

2020
RESILIENT
MATERIALS
4LIFE
INTERNATIONAL CONFERENCE

Organised by the UKRI-EPSCRC funded Programme Grant
Resilient Materials 4 Life (RM4L)

Conference Proceedings

Edited by R. Maddalena and M. Wright-Syed

20-22 September 2021

Online

ISBN 978-1-3999-0832-0



2020
RESILIENT
MATERIALS
4LIFE
INTERNATIONAL CONFERENCE

The abstracts and posters appearing in this book comprise the proceedings of the RM4L2020 International Conference, held between the 20th and 22nd of September 2021. The posters presented reflect the authors' opinions and are published as presented and without change (formatting and minor editing expected). Their inclusion in this publication does not necessarily constitute endorsement by the editors, RM4L, or Cardiff University.

ISSBN 978-1-3999-0832-0

Published by Cardiff University

For information

Cardiff University, Queen's Building, The Parade, CF24 3AA.

Email: MaddalenaR@cardiff.ac.uk

Please use the following format to cite material from these proceedings:

Author, AB, Author, XY, and Author, DE (2021), Title of paper, Proceedings Resilient Materials 4 Life 2020 (RM4L2020), Maddalena R, Wright-Syed M, (RM4L Eds), pp. a–b, Cardiff, UK, 20-22 Sep 2021, ISBN 978-1-3999-0832-0

Copyright © 2021 RM4L and Cardiff University.

Copying of material in these Proceedings for internal or personal use, or for the internal or personal use of specific clients is permitted without charge by RM4L and Cardiff University. Other copying for republication, resale, advertising, or promotion, or any form of systematic or multiple reproduction of any material from these Proceedings is prohibited except with permission in writing from Cardiff University.

The RM4L2020 is organised by the UKRI-EPSCRC funded Programme Grant Resilient Materials 4 Life (RM4L) and supported by



American Concrete Institute
Always advancing



The Institute of
Concrete Technology



The Institution of
StructuralEngineers



applied sciences

an Open Access Journal by MDPI

Preface

It is with great pleasure that we welcome you to the Resilient Materials 4 Life (RM4L) International Conference. Originally scheduled for September 2020, like so many events over the last, very difficult, 18 to 24 months, the conference has had to be first postponed and then moved entirely online. As such, it is even more pleasing to receive such a wide range of papers from around the world on the topic of smart, biomimetic infrastructure materials and we would like to thank all our contributors for taking the time to prepare and submit their papers.

The vision of the EPSRC funded RM4L Programme Grant was the generation of new construction materials that can adapt to their environment, develop immunity to harmful actions, self-diagnose the onset of deterioration and self-heal when damaged. The need to develop a sustainable and resilient built environment has never been greater. As will be evidenced in this conference, scientifically and technically, significant progress has been made towards achieving this vision. However, from an engineering perspective, what is still missing is a detailed assessment of how the structural design of components might be re-envisaged to maximise the advantages facilitated by the adoption of such materials and how asset owners might quantify and therefore justify their adoption. To this end, we are particularly grateful to our industrial contributors and for their support in delivering the Industry Session and round table discussions, which we are sure will help us address these challenges.

We trust you will find the conference challenging, but enjoyable, and that it will provide you with an opportunity to engage with others, both in your field of interest and in the wider context of smart, biomimetic infrastructure materials. We wish you well and we look forward to exploring with you the latest developments in this vitally important area of research and development.

Conference Chair, Prof Bob Lark and the RM4L Programme Grant Management Board

Acknowledgments

We would like to acknowledge The Concrete Society, American Concrete Institute, The Institute of Concrete Technology, The Institute of Materials, Minerals and Mining, The Institution of Structural Engineers, Institution of Civil Engineers and RILEM for supporting the conference.

We would like to acknowledge the journal manager of Applied Sciences (MDPI) for sponsoring the prizes for the best paper awards.

The Conference Chairs

Prof Bob Lark, Cardiff University, UK

Prof Tony Jefferson, Cardiff University, UK

Dr Diane Gardner, Cardiff University, UK

Prof Kevin Paine, University of Bath, UK

Prof Abir Al-Tabbaa, University of Cambridge, UK

The Organising Committee

Dr Riccardo Maddalena / Cardiff University / Chair

Dr Muaaz Wright-Syed / Cardiff University

Dr Hussameldin Abdalgadir / University of Bath

Dr Ioanna Papanikolaou / University of Cambridge

Dr Rami Alghamri / University of Cambridge

Dr Brunella Balzano / Cardiff University

Dr Regeani Bagonyi / University of Cambridge

Dr Pedro Bonilla Villalba / Cardiff University

Dr Cristina De Nardi / University of Bradford

Dr Brubeck Freeman / Cardiff University

Dr Ismael Justo-Reinoso / University of Bath

Dr Chrysoula Litina / University of Cambridge

Dr Magdalini Theodoridou / Newcastle University

Dr Bianca Reeksting / University of Bath

Dr Livia Ribeiro de Souza / University of Cambridge

Dr Cristina Tuinea-Bobe / University of Bradford

Dr Amir Zomorodian / University of Cambridge

Dr Sripriya Rengaraju / University of Cambridge

Dr Vahid Afroughsabet / University of Cambridge

The Scientific Committee

Dr Michael Harbottle / Cardiff University / Chair
Prof Gordon Airey / University of Nottingham
Dr Paola Antonaci / Politecnico di Torino
Dr Richard Ball / University of Bath
Dr Zeynep Basaran Bundur / Özyeğin University
Prof Ian Bond / University of Bristol
Prof Barry Clarke / University of Leeds
Mr Dave Cullen / Jacobs
Dr Robert Davies / Cardiff University
Dr Edurne Erkizia / Tecnalia technology center
Dr Paulina Faria / Universidade NOVA de Lisboa
Dr Susanne Gebhard / University of Bath
Dr Elke Gruyaert / KU Leuven
Prof Andrew Heath / University of Bath
Prof Andrea Hamilton / University of Strathclyde
Prof NingXu Han / Shenzhen University
Dr Henk Jonkers / Delft University of Technology
Prof Gopal Madabhushi / University of Cambridge
Dr Iulia Mihai / Cardiff University
Dr Jose Norambuena / University of Bío-Bío
Dr Alison Paul / Cardiff University
Dr Sanjay Pareek / Nihon University
Prof Chris Pearce / University of Glasgow
Dr Chunxiang Qian / Southeast University
Dr Mercedes Sanchez / Universidad de Córdoba
Prof Pedro Serna Ros / Universitat politecnica de Valencia
Prof John Sweeney / University of Bradford
Dr Magdalini Theodoridou / University of Newcastle
Prof Kim Van Tittelboom / Ghent University
Romildo Toledo Filho / Federal University of Rio de Janeiro
Mr Don Wimpenny / HS2
Prof Feng Xing / Shenzhen University

Table of contents

Plenary Lectures	1
<i>Resilient Materials 4 Life (RM4L) – An overview of research on biomimetic infrastructure materials</i>	<i>2</i>
<i>Upgrading the concept of UHPFRC for high durability in the cracked state: the concept of Ultra High Durability Concrete in the approach of the H2020 project ReSHEALience</i>	<i>4</i>
<i>Recent advances in self-healing concrete: stimulated and autonomous healing</i>	<i>5</i>
<i>Towards Self-repairing Cities.....</i>	<i>8</i>
<i>Fundamental Aspects and Modelling of Self-healing Construction Materials</i>	<i>10</i>
Session 1 Self-sensing in the built environment	13
<i>Robotically deployed self-sensing cements</i>	<i>14</i>
<i>A comparison of soft and hard PZT for damage detection in cement mortars</i>	<i>20</i>
<i>Graphite-silicone composite strain sensors for self-sensing structures.....</i>	<i>26</i>
<i>Self-sensing quantum tunnelling composite for smart infrastructures</i>	<i>32</i>
<i>Graphene-related materials for self-sensing infrastructure applications– Experimental results and lifecycle analysis.....</i>	<i>37</i>
Session 2A Biological Self-healing of soil and building materials	42
<i>Healing depth of early age cracks in cement-based materials by microorganism.....</i>	<i>43</i>
<i>Sporosarcina pasteurii induced carbonate formation for repairing and preventing damage in existing stone masonry structures.....</i>	<i>48</i>
<i>Biologically modified minerals for self-healing cement-based mortars</i>	<i>52</i>
<i>Calcite biomineralisation for the repair of damaged concrete.....</i>	<i>58</i>
<i>Engineering fungal networks for ground improvement</i>	<i>63</i>
Session 2B Bio-inspired building materials	69
<i>Strength properties of Limestone Calcined Clay Cement (LC³) in Malawi</i>	<i>70</i>
<i>Application of nanotechnology for the development of sustainable lignocellulosic materials</i>	<i>75</i>
<i>Evaluation of the reactivity of selected rice husk ash-calcined clay mixtures for sustainable cement production</i>	<i>81</i>
<i>Building couture: knitting as a strategy for bespoke bio architecture</i>	<i>85</i>
<i>Bacterial Cellulose as a Building Material: Identifying opportunities, limitations and challenges.....</i>	<i>90</i>
Session 3A Advanced modelling and simulation of smart infrastructure materials	95
<i>Coupled simulations of bacterial evolution and mineral dissolution/ precipitation.....</i>	<i>96</i>
<i>A two-phase reactive flow model of self-healing reactions</i>	<i>101</i>
<i>Time dependent micromechanical self-healing model for cementitious material</i>	<i>105</i>
<i>A CutFEM approach for simulating coupled 3D matrix - 2D crack plane flow of a healing agent in cementitious materials.....</i>	<i>110</i>
<i>Simulation of moisture transport through bio-based materials using independent measurements of water vapour diffusivity.....</i>	<i>115</i>
<i>A micro-mechanics-based element for modelling fibre bridging in embedded cracks.....</i>	<i>120</i>
Session 3B Concrete and ground healing and improvement.....	124

<i>The properties and microstructure of microbial mineralized steel slag cementitious materials.....</i>	<i>125</i>
<i>Challenges of Self-Healing Concrete Application.....</i>	<i>130</i>
<i>Microbial induced calcite precipitation as a viable ground improvement technique.....</i>	<i>136</i>
<i>Grouting of well leakage and migration pathways using colloidal silica: a preliminary experimental investigation.....</i>	<i>142</i>
Session 4A Smart resources for the built environment.....	147
<i>Large-scale soil improvement tests using microbially induced carbonate precipitation.....</i>	<i>148</i>
<i>Screening a suitable coating for expanded clay aggregate as bacteria carrier for manufacturing self-healing concrete.....</i>	<i>153</i>
<i>Contaminant-triggered self-healing cut-off wall materials incorporating oil sorbents.....</i>	<i>158</i>
<i>Direct-writing and embedding of functional materials into construction materials to enable smart cities ..</i>	<i>163</i>
Session 4B Encapsulation for infrastructure materials' healing.....	169
<i>Powder-based and capsule-based crack healing agents for concrete.....</i>	<i>170</i>
<i>Time-related performance of commercially applied microcapsule-based self-healing concrete</i>	<i>175</i>
<i>Evaluation of test methods for self-healing concrete with macrocapsules by inter-laboratory testing.....</i>	<i>180</i>
<i>Investigation of the micromechanical properties of the interface between PLA self-healing capsules and cementitious matrix</i>	<i>186</i>
<i>Biopolymeric capsules for asphalt self-healing</i>	<i>191</i>
<i>Fracture of cementitious material containing spherical microcapsules</i>	<i>197</i>
<i>Field investigation on the performance of smart aggregates for self-healing of concrete in different curing regimes.....</i>	<i>203</i>
Session 5 Bacteria and microorganisms for civil engineering	208
<i>Microorganisms inhabiting concrete in the marine environment.....</i>	<i>209</i>
<i>Microbial characterization for bio self-healing concrete applications</i>	<i>215</i>
<i>Micro-Scale Processes in Microbially Induced Carbonate Precipitation.....</i>	<i>220</i>
<i>Calcite precipitation by environmental bacteria as a method to improve durability of cementitious materials</i>	<i>225</i>
<i>Calcium carbonate precipitation as a function of alkaliphilic bacteria development</i>	<i>230</i>
Session 6 Bacteria-based self-healing of building materials	235
<i>Effect of microbial mineralization on microstructure of hardened C₃S paste</i>	<i>236</i>
<i>Self-healing bacterial concrete exposed to freezing and thawing associated with chlorides</i>	<i>241</i>
<i>Development of bacteria-based repair agents for external healing of cementitious materials.....</i>	<i>247</i>
<i>Bacteria-based self-healing concrete at low temperature</i>	<i>248</i>
<i>Evaluation of the self-healing of cracked mortars incubated within sterilized and non-sterilized natural soil</i>	<i>253</i>
<i>Microbial induced calcite precipitations of bio self-healing concrete underground exposure conditions... </i>	<i>258</i>
Session 7 Self-healing composites and advance monitoring	264
<i>Self-healing capability of fibre reinforced cementitious composites using different types of by-products....</i>	<i>265</i>
<i>Preliminary study of developing a self-healing strain-hardening cementitious composite (SHCC) for cyclic loading conditions</i>	<i>270</i>

<i>Polypropylene/CNT strain gauges for structures monitoring</i>	276
<i>Automatic smart concrete quality control using supercomputing</i>	281
Session 8A Advance Manufacturing for Civil Engineering and self-healing	285
<i>A high throughput microfluidic platform for production of microcapsules for self-healing in cementitious materials</i>	286
<i>Advanced 3D printed mini-vascular network for self-healing concrete</i>	292
<i>Advanced manufacturing platform for microcapsule-based self-healing cementitious materials</i>	297
<i>Injection moulding of ‘Spheritet’ component for concrete reinforcement</i>	302
<i>Concrete crack closure and reinforcement using high performance shape memory polymers (SMP)</i>	306
<i>Modified hybrid shape memory polymer tendons for enhanced concrete crack closure</i>	311
Session 8B Advances and measurements in self-healing and self-immunising materials	316
<i>Self-healing bio-concrete – a sustainable solution for structures and infrastructures</i>	317
<i>Self-Immunity in cementitious materials for protection against corrosion</i>	322
<i>Efficiency of Inhibitors in corrosion protection of reinforcing steel in synthetic pore water</i>	327
<i>Experimental investigation of water vapor diffusivity in bio-based building materials by a novel measurement method</i>	333

Plenary Lectures

Chair: Prof John Sweeney

Tony Jefferson, Diane Gardner, Kevin Paine and Abir Al-Tabbaa. Resilient Materials 4 Life (RM4L) – An overview of research on biomimetic infrastructure materials

Liberato Ferrara. Upgrading the concept of UHPFRC for high durability in the cracked state: the concept of Ultra High Durability Concrete in the approach of the H2020 project ReSHEALience

Nele De Belie. Recent advances in self-healing concrete: stimulated and autonomous healing

Mark Miodownik. Towards Self-repairing Cities

Erik Schlangen. Fundamental Aspects and Modelling of Self-healing Construction Materials

Resilient Materials 4 Life (RM4L) – An overview of research on biomimetic infrastructure materials

Tony Jefferson¹, Diane Gardner¹, Kevin Paine², Abir Al-Tabbaa³

1: School of Engineering, Cardiff University, United Kingdom

2: BRE Centre for Innovative Construction Materials, Department of Architecture and Civil Engineering, University of Bath, United Kingdom

3: Department of Engineering, University of Cambridge, United Kingdom

Introduction

Despite recent endeavours, structures remain susceptible to damage. The need to develop resilient structures, whilst being prudent with our natural resources has never been more pressing. Since planning the RM4L project in 2016, the landscape surrounding climate change has changed significantly. As a research consortium, we had and still have an ambition that by 2050 we can create a sustainable and resilient built environment and infrastructure comprising materials and structures that continually monitor, regulate, adapt and repair themselves without the need for external intervention. RM4L and its inception was a key enabler of this ambition, with its own vision of achieving (by the project end) a transformation in construction materials using the biomimetic approach that will adapt to their environment, develop immunity to harmful actions, self-diagnose the on-set of deterioration and self-heal when damaged. Although we are still en-route to achieving this vision, the innovative research into smart materials in RM4L will engender a step-change in the value placed on infrastructure materials and provide a much higher level of confidence and reliability in the performance of our infrastructure systems.

Progress on Self-healing Mechanisms

Cardiff University and University of Bradford – The work conducted in Cardiff University and University of Bradford falls under the main categories of vascular networks and their associated cargoes, novel polymer inclusions and numerical modelling of self-healing systems (see later). The team have successfully created and tested 2 and 3 dimensional hollow-channel vascular networks in concrete elements. Promising repeated healing has also been achieved through novel mini-vascular network systems. The encapsulation of healing agents within these systems has driven the investigation into a wide range of commercial and novel research-based agents. These have led to combinations of healing agents to extend encapsulation duration, enhance reactivity with the matrix and optimise healing efficiency. Novel polymer systems using shape memory fibres and polymer tendons have been successfully employed as crack closure techniques. Scale-up of the latter is underway, giving due consideration to activation and anchorage techniques and is soon to be combined with the sensing techniques developed at the University of Bath. Lastly, novel tetrahedral reinforcement for crack control has been developed with the University of Bradford and is soon to be coupled with concrete mixes that have been designed to offer an enhanced autogenic healing response to damage.

University of Bath – Research activities at the University of Bath have been largely focussed on bacteria-based self-healing (for RT1 and RT2) and on self-sensing technologies (for RT3). It is shown how research at Bath has developed a broader understanding of the capability of bacteria to precipitate calcium carbonate. A library of over 140 spore-forming alkali-tolerant bacteria has been obtained, and we have shown that non-ureolytic bacteria are the most suitable for self-healing concrete. Furthermore, it is shown that some bacteria in our library can heal cracks at much lower temperatures than research elsewhere. It is also demonstrated

that it is possible to take a non-calcite precipitating bacteria (*Bacillus subtilis* W168) and give it the genes necessary to do so, and even show that the morphology of the calcite produced is dependent on the urease genes added. The self-sensing work that has developed concretes that recognise that they have cracked is also described. Self-sensing has been achieved through two methods based on the electrical properties of concrete: external sensing using piezo-sensors and through intrinsic sensing using carbon-based powders and fibres.

University of Cambridge – Research activities at the University of Cambridge targeted a number of biomimetic systems (RT1-4) including (i) mineral-based additives (expansive mineral additives for enhanced autogenous healing and mineral inclusions as green corrosion inhibitors), carbon-based additives (graphite and graphene and carbon-based fibres for self-sensing), self-healing microcapsules (with sodium silicate or green corrosion inhibitors as cargo) using complex coacervation, microfluidics and membrane emulsification, smart aggregates (using lightweight Lytag and expanded clay impregnated with sodium silicates or corrosion inhibitors) using pelletisation and spray coating and vascular systems that obey Murray's law using 3D printing and modular construction. The work also included the deployment of embedded sensors with the above to monitor performance (RT3-4). The carbon footprint assessment of those developments and resulting cementitious products has been on-going hand in hand. Extensive laboratory characterisation and testing culminated in commercial deployment (RT1) of microcapsules and mineral additives in the Department of Engineering Dyson Building, in 200 concrete blocks, and the new Civil Engineering Building, in an outdoor reinforced concrete slab. Scale-up and potential commercialisation activities are underway.

Progress on numerical modelling - The research comprises a combined numerical and experimental study on healing-agent transport and mechanical damage-healing processes. The experimental programme includes mechanical tests on concrete specimens with inbuilt vascular healing systems, as well as tests to measure healing-agent transport properties. The coupled model employs elements with embedded strong discontinuities linked to a damage-healing constitutive model component for mechanical behaviour. This is coupled to flow models that simulate healing-agent transport. Some new results are presented on a statistical discrete model simulation that is used to derive the governing relationships of the homogenised crack-plane damage-healing model. A series of examples demonstrate the ability of the new coupled model to reproduce the experimentally observed behaviour of self-healing specimens subject to a range of loading scenarios.

The Future – Plans for the final year of the project and beyond include: scaling up our technologies: undertaking large scale tests and site trials: evaluating the sustainability of the technologies with a focus on low carbon self-healing concrete and other cementitious composites and LCA of our biomimetic systems: generally improving our biomimetic and linked technologies: and, expanding the capability of 3D models and using them to tailor systems.

Upgrading the concept of UHPFRC for high durability in the cracked state: the concept of Ultra High Durability Concrete in the approach of the H2020 project ReSHEALience

Liberato Ferrara

Department of Civil and Environmental Engineering, Politecnico di Milano, Milan, Italy

Abstract

Current solutions for new concrete constructions in Extremely Aggressive Exposures (EAE), as recommended and enforced by design codes, are not taking into account new cement-based construction materials, such as Ultra High Performance (Fibre Reinforced) Concrete - UHP(FR)C, neither new constituents and products specifically conceived to improve the concrete durability (including, e.g., nanoparticles or self-healing promoters), because of the lack of standards and technical awareness by most designers and contractors.

The use of UHPC/UHFRC still has significant limitations to be overcome and has so far failed to stand as the market breakthrough concept/product it was expected to be. This is due to the claimed superior durability of UHPC/UHPFRC, which has been almost exclusively proven in the laboratory, and with main reference to the un-cracked state. With reference to the cracked state a "superior durability" is generally heuristically justified because of the higher crack tightness characterising the material response under tensile loads. What is more, its use has hardly been accompanied by design considerations, due to the lack of internationally recognized regulations. Moreover, a clear quantitative evaluation of the structure service life is also lacking.

ReSHEALience

The H2020 funded ReSHEALience project, whose concept will be outlined in this paper, moves from the consideration that using materials with a high durability performance and durability based design approaches, the long-term behaviour of these structures will be highly improved. To this purpose, the UHPC/UHPFRC concept will be upgraded to the concept of Ultra High Durability Concrete (UHDC), combining nano-scale constituents (nano-cellulose, alumina nanofibers) and self-healing promoters (crystalline admixtures and nano-cellulose), as purpose-functionalities to increase the density of the paste and ITZ, control crack growth and heal small cracks. UHDC will develop, under the stress levels representative of the service state, a continuous smeared micro-crack pattern, instead of a discrete series of localised cracks (or macro cracks wider than 0.1 mm). The theoretical and experimental comprehension of the processes governing the long-term material behaviour and degradation will explain how the new functionalities can modify the nature and kinetics of the same processes.

The paper will present the approach pursued in the project and a synoptic view of the experimentally obtained results.

Recent advances in self-healing concrete: stimulated and autonomous healing

Nele De Belie

Magnel-Vandepitte Laboratory, Department of Structural Engineering and Building Materials,
Ghent University, Belgium

Introduction

The formation of small cracks (< 300 μm in width) in concrete is almost unavoidable. These cracks may not cause a direct risk of structural collapse, but do accelerate concrete degradation, and may hence reduce the structure's service life. It is clear that cracks above a certain critical width form a direct path along which aggressive agents can penetrate into the concrete towards the steel reinforcement. Especially penetration of carbon dioxide or chloride will increase the risk for initiation and propagation of steel reinforcement corrosion. When cracks would be healed upon occurrence, a significant extension in service life can be achieved and environmental burdens related to maintenance and repair can be avoided to a large extent.

Current status

Therefore, over the last decade the research on self-healing agents to incorporate in concrete, has grown exponentially. Certain self-healing agents, like superabsorbent polymers, can stimulate the autogenous healing properties that traditional concrete possesses. Autogenous healing in itself will proceed slowly and will lead to complete healing of small cracks only, and on the condition that liquid water is available in the crack. Stimulated autogenous mechanisms allow to heal larger cracks (although generally still limited to crack widths of about 100-150 μm) and additionally improve healing in an environment with high relative humidity. Furthermore, autonomous self-healing mechanisms have been developed, which can heal cracks of 300 μm and even sometimes up to more than 1 mm, and usually act faster. In this case complete healing can be obtained in a time span of 1 day (for polymer based systems) up to 3-4 weeks (for bacteria based or mineral based systems). In some self-healing systems, the healing agent needs to be encapsulated, and a whole range of shell materials have been investigated and tailored for use in cementitious matrices [1]. Researchers have made progress regarding improved bond with the cementitious matrix and changeable shell properties (flexible in fresh concrete to survive concrete mixing, while brittle in hardened concrete to release the contents at crack occurrence). For these self-healing agents, the optimum dosages usually range between 0.5% to 10% by weight of cement, in order to obtain sufficient healing in combination with a limited effect on concrete's mechanical properties. A point of concern remains the long-term stability of encapsulated polymers. This is less problematic when encapsulating bacterial spores or mineral additives, since their "reactivity" with moisture penetrating through the shell is much lower.

A comprehensive review on self-healing concrete, aiming for damage management of structures, was recently compiled in a combined effort by COST CA15202 "SARCOS" members [1, 2]. This review reveals the key challenge that the self-healing additions up-to-date are produced at lab scale and self-healing efficiency is only shown at paste/mortar level. It is further suggested that future research should focus on durability of the healed elements, regarding resistance to chloride ingress, carbonation, freeze/thaw, salt crystallization, etc.

Recent results

Therefore, our recent research has focused on durability and service life of different types of self-healing concrete. For self-healing concrete with macro-encapsulated polyurethane [3-5], chloride profiles and electron probe microanalysis indicated that this mechanism was efficient

to reduce the chloride penetration. Electrochemical measurements on reinforced concrete specimens subjected to cyclic exposure with a NaCl solution showed that autonomous crack healing could significantly reduce the corrosion propagation. Active corrosion was monitored after 10 weeks of exposure of cracked traditional concrete specimens to NaCl solution and after 26 weeks clear pitting damage was observed on the rebars. On the other hand, if cracks were self-healed with low viscosity polyurethane, the rebars showed no or very limited corrosion. While self-healing by encapsulated polyurethane is complete after one day, bacteria-based products take several weeks to heal a 300 µm crack. In this case, bacterial granules containing denitrifying cultures have the benefit to release nitrite as an intermediate metabolic product which can protect the reinforcement during the crack healing process [6-7]. In another recent study the potential of combining two metabolic pathways, urea hydrolysis and nitrate reduction, simultaneously in one bacteria strain for improving the bacterial CaCO₃ yield has been investigated [8].

The experimental self-healing efficiency obtained for each system could then be implemented in a probabilistic prediction model that estimates the time to chloride- or carbonation-induced steel depassivation in comparison with ordinary cracked concrete [9]. A significantly reduced maintenance and repair frequency was demonstrated for the polymer-based self-healing concrete. A subsequent life cycle assessment showed a substantial environmental benefit which can mainly be attributed to the service life extension possible with self-healing concrete which easily overcomes environmental burdens inherent to the polymers. A cradle-to-gate LCA study was also carried out for fibre reinforced Engineered Cementitious Composite (ECC) with Superabsorbent Polymers (SAP) to stimulate self-healing [10]. The environmental impacts of the SAPs, mainly due to expected high energy use during the drying step, could not be neglected, but remained limited to half or less of the environmental impact of the cement in the self-healing ECC mix.

Acknowledgment

The author acknowledges the support from SIM and VLAIO for the project ISHECO (Impact of Self-Healing Engineered Materials on steel CORrosion of reinforced concrete) - program SHE (Engineered Self-Healing materials). This paper is based on results obtained by the researchers in the Concrete and Environment team of the Magnel-Vandepitte laboratory for structural engineering and building materials, and especially the contribution of following researchers is gratefully acknowledged: Kim van Tittelboom, Philip Van den Heede, Bjorn Van Belleghem, Yusuf Ersan, Didier Snoeck, Adelaide Araujo, Xuejiao Zhu.

References

- [1] De Belie, N., Gruyaert, E., Al-Tabbaa, A., Antonaci, P., Baera, C., Bajare, D., Darquennes, A., Davies, R., Ferrara, L., Jefferson, T., Litina, C., Miljevic, B., Otlewska, A., Ranogajec, J., Roig, M., Paine, K., Lukowski, P., Serna, P., Tulliani, J.-M., Vucetic, S., Wang, J., Jonkers, H.A.. A review of self-healing concrete for damage management of structures. *Advanced Materials Interfaces* 2018 Vol 5, 1800074, 28 p.
- [2] Ferrara, L., Van Mullem, T., Alonso, M.C., Antonaci, P., Borg, R.P., Cuenca, E., Snoeck, D., Jefferson, A., Peled, A., Ng, P.I., Roig Flores, M., Serna Ros, P., Sanchez, M., Schroefl, C., Tulliani, J.M., De Belie, N. Experimental characterization of the self-healing capacity of cement based materials and its effects on the material performance: A state of the art report by COST Action SARCOS WG2. *Construction and Building Materials* 2018 Vol 167, 115-142.
- [3] Van Belleghem, B., Kessler, S., Van den Heede, P., Van Tittelboom, K., De Belie, N. Chloride induced reinforcement corrosion behavior in self-healing concrete with encapsulated polyurethane. *Cement and Concrete Research* 2018, 113, 130-139.
- [4] Van Belleghem, B., Van Tittelboom, K., De Belie, N. Efficiency of self-healing cementitious materials with encapsulated polyurethane to reduce the water ingress through cracks. *Materiales de Construcción* 2018, 68 (330), e159.

- [5] Van Belleghem B., Villagrán Zaccardi Y., Van Den Heede P., Van Tittelboom K., De Belie N. Evaluation and comparison of traditional methods and EPMA to determine the chloride ingress perpendicular to cracks in self-healing concrete. *Construction and building materials* 2019, 227, 116789 (12 p).
- [6] Erşan, Y.C., Verbruggen, H., De Graeve, I., Verstraete, W., De Belie, N., Boon, N. Nitrate reducing CaCO_3 precipitating bacteria survive in mortar and inhibit steel corrosion. *Cement and concrete research* 2016, 83, 19-30.
- [7] Erşan, Y.C., Van Tittelboom, K., Boon, N., De Belie, N. Nitrite producing bacteria inhibit reinforcement bar corrosion in cementitious materials. *Nature - Scientific Reports* 2018, 8: 14092.
- [8] Zhu, X., Wang, J., De Belie, N., Boon, N. Complementing urea hydrolysis and denitrification for improved microbially induced calcium carbonate precipitation. *Journal of applied microbiology* 2019, 103, 8825–8838.
- [9] Van Belleghem, B., Van den Heede, P., Van Tittelboom, K., De Belie, N. Quantification of the service life extension and environmental benefit of chloride exposed self-healing concrete. *Materials* 2017, Special issue "Self-healing Concrete", 10 (5), 22 p.
- [10] Van den Heede, P., Mignon, A., Habert, G., De Belie, N. Cradle-to-gate life cycle assessment of self-healing engineered cementitious composite with in-house developed (semi-)synthetic superabsorbent polymers. *Cement and Concrete Composites* 2018, 94, 166-180.

Towards Self-repairing Cities

Mark Miodownik

UCL Mechanical Engineering, University College London, United Kingdom

Introduction

By 2050, 86% of the UK (and two-thirds of global) population will live in cities. Their quality of life – critically dependent on infrastructure systems for water, power, transport etc. and natural systems for clean air, waste disposal and other associated services – will depend on the engineering and policy innovations of the next ten years. Many infrastructure artefacts are buried or elevated. Maintaining them through streetworks causes disruption costing the UK £4.3Bn pa. Each trench can reduce the life of a road by 30%; expenditure on potholes (£1.2Bn pa) is 10% of that actually required; half the material removed from trenches ends up in landfill; congestion doubles traffic pollution. This talk summarises work funding by EPSRC to create Self-repairing cities. The work presented is a collaboration between Leeds University, Birmingham University, University College London and Southampton University. See our website for more information about the individual teams: <https://selfrepairingcities.com/>

Our work

We have developed Robots and Autonomous Systems (RAS) to live within infrastructure, addressing defects at the millimetre/gram-scale, preventing them from growing to the metre/tonne-scale that requires disruptive intervention. We are on-target to achieve our technology vision, having demonstrated several prototype infrastructure robots.

Our impact activities inspire the public regarding robots in society and raise the profile of infrastructure, and have been the key contribution so far. Progress has exceeded expectations, generating unprecedented media, industry and educational interest. We are working with international infrastructure companies (e.g. Kier, Severn Trent, Anglian Water) to introduce RAS concepts at board-level. By engaging with academic institutions (via e.g. the UK-RAS White Papers, and collaborations with the OFGEM GRAID, and EPSRC Twenty65) we are setting national agendas and helping the community to work together (e.g. to access RAS Capital for Great Technologies funding). Our Robotics Challenge Event (RCE) attracted international participants, and we are negotiating with international philanthropic organisations to showcase our research and vision. As identified at the proposal stage, the key challenge has been recruitment and retention of suitably qualified research fellows (RF). We mitigated by scheduling major deliverables later in the programme, staggering recruitment of RFs and we remain on track.

Our objective was to “restore the balance between engineered and natural systems”. In cities, maintenance vehicles produce damaging air, noise and waste pollution, excavations cause transport delays and displace animal and plant life, and maintenance ‘at height’ (lighting, gantries) involves multiple H&S challenges; yet the demands of core maintenance tasks may be low. A 4-tonne vehicle might carry 3 people many km to insert a 30g lamp-post bulb; we dig metre-scale holes in roads to repair millimetre-scale defects in pipes. This causes imbalances: the energy used for auxiliary activities is orders-of-magnitude greater than that required for the core task; the scale and cost of equipment, human and material resources and waste generation are inflated; and the risk to natural ecosystems, human health and wellbeing is excessive. Our core objectives were to restore the balance by: developing technologies for autonomous defect detection, diagnosis and repair compatible with new and existing infrastructure; developing robotic platforms, control strategies, sensing and communication systems to autonomously operate in complex city environments; and understanding and managing, technology, society and the environment.

Our original vision proposed three technological RAS challenges: Perch & Repair (remote inspection and maintenance of structures at height, e.g. bridges); Perceive & Patch (autonomous diagnostics, repair and prevention of defects, e.g. potholes); and Fire & Forget (robots designed to operate indefinitely, e.g. in live water mains). Together with the UK RAS Network (<http://hamlyn.doc.ic.ac.uk/uk-ras/>) we have added further themes to coordinate with (inter)national activity: Plunge & Protect (the ability to operate robots underwater or underground); Dismantle & Dispose (cut, separate, and unfasten structures in extreme environments); Construct & Confirm (coordinating robots to build infrastructure from CAD models); and Data & Decisions (create and interpret data for robots interfaced with smart cities). This also aligns to the EPSRC Delivery Plan and HMG Industrial Strategy (IS). We aim to: increase productivity through more efficient infrastructure maintenance, reduced disruption and improved industry skills; improve connectivity by integrating robots, the smart city and the Internet of Things; increase resilience by providing new ways to maintain critical national infrastructure; and improve health by reducing pollution and workforce injury rates. Upgrading infrastructure is a foundation of the IS, and Artificial Intelligence and Data is an IS Grand Challenge (GC); embedding RAS and associated data systems into infrastructure will be a key contributor. Our interaction with road monitoring and management and autonomous vehicles also addresses another IS-GC; Future Mobility.

Our work integrates multiple disciplines and partners, generating significant impact, the acme being our 'Pothole Prevention Robot (PPR)'. Roads are designed for a finite life with minimal maintenance; potholes are an inevitable consequence. The PPR would be part of a system where maintenance is continuous from day 1, repairing small defects before they turn into potholes. It combines advances in understanding how road materials degrade, RAS that equips drones with sensors to detect cracks and 3D printers to repair them, integrating materials science, vision systems, signal processing, mechatronics and other disciplines. UCL developed the 3D asphalt printing nozzle; Birmingham University developed tests to validate the methods; Leeds University developed the UAV platform. We have research and economic models that promote continuous maintenance over 'build and replace' to develop business cases that include not only the capital cost/benefit analysis for robots, but also impacts on: employment and skills for workers; the environment through fewer road closures; and reduced vehicle damage claims.

More information and references can be found at our website: <https://selfrepairingcities.com/>

Fundamental Aspects and Modelling of Self-healing Construction Materials

Erik Schlangen

Faculty of Civil Engineering and Geosciences, Delft University of Technology, Delft, The Netherlands

Abstract

Self-healing concrete can be implemented by using various techniques. It is discussed when these different techniques are useful to solve certain problems that occur in concrete or concrete structures over the life-time. Practical applications where these techniques can be beneficial are given. Furthermore the challenges that remain in developing the self-healing agents, methods and techniques are listed and ways of using models to support the development are indicated.

Introduction

Applying self-healing concrete is only useful in case the self-healing method or agent is proven to be reliable, cost effective, durable and sustainable. Actually the performance of the structure with implemented self-healing should be better than structures for which traditional solution as various repair techniques are used. If a better performance and especially the reliability also in the long term is not yet obtained by using self-healing than the introduction and acceptance in practice will be difficult. Important aspect when considering self-healing techniques are the type of damage and the moment of occurrence of damage that the self-healing technique should solve or repair. These determine the working principle that the self-healing agent should have, which could be for instance mechanical repair, sealing of a crack or changing locally the relative humidity or chemical composition. When developing self-healing agents the use of modelling tools can be of great help since they can confirm a certain mechanism, reduce the number of experiments needed, help to make certain choices for particular healing agents or support the design.

Damage mechanisms

The different reasons for implementing self-healing can be categorised as shown below. For each category possible applications and challenges where modelling [1] can help are given.

Mechanics

Mechanical repair of cracks can be very beneficial for early age cracks which often occur in massive concrete structures. First of all there is plenty of unhydrated cement left that can bring autonomous healing. Modelling [2] on different scales can be applied to determine for instance:

- The crack opening for which healing can take place or for which reaction products can bridge the gap.
- The amount of strength and stiffness that is gained when the crack is (partially) filled with reaction products
- The amount of unhydrated cement left and the amount of water needed for the hydration when the crack is formed.
- The environment or circumstances for which healing can occur.

Mechanical repair of concrete can also be useful for cracks in old concrete. Although most structures in practice are reinforced and as a result they have to crack. For these cracks there is usually no need for mechanical repair. Cracks at the surface of a structure (roads, industrial floors) could lead to further damage and deterioration due to for instance abrasion or mechanisms as freeze-thaw. Also damage in repair patches on structures will benefit from mechanical repair. Finally, strengthened or hybrid structures made from UHPFRC or SHCC

could benefit from mechanical repair of the small cracks which usually develop in these materials. The modelling techniques are similar as given above for early age cracks. Other techniques that can be applied to get mechanical healing are the use of tubes, capsules or vascular filled with glue or epoxy or used as transport medium for these agents. Additional challenges for modelling are:

- The stiffness, strength and filling degree of the hardened epoxy or glue and how much that improves the strength of the material or structure.
- The stiffness and strength of the container and the influence of that on the fracture behaviour [3]
- How does the healing agent penetrate the crack?
- What should be the location and distribution of the tubes, capsules or vascular.
- What is the shelf life of the healing agent that is used inside the containers.

Leakage or ingress

Filling cracks to stop leakage of stopping the ingress of water and chloride (or other ions) for durability reasons is the most common application for self-healing. The methods described for mechanical healing would also work here. But in addition Super Absorbent Polymers (SAP), either encapsulated or not can be used to seal cracks. Healing agents containing bacteria are used to precipitate calcium carbonate. Or various kinds of crystalline admixtures are available to precipitate products in cracks that (partially) close them. Usually these methods do not provide enough mechanical strength to realise also mechanical recovery.

The modelling challenges are:

- The filling rate of the cracks, the expansion of that SAP [4] or the amount of reaction product that is formed
- The influence of the cracks width and the amount of healing agent required to fill the crack
- The size, distribution and properties of the healing agent.
- The influence of the environment, (H, T, pH) on the functionality of the healing agent.

Durability issues

There are several other durability related problems in concrete for which self-healing could give a cure. As examples could be given corrosion of reinforcement, damage due to freeze thaw and salt crystallisation in pores and cracks. However there might be much more durability issues where self-healing could be beneficial. Challenges for modelling in these cases are:

- Modelling of carbonation and chloride ingress process that leads to rebar corrosion.
- Simulation of oxygen consumption (due to bacterial activity) which could reduce rebar corrosion.
- Simulation of corrosion process, expansion mechanism of rebar and consequent damage of concrete.
- Modelling the fibre of rebar interfacial zone and pull-out behaviour before and after healing of the ITZ.
- Distribution and functionality of inhibitors against corrosion or salt crystallisation
- Simulation of distribution and effect of (encapsulated) PCM or NA-MFP for stopping or delaying freeze-thaw damage [5].

Discussion and Conclusions

Possible application of self-healing in concrete materials and structures is discussed. This overview is far from complete but gives direction of healing methods and agents and how modelling can assist in the development of these techniques. Several challenges for the modelling community are listed.

The combination of laboratory work, modelling and field applications is needed to make steps forward in the development of self-healing for concrete. Only then reliable methods can be realised. This is most important to get them accepted and applied in practice.

References

- [1] Erik Schlangen, Edward J Garboczi. Fracture simulations of concrete using lattice models: computational aspects, Engineering fracture mechanics, 1997.
- [2] Nynke ter Heide, Erik Schlangen. Self-healing of early age cracks in concrete. Proceedings of the First international conference on Self Healing Materials, 2007
- [3] CR Rodríguez, FF de Mendonça Filho, L Mercuri, Y Gan, E Rossi, G Anglani, P Antonaci, E Schlangen, B Šavija. Chemo-physico-mechanical properties of the interface zone between bacterial PLA self-healing capsules and cement paste. Cement and Concrete Research 138, 106228
- [4] CR Rodríguez, SC Figueiredo, M Deprez, D Snoeck, E Schlangen, B Šavija. Numerical investigation of crack self-sealing in cement-based composites with superabsorbent polymers. Cement and Concrete Composites 104, 103395
- [5] Romero Rodriguez, C., Chaves Figueiredo, S., França de Mendonça Filho, F., Schlangen, E. & Šavija, B. Frost damage progression studied through X-Ray tomography in mortar with Phase Change Materials, FraMCoS-10 2019.

Session 1 Self-sensing in the built environment

Chair: Prof Tomoya Nishiwaki

1101 *Perry et al.* Robotically deployed self-sensing cements

1188 *Taha et al.* A comparison of soft and hard PZT for damage detection in cement mortars

1263 *Gaumet et al.* Graphite-silicone composite strain sensors for self-sensing structures

1196 *Zheng et al.* Self-sensing quantum tunnelling composite for smart infrastructures

1103 *Papanikolaou and Al-Tabbaa.* Graphene-related materials for self-sensing infrastructure applications— Experimental results and lifecycle analysis

Robotically deployed self-sensing cements

Marcus Perry, Jack McAlorum, Christos Vlachakis, Lorena Biondi

Department of Civil and Environmental Engineering, University of Strathclyde, Glasgow, G1 1XJ, UK

Abstract

Self-sensing cements offer a unique opportunity to unify our approaches to the monitoring and maintenance of concrete assets. Here, we present our latest progress in the manufacturing and robotic deployment of self-sensing cement repairs, based on alkali-activated fly ash and metakaolin materials. We will outline our processes for 3D printing and spray-coating these materials using a six-axis robot, and provide highlights of results of mechanical and adhesion testing, and sensor responses to strain, cracking, temperature and moisture. We will also outline some of the results from active industry projects we have in the nuclear and transport sectors. Unifying concrete monitoring and maintenance is of key national importance to the UK, Europe and US, who now face an ageing population of reinforced concrete bridges, tunnels and support structures.

Introduction

Asset managers worldwide are struggling to optimise the maintenance of their growing, ageing population of concrete structures. Smart materials may in time help to address this challenge, imbuing structures with unique capabilities like self-monitoring, self-diagnosis and self-healing. The troubled history of conventional sensors in construction, however, suggests that new materials are probably only part of the solution. Electronic and fibre-optic sensors, for example, have now been around for decades. These are mature, affordable sensor technologies that offer clear benefits for structural health monitoring — and yet their use in construction is still uncommon. This is partly because of two practical challenges associated with technology deployment:

- Cost and risk: Technology installation campaigns pose significant labour costs, disruption and risks to productivity. These factors can suppress industry willingness to use new technology. This is especially true when there is a broken value chain: i.e. when the value added by a new technology is not directly seen by the firm shouldering its installation or management risks.
- In-field technical performance: The real-world performance of monitoring and maintenance technologies is usually limited by errors and variations in the quality of human workmanship, rather than limitations in the technologies themselves.

There is no reason to believe that smart materials will be immune to these factors. As such, our group have been investigating robotic deployment methods for the on- and off- site installation of self-sensing materials. In innovating the deployment process with automation, we seek to eliminate the risks and errors associated with manual installation. We hope that this will pave the way for more frequent industry uptake of smart materials in general.

The work outlined here demonstrates how automated 3D printing and robotic spray coating approaches can be used to deploy self-sensing cementitious repair materials onto concrete substrates. The “self-sensing cements” described in this paper are geopolymers, often also referred to as alkali-activated materials [1]. Geopolymers are a class of cementitious binders that exhibit similar thermal and mechanical properties to ordinary Portland cement. They adhere strongly to concrete substrates, are chemically stable, and due to the presence of free ions in their matrix, exhibit electrical conductivities in the range 10^{-6} S/cm to 10^{-3} S/cm, depending on mix design [2, 3]. In previous work, this enhanced ionic conductivity has been exploited to produce self-sensing cementitious materials for concrete monitoring and

maintenance applications [4 -11]. The remainder of this paper provides an overview of our approach to material fabrication, automated deployment, and sensor interrogation. We finally outline how our automated approach can be used to address the challenges faced by our industry collaborators in the oil and gas and nuclear sectors.

Materials and methods

Metakaolin geopolymer fabrication

In this work, geopolymers were produced by combining a metakaolin precursor with an alkaline activator. Metakaolin was formulated through the calcination of kaolin (china clay) at temperatures of 550 – 850 °C [12,13]. We have opted to use metakaolin, rather than fly ash or blast-furnace slag, to produce our geopolymers, as it tends to be quite compositionally consistent and reactive [14], and has a track record of producing suitable concrete repairs [15]. The alkaline activator was made by combining sodium silicate (Na₂O = 8.5%, SiO₂ = 27.8%, H₂O = 63.7%) and 10 M sodium hydroxide solutions. The mass ratio of sodium silicate to sodium hydroxide was 2. To reduce shrinkage of our geopolymer coatings after deposition on the concrete substrate [16], 0.5 wt% PVA fibres (3 mm length) were added to the dry metakaolin precursor prior to mixing. The metakaolin precursor was then mixed with the activator for 5 minutes until homogenous. For spray coating applications, we used a very low solid/liquid ratio of 0.65, while for 3D printing we use a solid/liquid ratio of 0.9 to allow the geopolymer to maintain shape stability.

Sensing principle

Due to the alkaline solution in their pores, geopolymers are solid electrolytic conductors which exhibit a reasonably high electrical conductivity [2,3]. They have therefore been employed in multiple self-sensing applications for strain and temperature, often free from conductive filler additives [4-11]. In general, sensing schemes seek to measure changes in the electrical impedance of geopolymer substrates. A sinusoidal voltage of magnitude V and frequency f , is applied to a cured sample and its current response, I is measured. Impedance is then calculated via [17]:

$$\vec{Z} = \frac{V}{I} e^{i(\phi_V - \phi_I)} = Z_{mod} e^{i \arg(Z)} \quad (1)$$

where $\Phi_V - \Phi_I$ is the phase difference between the applied ac voltage and measured current. Impedance is a complex value defined by an impedance magnitude, Z_{mod} , and argument $\arg(Z)$. In the work presented in this paper, we simply consider the sensing response to be defined by the fractional change in Z_{mod} in response to the measurand of interest: strain, temperature or moisture. For sensing, high frequency ($f > 1$ kHz) excitation is usually preferred over low frequency and dc, as it prevents electrolysis (in our case, the net migration of conductive Na⁺ ions towards the cathode). Our sensing schemes also typically employ a four-probe Van der Pauw sensing method to reduce the probability of cracking, and the spurious effects of lead and contact resistances [18,19].

Automated deployment

3D printing or spray coating a geopolymer begins with the use of a screw cavity extruder. The use of this dispensing method ensures precise and repeatable low-flow-rate deposition of the geopolymer, almost independently of viscosity. For 3D printing, the extruder is fitted with a nozzle of size 18G (0.84 mm), and mounted to the x-y gantry axis of a 3D printer or the tool end of a six-axis robot. A picture of the setup in a 3D printer is presented in Figure 1a. A cartridge, fit with an air supply pressure of 1 bar, ensures material flow into the screw cavity regardless of sprayer orientation, or whether the material is self-levelling.

For spray-coating, a similar principle applies, but the screw cavity extruder is followed by an atomiser. Figure 1b shows the attachment of the spray dispenser to the robot tool head. In the robot setup, an infrared sensor is connected to the robot's input to control the proximity between the extrusion nozzle and concrete substrate.

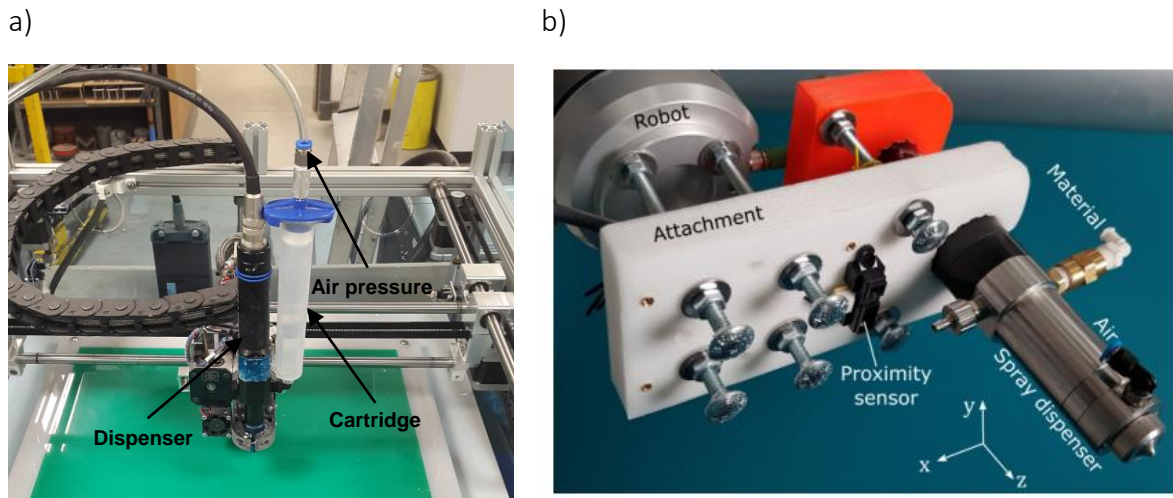


Figure 1: a) 3D printing setup showing the dispensing unit, and pressurised feed cartridge. b) spray coating setup mounted to the end of a six-axis robotic arm.

Results and discussion

Mechanical properties

Typical photographs of 3D printed and spray-coated patches with embedded wires and electrodes are shown in Figures 2a and 2b respectively. The 28-day compressive strengths of both mixes was bulk tested separately and found to be >20 MPa. This is adequate for a repair material (according to BS EN 1504:1999), but slightly lower than a typical geopolymer mix: likely due to the high water contents required to produce extrudable / sprayable mixes [20]. The average bond strength between the printed / spray coated patches and the concrete substrate was tested using a standard pull-off adhesion test, and was found to be 0.5 MPa. The failure type in all geopolymer overlays was adhesion failure (failure at the interface between the substrate and the repair).



Figure 2: Examples of a) 3D printed and b) spray coated metakaolin geopolymer patched on concrete substrates, with electrode wires and plates at the corners of the patch.

Sensing properties

Figure 3 plots example responses of sensors to temperature and moisture (characterised using an environmental chamber, as outlined in detail in [11]). The strain response, shown in Figure 4, was found by testing a patch adhered to a 100 mm side concrete cube under compressive load. The relationship between fractional shifts in Z_{mod} and temperature / moisture is exponential, while the response to strain is linear, at least for low levels of strain when the concrete substrate itself behaves approximately linearly. Further details may be found in [11, 21]. Typical sensor precisions for our geopolymers are 0.1 °C, 0.1 wt% and 1 - 10 $\mu\epsilon$. As with any sensing scheme, separation of variables could be achieved with nearby temperature and moisture reference sensors for compensation.

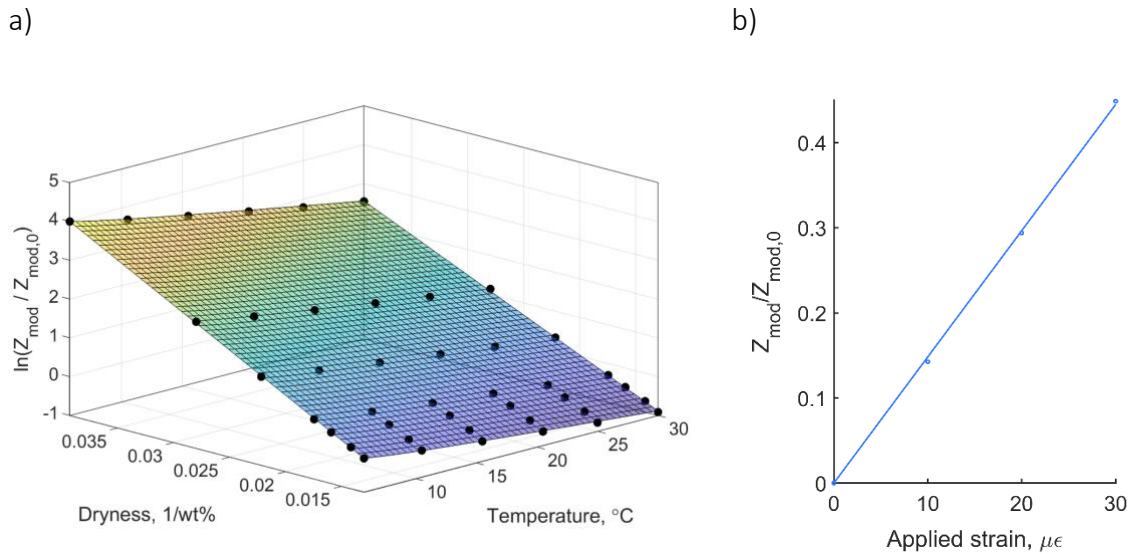


Figure 3: Example sensor response of geopolymers to a) temperature and moisture and b) low levels of applied strain.

Applications

Our active projects are currently looking at the deployment challenges faced in three environments:

1. *Nuclear storage facilities (for moisture and chloride monitoring)*: Here the ability to remotely deploy monitoring technologies in harsh environments could improve health and safety.
2. *Oil and gas concrete assets (for crack monitoring)*: In the case, the remote deployment offered by robotics represents clear cost and safety benefits for continuous monitoring of active and decommissioned assets in the North Sea.
3. *During precast concrete component manufacturing*: The use of repeatable, robotic processes synchronises well with the manufacturing environment of a precast concrete factory. Automated deployment of smart materials in this setting is less challenging than field deployment, and it could improve the repeatability of the material’s sensing performance.

While the cost or safety benefits of remotely deploying smart materials is already clear, our future work will be looking to quantify the relative benefits of automated deployment in terms of technical sensing performance and repeatability, especially when compared with manual deployment.

Conclusion

This paper has outlined some recent highlights in our ongoing projects which seek to demonstrate the viability of robotically deploying self-sensing cements for monitoring strain, temperature and moisture in concrete. The affordability of our sensing techniques are on par with direct measurements of concrete impedance, but the higher electrical conductivity of geopolymers could allow for monitoring over a broader range of measurands, and over larger areas. The techniques outlined could be used to remotely or automatically deploy other novel materials in the field or in manufacturing environments.

Acknowledgments

This work was funded in part by the National Nuclear Laboratory ICASE award (NNL/UA/022), EPSRC (EP/L014041/1), the Royal Society (RG160748), the Advanced Nuclear Research Centre and the Scottish Funding Council's Oil & Gas Innovation Centre. Our thanks to our industry partners: Sellafield, Cavendish Nuclear, Bruce Power, EDF Energy, Doosan Babcock and The Lloyd's Register.

References

- [1] J. L. Provis, Geopolymers and other alkali activated materials: Why, how, and what?, *Materials and Structures* 47 (1) (2014) 11–25. doi:10.1617/440s11527-013-0211-5.
- [2] S. Hanjitsuwan, P. Chindapasirt, K. Pimraksa, Electrical conductivity and dielectric property of fly ash geopolymer pastes, *International Journal of Minerals, Metallurgy, and Materials* 18 (1) (2011) 94–99.
- [3] X.-M. Cui, G.-J. Zheng, Y.-C. Han, F. Su, J. Zhou, A study on electrical conductivity of chemosynthetic Al₂O₃–2SiO₂ geopolymer materials, *Journal of Power Sources* 184 (2) (2008) 652–65.
- [4] J. He, G. Zhang, S. Hou, C. S. Cai, Geopolymer-based smart adhesives for infrastructure health monitoring: Concept and feasibility, *Journal of Materials in Civil Engineering* 23 (2) (2010) 100–109.
- [5] L. Biondi, M. Perry, C. Vlachakis, Z. Wu, A. Hamilton, J. McAlorum, Ambient Cured Fly Ash Geopolymer Coatings for Concrete, *Materials* 12 (6) (2019) 923.
- [6] F. Pacheco-Torgal, J. Castro-Gomes, S. Jalali, Alkali-activated binders: A review: Part 1., *Construction and Building Materials* 22 (7) (2008) 1305-1314. doi:10.1016/j.conbuildmat.2007.10.015.
- [7] M. Perry, M. Saafi, G. Fusiek, P. Niewczas, Hybrid optical-fibre/geopolymer sensors for structural health monitoring of concrete structures, *Smart Materials and Structures* 24 (4) (2015) 045011
- [8] M. Perry, M. Saafi, G. Fusiek, P. Niewczas, Geopolymeric thermal conductivity sensors for surface-mounting onto concrete structures, in: *9th International Concrete Conference, Dundee, UK, 2016*. 450
- [9] M. Saafi, G. Piukovics, J. Ye, Hybrid graphene/geopolymeric cement as a superionic conductor for structural health monitoring applications, *Smart Materials and Structures* 25 (10) (2016) 105018. doi:10.1088/0964-1726/25/10/105018.
- [10] M. Saafi, L. Tang, J. Fung, M. Rahman, F. Sillars, J. Liggat, X. Zhou, Graphene fly ash geopolymeric composites as self-sensing structural materials, *Smart Materials and Structures* 23 (6) (2014) 065006. doi:10.1088/0964-1726/23/6/065006.
- [11] L. Biondi, M. Perry, J. McAlorum, C. Vlachakis, A. Hamilton, Geopolymer-based moisture sensors for reinforced concrete health monitoring, *Sensors and Actuators B: Chemical*, Minor Revisions submitted.
- [12] J.L. Provis, S.A. Bernal, Geopolymers and Related Alkali-Activated Materials, *Annu. Rev. Mater. Res.* 44 (2014) 299–327. <https://doi.org/10.1146/annurev-matsci-070813-113515>.
- [13] A.M. Rashad, Metakaolin as cementitious material: History, scours, production and composition-A comprehensive overview, *Constr. Build. Mater.* 41 (2013) 303–318. <https://doi.org/10.1016/j.conbuildmat.2012.12.001>.
- [14] P. Duxson, A. Fernández-Jiménez, J.L. Provis, G.C. Lukey, A. Palomo, J.S.J. Van Deventer, Geopolymer technology: The current state of the art, *J. Mater. Sci.* 42 (2007) 2917–2933. <https://doi.org/10.1007/s10853-006-0637-z>.
- [15] S. Kramar, A. Šajna, V. Ducman, Assessment of alkali activated mortars based on different precursors with regard to their suitability for concrete repair, *Constr. Build. Mater.* 124 (2016) 937–944. <https://doi.org/10.1016/j.conbuildmat.2016.08.018>.
- [16] C. Zanotti, P.H.R. Borges, A. Bhutta, N. Banthia, Bond strength between concrete substrate and metakaolin geopolymer repair mortar: Effect of curing regime and PVA fiber reinforcement, *Cem. Concr. Compos.* 80 (2017) 307–316.

- [17] A. Lasia, *Electrochemical Impedance Spectroscopy*, Springer, 2014. <https://doi.org/10.1007/978-1-4614-8933-7>.
- [18] M. Chiarello, R. Zinno, Electrical conductivity of self-monitoring CFRC, *Cem. Concr. Compos.* 27 (2005) 463–469. <https://doi.org/10.1016/j.cemconcomp.2004.09.001>.
- [19] B. Han, X. Guan, J. Ou, Electrode design, measuring method and data acquisition system of carbon fiber cement paste piezoresistive sensors, *Sensors Actuators, A Phys.* 135 (2007) 360–369. <https://doi.org/10.1016/j.sna.2006.08.003>.
- [20] R. Pouhet, M. Cyr, R. Bucher, Influence of the initial water content in flash calcined metakaolin-based geopolymer, 201 (2019) 421–429.
- [21] C. Vlachakis, M. Perry, L. Biondi, J. McAlorum, 3D printed self-sensing repairs for concrete structures, submitted to *Additive Manufacturing*, In Review.

A comparison of soft and hard PZT for damage detection in cement mortars

Hussameldin Taha, Richard J Ball, Kevin Paine

BRE Centre for Innovative Construction Materials, Department of Architecture and Civil Engineering, University of Bath, Bath, Calverton Down, BA2 7AY, UK

Abstract

Lead zirconium titanate (PZT) have recently emerged as low-cost materials for non-destructive monitoring for civil structures. Different types of PZT materials with different properties are already commercially available. Depending on the dopant type used, soft PZTs and hard PZTs are the main two types of PZT materials. Most of the available studies which addressed the viability of PZT transducers in detecting damage in civil structures, have studied only the response of soft PZT transducers to damage. This is even though many studies have shown that the hard PZT transducers are less influenced by temperature fluctuations, which potentially makes the latter more electromechanically stable when used in real environment conditions. To this end, this study compared experimentally the effect of damage on the electromechanical response of both soft and hard PZT transducers, in order to assess the sensitivity of each type to localized damage. Mortar beam was used as a hosting structural element, and the electromechanical response of the two PZT types were compared through different damage stages. The damage effect on the electromechanical response was studied by comparing the electrical admittance response, the resonance frequency response and the root mean square deviation before and after imposing damage. This study is expected to highlight the differences between the soft and the hard PZT materials in the scope of structural health monitoring, which will help in the selection process for the most efficient PZT type in future damage detection applications.

Introduction

Damage detection's sensors in civil structures, are increasingly used in early warning systems to detect damages at early stages. Intervention during the early damage stages is often more feasible and more economically efficient. Nowadays and particularly in cementitious civil structures, researchers are exploring the capability of autonomous self-healing techniques to restore functionality and providing a methodology for cracks closure in cementitious members. Shape memory polymers [1], and the addition of bacterial spores during the casting process [2], both showed good results mitigating against cracks by either closing them mechanically or filling the crack by precipitated calcium carbonate, respectively. However, to achieve the goal of a fully automated self-healing cementitious structural system, the damage initiation and the extent to which the healing process is applied needs to be controlled. This requires both damage detection and quantification to initiate and end the healing process at the appropriate stage of each damage and healing cycle.

Throughout the last three decades, piezoelectric ceramics, particularly lead zirconate titanate (PZT), have attracted many researchers due to their ability to reflect changes which take place in hosting materials' properties, and its relative low cost when employed as sensors for damage detection in the electromechanical mode. Ranging from damage sensing [3], repairing detection [4], strength development [5], chloride and carbonation induced corrosion [6, 7], all these scenarios were used to validate PZTs electromechanical sensitivity to the changes in the properties of cementitious materials when they are used in the electromechanical mode.

Depending on the doping agent used to modify the chemical composition of the PZT ceramic, soft PZTs, in which donor doping agent is used, and hard PZTs, in which acceptor doping agent is used, can be produced. These two types of PZTs exhibit significant differences in their

domain's mobility, hence their piezoelectric properties and the thermal stability of their piezoelectric properties [8].

Studying the effect of different PZT types on damage sensing capabilities in civil structures, can pave the way for a future tailoring for an optimum PZT ceramic which has the required sensing ability as well as the required properties to withstand the challenging working conditions especially temperature variations. To this end, this paper presents studies of different PZTs types, mainly hard and soft, for their ability to sense damage in cementitious mortar, and to highlight the difference in the sensing ability for each type.

Materials and methods

In this study, a 500×100×100 mm mortar beam was used as a hosting sample for three different types of PZTs transducers, two soft types of PZT, which were denoted as S_1 and S_2 , and one hard type of PZT denoted as H, see Table 1.

The mix design used, and the methodology of attaching the sensors to the surface of the hosting sample are described elsewhere [4]. The thickness of the PZT transducers was 2 mm, and their diameters were 13 mm for S_1 , 10 mm for both the S_2 and the H PZTs. The damage was simulated by drilling a series of 4 mm diameter holes of depth 5 mm in a line, starting from the beam end and approaching the centre of the beam where the PZTs were located. The spacing between each consecutive hole was 20 mm and a total of 14 holes were drilled on the surface of the beam. The electromechanical response of the three PZTs before and post damage was used as a mean to assess the damage extent in the hosting material, this was done by collecting the electrical admittance signature for each PZT before and after each hole was drilled by a Newton4th PSM 3750 frequency analyser, interfaced with an impedance analyser. To quantify the damage effect on the sample, both the admittance signature and the root mean square deviation (RMSD) [6] were used for this purpose. The frequency range used to collect the admittance signature was 15 kHz – 350 kHz.

Results and discussion

PZT type effect on the admittance signature

Figure 2 shows the admittance signature for the three different PZT transducers attached to the sample before damage application. It is evident that the S_1 PZT transducer showed higher admittance amplitudes, this was clear when comparing the highest resonance peak for this particular PZT type with the other PZT types.

Table 1. Specifications of PZT transducers

Property	SOFT		HARD
	S_1	S_2	H
Electric Permittivity, $\epsilon_{33}^T/\epsilon_0$	4200	1750	1200
Piezoelectric Strain Coefficient, d_{31} (10 ⁻¹² C/N)	-600	-180	-120
Piezoelectric Strain Coefficient, d_{33} (10 ⁻¹² C/N)	600	400	265
Dielectric Loss Factor, $\tan\delta$ (10 ⁻³)	30	20	3
Mechanical quality factor (Q_m)	50	80	2000

The resonance peaks for the S_1 took place within the frequency range of 100 – 200 kHz and recorded a value of 2.9×10^{-3} S. On the other hand, both the S_2 and the H PZT transducers recorded lower values of 1.85×10^{-3} S and 0.87×10^{-4} S respectively for their highest resonance peaks. It was also evident from Figure 2 that the frequency ranges in which the resonance peaks for each PZT transducer took place, were dependent on the PZT type, as the maximum resonance peak for the two soft PZTs, denoted as f_{s1} and f_{s2} in figure 1, took place at lower

frequency ranges when compared with the hard PZT, denoted as f_H . Within the same context, the resonance frequency for the S_1 PZT, took place at a lower frequency in comparison to the S_2 .

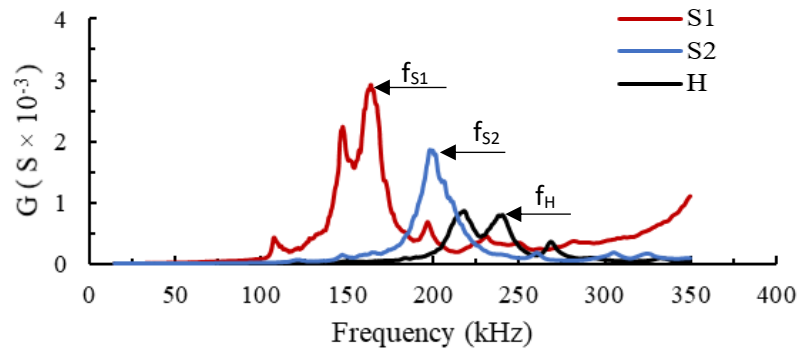


Figure 2. Admittance signatures for the three different PZTs

From the results it can be suggested that the higher admittance signature, and the lower resonance frequency ranges observed for the soft PZT transducers, means that these transducers are more dynamically fixable. Therefore, they are much easier to deform and to resonate at lower frequencies [9]. The higher electrical admittance values for the soft PZTs, suggests the higher voltage produced which is attributed to the enhanced deformability when compared to the hard PZTs. The differences in the resonance frequencies between the soft and the hard PZTs should be considered when designing an automated damage sensing system, as the frequency range over which the admittance signature is sensitive to changes which take place in the hosting material, is expected to change according to the PZT type used.

PZT type effect on damage sensing

Figure 3 (a), (b) and (c) show the admittance signature in the frequency range of 65 kHz – 75 kHz for the different PZTs before and after drilling the 14 holes on the surface of the beam. Noticeable differences in the admittance signature were observed between the pristine stage and the damaged stage signatures. In order to be able to quantify the changes in the admittance signature hence the effect of damage, the root mean square deviation statistical metric (RMSD) was used. Figure 3 (a`), (b`) and (c`) show the RMSD after each hole was drilled into the sample. The frequency range which demonstrated the highest sensitivity to damage for each PZT transducer, was used to calculate the RMSD. These were 65 – 115 kHz for both S_1 and S_2 , transducers and 165 – 215 kHz for the H transducer. Results demonstrate that the three different PZT transducers were capable of sensing the holes being drilled as they approached the PZT location. A difference in the damage sensitivity was observed between the three transducers, as the RMSD values for both the S_1 and the S_2 PZTs showed an increase in their values immediately after hole 4 as indicated by the red line in figure 2 (a`) and (b`). This shows that the S_1 and the S_2 PZTs were able to detect the damage at a 12 cm distance away from their position. In comparison, the H PZT exhibited an increase in the RMSD after hole number 7 which was 6 cm away from its location.

A comparison of the RMSD values obtained from the different PZTs types revealed that the highest value was 2.870%. for the S_1 PZT. On the other hand, the S_2 and the H PZTs recorded values of 2.38 and 2.06% respectively. This shows that for these selected frequency ranges, the S_1 admittance signature was affected by damage to a greater extent than the S_2 and the H PZTs admittance signatures.

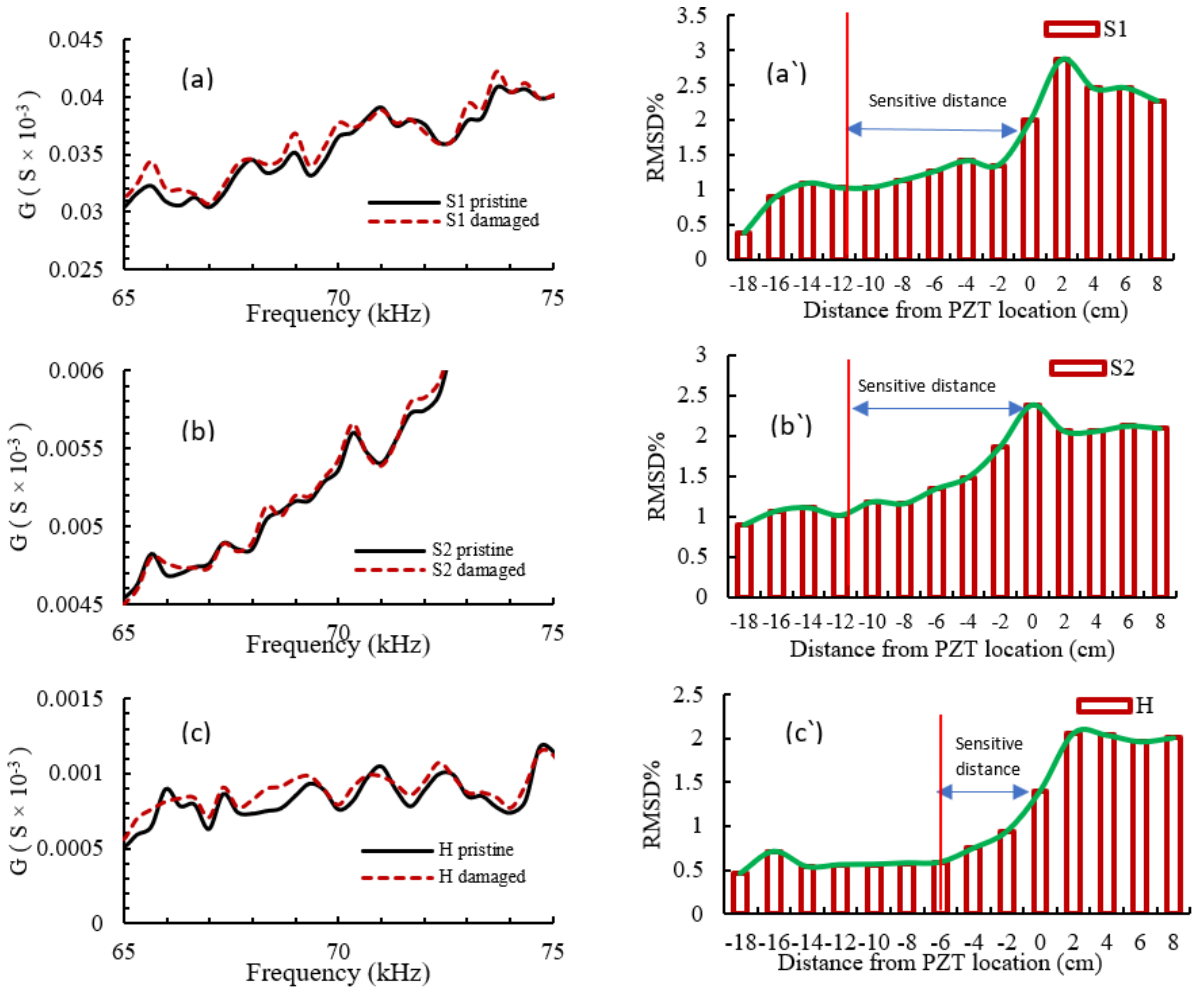


Figure 3. Admittance signature at the resonance peak before and after damage for (a) S1 PZT (b) S2 PZT and (c) for H PZT, and the corresponding RMSD% for (a') S1 PZT (b') S2 PZT and (c') H PZT.

The higher sensitivity of the S_1 PZT transducer admittance signature to damage was also confirmed by comparing the values of the averaged/ normalised RMSD for each PZTs transducer. The averaged/ normalised RMSD was calculated by normalising the RMSD of each hole by the RMSD of hole number1, then taking the average of the RMSDs over the 14 holes. This was done for seven different frequency intervals, and the results are as shown in Figure 3. The averaged and normalised RMSD values were used to minimize errors attributed to the bonding agent on the admittance signature, hence making it possible to compare the 3 different PZTs.

From Figure 3, it is noteworthy that the averaged normalised RMSD for the S1, except in the frequency ranges of 15 – 65 kHz and 165 – 215 kHz showed the highest values when compared with the other PZT transducers. In addition, and at higher frequency ranges, i.e.: 115 kHz to 350 kHz, the S_2 showed higher values than the H PZT.

This indicates that when accounting for the initial conditions which are expected to be different for each PZTs due to the random bonding process, and the local heterogeneity on the surface of the hosting material, the soft PZTs admittance signature showed more influence by the effect of damage than the hard PZT, despite the fact that both the mentioned PZT types have been shown to be sensitive to the damage scenario used in this study.

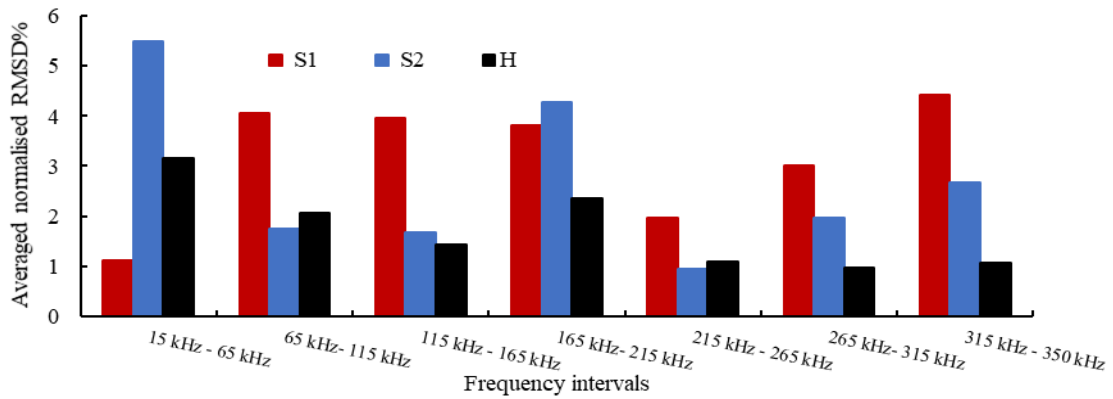


Figure 4. Averaged and normalised RMSD% for the 3 different PZTs through different frequency intervals

Conclusions

Three different PZTs transducers were studied to assess their performance on damage detection in cementitious materials. From this study the following conclusions can be drawn:

- Both the amplitude of the admittance signature and the operating frequency showed a close dependency with the PZT type. The hard PZT operated over a higher frequency range and lower admittance amplitudes, whilst the soft PZTs showed a lower operating frequency and higher admittance amplitudes. It is important to carefully consider the type of PZT used when designing automated self-sensing systems as the frequency range which is sensitive to damage is clearly dependent on the type of PZT employed.
- The hard and soft PZTs used in this study were all capable of sensing the damage as it approached the PZT location. The sensing distance of the hard PZT (6cm) was lower than that of the two soft PZTs (12cm).
- The averaged normalised RMSD values showed higher values for the soft PZTs in comparison to the hard one, which indicates that the admittance signatures for the soft PZTs were more affected by damage than the hard PZT admittance signature.

Future work

- Considering the sensing ability to damage which was assessed in this study, and the end working environmental conditions, these two factors would affect the selection of a suitable PZT type for damage sensing applications. Therefore, as a future work, the effect of different environmental conditions on the electromechanical response of these different PZTs types will be evaluated.
- More damage scenarios should be studied to accurately establishing the sensitivity distance range of each PZT type, as different damage scenarios might have an influence on the sensitivity range.

Acknowledgment

This research was funded by UK-EPSCRC, grant number No. EP/P02081X/1, Resilient Materials 4 Life, RM4L.

References

- [1] O. Teall, M. Pilegis, R. Davies, J. Sweeney, T. Jefferson, R. Lark, D. Gardner, A shape memory polymer concrete crack closure system activated by electrical current, *Smart Materials and Structures* 27 (7) (2018) 075016. doi:10.1088/1361-665X/aac28a.
- [2] Paine, K., Sharma, T., Alazhari, M., Heath, A., & Cooper, R. (2018). Application and performance of bacteria-based self-healing concrete. In A. Bertron, & H. Jonkers (Eds.), *Proceedings of Final Conference of RILEM TC 253-MCI: Microorganisms-Cementitious Materials Interactions* (Vol. 2, pp. 387-394)

- [3] Hu, X., H. Zhu, and D. Wang, A study of concrete slab damage detection based on the electromechanical impedance method. *Sensors*, 2014. 14(10): p. 19897-19909.
- [4] Taha, H., R.J. Ball, and K. Paine, Sensing of Damage and Repair of Cement Mortar Using Electromechanical Impedance. *Materials*, 2019. 12(23): p. 3925.
- [5] Su, Y.-F., et al., Instantaneous monitoring the early age properties of cementitious materials using PZT-based electromechanical impedance (EMI) technique. *Construction and Building Materials*, 2019. 225: p. 340-347.
- [6] Talakokula, V., et al., Diagnosis of carbonation induced corrosion initiation and progression in reinforced concrete structures using piezo-impedance transducers. *Sensors and Actuators A: Physical*, 2016. 242: p. 79-91.
- [7] Talakokula, V., S. Bhalla, and A. Gupta, Corrosion assessment of reinforced concrete structures based on equivalent structural parameters using electro-mechanical impedance technique. *Journal of Intelligent Material Systems and Structures*, 2014. 25(4): p. 484-500.
- [8] Zhu, X., *Piezoelectric ceramic materials: processing, properties, characterization, and applications*. 2010: Nova Science Publishers.
- [9] Erturk, A., H.-Y. Lee, and D.J. Inman. Investigation of Soft and Hard Ceramics and Single Crystals for Resonant and Off-Resonant Piezoelectric Energy Harvesting. in *ASME 2010 Conference on Smart Materials, Adaptive Structures and Intelligent Systems*. 2010.

Graphite-silicone composite strain sensors for self-sensing structures

Alizé V Gaumet¹, Alain R Nogaret¹, Richard J Ball²

1: Department of Physics and Centre for Nanoscience and Nanotechnology, University of Bath, Claverton Down, Bath, BA2 7AY, UK

2: BRE Centre for Innovative Construction materials (CICM), Department of Architecture and Civil Engineering, University of Bath, Claverton Down, Bath, BA2 7AY, UK

Abstract

Cracking and degradation of civil structures are driving demand for the development of self-sensing technologies which can detect damage effectively. Here we evaluate an alternative to traditional strain sensors which relies on piezoresistive films to map strain on the millimetre scale within concrete. We used graphite-polydimethylsiloxane composites to achieve high strain sensitivity and scalable devices while comparable strain sensors conventionally used to warn of structural weaknesses are large and costly. Our sensors were embedded in cementitious materials and their ability to sense early-stage changes in strain attributed to microcracking was evaluated. The simple sensor design and manufacturing process make our sensors industrially scalable and economical. The very high strain sensitivity (gauge factor of 65 for strains under 0.6%) of the composite was observed and attributed to quantum tunnelling within its percolation network.

The piezoresistive response of our sensors could be calibrated using a universal analytical formula depending on three material parameters; the potential barrier height, creep time and residual creep factor. Preliminary experiments indicate an optimized sensitivity for the composite strain sensors for loading frequencies of up to 1 Hz, and thus approaching bridges fundamental frequencies. Cylindrical smart aggregates 25 mm in diameter and 15 mm in height consisting of composite strain sensors embedded in rapid setting cementitious materials and epoxy that provide good compatibility with concrete have been fabricated and evaluated in the laboratory. Their implementation into large scale concrete specimens will allow their ability to detect and evaluate changes in strain attributed to cracking to be investigated.

Introduction

Cracking, corrosion and degradation of civil structures are driving demand for the development of non-destructive evaluation methods [1, 2] and intrinsic self-healing strategies [3-5]. Intrinsic self-healing includes autogenous and bio-related techniques which encompass smart functionalities such as self-sensing and self-adjusting [5]. Studies have highlighted several self-healing agents among which are a UV-curable resin [3] stored in unit cells embedded in the structure and concrete-healing fungi [4] using calcium carbonate precipitation. Self-sensing is achievable through the embedment of high sensitivity sensors networks with a rapid response time mimicking the human touch. The potential of a strain sensing graphite-silicone composite for the making of such a network has been previously evidenced through the interrogation of an array of 64 x 64 graphite-silicone composite strain sensors at a rate of 8 images per second with pressure resolution down to 50 Pa [6]. The pressure at each pixel was inferred from the quasi-instantaneous resistance spikes using a universal analytical formula that predicts the dynamic conductivity of the graphite-silicone composite with only three material parameters [6]. This formula originates from a tunnelling-percolation network model according to which resistance recovery occurs through a double exponential decay and the piezoresistance is symmetrical with respect to strain reversal [6, 7].

Here we evaluate the potential of graphite-silicone composite strain sensors to map strain within cementitious materials as an alternative to the large [8] and costly [8, 9] strain sensors conventionally used to detect structural changes.

Materials and methods

The graphite-silicone composite we used consists of highly oriented pyrolytic graphite nanoparticles 450 nm in diameter randomly dispersed in an insulating silicone matrix that is composed of a mixture of a polydimethylsiloxane rubber and a catalyst. We chose a filling fraction of 25% such that the strain sensitivity would be maximised while allowing a reliable operation away from the percolation threshold (24%). Figures 1a and 1b show the design and a photo of a six-contact graphite-silicone composite strain sensor we fabricated, respectively. The composite geometry was either in a six or a five contact Hall-bar shape on a thin printed circuit board. We selected Hall-bar shapes to allow four terminal measurement and, in the case of the five-contact Hall-bar shape (L shape), also study simultaneously both strain components in the plane of the L-shaped five-contact sensor. Both six-contact (Figures 1a and 1b) and five-contact L-shaped composite sensors were 10 mm x 10 mm squares. The simple manufacturing process of these composite sensors allows size scalability (we have also successfully manufactured 3 mm x 3 mm two-terminal composite sensors), industrial scalability and low-cost (their production only costs a few pence).

We tested our graphite-silicone composite strain sensors in three different testing geometries. Cylindrical blocks 39 mm in diameter and 60 mm in height, illustrated in Figures 1c and 1d, were prepared by embedding a six-contact composite strain sensor (Figures 1a and 1b) in a Portland cement mortar mix with very fine aggregates. Testing was also carried out with single L-shaped five-contact composite sensors mounted in columns of very fine sand (play sand) restrained by a steel tube of internal diameter 69 mm and height 140 mm. Cylindrical smart aggregates 25 mm in diameter and 14 mm in height each consisting of a L-shaped five-contact composite strain sensor embedded either in rapid setting cementitious materials (calcium aluminate mortar) or concrete repair epoxy that provided good mechanical compatibility with concrete were also fabricated and evaluated in our laboratory. All the tests were carried out using a universal testing machine (Figure 1d) simultaneously monitoring both the stress σ and the average strain ϵ_{avg} applied at the top of each specimen subjected to uniaxial compression loading. During these tests, a d.c. voltage was applied to the embedded composite sensor placed in series with a resistor. The voltages of the resistor and the embedded sensor were monitored with a sampling frequency of 100 Hz using a data acquisition card manufactured by National Instruments. While probing either voltage V1 or voltage V2 is sufficient when using six-contact composite sensors since both voltages provide same value (Figure 1a), monitoring these two voltages when L-shaped five-contact composite sensors are being employed is of the essence. In the case of the L-shaped five-contact composite sensors, voltages V1 and V2 are indeed perpendicular, allowing the study of both strain components in the plane of the sensor.

We subsequently calculated the relative change in resistance $\Delta R/R_0$ values of the sensor from the voltage measurements. Since the strain magnitudes in the monotonic uniaxial compression loading tests we have carried out remained in the 0 - 1.6 % range, the tunnelling-percolation network model developed for bent substrates [6, 7] remained valid for the monotonic uniaxial compression loading tests. We thus used the associated universal analytical formula [6], which depends solely on the potential barrier height, creep time and residual creep factor of the composite, to compute the theoretical calibration curve ($\Delta R/R_0$ dependence on strain) of the piezoresistive composite film. Since the piezoresistance of the graphite-silicone composite responds to changes in strain on the scale of the sensor, the strain involved in the theoretical calibration curve is a local strain, ϵ_{loc} . We then used this calibration curve to extract the local

strain ϵ_{loc} from the measured relative change in resistance of the composite. Examples of the resulting dependence of the local strain ϵ_{loc} on the average strain ϵ_{avg} are plotted in Figure 2.

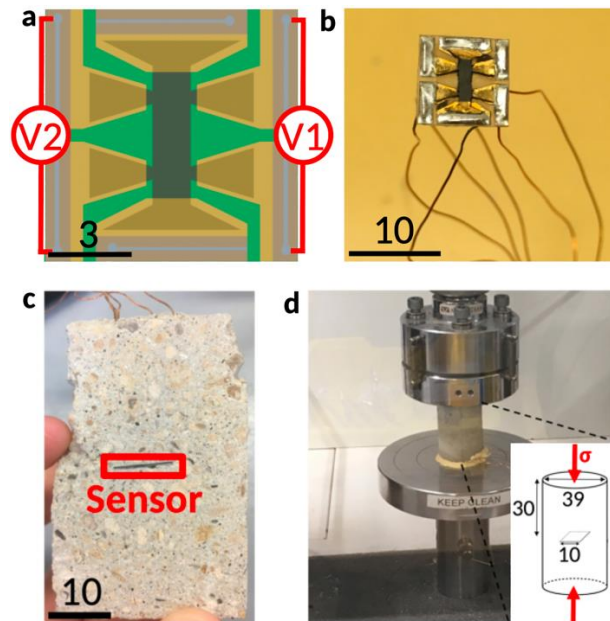


Figure 1. **a** Design of the graphite-silicone composite sensors containing six contact pads. In black, the graphite-silicone composite. In gold colour, the layer of gold covering the composite and the copper contacts. In green, insulating epoxy resin of the printed circuit board. In grey, the wires soldered to the copper pads. The voltage of the graphite-silicone composite can be obtained by probing either voltage V1 or voltage V2. **b** Photo of a graphite-silicone composite sensor whose design is illustrated in **a**. **c** Photo of the cross section of a Portland cement mortar block with a graphite-silicone composite sensor embedded midheight taken after being subjected to monotonic uniaxial compression loading. The irregularities of the side edges result from damage occurring during testing. **d** Schematic of the uniaxial compression loading of a Portland cement mortar block with embedded composite sensor. The red arrows indicate the compressive forces applied. The number units in all the scale bars are in millimetres.

Results and discussion

The dependences of the local strain ϵ_{loc} on the average strain ϵ_{avg} of the two Portland cement mortar specimens subjected to monotonic uniaxial compression loading (Figure 2) have a high degree of linearity so long as ϵ_{avg} remains below $\sim 1\%$, that is to say as long as the deformation is elastic (reversible) as can be inferred from the stress-strain curves (inset of Figure 2) of the two specimens. A high degree of linearity during elastic deformation resulting from monotonic uniaxial compression loading has also been found in our calcium aluminate mortar specimens. Although one would expect the local strain to be approximately equal to the average strain during these loading tests, this was only observed for specimen 1 (Figure 2). In order for the embedded composite sensor of specimen 2 to provide accurate quantitative strain reading, a prior experimental calibration is then necessary. The need for an experimental calibration to provide accurate quantitative strain reading has also been found for our calcium aluminate mortar specimens. This is validated by the piezoresistances of the two composite sensors embedded in different sand columns (Figures 3a and 3b) having very similar dependences on the average strain and by the piezoresistances sampled by the two voltage probes V1 and V2 (Figure 3) being almost superimposed on each other for both sand columns even though the

voltage probes V1 and V2 are at an angle of 90 degrees of each other, which is consistent with hydrostatic transmission of strain within a fluid-like environment.

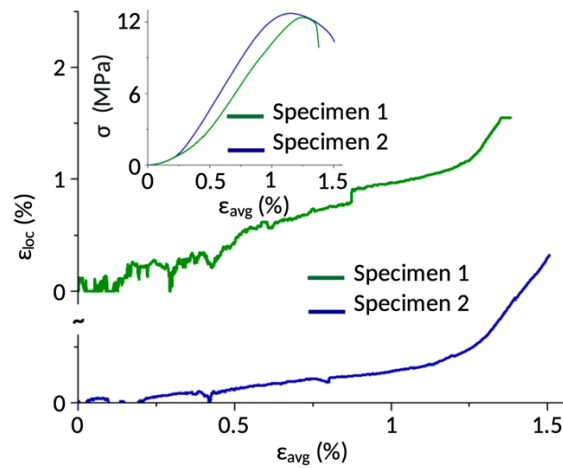


Figure 2. Monotonic uniaxial compression loading of two Portland cement mortar block specimens. The local strain ϵ_{loc} (%) evaluated by each embedded six-contact composite sensor was compared to the macroscopic strain ϵ_{avg} (%) obtained from the strain gauge of the universal testing machine. Inset shows the stress-strain curve of each specimen subjected to the monotonic uniaxial compression loading.

During elastic deformation (ϵ_{avg} below $\sim 1\%$), kinks were observed in the local strain signals of both Portland cement mortar specimens (Figure 2); they were most prominent for specimen 1. This suggests that the graphite-silicone composite sensors detect early-stage damage, in particular micro-cracking, in the Portland cement mortar. Similar kinks have also been found in the local strain signals of our calcium aluminate mortar specimens subjected to similar loading tests. In contrast, the piezoresistances of the two composite sensors each embedded in a very fine sand column, which was subjected to the same monotonic uniaxial compression loading, monotonically and very smoothly decreased during loading (Figure 3). This is consistent with both hydrostatic transmission of strain and the fluid-like nature of this environment, which is not expected to induce micro-cracking.

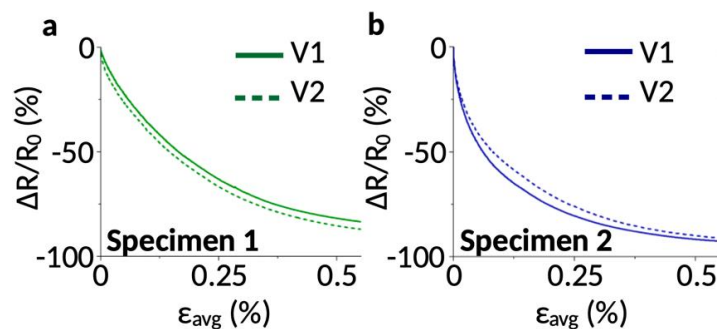


Figure 3. $\Delta R/R_0$ (%) for the monotonic uniaxial compression loading of two specimens consisting in very fine sand columns each with an embedded L-shaped five-contact composite sensor. ϵ_{avg} (%) corresponds to the macroscopic strain obtained from the strain gauge of the universal testing machine. V1 and V2 correspond to the voltage probes of the L-shaped composite, which are at an angle of 90 degrees from each other, allowing the study of both strain components in the plane of the composite sensor.

These findings demonstrate that the composite sensors detect micro-cracking in at least two materials: the Portland cement mortar and the calcium aluminate mortar.

The local strain signals of the two Portland cement mortar specimens share the same overall dependence on the average strain (Figure 2). The same observation was made for our calcium aluminate mortar specimens. This suggests that the graphite-silicone composite strain sensors are reliable.

This is validated by the piezoresistances of the two composite sensors embedded in different sand columns (Figures 3a and 3b) having very similar dependences on the average strain and by the piezoresistances sampled by the two voltage probes V1 and V2 (Figure 3) being almost superimposed on each other for both sand columns even though the voltage probes V1 and V2 are at an angle of 90 degrees of each other, which is consistent with hydrostatic transmission of strain within a fluid-like environment.

For specimen 1 of Portland cement mortar, we estimated the gauge factor of the embedded composite sensor at a value of about 13 for strains ϵ_{avg} up to 0.45%, and 127 for strains ϵ_{avg} comprised between 0.45% and 0.6%. This indicates that graphite-silicone composite strain sensors have a very high strain sensitivity. Furthermore, preliminary experiments of a composite sensor embedded in a concrete repair epoxy specimen subjected to a series of cyclic uniaxial compression loadings at different loading frequencies hinted at the strain sensitivity of the composite sensors being optimised for loading frequencies up to about 1Hz. This coincides with bridges fundamental frequencies [11].

Conclusions

Our results demonstrate that piezoresistive graphite-silicone composite strain sensors represent a potential alternative to strain sensors conventionally used to detect structural changes that are large and costly. The piezoresistive properties of the graphite-silicone composites, which allow the fabrication of economical highly strain sensitive and scalable devices, are attributed to quantum tunnelling within their percolation networks. Our results evidenced that the composite sensors are reliable, non-invasive, could be massively distributed within civil structures and detect the onset of micro-cracking. An implementation of rapid setting cementitious or epoxy smart aggregates with embedded graphite-silicone composite sensors into large scale concrete specimens could allow the ability of these sensors to detect and evaluate changes in strain attributed to cracking to be investigated.

Acknowledgments

The authors would like to acknowledge support of the EPSRC, grant number No. EP/P02081X/1, Resilient Materials 4 Life, RM4L. We also thank William Bazeley, Dr Tzoura, Dr Taha Abdalgadir, Dr Dams and Prof Ibell for helpful discussions and suggestions. This work has been financially supported by the Lloyd's Register Foundation International Consortium of Nanotechnologies (ICON).

References

- [1] Gao, Y., Tian, G.Y., Wang, P., Wang, H., Gao, B., Woo, W.L. and Li, K., 2017. Electromagnetic pulsed thermography for natural cracks inspection. *Scientific reports*, 7(1), pp.1-9
- [2] Taha, H., Ball, R. J., Paine, K., 2019. Sensing of Damage and Repair of Cement Mortar Using Electromechanical Impedance. *Materials MDPI*, 12, 3925; doi:10.3390/ma12233925
- [3] Davami, K., Mohsenizadeh, M., Mitcham, M., Damasus, P., Williams, Q. and Munther, M., 2019. Additively Manufactured Self-Healing Structures with Embedded Healing Agent Reservoirs. *Scientific reports*, 9(1), pp.1-8.
- [4] Menon, R.R., Luo, J., Chen, X., Zhou, H., Liu, Z., Zhou, G., Zhang, N. and Jin, C., 2019. Screening of fungi for potential application of self-healing concrete. *Scientific reports*, 9(1), pp.1-12.
- [5] Li, W., Dong, B., Yang, Z., Xu, J., Chen, Q., Li, H., Xing, F. and Jiang, Z., 2018. Recent advances in intrinsic self-healing cementitious materials. *Advanced Materials*, 30(17), p.1705679.

- [6] Chauhan, A.S., Taylor-Harrod, I., Littlejohn, S.D. and Nogaret, A., 2017. Ultrafast pressure sensing with transient tunnelling currents. *Nanoscale*, 9(13), pp.4544-4549.
- [7] Taylor-Harrod, I. and Nogaret, A., 2017. Piezoresistance of flexible tunneling-percolation networks. *Physical Review B*, 96(2), p.024205.
- [8] Gupta, S., Vella, G., Yu, I.N., Loh, C.H., Chiang, W.H., Loh, K.J., 2019. Graphene sensing meshes for densely distributed strain field monitoring. *Structural Health Monitoring*, p.1475921719877418.
- [9] Ostachowicz, W., Soman, R., Malinowski, P., 2019. Optimization of sensor placement for structural health monitoring: A review. *Structural Health Monitoring*, 18(3), pp.963-988.
- [11] Siringoringo, D.M. and Fujino, Y., 2012. Estimating bridge fundamental frequency from vibration response of instrumented passing vehicle: analytical and experimental study. *Advances in Structural Engineering*, 15(3), pp.417-433.

Self-sensing quantum tunnelling composite for smart infrastructures

Qiaofeng Zheng^{1, *}, Siqi Ding², Baoguo Han³, Abir Al-Tabbaa¹

1: Department of Engineering, University of Cambridge, Cambridge, CB2 1PZ, UK

2: Department of Civil and Environmental Engineering, The Hong Kong Polytechnic University, Hung Hom, Kowloon, Hong Kong

3: School of Civil Engineering, Dalian University of Technology, Dalian, 116024, China

Abstract

The significance of developing smart materials and infrastructures, in order to monitor facility serviceability and issue early warnings on damage or deterioration prior to costly repair or even catastrophic collapse, has been widely recognized by researchers and engineers worldwide. Developing smart infrastructures poses technological challenges at different levels, one of which is to select proper sensors with high sensitivity to reflect the inner changes of structures. In this paper, an innovative self-sensing composite, which is fabricated by adding spiky spherical nickel powders as functional fillers into silicone rubber, has been developed into sensors for various scenarios of traffic detection and structural health monitoring. The proposed composite is based on quantum tunnelling effect referring to the phenomenon that electrons can jump from metal surface to form conductive path even without direct physical contact between nickel particles. Test results show the composite is near-perfect insulator in unstressed state and extremely sensitive to any kind of external force and deformation. When embedded in road or integrated into rubber-based structural components such as pier fender, the composite endows the components with self-sensing property useful for monitoring stress/strain condition, detecting traffic information, and predicting possible bridge collapse after ship-bridge collision. Similarly, the use of graphene as a filler in polymers to form self-sensing fibres, is promising for applications in cementitious composite. The paper will present details and results related to both systems and their potential applications in self-sensing infrastructure.

Introduction

Modern cities are greatly dependent on their civil and marine infrastructure networks (e.g., highways, airports, bridges, tunnels and artificial islands) for social-economic development. However, once built, these infrastructures are subjected to the coupling effect of environmental corrosion, material deterioration, loading fatigue and natural disasters, inevitably resulting in structural damage accumulation and resistance attenuation. As such, it is essential to implement real-time monitoring on these infrastructures to understand their service status and evaluate potential risks before proper maintenance and demolition could be carried out timely. It is in situations like these that the field of health monitoring of concrete comes into its own. Structural health monitoring (SHM) refers to the process of measurement of the operating and loading environment and the critical responses of a structure to track and evaluate the symptoms of operational incidents, anomalies, and/or deterioration or damage indicators that may affect operation, serviceability, safety, and reliability. Developing an accurate and prompt monitoring system poses technological challenges at different levels, of which the most fundamental one is to select proper sensors to reflect the inner changes of structures.

The self-sensing property of a material is an ability to show detectable changes in response to applied stress/strain or environmental changes. Therefore, self-sensing materials such as

piezoresistive ceramics, magnetorheological fluid, optical fibres, shape memory alloys and carbon fibres, have been heavily investigated and fabricated into sensors for SHM. As novel self-sensing materials, quantum tunnelling composites (QTCs) are becoming highly attractive largely due to their extremely sensitive and robust performance and low cost. QTCs usually have an elastomeric rubber matrix filled with conductive nano- to micro- particles, and were firstly manufactured by a British company Peratech Ltd. in 1997 [1]. It is noteworthy that different from conventional conductive self-sensing materials that rely on the direct contact of conductive fillers/particles to form conductive networks, the conductive particles in QTCs are always coated with a thin film polymer when QTCs are deformed and transformed from perfect insulator to metal like conductor [2]. This is because of the so-called quantum tunnelling effect, meaning the electrons enriched at the nano-size tips on metal particles can ‘leap’ from one metal particle to the other, thus creating conduction path. Using this unique characteristic, researches have successfully applied QTCs to many sensing fields including electronics, aerospace, transportation, military, etc. [3,4].

In this paper, we propose a new type of sensor based on QTCs and investigate its performance for applications to ship-bridge collision monitoring and traffic detection.

Materials and methods

The QTC manufactured in this study is a rubber polymer-based composite filled with nickel particle. Two types of silicone rubber with different viscosities, Silicon T4 and Silicon 781, were purchased from Dow Corning Corporation, USA (see Table 1). T4 type was used for collision sensor, while 781 type for traffic detection sensor. The spiky nickel powders (type 123) provided by Inco Ltd, Canada, had an average diameter of 3.0~7.0 μm and nano-size tips on their surface that could amplify the local electrical field and quantum tunnelling effect (Table 2). A detailed manufacturing procedure is as follows: 1) use a commercial mixer to blend the nickel powder and liquid silicone polymer at low speed for 20 min; 2) pour the mixture into the moulds with 1 mm thickness, and degas in 0.1 MPa vacuum vessel for 10 min; 3) cure the composite at 60 °C for 10 h; 4) demould. The weight ratio of nickel to silicone polymer was selected as 3:1 for collision monitoring and 4:1 for traffic detection, according to reference [5].

Table 1. Typical characteristics of silicone rubber polymer.

Silicon type	Density (g/cm^3)	Hardness (A°)	Ductility (%)	Viscosity ($\text{mPa}\cdot\text{s}$)
T4	0.96	40	400	70000
781	1.087	43	400	51000

Table 2. Typical characteristics of nickel particles.

Fish sub-sieve size (μm)	Density (g/cm^3)	Electrical resistivity ($\Omega\cdot\text{cm}$)	Particle shape
3.0-7.0	8.9	6.84×10^{-4}	Spiky spherical

To simulate ship-bridge collision in lab, a model test was designed by releasing steel balls to hit the QTC sensors mounted on concrete block, as illustrated in Figure 1(a). For traffic detection, sensors were designed as shown in Figure 1(b), then mounted on road for real-time road test. For each type of sensor, several same sensors were connected to data acquisition system as shown in Figure 2, and the voltage across the sensors was collected for analysis. The circuit had a supply voltage of 1.5 V and a reference resistance of 120 Ω on each parallel branch.

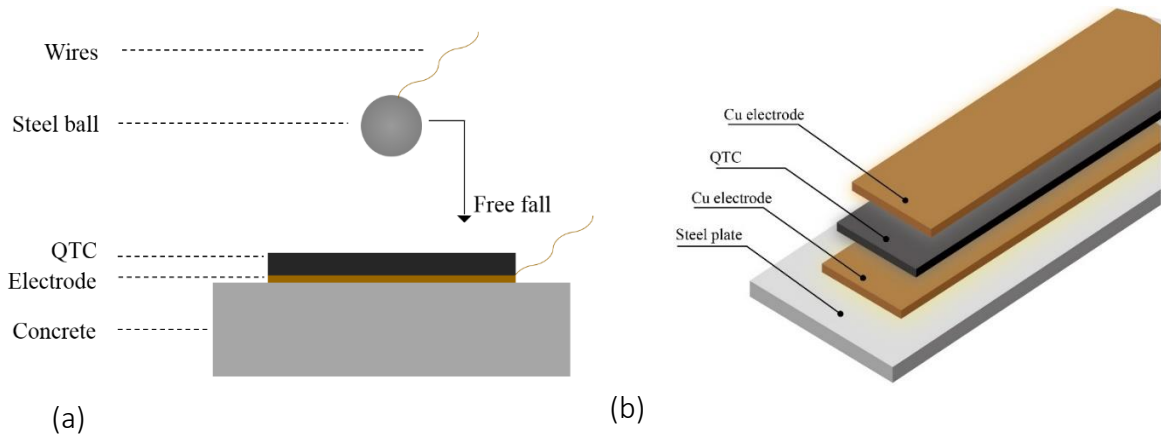


Figure 1 Schematic diagram of the sensors for (a) ship-bridge collision; (b) traffic detection.

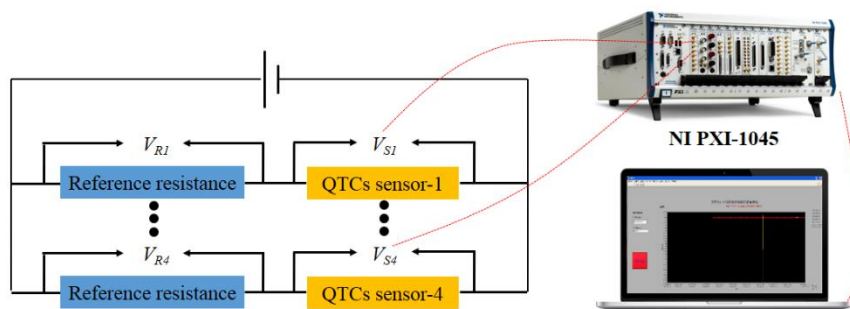


Figure 2 Circuit and data acquisition system.

Results and discussion

Figure 3(a) displays the voltage changes corresponding to collisions of different impact stress. When there is no collision, the voltage across the sensor is close to the voltage supply, suggesting the sensor is a good insulator when not deformed. Once the steel ball hits the sensor, the sensors respond immediately, and the voltage across the sensor consistently declines as the impact stress increases even over 50 MPa. According to finite element modelling of ship-bridge collision, the impact stress in bridge pier during collapse is normally within 40 MPa [6], therefore the working range of fabricated sensor is large enough to monitor the whole process of a collision. Also shown in Figure 3(b), the response of QTC sensor subjected to repeated impact loadings is reproducible and stable, indicating the sensor is capable of accurately monitoring a possibly second collision after the ship rebounds. The proposed sensor has great potential for monitoring the significant parameters in a ship-bridge collision, such as collision occurrence, position, impact stress.

Figure 4 shows the traffic detection results of QTC sensors mounted on a real road for around 300 s. The voltage curve shows a peak every single time a vehicle passes over the sensor. From the curve, the vehicle number (25) and vehicle density (around 5/min) can be easily counted and calculated. The correctness of counting is 100%, which is verified by the video record during the test. Besides, although the vehicle weight is not measured in this test, it appears the peak value increases when larger and heavier cars pass by.

Figure 5 gives an example of QTC sensors for detecting traffic parameters where sensors are buried before crosswalk, along double yellow lines and in controlled parking zones. Information such as vehicle weight, position, traffic density and violation of traffic rules, can be collected for better management of transportation.

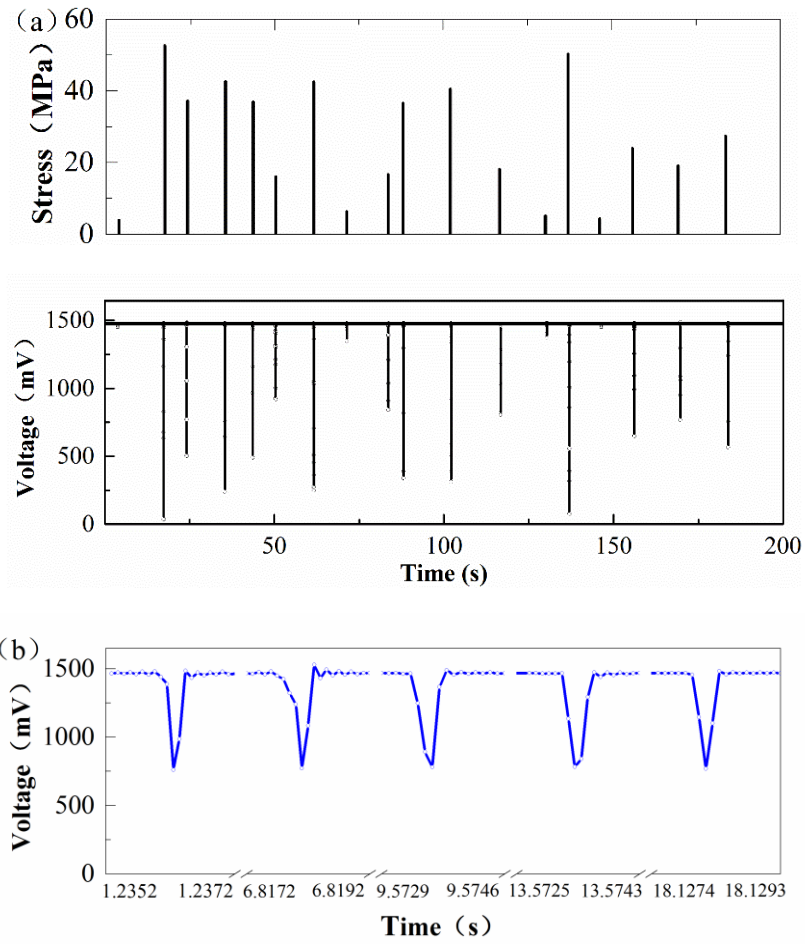


Figure 3 Detection results of collisions: (a) subjected to different impact loadings; (b) subjected to same impact loading.

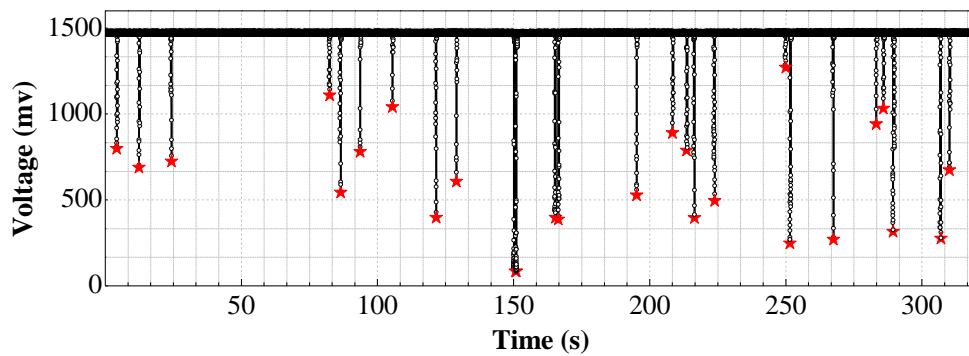


Figure 4 Detection results of traffic detection (Each red star means a vehicle passes).

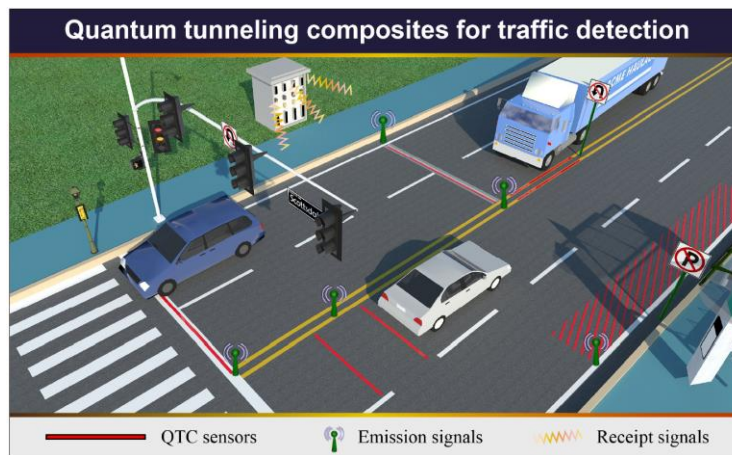


Figure 5 Schematic illustration of QTC sensors for traffic detection.

Conclusion

This paper proposes a self-sensing quantum tunnelling composite and preliminarily investigates its potential application to ship-bridge collision monitoring and traffic parameter detection. Both types of sensors have fast, accurate and stable response to the loading. The sensor is a perfect insulator when not working, thus saving energy compared to other sensors. In specific, test results show the collision sensor has a working range over 50MPa, enough to record the complete stress transmission process of ship-bridge collision. The collected information is useful for issuing early warning, estimating bridge damage, and positioning the collision that could save time for evacuation and rescuing. Test results of traffic detection sensor on real roads show the sensor can be used to collect significant traffic parameters including vehicle weight-in-motion, vehicle distribution along the road, and traffic density for improving transportation management. The research shows the great sensing properties of QTCs, and their potential for SHM and smart infrastructures. However, a major challenge lies with the incompatibility between the composite and most of concrete-based structures, which affects the accuracy of the detected information. In future work, the authors will further the research on polymer-based self-sensing composites, as well as their application in cementitious composite.

Acknowledgment

The authors thank the funding supported from the National Science Foundation of China (51428801).

References

- [1] Lussey D 1998 Peratech Ltd. UK Patent PCT/GB98/00206 (WO 98/33193).
- [2] Ding S, Han B, Dong X, et al. Pressure-sensitive behaviours, mechanisms and model of field-assisted quantum tunnelling composites. *Polymer*, 2017 vol 113 pp 105–118
- [3] Lantada AD, Lafont P, Sanz JLM, et al. Quantum tunnelling composites: Characterisation and modelling to promote their applications as sensors. *Sensors and Actuators A: Physical*, 2010 vol 164(1-2) pp 46-57.
- [4] Bloor D, Donnelly K, Hands P J, et al. A metal-polymer composite with unusual properties. *Journal of Physics D: Applied Physics*, 2005 vol 38(16): 2851.
- [5] Han B, Ding S, Yu X, et al. Design and implementation of a multiple traffic parameter detection sensor developed with quantum tunneling composites. *IEEE Sensors Journal*, 2016 vol 59 pp110–128.
- [6] Sha Y, Hao H. Nonlinear finite element analysis of barge collision with a single bridge pier. *Engineering Structures*, 2012 vol 41 pp 63-76.

Graphene-related materials for self-sensing infrastructure applications— Experimental results and lifecycle analysis

Ioanna Papanikolaou, Abir Al-Tabbaa

Department of Civil Engineering, University of Cambridge, Cambridge CB2 1PZ, UK

Abstract

This study focuses on the effect of three graphite types of varying sizes on the mechanical performance and electrical conductivity of cement composites. The finest graphite results in better mechanical properties and the lowest percolation threshold. A lifecycle assessment (LCA) study for the graphite nanoplatelet production and incorporation in concrete is also presented.

Introduction

Concrete is the most widely used construction material, however, concrete structures often suffer from poor durability performance. There is an impending need for reducing repair and maintenance by developing materials that look after themselves, i.e. have biomimetic attributes. One such material is self-sensing concrete; which can sense the presence of stresses, cracks and damage on its structure using conductive additives. These additives create a conductive network within the cementitious matrix and when there is damage or a change in loading conditions, there is a consequent change in the electrical conductivity of the specimen that can be monitored [1]. This paper focuses on the use of graphene-related materials (GRM) in cementitious composites for self-sensing. The effect of natural graphite on the electrical conductivity of cement composites has been investigated using a 4-probe method and the electrical percolation threshold has been found to reduce with reducing particle size. The effect of graphite on the microstructure and mechanical properties of cement composites is investigated through rheology, compressive strength testing and Scanning Electron Microscopy (SEM). The potential use of graphite nanoplatelets (GNPs) as a conductive additive is also discussed.

In terms of sustainability, it is estimated that each tonne of concrete has approximately 100-300 kg of embodied CO₂ [2]. The introduction of GNPs could lead to an improved structural performance and therefore reduce the need for cement. However, there is very limited literature on the environmental impact of producing GNPs and to the author's best knowledge, there is no study of the environmental performance of a GNP-cement composite. Therefore, a Life Cycle Assessment (LCA) was carried out to assess the environmental impact of concrete reinforced with GNPs by focusing on the "cradle-to-gate" of GNP production and their incorporation in concrete.

Materials and Methods

The materials used in this study were Portland cement CEM I 52.5R by Hanson and three different natural graphite products with varying sizes. The coarse graphite was supplied by AlfaAesar and had a lateral size of 2 mm (-10 mesh). Two other products were supplied by SigmaAldrich and were of mesh size -100 (150 μ m) and -325 (μ m). Cement paste mixes with a w/c = 0.45 containing natural graphite were prepared by dry mixing the required graphite dosage with cement first for two minutes and then adding water, following the BS EN 196-1 [3].

Rheology testing was undertaken using a smooth-walled Brookfield DV3T Rheometer with a SC4-27 spindle. A modified Bingham model was used for the analysis of the results. For the compressive strength testing, a CONTROLS Advantest9 machine was used with a maximum capacity of 250kN at a loading rate of 2400 N/s following BS EN 196-1. A ZEISS EVO LS 15 SEM-EDX, was used to obtain the microstructural images of the samples. Small chipped pieces were

extracted from the cracked faces of the specimens after compressive strength testing and all samples were gold-coated before testing. A four-probe method was used to assess the electrical conductivity. Perforated steel sheet electrodes of a thickness 0.55 mm and hole size 3 mm supplied by RS Components were used. The outer two electrodes were used to supply the direct current (DC) of 10V and the inner two electrodes measured the voltage, which was recorded with a datalogger every second.

The LCA study was carried out according to ISO standards [4]. The software SimaPro was used with the Ecoinvent 3.0 database. The life cycle environmental impacts were assessed using the Impact 2002+ methodology [5]. The functional unit was 1m³ of concrete and the LCA inventory comprised of primary and secondary data gather directly by the authors or through the Ecoinvent 3.0 database. The LCA covered the GNP production by Liquid Phase Exfoliation (LPE) and their subsequent incorporation in concrete.

Results and Discussion

Electrical conductivity and the percolation threshold (minimum additive dosage required to create a conductive network) were found to vary with graphite size (Figure 1). For the coarse graphite (-10 mesh size), the threshold is at 30% of graphite by weight of cement. As we move to finer types, the threshold reduces at 20%. At 20% graphite content, the specimens with finer graphite (-325 mesh) are more conductive than the -100-mesh graphite specimens. Overall, conductivity was found to reduce as the specimen age increases from 2 to 7 and then 28 days which is expected as cement hydration progressed and there is less free water available to enable electrolytic conduction. The microstructural analysis of the specimens at percolation threshold shows that graphite flakes are well integrated in the cement matrix and close proximity to each other; therefore, allowing for electronic conduction and a tunnelling mechanism to be developed.

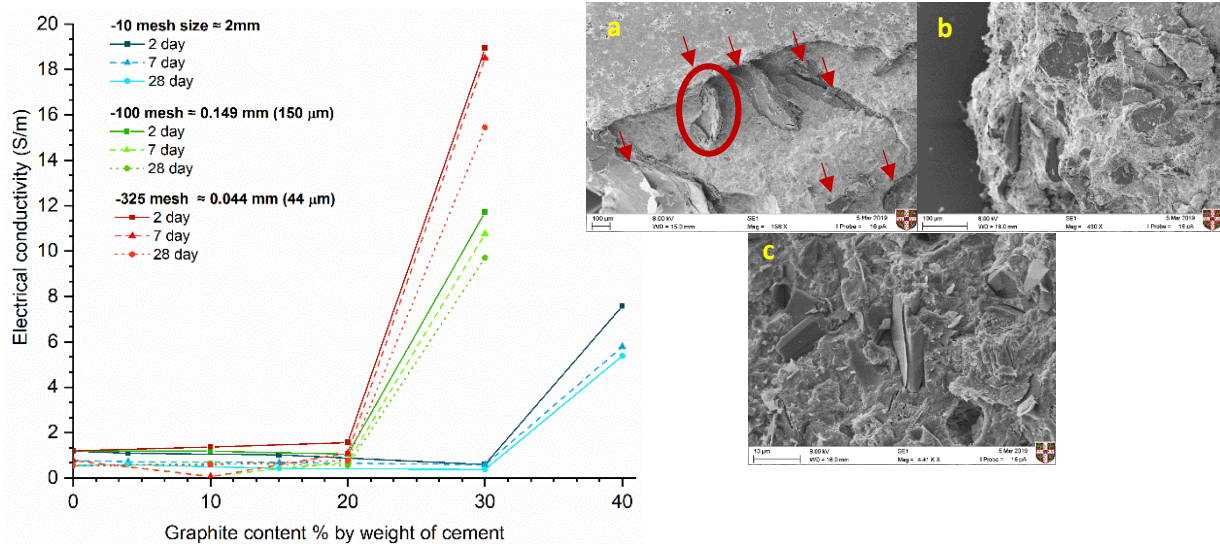


Figure 5: Electrical conductivity variation with age and graphite size (left) and SEM images of graphite in cement paste (w/c = 0.45) at 28 days of hydration, (a), AlfaAesar -10mesh (b) SigmaAldrich -100 mesh and (c) SigmaAldrich-325 mesh

However, the addition of natural graphite, has been found to affect some of the properties of cementitious composites. As shown in Figure 2 (left), for the very coarse graphite (AlfaAesar -10 mesh = 2 mm), rheology increased almost linearly with increasing dosage. As the graphite size became finer, the fluidity reduced dramatically. The viscosity at 10% graphite of size 0.15 mm was higher than that of 20% with the coarse (2 mm) graphite. As the graphite size reduced

to 0.044 mm, the paste became extremely stiff. At 20% dosage, it was very difficult to mix and therefore, the error is very high.

In terms of compressive strength, it was found that at all test ages, the samples with graphite addition have a lower compressive strength compared to the control. The coarsest graphite (-10mesh) produces the lowest strength, followed by the medium fineness (-100 mesh) and the finest graphite (-325 mesh). 20% graphite addition always reduces the strength more compared to 10% graphite addition, irrespective of graphite size. SigmaAldrich -325mesh (0.15 mm) at 10% dosage (by weight of cement) has been found to maintain the compressive strength the most, with only a 12% reduction at 28 days of testing.

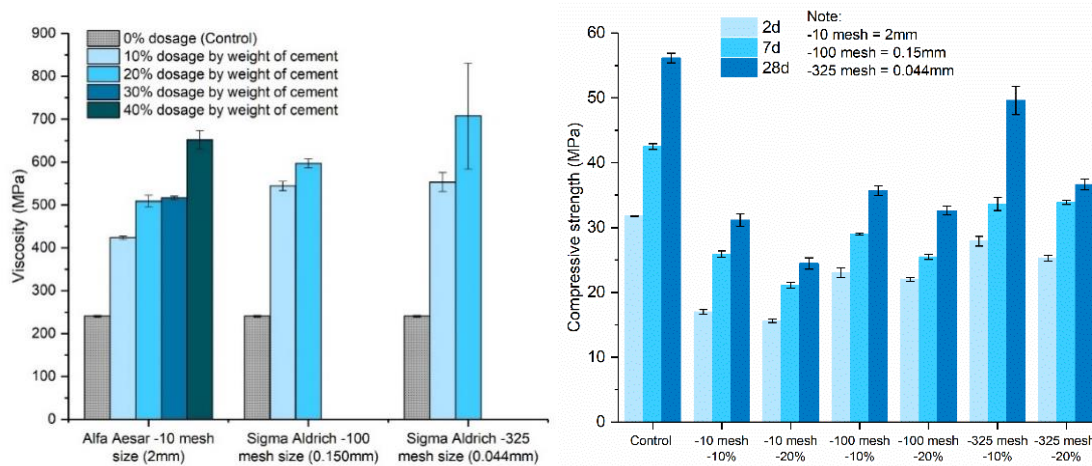


Figure 6: The effect of graphite size and dosage (by weight of cement) on the viscosity (left) and compressive strength of cement paste mixes (w/c = 0.45)

Overall, it is found that the finer graphite (44 μ m) results in a lower electrical conductivity percolation threshold compared to coarser graphite. With this graphite, the compressive strength is maintained the most compared to the control; however, the fluidity of the mix is compromised. GNPs, which are of even lower lateral size and higher electrical conductivity, are expected to reduce the percolation threshold even further whilst maintain the mechanical performance. However, as the size reduces further, the dispersion of the material becomes even more challenging. A previous study by the authors has shown that the use of a polycarboxylate superplasticiser is necessary to ensure sufficient mixing [6], which can in turn complicate the electrical conductivity performance. Nonetheless, the use of GNPs has been found to generate a conductive network whilst maintaining mechanical performance and improving some of the durability indicators.

From a lifecycle assessment perspective, the GNP production (of a product called G2NanPaste, supplied by Nanasa Ltd.) has been analysed and the results are shown in Figure 3. It is apparent that the greatest effect comes from the electricity consumption during the exfoliation and expansion of graphite, followed by thermal energy (heat) and the use of graphite as a raw material. The consumption of water appears to be negligible in the whole GNP manufacturing process. The production of 1 kg of CEM I corresponds to 0.86 kgCO₂eq whilst GNP production in this study has been found to correspond to only 0.17 kgCO₂eq.

The GNP incorporation in concrete was investigated next. A standard concrete mix design has been used as a base case to establish the baseline for this study and is then compared with the GNP-reinforced concrete mix.

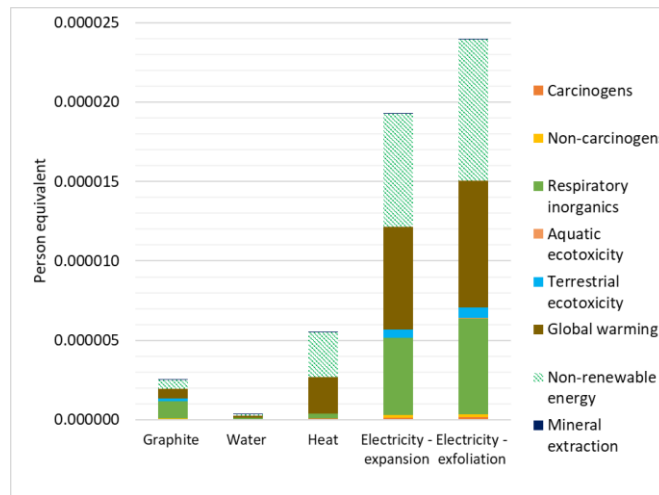


Figure 7: Normalized results in terms of impact (mid-point) categories of life cycle impact assessment of 1 kg of G2NanPaste production. Here and in the following figures the criteria for normalisation are per person equivalent units, where one-person equivalent represents the average global per capita annual average impact in the specific category [7]

From Figure 4 (left), it is evident that Portland cement (CEM I) is the largest contributor, followed by aggregates (sand and limestone as fine and coarse aggregate respectively). The use of water is found to have a negligible effect and the same applied to the electricity whilst GGBS has been considered as avoided impact. Global warming is found to be the largest mid-point impact category and the production of this specific 1m³ of concrete corresponds to 19.42 kgCO₂eq. The impact of global warming is followed by the consumption of non-renewable energy and respiratory inorganics. From Figure 4 (right), it is shown that even when GNPs are added in the mix, Portland cement remains the greatest contributor to overall impact followed by limestone and sand. Overall, the plasticiser is found to have a greater effect compared to G2NanPaste and its effect on the global warming it is 3.22 times that of the G2NanPaste whilst this increases to 6.13 times for respiratory inorganics. Portland Cement (CEM I) is 248 times more damaging than G2NanPaste in terms of global warming and 124 times more damaging in terms of respiratory inorganics (human health) for the specific concrete mix that was investigated.

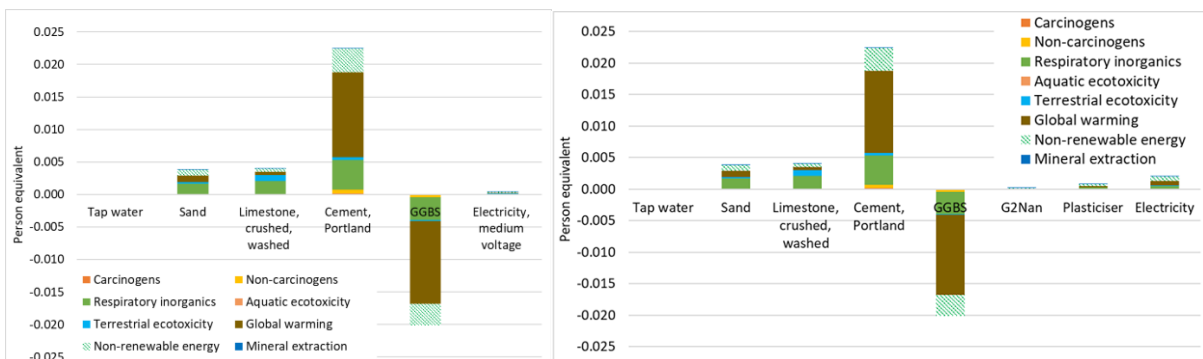


Figure 8: Normalized results in terms of impact (mid-point) categories of life cycle impact assessment of producing 1m³ of concrete for the base case (left) and for the GNP-reinforced concrete (right) [7]

Conclusion

Three graphite types of varying sizes have been tested and it was found that the finest graphite results in better mechanical properties compared to the rest and has the lowest percolation

threshold for electrical conductivity (therefore a lower dosage of graphite is needed). GNPs, which are of lower size and higher conductivity, can further reduce the percolation threshold whilst maintaining the mechanical performance. A lifecycle assessment (LCA) study showed that the production of 1 kg of G2NanPaste (GNPs product of the study) with Liquid Phase Exfoliation results in 0.17 kgCO₂eq which is less than the production of Portland cement (0.86 kgCO₂eq).

Acknowledgment

The authors would like to thank the Engineering and Physical Sciences Research Council (EPSRC Future Infrastructure and Built Environment (FIBE) Centre for Doctoral Training (CDT) Grant No. EP/L016095/1) and Costain Group for funding this research.

References

- [1] B. Han, X. Yu, and J. Ou, *Self-sensing concrete in smart structures*. Oxford: Elsevier Inc., 2014.
- [2] National Ready Mixed Concrete Association, "Concrete CO₂ Fact Sheet," NRMCA Publ. Number 2PCO₂, no. 2, p. 13, 2012.
- [3] British Standards Institution, "BS EN 196-1:2016 Methods of testing cement. Determination of strength." 2016.
- [4] ISO-14040, "Environmental Management- Life Cycle Assessment- Principles and Framework," Geneva, Switzerland, 2006.
- [5] O. Jolliet et al., "Impact 2002+: A new life cycle impact assessment methodology," *Int. J. Life Cycle Assess.*, vol. 8, no. 324, 2003.
- [6] I. Papanikolaou, C. Litina, and A. Al-Tabbaa, "A preliminary study into the effect of superplasticisers on the dispersion of graphene materials in cement," in *Proceedings of the 12th fib International PhD Symposium in Civil Engineering*, 2018.
- [7] I. Papanikolaou, N. Arena, and A. Al-Tabbaa, "Graphene nanoplatelet reinforced concrete for self-sensing structures – A lifecycle assessment perspective," *J. Clean. Prod.*, vol. 240, 2019.

Session 2A Biological Self-healing of soil and building materials

Chair: José Norambuena-Contreras

1243 *Zheng et al.* Healing depth of early age cracks in cement-based materials by microorganism

1177 *Theodoridou et al.* *Sporosarcina pasteurii* induced carbonate formation for repairing and preventing damage in existing stone masonry structures

1238 *Tezer et al.* Biologically modified minerals for self-healing cement-based mortars

1254 *Turner et al.* Calcite Biomineralisation for the Repair of Damaged Concrete

1194 *El-Mountassir et al.* Engineering Fungal Networks for Ground Improvement

Healing depth of early age cracks in cement-based materials by microorganism

Tianwen Zheng^{1, 2, 3, 4}, Chunxiang Qian^{1, 2, 3, 4}, Hengyi Zhou^{1, 2, 3, 4}

1: School of Materials Science and Engineering, Southeast University, Nanjing, 211189, China

2: Research Centre of Green Building and Construction Materials, Southeast University, Nanjing, 211189, China

3: Jiangsu Key Laboratory for Construction Materials, Southeast University, Nanjing, 211189, China

4: Key Lab of Microbial Bio-mineralization Technology, China Construction Materials Industry, Nanjing, 211189, China

Introduction

Concrete is the most widely used construction material in the world, its output was up to 2.5 billion m³ in 2019 in China. However, during its long service life and under the action of environment factors, cracking of concrete will be inevitable [1-2], which will affect the durability and bearing capacity of the concrete structure. In recent years, microbial induced calcium carbonate precipitation (MICP) has been developed to repair concrete cracks [3-5]. However, most research results showed that the healing depth in crack mouth was small. A self-healing method based on compound microorganisms was studied in the research in order to increase the healing depth of cracks.

Materials and methods

Microorganism

The microbial additive consisted of two kinds of bacteria, which had strong alkali resistance and could produce CaCO₃ by mineralization. Then spray drying was used to transform cells into spores. The spores were conserved in a refrigerator at 4°C.

Preparation of mortar samples

Mortar samples with the size of Φ100 mm × 50 mm were prepared by mixing sand, water, China P II 42.5 cement and microbial self-healing agent, which contained spores with 1.0 × 10¹⁰ CFU/g. The mix proportions are shown in Table 1. The samples were cured in standard curing room (RH = 90%, T = 20 ± 3 °C) for 7 d. The splitting method is used to make cracks between 0.20-0.30 mm. Subsequently, the samples were conducted dry-wet cycle healing. In each dry-wet cycle, the samples were placed in the water for 12 h and were then exposed to the air for 12 h. In addition, the healing temperature was maintained at 25 ± 2 °C, and the self-healing efficiency of samples was tested after 28 days healing time.

Table 1. Mix proportions of the mortar samples

Group	Cement (g)	Water (g)	Sand (g)	Spores (g)
Reference	500	250	1500	0
Microbial	500	250	1500	4

Characterization methods for self-healing efficiency

Image processing method

Using digital camera to take photos of cracks surface before and after healing, and Image-J was used to obtain the binary photograph and analyze the gray value. The area repair rate of samples can be calculated by Equation (1) [6]. Where A₀ is the number of crack area pixel dots before healing and A_t is the number of crack area pixel dots after healing.

$$\text{Area repair rate} = \frac{A_0 - A_t}{A_0} \times 100\% \quad (1)$$

Water permeability testing method

Permeability coefficient of cylinder samples before and after healing could be calculated according to Darcy's Law shown in Equation (2) [7]. Where k is permeability coefficient, m/s; Q is amount of water flow, m³/s; L is height of sample, m; A is area of section, m²; Δh is head difference, m.

$$k = Q \cdot L/A \cdot \Delta h \quad (2)$$

The depth of the cracks repaired

The repaired sample was broken along the crack mouth, and then the distribution of mineralization products at different depths (along the Z direction of crack) at the cross section was analyzed by stereo microscope. The schematic diagram is shown in Figure 1.

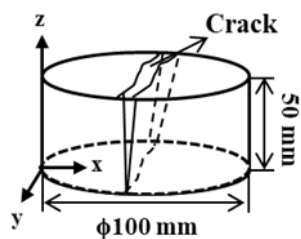


Figure 1. Schematic diagram of cracking sample

Characterization of precipitations at the crack mouth

The precipitation produced on the surfaces of the samples was analyzed by Scanning Electron Microscope (SEM) equipped with an Energy Dispersive X-ray Spectrometer (EDS), and then examined by X-ray Diffraction (XRD).

Results and discussion

Area repairing rate

Figure 2 shows the repair of crack within different healing time. It can be seen that with the increase of healing time, the crack was gradually filled with white precipitations. The crack of microbial group was mostly repaired after 28 days, and the area repair rate could reach 98.2%. While the reference group was hardly repaired, and the area repair rate was only 3.6% (Figure 3), which was mainly due to the late hydration of cement particles.

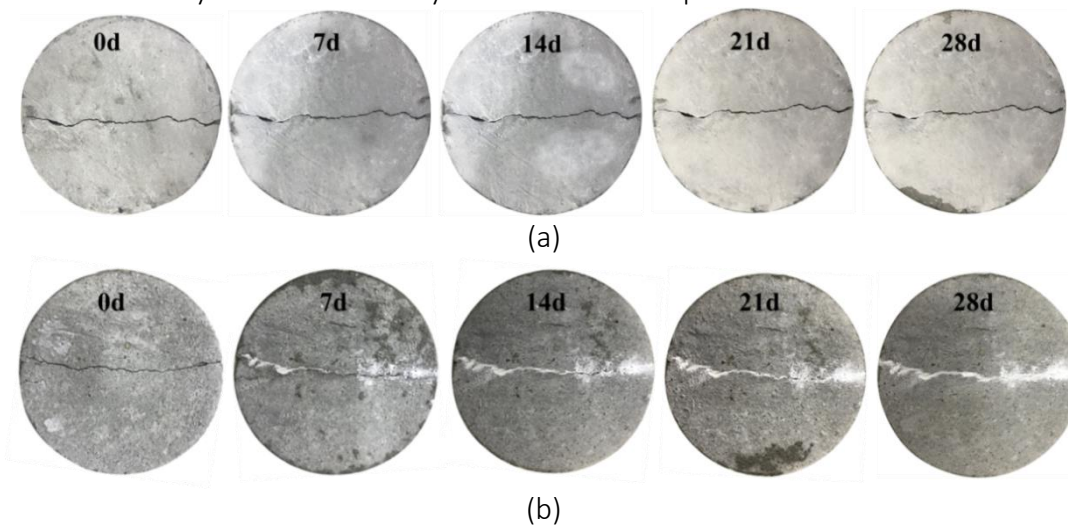


Figure 2. Surface image of crack before and after different healing time, (a) reference, (b) microbial

Permeability coefficient

Figure 4 shows the permeability coefficient calculated according to Darcy's law. It can be seen that with the increase of healing time, the permeability coefficient of the reference group remained unchanged. While the permeability coefficient of the microbial group was significantly reduced by two orders of magnitude. Comparing with the reference group, the water permeability resistance of the microbial group was greatly improved.

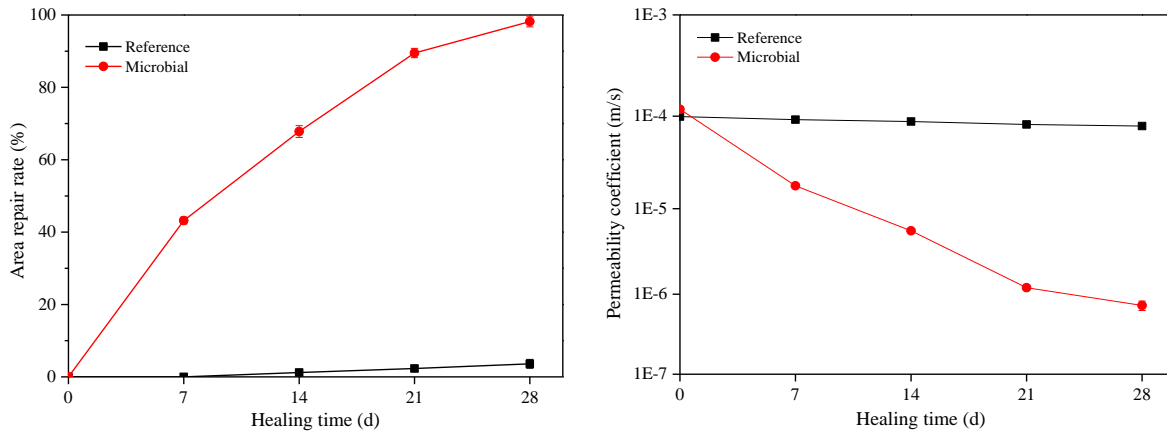


Figure 3. Area repair rate of samples Figure 4. Permeability coefficient of samples

Depth of repair

Figure 5 is the distribution of mineralization products at the crack mouth of microbial group observed by stereo microscope. It can be seen that the cracks of different depth were full of white precipitations. With the increase of crack depth, the white precipitations gradually reduced. The average repair depth of cracks was around 8.0 mm (Figure 6).

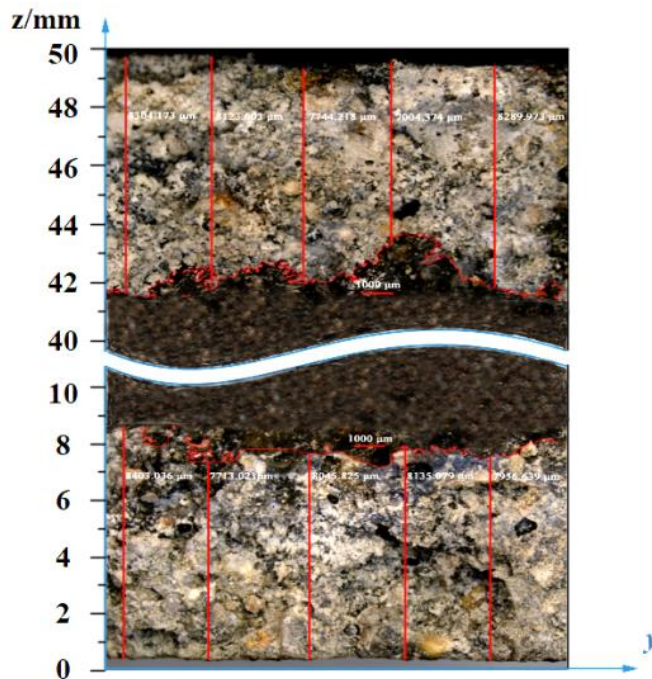


Figure 5. Images of repair depth of crack in the microbial group sample after healing 28 days

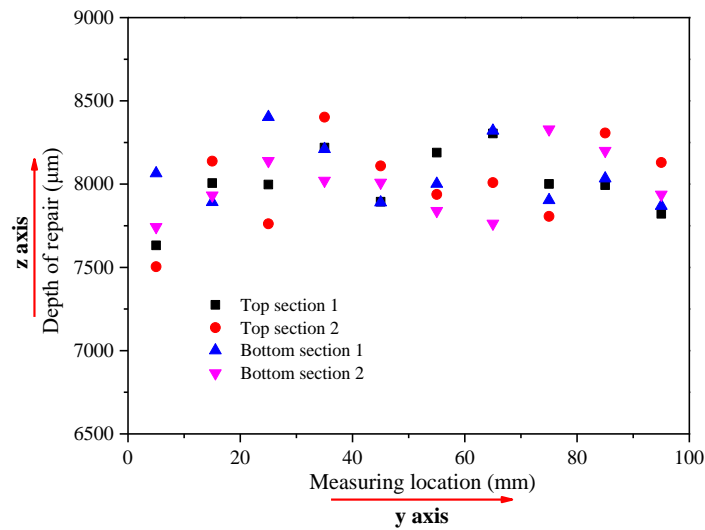


Figure 6. Depth of repair at different measuring locations after healing 28 days

Morphology and component of crack fillers

Figure 7 (a) shows the SEM images of crack fillers of the microbial sample. It can be seen that the crystallized products were irregular massive particles formed by the accumulation of small particles. According to the EDS (Figure 7 (b)) and XRD (Figure 8) analysis, the products were CaCO₃ in the form of calcite.

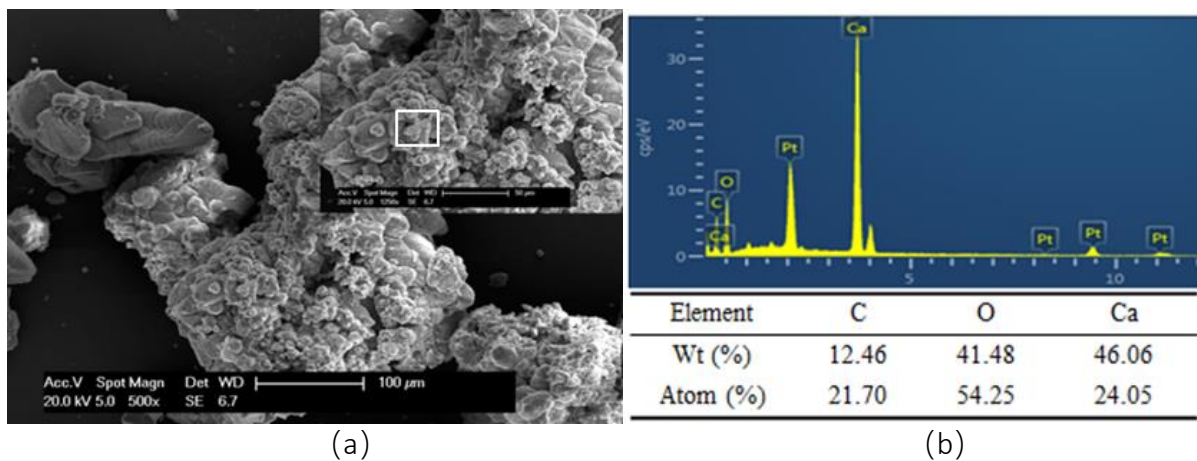


Figure 7. Precipitates at the crack mouth in the microbial samples after healing 28 days, (a) SEM micrograph, (b) Energy spectrum analysis

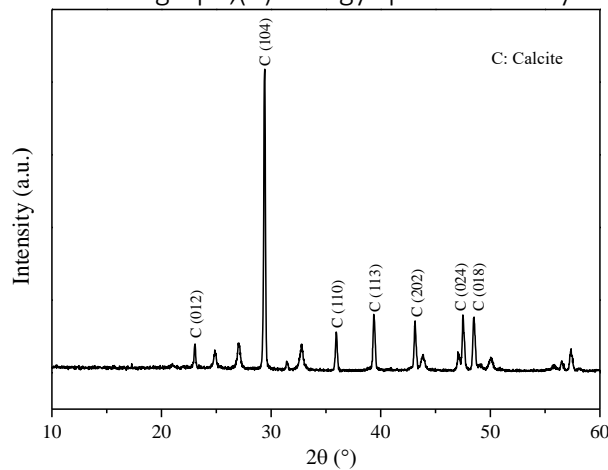


Figure 8. XRD analysis of precipitates at the crack zone after healing 28 days

Conclusion

(1) Compared with the reference group, the cracks between 0.2 - 0.3 mm of cement-based materials could be mostly repaired after healing 28 days by adding microorganism. The area repair rate on surface of cracks was up to 98.2%, and the permeability coefficient was reduced by two orders of magnitude.

(2) The repair depth of the cracks in the microbial sample was greatly improved, and the average repair depth was 8.0 mm. The results show that the precipitates at the crack mouth were calcite CaCO_3 with irregular morphology.

Acknowledgment

The financial help of the National Nature Science Foundation of China (Grant No. 51738003) is gratefully acknowledged.

References

- [1] Li W T, Dong B Q, Yang Z X, et al. Recent Advances in Intrinsic Self-Healing Cementitious Materials[J]. *Advanced Materials*, 2018:1705679.
- [2] Joshi S, Goyal S, Mukherjee A, et al. Microbial healing of cracks in concrete: a review[J]. *Journal of Industrial Microbiology & Biotechnology*, 2017, 44(11):1-15.
- [3] Ramachandran S K, Ramakrishnan V, Bang S S. Remediation of concrete using micro-organisms [J]. *ACI Materials Journal*, 2001, 98(1): 3-9.
- [4] Jonkers H M, Thijssen A, Muyzer G, et al. Application of bacteria as self-healing agent for the development of sustainable concrete[J]. *Ecological Engineering*, 2010, 36(2):230-235.
- [5] Qian C X, Ren L F, Xue B, et al. Bio-mineralization on cement-based materials consuming CO_2 from atmosphere[J]. *Construction and Building Materials*, 2016. 106:126-132.
- [6] Luo M, Qian C X. Performance of two bacteria-based additives used for self-healing concrete [J]. *Journal of Materials in Civil Engineering*, 2016,28 (12): 04016151.
- [7] Chen H C, Qian C X, Huang H L. Self-healing cementitious materials based on bacteria and nutrients immobilized respectively[J]. *Construction and Building Materials*, 2016, 126(15):297-303.

Sporosarcina pasteurii induced carbonate formation for repairing and preventing damage in existing stone masonry structures

Magdalini Theodoridou¹, Oana Adriana Cuzman², Piero Tiano², Brunella Perito³, Michael Harbottle⁴

1: Hub for Biotechnology in the Built Environment, School of Engineering, Newcastle University, Newcastle Upon Tyne NE1 7RU, UK

2: Institute for Heritage Science, National Council of Research–ISPC-CNR, Via Madonna del Piano 10, Sesto Fiorentino 50019, Italy

3: Department of Biology, University of Florence, Via Madonna del Piano 6, Sesto Fiorentino 50019, Italy

4: School of Engineering, Cardiff University, Cardiff CF24 3AA, UK

Abstract

Natural stone is one of the most widely used geological construction materials. Although stone masonry structures have the potential to survive over centuries, they may be subject to significant damage and deterioration. Various conservation treatments have been explored for modifying the characteristics of stone, often in the layer closer to the surface. However, treatments may limit the breathability of the material triggering further damage.

This work studies microbially induced carbonate precipitation by bacteria as a breathable alternative for the protection of building stone from deterioration. The mineralogical composition and pore structure of most stone types used in construction are favourable for the growth of bacterial communities, while calcium carbonate as the healing product is highly compatible with the substrate.

A protocol for the application and assessment of biological healing was determined, taking into consideration the specific needs of bulk materials and existing structures. *Sporosarcina pasteurii*, an aerobic, ureolytic bacterium, was applied to two different types of stone: i) a massive calcitic chalk from Cyprus, popularly called Lympia stone, ii) a dolomitic limestone from Italy, popularly known as Pietra d'Angera. The healing effect of the newly formed minerals was determined and compared to reference samples by recording changes in water absorption and drilling resistance, as well as by means of SEM/EDS and confocal microscopy on calcein stained samples. The results demonstrated that *Sporosarcina pasteurii* induced sufficient cementation in the near surface region of the specimens to an extent that could be considered protective, yet compatible with the natural properties of the materials.

Introduction

Geological materials comprise most cultural heritage building materials worldwide. However, they are subject to damage and deterioration [e.g., 1-2]. Surface treatments [3] may reduce the 'breathability' of the material and can be limited to specific stones [4].

Biological methods of strengthening a range of materials can be found in the literature [e.g., 5-9]. However, self-healing concepts have yet to be explored for building stones in construction. This work investigates the potential for providing building stone with a system that could heal damage and prevent further deterioration. Taking the advantage of the stones' bioreceptivity and suitability for biomineralisation, the system developed in this study is based on the use of naturally occurring biological mechanisms, which can induce calcium carbonate precipitation. *Sporosarcina pasteurii*, one of the most commonly used microorganisms in biocementation of particulate media [10-12], has been selected for this study. This paper discusses the potential of biological systems to change the microstructure of porous natural stone in order to increase resilience to deterioration.

Materials and methods

Lympia stone, a massive chalk from Cyprus (>99% calcite), was chosen as the model rock for this study due to its relatively homogeneous microstructure and mineral composition [13]. Angera stone, a dolomitic limestone from Italy [14], was also added the investigation as a substrate of different mineralogical composition (>98% dolomite) compared to the healing products (CaCO₃).

Lympia stone specimens (2×2×2 cm) were divided in three groups (i.e., A, B, C), while one more group (D) was added in the study of Angera specimens (Table 1); group A was treated in aseptic conditions with a *Sporosarcina pasteurii* bacteria solution (NCIMB 8221, UK) and cementation medium (per litre of water: 3 g nutrient broth CM0001-Oxoid, UK, 10 g NH₄Cl, 2.12 g NaHCO₃, 22.053 g CaCl₂ · 2H₂O, 20 g urea), group B was treated only with cementation medium (aseptic), group C only with water and group D with dead bacteria and cementation medium (aseptic). Groups A, B and D were treated two more times with cementation medium, while group C was only supplied with water. The specimens were stored at 30 °C during all healing stages.

Table 1: Groups of specimens

group	Bacteria	Cementation medium	Water
A	+ (living cells)	+	-
B	-	+	-
C	-	-	+
D	+ (dead cells)	+	-

The efficiency of the treatments was assessed through the implementation of various tests and analysis; here we present indicative results/observations from (i) water absorption measurements by capillary action (i.e., mass changes at different time intervals), (ii) micro-drilling resistance measurements (DRMS by SINT Technology) [15], (iii) the use of SEM/EDS (GAIA 3 TESCAN), (iv) the use of confocal microscopy (LEICA TCS SP5) on calcein stained specimens, (v) the use of colourimetry (MINOLTA CM 700D) and the determination of colour changes according to the CIELAB 1976 system.

Results and discussion

Indicative results of the capillary absorption tests are presented in Table 2, where a decrease of 5.68% in capillary absorption was observed for the Lympia specimens treated with *S. pasteurii* (group A), while no significant change is observed in the cases of group B and C. This result proves the potential of the treatment to change the microstructure of the specimens in a promising way which can prohibit deterioration related to water transport.

Table 2: Indicative decrease in capillary absorption (average values) after treatment on one of the stone types (Lympia stone). Negative values correspond to increase in capillary absorption. All measurements took place after 40 mins (Δ CA40 %) of partial immersion in deionised water.

group	Average Δ CA40 (%)	Standard deviation
<i>Lympia stone</i>		
A	5.68	0.63
B	-0.14	0.22
C	-1.00	0.18

The drilling profiles of *Lympia* specimens showed a clear peak of higher resistance to drilling in the case of group A (data not shown). This agrees well with the capillary absorption results shown in Table 2 and it can be attributed to the effective consolidation of the material in the area close to the treated surface. No similar peak was recorded for the specimens of group B and C.

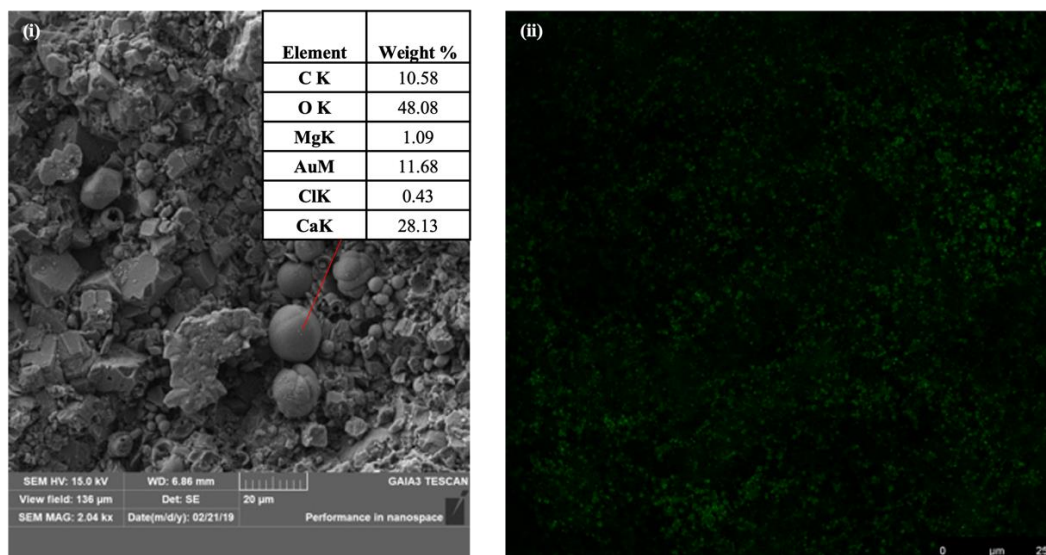


Figure 1: (i) SEM/EDS and (ii) confocal microscopy evidence of new CaCO_3 formation on a stone specimen (Angera type) treated with bacteria and nutrients (group A).

The determination of the changes in the chromatic components is reported in Table 3. The overall colour changes (ΔE^*_{ab}) of the specimens treated with bacteria and/or cementation medium compared to the relevant group C values, are equal to less than 3, which is the value under which the average human eye cannot detect colour differences (Tiano et al. 2006). Therefore, the biological treatments performed in this study may be considered that they do not cause any aesthetic change on the surface of the treated materials.

Table 3: Chromatic coordinates of the surface of all specimens after treatment. Δ values for groups A, B and D were calculated in comparison with the relevant groups C.

group	ΔL^*	Δa^*	Δb^*	ΔE^*_{ab}
<i>Lympia stone</i>				
A	-0.73	0.26	1.93	2.07
B	0.08	0.79	1.07	1.33
<i>Angera stone</i>				
A	-0.31	0.11	0.54	0.63
B	0.24	0.08	-0.05	0.25
D	0.11	-0.13	-1.01	1.02

Conclusion

This work presents the application and evaluation of biological treatments in natural building stone using the bacteria strain *Sporosarcina pasteurii*. *S. pasteurii* induced significant differences in the microstructure of laboratory stone specimens, which is proved by the decrease in capillary absorption, increase in drilling resistance, microscopic observations and elemental analyses. Sufficient supply of nutrients and the use of living cells was found to be the treatment that better promoted healing in both stone types. Dead cells with nutrients also

led to new formation of CaCO₃, however further research and optimisation of the treatment is needed. None of the biological treatments performed in this study was found to cause colour alterations that can be detected by the average human eye.

Acknowledgment

This project has received funding from the European Union's Horizon 2020 research and innovation programme under the Marie Skłodowska-Curie grant agreement No 745891, the Engineering and Physical Sciences Research Council (EPSRC), grant number EP/P02081X/1 and from Research England and The Hub for Biotechnology in the Built Environment (E3 Fund), Newcastle University. The help of Dr Giada Magni (IFAC-CNR Florence) is acknowledged for the use of confocal microscopy.

References

- [1] Amoroso GG, Fassina V. 1983. *Stone decay and conservation*. Elsevier, Amsterdam 453p.
- [2] Theodoridou M, Török Á. 2019. In situ investigation of stone heritage sites for conservation purposes: a case study of the Székesfehérvár Ruin Garden in Hungary. *Progress Earth Plan Sci* 6:15.
- [3] Pinna D, Salvadori B, Porcinai S. 2011. Evaluation of the application conditions of artificial protection treatments on salt-laden limestones and marble. *Const Build Mater* 25: 2723-2732.
- [4] Maravelaki-Kalaitzaki P, Kallithrakas-Kontos N, Agioutantis Z, Maurigiannakis S, Korakaki D. 2008. A comparative study of porous limestones treated with silicon-based strengthening agents. *Prog org Coat* 62:49-60.
- [5] Perito B, Marvasi M, Barabesi C, Mastromei G, Bracci S, Vendrell M, Tiano P. 2014. A *Bacillus subtilis* cell fraction (BCF) inducing calcium carbonate precipitation: Biotechnological perspectives for monumental stone reinforcement. *J Cult Herit* 15: 345-351.
- [6] Jroundi F, Gómez-Suaga P, Jimenez-Lopez C, González-Muñoz MT, Fernandez-Vivas MA. 2012. Stone-isolated carbonatogenic bacteria as inoculants in bioconsolidation treatments for historical limestone. *Sci Tot Envir* 425:89-98.
- Tiano P, Cantisani E, Sutherland I, Paget JM. 2006. Biomediated reinforcement of weathered calcareous stones. *J Cult Herit* 7: 49-55.
- [7] De Muynck W, De Belie N, Verstraete W. 2010. Microbial carbonate precipitation in construction materials: A review. *Ecol Eng* 36:118-136.
- [8] Le Métayer-Levrela G, Castaniera G, Oriol J, Floubière J, Perthuisot P. 1999. Applications of bacterial carbonatogenesis to the protection and regeneration of limestones in buildings and historic patrimony. *Sediment Geol* 14:25-34.
- [9] Van Tittelboom K, De Belie N, De Muynck W. 2010. Use of bacteria to repair cracks in concrete. *Cement Concrete Res* 40: 157-166.
- [10] Botusharova S, Gardner D, Harbottle M. 2020. Augmenting Microbially Induced Carbonate Precipitation of Soil with the Capability to Self-Heal. *J Geotech Geoenviron Eng* 146(4): 04020010.
- [11] Harbottle, M, Lam MT, Botusharova SP, Gardner DR. 2014. Self-healing soil: Biomimetic engineering of geotechnical structures to respond to damage. In: *Proc. 7th Int. Congress on Environmental Geotechnics*, edited by A Bouazza, S Yuen and B Brown, Melbourne, Australia: Engineers Australia, 1121–1128.
- [12] Montoya BM, DeJong JT. 2013. Healing of biologically induced cemented sands. *Geotech Lett* 3 (3): 147–151.
- Botusharova SP. 2017. *Self-healing geotechnical structures via microbial action*. PhD thesis, School of Engineering, Cardiff University.
- [13] Modestou S, Theodoridou M, Fournari R, Ioannou I. 2016. Physico-mechanical properties and durability performance of natural building and decorative carbonate stones from Cyprus. In: *Sustainable Use of Traditional Geomaterials in Construction Practice*, edited by R Pšikryl, Á Török, M Gómez-Heras, KnMiskovsky and M Theodoridou, London: Geological Society, Special Publications, 416, pp. 145-163.
- [14] Alessandrini G. et al. La Ca' Granda di Milano. L'intervento conservativo sul cortile richiniano. Milano, Silvana Editoriale, 1993.
- [15] Theodoridou M, Dagrain F, Ioannou I. 2015. Micro-destructive cutting techniques for the characterization of natural limestone. *Int J Rock Mech Min Scie* 76: 98-103.
- [16] Tiano P, Cantisani E, Sutherland I, Paget JM. 2006. Biomediated reinforcement of weathered calcareous stones. *J Cult Herit* 7: 49-55.

Biologically modified minerals for self-healing cement-based mortars

Mustafa Mert Tezer¹, Ilgin Sandalci¹, Zeynep Basaran Bundur¹

1: Department of Civil Engineering, Ozyegin University, Cekmekoy, Istanbul, TR

2: Faculty of Bioscience Engineering, Ghent University, Ghent, Belgium

Abstract

While concrete is a widely used building material, microcracks occurring during casting and placing could be a major drawback in applications. Limited research on biomineralization in cement-based systems suggested that self-healing of surface cracks could be obtained by triggering biogenic calcium carbonate precipitation within the cracks. While this is encouraging, studies continue to improve the extend of the possible applications of the biomineralization. Recent studies suggested that natural minerals could be used as protective barriers, which might increase the efficiency of self-healing. This paper summarizes a study undertaken to investigate the self-healing efficiency of *Sporosarcina pasteurii* (*S. pasteurii*) cells immobilized on different natural minerals such as diatomaceous earth, bentonite and metakaolin to remediate flexural cracks on mortar in early ages (7 and 28 days). To obtain a 2-phase bio-mineral additive, half of the minerals were saturated with a nutrient medium consisting of urea, corn steep liqueur and calcium acetate, while the bacterial cells were immobilized to the other half of the minerals without nutrients. Evaluation of the healing process was done with stereomicroscopy and water absorption tests. With this approach, the cracks on mortar surface were sealed and the water absorption capacity of the so-called self-healed mortar decreased compared to its counterpart cracked mortar samples. Complimentary Scanning electron microscope (SEM) analysis revealed that the cracks were sealed by calcium carbonate.

Introduction

Despite its negative perception in society, concrete is still the most used building material in the construction sector. Nevertheless, early age cracks occurring in concrete can decrease the strength of the materials and limit the service life of the concrete structures. Recent studied in the field showed that it might be possible to develop a bio-based self-healing system where bacterial cells are being used to remediate cracks by triggering microbial induced calcium carbonate precipitation (MICP) within very narrow microcracks [1–3]. The main challenge of the application is to find a microorganism that can tolerate highly alkaline conditions of cement paste, can survive the mixing process and can remain viable with limited access to nutrients [4]. A simple approach is adding the vegetative bacterial cells directly to the mix. Previously, Bundur et al.[5] showed that vegetative *Sporosarcina pasteurii* cells could survive in mortar up to 11 months when they were added to the mix without any encapsulations. These remaining cells were found to be effective in remediation of the microstructure when internal microcracks[6] and flexural surface cracks in 7-day old samples [7]. However, limited viability and lack of O₂ decreased the performance of CaCO₃ yield through all crack the depth [7]. Concerns regarding the viability of the cells and limited crack healing led researchers to propose various encapsulation methodologies. The encapsulation methods consist of embedding the endospores in a protective covering, e.g. inorganic lightweight porous aggregates (LWAs)[8], polymeric membrane [9,10], microcapsules [11], hydrogels [12], and natural minerals [13,14]. Instead of using synthetic encapsulation covering, a more sustainable approach could be achieved by using natural additives or natural lightweight aggregates. Throughout the literature, studies showed that among several alternatives such as diatomaceous earth (DE), metakaolin, zeolites, and expanded clay could be suitable for the

protection of the bacteria based on their effects on compressive strength and setting, in particular, DE was found to be effective in self-healing of cracks [14,15]. To achieve effective self-healing in cement-based materials, an appropriate protection barrier should be chosen along with a correct application methodology.

This paper summarizes a study undertaken to investigate the self-healing efficiency of *S. pasteurii* cells immobilized on different natural minerals such as DE and bentonite to remediate flexural cracks on mortar in 28 days.

Materials and methods

Microorganism Selection and Growth

A urease-enzyme active, endospore-forming *S. pasteurii* (Leibniz Institute- German Collection of Microorganisms and Cell Cultures DSMZ 33) cells were selected as a self-healing agent. *S. pasteurii* cells were grown in a Urea-corn steep liqueur (CSL)-sodium acetate nutrient medium (UCSL) which includes tris base (0.13M), CSL (15 g), sodium acetate (10g) and urea (20 g) per litre of distilled (DI) water. The pH of the medium was adjusted to 9. The cells were incubated aerobically in a sterilized liquid medium with shaking conditions (175 rpm) at 30°C until the stationary phase (10^9 CFU/mL) was reached. Then, the cells were collected from the culture by centrifuging at 6300g for 15 min. The cells were washed twice by PBS (Phosphate buffered solution) and stored at 4°C until immobilizing.

Material selection

Throughout the study, DE and bentonite were used to immobilize the bacterial cells. The average particle sizes of DE, bentonite, and cement were determined as 19.20, 22.1, and 23.2 μm , respectively. In particular, the immobilization procedure was achieved by submerging the barriers to an aqueous medium for 24 hours, thus the *so-called* absorption capacity of the minerals could be specified as 24-hour absorption capacity. The *24-hour water absorption capacity* by weight for DE and bentonite was found to be 110% and 300%, respectively. Besides the additions or replacements, mortar samples were prepared using OPC CEM I 42.5R and standard sand accordingly to the norm EN 196-1. A polycarboxylate superplasticizer was used to maintain the same workability criterion for all samples. The water to cement ratio (w/c) was kept at 0.45. While the dry mineral content was 5% (w/w) of cement weight, the total biological self-healing agent content including cells and the aqueous solution was used calculated as 10% (w/w) and 15% (w/w) for DE and bentonite, respectively. This difference was mainly due to the different absorption capacities of these minerals affecting the weight of the absorbed solution.

Immobilization procedure

To immobilize the cells on minerals, 1 gram of viable *S. pasteurii* cells were collected and they were resuspended in a sterilized 45 mL PBS solution. Then, 11.25 g of the mineral was added to the suspension. Then, the other half of the minerals (11.25) were submerged in a 45 mL nutrient medium (UCSLC) including of urea (20g/L), CSL (10g/L), and calcium acetate 10g/L. Immobilization was achieved with shaking conditions (175 rpm) at 30°C for 24 hours. Then, the slurry was removed from incubation and kept at 40°C in an oven for an additional 12 hours. Excess moisture content was calculated by subtracting the known weight of minerals, bacterial cells, and theoretical absorbed aqueous content from the final weight of oven-dry slurry. This value was subtracted from the mixing water content. To evaluate if the immobilization was achieved, the morphology of the DE and bentonite were evaluated before and after treatment by an FEI-Philips XL30 Environmental SEM with Field Emission Gun (FEG). Figure 1 shows the SEM images obtained before and after the immobilization procedure.

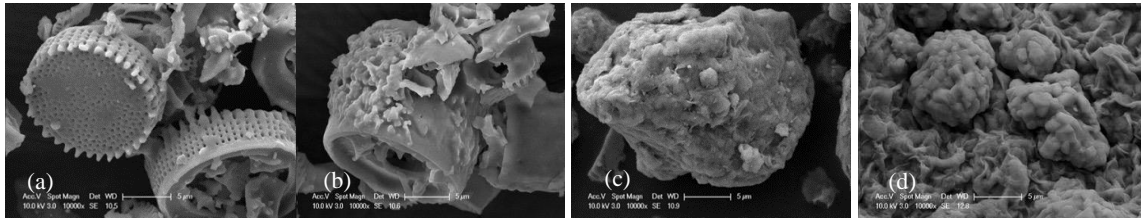


Figure 1. Morphology of minerals before and after immobilization: (a) diatomaceous earth before immobilization; (b) diatomaceous earth after immobilization; (c) bentonite before immobilization; (d) bentonite after immobilization. Scale: 5 μm

Crack formation and evaluation of self-healing

Mortar samples were prepared based on ASTM C305-14 [16]. Samples were made with a water to cement ratio (w/c) of 0.45 and a sand-to-cement ratio of 3. The mortar samples were then cast into 40 x 40 x 160 mm molds and kept in a humid environment at 21°C for 24 h. Then the molds were removed, and the samples were further cured in a moist environment until testing (22°C). To provide flexural resistance during crack initiation, 12-mm micro synthetic fiber were added to mortar (4 g/m³ of mortar). A polycarboxylate ether (PCE)-based superplasticizer was used to maintain the required workability of mortars. Samples containing *S. pasteurii* cells immobilized on DE were noted as *DE-2P* and samples containing cells immobilized on bentonite were noted *BT-2P*. Twenty-eight days after mixing, the samples were removed from the curing environment and cracked under flexural loading using a servo-hydraulic displacement-controlled device (0.05 mm/sec). Upon unloading, the remaining crack width was determined as 0.35 mm. Once the cracks were formed a set of cracked samples were treated in water and another set was treated in UCSLC nutrient medium. The treatment process for healing was done by submerging the samples into curing solutions for 2-days and then, subsequently leaving them at ambient conditions for 2 days. This “2- days period” treatment process was applied until at least 90% crack sealing was observed. To investigate the self-healing in cement-based mortar, cracked beams were periodically observed under NIKON Inc. SMZ745T Stereomicroscope. Complementary quantification was done by calculating water absorption capacity (RILEM 25 PEM II-6) of the beams were evaluated with respect to RILEM morphology of the precipitate was analyzed with an FEI-Philips XL30 ESEM with FEG.

Results and discussion

Visual evaluation of self-healing

Upon 28 days of solution (or water) treatment, the cracks were visually sealed in specimens containing bacterial cells (*DE-2P* and *BT-2P*) when additional nutrients were provided during the treatment. There was not any visual crack closure in control samples without any bacterial cells and the samples containing cells but rather kept in water. Since the visual crack healing was almost the same for each set, one representative image of series with 28-day old samples containing bacterial cells is shown in Figure 2.

Based on the visual crack evaluation, both minerals were found to be effective in terms of immobilizing the bacterial cells and trigger self-healing. The possible mechanism of these minerals could be attributed to their relatively high capacity to absorb and hold bacterial cells on the surfaces. This was attributed to its relatively higher absorption capacity and high specific surface area of these minerals which could enable a more homogenous distribution. A critical point of the results obtained is the importance of nutrients for self-healing. As abovementioned crack healing was observed in any sample containing bacterial cells when they were cured in the nutrient medium. Results showed that cells require additional nutrient source as urea and calcium acetate either in the mix or externally in treatment solution

regardless of the type of the immobilization barrier. Besides, the cracks were sealed faster in samples containing bentonite than that of in samples prepared with DE. While full crack sealing in *DE-2P* samples could only be achieved in 28 days, this duration was 14 days in *BT-2P* samples. This might be attributed to the autogenous healing effect of bentonite by itself. Suleiman et al. [17] showed that partial crack healing was observed in concrete samples containing bentonite in 1 year. Thus, the incorporation of bentonite with bacterial cells significantly improved the rate of crack remediation compared to the cases where these 2 agents were used separately [17].

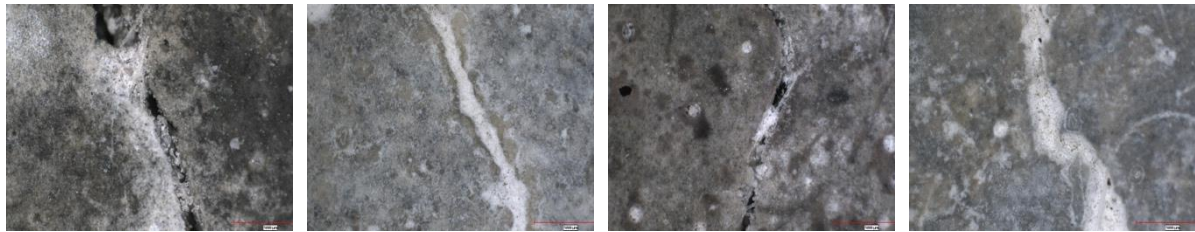


Figure 2. Stereomicroscopy images of the cracks (0.3 to 0.4 μm) induced in 28-day old specimens (a) *DE-2P* after 28-days of water treatment (b) *DE-2P* after 28-days nutrient treatment (c) *BT-2P* after 21 days of water treatment and (d) *BT-2P* after 21 days nutrient treatment.

Figure 3 shows the SEM images obtained from the crack surface area in *DE-2P* and *BT-2P* samples in which crack healing was observed. The precipitates were collected from the cracked surface after the water absorption test. In fact, upon fracturing the beams from the cracking, it was found that precipitation was found to be distributed through the crack depth not particularly at the edges (*data not shown*). Crystals of aragonite and calcite were found formation were observed in the *DE-2P* sample. Similarly, SEM analysis showed that calcite and vaterite was the dominant crystal within the cracks of *BT-2P* sample. Also, there were rod-shaped indications of bacterial cells (showed with red arrows). SEM images revealed that the bacterial cells were immobilized in bentonite and triggered MICP when cracks were induced.

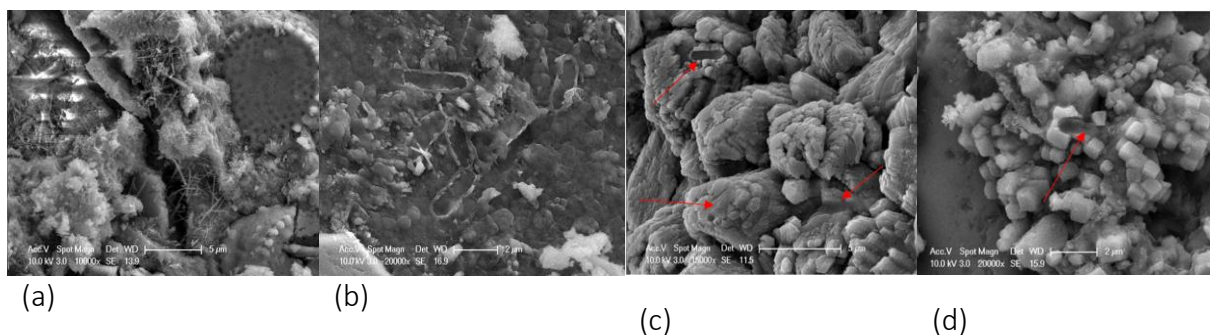


Figure 3. SEM images of the crack surfaces in (a) and (b) *DE-2P* samples after 28 days of UCSLC medium treatment, (c) and (d) *BT-2P* samples after 21 days of UCSLC medium treatment. Red arrows highlighting the indications of the possible presence of *S. pasteurii* treatment.

Change in water absorption

Figure 4 below summarizes the water absorption coefficients, k , obtained from the test. Samples containing DE (*DE-C* and *DE-2P*) showed consistent results with the visual inspection. There was approximately a 50% decrease in k -value in *DE-2P* samples compared to their

counterpart control DE-C samples, regardless of the treatment regime. Relatedly, there was a considerable improvement in k value (almost 50 %) in 28 days cracked DE-2P sample kept in water compared to its counterpart control sample DE-C kept in water. This is slightly inconsistent with the visual inspection result where there was only a partial precipitate observed around the crack mouth. This might indicate that the healing process in this sample yield through the crack depth rather than the crack mouth. Even though the cracks were sealed in BT-2P samples, the water absorption coefficient was found to be higher than their counterpart control BT-C samples. One sound explanation for this is the inconsistent trend in water absorption of samples containing bentonite. This could be again related to the high absorption capacity of the mineral leading to an experimental error due to the use of paraffin. Even though the absorption capacity of bentonite was recorded as 300% for 24 hours, extended saturation might lead to a higher degree of absorption capacity.

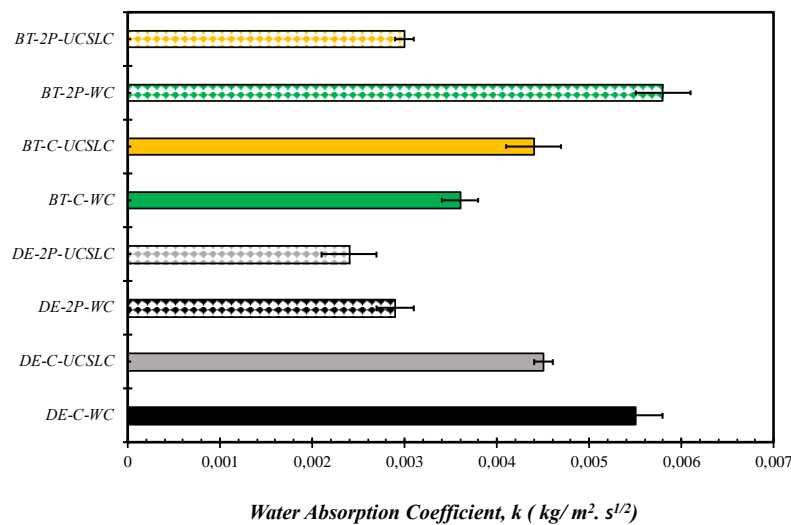


Figure 4. Water absorption coefficient, k after crack healing. DE: Diatomaceous earth; BT: bentonite; 2P:2-Phase; WC: Water curing; UCSLC: Urea-CSL and calcium acetate nutrient medium curing.

Conclusion

This study was undertaken to investigate the use of diatomaceous earth and bentonite as protective barriers for bacterial cells to trigger self-healing of cracks. Our study showed that both minerals could be used to immobilize *S. pasteurii* cells. Visual evaluation and water absorption test also showed that this methodology could be used as a self-healing methodology for flexural cracks as large as 0.4 mm. Complete crack sealing was observed in all samples containing bacterial cells when the nutrient medium was provided. Besides, SEM results revealed mostly calcite and vaterite precipitation in BT-2P samples, while ACC was found in cracks in DE-2P samples. The mineral precipitation was through the crack depth rather than only occurring at the crack mouth. Upon crack healing, samples containing DE showed a higher degree of improvement in water absorption compared to samples containing bentonite.

Acknowledgment

This research was conducted by financial assistance of the Scientific and Technical Research Council (TUBITAK) of Turkey Project: MAG-118M327. SEM analysis was conducted in Advanced Technologies Research and Development Center facilities of Bogazici University, Istanbul. The authors graciously acknowledge Dr.Bilge Gedik Uluocak for her assistance during the analysis.

References

- [1] W. De Muynck, N. De Belie, W. Verstraete, Microbial carbonate precipitation in construction materials : A review, *Ecol. Eng.* 36 (2010) 118–136. doi:10.1016/j.ecoleng.2009.02.006.
- [2] J. Wang, Y.C. Ersan, N. Boon, N. De Belie, Application of microorganisms in concrete: a promising sustainable strategy to improve concrete durability, *Appl. Microbiol. Biotechnol.* 100 (2016). doi:10.1007/s00253-016-7370-6.
- [3] B. Zhang, Z.B. Bundur, P. Mondal, R.D. Ferron, Use of biomineralisation in developing smart concrete inspired by nature, *Int. J. Mater. Struct. Integr.* 9 (2015) 39–60.
- [4] I. Tiago, A.P. Chung, A. Verissimo, Bacterial Diversity in a Nonsaline Alkaline Environment : Heterotrophic Aerobic Populations, *Appl. Environ. Microbiol.* 70 (2004) 7378–7387. doi:10.1128/AEM.70.12.7378.
- [5] Z.B. Bundur, S. Bae, M.J. Kirisits, R.D. Ferron, Biomineralization in self-healing cement-based materials: Investigating the temporal evolution of microbial metabolic state and material porosity, *J. Mater. Civ. Eng.* 29 (2017).
- [6] S. Liu, Z.B. Bundur, J. Zhu, R.D. Ferron, Evaluation of self-healing of internal cracks in biomimetic mortar using coda wave interferometry, *Cem. Concr. Res.* 83 (2016). doi:10.1007/s13398-014-0173-7.2.
- [7] A. Amiri, M. Azima, Z.B. Bundur, Crack remediation in mortar via biomineralization : Effects of chemical admixtures on biogenic calcium carbonate, 190 (2018) 317–325. doi:10.1016/j.conbuildmat.2018.09.083.
- [8] V. Wiktor, H.M. Jonkers, Quantification of crack-healing in novel bacteria-based self-healing concrete, *Cem. Concr. Compos.* 33 (2011) 763–770. doi:10.1016/j.cemconcomp.2011.03.012.
- [9] S.S. Bang, J.J. Lippert, U. Yerra, S. Mulukutla, V. Ramakrishnan, Microbial calcite, a bio-based smart nanomaterial in concrete remediation, *Int. J. Smart Nano Mater.* 1 (2010) 28–39. doi:10.1080/19475411003593451.
- [10] J. Wang, K. Van Tittelboom, N. De Belie, W. Verstraete, Use of silica gel or polyurethane immobilized bacteria for self-healing concrete, *Constr. Build. Mater.* 26 (2012) 532–540. doi:10.1016/j.conbuildmat.2011.06.054.
- [11] J.Y. Wang, H. Soens, W. Verstraete, N. De Belie, Self-healing concrete by use of microencapsulated bacterial spores, *Cem. Concr. Res.* 56 (2014) 139–152. doi:10.1016/j.cemconres.2013.11.009.
- [12] J.Y. Wang, D. Snoeck, S. Van Vlierberghe, W. Verstraete, N. De Belie, Application of hydrogel encapsulated carbonate precipitating bacteria for approaching a realistic self-healing in concrete, *Constr. Build. Mater.* 68 (2014) 110–119.
- [13] M. Alazhari, T. Sharma, A. Heath, R. Cooper, K. Paine, Application of expanded perlite encapsulated bacteria and growth media for self-healing concrete, *Constr. Build. Mater.* 160 (2018) 610–619.
- [14] J.Y. Wang, N. De Belie, W. Verstraete, Diatomaceous earth as a protective vehicle for bacteria applied for self-healing concrete, *J. Ind. Microbiol. Biotechnol.* 39 (2012) 567–577. doi:10.1007/s10295-011-1037-1.
- [15] Y.Ç. Erşan, F.B. Da Silva, N. Boon, W. Verstraete, N. De Belie, Screening of bacteria and concrete compatible protection materials, *Constr. Build. Mater.* 88 (2015) 196–203. doi:10.1016/j.conbuildmat.2015.04.027.
- [16] ASTM International, ASTM C305-14 Standard Practice for Mechanical Mixing of Hydraulic Cement Pastes and Mortars of Plastic Consistency, West Conshohocken, 2014. doi:10.1520/C0305-14.2.
- [17] A.R. Suleiman, A.J. Nelson, M.L. Nehdi, Visualization and quantification of crack self-healing in cement-based materials incorporating different minerals, *Cem. Concr. Compos.* 103 (2019) 49–58.

Calcite biomineralisation for the repair of damaged concrete

Ronald J Turner, James M Minto, Grainne El Mountassir, Rebecca J Lunn

Department of Civil and Environmental Engineering, University of Strathclyde, Glasgow, G1 1XJ

Abstract

UK Civil Nuclear sites contain significant volumes of concrete infrastructure, including both external and internal structures. As a consequence, different concretes are exposed to differing environmental conditions, resulting in variable mechanisms and rates of concrete degradation. For example, external structures may be exposed to salt water and freeze-thaw cycles, while internal structures may be exposed to high temperatures and/or high levels of radiation.

Key to minimising the degradation of concrete structures is the reduction of concrete permeability. High permeability permits the ingress of damaging chemical compounds such as sulfate, and permits carbonation which may damage steel-bearing reinforcements. Consequently, techniques to reduce permeability will improve durability of the concrete. Specifically, very low permeability concrete is highly desirable for radiation shielding structures, which must be impermeable to radioactively contaminated air and liquids.

Microbially-induced calcite precipitation (MICP) may provide a low-cost, low-carbon method for the reduction of permeability in aged or damaged concrete infrastructure. The method used in this study relies upon the ureolytic capacities of the bacterial strain *Sporosarcina pasteurii*. We treat fractured concrete cores in the laboratory and show that our newly developed concrete treatment protocol successfully reduces hydraulic conductivity by at least 2 orders of magnitude in concrete samples collected from UK Civil Nuclear sites. We utilise X-CT imaging to quantify and visualise the calcite deposited within the fracture network present in the concrete samples. Our research indicates this treatment protocol can significantly reduce concrete permeability and thus could be deployed to increase the longevity of degraded concrete nuclear assets.

Introduction

Concrete makes up a large proportion of infrastructure and assets comprising the built environment. This results in concrete and cement being exposed to a broad range of environmental conditions. Concrete is therefore subject to many forms of deterioration, typically leading to the formation of cracks or fractures; and consequently increased permeability, leading to even further deterioration due to corrosion of reinforcement. Traditional repair methods used depend upon the purpose of the concrete structure and include patching with concrete or bitumen, or the injection of new concrete or other grouting materials into deeper fractures [1], [2]. These methods are expensive in both time, materials, and have associated negative environmental impacts.

The development of low embodied carbon materials and methods for the repair of concrete may contribute to reducing the environmental impact of concrete usage.[3] The use of industrial waste materials to act as nutrient sources for microbial growth may also allow contribution to a sustainable 'circular economy'.[4] Microbially induced calcite precipitation (MICP) relies upon the ureolytic activity of bacteria to trigger biomineralisation. This process occurs via the enzymatic breakdown of urea to produce ammonium and carbonate ions. These carbonate ions will bond to any free calcium ions present in the system, and in a high pH environment the formation of calcium carbonate (calcite) will be promoted.

Most laboratory studies of the treatment of concrete have relied on pouring/dripping treatment solutions onto concrete blocks or immersing blocks fully in treatment solutions.[5]

Neither of those approaches may be practical for in situ application. In comparison, injection enables treatment fluids to be applied to non-horizontal surfaces such as walls and roofs, and also allows application into internal fracture networks. Most studies treating natural/created fractures and artificially planar fractures have relied on visual assessment of the repair at the surface.[5] Few studies have investigated strength gains from MICP treatment of damaged concrete. In this study we (1) inject the MICP treatment solutions under controlled conditions, (2) visualise and quantify the deposition of calcite in the core using X- μ CT and (3) demonstrate that MICP can effectively regain strength in an initially fragmented concrete core.

Materials and methods

Concrete Sample Collection and Preparation

Concrete blocks were provided by Babcock Marine Ltd, taken from concrete caissons/dock blocks used as part of a dry dock structure at Devonport Royal Dockyard facility, within HMNB Devonport. The dimensions of each block were W: 100 cm, L: 181 cm, H: 80 cm, weighing approximately 3.3 tonnes.

From these blocks, a 36 mm diameter by 72 mm length core was cut to produce samples suitable for laboratory scale testing. An unconfined compressive strength (UCS) test was conducted to determine the UCS value of the concrete and also to artificially induce fracturing. Once visible fracturing was observed the core was then split along the predominant fracture into two halves through impact with a chisel.

The core was reassembled, wrapped in heat-shrink tubing and confined at 1000 kPa in a core holder for 1 hour to compress the halves of the core firmly together. After this, the core was vacuum-saturated with tap water and scanned via X- μ CT. Finally the core was remounted in the core holder and a confining pressure of 1000 kPa was applied to ensure no by-pass of MICP treatment fluids around the core.

Bacterial growth and preparation for injection

S. pasteurii was grown from cryopreserved stock cultures in a solid medium consisting of 5.5 gL⁻¹ Yeast Extract (Sigma-Aldrich), 5 gL⁻¹ sodium chloride (Fisher scientific), 0.4 gL⁻¹ D-glucose (Sigma-Aldrich), 0.4 gL⁻¹ K₂HPO₄ (Sigma-Aldrich), 20 gL⁻¹ urea, and 15 gL⁻¹ agar (Sigma-aldrich). Urea was added aseptically after autoclaving. A single bacterial colony was then transferred into a liquid growth media consisting of 5.5 gL⁻¹ Yeast Extract (Sigma-Aldrich), 5gL⁻¹ sodium chloride (Fisher scientific), 0.4 gL⁻¹ D-glucose (Sigma-Aldrich), 0.4 gL⁻¹ K₂HPO₄ (Sigma-Aldrich), and 20 gL⁻¹ urea (Sigma-Aldrich). Urea was added aseptically after autoclaving. The culture was incubated overnight at 30 °C. The culture was then centrifuged at 6000 G for 7 minutes. The supernatant was discarded, and the bacterial cell pellet resuspended in mains tap water to an OD₆₀₀ of 1.0. This solution was prepared immediately prior to injection into the core.

MICP Treatment and Permeability Measurements

A HPLC pump was used to inject water and treatment fluids through the core. Initial absolute permeability (units m²) was determined during injection of tap water by controlling the flow rate at the pump, and measuring the differential pressure across the core. This calculation utilised Darcy's law (formula below) to measure permeability (k):

$$q = -\frac{k}{\mu} \nabla p.$$

Where k = permeability (m²), μ = dynamic viscosity of the fluid (Pa.S), ∇p = pressure drop (Pa), and q = instantaneous flux (m³/s).

Treatment cycles consisted of seven main injection stages through the core, interspersed with water pulses to prevent blockage of the pump and tubing. For each bacterial and cementing solution injection stage, 5 ml of fluid was injected per cycle at a flow rate of 0.1 ml/min. Cementing solution consisted of 111 gL⁻¹ calcium chloride (Sigma-Aldrich), and 60 gL⁻¹ urea (Sigma-Aldrich).

The order of these injection steps for a single treatment cycle are listed below (Table 1). Permeability measurements were taken with water after each treatment cycle.

Table 1: Treatment Cycle Steps for Cycles 1-6

Treatment Step	Treatment Solution	Flow Rate (ml/min)	Duration (minutes)	Total Volume (ml)
1	Bacterial Injection	0.1	50	5
2	Static Period	N/A	120	N/A
3	Water Injection	0.1	20	2
4	Cementing Injection	0.1	50	5
5	Static Period	N/A	960 (overnight)	N/A
6	Water Injection	0.1	20	2

Between treatment cycles, the tubing lines and pump were flushed thoroughly with tap water. This treatment cycle was repeated several times.

After 6 treatment cycles, permeability had decreased significantly. At this point, the flow rate for all injection stages was halved to 0.05 ml/min, with the treatment duration doubled to maintain the same volume of treatment fluid as in Cycles 1-6 (Table 2).

Table 2: Treatment Cycle Steps for Cycles 7-9

Treatment Step	Treatment Solution	Flow Rate (ml/min)	Duration (minutes)	Total Volume (ml)
1	Bacterial Injection	0.05	100	5
2	Static Period	N/A	120	N/A
3	Water Injection	0.05	40	2
4	Cementing Injection	0.05	100	5
5	Static Period	N/A	960 (overnight)	N/A
6	Water Injection	0.05	40	2

Tomography (X-μCT) Method

X-ray micro computed tomography of the concrete core was carried out using a Nikon XT H 225 LC X-ray computed tomography system. This generated a 2D stack of projections from the scan. The core was scanned once before MICP treatment, and once afterwards. Following reconstruction, pre- and post-treatment stacks were aligned using the registration software Elastix.[6] Thresholding and processing of the stacks was performed using the FIJI distribution of ImageJ [7] which allowed the solid components (concrete: cement matrix or aggregates) to be distinguished from the void or fracture spaces. The data was binarized based on grey values (255/White or 0/Black), with 255 representing concrete/calcite, and 0 representing void/fracture space. By subtracting the pre- and post-treatment binarized stacks, it was possible to visualise where calcite was deposited within the fracture network. It was also

possible to count the number of these voxels, which corresponds to a measurement of deposited calcite volume.

Results and discussion

Permeability was observed to continually decrease with each treatment cycle completed (Fig 1). After 9 treatment cycles a permeability reduction of 3 orders of magnitude was achieved. After 9 treatment cycles, the core was removed from the core holder and imaged under X- μ CT. X- μ CT analysis revealed that the initial fracture network within the core had been coated with a new solid phase, (i.e. calcite), see Fig 2. Based on X- μ CT data, the measured volume of the precipitated phase was 46.42 mm³.

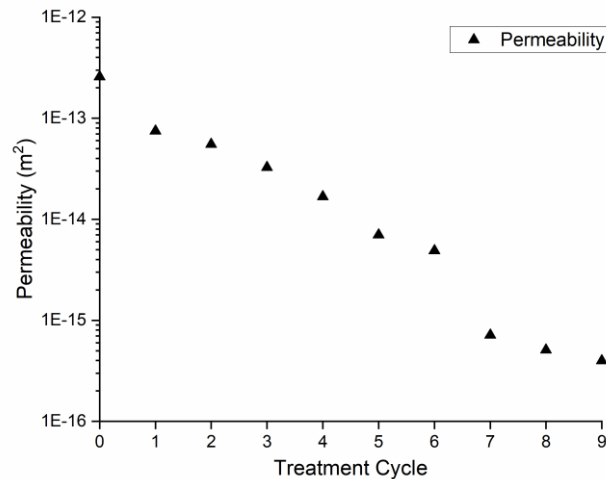


Figure 1: Permeability change vs. Treatment Cycle Number

The initial measured compressive strength of the core was 14.41 MPa. After X-CT imaging another UCS test was conducted, and the new compressive strength measured as 1.58 MPa, indicating that ~10% of the initial strength of the concrete core had been regained via MICP treatment.

Conclusion

In this study we have demonstrated that MICP treatment via controlled injection can be used to effectively reduce the permeability of damaged concrete, and also results in strength gain in an initially fragmented concrete specimen. Using X- μ CT we show that the location of the calcite precipitated maps onto the initial fracture network within the core and that calcite was precipitated along the full length of the core (72 mm length).

Acknowledgments

We gratefully acknowledge funding from EPSRC-UKRI and various industrial partners, who funded this research through the grant “EP/R004889/1 - Delivering Enhanced Through-Life Nuclear Asset Management”. We also thank Babcock International Group Plc for supplying concrete samples.

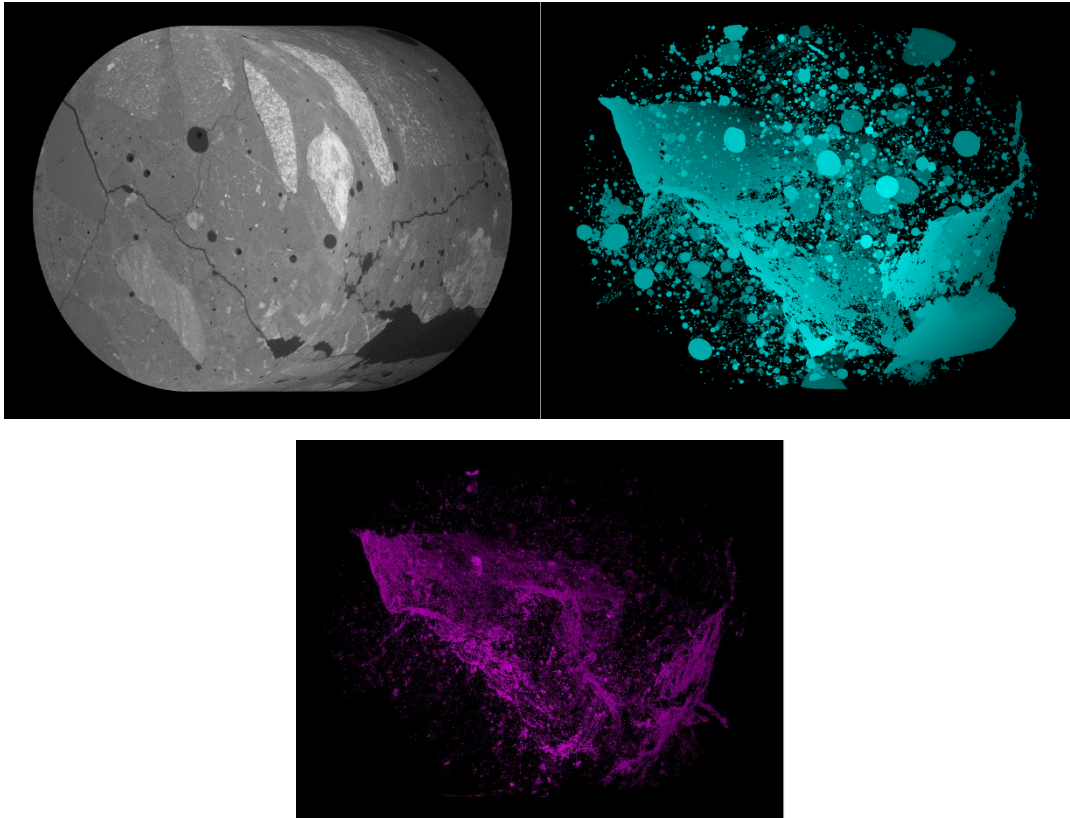


Figure 2: X-CT visualisations of the concrete core, showing front $\frac{3}{4}$ view relative to the base of core. 3D reconstruction of the scan shows that fractures are present in the concrete, along with voids and aggregate pieces (top left). Image segmentation allowed the initial void and fracture space to be visualised pre-treatment (top right, Cyan). Subtracting the post-treatment void space from the pre-treatment void space allowed direct visualisation of the location of calcite in the fracture network (lower image, Pink).

References

- [1] Y. Jung, T. J. Freeman, and D. G. Zollinger, "Guidelines for Routine Maintenance of Concrete Pavement," 2008.
- [2] H. Wang, *Life-cycle analysis of repair of concrete pavements*. Elsevier Ltd, 2018.
- [3] R. Muigai, *Eco-efficient design of concrete repair and rehabilitation*. Elsevier Ltd, 2018.
- [4] H. Y. Leong *et al.*, "Waste biorefinery towards a sustainable circular bioeconomy: a solution to global issues," *Biotechnol. Biofuels*, vol. 14, no. 1, pp. 1–15, 2021, doi: 10.1186/s13068-021-01939-5.
- [5] K. Van Tittelboom, N. De Belie, W. De Muynck, and W. Verstraete, "Use of bacteria to repair cracks in concrete," *Cem. Concr. Res.*, vol. 40, no. 1, pp. 157–166, 2010, doi: 10.1016/j.cemconres.2009.08.025.
- [6] S. Klein, M. Staring, K. Murphy, M. A. Viergever, and J. P. W. Pluim, "elastix: a toolbox for intensity-based medical image registration.," *IEEE Trans. Med. Imaging*, vol. 29, no. 1, pp. 196–205, Jan. 2010, doi: 10.1109/TMI.2009.2035616.
- [7] J. Schindelin *et al.*, "Fiji: an open-source platform for biological-image analysis," *Nat. Methods*, vol. 9, p. 676, Jun. 2012, [Online]. Available: <http://dx.doi.org/10.1038/nmeth.2019>.

Engineering fungal networks for ground improvement

Grainne El Mountassir¹, Alexandra Schellenger¹, Emmanuel Salifu^{1,2},
Rebecca J. Lunn¹

1: Department of Civil and Environmental Engineering, University of Strathclyde, Glasgow, UK, G1 1XJ

2: Università di Napoli, Dipartimento di Ingegneria Civile, Edile e Ambientale, Federico II, Italy.

Abstract

Conventional ground improvement techniques are energy intensive, highly invasive and require the introduction of environmentally damaging chemicals or carbon intensive materials. There is a clear need for the development of sustainable, low-carbon technologies for ground improvement. Recently, geotechnical engineers have started to consider biological-based solutions including engineered vegetation, biopolymers, and bio-mineralisation (e.g. microbially induced carbonate precipitation) for ground improvement. At the University of Strathclyde, we are investigating the use of fungal networks for ground engineering applications. Fungi produce hyphae, long filamentous structures which collectively are called a mycelium. Mycelia can grow to vast sizes, with individual mycelium (in forest floors) covering areas up to 9km² in North America. As such there is great potential 'to grow' fungal mycelia for earth infrastructure applications over vast areas.

This study investigates the influence of fungal hyphae growth on erosion behaviour. Jet erosion tests were performed on sands inoculated with different fungal species: *Pleurotus ostreatus*, *Trichoderma harzianum*, *Mucor racemosus* with periods of incubation up to 9 weeks. Laser scans were carried out to determine the total eroded soil volume and final geometry. Results show that fungal treatment significantly reduces soil erodibility compared to untreated control specimens. Growth behaviour varies for different fungal and as such so too does the protection offered against erosion: some species form dense mycelium mats at the soil-air interface whereas other species prefer to penetrate deeper into the soil providing reinforcement with depth. Our results demonstrate the great potential of fungal-based technologies as low cost, minimally-invasive techniques for ground improvement.

Introduction

Conventional ground improvement techniques contribute to global CO₂ emissions, directly and indirectly. It is estimated that there are approximately 40,000 soil and ground improvement projects, carried out annually worldwide, at a total value over US\$6 billion [1]. Conventional ground improvement includes: (i) mechanical techniques, i.e. compaction, external loading, construction of drains or the introduction of reinforcement; (ii) chemical techniques that involve the introduction of chemical reagents to produce soil binding products and or fill pore space, (iii) thermal techniques (heating/freezing) and (v) electrical techniques (e.g. electro-osmosis). These processes are often expensive, energy intensive, highly invasive and require the introduction of environmentally damaging chemicals or carbon intensive materials. Chemicals (including cements) often used for soil improvement are toxic/hazardous to soil organisms and groundwater (e.g. resulting from high pH plumes induced by cements). Furthermore, the production of cement, which is widely used in ground engineering, is the third largest source (estimated to contribute ~5%) of global anthropogenic CO₂ emissions [2]. There is a clear need for the urgent development of sustainable low-carbon technologies for ground improvement.

In a bid to find alternatives to traditional ground engineering techniques, geotechnical engineers have in the last 15 years begun to actively collaborate with geochemists and

microbiologists to investigate bio-geo-chemical approaches to modifying the hydraulic and mechanical behaviour of soil [3, 4, 5], with the creation of the new subdiscipline *biogeotechnics*. Much of the research in this area to date has been focused on bacterial biomineralization and in particular on the process of microbially inducing calcite precipitation via ureolysis using the bacterium *S. pasteurii*. This process has wide ranging applications for soil stabilisation, erosion control, rock fracture grouting, concrete and building repair [6,7,8,9]. On the basis of this success, we should continue to explore the potential for the deployment of other microorganisms in ground engineering.

Over the last four years at the University of Strathclyde we have been investigating the influence of multi-cellular fungi on soil behaviour. Multi-cellular fungi grow via the development of hyphae. Hyphae are elongated, tubular structures, consisting of an outer cell wall made up of polysaccharides (chitin). Hyphae possess high mechanical resistance due to their structural configuration such that some species are capable of boring through rocks and hard mineral substrates [10, 11]. Hyphal diameters range between 1 – 30 μm and lengths can span from several microns to several metres [12]. Hyphae of filamentous fungi can branch into multiple hyphae and can anastomose, creating a massive three-dimensional vegetative structure called the mycelium.

Studies by soil and agricultural scientists have observed increased size of aggregates formed in soils inoculated with fungi and enhanced resistance to breakdown upon wetting, for a range of different fungal species, e.g. [13, 14]. There are three main categories of mechanisms by which fungi can contribute to soil aggregate stability: (i) Biophysical, (ii) Biochemical and (iii) Biological mechanisms [15]. We propose that fungal growth could thus be engineered to promote binding of soil particles and enhance soil resistance to erosion.

In this study the influence of fungal inoculation on the erosion behaviour of sandy soil is investigated via Jet erosion tests. These results show that fungal treatment can reduce soil erosion and hence could be a promising new low-cost technology for erosion protection.

Materials and methods

Fungal treatment



Fig 1. Radial hyphal development of *T. harzianum*.

In this study the fungal species: *Trichoderma harzianum* was selected for treatment of the soil specimens. *T. harzianum* is a non-pathogenic saprotrophic fungus, i.e. it degrades organic matter, and is known to be capable of altering surface wettability [16]. It is also used as a biocontrol agent to suppress disease causing fungal pathogens in agriculture [17]. Figure 1 shows the typical radial hyphal growth of *T. harzianum*, extending from a central inoculation point in a mixture of sand and leaf litter. It has a fast growth rate (~ 1 cm/day) and forms a dense mass of hyphae at the surface and throughout the soil.

To inoculate the soil specimens, a fungal treatment suspension (FTS) was prepared. *T. harzianum* was cultivated in 50 mL malt extract broth at 25 °C for four days prior to sample preparation. The mass of fungal hyphae was then extracted from the broth solution using sterilised tweezers, rinsed in sterile distilled water, and placed in a blender with 100mL sterile distilled water and homogenised (i.e. blended). This produced the FTS containing fungal hyphae and spores.

Specimen preparation

All specimens were prepared under sterile conditions, using autoclaved soil, solutions, and glassware. Soil specimens were composed of sand with a particle size < 600 µm mixed with 5% leaf litter by mass. For the control specimens, 800 g of the soil mixture (sand + leaf litter) were then mixed with water and compacted into the 100 mm diameter x 100 mm high mould, achieving an initial degree of saturation of 50%.

In the fungal treated specimens, 5ml of FTS was mixed with the uppermost 200 g of soil before compacting into the mould, i.e. the top 25% of soil was fungal treated. In these samples, water was replaced with malt extract broth, to give the same initial degree of saturation of 50%, to test the performance of fungi in conditions that gave adequate access to nutrients for growth. Specimens were left to incubate at 25 °C for 3 weeks.

Jet Erosion Test

Figure 1 shows the JET apparatus constructed at the University of Strathclyde based on the mini-JET apparatus designs of [18]. It consists of an acrylic jet tube (50 mm dia, 920 mm length), a nozzle plate with an orifice of diameter 6.4 mm, a deflector plate with handle control and a 300 mm high x 300 mm in diameter submergence tank made of transparent acrylic plastic. The apparatus is supported by screw rods and acrylic sheets and can be easily dismantled and re-assembled. A mould holder is provided at the bottom of the submergence tank for fitting the soil specimen mould. The soil specimen mould is 100 mm high x 100 mm diameter, and made of acrylic. Inlet valves at the bottom of the submergence tank are used for draining and filling the tank; and at the top of the jet tube for filling the tube and maintaining a constant hydraulic head. A graduated thin rod (63 mm dia) which can pass through the jet nozzle, was used as the point gauge. The Jet erosion test (JET) imposes a submerged impinging jet on to the specimen surface which induces erosion/scour; the shear stress imposed on the soil surface is controlled by the head of water in the Jet tube (measured relative to the water level in the submergence tank). Erosion continues until equilibrium is reached at a given head. Measurements of scour depth were recorded over a period of 60 mins at each head or until all soil was washed from the specimen mould. The head in the jet tube was then increased. The surface of the soil specimens after erosion at each head was then scanned using a 2D/3D scanCONTROL 2700-100/BL laser from Micro-Epsilon. Data were exported as ASCII files for further processing using CloudCompare, a 3D point cloud open source processing software. In this software, the initial specimen surface was used as the reference against which the subsequent eroded volumes were determined.

Figure 3 presents the cumulative percentage soil volume eroded against head determined from the laser scanning data, for both the control and fungal treated specimens. It is evident that the % soil volume eroded is greatly reduced by fungal treatment. For the control specimen (sand + 5% leaf litter) 100% of the soil volume is eroded when the head of water in the jet tube is increased to 50 cm, whereas for the fungal treated specimens subjected to a jet at the same head, only 14% of the soil volume was eroded.

Results and discussion

Figure 4 presents the surfaces of the soil specimens at the beginning of the test and after erosion at heads equal to 10 cm and 25 cm. In the control specimens as erosion progresses, almost all soil volume down to a given depth is removed, due to the cohesionless nature of the

soil. Whereas in the fungal treated specimens, due to binding of the soil particles, as a result of enmeshment by fungal hyphae, soil removal occurs only in a central hole directly under the impinging jet; this is more representative of the behaviour exhibited by cohesive materials. Indeed, the fungal treatment has transformed the soil from being a very erodible material to being moderately resistant to erosion.

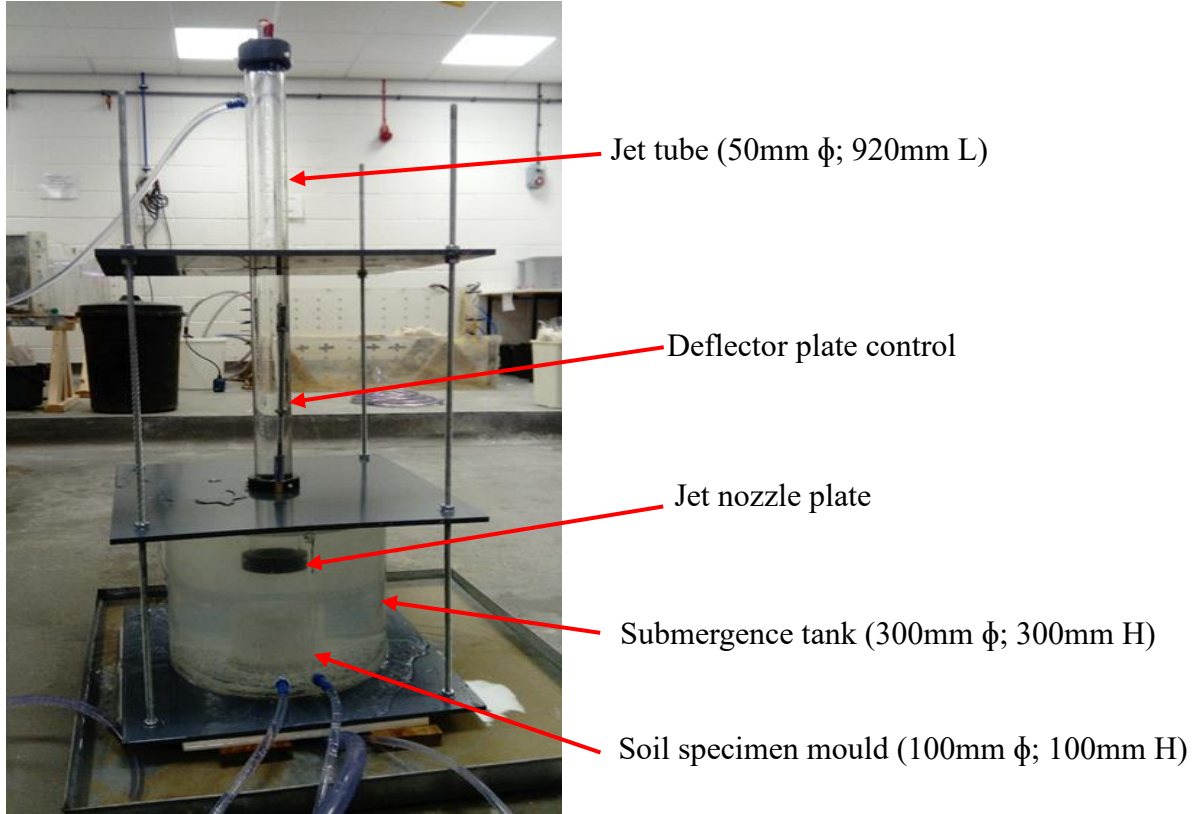


Figure 2. Jet erosion test apparatus at University of Strathclyde

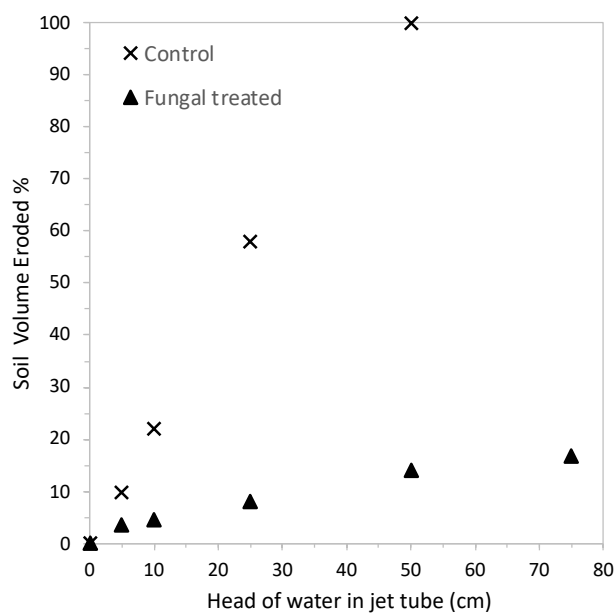


Figure 3. Cumulative soil volume eroded (%) against head for control and fungal treated specimens.

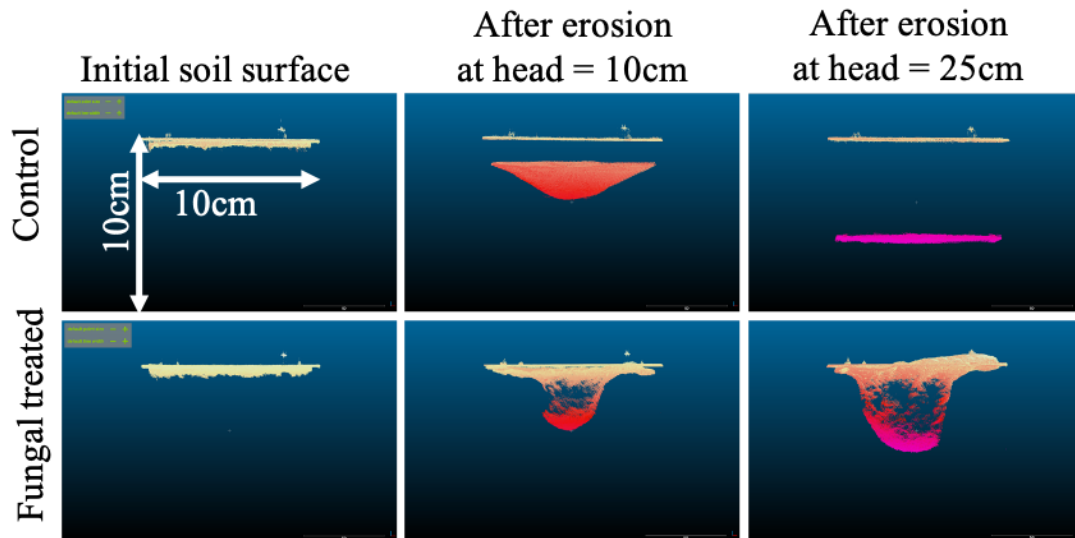


Figure 4. Specimen surfaces for control and fungal treated specimens: (i) at start of tests, (ii) after erosion at $h = 10\text{cm}$, and (iii) after erosion at $h = 25\text{cm}$.

Conclusions

This study has demonstrated that inoculation of a sandy soil with *T. harzianum* can greatly increase its resistance to erosion. Fungal treatment of soils shows potential as a low-cost technique to reduce soil erosion in fragile environments, e.g. after wildfires, to mitigate against aeolian desertification and to prevent shallow landslides.

Acknowledgments

The authors wish to acknowledge the support of the European Commission via the Marie Skłodowska-Curie Innovative Training Networks project TERRE 'Training Engineers and Researchers to Rethink geotechnical Engineering for a low carbon future' (H2020-MSCA-ITN-2015-675762) and the Engineering and Physical Sciences Research Council via Grant EP/N035526/1. The authors also wish to acknowledge the contribution of Derek McNee in manufacturing the JET erosion test apparatus.

References

- [1] DeJong, J. T. *et al.* 2010. 'Bio-mediated soil improvement', *Ecological Engineering*, 36(2), pp. 197–210.
- [2] Andrew, R. M. 2017. 'Global CO₂ emissions from cement production', *Earth System Science Data*, pp. 1–52.
- [3] Mitchell, J. K., & Santamarina, J. C. 2005. Biological considerations in geotechnical engineering. *Journal of Geotechnical and Geoenvironmental Engineering*, 131(10), 1222–1233.
- [4] DeJong, J. T., Soga, K., Kavazanjian, E., Burns, S., van Paassen, L. A., Al Qabany, A., *et al.* 2013. Biogeochemical processes and geotechnical applications: Progress, opportunities and challenges. *Géotechnique*, 63(4), 287–301.
- [5] El Mountassir, G., Minto, J. M., Van Paassen, L.A., Salifu, E., Lunn, R.J. 2018. Applications of Microbial Processes in Geotechnical Engineering. *Advances in Applied Microbiology*. Vol. 104, Chapter 2. Elsevier Inc.
- [6] van Paassen, L. A., Ghose, R., van der Linden, T. J. M., van der Star, W. R. L., & van Loosdrecht, M. C. M. 2010. Quantifying biomediated ground improvement by ureolysis: Large-scale biogROUT experiment. *Journal of Geotechnical and Geoenvironmental Engineering*, 136, 1721–1728.
- [7] Gomez, M. G., Martinez, B. C., DeJong, J. T., Hunt, C. E., DeVlaming, L. A., Major, D. W., *et al.* 2015. Field-scale bio-cementation tests to improve sands. *Proceedings of the Institution of Civil Engineers—Ground Improvement*, 168, 1–11.
- [8] Minto, J. M., MacLachlan, E., El Mountassir, G., & Lunn, R. J. 2016. Rock fracture grouting with microbially induced carbonate precipitation. *Water Resources Research*, 52(11), 8827–8844.

- [9] Minto, J. M., Tan, Q., Lunn, R. J., El Mountassir, G., Guo, H., & Cheng, X. 2018. "Microbial mortar"—restoration of degraded marble structures with microbially induced carbonate precipitation. *Constr. Build. Mater.*, 180, 44–54.
- [10] Jongmans, A. G. *et al.* 1997. 'Rock-eating fungi', *Nature*, 389(October), p. 682. doi: 10.1038/39493.
- [11] Van Schöll, L. *et al.* 2008. 'Rock-eating mycorrhizas: Their role in plant nutrition and biogeochemical cycles.', *Plant Soil*, 303, pp. 35–47.
- [12] Islam, M. R., Tudryn, G., Bucinell, R., Schadler, L., & Picu, R. C. 2017. Morphology and mechanics of fungal mycelium. *Scientific Reports*, 7(1), 13070.
- [13] Tisdall, J.M., & Oades, J.M. 1982. Organic matter and water-stable aggregates in soils. *J. of Soil Sci.*, 33(2), 141–163.
- [14] Caesar-Tonthat, T.-C., & Cochran, V. L. 2000. Soil aggregate stabilization by a saprophytic lignin-decomposing basidiomycete fungus I. Microbiological aspects. *Biology and Fertility of Soils*, 32(5), 374–380.
- [15] Rillig, M. C., & Mummey, D. L. (2006). Mycorrhizas and soil structure. *New Phytologist*, 171(1), 41–53.
- [16] Chau, H.W., Si, B. C., Goh, Y. K. and Vujanovic, V. (2009). A novel method for identifying hydrophobicity on fungal surfaces, *Mycological Research*, vol. 113, 1046-1052.
- [17] Poveda, J. Hermosa, R., Monte, E. and Nicolás, C. 2019. *Trichoderma harzianum* favours the access of arbuscular mycorrhizal fungi to non-host Brassicaceae roots and increases plant productivity. *Scientific Reports*, 9:11650.
- [18] Al-Madhhachi, A. T., Hanson, G. J. and Fox, G. A. 2013. Measuring soil erodibility using laboratory "mini" JETs. *Transactions of the ASABE*, 56(3), pp. 901–910.

Session 2B Bio-inspired building materials

Chair: Dr Ana Bras

1265 *Kafodya et al.* Strength properties of Limestone Calcined Clay Cement (LC3) in Malawi

1249 *Jiang et al.* Application of Nanotechnology for the Development of Sustainable Lignocellulosic Materials

1267 *Mwiti et al.* Reactivity of selected rice husk ash-calcined clay mixtures for sustainable cement production

1253 *Scott et al.* Building Couture: Knitting as a Strategy for Bespoke Bio Architecture.

1240 *Yang et al.* Bacterial Cellulose as a Building Material: Identifying opportunities, limitations and challenges

Strength properties of Limestone Calcined Clay Cement (LC³) in Malawi

Innocent Kafodya¹, Tania Sharmin², Viviana Novelli³

1: Civil Engineering Department, Malawi University of Business and Applied Sciences, Malawi

2: Welsh School of Architecture, Cardiff University, United Kingdom

3: School of Engineering, Cardiff University, United Kingdom

Abstract

Malawi is a developing country in the Sub-Saharan Africa with 84 % of population living in rural areas. The socio-economic status of the population is characterised by low income and poor housing structures that are vulnerable to natural disasters. The construction industry in Malawi uses Ordinary Portland Cement (OPC) and Portland Pozzolana Cement (PPC) produced with high clinker factor. Limestone Calcined Clay Cement (LC³), is already proven to be cost-effective and sustainable material. However, LC³ production in Malawi is not exploited due to lack of guidelines on product formulations, strength, and durability. Replacing OPC with LC³ ensures more durable and resilient construction and reduces CO₂ emissions from OPC production.

In this study, strength properties of limestone calcined clay cement (LC³) in Malawi were investigated to explore potential replacement for Ordinary Portland cement (OPC). The raw materials of LC³ were characterised using X-ray fluorescence (XRF) analyser. The 7-day and 28-day compressive strengths of LC³-50 and LC³-40 were investigated with varying calcined clay to limestone (CC/LS) ratios of 1:1, 2:1 and 3:1) and water to cement (w/c) ratios of 0.45, 0.5 and 0.6. The results revealed that LC³-50 achieved maximum compressive strength of 39.2 MPa with 0.5 w/c ratio at CC/LS ratio of 2:1. On the other hand, LC³-40 showed maximum strength of 31.9 MPa with 0.5w/c ratio at CC/LS ratio of 1:1. The strength of LC³-50 was comparable with the required strengths for Portland Pozzolana cement (PPC-32.5) while LC³-40 met requirements for masonry cement (MC 22.5).

It is anticipated that LC³ production could foster job creating in the small-scale mining sector. This work has the potential for enormous benefits in the Sub-Saharan Africa and is aligned with the UN Sustainable Development Goals (SDGs) in developing sustainable and resilient materials.

Introduction

Malawi is a land-locked country to the east of the Sub Saharan Africa. It is located within East Africa lift system that is prone to natural hazards such as earthquakes. Malawi is one of the list developed countries with prevailing poor socio economic conditions [1]. The construction industry in Malawi uses Ordinary Portland Cement (OPC) produced from clinker. The consumption of cement is around 370,000 tonnes per annum [2]. Due to the poor economic status of the country, majority of locals do not afford cement, a situation that has resulted into poor infrastructure that is vulnerable to natural disasters.

Limestone calcined clay cement (LC³) has been proven to be low-cost and a potential replacement of Ordinary Portland Cement (OPC) [3]. The literature [2] shows that there is availability of large quantities of naturally occurring minerals in Malawi to produce low-cost and sustainable limestone calcined clay cement (LC³). Replacing OPC with low-cost LC³ will ensure more durable and resilient construction and also reduce CO₂ emission emanating from OPC production [3, 4].

This study aimed at investigating properties of limestone calcined clay cement in Malawi as a low-cost and sustainable construction material. LC³ was developed from the locally available clay and limestone at 50 % and 40 % clinker factors. A series of tests were performed to

establish compressive strength of LC³-50 and LC³-40 produced from the local clay. The maximum strength was determined by varying calcined clay to limestone (CC/LS) ratio and also water to cement (w/c) ratios. The acquired strengths of LC³ were compared with specifications for Portland pozzolana cement (PPC) and masonry cement (MC 22.5) in accordance with EN 197-1 and EN 413-1, respectively in order to assess the potential application of LC³ in Malawi.

Materials and methods

Raw Materials

The materials for manufacturing LC³ were clay, limestone, clinker and gypsum. Clay soil was collected from Lithipe in the central Malawi. Limestone was obtained from the mining site in Balaka, Southern Malawi. Clinker and gypsum were obtained from the local cement manufacturing company. Limestone, gypsum and clinker were ground in the laboratory to produce powder. Clay soil was initially pulverised and sieved using 75 µm sieve. Calcined clay was produced by static calcination process of a clay sample of total mass of 50 g at 800 °C in a laboratory muffle furnace for 30 min. The cement constituents were analysed using X-ray fluorescence (XRF) analyser and the results are shown in Table 1.

Table 1: XRF analysis of LC³ constituents

Compound	Element composition (%)				
	Clinker	Clay	Calcined Clay	Limestone	Gypsum
Na ₂ O	0.03	0.009	0.003	0.003	0.003
MgO	4.00	0.12	0.20	9.20	4.80
Al ₂ O ₃	7.35	29.44	36.03	1.65	1.90
SiO ₂	34.07	48.15	46.71	6.45	1.50
P ₂ O ₅	0.36	0.06	0.06	0.034	0.00
SO ₃	1.19	0.06	0.83	0.34	52.5
Cl	0.03	0.007	0.004	0.002	0.005
K ₂ O	0.65	0.3	0.35	0.05	0.01
CaO	52.17	0.44	0.71	47.26	32.01
TiO ₂	0.3	0.40	0.43	0.057	0.02
MnO	0.004	0.02	0.022	0.018	0.004
Fe ₂ O ₃	2.58	2.9	3.35	0.61	0.07
LOI	0	18.09	11.30	34.32	7.17

Specimen preparations

Two cement samples namely, LC³-50 and LC³-40 were manufactured in the laboratory. The composition of LC³-50 by mass comprised of 50 % of clinker, 45 % of combined calcined clay and limestone and 5 % of gypsum. On the other hand LC³-40 composed 40 % of clinker, 55 % of combined calcined clay and clinker and 5 % of gypsum. Calcined clay and limestone were mixed at the ratios of 1:1, 2:1 and 3:1.

For each calcined clay and limestone ratio, the specimens for compression test were prepared at (w/c) ratios of 0.45, 0.5 and 0.6. Three mortar cylinder specimens were prepared using standard sand and were tested after 7 days and 28 days of curing periods according to EN 196-1. Eighteen (18) laboratory mixtures were prepared for both LC³-40 and LC³-50. The experimental programme for mix designs is summarised in Table 2.

Table 2: Experimental mix designs for compressing tests

Mix No	Clay/Limestone ratio (CC/LS)	Water/Cement ratio (w/c)
1	1:1	0.45
2	1:1	0.5
3	1:1	0.6
4	2:1	0.45
5	2:1	0.5
6	2:1	0.6
7	3:1	0.45
8	3:1	0.5
9	3:1	0.6

Results and discussion

Variation of compressive strength with calcined clay and limestone ratios (CC/LS)

The variations of 28-day compressive strength of LC³-50 and LC³-40 with CC/LS ratios at various w/c ratios are shown in Figure 1.

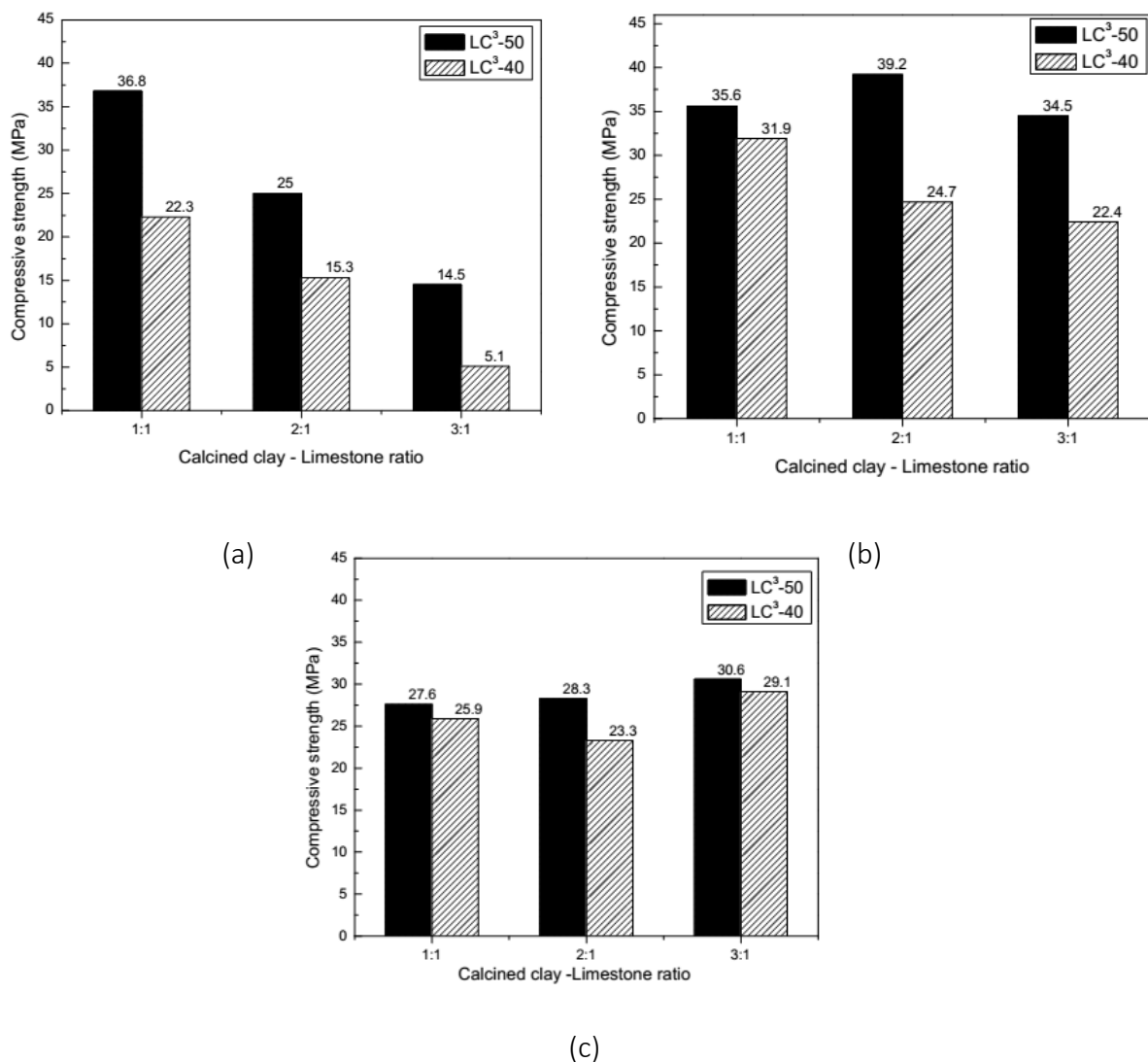


Figure 9: Compressive strength after 28 days of curing (a) 0.45 w/c (b) 0.5 w/c (c) 0.6 w/c

It is noted that at 0.45 w/c ratio, compressive strength reduces with an increase in CC/LS ratio for both LC³-50 and LC³-40. The maximum compressive strengths for LC³-50 is shown to be

36.8 MPa with 0.45 w/c ratio at CC/LS ratio of 1:1, 39.2 MPa with 0.5 w/c ratio at CC/LS ratio of 2:1 and 30.6 MPa with 0.6 w/c ratio at CC/LS ratio of 3:1. On the other hand, LC³-40 shows maximum strength of 22.3 MPa with 0.45 w/c ratio at CC/LS ratio of 1:1, 31.9 MPa with 0.5 w/c ratio at CC/LS ratio of 1:1 and 29.1 MPa with 0.6 w/c ratio at CC/LS ratio of 3:1. The lowest strength is indicated to be 5.1 MPa with 0.45 w/c ratio at 3:1 CC/LS ratio and is attributed to low workability of cement mixture that renders it difficult to be properly placed in a mould and this in turn increases porosity of hardened mortar and ultimately reduces strength [5, 6]. Further, mix design of 3:1 CC/LS ratio has high clay content which is associated with high pozzolanic activity that produces a significant reduction of portlandite level in liquid phase of the cement mortar. The activated clay therefore does not develop all its pozzolanic activity to generate hydration products due to insufficient Ca(OH)₂ hence low strength is developed [7]. In addition, water in excess of the amount required for hydration causes segregation of aggregates in the cement mortar mixture. When free water evaporates, it leaves pore spaces in the mortar that cause a decrease in strength [6, 8, 9]. It could be deduced from the results that each mix design had different favourable water-cement ratio. LC³-40 was expected to exhibit lower strength irrespective of calcined clay and limestone content. This was attributed to the reduced amount of clinker available for hydration.

Comparative analysis of LC³ strengths with specifications for PPC and masonry cement

The comparison of LC³ strengths with PPC and masonry cement (MC 22.5) specifications is shown in Tables 3a-3c in order to assess the potential of LC³ for application in the Malawian construction industry.

Table 3a: Compressive strength of LC³ at 0.45 w/c ratio

Properties	Type of LC ³						Specificati on EN 197-1	Specification EN 413-1
	LC ³ -50			LC ³ -40			PPC	MC 22.5
	1:1	2:1	3:1	1:1	2:1	3: 1		
Compressive strength 7 days (MPa)	28.0	16.7	14.0	15.6	12.1	3.7	16 ≥	10
Compressive strength 28 days (MPa)	36.8	25.0	14.5	22.3	15.3	5.1	≥ 32.5 ≤ 42.5	≥ 22.5 ≤ 32.5

Table 3a shows that at 0.45 w/c ratio, LC³-50 with CC/LS ratio of 1:1, met requirements for PPC while LC³-40 met requirements for masonry cement (MC 22.5). Table 3b indicates that at 0.5 w/c ratio, LC³-50 met requirements for PPC for all CC/LS ratios while LC³-40 met requirements for MC 22.5. Table 3c shows that at 0.6 w/c ratio and for all CC/LS ratios, both LC³-50 and LC³-40 met requirements for MC 22.5.

Conclusion

The investigation revealed that strength of LC³ in Malawi is comparable with the required strengths for PPC (32.5) and MC 22.5. LC³-50 could achieve strength of more than 32.5 MPa and LC³-40 could achieve strength of more than 22.5 MPa. The acquired strength indicated high potential of LC³ for application in Malawi and Sub-Saharan Africa in order to realise

resilient and sustainable construction aligned with the UN Sustainable Development Goals (SDGs).

Table 3b: Compressive strength of LC³ at 0.5 w/c ratio

Properties	Type of LC ³						Specification EN 197-1 PPC	Specification EN 413-1 MC 22.5
	LC ³ -50			LC ³ -40				
	1:1	2:1	3:1	1:1	2:1	3:1		
Compressive strength 7 days (MPa)	25.9	29.1	25.5	27.8	21	14.9	16 \geq	10
Compressive strength 28 days (MPa)	35.6	39.2	34.5	31.9	24.7	22.4	≥ 32.5 ≤ 42.5	≥ 22.5 ≤ 32.5

Table 3c: Compressive strength of LC³ at 0.6 w/c ratio

Properties	Type of LC ³						Specification EN 197-1 PPC	Specification EN 413-1 MC 22.5
	LC ³ -50			LC ³ -40				
	1:1	2:1	3:1	1:1	2:1	3:1		
Compressive strength 7 days (MPa)	16.8	20	20.9	15.7	20.4	20	16 \geq	10
Compressive strength 28 days (MPa)	27.6	28.3	30.6	25.9	23.3	29.1	≥ 32.5 ≤ 42.5	≥ 22.5 ≤ 32.5

Acknowledgment

The authors sincerely acknowledge financial support from Cardiff University HEFCW-GCRF fellowship scheme.

References

- [1] Novelli et al. Fragility curves for non-engineered masonry buildings in developing countries derived from real data based on structural surveys and laboratory tests. Soft Computing 2021 Vol 25 pp 6113-6138.
- [2] TARA. Analysis of raw materials and assessment of the reactivity of china clay from Malawi for LC³ application, New Dehli, India, 2016.
- [3] Scrivenera K, Martirenab F, Bishnoic S, Maity S. Calcined clay limestone cements (LC³). Cement and Concrete Research. 2018 Vol 114 pp 49-56.
- [4] Akindahunsia A.A, Avetb F, Scrivener K. The Influence of some calcined clays from Nigeria as clinker substitute in cementitious systems. Case Studies in Construction Materials. 2020 Vol 13 pp 1-10.
- [5] Marangu J.M. Physico-chemical properties of Kenyan made calcined Clay-Limestone cement (LC³). Case Studies in Construction Materials. 2020 Vol 12 pp 1-7.
- [6] Chan N, Young-Rojanschi C and Li S. Effect of water-to-cement ratio and curing method on the strength, shrinkage and of the biosand filterconcrete body. Water and Science Technology. 2018 Vol 77.6
- [7] Carlos H. Aramburo, Pedrajas C, Talero R. Portland Cements with High Content of Calcined Clay: Mechanical Strength behaviour and sulfate durability. Materials. 2020 Vol 23 pp 4506.
- [8] Jaskulski R, Jó'zwiak-Nied 'zwiadzka D, Yakymchko Y. Calcined Clay as Supplementary Cementitious Material. Materials. 2020 Vol 13 pp 1-36.
- [9] Avet F and Scrivener K. Investigation of the calcined kaolinite content on the hydration of Limestone Calcined Clay Cement (LC³). Cement and Concrete Research. 2020 Vol 107 pp 124-135

Application of nanotechnology for the development of sustainable lignocellulosic materials

Yunhong Jiang^{1,2*}, Mike Lawrence², Atif Hussain^{2,3}, Davoud M Heidari⁴ and Martin Ansell²

1: HBBE, Department of Applied Science, Northumbria University, NE1 8ST, UK

2: Department of Architecture and Civil Engineering, University of Bath, BA2 7AY, UK

3: Department of Wood and Forest Sciences, Université Laval, Quebec, QC G1V 0A6, Canada

4: Department of Civil and Building Engineering, Université de Sherbrooke, J1K 2R1, Canada

Abstract

Environmental and sustainability concerns have driven the building industry to develop new and more durable sustainable building materials. Much attention has been focused on the utilisation of bio-based lignocellulosic materials for sustainable construction with low thermal conductivity and high hygrothermal efficiency as well as desirable environmental characteristics such as sustainability and renewability. The development of nanotechnology and nanomaterials offers an opportunity for the development of innovative, durable and multifunctional building materials. In this study, the combination of the hemp aggregates with natural matrix materials results in exceptionally low thermal conductivity and high hygrothermal efficiency compared to conventional materials of construction as a result of their microporosity and breathability. In addition, the developed bio-based composites with nanotechnology improve resistance to liquid water and protect the hemp shiv from biodegradation without impacting the natural ability of the shiv to buffer moisture vapor. Hemp-concrete and novel Hemp-organic composite have been studied and compared. Measurements of the thermal conductivity of hemp-composite panels are described which confirm their highly insulating properties. Hygroscopic testing demonstrates their effectiveness in absorbing and releasing moisture. The thermal and hygroscopic performance of hemp-composite panels in test cells is reported together with their application in construction. The life cycle assessment of hempcrete and hemp organic composite were performed. This study is part of the output of the ISOBIO programme supported by the European Union Horizon 2020 program, within the 'Materials for Building Envelopes' call for Energy Efficient Buildings.

Introduction

Using environmental-friendly and sustainable bio-based plant aggregates as raw materials for building insulation and construction is a new approach to address climate change and reduction in carbon dioxide emission. The bio-based insulation materials can form a breathable wall by readily absorbing and desorbing moisture in response to changes in relative humidity (RH) and vapour pressure gradients in the surrounding environment. They can act as a hygric buffer, reducing the energy requirements of air conditioning and increasing the comfort of the occupants in the building. Tran et al. reported the hierarchical cell wall structure of bio-based plant aggregates resulted in good air tightness and minimal thermal bridging of the building. They have huge potential to be used in mainstream building insulation industrial [1]. Collet et al. reported the hemp concretes are excellent hygric regulators and the total porosity and manufacturing method have a slight effect on the hygric performance of hemp concrete [2]. Although the bio-based plant aggregates have drawn great attention, the bio-based plant aggregates are still needed to be developed for the bio decay. Because the bio-based plant aggregates formed by Cellulose (40-48%), hemicellulose (18-28%) and lignin (20-26%), which are moisture sensitivity. The amount of moisture in the aggregates normally resulted in

microbial growth causing degradation of the aggregate cell wall and deterioration of the composite durability. The development of nanotechnology offers an opportunity for the development of innovative, durable and multifunctional building materials. Previous research showed that the developed bio-based composites with nanotechnology improving resistance to liquid water and protecting the hemp shiv from biodegradation without impacting the natural ability of the shiv to buffer moisture vapour [3]. Some of the approaches include addition of silanes, acetylation or in situ polymerization that involve chemical modification of the aggregate cell wall to enhance the hydrophobicity of plant-based aggregates and prevent materials from fungal, damp and keep their durability [4, 5]. However, there is limited knowledge on the impact of nano-coating on hygrothermal and moisture buffer value of the modified bio-composite and bio-composite panel, which have been developed for sustainable construction with low thermal conductivity and high hygrothermal efficiency. Moreover, environmental assessment is required to make a strategic decision related to the use of these bio-based materials instead of their fossil-based ones. This work compared the MBV value, water absorption and vapour permeability of untreated hemp composite and treated hemp composite. The thermal and hygroscopic performance of hemp-composite and hemp-composite panels in test cells is reported together with their application in construction. The life cycle assessment (LCA) of hempcrete and hemp organic composite were performed.

Materials and methods

Two sets of hemp organic composites were developed consisting of, (i) Untreated hemp composite: raw hemp shiv aggregates and bio-based binder; and (ii) Treated hemp composite: modified hemp shiv aggregates using a hydrophobic pre-treatment and bio-based binder. Generally, the sol-gel process was followed. 0.015M of hexadecyltrimethoxysilane (HDTMS) was added to the above mixture as the hydrophobic agent. The hemp shiv aggregates were dipped in the sol for 10 mins, transferred to an open tray and then dried at room temperature for one hour. Finally, the hemp shiv aggregates were placed in an oven at 80 °C for one hour. For preparation of the composites, the mixture of the constituent materials was placed into a steel mold of desired dimension and compacted at 0.5 MPa using a hot press (PressMasters 40T GEM series). The upper and lower plates were then heated to 180 °C and the temperature was maintained for one hour.

The specimens were demolded after cooling down to room temperature and then transferred to a conditioning room at 19 °C and 50% relative humidity. The details of moisture buffering test, vapour permeability test and water absorption test can be found in our previous publications [5]. The hemp organic composite which is the subject of this study was developed as part of the EU funded ISOBIO project and three ISOBIO wall systems and four reference walls were monitored at test facilities in the UK and Spain, for the purpose of measuring thermal transmittance using the Heat Flow Meter method to ISO 9869, and comparing results with calculated U-values to ISO 6946. Treated hemp shiv as a bio-based composite wall with thermal transmittance U-value of 0.15 W/m² K is compared to two other walls with same U-value, which were a wall made with untreated hemp shiv and a reference cavity wall constructed using traditional masonry techniques. Damage to the terrestrial ecosystem due to land use, acidification, photochemical ozone formation, ecotoxicity, water use and climate change were included. Potentially disappeared fraction of species (PDF), as a damage to the terrestrial biodiversity, integrated over area and time in m² y, was analysed for the functional unit of one kg of hemp shiv and sol-gel produced and subsequently per one square meter of insulation wall with a U-value of 0.15 W/m² K for one year of its service life.

Results and discussion

The MBV of the usual building materials reported in literature is shown in Figure 1 and compared with the MBV obtained for the organic hemp composites. It can be seen that the prepared hemp organic composites show excellent moisture buffering capacity. The MBV of the both untreated and treated hemp composites is higher than hemp concrete reported in literature (1.75-2.15 g/m².RH) [1, 2]. The high hemp shiv binder ratio in these composites result in lower density and thereby enhancing their vapour permeability.

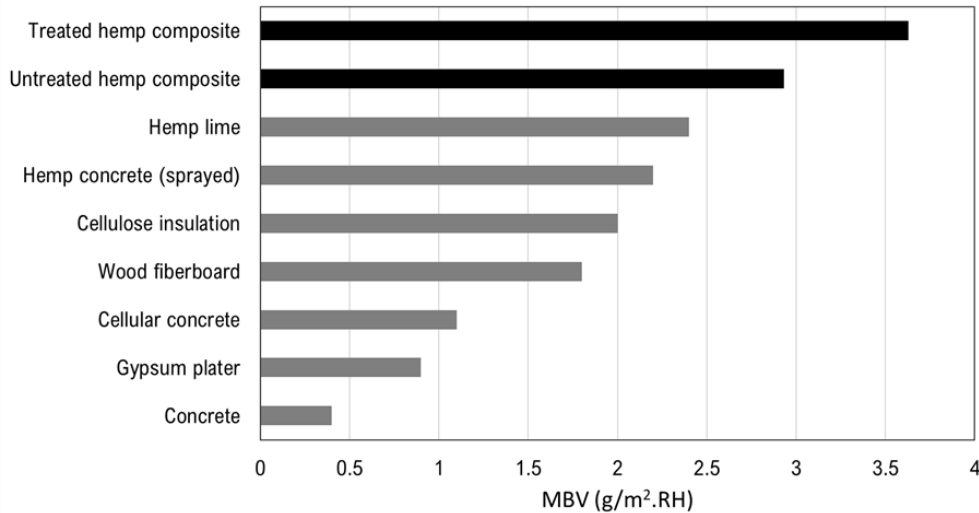


Figure 1. Moisture buffer value of general building materials vs the hemp organic composites [1-3]

The composites show promising results as seen in Table 1, behaving as a good vapour permeable material. It can be seen from the results that hydrophobic treatment of hemp shiv did not affect the vapour permeability of the material. Bio-based aggregates such as hemp shiv have very high porosity and as a result they have very low water vapour resistance. On the other hand, solid concrete has a very high water vapour diffusion resistance factor at about 130 while for hemp concrete it ranges between 5 and 12.

Table 1. Vapour permeability results of the hemp organic composites

Parameters	Untreated hemp composite		Treated hemp composite	
	Dry cup	Wet cup	Dry cup	Wet cup
Water vapour transmission rate, g (mg/hr)	6343.75	9833.33	7224.3	9605.6
Water vapour permeance, W (mg/m ² hr Pa)	4.72	8.13	5.37	7.94
Water vapour resistance, Z (m ² hr Pa/mg)	0.21	0.12	0.18	0.13
Water vapour permeability δ (mg/m hr Pa)	0.09	0.16	0.11	0.16
Water vapour resistance factor μ	7.54	4.37	6.62	4.48

The water absorption results are presented in Table 2. The untreated hemp composite shows higher values for WA and WA% due to the absence of hydrophobic silica treatment on hemp shiv in the composites. The hydrophobic treatment significantly reduced the WA by 50% and the WA% reduced by 123%. High sensitivity to moisture can be responsible for colonial fungal growth leading to cell wall degradation and affecting the durability of the material. High water absorption capacity can also affect the manufacturing quality of the final product if it

encounters water or is exposed to humid surroundings. The silica treatment used in this research reduced the hydrophilicity of hemp shiv as seen with the water absorption tests making them water resistant and less susceptible to degradation.

Table 2. Water absorption measurements of the hemp organic composite panels

Sample	Water Absorption (kg/m ²)	Water Absorption (%)
Untreated hemp composite	22.11 ± 0.7	221.10 ± 1.3
Treated hemp composite	11.04 ± 0.6	98.02 ± 3.5

Figure 2 shows a comparison of the measured U-value of the ISOBIO New-build panel, compared with the Reference New-build cavity wall. The results show a 65 % reduction in thermal transmittance of the ISOBIO panel compared with the New-build cavity wall. If we consider the ISOBIO New-build panel’s moisture buffering performance and impact on internal relative humidity, we can see that the panel offers superior performance compared to the Reference cavity wall.

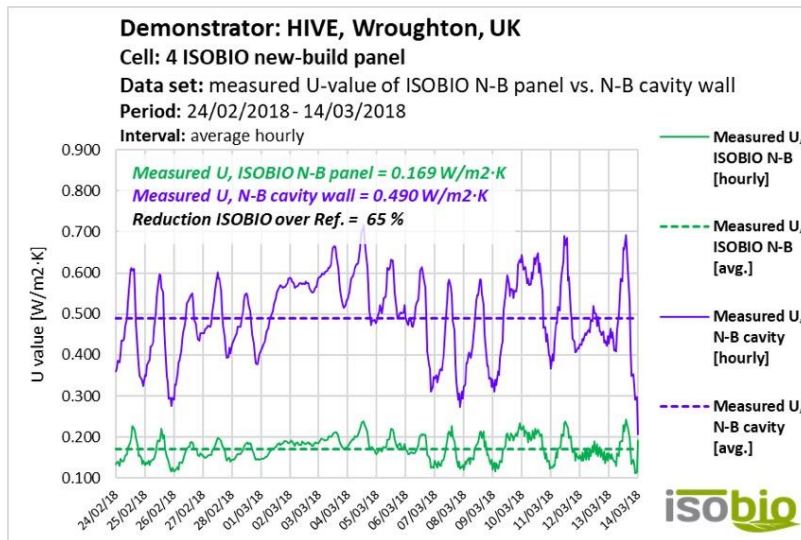


Figure 2. Measured U-value of ISOBIO New-build panel vs. Reference New-build cavity wall, HIVE, United Kingdom

Figure 3 below shows the relative humidity in Cell 4 (ISOBIO New-build panel) compared with Cell 1 (Reference New-build cavity wall), during the same period (24/02 - 14/03). The ISOBIO panel in Cell 4 helps maintain an average RH of 42 % (within the optimum comfort range for indoor relative humidity), while in Cell 1, the New-build cavity wall (being vapour impermeable), does not allow water vapour to dissipate, and RH remains at an average of 72 %. The ISOBIO External retrofit system reduced thermal transmittance by 55 % (UK) and 71 %, (Spain), in comparison with their respective reference walls.

Carbon footprint of one square meter of a wall, using treated and untreated hemp shiv was calculated using the IPCC 2013 GWP 100a method. The results based on mass allocation and untreated hempcrete wall are shown in Figure 4. Using economic allocation, the total carbon footprint of one m² of treated hempcrete wall (for its entire service life) is 24.65 kg CO₂-eq and 22.51 kg CO₂-eq based on end-of-life treatment as composting and landfilling, respectively.

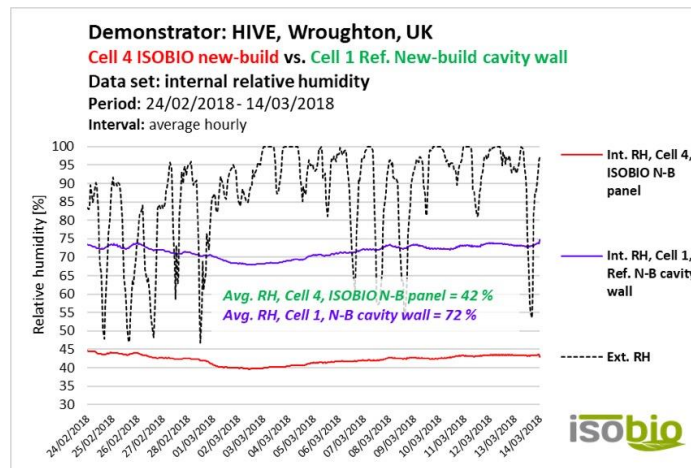


Figure 3. Average internal relative humidity of Cell 1 (ISOBIO New-build panel) vs. internal relative humidity of Cell 1 (Reference New-build cavity wall), HIVE, United Kingdom

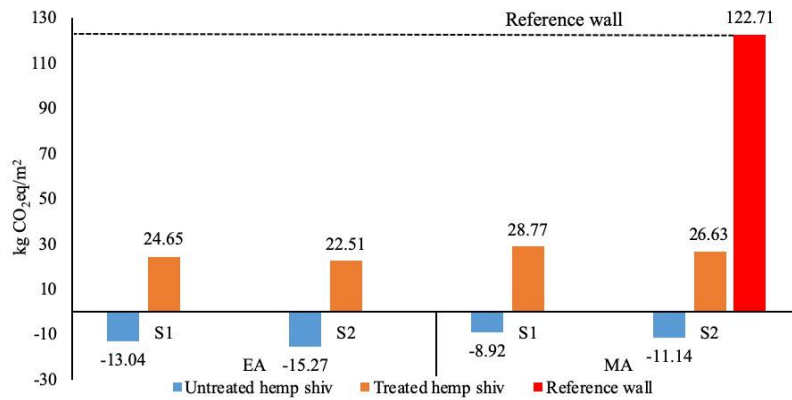


Figure 4. Carbon footprint of 1m² walls for their entire service life. EA and MA show the results based on economic and mass allocation. S1 and S2 are waste scenarios (S1: composting hemp shiv and landfilling the rest, S2: landfilling all the materials)

Conclusion

In this work, vapour permeability and Nordtest results validate that hemp shiv composites retain their hygroscopic and moisture buffering ability even after hydrophobic treatment of the aggregate. The silica treatment reduced the hydrophilicity of hemp shiv as seen with the water absorption tests making them water resistant and less susceptible to degradation. The UK monitoring results show that the ISOBIO new-build panel is a high-performance composite wall system, with a very good correlation between calculated and measured values and a near-zero performance gap. The data suggests that bio-based materials, when combined in a structural insulated panel with an air barrier, can provide predictable performance and high thermal resistance that will reduce heating and cooling energy consumption at building scale. The LCA results showed that using treated hemp shiv with sol gel can decrease the carbon footprint of a building envelope through carbon sequestration.

Acknowledgment

The work was supported by the ISOBIO project funded by the Horizon 2020 programme [Grant number 636835 – ISOBIO – H2020-EeB-2014-2015].

References

- [1] Tran Le AD, Maalouf C, Mai TH, Wurtz E, Collet F. Transient hygrothermal behaviour of a hemp concrete building envelope. *Energy Buildings*. 2010 42:1797-1806.
- [2] Collet F, Chamoin J, Pretot S, Lanos C. Comparison of the hygric behaviour of three hemp concretes. *Energy Buildings*. 2013 62:294-303.
- [3] Jiang Y, Bourebrab M, Sid N, Taylor A, Collet F, Pretot S, Hussain A, Ansell M, Lawrence M. Improvement of water resistance of hemp woody substrates through deposition of functionalized silica hydrophobic coating, while retaining excellent moisture buffering properties. *ACS Sustainable Chemical and Engineering* 2018 10151-10161
- [4] Bourebrab M, Durand G, Taylor A. Development of highly repellent silica particles for protection of hemp shiv used as insulation materials. *Materials*. 2018 11 4
- [5] Hussain A, Calabria J, Lawrence M, Jiang Y. Hygrothermal and mechanical characterisation of novel hemp shiv based thermal insulation composites. *Construction and Building Materials*. 2019 212 561-568.

Evaluation of the reactivity of selected rice husk ash-calcined clay mixtures for sustainable cement production

Joseph Mwiti Marangu¹, Eshrar Latif², Riccardo Maddalena³

¹Department of Physical Sciences, Meru University of Science and Technology, Meru-Kenya

²School of Architecture, Cardiff University, Cardiff-United Kingdom

³ School of Engineering, Cardiff University, Cardiff- United Kingdom

Abstract

There is an increasing demand for concrete in the construction industry globally. The use of locally available Supplementary Cementitious Materials (SCM) such as Rice Husk Ash (RHA) is considered an innovative strategy to lower the cost of cement production as well as promotion of environmentally friendly methods of waste disposal. This study presents the preliminary findings on the evaluation of the reactivity of selected RHA and Calcined Clay (CC) systems as potential SCMs for blended cement production. Different RHA/CC mixtures were formulated and subjected to chemical, mineralogical analysis and pozzolanicity analysis, as well as compressive strength tests using 40 mm x 40 mm x160 mm mortars prisms. Results showed that locally sourced RHA and CC were highly pozzolanic, providing the viable alternative materials for concrete production in Kenya.

Introduction

More than half of the world population live in cities. It is estimated that by the year 2050, two thirds of all humanity—6.5 billion people—will be living in urban areas [1]. Sustainable development cannot be achieved without significantly transforming the way we build and manage our urban spaces. The population of the world's urban areas is increasing by 200,000 people per day, all of whom need affordable housing as well as social, transportation and utility infrastructure. Hence there is an increasing demand for sustainable construction materials globally [1]. Concrete has been the most used construction material globally [2]. The potential of the use of CC blended with RHA in cement production and use in concrete has not been fully explored in Kenya. To achieve this, the reactivity of the CC-RHA blends required to be assessed. The present study therefore aimed at the evaluation of the reactivity of selected RHA-CC mixtures for mortar production.

Experimental

Materials

The clay was obtained from Mûkûrwe'inî (Nyeri, Kenya) (0.5609° S, 37.0488° E) and calcined at 800 °C for one hour to form the Calcined Clay (CC). Rice Husk (RH) was obtained from a rice processing plant (Mwea – Kenya). The RH was incinerated at 600 °C for 24 hours using a standard fixed bed kiln to obtain the RHA. Commercial Portland Cement (PC) used in this study was procured from East African Portland Cement Company Ltd (EAPCC) in Athi River, Machakos County in Kenya. The PC conformed to ASTM C 150 Type 1 (42.5 N/mm²). X-Ray Fluorescence (XRF) analysis was conducted on clay, RHA and PC to determine their chemical composition. The sum of SiO₂, Al₂O₃ and Fe₂O₃ was found to exceed 70 %. Therefore both RHA and CC met the KS 02 1260(1994) and ASTM C618 (2003) specification for use as pozzolana/SCM. Different proportions of CC, RHA and PC were mechanically mixed in an automatic mixer to make a formulation in nine batches varying proportions of CC, RHA and PC, as summarized in Table 1.

Materials and methods

Pozzolanic activities of the test RHA-CC-PC blends (marked as series 1-9) were evaluated using the saturated lime test method [3]. Mortar prisms measuring 160 mm x 40 mm x 40 mm for different binders (series 1-9) were separately cast at water/cement ratio (w/c) of 0.50 and cured in water in accordance with the EAS 148-1(2000) specifications. The compressive strength for the mortars was determined on triplicate samples after 2, 7, 14 and 28 days, using a uniaxial compressive machine.

Table 1. Sample series and their composition

Sample	Blend Composition (% w/w)		
	Portland Cement (PC)	Rice Husk Ash (RHA)	Calcined clay (CC)
Series 1	100	0	0
Series 2	50	50	0
Series 3	50	0	50
Series 4	50	40	10
Series 5	50	25	25
Series 6	50	10	40
Series 7	40	50	10
Series 8	40	35	25
Series 9	40	10	50

Results and Discussions

Pozzolanicity

The quantity of Ca(OH)₂ in the test cement solution containing RHA-CC-PC blends from each series was assessed in terms of the concentration of CaO and OH⁻ at different curing ages as represented Figure 1 and Figure 2 respectively. In principle, the lower the resulting quantity of CaO and OH⁻, the higher the pozzolanicity and vice versa.

From Figure 1 and 2, it was observed that with the exception of series 1, there was a progressive decrease in the concentration of CaO and OH⁻ in all the in series 2 to 9 for all the RHA-CC-PC blends with increased curing age. The difference can be attributed to the differences in their cement hydration actions. In the hydration of PC, the C₃S and C₂S phases undergo hydration reactions to produce CH as shown in Equation 1 and 2[4];



The CSH formed in Equation (1) and (2) is mainly responsible for strength development in the cement based structures. The increase in concentration of CaO and OH⁻ in PC (series 1) can be attributed to the production of CH with continued curing.

On the other hand, a notable decrease in concentration of OH⁻ and CaO in all the other RHA-CC-PC blends (series 2 to 9) which can be attributed to the consumption of CH during pozzolanic reaction in RHA-blended cements. Both RHA and CC contains amorphous silica and alumina and therefore exhibits pozzolanic properties [5].

The hydration of PC produces CH which reacts with silica and alumina present in both RHA and CC during the pozzolanic reaction, as shown in Equation 3 and 4 [6-7];



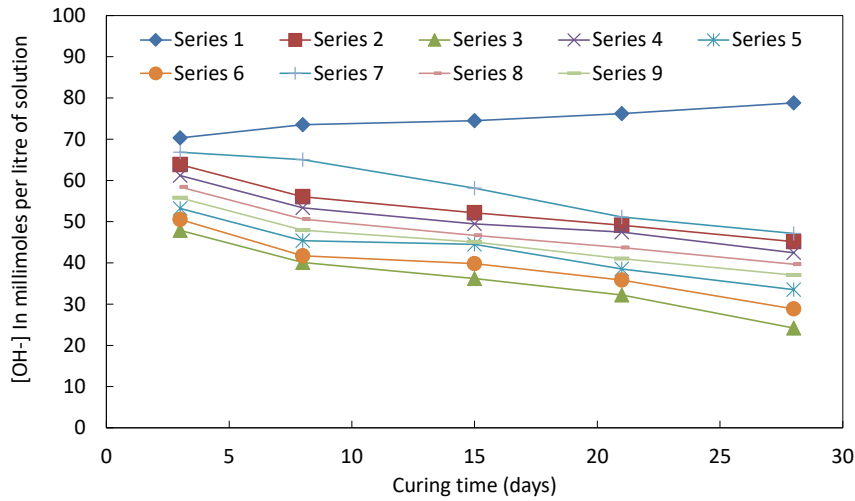


Figure 1: Concentration of OH⁻ in RHA-CC-PC blends

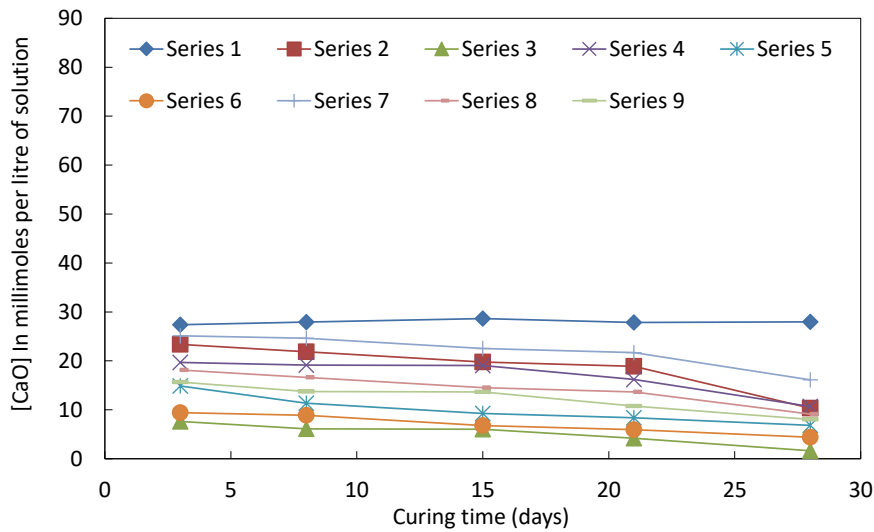


Figure 2: Concentration of CaO in RHA-CC-PC blends

Increased curing period results in higher consumption of CH in pozzolanic reactions results in progressive decrease in the amount of CH in the hydrated RHA-CC-PC blends matrix. In conclusion, RHA-CC-PC blends were found to exhibit pozzolanic properties.

Compressive Strength

The compressive strength results for various RHA-CC-PC blends at different curing ages are shown in Figure 3. It was observed that compressive strength increased with increased duration of curing for all the RHA-CC-PC blends. This can be attributed to the hydration reactions occurring in the hydrated cement matrix resulting in the formation of CSH as shown in Equation 1 and 2. The reference non-blended binder (series 1) exhibited higher compressive strength than the other RHA-CC-PC blends. This can be attributed to the fact that series 1 was neat PC hence contained the highest content of the clinker phases (C₃S and C₂S) which are mainly responsible for strength in comparison to the other series of RHA-CC-PC blends. Progressive decline in compressive strength with increased substitution of PC with either RHA or CC was noted. This could further be due to the progressive decrease in the content of PC in RHA-CC-PC blends. In conclusion, the KS EAS 18:1-2001 requires that pozzolana cements should have a minimum compressive strength of 32.5 MPa at 28 days of curing. In this study, only RHA-CC-PC blends represented by series 3, 5 and 6 of the RHA-CC-PC blends met this requirement. The

durability of series 3, 5 and 6 of the RHA-CC-PC blends was evaluated by subjecting the samples to accelerated ingress chloride test.

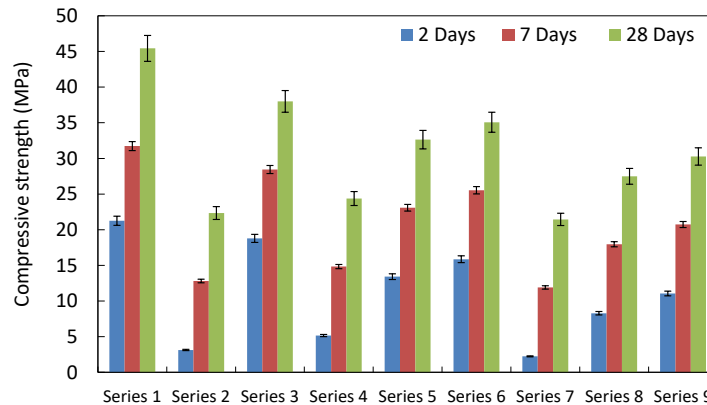


Figure 3: Compressive Strength Verses Various Binder Types (RHA-CC-PC blends)

Conclusions

From the study the following conclusions were made:

1. Locally sourced RHA and CC were highly pozzolanic, providing the viable alternative materials for concrete production in Kenya.
2. Only the RHA-CC-PC blend in series 3, 5 and 6 met the standard for use as blended cements.

Acknowledgement

This research was funded by the HEFCW GCRF Fellowship Award: Circular-Cement: local resources for affordable and sustainable infrastructures in Kenya.

References

1. United Nations; Department of Economic and Social Affairs; Population Division *World Urbanization Prospects: The 2018 Revision*; 2019; ISBN 978-92-1-148319-2.
2. Naik, T.R. Sustainability of Concrete Construction. *Practice Periodical on Structural Design and Construction* 2008, *13*, 98–103, doi:10.1061/(ASCE)1084-0680(2008)13:2(98).
3. Donatello, S.; Tyrer, M.; Cheeseman, C.R. Comparison of Test Methods to Assess Pozzolanic Activity. *Cement and Concrete Composites* 2010, *32*, 121–127, doi:10.1016/j.cemconcomp.2009.10.008.
4. Marangu, J.M.; Thiong'o, J.K.; Wachira, J.M. Chloride Ingress in Chemically Activated Calcined Clay-Based Cement. *Journal of Chemistry* 2018, *2018*, 1–8, doi:10.1155/2018/1595230.
5. Krishnan, S.; Emmanuel, A.C.; Bishnoi, S. Hydration and Phase Assemblage of Ternary Cements with Calcined Clay and Limestone. *Construction and Building Materials* 2019, *222*, 64–72, doi:10.1016/j.conbuildmat.2019.06.123.
6. Mwiti, M.J.; Karanja, T.J.; Muthengia, W.J. Properties of Activated Blended Cement Containing High Content of Calcined Clay. *Heliyon* 2018, *4*, e00742, doi:https://doi.org/10.1016/j.heliyon.2018.e00742.
7. Walker, R.; Pavía, S. Physical Properties and Reactivity of Pozzolans, and Their Influence on the Properties of Lime–Pozzolan Pastes. *Materials and Structures* 2011, *44*, 1139–1150, doi:10.1617/s11527-010-9689-2.

Building couture: knitting as a strategy for bespoke bio architecture

Jane Scott, Romy Kaiser, Paula Nerlich

Hub for Biotechnology in the Built Environment, Newcastle University, Newcastle NE1 7RU, UK

Abstract

The interest in mycelium, the root network of fungus, as a biomaterial for architecture is expanding as international research groups demonstrate the strength and durability of mycelium composites as a replacement for traditional building materials [1][2][3][4]. The transition to biocomposite systems in architecture offers an opportunity to fundamentally rethink material strategies moving away from the homogeneous, to a design approach that tailors material properties to specific functional requirements [5].

Textile fabrication is ideally suited to the production of highly specialised bio-composites, because the hierarchical nature of fabrics permits variable properties to be incorporated within a continuous material [6].

Knitting in particular, enables this functionalisation. Using knitting processes, specific yarns and fabric structure can provide localised sites for mycelium growth. Knit scaffolds can be designed in complex 2D and 3D shapes and knitted to shape with no waste. This research outlines the design of a series of experimental knitted scaffolds tested for mycelium growth. The paper details how fabric structure impacts mycelium growth and resulting integrity.

The significance of this research is twofold; firstly the research demonstrates the efficiency of the knitting process as a scaffold for mycelium growth with reference to specific knit parameters. In addition, the research creates knowledge for potential upscaling with digital fabrication techniques for architectural applications.

Introduction

The drive to net zero carbon requires a fundamental rethink of materials in the building sector, and mycelium-bound bulk composites have come into focus as a low impact, sustainable alternative to conventional bulk materials. Mycelium, the root network of fungus, as a living organism is dependent on water, light, temperature, airflow and nutrition's during growth and therefore requires different fabrication methods compared to traditional building materials. This is particularly explored in form of bricks, or panels shaped by growth in removable molds and used to demonstrate mycelium acoustic or thermal insulation qualities [2][4][8]. For strong and self-supporting structures in architecture however, it is argued that a geometrical assembly is the key aspect for creating stable structures, since mycelium itself is considered to be a rather weak material [1][3][8]. The performance, therefore, is highly dependent on its molding possibilities. Similarly, it is shown that mycelium composites can provide a wide range of properties depending on the given food, fungal species and mixed inoculation medium which results as bulk composite. [9][8][7].

In contrast to removable molds, introducing a textile form to scaffold mycelium enables both shaping of complex 3D structure and interaction with the material as reinforcement. This not only saves processing steps and time but also enhances the tailoring of material's properties. While mycelium as a surface treatment for textiles shows the expansion on the qualities of the textile like increased stiffness and water repellency [6], a rattan kagome weave framework [10] or filled cotton tubes [11], demonstrate the ability shape physical and aesthetical qualities by using textile-led methods for shape generation. Similarly, the Dynamic Assembly Lab suggests a modular system for architecture generated by complex branched 3D knitted shapes on an industrial machine [12]. Here bindings and yarns are adjusted to non-stretch qualities for molding purposes, relying on a small stitch size and synthetic yarns to generate a robust mold.

Knitted fabric is composed of loops of yarn, and this construction processes produces inherent multi-directional extensibility as the loops readily deform under tension [13]. The fundamental unit of knitting is the loop, therefore loop length is critical to determine both fabric properties and fabric dimensions. Knitted fabrics can be produced using a range of technologies, from industrial 3D knitting machines to handknitting using needles, but handknitting remains the most versatile production method in terms of the range of yarns and the variation to loop length achievable. Hand knitted samples can be produced from yarns with low/no twist, and with very high linear density, neither of which is readily achievable using current industrial technologies.

Despite previous examples which demonstrate successful application of fine gauge knitted molds, research has also shown that loose fibres encourage dense mycelium growth [14]. This paper, therefore, proposes the use of hand knitting, instead of machine knitting, incorporating lower twist yarns and lower density fabric structures within 3D knitted forms to investigate the integrity of mycelium growth and lower gauge knitting.

Materials and methods

The aim of this research was to analyse mycelium growth on a range of experimental tubular knitted scaffolds constructed from different fibre types to inform development of self-supporting textile biocomposites as preliminary studies for large-scale building composites. Initial experiments determined how mycelium growth varied on different handknit scaffolds and whether it results in lasting integrity for a biocomposite. Stitch density was explored in initial samples, to ascertain if the tightness of a fabric impacted mycelium growth.

Tests were undertaken using two fibre types; 100% merino wool, and 100% paper cellulose. Fabric specifications are included within table 1. Fabrics were constructed using hand knitting to produce seamless tubes. Knitted Tubes were filled with barley straw (as a substrate) and inoculated with spawn of oyster mushroom mycelium (*Pleurotus ostreatus*). Fabrics and substrate were pasteurised through submersion in boiling water. After cooling the tubes were filled with substrate and the mycelium spawn applied to the exterior of the tube along with millet acting as a nutrition source. During the growth stage samples were wrapped in plastic, kept in dark conditions and left at room temperature (approximately 20°C). Samples were grown in these conditions for 26 days. After growing samples were air dried in ambient conditions. All samples reduced in size after drying, with samples constructed from cellulose, and samples knitted as a lower fabric density (ie using larger needle size) demonstrating the highest dimensional shrinkage (table 1).



Figure 1: Mycelium Growth Experiments

Table 1. Mycelium Growth Experiments

	Fabric specification W (wales) C (courses) n (needle size)	Fibre Composition	Initial Dimensions HxD (mm)	Resultant Dimension HxD (mm)	Resultant Weight
1	18W25C (n3)	Wool	105 x 45	96 x 40	9 g
2	18W25C (n5)	Wool	180 x 55	150 x 50	20 g
3	18W25C (n3)	Cellulose	130 x45	110 x 38	13 g
4	18W25C (n5)	Cellulose	185 x 68	140 x 50	23 g

Visual analysis recorded the level of mycelium growth observable on the outside of the knitted samples, and this was analysed in reference to the transformation of the visible fabric structure. Samples 1 and 2 (wool) recorded minor changes to the surface of the fabric, the knitted stitches remained clearly visible. However mycelium growth on samples 3 and 4 completely covered the knitting, the greatest transformation was achieved on sample 4 with the lowest stitch density. Using a digital microscope the integrity of the binding was analysed further in relation to the different yarn types. Figure 2,3, and 4, illustrate different ways that the mycelium has interacted with textile fibres, suggesting the level of integration with the fabric varied dependent on fibre type or yarn structure.



Figure 2: Paper tape yarn: mycelium binds with yarn, high level of integration with mycelium



Figure 3: Wool yarn: mycelium binds with individual fibres some disintegration of yarn structure

Results and Discussion

From a textile design perspective, the observations regarding mycelium growth are significant to determine yarn selection for experimental development into self-supporting textile biocomposites. Using the findings of the initial tests, a series of 3 experimental 3D knit scaffolds were developed. These complex forms were handknitted (needle size 5) using a cotton knitted tape yarn, selected due to previous high level of integration between cellulose fibres and mycelium. However to retain the integrity of the yarn structure, a knitted tape with high strength was chosen for experimental work. The scaffolds were designed to incorporate techniques enabling the production of 1: branching structures and 2: variation to surface texture and structure. Each scaffold was knitted integrally, with no waste and no post-knitting

assembly required. 1 and 3 were prepared for growth using a sawdust substrate mixed with *Pleurotus ostreatus* mycelium spawn, 2 contained no substrate. The growth period was 3 weeks.

Visual analysis identified excellent mycelium growth, visible on the surface of each structure. Fabric properties were transformed by the mycelium; the biocomposite is stiff and rigid rather than soft and flexible, the multiple connecting tubes have been bound together by the mycelium solidifying the resulting geometry. Each biocomposite is self-supporting, standing at 25-30 cm high. The surface texture created by the garter stitch has less mycelium growth, however this has resulted in variable textures and changing surface qualities.

Table 2. Experimental Knit biocomposites

1 branching structure	2 surface texture (garter stitch)	3 multiple connected tubes
		

Resulting self-supporting experimental knit biocomposites



Conclusion

The visual result shows that hand-knitting enables lasting integrity in the composite acting as strength giving component, possibly due to higher permeability. This might lead to the assumption that fine gauge bindings and high twisted yarns required by the machines, could hinder airflow as well as the digestion of the material by mycelium growth. Due to the current Covid-19 situation, lab access was not available.

In this regards the visual conclusions regarding strength and integrity of growth are invite further examination by tensile strength/compression testing.

This preliminary study identifies the potential for the development of unconventional construction materials using knitted scaffolds for mycelium textile biocomposites. Whilst this research reports on handknitted samples, the knowledge of material qualities and bindings can be transferred for scale up to the built environment using digital fabrication via knitting technologies such as Shima Seiki. Further research is underway by the team focuses on scale up for the production of knit biocomposites at a building scale.

References

- [1] Benjamin, D. Living Matter. in Eds. Tibbit, S. (2017). Active Matter. The MIT Press, Cambridge.
- [2] Lelivelt, R.J., Lindner, G., Teuffel, P., & Lamers, H., (2015). The production process and compressive strength of Mycelium-based materials. In First International Conference on Bio-based Building Materials. 22-25 June 2015, Clermont-Ferrand, France. pp. 1-6
- [3] Frearson, A., (2017). "Tree-shaped structure shows how mushroom roots could be used to create buildings". <https://www.dezeen.com/2017/09/04/mycotree-dirk-hebel-philippe-block-mushroom-mycelium-building-structure-seoul-biennale/> Accessed 26.02.2021
- [4] Superflux, (2014). MOMA, Design and Violence, Mycotecture (Phil Ross). [online] Available at: <https://www.moma.org/interactives/exhibitions/2013/designandviolence/mycotecture-phil-ross/> Accessed 26.02. 2021
- [5] Colmo, C. and Ayres, P. (2020). 3D Printed Bio-hybrid Structures: Investigating the architectural potentials of mycoremediation. Werner, L and Koering, D (eds.), Anthropologic: Architecture and Fabrication in the cognitive age - Proceedings of the 38th eCAADe Conference - Volume 1, TU Berlin, Berlin, Germany, 16-18 September 2020, pp.573-582
- [6] Collet, C., (2017). "Grow-made" textiles, Alive. Active. Adaptive: International Conference on Experiential Knowledge and Emerging Materials, EKSIG 2017, pp. 24–37.
- [7] Elsacker, E., Peeters, E., Van Wylick A., De Laet, L., (2020). Growing living and multifunctional mycelium composites for large-scale formwork applications using robotic abrasive wire-cutting', Construction and Building Materials, 283(May). doi: 10.1016/j.conbuildmat.2021.122732.
- [8] Jones, M., et al., (2020). Engineered mycelium composite construction materials from fungal biorefineries: A critical review. Materials & Design 187: 108397.
- [9] Haneef, M., et al., (2017). Advanced Materials From Fungal Mycelium: Fabrication and Tuning of Physical Properties. Scientific Reports 7(1): 41292.
- [10] Adamatzky, A., Gandia, A., Ayres, P., Wösten, H., & Tegelaar, M., (Accepted/In press). Adaptive Fungal Architectures. *LINKs-series*, 5-6, 66-77.
- [11] Morby, A., (2017). Structure grown from "mushroom sausages" shows potential for zero-waste architecture. Available at: <https://www.dezeen.com/2017/06/20/aleksi-vesaluoma-mushroom-mycelium-structure-shows-potential-zero-waste-architecture/> Accessed 22.04.2021
- [12] Yogiaman, C., Pambudi, C.P., Jayahankar, D.K., Tracy, K.J., (2020). Knitted Bio-Material Assembly, ACADIA 2020: Distributed Proximities: Biological Interactions and Ecological Adaption. Publication in Press.
- [13] Munden, DL., (1959). The Geometry and Properties of Plain Knit Fabrics. Journal of the Textile Institute Transactions 50(7) pp448-4
- [14] Tabellini, G., (2015). Mycelium Tectonics, Available at: <http://mycelium-tectonics.com/> Accessed 28.04.2021

Bacterial Cellulose as a Building Material: Identifying opportunities, limitations and challenges

Heran Yang^{1,3}, Ruth Morrow^{1,3}, Ben Bridgens^{1,3}, Meng Zhang^{2,3}, Joshua Loh^{2,3}, Martyn Dade-Robertson^{1,3}

1: School of Architecture, Planning and Landscape, Newcastle University, Newcastle, NE1 7RU, UK

2: Department of Applied Sciences, Northumbria University, Newcastle, NE1 8ST, UK

3: Hub for Biotechnology in the Built Environment

Abstract

Bacterial cellulose (BC), a bacteria-synthesised cellulose material, has been intensively researched in biomedical, food and packaging over several decades. However, its application in the built environment (BE) has received less attention. This paper scopes out BC's original properties and the methods used to modify them. This capability to modify the properties of BC offers exciting possibilities for creating building components with low environmental impact, enhanced properties and targeted performance. In its unprocessed hydrogel state, BC yields promising strength and durability. This biodegradable material's production process can be sustained by several waste streams, making it a promising material for the circular economy. When used in composites, BC can act as a scaffold for multiple nanoparticles and polymers, extending its properties to, for example, provide electrical conductivity or antimicrobial surfaces. However, to support BC's application in the BE, the material must be studied at multiple scales, namely nano-, micro- and macro-scale. Standardised tests need to be developed and tailored to measure BC behaviour under complex BE scenarios. Its interaction with humidity, durability and its regenerative properties are identified as potentially fruitful areas for further investigation.

Introduction

Bacterial cellulose, usually generated as a pure cellulose gelatinous mat, secreted by a genus of bacteria known as *Komagataeibacter*, has garnered increased attention over recent years. Its first appearance in scientific paper dates to 19th century. Since then, traditional modification methods applicable to other cellulosic materials have been tested on BC, such as acetylation: a chemical surface treatment that makes this hydrophilic hydrogel repellent to water [1]. Other modification methods followed, attempting to add additional functionality or to optimise its performance. Hu et al., have made BC membranes that are antimicrobial or resistant to water [2]. Due to its high purity and biocompatibility, BC has been the focus of biomedical research, as a drug delivery substrate or as artificial tissue [3]. It has also been studied as a bio-degradable material source for packaging [4]. To date, the only BE-related application identified for BC has been as a reinforcing admixture for concrete [5].

BC is a product of a distinctive group of bacteria. Its formation, or fermentation, is typically sustained in a liquid nutritious culture medium in the presence of oxygen. The culture medium provides the bacteria with carbon and nitrogen sources, both indispensable to support the producer bacteria's metabolism. Several additives can be used in the culture medium to alter the BC membrane property, embedding extra functionality or interfering with its formation. The cellulose-genesis process will initiate once the required conditions are met, when the carbon source is consumed and extruded into β -1,4-glucan chains, a polysaccharide [6]. During extrusion, the cellulose-producing bacterium cell divides, creating numerous entangled and interconnected branches of polysaccharide chains, forming cellulosic ribbons, approx. 40 – 60 nm wide [7]. With hydroxyl groups interacting with each other and with the water, these

ribbons form a 3D meshed polysaccharide network in the form of a hydrogel mat that floats on the liquid-to-air interface [8].

This paper draws on an extensive body of BC research. Over 250 sources from both fundamental science, applied science and DIY experimentation were reviewed, with only the most significant sources cited in this abstract. The paper reflects on the demands and requirements of BC as a building material in terms of production efficiency (yield), mechanical properties, durability, aesthetics and functionality. Chemical substances, treatments and growing methods are reviewed in terms of their utility and efficiency. The paper also looks for a trajectory of research that indicates possible application of BC in the built environment.

Intrinsic properties

The key properties of BC are hydrophilicity, high crystallinity, high purity, excellent biocompatibility and UV-resistance. BC hydrogel membrane has a high water holding capacity, thanks to the hydroxyl groups on the entangled cellulose chains [8]. The consistently repeating biosynthetic process also gives BC a high crystallinity, as well as purity [6]. Its high crystallinity indicates higher tensile strength in comparison with other cellulosic materials [9]. Some researchers have suggested that BC is formed by the producer bacteria as a protection mechanism against UV radiation, whilst allowing liquid culture media to access oxygen [8]. Whilst these properties show potential for a range of applications in the built environment, a deeper understanding of both BC properties and the functional requirements of different building components is required to identify beneficial applications. In terms of the tensile strength and elastic modulus of BC, there is considerable variation, across scientific papers due to the varied nature of BC and means of testing. For example, following some simple loading experiments Cazón et al, record them as 20 MPa and 1GPa respectively [10]; Dayal and Catchmark report the elastic modulus to be around 7.55 MPa [11]; and according to Damsin, an unsterilised wet BC pellicle has an elastic modulus of 25 MPa, compared to 100 MPa for a sterilised, dried BC pellicle [12]. The literature search revealed little data regarding durability against chemical, biological or atmospheric corrosive agents, all of which are present in external BE applications. As a biopolymer, BC's resistance to photo-degradation is comparable to petrochemical-based polymers whose UV resistance and long-term integrity can be enhanced by antioxidants or stabilizers [13]. Furthermore, BC mechanical performance, UV resistance and insulative properties are reported to be humidity-sensitive [10].

Properties enhanced through modifications

In-situ modification methods can be carried out in nano- and micro-scale, through editing and selecting producer bacteria, co-culturing, choosing nutritional sources, additives and bioreactors.

The type of *producer bacteria* can influence production efficiency and BC grown form, among them *Komagataeibacter* is the most productive genus, producing long, consistent fibrils in the form of a gelatinous mat [14]. As the core concept of engineered living materials, the producer bacteria can be genetically edited at a nano-scale [15] and material microstructural patterns can be generated through a genetic strategy [16]. Levantis, a biodesigner, has proposed editing bacteria in a way that allows their production to be activated by light, enabling localised control of cellulose production, similar to a 3D printer [17]. This method could potentially be used to *grow* BC with complex geometries.

Co-culturing is a process whereby multiple microorganisms are hosted in a single culture medium. This method can be used to increase the yield or build in additional functions. It was proved feasible by Liu and Catchmark, who co-cultured *Escherichia coli* to produce a yield-boosting substance for BC producer bacteria [18]. Das et al. have co-cultured BC with

photosynthesising microalga, exploring their symbiotic relationship to fabricate a new type of living biomaterial [19].

Carbon and nitrogen sources are indispensable as *nutrition* and, in many cases, influence the yield and mechanical properties. Some carbon sources can boost the production, such as arabitol [20]. In comparison, lactose and sucrose are less effective [6]. Some are reported to increase mechanical performance, like mannose [21]. An increased fire-resistance can be achieved by using glucose phosphate as carbon source [22]. Typical nitrogen sources include yeast extract and peptone and among them, substances like vitamins and nicotinic acid can increase yield [23]. It should be noted, however, that the use of refined chemicals, involves intensive energy and material input [24].

Additives can affect production efficiency, mechanical properties and functionality. Antibiotics, such as nalidixic acid, are reported to interfere with cell division and protein activities, influencing mechanical properties [7]. Some additives, including agar, can alter the viscosity of the medium, and influence the yield and mechanical properties [25]. Starch can also change the medium viscosity, causing reduced crystallinity and changes in mechanical properties with different water content [26]. Sodium carboxymethyl cellulose can inhibit the formation of nanofibril bundles, changing the material crystallisation and internal stress [27]. Caffeine is reported to stimulate the BC growth, increasing the yield [23]. Vegetable oil is reported to significantly increase the yield and water-holding capacity and potentially the mechanical strength [28]. Metal and metal oxides have been used in the biomedical context to add functions, such as antibacterial [29].

Bioreactors, reviewed by Campano et al., are the containers where the BC biosynthesis process occurs. Increasing the air transfer ratio is critical for biodesigners, who often use tray-like containers to produce large BC membranes [30]. Multiple designs of airlift bioreactors have also been proposed [31]. Strategies, such as intermittent feeding, can make use of limited volume to effectively interact with air [32]. Agitation or air-pumping can increase oxygen exchange and the yield at the cost of forming a disrupted BC mass [33]. Plastics such as polyvinylchloride can be used as substrate or scaffold to host BC growth [34].

Ex-situ methods at a macro-scale involve sterilisation, drying, chemical and mechanical treatment.

Typically the BC hydrogels discussed in the literature are *sterilised* in boiling sodium hydroxide solution, thus disabling its bacterial activity. *Drying* can be achieved using air-convection, heat-press-drying, vacuum-drying and freeze-drying, though properties of BC are subject to change [35]. *Chemical treatment* on the surface or through impregnation has been found to change BC's water-resistance, thermal stability or structure performance and ethylene glycol etc. can alter the BC mechanical properties [12]. For example, BC impregnated with glycerol is reported to develop long-term water resistance [36]. And application of chitosan acetic acid solution allows BC to develop resistance against thermal degradation [37]. Chemical grafting is a common surface treatment to make BC antibacterial, water-repellent or transparent [38]. *Mechanical treatments* can alter physical appearance and form. Dry moulding results in shrinkage [39] and hot pressing alters the physical appearance, making it brittle but stiffer [12]. Grinding and casting BC is commonly used by designers, where BC is first shredded and a chemical binder added, before being added to a mould [40]. Stitching BC components together also appears to be durable enough for use in clothing [36].

Opportunities and Reflection

BC can be modified at multiple scales and at many stages within the manufacturing process, but to date its behaviour and performance has been investigated in limited contexts. However the growing body of research indicates that BC has characteristics that are conducive to BE applications, in terms of production efficiency (yield), durability, mechanical properties,

aesthetics and potentially other unique functionalities. Large scale BC production faces challenges, in terms of energy and material input, when using refined substances to support BC growth. However, research indicates that utilisation of waste streams offer potential nutritional alternatives for BC growth [38]. More data is needed to reveal its durability in outdoor environments, but given its similarity to other polymers, its exterior applications might be evaluated as a trade-off between decomposability and durability. However, it should be noted that when used as a blood vessel substitute, BC is relatively durable with only negligible degradation [41]. Vegetable oil offers an interesting path for further investigation, given its protective nature and ability to boost production and since some types of oil are used as wood stabilisers, this might also inform future weathering strategies [28]. Oil might also turn out to be an interesting method to achieve insulative performance, interfering with BC mesh formation and entrapping air bubbles. BC is likely to exhibit low UV-resistance, a similar challenge faced by many polymers, especially in the absence of antioxidants or stabilizers [13]. Its mechanical performance and UV resistance are also reported to be humidity-sensitive, which is a significant issue for external built environment applications [10]. In addition BC's reaction to water may offer unique strategies to manage water-related aspects. Its mechanical and aesthetic properties are demonstrated through apparel designs [42]. Although exhibiting limited strength and stiffness in its raw form, this can be compensated for by selecting the right nutrition, additives, in-situ and ex-situ composites and treatment. Notably, similar to an elastomer, BC's microstructure can realign to applied load [43]. Without sterilisation, the bacteria are likely to remain alive, maintaining a certain level of self-healing for the material. BC's unique properties, in relation to changes over time and in respect to built environmental context, need further study.

References

- [1] Kim DY, Nishiyama Y, Kuga S Surface acetylation of bacterial cellulose. *Cellulose*, 2002 9:361–367
- [2] Hu W, Chen S, Yang J, Li Z, Wang H Functionalized bacterial cellulose derivatives and nanocomposites. *Carbohydr Polym*, 2014. *Carbohydr. Polym*.
- [3] Heßler N, Klemm D Alteration of bacterial nanocellulose structure by in situ modification using polyethylene glycol and carbohydrate additives. 2009 899–910
- [4] Cazón P, Velázquez G, Vázquez M Bacterial cellulose films: Evaluation of the water interaction. *Food Packag Shelf Life*, 2020 25:100526
- [5] Akhlaghi MA, Bagherpour R, Kalhori H Application of bacterial nanocellulose fibers as reinforcement in cement composites. *Constr Build Mater*, 2020 241:118061
- [6] El-Saied H, Basta AH, Gobran RH Research progress in friendly environmental technology for the production of cellulose products (Bacterial cellulose and its application). *Polym - Plast Technol Eng*, 2004 43:797–820
- [7] Yamanaka S, Sugiyama J Structural modification of bacterial cellulose. *Cellulose*, 2000 7:213–225
- [8] Gama M, Gatenholm P, Klemm D Bacterial NanoCellulose: A Sophisticated Multifunctional Material *J Chem Inf Model*, 2012
- [9] Lee KY, Tammelin T, Kiiskinen H, Samela J, Schlufte K, Bismarck A Nano-fibrillated cellulose vs bacterial cellulose: Reinforcing ability of nanocellulose obtained topdown or bottom-up. *ECCM 2012 - Compos Venice, Proc 15th Eur Conf Compos Mater*, 2012 24–28
- [10] Cazón P, Velázquez G, Vázquez M Characterization of mechanical and barrier properties of bacterial cellulose, glycerol and polyvinyl alcohol (PVOH) composite films with eco-friendly UV-protective properties. *Food Hydrocoll*, 2020 99:105323
- [11] Dayal MS, Catchmark JM Mechanical and structural property analysis of bacterial cellulose composites. *Carbohydr Polym*, 2016 144:447–453
- [12] Damsin B, Bacterial Cellulose: New bio-composites based on bacterial cellulose for architectural membranes. 2019. Vrije Universiteit Brussel
- [13] Ashby M, Shercliff H, Cebon D *Engineering , Science , Processing and Design* 2007
- [14] Jonas R, Farah LF Production and application of microbial cellulose. *Polym Degrad Stab*, 1998 59:101–106
- [15] Nguyen PQ, Courchesne NMD, Duraj-Thatte A, Praveschotinunt P, Joshi NS Engineered Living Materials: Prospects and Challenges for Using Biological Systems to Direct the Assembly of Smart Materials. *Adv Mater*, 2018 30:1–34
- [16] Walker KT, Goosens VJ, Das A, Graham AE, Ellis T Engineered cell-to-cell signalling within growing bacterial

- cellulose pellicles. *Microb Biotechnol*, 2019 12:611–619
- [17] Levantis I Project:JuicyPrint. 2014. <https://biohackspace.org/projects/juicyprint/>
- [18] Liu K, Catchmark JM Enhanced mechanical properties of bacterial cellulose nanocomposites produced by co-culturing *Gluconacetobacter hansenii* and *Escherichia coli* under static conditions. *Carbohydr Polym*, 2019 219:12–20
- [19] Das AAK, Bovill J, Ayes M, Stoyanov SD, Paunov VN Fabrication of living soft matter by symbiotic growth of unicellular microorganisms. *J Mater Chem B*, 2016 4:3685–3694
- [20] Mikkelsen D, Flanagan BM, Dykes GA, Gidley MJ Influence of different carbon sources on bacterial cellulose production by *Gluconacetobacter xylinus* strain ATCC 53524. *J Appl Microbiol*, 2009 107:576–583
- [21] Liu K, Catchmark JM Effects of exopolysaccharides from *Escherichia coli* ATCC 35860 on the mechanical properties of bacterial cellulose nanocomposites. *Cellulose*, 2018 25:2273–2287
- [22] Basta AH, El-Saied H Performance of improved bacterial cellulose application in the production of functional paper. *J Appl Microbiol*, 2009 107:2098–2107
- [23] Fontana JD, Franco VC, De Souza SJ, Lyra IN, De Souza AM Nature of plant stimulators in the production of *Acetobacter xylinum* (“tea fungus”) biofilm used in skin therapy. *Appl Biochem Biotechnol*, 1991 28–29:341–351
- [24] de Araújo e Silva R, Santa Brígida AI, de Freitas Rosa M, da Silva Neto RM, Spinosa WA, Benício de Sá Filho E, Brito de Figueirêdo MC An approach for implementing ecodesign at early research stage: A case study of bacterial cellulose production. *J Clean Prod*, 2020. *J Clean Prod*. <https://doi.org/10.1016/j.jclepro.2020.122245>
- [25] Ishida T, Sugano Y, Nakai T, Shoda M Effects of acetan on production of bacterial cellulose by *acetobacter xylinum*. *Biosci Biotechnol Biochem*, 2002 66:1677–1681
- [26] Grande CJ, Torres FG, Gomez CM, Troncoso OP, Canet-Ferrer J, Martínez-Pastor J Development of self-assembled bacterial cellulose-starch nanocomposites. *Mater Sci Eng C*, 2009 29:1098–1104
- [27] Chen HH, Chen LC, Huang HC, Lin S Bin In situ modification of bacterial cellulose nanostructure by adding CMC during the growth of *Gluconacetobacter xylinus*. *Cellulose*, 2011 18:1573–1583
- [28] Żywicka A, Junka AF, Szymczyk P, Chodaczek G, Grzesiak J, Sedghizadeh PP, Fijałkowski K Bacterial cellulose yield increased over 500% by supplementation of medium with vegetable oil. *Carbohydr Polym*, 2018 199:294–303
- [29] Shah N, Ul-Islam M, Khattak WA, Park JK Overview of bacterial cellulose composites: A multipurpose advanced material. *Carbohydr Polym*, 2013 98:1585–1598
- [30] Ōun R Crafting organic waste for fashion. 2019. <https://www.riinao.com/lab>
- [31] Lee KY, Buldum G, Mantalaris A, Bismarck A More than meets the eye in bacterial cellulose: Biosynthesis, bioprocessing, and applications in advanced fiber composites. *Macromol Biosci*, 2014. *Macromol Biosci*. <https://doi.org/10.1002/mabi.201300298>
- [32] Hsieh YC, Yano H, Nogi M, Eichhorn SJ An estimation of the Young’s modulus of bacterial cellulose filaments. *Cellulose*, 2008. *Cellulose*. <https://doi.org/10.1007/s10570-008-9206-8>
- [33] Damsin B Higher BC yield with aquarium air filter. 2019
- [34] Cacicedo ML, Castro MC, Servetas I, Bosnea L, Boura K, Tsafrakidou P, Dima A, Terpou A, Koutinas A, Castro GR Progress in bacterial cellulose matrices for biotechnological applications. *Bioresour Technol*, 2016 213:172–180
- [35] Clasen C, Sultanova B, Wilhelms T, Heisig P, Kulicke WM Effects of different drying processes on the material properties of bacterial cellulose membranes. *Macromol Symp*, 2006 244:48–58
- [36] Kamiński K, Jarosz M, Grudzień J, Pawlik J, Zastawnik F, Pandyrza P, Kołodziejczyk AM Hydrogel bacterial cellulose: a path to improved materials for new eco-friendly textiles. *Cellulose*, 2020 27:5353–5365
- [37] Cai Z, Chen P, Jin HJ, Kim J The effect of chitosan content on the crystallinity, thermal stability, and mechanical properties of bacterial cellulose-chitosan composites. *Proc Inst Mech Eng Part C J Mech Eng Sci*, 2009 223:2225–2230
- [38] Andriani D, Apriyana AY, Karina M The optimization of bacterial cellulose production and its applications: a review. *Cellulose*, 2020 27:6747–6766
- [39] Bloch K Micro - Design Potential of Microbial Cellulose in Growing Architecture Master. 2019. Chalmers School of Architecture
- [40] Iguchi M, Mitsuhashi S, Ichimura K, Nishi Y, Uryu M, Yamanaka S, Kunihiko W Bacterial Cellulose-Containing Molding Material Having High Dynamic Strength. *United States Pat*, 1988. *United States Pat*.
- [41] Pértile RAN, Moreira S, Gil Da Costa RM, Correia A, Guardão L, Gartner F, Vilanova M, Gama M Bacterial cellulose: Long-term biocompatibility studies. *J Biomater Sci Polym Ed*, 2012 23:1339–1354
- [42] Suzanne Lee, Congdon A, Parker G, Borst C UNDERSTANDING “ BIO ” MATERIAL INNOVATIONS : a primer for the fashion industry. 2020
- [43] Gao X, Sözümert E, Shi Z, Yang G, Silberschmidt V V. Mechanical modification of bacterial cellulose hydrogel under biaxial cyclic tension. *Mech Mater*, 2020 142:103272

Session 3A Advanced modelling and simulation of smart infrastructure materials

Chair: Dr Cristina Tuinea-Bobe

1172 *Masoero et al.* Coupled simulations of bacterial evolution and mineral dissolution/ precipitation

1197 *Javierre.* A two---phase reactive flow model of self---healing reactions

1262 *Sayadi et al.* Time dependent micromechanical self-healing model for cementitious material

1119 *Freeman et al.* A CutFEM approach for simulating coupled 3D matrix - 2D crack plane flow of a healing agent in cementitious materials

1138 *Antonov et al.* Simulation of moisture transport through bio-based materials using independent measurements of water vapour diffusivity

1117 *Bonilla-Villalba et al.* A micro-mechanics-based element for modelling fibre bridging in embedded cracks

Coupled simulations of bacterial evolution and mineral dissolution/precipitation

Enrico Masoero, Denis Taniguchi, Irina Dana Ofiteru

School of Engineering, Newcastle University, Newcastle upon Tyne NE1 7RU, UK

Abstract

The engineering of bacterial activity for material production is subject of increasing interest from the scientific community. An important example is controlling microbially induced calcium carbonate precipitation to repair cracks in self-healing concrete. The current understanding of such processes is mainly empirical, due to the difficulty to model the underlying complex coupling between chemical reactions, mechanical interactions, and morphology evolution. Here we present a new simulator which combines state-of-the-art computational models of bacterial metabolism and mineral dissolution/precipitation. The simulator is based on the Kinetic Monte Carlo method and predicts evolutions of bacterial colonies within the pore of concrete, where the evolving chemical composition of the pore solution controls the coupling between bacteria and minerals over time. Results include temporal evolutions of the pore chemistry and of the chemical compositions, morphologies, and mechanical properties of both the bacterial colony and the minerals. The presented simulator provides a new way to predict the interaction between bacteria and minerals in concrete, with potential to support the development of future designs for self-healing materials in engineering.

Introduction

There is a growing interest in engineering the activity of bacteria to produce bespoke materials. An important example is controlling microbially induced calcium carbonate precipitation to repair cracks in self-healing concrete. The current understanding of such processes is mainly empirical, due to the difficulty to model the underlying complex coupling between chemical reactions, mechanical interactions, and morphology evolution.

Here we present a new simulator which combines state-of-the-art computational models of bacterial metabolism and mineral dissolution/precipitation. It features a bottom-up approach based on first principles that allows a more generic representation of the phenomena. The simulator is based on the Kinetic Monte Carlo method and predicts evolutions of bacterial colonies within the pores of concrete, where the evolving chemical composition of the pore solution controls the coupling between bacteria and minerals over time. Results include temporal evolutions of the pore chemistry and of the chemical compositions, morphologies, and mechanical properties of both the bacterial colony and the minerals. The presented simulator provides a new way to predict the interaction between bacteria and minerals in concrete, with potential to support the development of future designs for self-healing materials in engineering.

Materials and methods

The simulations consider the co-evolution of cement minerals and bacteria in a representative volume with linear length-scale of some tens of micrometres. Bacteria are modelled individually as micrometre-sized spherical particles that can grow, duplicate, and die, while consuming a background aqueous solution of nutrients and ions. The cement minerals are also represented as micrometre-sized spherical particles, each coarse-graining billions of molecules of the corresponding solid. The mineral particles can dissolve or nucleate depending on the surrounding solution chemistry and on the mechanical interactions with other mineral particles or bacteria.

Bacteria growth is governed by the stoichiometry of the chemical reactions for the intake and products of the bacteria metabolism allowing different chemical forms to coexist and therefore take into account the variation in pH. Spatial distribution is highly affected by the mechanical interactions and division. Diffusion of chemical species within the simulated environment is also taken into consideration, as well as the increase/decay in concentration due to bacterial activity. A detailed description of the software framework developed for the simulation of bacteria can be seen in [1] and its application with focus on the thermodynamics and the impact of chemical speciation in [2].

Bacterial processes are modelled as a continuous integration of changing rates for growth, nutrient consumption, etc. Mineral evolution instead is simulated as a sequence of discrete events constructed with the Kinetic Monte Carlo method. At any given configuration of the system, the algorithm computes the rate of each possible discrete event, which here are the dissolution of any mineral particle, or the nucleation of a particle of any allowed type at a sufficiently large number of locations within the simulation box. More details about the algorithm for particle insertion and deletion are available in a separate publication [3]. The rate of a dissolution or nucleation event is computed following classical Transition State Theory, which provides rate equations for one-molecular reactions. These rate equations depend on the stoichiometry of the underlying chemical reaction, on the corresponding equilibrium constant, on the concentrations of involved ions in solution (more specifically, on the saturation index Ω of the chemical reaction), on the surface energy of the mineral, and on the interaction energy between the mineral particle to be dissolved or nucleated and other particles. The interaction energy is computed using LAMMPS, as a position-dependent pairwise spherical interaction potential of harmonic type (viz. a linear spring) parametrised to represent the surface energy and mechanical properties of the mineral at the nanoscale [3, 4].

The rates provided by Transition State Theory refer to a one-molecular chemical reaction, but dissolution and nucleation of a mineral particle in our simulations are a coarse-grained representation of billions of such reactions for each event. Rigorous coarse-graining schemes can be developed (e.g. in [3]) but for the sake of simplicity and given the demonstrative nature of this manuscript, here we decided to assume that all the chemical reactions involved in the dissolution or nucleation of a mineral particle occur in parallel, at the same time. This means that the coarse-grained rate to dissolve or nucleate a one-micrometre particle is taken to be the same as the rate for a uni-molecular chemical reaction from Transition State Theory. This approximation leads to a significant underestimation of the time scale for dissolution and nucleation, but this is compensated for by fitting the activation free energy for the chemical reaction, which defines the rate prefactor in the Transition State Theory equations, until the time scale goes back to one that is reasonably close to the experimental one.

To combine the evolution of bacteria with that of minerals, our new simulator considers a single timeline for all the possible events and, at the generic time t , it evaluates when the next discrete event of mineral dissolution or nucleation will take place. This is based on the Kinetic Monte Carlo which specifies that the average time for a discrete event to occur is linked to the inverse of the total rate of all possible events, all of which can be calculated referring to the Transition State Theory approach described above. For the continuous integration of the bacterial evolution, instead, the simulator requires the user to specify the time step dt of integration and the number of steps n to be carried out before considering whether a discrete event of mineral dissolution or precipitation should occur. If the time of occurrence of the next discrete event is greater than ndt , then the bacterial evolution is integrated, otherwise the discrete event is carried out. Care is taken to synchronise the time scales but such a level of detail in the explanation is left to future contributions.

The coupling between mineral and bacterial evolution emerges from two aspects. First, bacteria and minerals occupy the same simulation box and interact mechanically via potentials,

similar to the harmonic one that has been mentioned already for the mineral particles. Second, bacteria and minerals are in contact with the same aqueous solution, whose chemical composition changes over time due to bacterial activity and mineral dissolution and precipitation. For the biomineralization process, this makes it possible for bacteria to release CO₂ into the solution and for minerals to take it up and form calcium carbonate.

This manuscript presents first results from our new coupled simulations. For now, the only minerals that have been considered are calcium hydroxide and calcium carbonate, whose dissolution reactions follow the stoichiometries and feature the rate parameters listed in Table 1. Precipitation rates are obtained as inverse dissolution rates, thus using the same parameters as in Table 1.

Table 1. Stoichiometry and rate parameters of the mineral dissolution and precipitation reactions [5,6]

Reaction	$\text{Ca(OH)}_2 \rightarrow \text{Ca}^{2+} + 2\text{OH}^-$
Equilibrium constant K_{eq}	$5.5 \cdot 10^{-6}$
Water-solid interfacial energy γ (mJ/m ²)	68.4
Activation energy ΔG^* (mJ)	$4.932 \cdot 10^{-17}$
Reaction	$\text{CaCO}_3 \rightarrow \text{Ca}^{2+} + \text{CO}_3^{2-}$
Equilibrium constant K_{eq}	$3.7 \cdot 10^{-9}$
Water-solid interfacial energy γ (mJ/m ²)	120
Activation energy ΔG^* (mJ)	$5.836 \cdot 10^{-17}$

Results and discussion

Two sets of results are presented here, to show the capabilities of the new simulation technique. The first set of results concerns the self-healing of a crack in calcium hydroxide without bacteria involved. The second result shows the co-evolution of a calcium hydroxide, calcium carbonate, and bacterial colony system. Figure 1.a shows a micro-cracked domain of calcium hydroxide that is coarse-grained as an ordered arrangement of spherical particles of Ca(OH)₂ with diameter of 1 μm. The crack is filled with an aqueous solution of CO₃²⁻, with initial concentration of 1 mol/L. The system is considered as a closed one, meaning that chemicals cannot diffuse into or out of the simulation box. Periodic boundary conditions are set in all directions. Since no bacteria are present, the only chemical reactions that can occur are the dissolution and precipitation of calcium hydroxide and carbonate.

These initial results predict the expected evolution of the system (Figure 1). Initially, the absence of Ca ions in solution promotes dissolution of Ca(OH)₂. As the concentration of Ca in solution increases, the high concentration of CO₃²⁻ will rapidly lead to supersaturation with respect to CaCO₃ precipitation, and the higher molar volume of the carbonate compared to the hydroxide will lead to progressive filling of the crack. The beneficial impact of this autogenous (viz. without bacteria) self-healing process are shown in Figure 2, which indicates a significantly improved stress-strain behaviour of the healed system when subjected to uniaxial tension in the direction perpendicular to the plane of the crack.

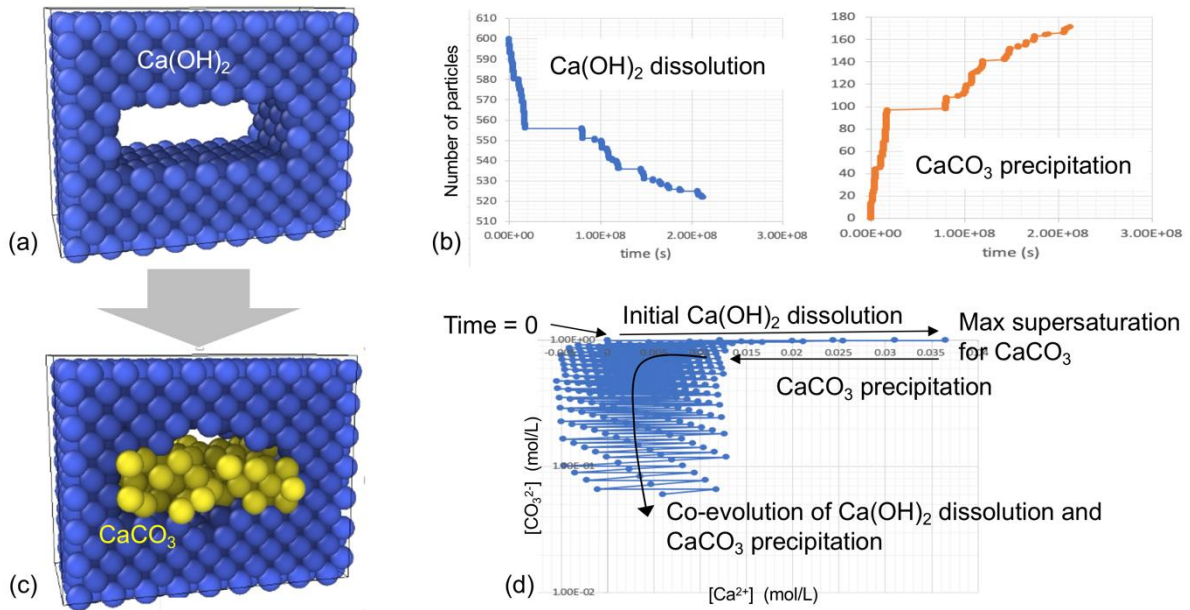


Figure 1. Cracked domain of calcium hydroxide (a) before and (c) after autogenous self-healing due to calcium carbonate precipitation. (b) Temporal evolution of number of solid particles, discretising the domains of calcium hydroxide and carbonate. (d) Solubility plot of the solution as it evolves during the simulation.

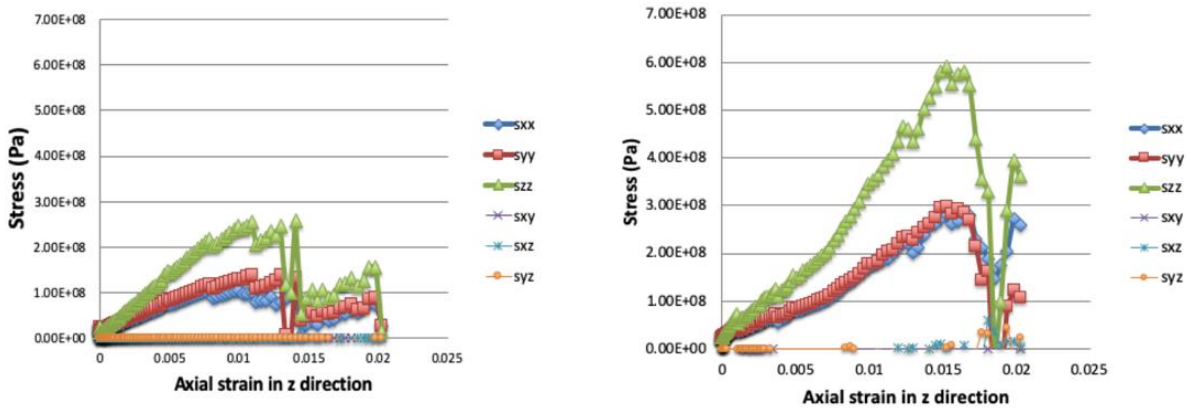


Figure 2. Stress-strain curves of the system in Figure 1, before (left) and after (right) self-healing.

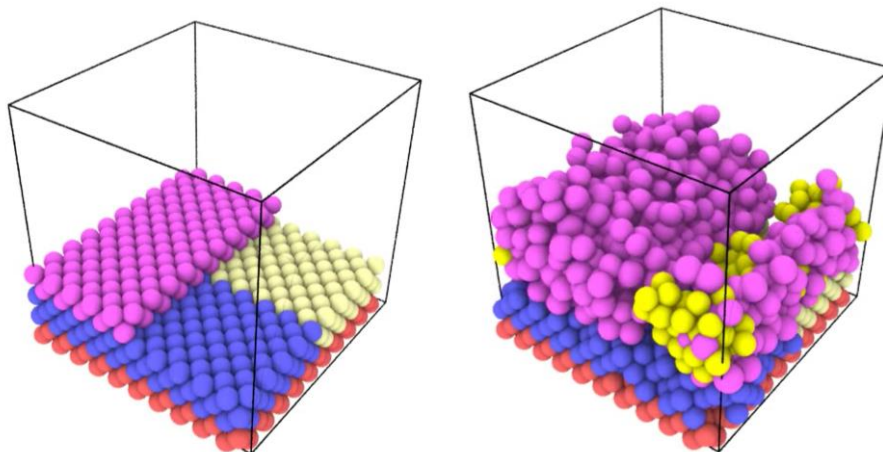


Figure 3. The evolution of the coupled mineral (red, blue, and light yellow are Ca(OH)_2 , darker yellow is CaCO_3 forming) and bacteria (pink) simulation

Figure 3 shows the evolution of a system containing $\text{Ca}(\text{OH})_2$ and CaCO_3 with the addition of bacteria. The model employed for bacterial growth consists of simple oxygen consumption leading to biomass growth with no coupling with the precipitation kinetics. Therefore, the input parameters were chosen just to allow growth and division, as an initial exploration on how bacteria and mineral share the same space and to investigate the feasibility of coupling the two simulations. Further stages of this study will include the proper representation of the stoichiometry related to the bacteria catalysing precipitation, and the definition of the input parameter values for the phenomenon as per [1, 2].

Conclusion

The simulator presented here is the first to simulate the co-evolution of bacterial colonies and minerals in concrete. First results have showcased some key capabilities of the simulators, namely its ability to:

- simulate the concomitant kinetics of chemical reactions inducing mineral dissolution/precipitation and bacterial metabolism;
- follow the evolving chemistry of the solution with which minerals and bacteria are interfaced;
- predict the change of mechanical properties of the material system as a result of self-healing.

The simulator is part of an EPSRC-funded research project which also includes experiments that will be used to calibrate the simulations. The experiments will be performed in similar conditions (one bacterial strain capable of biomineralization, one nutrient source, one Ca^{2+} source, same pH) and results will be compared in terms of CaCO_3 precipitation extent and rates. Once validated, the capabilities of the simulator can be leveraged to inform macroscale models of self-healing [7], providing a pathway for multi-modelling of the process which can guide the optimisation of bacteria-concrete formulations.

Acknowledgment

Research funded by the UK Engineering and Physics Research Council, EPSRC, grant EP/S013997/1

References

- [1] Li B, Taniguchi D, Gedara JP, Gogulancea V, Gonzalez-Cabaleiro R, Chen J, McGough AS, Ofiteru ID, Curtis TP, Zuliani, P. NUFEB: A massively parallel simulator for individual-based modelling of microbial communities. *PLOS Computational Biology*. 2019 Vol 15.
- [2] Gogulancea V, González-Cabaleiro R, Li B, Taniguchi D, Jayathilake PG, Chen J, Wilkinson D, Swailes D, McGough AD, Zuliani P, Ofiteru ID, Curtis TP. Individual Based Model Links Thermodynamics, Chemical Speciation and Environmental Conditions to Microbial Growth. *Front. Microbiol.* 2019 Vol 10.
- [3] Shvab I, Brochard L, Manzano H, Masoero E. Precipitation mechanisms of mesoporous nanoparticle aggregates: off-lattice, coarse-grained, kinetic simulations. *Crystal Growth & Design*. 2017 Vol 17 pp.1316-27.
- [4] Masoero E, Jennings HM, Ulm FJ, Del Gado E, Manzano H, Pellenq RJ, Yip S. Modelling cement at fundamental scales: From atoms to engineering strength and durability. *Computational Modelling of Concrete Structures*. 2014 Vol 1 pp. 139-48.
- [5] Estrela C, Estrela CR, Guimarães LF, Silva RS, Pécora JD. Surface tension of calcium hydroxide associated with different substances. *Journal of Applied Oral Science*. 2005 Vol 13 pp. 152-6.
- [6] Fernandez-Martinez A, Hu Y, Lee B, Jun YS, Waychunas GA. In situ determination of interfacial energies between heterogeneously nucleated CaCO_3 and quartz substrates: thermodynamics of CO_2 mineral trapping. *Environmental science & technology*. 2013 Vol 47 pp. 102-9.
- [7] Jefferson, T., Javierre, E., Freeman, B., Zaoui, A., Koenders, E. and Ferrara, L., 2018. Research progress on numerical models for self-healing cementitious materials. *Advanced materials interfaces*, 5(17), p.1701378.

A two-phase reactive flow model of self-healing reactions

Etelvina Javierre^{1,2}

1: Centro Universitario de la Defensa, Academia General Militar, Ctra. Huesca s/n, 50090 Zaragoza, Spain

2: Instituto Universitario de Investigación en Matemáticas y Aplicaciones (IUMA), Universidad de Zaragoza, Zaragoza, Spain

Abstract

Self-repair of cracks in concrete can be achieved by the timely activation of different multi-physics and multiscale approaches. The efficiency of these can, in turn, be improved by tuning the progress of specific chemical reactions within enhanced concrete matrices. For instance, the performance of autogenous healing reactions can be improved by the incorporation of fibres that restrain crack growth, of encapsulated bacteria as additional sources for the carbonation reaction or of superabsorbent polymer particles as active elements in the sealing of a crack. In this work we consider a two-phase reactive flow problem to describe the physicochemical coupling of the healing reactions. This general framework allows to consider a wide range of experimental conditions (i.e., moisture and air exposure conditions) as well as to address changes in the matrix microstructure during the course of the considered reactions. In particular, the calcite carbonation reaction is considered here, although the proposed approach can be generalized to other chemical reactions.

Introduction

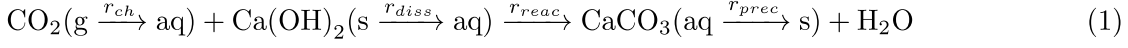
Self-repair of cracks in concrete can be achieved by the timely activation of different multi-physics and multiscale approaches. The efficiency of these can, in turn, be improved by tuning the progress of specific chemical reactions within enhanced concrete matrices. Autogenous healing reactions are efficient to seal small cracks, and their performance depends on concrete composition and age and healing conditions [1]. In this last aspect, results indicate that healing under cycling wet-dry conditions outperforms the autogenous healing under immersion and/or air exposure conditions [2]. Additionally, a number of approaches aim at synergistically cooperate with the healing reactions by limiting crack growth (incorporation of fibres or SMP tendons in the matrix), by enhancing healing reactions (encapsulation of bacteria or the incorporation of admixtures) or by managing water content within the matrix (incorporation of superabsorbent polymers in the matrix) [3].

Thus, the chemical reactions driving the precipitation of solid compounds at the crack site are common and central step in many of the different self-healing approaches. In general terms, the progress of the active chemical species can be modelled (at the macroscopic scale) as a reactive flow problem [4] with potentially many coupled convection-diffusion-reaction equations. A generic autogenous self-healing mechanism is considered in [5] for early-age cementitious materials. The model is formulated in terms of the transport phenomena in porous media, and provide a detailed representation of the porosity evolution as a result of changes in the water content caused by the ongoing hydration reactions. The healing of the crack is modelled as the precipitation of a generic cementitious compound without considering the specific reaction kinetics of the individual chemical species. In this work we consider a two-phase reactive flow problem to model a generic purpose healing reaction. We consider the calcium hydroxide carbonation reaction, and the presented model builds up on its physicochemical description [6], and on the multiphase flow in porous media [7,8].

Materials and methods

The calcium hydroxide carbonation reaction is considered here as a prototype model. This reaction proceeds through a number of steps, that include absorption of carbon dioxide,

dissolution and reaction of the involved species and finally the precipitation of calcium carbonate, as briefly summarized in Eq. (1):



where r_i denotes the rate of reaction i . This reaction requires of the presence of both carbon dioxide and water in the porous matrix to proceed, and hence a two-phase flow description is convenient.

In the remaining of this paper, we will denote by ϕ the porosity of the matrix, S_α , ρ_α , p_α and \mathbf{q}_α the degree of saturation, density, pressure and flux vector of phase α ($\alpha = \text{air or water}$), and by $c_{k\alpha}$ the concentration of compound k in phase α . Thus, c_{Ag} , c_A , c_{Bs} , c_B , c_C and c_{Cs} refer, respectively, to the concentration of $\text{CO}_2(\text{g})$, $\text{CO}_2(\text{aq})$, $\text{Ca}(\text{OH})_2(\text{s})$, $\text{Ca}(\text{OH})_2(\text{aq})$, $\text{CaCO}_3(\text{aq})$ and $\text{CaCO}_3(\text{s})$. The conservation equations of the water and the air phases are given by:

$$\frac{\partial[\phi\rho_\alpha S_\alpha]}{\partial t} + \nabla \cdot (\rho_\alpha \mathbf{q}_\alpha) = f_\alpha, \quad \mathbf{q}_\alpha = -\frac{\mathbf{k}k_{r\alpha}}{\mu_\alpha} (\nabla p_\alpha - \rho_\alpha \mathbf{g}), \quad (2)$$

where \mathbf{k} denotes the permeability of the material, and $k_{r\alpha}$ and μ_α the relative permeability and dynamic viscosity of phase α . The following constitutive relations are used:

$$S_w(p_c) = [1 + (ap_c)^n]^m, \quad p_c = p_a - p_w, \\ k_{rw}(S_w) = \sqrt{S_w} \left[1 - (1 - S_w^{\frac{1}{m}})^m \right]^2, \quad k_{ra} = (1 - S_w)^2 (1 - S_w^2).$$

The mass conservation of the dispersed/dissolved compounds k in phase α is given by the equation:

$$\frac{\partial[\phi S_\alpha c_{k\alpha}]}{\partial t} + \nabla \cdot (-\phi S_\alpha D_{k\alpha} \nabla c_{k\alpha} + c_{k\alpha} \mathbf{q}_\alpha) = f_{k\alpha}, \quad (3)$$

where $D_{k\alpha}$ denotes the diffusion coefficient of species k in phase α . Finally, the mass conservation of the solid compounds k reads:

$$\frac{\partial[(1 - \phi)c_{ks}]}{\partial t} = f_{ks}. \quad (4)$$

The model is closed with the net production of phase α /compound k by the action of reaction (1), functions f_α , $f_{k\alpha}$ and f_{ks} . Following [6, 7], we have that:

$$f_w = M_w \phi S_w k^{reac} g^{hum}(RH) c_A c_B, \quad f_a = 0, \\ f_{A_g} = k^{ch} (C^{Henry} \phi S_a A_g - \phi S_w A), \\ f_A = -f_{A_g} - M_A \phi S_w k^{reac} g^{hum}(RH) c_A c_B, \\ f_B = \phi S_w k^{diss} (c_B^{eq} - c_B) - M_B \phi S_w k^{reac} g^{hum}(RH) c_A c_B, \\ f_C = M_C \phi S_w k^{reac} g^{hum}(RH) c_A c_B - \phi S_w k^{prec} (c_C - c_C^{eq}), \\ f_{B_s} = -\phi S_w k^{diss} (c_B^{eq} - c_B), \quad f_{C_s} = \phi S_w k^{prec} (c_C - c_C^{eq}),$$

where M_k denotes the molar mass of compound k , k^r the rate of reaction r and c_k^{eq} the solubility of compound k in water. The function g^{hum} inhibits the carbonation reaction when the water content is insufficient [9]:

$$g^{hum}(RH) = \begin{cases} 0, & \text{si } RH < 0.5, \\ \frac{RH-0.5}{0.4}, & \text{si } 0.5 \leq RH < 0.9, \\ 1, & \text{si } RH \geq 0.9, \end{cases}$$

and the relative humidity RH is related to the capillary pressure p_c through the Kelvin-Laplace law. The model equations (1)-(4), supplemented with the corresponding initial and boundary conditions, are discretized in time with the backward Euler method and in space with linear finite elements. The modified Picard method [10], which is mass conservative, is applied to solve the nonlinear flow problem.

Results and discussion

We consider the progress of the carbonation reaction on a concrete sample as sketched in Figure 1. The sample is subjected to environmental conditions through the boundary Γ_{env} , while it remains isolated (no-flux boundary conditions) on Γ_N . Under this simplified geometry and boundary conditions, the problem can be formulated in one spatial dimension.

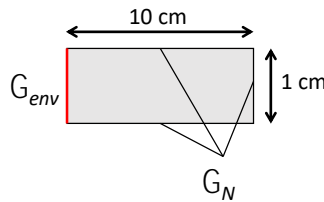


Figure 1: Schematic representation of the computational domain and boundaries.

The temperature, relative humidity and CO_2 concentration (A_g^{env}) at the environment are set to 30 °C, 60% and 0.007 kg/m³, respectively. We furthermore assume that the air phase fulfils $p_a = 0$ Pa at Γ_{env} . The initial relative humidity of the matrix is set equal to 35%. We consider two healing conditions, that try to mimic the healing reaction under air exposure conditions and under one wet/dry cycle. In the second case, a water infiltration step (with 98% of relative humidity at Γ_{env}) is considered prior to the carbonation reaction.

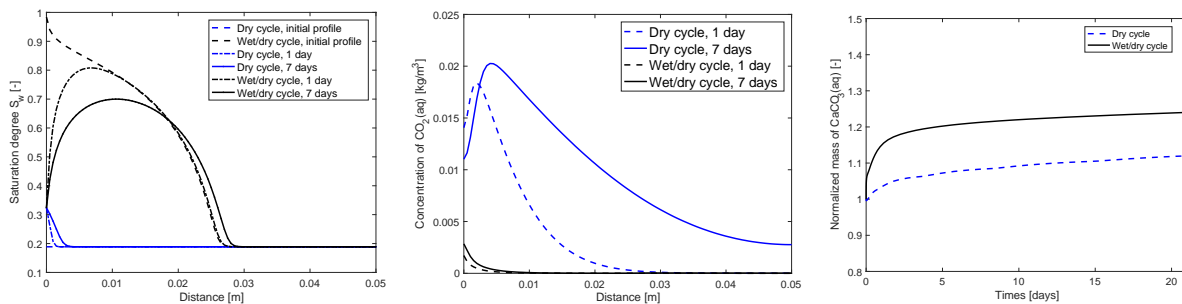


Figure 2. Left: water saturation profiles at different times. Centre: concentration of $\text{CO}_2(\text{g})$ at different times. Right: normalized mass of produced $\text{CaCO}_3(\text{aq})$ over time.

This infiltration step creates an inhomogeneous water (and consequently air) profile within the matrix, see Figure 2 (left). The differences in the water (and air) profile strongly affect the progress of the carbonation reaction. For the carbonation under environmental conditions (labelled as dry cycle in the figures), the low content of water in the pores on one hand facilitates the absorption of carbon dioxide and on the other hand inhibits the carbonation reaction. In the wet/dry cycle, however, the high content of water activates the carbonation reaction and the absorbed carbon dioxide is rapidly consumed in the reaction, see Figure 2 (centre). The consequence of these different trends is that the production of $\text{CaCO}_3(\text{aq})$, and

hence the efficiency of the healing reaction, is improved by the initial infiltration step, see Figure 2 (right).

Conclusion

A two-phase reactive flow model has been presented in the context of autogenous self-healing reaction in concrete materials. The model allows to estimate the evolution of the active chemical species, and in consequence to obtain measurements of the depletion/production of specific compounds. Changes in the microstructure, through local changes in the porosity with the concentrations of the solid compounds has not been considered yet but can be easily implemented [6]. Though the carbonation reaction has been considered here, the presented framework is applicable to other healing reactions. Thus, the model offers the potential to gain a better knowledge of the performance of the healing reaction under different healing conditions. However, the model also presents a number of limitations. It should be remarked that an accurate estimation of certain parameters needs to be undertaken. Although the qualitative behaviour of the solution reproduces the main aspects of the carbonation reaction under environmental conditions and wet/dry cycles, a detailed comparison with experimental results is necessary to supply the model with a quantitative predictive power. These are the lines of future research.

Acknowledgment

The author acknowledges the support from the Spanish project PID2019-105574GB-I00 (MCI/AEI/FEDER, EU) and from the Aragon Government and European Social Fund (group E24_17R).

References

- [1] De Belie N, Gruyaert E, Al-Tabbaa A, Antonaci P, Baera C, Bajare D, Darquennes A, Davies R, Ferrara L, Jefferson T, Litina C, Miljevic B, Otlewska A, Ranogajec J, Roig-Flores M, Paine K, Lukowski P, Serna P, Tulliani JM, Vucetic S, Wang J, Jonkers H. A Review of Self-Healing Concrete for Damage Management of Structures. *Advanced Materials Interfaces*. 2018 Vol 5 pp. 1800074–28.
- [2] Snoeck D, De Belie N. Autogenous Healing in Strain-Hardening Cementitious Materials with and without Superabsorbent Polymers: an 8-year study. *Frontiers in Materials*. 2019 Vol 6 pp. 11-12.
- [3] Al-Tabbaa A, Lark B, Paine K, Jefferson T, Litina C, Gardner D, Embley T. Biomimetic cementitious construction materials for next-generation infrastructure. *Proceedings of the Institution of Civil Engineers - Smart Infrastructure and Construction*, 2018 Vol 171 pp. 67–76.
- [4] Jefferson T, Javierre E, Freeman B, Zaoui A, Koenders E, Ferrara L. Research Progress on Numerical Models for Self-Healing Cementitious Materials, *Advanced Materials Interfaces*. 2018 Vol 5 pp. 1701378-19.
- [5] Chitez AS, Jefferson AD. A coupled thermo-hygro-chemical model for characterising autogenous healing in ordinary cementitious materials. *Cement and Concrete Research*. 2016 Vol 88 pp. 184–197.
- [6] Papadakis VG, Vayenas CG, Fardis MN. A reaction engineering approach to the problem of concrete carbonation. *AIChE Journal*, 1989 Vol 35 pp. 1639–1650.
- [7] Radu FA, Muntean A, Pop IS, Suci N, Kolditz O. A mixed finite element discretization scheme for a concrete carbonation model with concentration-dependent porosity. *Journal of Computational and Applied Mathematics*. 2013, Vol. 246, pp. 74–85.
- [8] Gawin D, Pesavento F, Schrefler BA. Modeling of cementitious materials exposed to isothermal calcium leaching, considering process kinetics and advective water flow. Part 1: Theoretical model. *International Journal of Solids and Structures*, 2008 Vol 45 pp. 6249–6268.
- [9] Saetta AV, Schrefler BA, Vitaliani RV. The carbonation of concrete and the mechanism of moisture, heat and carbon dioxide flow through porous materials. *Cement and Concrete Research*. 1993 Vol 23 pp. 761–772.
- [10] Celia MA, Bouloutas ET, Zarba RL. A General Mass-Conservative Numerical-Solution for the Unsaturated Flow Equation. *Water Resources Research*. 1990 Vol 26 pp. 1483–1496.

Time dependent micromechanical self-healing model for cementitious material

Sina Sayadi, Iulia Mihai, Anthony Jefferson

School of Engineering, Cardiff University, Cardiff CF24 3AA, UK

Abstract

The need for more sustainable systems for construction applications has led researchers to develop a range of self-healing materials for designing or repairing structures. Unsurprisingly, concrete, as the most used construction material, has received considerable attention from the biomimetic research community. Despite much research over the past two decades, there is not yet a comprehensive reliable model for predicting the behaviour of self-healing concrete under a range of conditions. Concrete itself is a complex heterogeneous brittle material that is challenging to simulate. When healing is also considered, its behaviour becomes even more complex. This contribution presents a constitutive model based on a micromechanical formulation, with time dependent cracking and healing functions. The model employs an Eshelbian solution, as well as a range of homogenization techniques, to estimate overall properties and the nonlinear response of self-healing concrete. A key assumption in the formulation is that the new healing material forms in a stress-free state. The initial results show that the mechanical healing efficiency and post-healed response are strongly dependent on the properties of the matrix and healing materials, curing time of the healing agent and the damage threshold at which healing is activated.

Introduction

Self-healing materials are able to reduce the vulnerability of cracked concrete structures, especially under extreme environmental conditions. Experimental research has shown that the healing process includes both crack sealing and the regain of mechanical properties [1–3]. Alongside these experimental studies, scientists have also investigated the numerical simulation self-healing materials. Some have employed the damage-healing approaches and have used the concept of an effective medium in their formulations [4–6]. Many of these methods have restrictions; for example, they are limited to a single damage-healing-redamage cycle; and/or, simultaneous damage and healing processes can not be simulated. Other approaches use micromechanical theories [7–9] to simulate the recovery of anisotropic mechanical properties. This paper presents a self-healing modelling approach in which simultaneous time dependent damage healing processes are considered.

Materials and methods

Continuum damage mechanics allows us to determine the amount of damage and the loss of area of a representative volume of material with either a scalar or a tensor variable. The damage variable (tensor) provides a measure of the material available for healing. The contribution of the healed portion of materials is considered by superposing the constitutive behaviour of the healing part and the undamaged component of the original material. The governing constitutive equation of the self-healing material comprises the sum of these two components, as follows:

$$\boldsymbol{\sigma} = (1 - \omega)\mathbf{D}_{el}:\boldsymbol{\varepsilon} + h_v(1 - \omega_h)\mathbf{D}_{eh}:(\boldsymbol{\varepsilon} - \boldsymbol{\varepsilon}_h) \quad (1)$$

where, the amount of damage is quantified by ω and ω_h (which vary from 0 to 1) for the original and healed materials, respectively; \mathbf{D}_{el} and \mathbf{D}_{eh} are the elastic stiffness matrices for the original material and for the healed material respectively; h_v denotes the amount of the newly healed

material. The derivation of this variable as well as ε_h , which represents the strain shift for the healed material, will be discussed in later in the paper.

For a cementitious material, the damage evolution is a function of the effective strain (Eq 2) which is referred to by ζ . This variable is derived based upon the damage yield surface equation (Eq 3) which is used by many researchers and consists of experiments [10].

$$\omega(\zeta) = 1 - \frac{\varepsilon_t}{\zeta} e^{-5\left(\frac{\zeta - \varepsilon_t}{\varepsilon_0 - \varepsilon_t}\right)} \quad (2)$$

$$\zeta(\varepsilon_L) = \frac{\varepsilon_{Lrr}}{2} \left[1 + \left(\frac{\mu}{q}\right)^2 \right] + \frac{1}{2q^2} \left(\sqrt{(q^2 - \mu^2)^2 \varepsilon_{Lrr}^2 + 4q^2 \gamma_L^2} \right) \quad (3)$$

where ε_t and ε_0 are the initial strain in the first damage, and strain at the end of stress-strain curve, respectively; ε_L is the local strain in a crack plane, which is calculated by using a plane transformation matrix consisting of three components $\varepsilon_L = (\varepsilon_{rr}, \gamma_{rs}, \gamma_{rt})$; q and μ are shear parameters.

For cementitious composite materials, the overall homogenized elastic stiffnesses were derived using Eshelby theory and the Mori-Tanaka homogenisation scheme. The stiffness matrix is as follows:

$$\mathbf{D}_{\text{eff}} = \mathbf{D}_m + \{f_\Omega (\mathbf{D}_\Omega - \mathbf{D}_m) \mathbf{A}^{\text{dill}}\} [f_m \mathbf{I}^{4s} + f_\Omega \mathbf{A}^{\text{dill}}]^{-1} \quad (4)$$

$$\mathbf{A}^{\text{dill}} = [\mathbf{I}^{4s} + \mathbf{S} \mathbf{C}_m (\mathbf{D}_\Omega - \mathbf{D}_m)]^{-1} \quad (5)$$

where \mathbf{D}_{eff} is the overall composite stiffness matrix, \mathbf{D}_m and \mathbf{D}_Ω are the matrix and inclusions stiffness with the corresponding volume fracture f_m and f_Ω , respectively; Finally, the strain concentration tensor for the dilute case, \mathbf{A}^{dill} , is defined in (Eq 4). In this equation, \mathbf{A}^{dill} is the Eshelby concentration tensor based on inclusion shape and matrix properties and \mathbf{I}^{4s} is fourth order identity tensor.

The portion of the representative crack area which is available for healing is based on the damage variable. It is assumed that, increasing the strain, newly damaged areas are available for healing immediately.

The healing process is assumed to be governed by the curing reaction of the healing material. Mathematically, this phenomenon is modelled with the following exponential function [11]. This convolution integral (Eq 6) shows the amount of accumulated healed material created from the incremental damaged material which is gradually healed.

$$h(t) = \int_{t=0}^t \omega(s) \left(1 - e^{-\frac{t-s}{\tau_0}} \right) ds \quad (6)$$

where τ_0 is the curing constant that depends on the healing agent chemical properties and h is accumulated amount of healed material at a specific time (t).

Microcracking in the healed material is considered by the parameter ω_h . When the system has the ability to re-heal, the equivalent value of ω_h is updated on the basis of the total amount of the available healed material. During the healing process, it is imperative that a healing event takes place without causing a change in the stress so that no strain energy is created due to healing alone. Therefore, in each step, ε_h has to be determined by solving an equation which ensures that this zero-stress-change criterion is satisfied. These criteria were used to derive the following equations that are used to update the re-damage variable and healing strain, as follows:

$$\omega_{h_{eq}}(\zeta_{h_{eq}}) = 1 - \frac{h_v(1 - \omega_h) + \Delta h}{h_v + \Delta h} \quad (7)$$

$$\varepsilon_h = \varepsilon_h + \frac{\Delta h}{h_v + \Delta h} (\varepsilon - \varepsilon_h) \quad (8)$$

where Δh represents the incremental healed material component from both the newly damaged material and the re-damaging of the healed material.

The following example demonstrates the differences in behaviour of self-healing material with different curing rates as well as their re-healing abilities. For the sake of clarity and simplicity, only a 1D loading condition was considered. A typical cementitious material subjected to under monotonic loading at a strain rate of $7.5E-6s$ is investigated. The time step size employed is 1s. The elastic properties, mechanical strength and nonlinear characteristics of the original and healing agent material are given in Table 2. To investigate the re-damaging, and re-healing effects on the overall behaviour of the system, different healing scenarios, such as a single healing event and multiple healing events are considered. The effect of healing rate is also studied with different curing constants ranging from 1s, which represents the instantaneous healing, to 2000s which represents the extremely slow curing agent. For all these cases it is assumed that healing initiated at ω is equal to 0.9, and finally the effect of different damage thresholds will be investigated to explore the difference responses.

Table 2 Material Properties

E (N/mm ²)	ν	K(N/mm ²)	f_t (N/mm ²)	ε_0	ε_{0h}	ε_{tv}	ε_{tvh}	τ_0 (s)	Δt (s)
24000	0.15	11429	1	6.67×10^{-3}	6.67×10^{-3}	4.17×10^{-5}	8.33×10^{-5}	200	1

Results and discussion

Figure 1 illustrates the self-healing behaviour for material with different healing abilities with $\tau_0 = 200s$, which represents a medium curing rate. The results shows that both stiffness and strength is partially recovered compared to the non-healing case (black dotted line). Recovery degree is strongly dependent on healing material characteristics as well as the damage threshold for initiating healing. Moreover, the response for the self-healing system with re-healing and re-damaging capabilities shows that the amount of the damaged portion of representative material gradually becomes equal to the healed material and they reach equilibrium. As may be seen by comparing the green line with those for single healing or multiple healing, the re-healing system has the ability to prevent full damage and is able to partially bear the stress under large strains.

The new formulation can also capture the healing process with different rates. Figure 2a shows different healing rates in the colour spectra from fast to slow curing. It could be interpreted from this figure that if the healing rate is much smaller than the damage rate, there would not be significant tangible healing, so it is important to choose proper a healing agent based on the loading characteristics.

The effect of initiating healing at different damage thresholds is depicted in Figure 2b. The results show that the maximum strength after healing is strongly dependent on the level of damage when healing commences. However, recovered stiffness as well as residual strength are the same for all the cases and are independent of damage threshold.

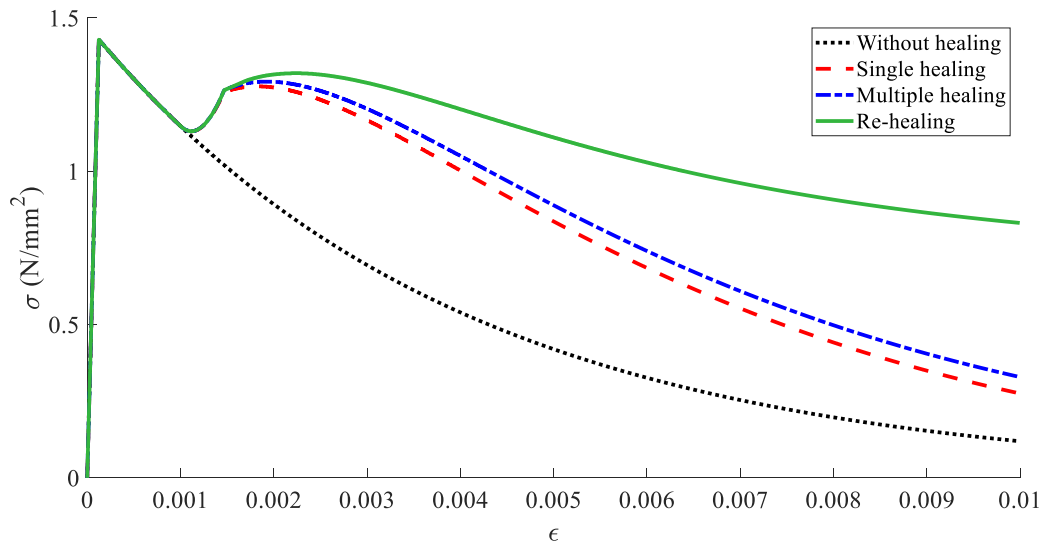


Figure 1. Material Behaviour under different damaging-healing scenario

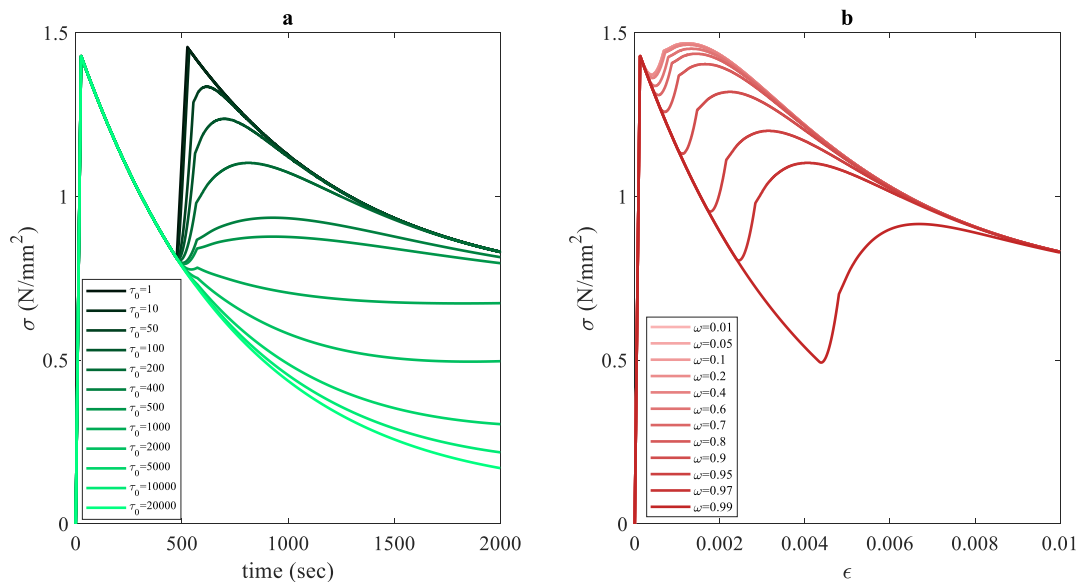


Figure 2. Self-healing responses with different material properties a) Healing rate, b) activation limit

Conclusion

The behaviour of a self-healing system was investigated using a model in which rate dependent healing was simulated with an exponential chemical curing function. A series of simulations, including a parametric study, shows that the overall damage-healing response is strongly dependent on the curing function parameters as well as the damage level at which healing is assumed to commence.

Acknowledgment

The authors acknowledge support from EU Horizon 2020 Action. The result of this paper is part of SMARTINCS project funded under the Marie Skłodowska-Curie grant agreement No 860006.

References

- [1] De Belie N, Gruyaert E, Al-Tabbaa A, Antonaci P, Baera C, Bajare D, et al. A Review of Self-Healing Concrete for Damage Management of Structures. *Adv Mater Interfaces* 2018;5.
- [2] Ferrara L, Van Mullem T, Alonso MC, Antonaci P, Borg RP, Cuenca E, et al. Experimental characterization of the self-healing capacity of cement based materials and its effects on the material performance: A state of the art report by COST Action SARCOS WG2. *Constr Build Mater* 2018;167:115–42.

- [3] Van Tittelboom K, De Belie N. Self-healing in cementitious materials-a review. *Materials (Basel)* 2013;6.
- [4] Abu Al-Rub RK, Darabi MK. A thermodynamic framework for constitutive modeling of time- and rate-dependent materials. Part I: Theory. *Int J Plast* 2012;34.
- [5] Barbero EJ, Greco F, Lonetti P. Continuum Damage-Healing Mechanics with application to self-healing composites. *Int J Damage Mech* 2005;14:51–81.
- [6] Darabi MK, Abu Al-Rub RK, Little DN. A continuum damage mechanics framework for modeling micro-damage healing. *Int J Solids Struct* 2012;49.
- [7] Davies R, Jefferson A. Micromechanical modelling of self-healing cementitious materials. *Int J Solids Struct* 2017;113–114:180–91.
- [8] Han K, Ju JW, Zhang H, Zhu Y, Chang T-S, Wang Z. Mechanical response analysis of self-healing cementitious composites with microcapsules subjected to tensile loading based on a micromechanical damage-healing model. *Constr Build Mater* 2021; 280:122251.
- [9] Zhou S, Zhu H, Yan Z, Ju JW, Zhang L. A micromechanical study of the breakage mechanism of microcapsules in concrete using PFC2D. *Constr Build Mater* 2016;115:452–63.
- [10] Jefferson A, Bennett T. Micro-mechanical damage and rough crack closure in cementitious composite materials. *Int J Numer Anal Methods Geomech* 2007;31:133–46. <https://doi.org/10.1002/nag.551>.
- [11] Mergheim J, Steinmann P. Phenomenological modelling of self-healing polymers based on integrated healing agents. *Comput Mech* 2013;52.

A CutFEM approach for simulating coupled 3D matrix - 2D crack plane flow of a healing agent in cementitious materials

Brubeck L. Freeman, Anthony D. Jefferson

School of Engineering, Cardiff University, Cardiff CF24 3AA, UK

Abstract

In recent years, a wide range of self-healing (SH) mechanisms have been developed, which help to mitigate the durability issues intrinsic to cementitious materials. Whilst the techniques differ in the method of delivery and release of the healing agent, as well as in the healing agent used, they all enhance the ability of the material to heal cracks as they form. The large number of physical processes involved in the SH mechanisms make the modelling of such systems complex; however, significant progress has been made.

The focus of the present work is on the transport processes associated with a SH system utilising embedded vascular networks for the delivery of the healing agent. A 3D finite element model is developed that considers the coupled matrix and crack flow of the healing agent, which allows for curved and branching cracks. The model employs Richard's equation for the matrix flow, which is coupled to the Navier-Stokes equations for the flow in the crack plane through a source/sink term representing flow through crack faces. For the crack flow, a CutFEM framework is employed to deal with the discontinuities found at the fluid interface, which is stabilised using a continuous interior penalty; whilst the movement of the interface is tracked using the level-set method.

Introduction

Self-healing systems have been the subject of a great deal of research effort due to their ability to mitigate the durability problems associated with cementitious materials. The simulation of these materials is complex due to the many interacting physical processes involved, all of which need to be accurately captured. In spite of this, the last decade has seen an ever-expanding body of literature on the numerical simulation of such systems [1].

The focus of this study is the simulation of the transport processes associated with a vascular healing system [2]. To this end, a finite element model that couples the 3D matrix to the 2D crack plane flow, of a healing agent, is developed. The simulation of flow in the crack plane presents two key challenges, the first is the tracking of the interface between the healing agent and air, the second is the representation of the strong discontinuities in material properties and fluid stresses found at this interface. In the present work, the discontinuities are represented using the CutFEM approach, whilst the level-set method is preferred for tracking the movement of the interface [3-4]. The CutFEM approach allows for discontinuities internal to the element, whilst still utilising the standard finite element shape functions. This paper presents an outline description of the model along with an illustrative example.

Theoretical basis

The flow of healing agent through the concrete matrix is governed by Richard's equation, given as:

$$\frac{\partial(\rho_h n S_h)}{\partial t} + \nabla \cdot \mathbf{J}_h + Q_{mtx} = 0 \quad (1)$$

where n is the porosity, S_h is the degree of saturation, ρ_h is the healing agent density, Q_{mtx} is a source/sink term and \mathbf{J}_h is the healing agent flux given as:

$$\mathbf{J}_h = -\rho_h \frac{\mathbf{K}_{int} K_{hrel}(S_h)}{\mu} (\nabla P_h - \rho_h \mathbf{g}) \quad (2)$$

where $P_h = P_g - P_c$ is the healing agent pressure (P_g is the gas pressure), \mathbf{K}_{int} is the intrinsic permeability tensor, μ is the dynamic viscosity of the healing agent, \mathbf{g} is the acceleration due to gravity and K_{hrel} is the relative permeability, which depends on the degree of saturation according to the van Genuchten-Mualem relationship [5]:

$$K_{hrel}(S_h) = S_h^\kappa \left[1 - \left(1 - S_h^{\frac{1}{m}} \right)^m \right]^2 \quad (3)$$

where κ is the pore interaction factor which accounts for the connectivity and tortuosity of the pores.

The degree of saturation is related to the capillary pressure through the moisture retention curve, which reads [5]:

$$P_c(S_h) = a(S_h^{-1/m} - 1)^{1-m} \quad (4)$$

where a and m are constants that depend on the medium.

The source/sink term in equation (1) represents the flow between the concrete matrix and the discrete cracks and is given as:

$$Q_{mtx} = 2n\beta_{crk}(P_h - P_{hcrk}) \quad (5)$$

where β_{crk} is a transfer coefficient and P_{hcrk} is the healing agent pressure in the crack.

The flow of healing agent in the crack plane is governed by the Navier-Stokes equations, which are given as:

$$\frac{\partial(\rho_h \mathbf{u})}{\partial t} + \rho_h(\mathbf{u} \cdot \nabla)\mathbf{u} + \eta\mathbf{u} = \rho_h \mathbf{g} \sin\phi - \nabla P_{hcrk} + \rho_h \mathbf{u} Q_{inlet} - \rho_h \mathbf{u} Q_{crk} \quad (6)$$

$$\frac{\partial(\rho_h A)}{\partial t} + \nabla \cdot (\rho_h A \mathbf{u}) - \rho_h A Q_{inlet} + \rho_h A Q_{crk} = 0 \quad (7)$$

where \mathbf{u} is the vector of healing agent velocities, $A = w * 1$ is the flow channel area (where w is the crack width), Q_{inlet} is a source term representing flow of healing agent into the crack plane from embedded channels or macro-capsules, ϕ is the inclination of the crack plane and η is the viscous resistance to flow, given as [6]:

$$\eta = \frac{\mu}{k + 0.5\mu w \beta_w} \quad (8)$$

where $k = w/12$ is the permeability of the crack and β_w is a wall factor.

Finally Q_{crk} is the sink of mass to the surrounding matrix, given as:

$$Q_{crk} = -\frac{2}{\rho_h} n \beta_{crk} (P_h - P_{hcrk}) \quad (9)$$

The total driving force for the flow reads:

$$F = P_c(\theta_d)(1 - \beta_s) - 2 \frac{\beta_m}{w} u + P_{app} \quad (10)$$

where β_s is a factor allowing for stick-slip of the meniscus, β_m is a factor allowing for frictional dissipation at the meniscus, P_{app} denotes the applied pressure and θ_d is the dynamic contact angle which is a function of the meniscus velocity [2].

The CutFEM approach, when applied to two-phase flow problems, divides the domain into two transient subdomains, Ω_1 and Ω_2 , each representing one of the fluids (healing agent or air). The interface between these two domains is denoted Γ . A schematic of the subdivision of the domain can be seen in Figure 1. The domains are coupled through interface conditions, which can be enforced using a variant of Nitsche's method [3-4]. The interface conditions considered here are given as [3]:

$$[[\mathbf{u}]] = 0 \quad \text{on } \Gamma \quad (11)$$

$$[[\boldsymbol{\sigma} \cdot \mathbf{n}]] = -\gamma \zeta \mathbf{n} \quad \text{on } \Gamma \quad (12)$$

where $[[x]]$ represents a jump in the quantity x over the interface, $\boldsymbol{\sigma}$ represents the Cauchy stress tensor, γ denotes the surface tension, ζ is the curvature of the interface and \mathbf{n} denotes the unit normal to the interface. At the intersection between the crack plane and any embedded channels, mass continuity is ensured through the following condition:

$$\int_{\Gamma_{ch}} \mathbf{N}^T (A \mathbf{u} \cdot \mathbf{n}_{\Gamma_{ch}}) d\Gamma_{ch} = A_{ch} Q_{inlet} \quad \text{on } \Gamma_{ch} \quad (13)$$

where Γ_{ch} and A_{ch} denote the perimeter and cross-sectional area of the embedded channel respectively.

In the present work, the stability of the CutFEM model is ensured using a continuous interior penalty approach, details of which can be found in [3-4].

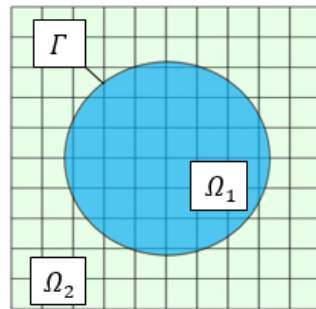


Figure 1 – Schematic of domain subdivision

The interface is tracked using a level-set function that is given as [3]:

$$\frac{\partial \varphi}{\partial t} + \mathbf{u} \cdot \nabla \varphi = 0 \tag{14}$$

where φ denotes the level-set value and the zero level-set represents the interface.

Example problem

To illustrate the performance of the model an example problem is considered. A number of examples, including the validation of the model against experimental data, will be presented in a forthcoming journal paper. The example considered here concerns the flow of a healing agent in a fractured concrete specimen. The main parameters used in the simulation can be seen in Table 1, the crack width considered was 0.15mm. The flow of the healing agent predicted by the model can be seen in Figure 2.

Table 1 - Parameters used in the simulation

Parameter	Value	Parameter	Value
ρ_h (kg/m ³)	1060	β_s (-)	0.0
θ (rad)	0.1754	β_w (m ³ /Ns)	0.0
μ (Ns/m ²)	0.004	P_{app} (N/m ²)	0.0
γ (N/m)	0.033	β_{crk} (s/m)	1.0x10 ⁻⁸
β_m (Ns/m ²)	0.0	K_{int} (m ²)	1.0x10 ⁻¹⁷

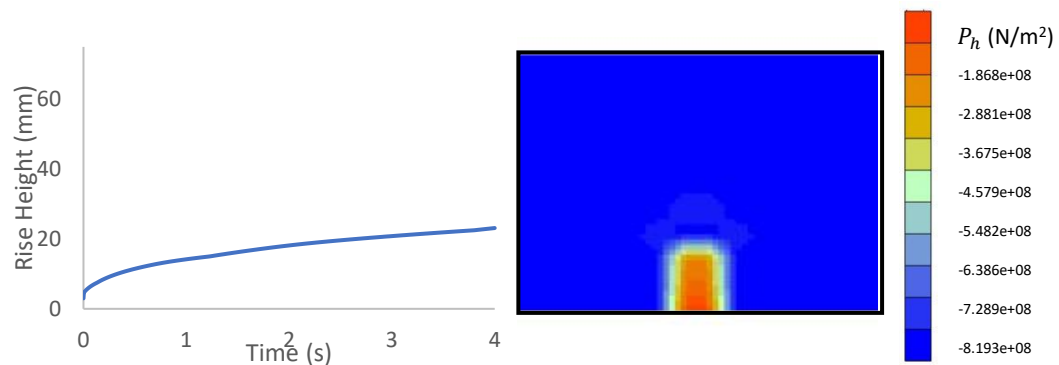


Figure 2 – Predicted rise height in the crack (left) and contour of the pressure in the matrix at time t=4s (right)

In this example, the flow was simulated as a 2D problem. An illustration of the characteristic behaviour of the model in simulating the crack plane flow for a similar problem in 3D, can be seen in Figure 3.

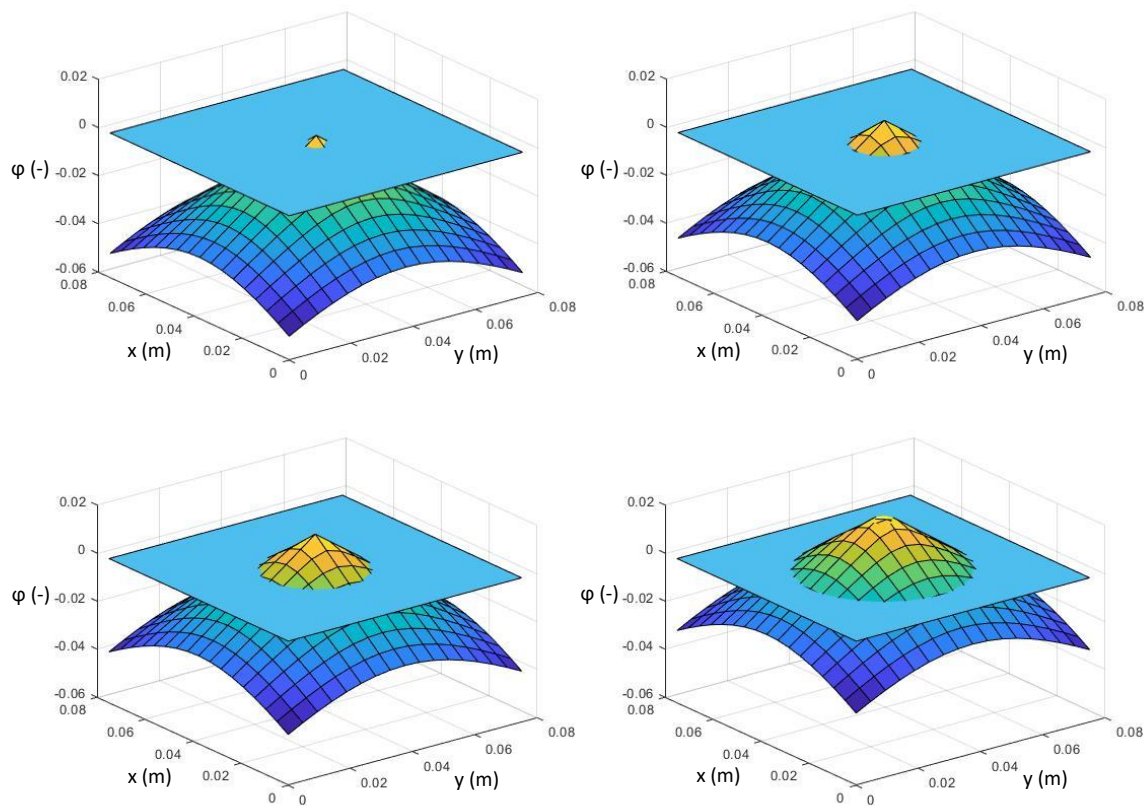


Figure 3 – Transient model predictions of crack plane flow from a central channel, at times $t=0s$, $t=0.25s$, $t=2s$ and $t=4s$ (from top left to bottom right). The blue plane indicates the zero value (the fluid interface), positive values indicate the part of the domain filled with healing agent and negative values indicate the part of the domain filled with air

Conclusion

This paper has presented an outline description of a new finite element model for simulating the coupled 3D matrix – 2D crack plane flow of a healing agent. Richard’s equation is used to simulate the matrix flow, which is coupled to the Navier-Stokes equations that are used to simulate the flow in the crack plane. The CutFEM approach is employed to capture the discontinuities associated with the healing agent-air interface, which is tracked using the level-set method. An example problem has shown the performance of the model in simulating the flow of healing agent in a fractured concrete specimen and illustrated the behaviour of the model in simulating crack plane flow, from a central channel, for a 3D problem. The validation of the model with experimental data is the subject of further research and will be presented in a forthcoming journal paper.

Acknowledgments

Financial support from the UKRI-EPSC Grant EP/P02081X/1 “Resilient materials for life (RM4L)” is gratefully acknowledged.

References

- [1] Jefferson AD, Javierre E, Freeman BL, Zaoui A, Koenders E, Ferrara L. Research progress on numerical models for self-healing cementitious materials. *Advanced Materials Interfaces*. 2018 Vol 5 pp. 1701378
- [2] Freeman BL, Jefferson AD. The simulation of transport processes in cementitious materials with embedded healing systems. *International Journal for Numerical and Analytical Methods in Geomechanics*. 2020 Vol 44 pp. 293-326
- [3] Claus S, Kerfriden P. A CutFEM method for two-phase flow problems. *Computer Methods in Applied Mechanics and Engineering*. 2019 Vol 348 pp. 185-206
- [4] Burman E, Claus S, Hansbo P, Larson MG, Massing A. CutFEM: discretizing geometry and partial differential equations. *International Journal for Numerical Methods in Engineering*. 2015 Vol 104 pp. 472-501
- [5] van Genuchten MT. A closed-form equation for predicting the hydraulic conductivity of unsaturated soils. *Soil Science Society of America Journal*. 1980 Vol 44 pp. 892-898
- [6] Gardner DR, Jefferson AD, Hoffman A, Lark R. Simulation of the capillary flow of an autonomic healing agent in discrete cracks in cementitious materials. *Cement and Concrete Research*. 2014 Vol 58 pp. 35-44

Simulation of moisture transport through bio-based materials using independent measurements of water vapour diffusivity

Yovko Ivanov Antonov, Kirstine Meyer Frandsen, Rasmus Lund Jensen, Per Møldrup

Aalborg University, Department of the Build Environment, Thomas Manns vej 23, 9000 Aalborg, Denmark

Abstract

Hemp-lime is a bio-based multi-functional building material, which has been proven to have excellent moisture buffering capacity, good thermal insulation and negative embodied energy. Due to its moisture buffering properties, hemp-lime materials can influence the indoor relative humidity by adsorbing, storing or desorbing water vapor to/from the ambient air. This provides passive design possibilities for improved indoor environment. The prediction of the indoor air quality is often done by the use of dynamic simulation models, where material properties are necessary input for successful simulation.

The work presented in this paper utilizes the dynamic simulation software BSim for the investigation of moisture transfer between ambient air and two different hemp-lime building materials. Two material properties, the water vapor sorption isotherm and the water vapor diffusivity (denoted vapor permeability in BSim), are required for a simulation. Obtaining both of those material properties by standard experimental procedures is a time- and resource-intensive process. Recent research has validated commercially available equipment, allowing for obtaining detailed isotherms of building materials in a time efficient manner. However, it has been shown that detailed isotherms alone are not enough to achieve meaningful moisture transfer simulation results.

A new method for experimental determination of sorption independent vapor diffusivity (companion paper) has been applied to the two hemp-lime materials simulated in this paper. The aim is to quantify the difference in simulation results, when using both experimentally derived isotherms and diffusivity, rather than derived isotherms and assumed diffusivity.

Introduction

Hemp-lime is a bio-based multi-functional building material, which has been proven to have excellent moisture buffering capacity [1], good thermal insulation [2] and negative embodied energy [3]. It has been shown that buildings with hempcrete provide stable indoor relative humidity and temperature by considerably reducing daily fluctuations [4]. This is due to the moisture buffering properties of hemp-lime materials, which influences the indoor relative humidity by adsorbing, storing or desorbing water vapor to/from the ambient air. This provides passive design possibilities for improved indoor environment.

The prediction of the indoor air quality is usually carried out by the use of dynamic simulation models, where the true hygrothermal behavior of hemp-lime buildings is quite difficult to predict. Varying approaches to obtain better prediction of relative humidity by tabulating material properties or imposing additional parameters have previously been suggested [5,6]. Two material properties, the water vapor sorption isotherm and the water vapor diffusivity are required for a successful calculation of moisture balance in most simulation tools. Both of those are typically derived by standard experimental methods (water adsorption-desorption isotherms [7], water vapor diffusivity [8]), which are time- and resource-intensive processes. Recent research has validated commercially available equipment, allowing for obtaining detailed isotherms of building materials in a time efficient manner [9]. However, it can be shown that high-resolution isotherms alone are not enough to achieve more precise moisture transfer simulation results and water vapour diffusivity should be determined for the specific

simulated material [10]. Wet/dry cup methods [8] are the common method for determination of water vapour diffusivity in buildings materials. While the method is used widely, its nature combines several physical processes occurring in building materials at the same time – water vapor transport, adsorption, desorption, capillary condensation, capillary transport, surface adsorption/desorption (effusion and liquid transfer [1]). A new method for experimental determination of water vapour diffusivity (presented in companion paper no. 137) has been applied to two hempcrete materials simulated in this paper. The method uses oxygen as a tracer gas for determining the diffusion coefficient, which is a novel, faster and specific approach within the field of building physics. The use of gas as a medium instead of water vapour allows for fast measurement time (approximately 1 hour), which results in separation of the water vapour related processes. For enhanced clarity, results from the novel method are hereafter referred to as gas diffusivity.

The aim of the paper is to investigate and quantify the difference in simulation results, when using both experimentally derived isotherms and water vapor diffusivity using standard and novel method. The work presented in this paper utilizes the dynamic simulation software BSim for the investigation of moisture transfer between ambient air and two different hempcrete building materials.

Materials and methods

The materials chosen for this study are two different hempcrete mixes. The mixes vary mainly in the amount of hemp used in the mix, one with high amount of hemp shives (denoted as HH mix) and one with low amount of shives, compared to the binder (denoted as LH). Binder composition used for HH and LH mixes is the same as specified in [11]. The HH and LH mixes provide ready materials with respective dry densities of approximately 155 and 320 kg/m³. The low density HH mix be used for insulating fill in floors, walls and roofs, while the higher density LH mix is suitable for external plasters and internal renders.

Figure 1 shows the obtained isotherms for HH and LH materials mixes, using the standard salt solution method, described in [7]. The resulting isotherms have been validated in [10], and are used as direct input to the performed dynamic building simulations.

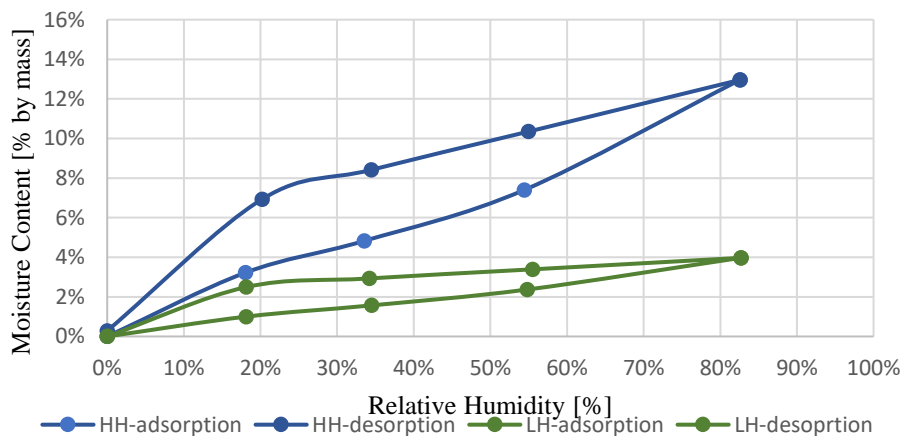


Figure 1 Water vapor isotherms for High-Hemp (HH) and Low-Hemp mixes, derived using the standard saturated salt solution method, specified in [7].

Water vapor transport properties for the two simulated materials are obtained using a novel measurement method within the field of building physics, explained in detail in a companion paper (number 137). The method applies a fast measurement technique, based on oxygen diffusion through a material sample, obtaining a gas diffusivity value (D_p/D_0 [m²/s]). The vapor diffusivity can then be calculated using relative diffusivity factor [12]. The measurement time

for each sample of about 1 hour and the use of oxygen as tracer gas, allows for obtaining independent measurement of diffusion. The term independent is used as gas diffusion is separated from other simultaneously occurring processes, included in the cup method. Those are water transport by effusion and liquid transfer [1,8]. It can be argued that to some extent adsorption and desorption occur due to vapor pressure gradient and vapor mitigation within the material matrix. As explained in paper 137, the results from cup method are about 360 times smaller than those obtained by using gas diffusion.

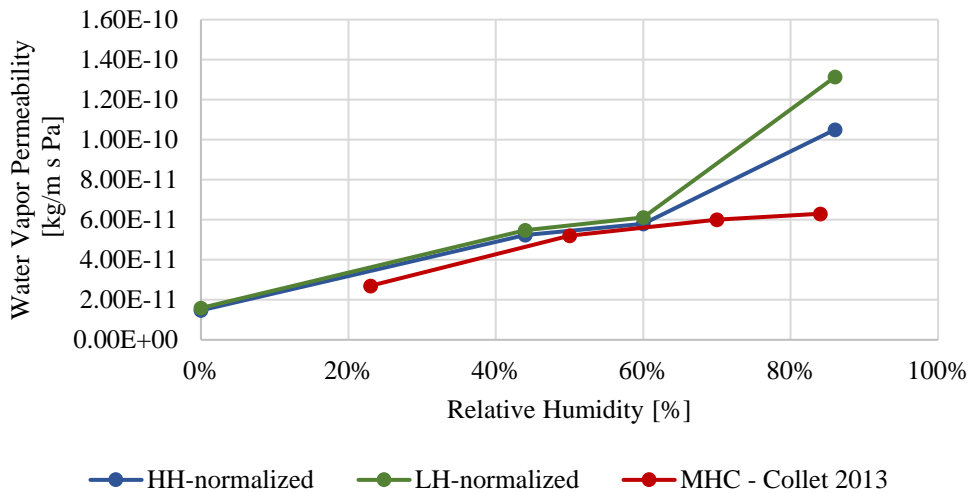


Figure 2 Water vapor permeability as a function of relative humidity. Normalized results for HH and LH mixes, compared to Molded Hemp Concrete adapted from Collet et al. [1]

Figure 2 shows comparison of the results for the HH and LH materials obtained by the novel method. The independent diffusion is normalized with retardation factor of 360 accounting for excluded transport processes, compared to the cup method. The factor is determined based on comparison with the results from Collet et. al [1] for a similar hempcrete mix. The water vapor diffusivity is expressed in (kg/m s Pa), also denoted as vapor permeability in building physics terms. Simulations in the paper use experimental results show in Figure 1 and Figure 2 and seek to find the obtained effect on the numerical simulations results on relative humidity in a house and moisture accumulation in a wall. The tool BSim is used for dynamic hourly building simulation, incorporating coupled heat and mass transfer models in a finite volume discretization. The building model is a single-family house with detailed heat and moisture loads from people and equipment. The investigated cases are specified in Table 1.

Table 3 Investigated simulation cases

Case	Applied isotherm	Applied diffusivity
1	Derived by standard method	Derived by cup method by [1]
2	Derived by standard method	Derived by novel method explained in paper no. 1137 and normalized with data used in case 1
3	Derived by standard method	Derived by novel method explained in paper no. 1137 -Not normalized
4	Minimal isotherm corrected to account for the combined sorption cup method	

Results and discussion

The extreme difference between results for gas and vapour diffusivity derived by the cup method, resulted in inability of the numerical model to converge to a tangible result in case 3.

The vast magnitudal increase of permeability (360 times) required an unreasonably large number of time-steps for stable calculation. Normalizing the isotherms with the same ratio as for vapour diffusivity, in case 4, resulted in constant accumulation of moisture in the construction, therefore these results are omitted in Figure 3.

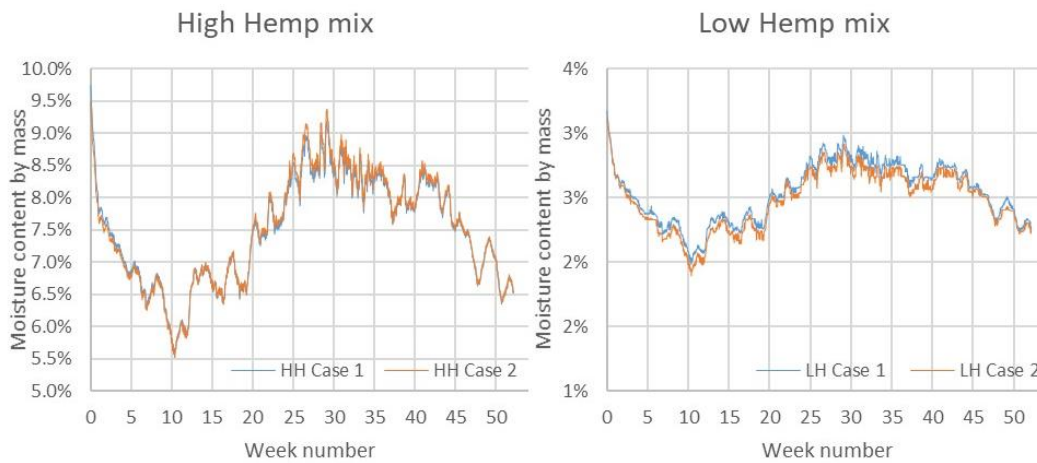


Figure 3 Average moisture content in construction in a year for HH (left) and LH (right), note different y-axis

Figure 3 shows average moisture content variation across a wall, calculated on hourly basis using Design Reference Year for Denmark. Both cases follow nearly the same variation on all time scales (annual, monthly, weekly and daily). Comparing the two cases for HH materials, case 1 results in slightly higher moisture content in winter and slightly lower in summer. For LH mix, case 1 is always higher than case 2, with nearly constant offset.

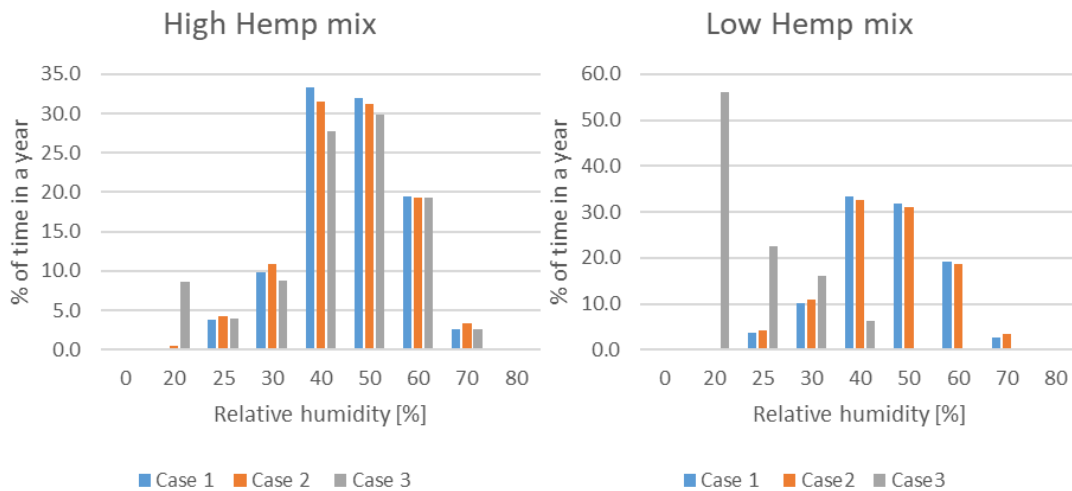


Figure 4 Distribution of indoor air relative humidity in a year

When considering the distribution of indoor air relative humidity for the two materials and investigated simulation cases, shown in Figure 4, one can see that case 1 and 2 provide comparable results with nearly the same distributions.

Conclusion

This paper provides a short introduction to novel experimental method and investigates how the experimentally derived results for gas diffusivity affect building simulation results related to indoor environment. Results show that by applying gas diffusivity, the simulation model

could not converge, due to the significantly higher diffusion curves (factor of 360) compared to standard methods.

Normalizing the gas diffusion to account for the separated physical processes such as effusion and liquid transport, yielded comparable results with simulations using diffusion curves derived by standard methods. However, determining the normalization factor requires knowledge of the combined water vapour diffusion processes. In this paper, the normalization factor is obtained by values from literature for similar building materials.

The work presented in the paper is a small initial step towards deeper understanding in the importance and magnitude of the different, simultaneously occurring physical processes related to water vapour behaviour. The calculated retardation factor of 360 entails that the excluded processes have large influence on the vapour diffusion obtained by the cup method. Separation and quantification of the physical processes occurring with vapour exchange between environment and materials play an important role in recognising which dominant effects are to be accounted, when scaling from small lab samples to full scale, real life behaviour of porous media materials.

Acknowledgment

The work in this paper is funded by the Independent Research Fund Denmark grant for “Non-Equilibrium Water Vapor Sorption in Building Materials [NOWA]” with project number 8022-00032B.

References

- [1] F. Collet, J. Chamoin, S. Pretot, C. Lanos, Comparison of the hygric behaviour of three hemp concretes, *Energy Build.* 62 (2013) 294–303. doi:10.1016/j.enbuild.2013.03.010.
- [2] P. De Bruijn, P. Johansson, Moisture fixation and thermal properties of lime-hemp concrete, *Constr. Build. Mater.* 47 (2013) 1235–1242. doi:10.1016/j.conbuildmat.2013.06.006.
- [3] K. Ip, A. Miller, Life cycle greenhouse gas emissions of hemp-lime wall constructions in the UK, *Resour. Conserv. Recycl.* 69 (2012) 1–9. doi:10.1016/j.resconrec.2012.09.001.
- [4] A. Shea, M. Lawrence, P. Walker, Hygrothermal performance of an experimental hemp–lime building, *Constr. Build. Mater.* 36 (2012) 270–275. doi:10.1016/j.conbuildmat.2012.04.123.
- [5] A.I.T.O. Yacine, B. Marjorie, M. Sophie, L. Christophe, P. Sylvie, C. Florence, Hygrothermal behaviour of a hemp concrete wall Influence of sorption isotherm modelling, in: IXth Nord. Symp. Build. Phys. Tampere, Finl. Monday, 30th May 2011, 2011: p. 9.
- [6] M. Barclay, N. Holcroft, A.D. Shea, Methods to determine whole building hygrothermal performance of hemp–lime buildings, *Build. Environ.* 80 (2014) 204–212. doi:10.1016/j.buildenv.2014.06.003.
- [7] CEN, Hygrothermal performance of building materials and products - Determination of hygroscopic sorption properties (ISO 12571:2013), 2013.
- [8] CEN, Hygrothermal performance of building materials and products - Determination of water vapour transmission properties - Cup method (ISO 12572:2016), 2016.
- [9] *In Preparation* Y.I. Antonov, K.M. Frandsen, P. Møldrup, E. Arthur, L. Wollesen de Jonge, M. Pomianowski, R.L. Jensen, Linking Three Methods for Quantifying Water Vapor Sorption Dynamics in Bio-Based Building Materials, 2020.
- [10] Y.I. Antonov, R.L. Jensen, P. Møldrup, M. Pomianowski, Comparison of salt solution and air drying methods for moisture fixation in highly porous building materials, *Energy Procedia.* 132 (2017) 189–194. doi:10.1016/j.egypro.2017.09.753.
- [11] Y.I. Antonov, R.L. Jensen, P. Møldrup, Hemp-Lime Performance in Danish Climatic Context. Thermal Conductivity as a Function of Moisture Content, in: P.K. Heiselberg (Ed.), CLIMA 2016 - Proc. 12th REHVA World Congr., Department of Civil Engineering, Aalborg University, Aalborg, 2016. http://vbn.aau.dk/files/233778874/paper_753.pdf.
- [12] P. Schjøning, M. Eden, P. Moldrup, L.W. de Jonge, Two-Chamber, Two-Gas and One-Chamber, One-Gas Methods for Measuring the Soil-Gas Diffusion Coefficient: Validation and Inter-calibration, *Soil Sci. Soc. Am. J.* 77 (2013) 729–740. doi:10.2136/sssaj2012.0379.

A micro-mechanics-based element for modelling fibre bridging in embedded cracks

Pedro Bonilla-Villalba, Iulia C. Mihai and Anthony D. Jefferson

Cardiff University, School of Engineering Cardiff CF24 3AA

Abstract

This work focuses on modelling the mechanical behaviour of fibre reinforced cementitious composites by developing a novel finite element with embedded discontinuity. The macro-crack initiation is determined by an exterior point Eshelby based criterion within a smeared crack approach. Thereafter, a (bi)linear plane divides the element in two complementary sub-domains. The element derivation is based in enforcing a split in the element's conforming kinematics. On the one hand all inelastic phenomena due to the discontinuity is segregated from the elastics by enforcing local equilibrium in a crack band. The inelastic conforming kinematics consists of crack opening, sliding and rotation. On the other hand, the overall elemental stiffness matrix is attained in a split manner. The elastic part comes from virtual work after subtracting the segregated inelastic part, allowing separate explicit inclusion of the inelastic component according to any desired constitutive law. Here, the fibre micro-mechanics model starts from simulating the force needed to extract a single fibre. It has only two phenomenological parameters being: (i) the initial shear force at the end of the debonding phase, and (ii) the hardening parameter governing the pull-out phase of the fibre slippage. The global fibre bridging effect is computed by integrating any probability distribution of those fibres activated by the rift development. The formulation allows crack continuity enforcement to explicitly represent the fracture, and thus accurately predict its opening, sliding and rotation. Finally, the model performance is validated by simulating several examples for which experimental data is available.

Introduction

Fibre Reinforced Concrete (FRC) is an increasingly significant material in construction. Devising accurate and efficient predictive models of these materials is a key factor to reduce the costs of the experimental work and to aptly design not only FRC materials but also subsequent FRC containing structures. The main aspects of these models can be reduced to three, first the general constitutive model, second the discretisation of the crack and its evolution and third how to consider bridging effects due to fibres and their distribution. References to literature was omitted in this introduction.

The present work choses a (micro)mechanical approach to the constitutive model over macroscopic mathematical models. The reason is the lower number of phenomenological parameters to be fitted, and more importantly, that in the first approach those parameters are directly link to mechanical properties of the micro/meso elements. That makes fitting the model to experimental data a more intuitive and meaningful process.

Regarding crack evolution modelling, embedded strong discontinuities in allow a very accurate model without the computational burden of lattice models, remeshing or having either a prior knowledge of the crack location or a mesh allowing enough crack growing directions (needed for the vast range of interface elements). Other options are considering all damaged elements for the crack, cohesive models and non-surface particle cohesive models. Within the embedded discontinuities approach a comparative study [1] showed that X-FEM family (which increases the degrees of freedom of the system) and E-FEM family (which condense the enrichments into standard degrees of freedom, enforcing physically acceptable

displacements/strains) converge with equivalent rate to the same solution, being E-FEM more computationally efficient for multiple cracks and more suitable for coarser meshes.

Finally, for fibre distribution this paper relies in probability integration within the element. The alternatives of explicit discretisation either with extra degrees of freedom or with a background mesh increase the computational cost. Furthermore, real applications require either scanning the reinforced concrete or making assumptions that generate a similar error than the probability integration.

Equilibrium Formulation

Equilibrium of Potential Energy

The broached formulation discretises a simplified version of the continuum constitutive model formulation advanced in [2], [3]. However, for the sake of simplicity, contact is not included, and only the angular direction of the formed macrocrack is considered due to its predominance. It is considered that all inelastic phenomena can be segregated from the elastic one from the displacement to the stress level, and that the inelastic stress can be enforced with negligible error by means of equilibrium at the same thin band that in the continuous model comprises all the micro cracks. The exact width of this band is the adjustable parameter. Hereafter, the notation for the aforementioned segregation of any physical quantity (such as displacement, strain, stress or potential energy) is $\tilde{\square}$, \square_e and \square standing for its total, elastic part and inelastic part respectively.

The ad hoc element is obtained by enhancing a Q4 bilinear quadrilateral finite element with the addition of a discontinuity assumed to be linear, the constricting of all considered conforming inelastic displacements, its segregation from the standard finite element formulation, and finally its reintroduction subjected to the desired model for fracture. For the sake of simplicity, the present work assumes that the angular direction of the crack ψ_{CK} is known and that the fissure goes through the centroid of the element. However, a criterion to enforce crack continuity based on finding elemental ψ_{CK} complying continuity and minimising the potential energy is easy to implement.

Using the minimisation of the equilibrium of internal $\tilde{\Pi}_{INT}$ and external virtual work $\tilde{\Pi}_{EXT}$ in a piece of concrete described by the domain Ω , and defining the Sobolev spaces $U = \{u \in H^1(\Omega) | u = u_D \text{ on } \Gamma_D\}$ for the unknown displacement field $u(\mathbf{x}, t)$ and $V = \{v \in H^1(\Omega) | v = 0 \text{ on } \Gamma_D\}$ for the virtual displacements $v(\mathbf{x}, t)$, leads to the following variational problem. Find $u(\mathbf{x}, t)$ such that

$$\begin{aligned} \tilde{\Pi}_{INT} &:= \int_{\Omega} \frac{1}{2} \boldsymbol{\varepsilon}_v(v(\mathbf{x})) : \boldsymbol{\sigma}(u(\mathbf{x}, t)) d\Omega = \int_{\Omega} \frac{1}{2} v(\mathbf{x}, t)^T F_B(\mathbf{x}, t) d\Omega + \int_{\partial\Omega} \frac{1}{2} v(\mathbf{x}, t)^T F_{\partial\Omega}(\mathbf{x}, t) d\Omega =: \tilde{\Pi}_{EXT}, \quad \forall v(\mathbf{x}) \in V \\ u(\mathbf{x}, t) &= u_D(\mathbf{x}, t) && \text{on } \Gamma_D, \\ \boldsymbol{\sigma}(u(\mathbf{x}, t)) \cdot \bar{\mathbf{n}} d\Omega &= g_D(\mathbf{x}, t) && \text{on } \Gamma_N. \end{aligned} \quad (1)$$

where \mathbf{x} is the cartesian basis, t is the time, Γ_D and Γ_N are the complementary subsets of the boundary where the prescribed displacements $u_D(\mathbf{x}, t)$ and tractions $g_D(\mathbf{x}, t)$ are applied, $\boldsymbol{\varepsilon}_v(v(\mathbf{x}))$ is the strain due to virtual displacement, $\boldsymbol{\sigma}(u(\mathbf{x}, t))$ is the stress in the concrete satisfying a constitutive model that will be introduced on due course, $F_B(\mathbf{x}, t)$ and $F_{\partial\Omega}(\mathbf{x}, t)$ describe the external body and surface forces, and $\bar{\mathbf{n}}$ are unit vectors on the boundary.

Enforcement of Conforming Kinematics

Using the Heaviside function $H_{g_{CK}}$ placed at this discontinuity $\mathcal{G}_{CK}(\mathbf{x}; \mathbf{x}_C, \psi_{CK})$, the elemental displacement can be split as the sum of two smooth functions u_e and u , the later representing the jump. In other words

$$u(\mathbf{x}, t) := u_e(\mathbf{x}, t) + H_{g_{CK}} u(\mathbf{x}, t). \quad (2)$$

This segregation can be forwarded to the potential energy level $\tilde{\Pi}_{INT} = \Pi_e + \tilde{\Pi}$. The elastic stress $\boldsymbol{\sigma}_e$ is formulated subtracting the crack inelastic part of the usual FE stress-strain constitutive relation $\boldsymbol{\sigma}_e = \mathbf{D} : (\boldsymbol{\varepsilon} - \boldsymbol{\varepsilon}_{CK})$. Here, \mathbf{D} is the elasticity tensor and the strains are $\boldsymbol{\varepsilon}(u(\mathbf{x}, t))$ and $\boldsymbol{\varepsilon}_{CK}(H_{g_{CK}} u(\mathbf{x}, t))$. The present work restricts the conforming fracture-induced displacements to the crack opening, crack sliding and rotation (which are needed to solve the integration along the discontinuity). Henceforth, $\tilde{\mathbf{w}}_j$ will denote these inelastic components at any point \mathbf{x}_j . And they will be related to the crack-induced displacements at the centre of the crack. Namely

$$\tilde{\mathbf{w}}_C := [\tilde{w}_{r,C}, \tilde{w}_{s,C}, \tilde{\alpha}_C]^T. \quad (3)$$

To be consistent, $\tilde{\mathbf{w}}_j$ will be used for total displacement in local coordinates.

It is also assumed that the rotation is small enough so that the relative inelastic displacement at any point $\mathbf{x}_j \in \Omega^+$ with respect to Ω^- can be accurately approximated by the expression

$$\tilde{\mathbf{u}}_{j*} = \tilde{\mathbf{u}}_C + \tilde{\mathbf{u}}_{j,\alpha} \square \tilde{\mathbf{u}}_C + R(\mathbf{x}_j; \tilde{\alpha}_C, \mathbf{x}_C) := \tilde{\mathbf{u}}_C + |\mathbf{x}_j - \mathbf{x}_C| \cdot \tilde{\alpha}_C \cdot \left(\tilde{\mathbf{t}} \times \frac{\mathbf{x}_j - \mathbf{x}_C}{|\mathbf{x}_j - \mathbf{x}_C|} \right) = \tilde{\mathbf{u}}_C + \tilde{\alpha}_C \cdot (\tilde{\mathbf{t}} \times (\mathbf{x}_j - \mathbf{x}_C)) \quad (4)$$

where $\tilde{\mathbf{t}} = \tilde{\mathbf{r}} \times \tilde{\mathbf{s}}$ and the definition of the approximation $R(\mathbf{x}_j; \tilde{\alpha}_C, \mathbf{x}_C)$ is developed (see Figure 10).

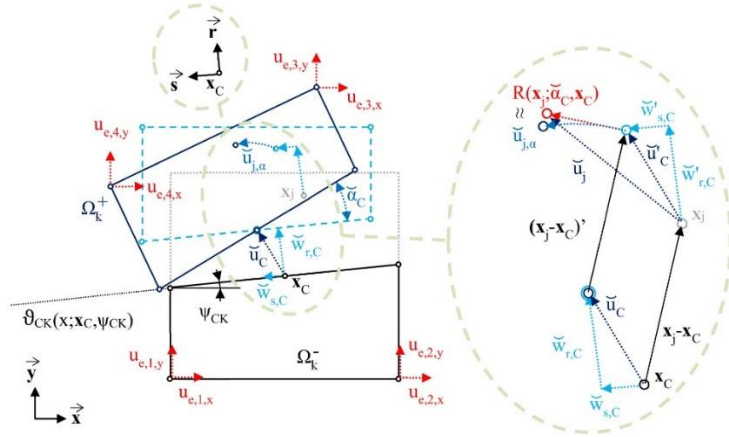


Figure 10. Inelastic relative displacement of Ω_k^+ with respect to Ω_k^- in the strong discontinuity element (left) and detail of the inelastic displacement of an arbitrary node \mathbf{x}_j (right)

Formulation of the Element from the Constitutive Law

The inelastic potential energy $\tilde{\Pi}$ can be computed as a combination of two 1D springs. Using $\{\tilde{\mathbf{r}}, \tilde{\mathbf{s}}\}$ as the orthonormal local basis at the discontinuity ($\tilde{\mathbf{r}}$ perpendicular to $g_{CK}(\mathbf{x}; \mathbf{x}_C, \psi_{CK})$), $\tilde{\boldsymbol{\sigma}}_r = \tilde{\boldsymbol{\sigma}}_r - \boldsymbol{\sigma}_{e,r}$ and $\tilde{\boldsymbol{\sigma}}_s = \tilde{\boldsymbol{\sigma}}_s - \boldsymbol{\sigma}_{e,s}$ are computable by means of equilibrium of forces and momentum along the fissure.

$$\tilde{\mathbf{F}}_Z = \mathbf{K}_Z \cdot \tilde{\mathbf{w}}_C \quad (5)$$

Here, \mathbf{K}_Z is a 3x3 matrix derived from model described in [2], [3] and its components come from

$$\begin{aligned} \tilde{F}_{r,Z} &= h \int_{-l_{CK}/2}^{l_{CK}/2} \tilde{\boldsymbol{\sigma}}_r \cdot dZ = h \int_{-l_{CK}/2}^{l_{CK}/2} \left(\omega_{\psi_{CK}} (1 - \omega_{F,\psi_{CK}}) \frac{E_{df}}{h} + (1 - \omega_{\psi_{CK}}) k_r \right) (\tilde{w}_{r,Z}) dZ, \\ \tilde{F}_{s,Z} &= h \int_{-l_{CK}/2}^{l_{CK}/2} \tilde{\boldsymbol{\sigma}}_s \cdot dZ = h \int_{-l_{CK}/2}^{l_{CK}/2} \left(\omega_{\psi_{CK}} (1 - \omega_{F,\psi_{CK}}) \frac{E_{df}}{h} + (1 - \omega_{\psi_{CK}}) k_s \right) (\tilde{w}_{s,Z}) dZ, \\ \tilde{M}_Z &= h \int_{-l_{CK}/2}^{l_{CK}/2} \tilde{\boldsymbol{\sigma}}_r \cdot Z dZ = h \int_{-l_{CK}/2}^{l_{CK}/2} \left(\omega_{\psi_{CK}} (1 - \omega_{F,\psi_{CK}}) \frac{E_{df}}{h} + (1 - \omega_{\psi_{CK}}) k_r \right) (\tilde{w}_{r,Z}) Z dZ. \end{aligned} \quad (6)$$

where $Z \in 0.5 \cdot [-l_{CK}, l_{CK}]$ spans the crack length l_{CK} in direction $\bar{\mathbf{s}}$; $\omega_{\psi_{CK}}$, $\omega_{F, \psi_{CK}}$ are damage variables of the concrete and fibres respectively; and k_r , k_s , E_{df} are material properties. Symbol $\mathbf{K}_{e,Z}$ denotes the particular elastic case satisfying both damage variables equal zero. Once all definitions needed to compute the elastic and inelastic phenomena in the element are set, the equilibrium of works, neglecting body forces reads

$$\tilde{\Pi}_{INT} := \int_{\Omega_k} \frac{1}{2} (\bar{\boldsymbol{\varepsilon}} - \boldsymbol{\varepsilon}_{CK})^T \mathbf{D} (\boldsymbol{\varepsilon} - \boldsymbol{\varepsilon}_{CK}) d\Omega_k + \frac{1}{2} (\tilde{\mathbf{w}}_C^T \cdot \tilde{\mathbf{K}}_Z \cdot \tilde{\mathbf{w}}_C - \mathbf{w}_{e,C}^T \cdot \mathbf{K}_{e,Z} \cdot \mathbf{w}_{e,C}) = \int_{\tilde{\Omega}} \frac{1}{2} \left(\sum_{in} \bar{\mathbf{v}} \cdot N_{in} \right)^T F_{\tilde{\Omega}} d\Omega =: \tilde{\Pi}_{EXT} \quad (7)$$

After condensation of the 3 additional unknowns $\tilde{\mathbf{w}}_C$ for fracture-induced displacements (which also determine $\boldsymbol{\varepsilon}_{CK}$) the elemental stiffness matrix \mathbf{K}_{SD} of the ad hoc element with embedded discontinuities satisfying $\mathbf{K}_{SD} \bar{\mathbf{u}} = \int_{\tilde{\Omega}} \sum_{in} N_{in} F_{\tilde{\Omega}} d\Omega$ (condensed version of equation (7)) reads

$$\mathbf{K}_{SD} := \left(\int_{\Omega_k} (\mathbf{B} - \tilde{\mathbf{M}} \mathbf{C}_Z)^T \bar{\mathbf{D}} (\mathbf{B} - \tilde{\mathbf{M}} \mathbf{C}_Z) d\Omega_k + (\mathbf{C}_Z^T \tilde{\mathbf{K}}_Z \mathbf{C}_Z) \right) \quad (8)$$

where $\mathbf{B} = \nabla_s \cdot \sum_{in=1}^{in=m} N_{in}$; $\tilde{\mathbf{M}}$ satisfies $\boldsymbol{\varepsilon}_{CK} = \tilde{\mathbf{M}} \cdot \tilde{\mathbf{w}}_C$; and \mathbf{C}_Z satisfies $\tilde{\mathbf{w}}_C = \mathbf{C}_Z \bar{\mathbf{u}}$.

Results

Preliminary results show a correct characteristic response.

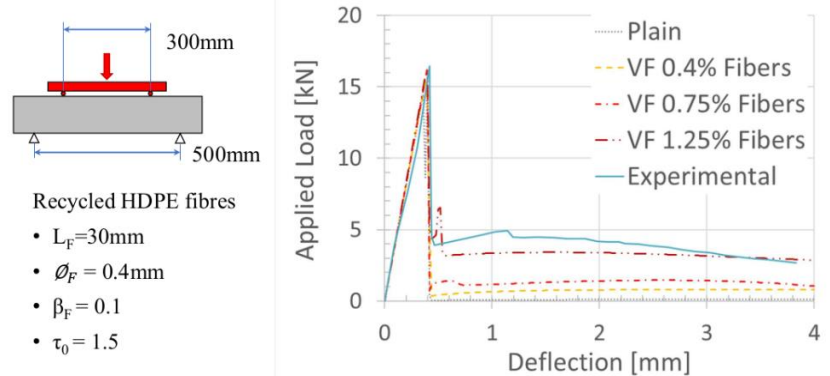


Figure 11 Load-deflection curves for a 4-point bending test

Acknowledgement

This work is supported by UK-EPSC (Grant No. EP/P02081X/1, Resilient Materials 4 Life, RM4L) and (Grant No. EP/P033792/1, Two-scale numerical simulations for fibre reinforced composites).

References

- [1] J. Oliver, A. E. Huespe, and P. J. Sánchez, "A comparative study on finite elements for capturing strong discontinuities: E-FEM vs X-FEM," *Comput. Methods Appl. Mech. Eng.*, vol. 195, no. 37–40, pp. 4732–4752, 2006.
- [2] I. C. Mihai and A. D. Jefferson, "A micromechanics based constitutive model for fibre reinforced cementitious composites," *Int. J. Solids Struct.*, vol. 110–111, pp. 152–169, Apr. 2017.
- [3] A. D. Jefferson, I. C. Mihai, R. Tenchev, W. F. Alnaas, G. Cole, and P. Lyons, "A plastic-damage-contact constitutive model for concrete with smoothed evolution functions," *Comput. Struct.*, vol. 169, pp. 40–56, 2016.

Session 3B Concrete and ground healing and improvement

Chair: Dr Susanne Gebhard

1242 *Zhang et al.* The properties and microstructure of microbial mineralized steel slag cementitious materials

1147 *Reda et al.* Challenges of Self-Healing Concrete Application

1239 *Anderson et al.* Microbial Induced Calcite Precipitation as a Viable Ground Improvement Technique

1206 *Pagano et al.* Grouting of well leakage and migration pathways using colloidal silica: a preliminary experimental investigation

The properties and microstructure of microbial mineralized steel slag cementitious materials

Xiao Zhang^{1,2}, Chunxiang Qian^{1, 2}, Hengyi Zhou^{1, 2}, Haihe Yi^{1, 2}

1: School of Materials Science and Engineering, Southeast University, Nanjing, 211189, China;

2: Research Centre of Green Building and Construction Materials, Southeast University, Nanjing, 211189, China

3: Jiangsu Key Laboratory for Construction Materials, Southeast University, Nanjing 211189, China

4: Key Lab of Microbial Bio-mineralization Technology, China Construction Materials Industry, Nanjing 211189, China Corresponding

Introduction

As the world's largest steel producer, China's crude steel output in 2019 has reached 996 million tons, accounting for more than 53% of the world's total output [1]. Steel slag is a by-product of the steelmaking process. For every ton of steel produced, 15%~20% of steel slag is produced. China's total output of steel slag exceeds 300 million tons, covering land of more than 1,600 acres, and it continues to grow by more than 30 million tons each year. However, most of these steel slags have not been effectively used, occupying more and more land, polluting the environment, and resulting in the waste of resources. The main factors restricting the utilization of steel slag are, on the one hand, the activity of steel slag is relatively low and the hydration of silicate mineral is slow, on the other hand, the free CaO and hard burnt MgO in the steel slag expand in the presence of water leading to cracks, causing poor stability and great harm for structure safety [2-4]. To solve the problems of stability and activity of steel slag, the microbial mineralization technology was proposed in this study to increase the strength of steel slag cementitious materials and reduce the linear expansion rate.

Materials and methods

Raw materials

Microbial additives

The appearance of the Bacillus powder used in the experiments is shown in Figure 1(a), the spores observed under SEM are shown in Figure 1(b), and the rate of spore germination into cells in the slag pore solution is shown in Figure 1(c).

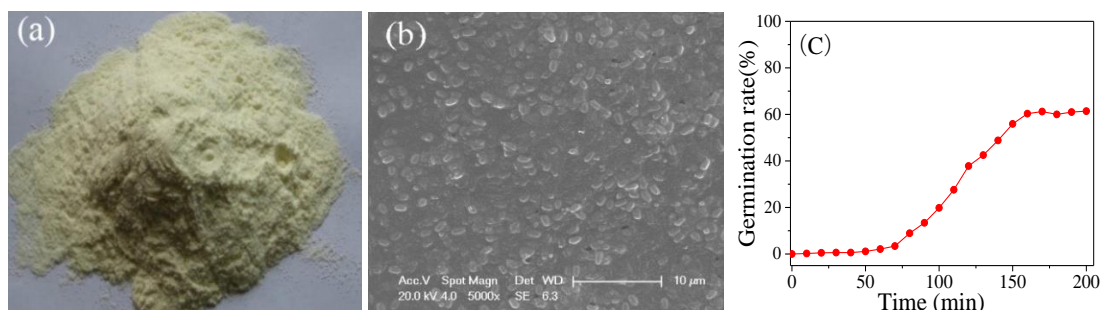


Figure 1. Appearance (a), micro-morphology (b) and spore germination rate (c) of microbial additives

Steel slag

The chemical composition of the steel slag used in the experiment is shown in Table 1. The specific surface area of the steel slag is 425 m²/kg, the f-CaO content is 5.6%, and the f-MgO content is 3.9%.

Table 1. Chemical composition of the steel slag (%)

CaO	SiO ₂	Al ₂ O ₃	FeO	MgO	MnO	Others
44.83	17.22	4.86	14.29	8.29	3.06	7.45

Sample preparation

In order to study the effect of microorganism amount on the strength of the steel slag cementitious material, it is incorporated at 0, 2%, 4%, 6%, 8%, and 10% of the cementitious material mass. The mix proportion of mortar samples are shown in Table 2. Paste samples were prepared at a mass ratio of bacteria at 6% for analysis of phase and pore structure. Formed samples were first put into the standard curing room (20±2 °C, 95% RH) for 2 days, and then in the carbonation kettle at (20±1 °C, 70±5% RH, 99% CO₂ concentration, 0.3MPa) for 4 hours of curing. The properties of each group of steel slag cementitious materials were tested after curing. The simulated steel slag pore solution was prepared under the steel slag power / deionized water ratio of 1g/10mL, which was sealed and shaken in a container for 10 minutes and was filtered after 1 hour of resting. Take 50mL of the solution and add it to a conical flask containing 200mL of microbial solution, mix thoroughly, place it in a constant temperature carbonation device at 25 °C for 24 hours, and filter to obtain mineralization products. Rinse with deionized water and absolute ethanol to remove impurities, and dry at 60 °C to obtain CaCO₃ synthesized by microbial method. 0.1 mol/L CaCl₂ and Na₂CO₃ solutions were prepared and placed in a reaction flask under the conditions of 200 r/min and 25 °C, and the precipitates were washed and filtered with deionized water and dried to obtain chemically synthesized CaCO₃.

Table 2. Mix proportion of mortar samples (g)

Code	Steel slag	Sand	Microbial additives	Water
S	450	1350	0	225
B2	450	1350	9	230
B4	450	1350	18	235
B6	450	1350	27	240
B8	450	1350	36	245
B10	450	1350	45	250

Testing methods

The test of the compressive strength of the samples was carried out according to China standard GB/T 17671-2011 'Method of testing cements – Determination of strength'. After CO₂ curing of the samples in Table 2, the linear expansion ratio is tested after autoclaving (215 °C, 2 MPa) for 3h according to the China standard GB/T 750 'Autoclave method for soundness of Portland cement'. Q-XRD was used to analyse the mineral composition of the steel slag cementitious material, and the mercury intrusion apparatus AutoPore IV 9500 was used to test the pore structure. The automatic X-ray diffractometer D8 Discover, the TEM Tecnai G2T20, the ATM Veeco Dimension ICON, and the synchronous thermal analyzer STA449 F3 were used to analyse the crystal size, morphology, adhesion, and decomposition temperature of microbial and chemical CaCO₃.

Results and discussion

Effect of microbes on the strength of steel slag cementitious materials

It can be seen from Figure 2 that microorganisms have a significant effect on enhancing the strength of the steel slag cementitious material, and the strength has been continuously

improved as the content of microorganisms increased. When the amount exceeds 6%, the strength can reach more than 50MPa, but when the amount continues to increase, the strength improvement effect weakens. Considering the cost, it can be determined that the optimal amount is about 6%.

Effect of microbes on the volume stability of steel slag cementitious materials

As shown in Figure 3, the linear expansion rate of the microbial-slag cementitious material samples is lower than that of the pure steel slag cementitious material samples, and the linear expansion rate decreases with increasing carbonation curing time. The linear expansion rate can be controlled below 0.5‰ under more than 3 hours of carbonation curing time.

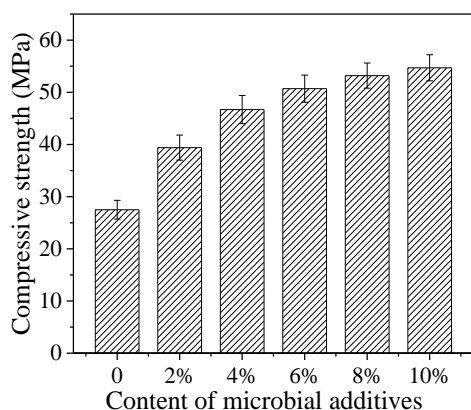


Figure 2. Effect of microbes on the strength

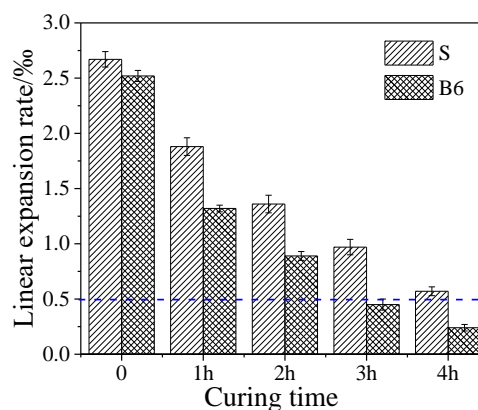


Figure 3. Volume stability at different carbonation curing time

Microstructure of microbial mineralized steel slag samples

Phase composition

It can be seen from Table 3 that the addition of microorganisms can reduce the content of f-MgO and f-CaO in the steel slag cementitious material, and promote the formation of carbonate minerals. After carbonation curing of the microorganism-steel slag samples (Sample B6), CaCO₃ in products was increased by 79.0%, MgCO₃ by 24.3%, and amorphous phase by 43.8% compared to Sample S without bacteria.

Table 3. Effect of microorganisms on mineral phase content of steel slag cementitious materials

Minerals (%)	Sample S	Sample B6
CaCO ₃	22.41	40.15
MgCO ₃	3.72	4.61
Amorphous phase	7.30	10.50
f-MgO	0.71	0.22
f-CaO	0.31	0.12

Pore structure

As shown in Table 4 and Figure 4, the analysis by MIP showed that the porosity of the steel slag cementitious material decreased after the microorganisms were added, and the most probable pore size decreased.

Table 4. Effect of microorganisms on pore structure of steel slag cementitious materials

Code	The most probable pore size /nm	Porosity (%)
Sample S	397.61	37.97
Sample B6	81.46	27.34

Characteristics of microbial CaCO₃

As shown in Table 5, the average crystal sizes of the CaCO₃ prepared by the microbial method and the chemical method calculated by Scherrer's formula are 42.1 nm and 59.3 nm, and the CaCO₃ crystal size formed by microbial mineralization is smaller than that of chemically synthesized CaCO₃. Calcite is the crystal form of CaCO₃ as shown in XRD pattern in Figure 5. DSC results (Figure 5) indicate that the decomposition temperature of microbial CaCO₃ is higher than that of chemical CaCO₃. TEM images (Figures 6 and 7) shows different crystal orientations between microbial CaCO₃ and chemical CaCO₃. The calibration results of diffraction pattern indicate that both crystals are closest to the lattice constant of calcite calcium carbonate of PDF card 05-0586. SEM images (Figure 8) shows that the morphology of microbial CaCO₃ particles is oriented to spherical or ellipsoidal, while the morphology of chemical CaCO₃ is mostly a regular polyhedron. And AFM results show that the adhesive force of microbial CaCO₃ is 45nN, which is higher than that of chemical CaCO₃ as 25 nN.

Table 5. Average crystal size of CaCO₃ prepared by microbial and chemical methods

Sample	θ (deg)	$\beta_{1/2}$ (deg)	D (nm)
Chemical CaCO ₃	29.469	0.137	59.3
Microbial CaCO ₃	29.431	0.193	42.1

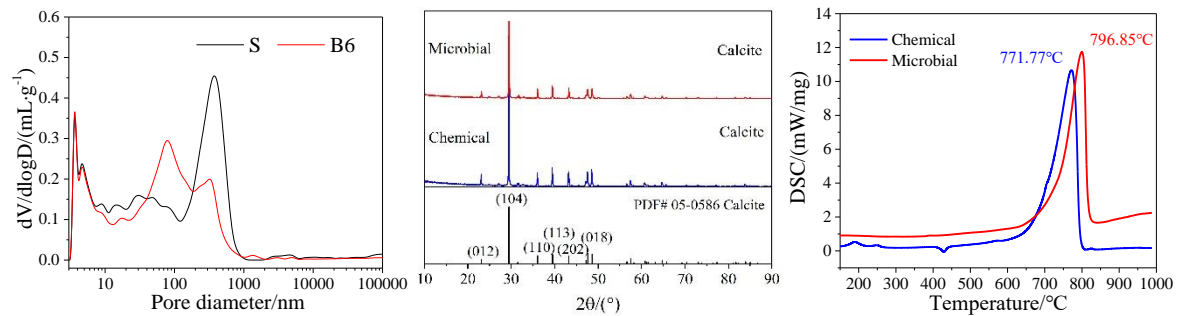


Figure 4. Paste pore size differential curve temperature of 2 types of CaCO₃

Figure 5. XRD pattern and decomposition

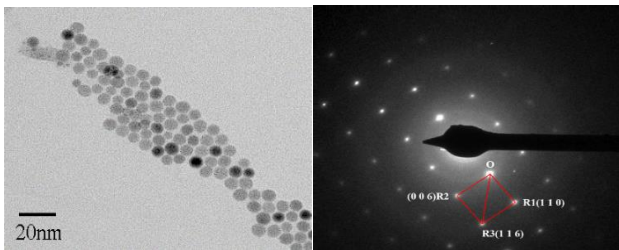


Figure 6. TEM image and electron diffraction pattern of microbial CaCO₃

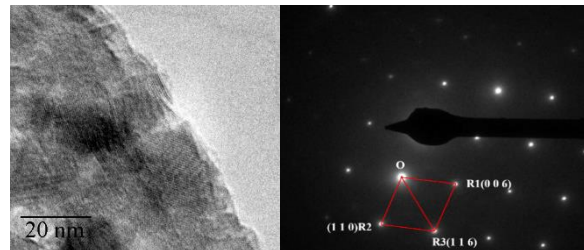


Figure 7. TEM image and electron diffraction pattern of chemical CaCO₃

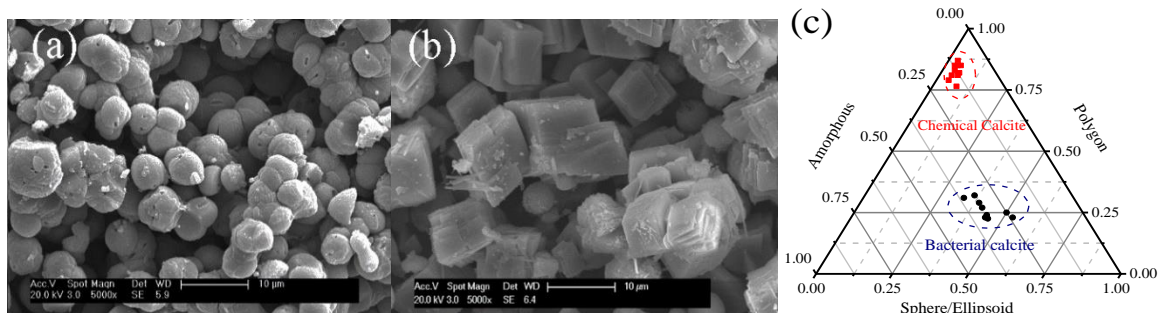


Figure 8. SEM images of microbial CaCO₃ (a), chemical CaCO₃ (b) and statistical diagram of morphology characteristics(c)

Conclusion

- Microbial mineralization can significantly improve the strength and stability of steel slag cementitious materials, reduce porosity and the most probable pore size.
- After the steel slag is mineralized by microorganisms, CaCO_3 and MgCO_3 increase in the product, and f-CaO and f-MgO decrease.
- Compared with chemical CaCO_3 , the microbial CaCO_3 has a smaller crystal size, higher decomposition temperature, and higher adhesion force, with crystal particles oriented to spherical or ellipsoidal.

Acknowledgment

The authors would like to thank the National Natural Science Foundation of China (Grant No.51572047) for the financial support.

References

- [1] E. B, A cross-section of steel industry statistics 2010-2019, Steel statistical yearbook by World Steel Association. 2020: 8-9.
- [2] Yi H, Xu G, Cheng H, et al. An overview of utilization of steel slag. *Procedia Environmental Sciences*, 2012(16): 791-801.
- [3] Shi, Caijun. Steel Slag: Its production, processing, characteristics, and cementitious properties. *Journal of Materials in Civil Engineering*, 2004, 16(3): 230-236.
- [4] Yi Haihe, Chun-xiang Qian. The Influence of Microbial Agent on the Mineralization Rate of Steel Slag. *Advances in Materials Science and Engineering*. 2018(4): 1-10.

Challenges of Self-Healing Concrete Application

Mouna A. Reda, Shannon Guo, Samir E. Chidiac

Department of Civil Engineering, McMaster University, Hamilton, Ontario, Canada

Abstract

Concrete, the most used construction material in the world, is susceptible to cracking as an inevitable natural phenomenon. It could occur in the plastic and hardened states as symptoms of volumetric stability issues, environmental actions, or mechanical loading of concrete elements. Without proper repair, cracks continue to grow and affect the performance, durability, and mechanical properties of concrete structures. The concept of self-healing and self-repairing naturally is being studied for concrete. Although cracks have been shown to heal in concrete either autogenously or autonomously, the field application of self-healing concrete remains challenging. Micro-encapsulation, which is one of the most promising technique in self-healing, faces similar challenges starting with the lack of consistent and standard test method to evaluate the healing efficiency of the microcapsules and of the system.

This study examines the postulated test methods in the literature pertaining to the effects of adding microcapsules on the properties and performance of concrete. Particularly, the distribution, number, and geometry of the microcapsules are investigated as well as the compatibility requirements of the material and system. The study will note the strengths and weaknesses of current test methods as well as identify the necessary test requirements for evaluating the healing efficiency and efficacy of microcapsules in concrete.

Introduction

Concrete, the most used construction material in the world, emerged in the early 1900's as a durable and maintenance-free construction material. However, concrete is susceptible to cracking at early age due to chemical reactions and volumetric instability. Without proper repair, crack openings provide deleterious gases and liquids pathways to the concrete core that compromise the performance and longevity of concrete structures. Self-healing, observed in nature and successfully developed for metals and polymers, has emerged as an option for concrete. Although cracks with very small openings in concrete have been shown to heal autogenously, the results are inconsistent and environment dependent. The application of autonomous healing, which is a possible alternative, is challenging.

Encapsulation, which involves the sealing of healing agents in microcapsules whose release is controlled by either a mechanical or environmental trigger, provides the vessels for autonomous self-healing concrete. The challenge with embedding these microcapsules for self-healing concrete is determining the shell geometrical and mechanical properties such that it can survive the concrete mixing and placement while still trigger the release of the healing agents when young concrete cracks [1,2]. This paper aims to critically analyze the proposed test method for evaluating the properties of the capsules as well as their efficiency as autonomous self-healing in young concrete.

Methodology and testing procedures

Microcapsules geometrical and mechanical compatibility requirements

The geometrical properties of the capsule, such as shape, size, surface morphology, and ratio of shell thickness to capsule diameter, influence the mechanical and fracture behavior of the capsule as well as its durability. The size of the capsule should be large enough to host the healing agents, yet not too large to adversely affect the mechanical and transport properties

of concrete. The capsules' diameter used in self-healing concrete ranges between 10-1000 μm , while the capsules' diameter ranges between 100 and 200 μm in self-healing polymers industry [3]. For reference, the diameter of air-entrained voids in concrete is between 10 and 100 μm , and with every 1% increase in air content yields 5 to 6% decrease in the concrete compressive strength [4]. A spherically shape capsule is preferred as it mitigates geometric discontinuities due to sharp edges and presents the least effects on the mechanical properties of the matrix. The morphology of the outer shell, specifically its roughness, is also due to the enhanced mechanical bond. Proper sizing of the capsule also requires a delicate and complex balance between the diameter that controls the storage capacity and the ratio of shell thickness to diameter of the capsule that controls the survivability and trigger of the capsule [5].

The mechanical trigger of capsules during the initiation or propagation of cracks in concrete is essential for healing to occur. Accordingly, the stiffness and strength of the capsule shell relative to those of the matrix are important. Ratio of matrix stiffness to that of the capsule controls the distribution of stress and ratio of their strength affects the fracture plane. As presented with these 4 scenarios of incompatibility, the properties of the capsule and matrix need to be equal: A stiffer and stronger capsule will attract more load and results in debonding of the capsule; A softer and stronger capsule will not attract the load and if cracking is in the vicinity of the capsule it will cause the interface to debond or the plane near the interface to crack, most likely will not lead to a crack in the vicinity of the capsule; A stiffer and weaker capsule will most likely not survive the rigorous mixing and placing of concrete; A softer and weaker capsule may survive the initial mixing and placing of concrete, however it may not fracture unless it is stretched which is not likely in concrete. Moreover, the bonding strength of the capsule to the matrix needs to be greater than the mechanical trigger of the capsule.

Microcapsules strength and stiffness properties

Characterization of the capsule's properties is yet to be standardized. Different test methods have been proposed in the literature to evaluate the stiffness and strength of a single capsule. These tests include Liu et al. [6] who tested poly-urethane microcapsules by compressing a single capsule between two parallel glass plates until the capsule started to burst, Keller and Sottos [7] who tested the mechanical properties of poly-urea-formaldehyde capsules by compressing a single-capsule, Lee et al. [8] who used nanoindentation and a cone tip of approximately 3 μm radius to measure the micromechanical properties of the capsule, and Lv et al. [9] who also used nanoindentation to evaluate the mechanical properties of phenol-formaldehyde shell-interlayer-cement paste zone (SIC). The corresponding results are summarized in Table 1.

Microcapsules healing efficiency

Testing the healing efficiency of capsules in concrete poses a multitude of challenges as one needs to account for the maturity of the concrete and the type of healing. The compatibility between the capsule mechanical properties and the matrix and the bonding strength are a necessary requirement for the mechanical trigger to work. Recognizing that the properties of concrete evolve with maturity, especially at its early age, the enforcement of the compatibility requirements is very difficult if not impossible. Moreover, the healing can have two performance requirements, sealing the crack to restore the concrete water and gas tightness or repairing the crack to restore the concrete stiffness and strength. As a priori, the test method must account for these specificities before it can be applied. Therefore, the properties of the shell and the healing agent must be selected accordingly.

Table 1. Microcapsule shell properties

Shell Material	Average size (D) (μm)	Shell thickness (t) (μm)	t/D	Elastic Modulus (GPa)	Rupture stress (MPa)
Poly(urethane) (PU) [6]	50-100	1-2	~ 0.02	0.0029	0.026
Urea-formaldehyde (UF) [7]	58-225	0.175 ± 0.033	~ 0.001	3.7 ± 0.2	0.24 ± 0.04 ($D=187 \pm 15 \mu\text{m}$)
Melamine-formaldehyde (MF) [8]	50-150	0.2	~ 0.003	4.66	1.5
Phenol-formaldehyde (PF) [5], [9]	50-600	29.96	~ 0.1	2.2 ± 0.8	1.37 ± 0.3 ($D=200-400 \mu\text{m}$)

Proposed test methods to evaluate the healing efficiency do not appear to account for the type of healing and the age of the concrete. Most test methods employ either the 3-point or 4-point flexural test or a compressive test to induce cracking in the concrete sample and then measure the healing effectiveness by measuring the flexural or compressive strength recovery of the sample [10–12]. The testing approach reported in the literature is problematic for many reasons. First, these tests do not reproduce the predominant failure mechanism caused by shrinkage at early age and environmental loading at a later age. Second, the sequences of the test and test results need to be time dependent to assess both the healing efficiency of the capsules in concrete. Thirdly, these tests are missing the most important problem in concrete, shrinkage due to hydration or drying which occurs when the concrete is very young. In brief, new testing methodology is needed to evaluate the efficiency of capsules in early and later age, and for sealing or structural repairing the concrete.

Preliminary results and discussion

To illustrate some of the issues raised with the current testing methods, the geometrical and mechanical properties of the prevalent polymeric capsules used in concrete for autonomous healing, documented in Table 1, are compared with the evolving properties of concrete that are reproduced in Table 2 for water to cement ratio w/c equals to 0.33 [13]. For reference, the shrinkage strains and corresponding stresses developed in concrete were estimated according to CEB [14] and reproduced in Table 1. Comparing the stress values to the capsule rupture strength of Table , the likelihood of rupturing the capsules due to shrinkage is very high but not high enough to crack the concrete as per the tensile strength. These results suggest that the capsules will rupture inside the concrete even if the concrete does not crack.

Table 2. Mechanical properties of concrete with $w/c = 0.33$ [13]

Age (h)	Young's modulus (GPa)	Tensile strength (MPa)	Shrinkage stress (MPa)
6	15.4	0.83	0.59
12	28.1	2.49	1.08
24	31.2	3.32	1.20
48	35.1	4.02	1.35
72	35.4	4.19	1.36
168	36.2	4.34	1.39
672	40.3	5.30	

The addition of surface drying strains to the shrinkage strains will most likely cause the concrete to crack at the exposed surface. From fracture mechanics, a magnification of 1.8 in the stress values can develop at the tip of the crack. Accordingly, the stress values would be large enough to rupture the capsules provided the bonding strength between the capsule and the matrix are not lower to cause debonding of the capsule.

The mechanical properties of concrete evolve as concrete matures. A plot of the ratio of concrete stiffness at different ages to that of the capsules, shown in Figure 1, reveals an increase in the first 24h with the magnitude depending on the material used to form the capsules. These results show that the state of stress in the vicinity of the capsule will be different for the different polymeric material and age of concrete [15]. A plot of the ratio of concrete tensile strength to that of the capsule rupture strength, shown in Figure 1, reveals that cracking can occur in the matrix for the cases where ratio is close to one, i.e. at early age. Therefore, a proper characterization of the capsule material properties is pivotal to ensure that the capsules rupture when it intercepts a crack. Moreover, testing the performance of the healing system needs to be carried out at the most critical age of concrete.

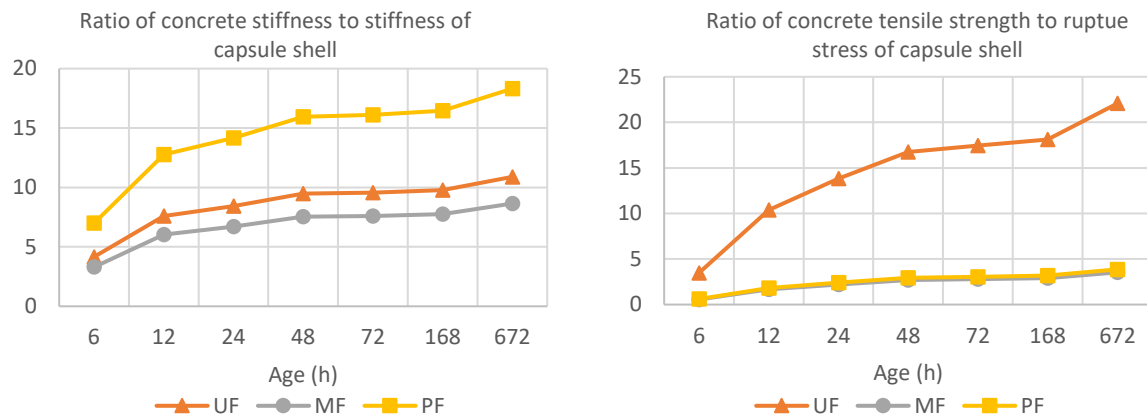


Figure 1. Mechanical properties of concrete with age and polymeric capsules

Table 3 documents the reported increase in the recovered mechanical properties of concrete due to self-healing for 2 different capsules. Although the results are appealing, they are most likely difficult to reproduce in the laboratory and in the field for the following reasons.

Table 3. Mechanical recovery of self-healing cementitious materials

Shell material	Average size (D) (μm)	Shell thickness (t) (μm)	t/D	Recovered property	Recovery
Urea-Formaldehyde [16], [17]	80-1000	0.14-0.20	~ 0.002	Elastic modulus	11-30%
	132-230	-	-	Compressive strength (pre-damage of 60% σ_{max})	10%
Melamine urea-formaldehyde [10]	10-1000	1.1~1.3	~ 0.003	Normalized flexural strength (pre-damage of 30% f_{max})	1.8

In addition to the concerns raised previously, the healing efficiency of capsules in concrete also depends on the flow properties and hardening kinetics of the healing agent as well as the testing environment. The former is critical for the healing agent to flow and fill the crack before it hardens.

The environment of the laboratory where the tests are carried out to assess the healing efficiency of the capsules in concrete is not representative of the concrete inner and outer environment, i.e. the moisture condition and temperature within the concrete and the environment surrounding the concrete will be different. These environmental conditions affect the flow, hardening kinetic and bonding strength of the healing agent.

Conclusions

The results from this study reveals the followings:

- Testing the mechanical properties of the capsules need to account for the confined and bonding condition of the capsules in concrete.
- Mechanical and geometric properties of the capsules must be compatible with those of the concrete at early age to mitigate cracks due to shrinkage.
- Capsule mechanical trigger is a balance between the mechanical properties of the concrete and the capsule and the bond strength at the interface between the capsule and concrete.
- Flow properties, hardening kinetic and bond strength of the healing agent need to be characterized for different temperature and moisture conditions.
- Test method for determining the efficiency of self-healing concrete needs to be specific to the type of healing, age of concrete and root causes of the cracks.
- Current test methods for the capsules and healing efficiency fail to meet their objectives.

Acknowledgment

This research was funded by the Natural Sciences and Engineering Research Council of Canada.

References

- [1] De Belie N, Gruyaert E, Al-Tabbaa A, Antonaci P, Baera C, Bajare D, et al. A Review of Self-Healing Concrete for Damage Management of Structures. *Advanced Materials Interfaces*. 2018 Vol 5 pp. 1800074.
- [2] Guo S, Chidiac SE. Self-healing concrete: A critical review. *CSCCE Annual Conference Growing with youth – Croître avec les jeunes*. Laval, ON, Canada: June 12 - 15, 2019 pp. 1–10.
- [3] Nesterova T, Dam-Johansen K, Pedersen LT, Kiil S. Microcapsule-based self-healing anticorrosive coatings: Capsule size, coating formulation, and exposure testing. *Progress in Organic Coatings*. 2012 Vol 75 pp. 309–318.
- [4] Kosmatka SH, Wilson ML. *Design and Control of Concrete Mixtures – The Guide to Applications, Methods and Materials*. (15th edition. Portland Cement Association PCA 2011).
- [5] Lv L, Schlagen E, Yang Z, Xing F. Micromechanical Properties of a New Polymeric Microcapsule for Self-Healing. *Materials*. 2016 Vol 9 pp. 1–16.
- [6] Liu KK, Williams DR, Briscoe BJ. Compressive deformation of a single microcapsule. *Physical Review E*. 1996 Vol 54 pp. 6673–6680.
- [7] Keller MW, Sottos NR. Mechanical Properties of Microcapsules Used in a Self-Healing Polymer. *Experimental Mechanics*. 2006 Vol 46 pp. 725–733.
- [8] Lee J, Zhang M, Bhattacharyya D, Yuan YC, Jayaraman K, Mai YW. Micromechanical behavior of self-healing epoxy and hardener-loaded microcapsules by nanoindentation. *Materials Letters*. 2012 Vol 76 pp. 62–65.
- [9] Lv L-Y, Zhang H, Schlagen E, Yang Z, Xing F. Experimental and numerical study of crack behaviour for capsule-based self-healing cementitious materials. *Construction and Building Materials*. 2017 Vol 156 pp. 219–229.
- [10] Li W, Zhu X, Zhao N, Jiang Z. Preparation and Properties of Melamine Urea-Formaldehyde Microcapsules for Self-Healing of Cementitious Materials. *Materials*. 2016 Vol 9 pp. 152.
- [11] Hu Z-X, Hu X-M, Cheng W-M, Zhao Y-Y, Wu M-Y. Performance optimization of one-component polyurethane healing agent for self-healing concrete. *Construction and Building Materials*. 2018 Vol 179 pp. 151–159.
- [12] Milla J, Hassan MM, Rupnow T, Daly WH. Measuring the crack-repair efficiency of steel fiber reinforced concrete beams with microencapsulated calcium nitrate. *Construction and Building Materials*. 2019 Vol 201 pp. 526–538.

- [13] Oluokun FA, Burdette EG, Deatherage JH. Rates of development of physical properties of concrete at early ages. *Transportation Research Record*. 1990 Vol 1284 pp. 16–22.
- [14] International Recommendations for the Design and Construction of Concrete Structures (CEB-FIP). (1st edition. FIP Sixth Congress, Prague: The cement and concrete association 1970).
- [15] Guo S, Reda MA, Chidiac SE. Fracture of cementitious material containing spherical microcapsules. *Resilient Materials 4 Life 2020 International Conference (RM4L2020)*. Churchill College, Cambridge, UK: Sept. 14-17, 2020 pp. 1-4.
- [16] Gilford J, Hassan MM, Rupnow T, Barbato M, Okeil A, Asadi S. Dicyclopentadiene and Sodium Silicate Microencapsulation for Self-Healing of Concrete. *Journal of Materials in Civil Engineering*. 2014 Vol 26 pp. 886–896.
- [17] Dong B, Han N, Zhang M, Wang X, Cui H, Xing F. A Microcapsule Technology Based Self-Healing System for Concrete Structures. *Journal of Earthquake and Tsunami*. 2013 Vol 7 pp. 1350014.

Microbial induced calcite precipitation as a viable ground improvement technique

Mary Anderson, Rebecca J Lunn, James Minto, Grainne El Mountassir

Department of Civil and Environmental Engineering, University of Strathclyde, Glasgow G1 1XJ, UK

Abstract

Traditional ground improvement techniques, such as grouting or compaction, can be invasive, energy demanding and expensive. Microbially induced calcite precipitation (MICP) offers a sustainable alternative by utilizing a natural process, and has therefore been the focus of extensive interest and laboratory research over the past decade. Most of that research has been at laboratory-scale on the factors that affect process efficiency. The use of MICP in the field have been discussed in numerous research papers but remains largely theoretical and examples of field-scale trials are rare.

MICP uses ureolytic bacteria, such as the common soil bacteria *Sporosarcina pasteurii*, which are given access to an ample supply of urea and calcium chloride. The bacteria hydrolyse the urea into ammonium and carbonate, raising the pH and in the presence of calcium in solution, facilitating the precipitation of calcite crystals (CaCO_3). It is particularly effective when used with fine grained sands as those calcite crystals form a bridge between the individual sand grains, cementing them together and creating a weak bio-sandstone.

This project, through bench-scale column experiments on MICP treated sands, has investigated optimization of the influencing factors of the bacteria concentration, the treatment strategy employed and the number of treatment cycles administered. The influence these parameters have on the ultimate core strength, from unconfined compressive strength (UCS) tests, and the homogeneity of the calcite distribution, have been determined. These results have then been used to design an efficient treatment process to underpin large-scale trials of MICP for ground improvement and erosion protection.

Introduction

Soil as a construction material has typically been viewed by engineers as a passive substance, with poor engineering properties, that often requires intervention to make fit for purpose [1]. One commonly used soil improvement technique is chemical grouting, involving the injection of cement or chemical grouts into the ground to bind the soil particles together, creating strength and stiffness within the soil [2]. Unfortunately, such treatments “increase the pH of groundwater to highly alkaline levels”, which can alter the local ecosystem and generate a number of environmental concerns [3]. In response to this, Wang *et al.* [1] state that “it is necessary to develop a new type of environmental friendly and cost-effective material which can be used for ground improvement for sustainable development”.

Microbial induced calcite precipitation (MICP) has the potential to offer that sustainable alternative to traditional ground improvement techniques. Bao *et al.*, [4] note that, “Soil is a living ecosystem in which biogeochemical processes such as mineral precipitation, gas generation, biofilm formation, and biopolymer generation are ubiquitous”. MICP is a biogeochemical process that involves the artificial inducement of calcium carbonate (calcite) precipitation by “microbial metabolic activity” [4]. It is sustainable as it can be applied in-situ and can utilize common bacteria such as the ureolytic soil bacteria *Sporosarcina pasteurii* (*S. pasteurii*). By giving the bacteria access to a supply of urea and calcium chloride, the urease positive bacteria hydrolyse the urea into ammonium and carbonate (Equation 1), raising the pH and facilitating the precipitation of calcite crystals [5].

The bacteria also play a critical role as nucleation sites for mineral growth within the soil matrix. This encourages calcite development between the grains, effectively cementing them together and increasing the mechanical properties of the soil such as the shear strength, compressibility and stiffness [4]. It is particularly effective when used with fine grained sands as those calcite crystals form bridges between the individual sand grains and create a weak bio-sandstone [6]. Figure 1 illustrates the calcite crystals bridging the gaps between the larger quartz sand grains, cementing them together.

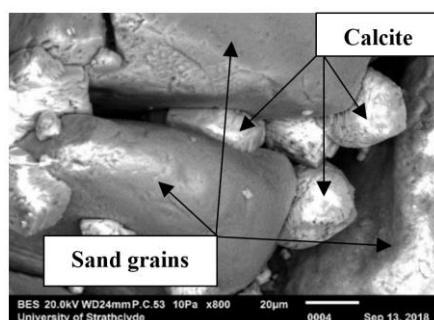


Figure 1 - S.E.M. image

In practice, the MICP process must be both economical and efficient if it is to be used as a sustainable and eco-friendly alternative to traditional methods [7]. To become a viable ground improvement technique there are a number of influential factors that first need to be optimised at the bench-scale. These factors include, but are not limited to, the concentration of the bacteria suspension, the treatment strategy employed and the number of completed treatment cycles [7]. This project, through bench-scale column experiments on MICP treated sands, has investigated optimization of some influencing factors. The impact these parameters have on the ultimate core strength, from unconfined compressive strength (UCS) tests, and the homogeneity of the calcite distribution, have been determined. These results have then been used to design an efficient treatment process to underpin large-scale trials of MICP for ground improvement and erosion protection.

Materials and methods

Bacteria and cementing fluid

The species of bacteria used in all experiments were *Sporosarcina pasteurii* (*S. pasteurii*), taken from cold-stored plated colonies and inoculated into autoclaved flasks of yeast extract broth media, with 20 g/l urea. Those flasks were then placed in a floor shaker at 115 rpm and 30 °C for up to 24-hr until adequate growth and an optical density (OD₆₀₀) greater than 1 was achieved. Fresh batches of broth media were prepared and inoculated with bacteria daily, to grow and be ready for use the following day.

Two main approximate concentrations of bacteria were used for the experiments; *in water* and *in broth*. For the *in water* concentration, each batch of bacteria were first separated from the supernatant by centrifuge before being re-suspended with tap water and restored to the original volume and a concentration which was measured as just above 1 OD₆₀₀. As the name suggests, *in broth* refers to the bacteria being kept in the original growth media with a measured optical density also just above 1.

To facilitate the MICP process, the bacteria must have a supply of urea to hydrolyse and a source of calcium to precipitate into calcite. These were supplied through the addition of a

cementing solution made from 0.5 equimolar of urea and calcium chloride dissolved in de-ionised water.

Soil

To create a fine soil only three sizes of sand were used; 28% at 0.15 mm, 33% at 0.212 mm and 39% at 0.3 mm. After initial fraction separation, the sand was washed and dried before the exact composition for each sample was individually weighed and mixed to ensure all contained the correct proportion. The initial average flow rate through the samples was 11ml/min, with a discharge velocity of 58 cm/hr, however it was possible to reduce that to roughly 6 ml/min, and a discharge velocity of 32 cm/hr, by including 3% of silica flour in the mix. Finally, the samples were vibrated to increase the bulk density to 1.7 Mg/m³, with a sample porosity between 35 and 37%.

Set-up

Clear plastic tubing, of 38mm inner diameter, was cut into lengths to create experiment moulds. As shown in Figure 2, a fine net material was secured over the bottom to prevent any loss of sand when the fluids were added, and to allow the samples to free drain under gravity. Prior to initial treatment, the samples were flushed with 2 pore volume (PV) of tap water to create a partially saturated state. At the end of the treatment, the samples were flushed with 10PV of tap water to stop all reactions and expel any unused fluids. Finally, the samples were allowed to air dry for approx. 1 week before being removed from their moulds and prepared for testing.

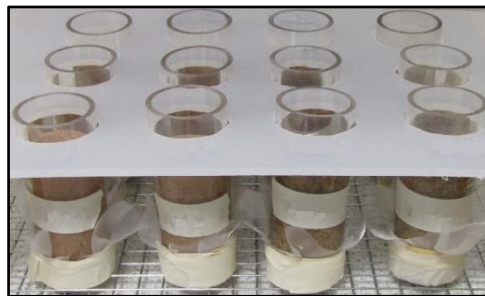


Figure 2 - Prepared samples for treatment

Treatments

Each treatment cycle began with 2PV of the bacteria, at each concentration, simply poured into the top of the sample and creating a temporary head. A static period of approximately 1-hr was allowed so the fluid would percolate through the sample and the bacteria would attach themselves. 2PV of cementing fluid was then added in the same manner as the bacteria and the samples were then left static until the next day (approx. 22-hr). A further 2PV of cementing fluid was then added to each sample before a further static period of approx. 24-hr to complete the cycle. The MICP treatment process was continued for 12 days until a total of 6 treatment cycles were completed on all samples.

Testing

Samples extracted intact from the moulds were adjusted to a ratio of 2:1 (76mm x 38mm) and tested by unconfined compression (UCS) to ascertain the strength properties. Each test was continued until failure was observed by a sudden drop in peak strength displayed on the real-time results graph.

Using a Jeol JSM-IT100 machine, scanning electron microscope (SEM) images were taken of sample fragments to ascertain the crystal growth with the sand grains. Using the same machine, it was also possible to conduct further analysis on the samples with energy-dispersive X-ray spectroscopy (EDS), giving an overview of the main chemical elements present.

Supplemental investigation

Further investigation was conducted to ascertain any difference in precipitation from administering the bacteria in different media. Simple bench experiments using bacteria in broth media, bacteria re-suspended in tap water, and supernatant that the re-suspended bacteria had been removed from, were performed in triplicate. 40ml of cementing fluid was added to beakers that already contained 40ml of the fore mentioned three varieties of fluid, then left static for 2-hr to allow for precipitation. Figure 3 shows an example of the supernatant during the 2-hr static period. The fluid was then vacuumed off through filter paper, which was dried and weighed to give the quantity of precipitate produced.



Figure 3 – Supernatant and CaCl

Results and discussion

It can be seen from Figure 4, that the samples treated with the bacteria still in broth produced higher strengths and total calcite contents than the samples treated with re-suspended bacteria. Despite the small number of results attained, the *in broth* results appear linear, with increasing calcite contents relating to increasing UCS, which corresponds with observations from other authors such as Cheng et al. [8] and Whiffin et al. [9].

Closer examination from the SEM images, Figure 5 and 6, show that there is a distinct difference in the formation/growth of the calcite crystals between the *in water* and *in broth* samples. Most notable is that the re-suspended bacteria has effectively formed a uniform blanket of calcite that is coating or encapsulating the sand grains. In contrast, the crystals created with *in broth* bacteria are more irregular in shape and size, while also appearing to be amassed between the sand grains rather than coating them. Crystal growth at the contact points between the sand grains is desired in MICP treatment and is associated with an increase in mechanical properties, such as strength and stiffness, of treated sands [2].

Apart from the bacteria suspension fluid, both samples were the same, from composition to post treatment, so any difference in results must be due to that fluid. The results of the simple experiments, shown in Figure 7, reveal that the supernatant alone is able to produce a significant amount of calcite. As the bacteria had been removed and there was no ureolytic activity present, there must be carbonate ions (from the bacteria growth) present in the supernatant fluid [10]. Those ions react instantaneously with the calcium chloride in the cementing fluid to precipitate calcite.

This means that the *in broth* samples effectively have an initial burst of precipitation forming calcite crystals before the bacteria start the hydrolysis of the urea. The impact of this phenomenon has both positive and negative implications and associations.

Although that initial precipitation from the supernatant may produce a boost for the MICP process, it may also significantly reduce the pore space and flow paths at the inlet, preventing fluids freely migrating through the entire sample [11]. Such an occurrence would effectively prevent homogeneous calcite distribution, instead creating samples with a strong top/inlet and a high calcite content, while the bottom/outlet was weak with a low calcite content.

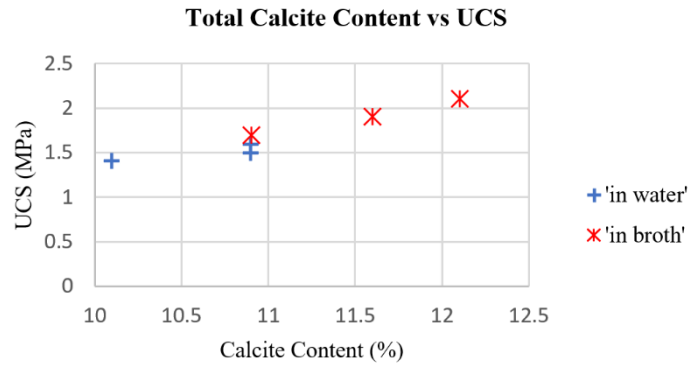


Figure 4 - Experiment results by bacteria concentration

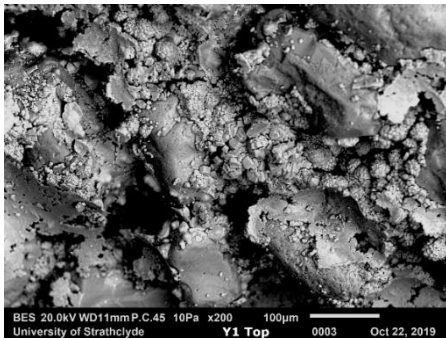


Figure 5 - SEM image of 'in water' sample

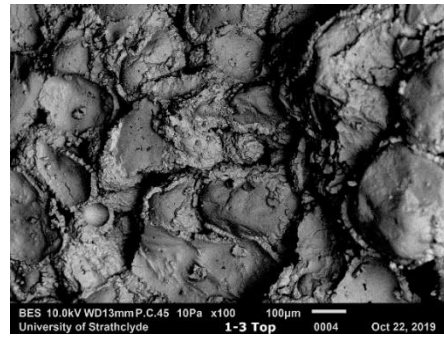


Figure 6 - SEM image of 'in broth' sample

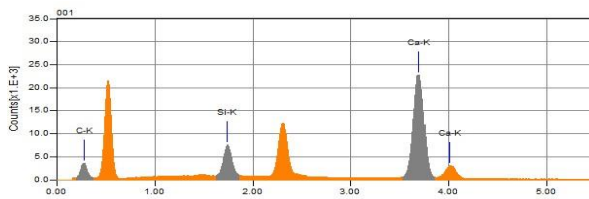


Figure 7 - EDS analysis of 'in broth' sample

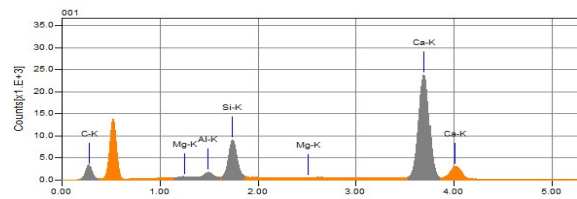


Figure 8 - EDS analysis of 'in water' sample

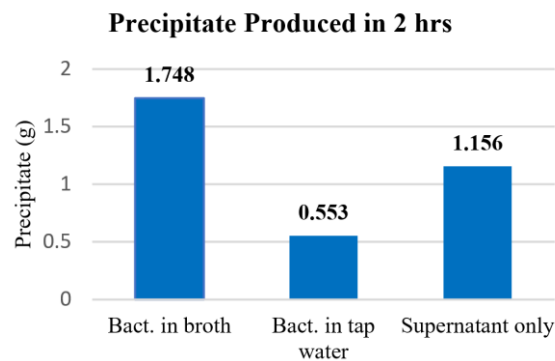


Figure 9- Precipitate results

EDS analysis of the samples reveals that the *in broth* sample, shown in Figure 8, has more impurities than the *in water* sample, shown in Figure 9, which has the basic chemical elements of only carbon, silicon and calcium. According to the analysis the *in broth* samples also have a small percentage of magnesium and aluminium present, although only at trace levels within these samples.

Conclusion

MICP offers an environmentally friendly and sustainable alternative to traditional ground improvement techniques by generating calcite within the soil matrix and increasing the strength properties of the soil. Although treatment with bacteria kept in their growth media increases calcite content, that initial precipitation could prove a hindrance to continuing a treatment programme. Ideally, for ground improvement, MICP treatment should result in homogeneous distribution of calcite to ensure consistent improvement of the engineering properties throughout the treated area. In contrast, coastal erosion prevention or dust suppression improvement may be able to utilise that fast precipitation to create a strong protective crust on the surface, effectively protecting the underlying soil layers.

Sufficient knowledge and understanding of these factors, and others, will ensure that any large-scale trials will be appropriately designed and targeted for that application, ensuring an efficient process.

Acknowledgment

This project has been jointly funded by Construction Scotland Innovation Centre (CSIC), Engineering and Physical Sciences Research Council (EPSRC), and BAM Nuttall.

References

1. Wang, Z., et al., *Review of ground improvement using microbial induced carbonate precipitation (MICP)*. Marine Georesources & Geotechnology, 2017. 35(8): p. 1135-1146.
2. Dejong, J.T., et al., *Bio-mediated soil improvement*. Ecological Engineering, 2010. 36(2): p. 197-210.
3. Mujah, D., M.A. Shahin, and L. Cheng, *State-of-the-Art Review of Biocementation by Microbially Induced Calcite Precipitation (MICP) for Soil Stabilization*. Geomicrobiology Journal, 2017. 34(6): p. 524-537.
4. Bao, R., et al., *Effect of Microbial-Induced Calcite Precipitation on Surface Erosion and Scour of Granular Soils: Proof of Concept*. Transportation Research Record, 2017. 2657(1): p. 10-18.
5. Amin, M., S.M.A. Zomorodian, and B.C. O'Kelly, *Reducing the hydraulic erosion of sand using microbial-induced carbonate precipitation*. Proceedings of the Institution of Civil Engineers: Ground Improvement, 2017. 170(2): p. 112-122.
6. Dharni, N.K., M.S. Reddy, and A. Mukherjee, *Biomineralization of calcium carbonates and their engineered applications: A review*. Frontiers in Microbiology, 2013. 4: p. 1 - 13.
7. Ng, W.-S., M.-L. Lee, and S.-L. Hii, *An Overview of the Factors Affecting microbial-induced calcite precipitation and its Potential Application in Soil Improvement*. World Academy of Science, Engineering and Technology, 2012. 62: p. 723-729.
8. Cheng, L., R. Cord-Ruwisch, and M.A. Shahin, *Cementation of sand soil by microbially induced calcite precipitation at various degrees of saturation*. Canadian Geotechnical Journal, 2013. 50(1): p. 81-90.
9. Whiffin, V.S., L.A. Van Paassen, and M.P. Harkes, *Microbial Carbonate Precipitation as a Soil Improvement Technique*. Geomicrobiology Journal, 2007. 24(5): p. 417-423.
10. De Muynck, W., N. De Belie, and W. Verstraete, *Microbial carbonate precipitation in construction materials: A review*. Ecological Engineering, 2010. 36(2): p. 118-136.
11. Phillips, A.J., et al., *Engineered applications of ureolytic biomineralization: a review*. Biofouling, 2013. 29(6): p. 715-733.

Grouting of well leakage and migration pathways using colloidal silica: a preliminary experimental investigation

Arianna Gea Pagano, Grainne El Mountassir, Rebecca Jane Lunn

Department of Civil and Environmental Engineering, University of Strathclyde, Glasgow G1 1XJ, UK

Abstract

Hydrocarbon well decommissioning and abandonment require the long-term sealing of potential fluid migration pathways. Current grouting technologies based on the use of cementitious grouts may not be able to achieve proper penetration and sealing of migration pathways, this resulting in an environmental risk due to the migration of hydrocarbons or other well fluids out of the well and into the environment.

Colloidal silica (CS) based grouts differ from traditional cement grouts due to their low viscosity (similar to water), and their excellent penetrability governed by the size of the silica nanoparticles (~15nm). As a result, CS grouts have the potential to seal migration pathways (i) at cement/casing or casing/cement interfaces where the cement bond is compromised, and (ii) due to micro-channels and micro-annuli within the cement annulus. This study presents a preliminary laboratory investigation to demonstrate the suitability of CS grout for the purpose of creating multiple barriers within hydrocarbon wells. To this end, CS grout was injected into fractured cement cores using a high pressure/high temperature core-holder apparatus to simulate target downhole scenarios. Microstructural analysis (micro-CT scanning) prior and post treatment were conducted to image the spatial distribution of the grout within the fracture network. The effectiveness of the treatment was measured by evaluating i) the core permeability before and after treatment with CS, and ii) the unconfined compressive strength of treated cement cores.

Introduction

Hydrocarbon well decommissioning and abandonment requires the long-term sealing of potential fluid migration pathways. Current grouting technologies based on the use of cementitious grouts are not able to penetrate fine fissures and cracks and therefore may not seal all potential migration pathways, resulting in the possible long-term migration of hydrocarbons or other well fluids out of the well and into the environment.

Colloidal silica (CS) based grouts are an alternative to traditional cementitious grouts [1] – [4]. CS is a non-toxic, low viscosity aqueous suspension of silica particles which forms a gel upon destabilisation, typically triggered by the addition of an accelerator (electrolyte solution). The gelation process is controlled by several factors, including particle size, particle concentration, pH, electrolyte concentration and valency, and temperature [5]. Analytical models able to predict gelling depending on the grout composition are available in the literature [6].

CS grouts differ from traditional cement grouts due to their low viscosity (similar to water), and their excellent penetrability governed by the size of the silica nanoparticles (~15nm). As a result, CS grouts have the potential to seal migration pathways (i) at cement/casing or casing/cement interfaces where the cement bond is compromised, and (ii) due to micro-channels and micro-annuli within the cement annulus. Moreover, the well-established pozzolanic activity of colloidal silica particles may offer further benefit to treated cement by promoting the generation of additional cementitious compounds, making use of available calcium sources naturally occurring in hydrated cement pastes [7] – [9].

This study presents a preliminary laboratory investigation to demonstrate the suitability of CS grout for sealing cracks within the cement annulus. To this end, CS grout was injected into a fractured cement core with constant fracture aperture and cured at reservoir conditions.

Experiments were carried out within a high pressure/high temperature core-holder apparatus to simulate target downhole scenarios. The effectiveness of the treatment was measured by evaluating the core hydraulic conductivity before and after treatment with CS.

Materials and methods

Cylindrical cement cores (75mm height x 38mm diameter) with constant fracture aperture of 0.2 mm were prepared using Ordinary Portland Cement. Cement paste was prepared by mixing cement powder with de-ionised water by means of a rotary mixer at a water-to-cement ratio $w/c = 0.375$. The two halves of each cement core were cast in silicon rubber moulds, specially designed to obtain a constant fracture aperture of 0.2 mm. The cement mix was left to cure in the moulds for 24 hours under controlled humidity and temperature. Then, the hardened cement pastes were de-moulded and placed in deionised water to cure for an additional 27 days. The specimen preparation procedure carried out in this study is showed in Figure 1.

A commercially available colloidal silica (CS) suspension, Meyco MP320, was used in this work. Meyco MP320 is a solvent-free, low viscosity suspension of nanometric colloidal silica particles (viscosity ~ 10 mPa.s, particle size ~ 15 nm). CS grout was prepared by mixing the as-delivered CS suspension with de-ionised water (5:1 CS-to-water ratio by volume). No accelerator (i.e. electrolyte solution) was added to the grout.

Hydraulic conductivity measurements and flow-through experiments at relevant downhole conditions were performed in a bespoke high pressure/high temperature core holder (Figure 2). A pre-treatment hydraulic conductivity measurement was carried out on the fully cured core by injecting tap water at varying flow rates. The resulting inlet pressure was continuously monitored in order to derive hydraulic conductivity using Darcy's law:

$$k = \gamma_w \cdot \frac{Q}{A} \cdot \frac{L}{\Delta P_{IN-OUT}}$$

where k is the hydraulic conductivity [m/s], γ_w is the unit weight of water [kN/m³], Q is the flow rate [m³/s], A and L are the whole cross sectional area [m²] and length [m] of the core respectively, and ΔP_{IN-OUT} is the pressure differential across the core [Pa].

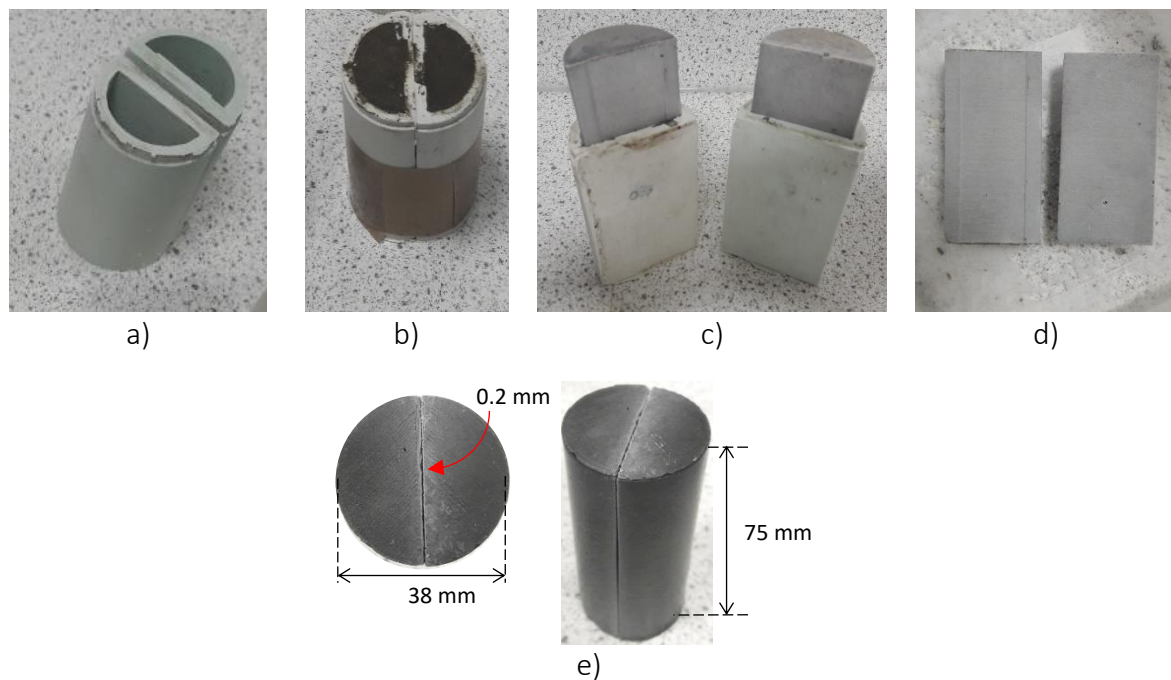


Figure 1. Specimen preparation: a) silicon rubber moulds; b) curing of wet cement paste (24 hours); c) de-moulding; d) curing under water (27 days); e) cured cement core.

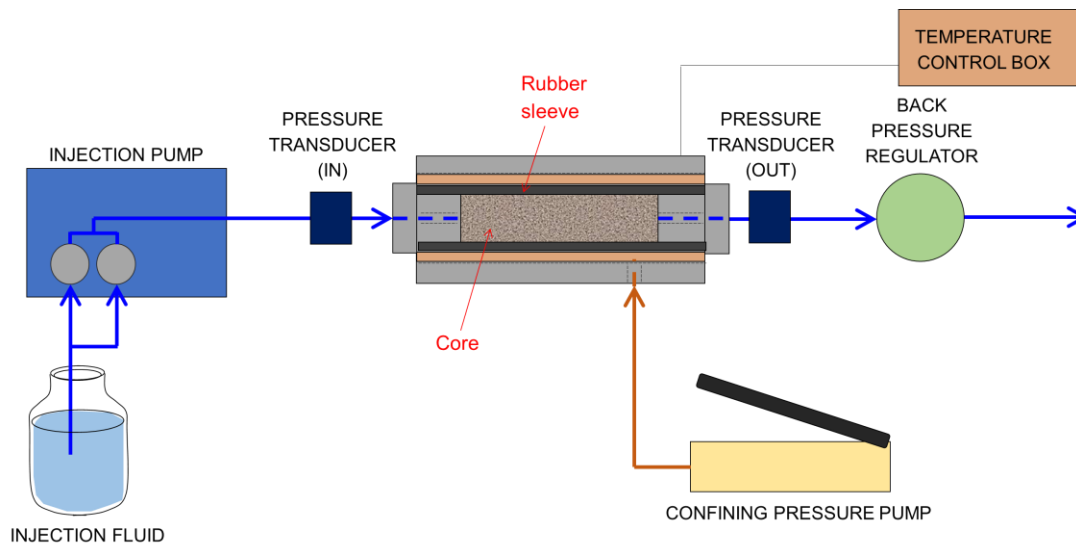


Figure 2. Schematic view of the bespoke high pressure/high temperature core holder.

Hydraulic conductivity was derived by considering the average value of Q and ΔP_{IN-OUT} once stable values had been reached during the test. Once the initial hydraulic conductivity had been determined, the cement core was then treated by injecting CS grout. The treated core was cured in the core holder at a selected high temperature and high pressure combination ($P = 15$ MPa, $T = 80$ °C, simulating 1.6 km depth) for 10 hours, then left to equalise to ambient conditions for a further 62 hours (total curing time: 72 hours). Hydraulic conductivity measurements were carried out after treatment by injecting tap water through the core at increasing inlet pressure, from 0 to 1.4 MPa. Inlet pressure was ramped up in steps. During each step, the resulting flow rate through the core was continuously monitored to derive hydraulic conductivity. The selected values of confining pressure, back pressure, injection pressure and flow rate adopted for each stage of the experiment are shown in Table 1.

Table 1. Core-holder experimental parameters during flow-through core tests and curing

	Before treatment	Curing	After treatment
Confining pressure [MPa]	3	15	3
Flow rate [mL/min]	4 to 10	-	measured
Inlet pressure [MPa]	measured	15	0 to 1.4
Outlet pressure [MPa]	0 (atmospheric)	15	0 (atmospheric)
Temperature [°C]	20	80	20

Results and discussion

The results of the hydraulic conductivity measurements obtained before and after treatment are shown in Figure 3a and 3b respectively. Before treatment, the fractured core exhibited a hydraulic conductivity of $\sim 10^{-6}$ m/s. After treatment, a hydraulic conductivity reduction of 4 orders of magnitude (down to $\sim 10^{-10}$ m/s) was observed. The treated cement core was able to withstand injection pressures up to 1.4 MPa for 12 hours, with no sign of water breakthrough. Furthermore, the CS grout treatment successfully bonded together the two halves of the core. The observed decrease in hydraulic conductivity and fracture sealing may be ascribed to two separate processes occurring within the fracture when colloidal silica comes into contact with cement: i) gel formation, and ii) calcium silicate hydrate (C-S-H) production. Gel formation is the consequence of the destabilisation of the colloidal suspension, usually induced by the addition of an accelerator (electrolyte solution). Since no accelerator was added during the preparation of the grout, the formation of siloxane bonds between colloids and consequent

gelling is to be attributed only to the presence of cations (predominantly calcium ions) released by the cement into the fluid present in the fracture. In addition, the exposure to high temperature (80°C) to simulate reservoir conditions is expected to increase the collision rate of particles in suspension, thus facilitating the gelation process.

On the other hand, silica nanoparticles, interacting with calcium sources present on the fracture surfaces (e.g. portlandite, $\text{Ca}(\text{OH})_2$), may undergo pozzolanic reactions to form additional cementitious compounds, such as calcium silicate hydrate (C-S-H). The formation of C-S-H may reduce or even bridge the gap between the two fracture surfaces, resulting in a hydraulic conductivity reduction and/or bonding of the two halves of the core.

The formation of siloxane bonds (gelling) and C-S-H products are competing phenomena: the higher the gelation rate, the lower the amount of available reactive sites for C-S-H formation and vice versa. Further investigations quantifying the amount of silica gel versus C-S-H produced upon treatment and their dependence on silica concentration and pore water composition are ongoing.

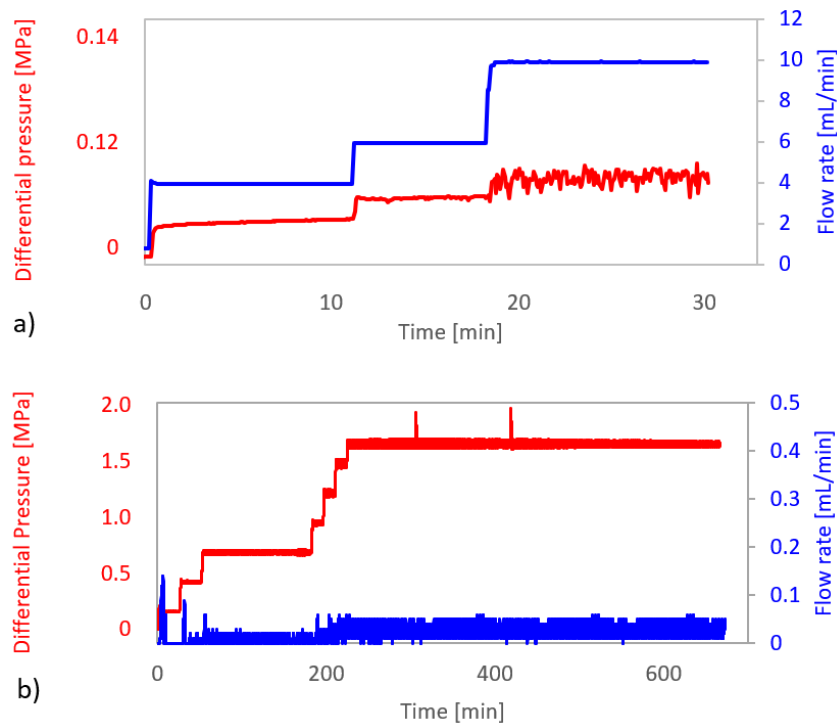


Figure 3. Flow-through experiment results: a) before treatment ($k = \sim 10^{-6}$ m/s), and b) after treatment ($K = \sim 10^{-10}$ m/s).

Conclusion

This preliminary experimental investigation shows the promising potential of CS grout treatment for the long-term sealing of fluid migration pathways in oil and gas wells for decommissioning and abandonment. The injection of CS grout cured at reservoir conditions was observed to successfully reduce hydraulic conductivity by 4 orders of magnitude, even in the absence of an accelerator. Colloidal silica makes use of calcium sources naturally occurring within the pore space and fracture network of cementitious materials to i) induce grout gelling, and ii) encourage the formation of additional cementitious compounds, thus activating a self-healing process within degraded cements. Further understanding of the mechanisms of gel formation and C-S-H production will be investigated via microstructural and mineralogical analyses, taking into account the composition of the water within the pore space and for a range of fracture geometries.

Acknowledgment

The authors gratefully acknowledge the financial support of the OGTC (Aberdeen, Scotland) under project WC-P-018, "Grouting of well leakage and migration pathways: Biogrouting and colloidal silica".

References

- [1] Moridis G, Persoff P, Apps J, Myer L, Pruess K, Yen P. A field test of permeation grouting in heterogeneous soils using a new generation of barrier liquids. Presented at the ER '95 Conference Committed To Results: Barriers for Long-Term Isolation 1995.
- [2] Moridis GJ, Finsterle S, Heiser J. Evaluation of alternative designs for an injectable barrier at the Brookhaven National Laboratory Site, Long Island, New York. 1999 *Water Resources Research* Vol 35, pp. 2937–2953.
- [3] Hakem N, Al Mahami, I, Apps J, Moridis G. Sorption of cesium and strontium on Savannah River soils impregnated with colloidal silica. 1997 *International Containment Technology Conference*, Petersburg pp. 652–657.
- [4] Manchester K, Zaluski M, North-Abbott M, Trudnowski J, Bickford J, Wraith J, Grout selection and characterization in support of the colloidal silica barrier deployment at Brookhaven National Laboratory. 2001 *Proceedings International Containment and Remediation Technology Conference and Exhibition*, Orlando, FL.
- [5] Iler RK. *The Chemistry of Silica: Solubility, Polymerization, Colloid and Surface Properties, and Biochemistry*. (John Wiley & Sons 1979).
- [6] Pedrotti M, Wong C, El Mountassir G, Lunn RJ. An analytical model for the control of silica grout penetration in natural groundwater systems. *Tunnelling and Underground Space Technology*. 2017 Vol 70 pp. 105-113.
- [7] Li H, Xiao HG, Yuan J, Ou J, Microstructure of cement mortar with nanoparticles. *Composites Part B: Engineering*. 2004 Vol 35 pp. 185–189,
- [8] Cardenas H, Struble LJ. Electrokinetic nanoparticle treatment of hardened cement paste for reduction of permeability. *Journal of Materials in Civil Engineering*. 2006 Vol 18 pp. 554-560.
- [9] Maddalena R, Hamilton A. Low-pressure silica injection for porosity reduction in cementitious materials. *Construction and Building Materials*. 2017 Vol 134 pp. 610-616.

Session 4A Smart resources for the built environment

Chair: Dr Richard Ball

1189 *Lunn et al.* Large-scale soil improvement tests using microbially induced carbonate precipitation

1125 *Risdanareni et al.* Screening a suitable coating for expanded clay aggregate as bacteria carrier for manufacturing self-healing concrete

1100 *Cao and Al-Tabbaa.* Contaminant-triggered self-healing cut-off wall materials incorporating oil sorbents

1257 *Vasanthanayagam et al.* Direct-writing and embedding of functional materials into construction materials to enable smart cities

Large-scale soil improvement tests using microbially induced carbonate precipitation

Rebecca J. Lunn, James M. Minto, Grainne El Mountassir, Mary Anderson

Department of Civil and Environmental Engineering, University of Strathclyde, Glasgow G1 1XJ, UK

Abstract

Bacterial biomineralization provides a greener solution to a diverse range of civil engineering applications, reducing the carbon footprint of construction. Most successful to-date is microbially induced carbonate precipitation (MICP). MICP is being developed for a diverse range of applications including plugging fractures, stabilising soils and repairing building surfaces. In MICP, bacteria are injected within the soil, followed by injection of a fluid containing urea and calcium chloride. The bacteria hydrolyse the urea, which generates bicarbonate ion, increases pH and precipitates calcite. Advantages of MICP include: better penetration due to the low viscosity of the fluids, the ability to maintain free drainage in treated materials and the thousand-year durability of calcite.

Despite the growing interest in MICP for geotechnical applications, MICP still remains largely confined to the laboratory with only a very small number of large-scale experiments having been completed and one commercial project. Use is constrained by (1) the ability to grow bacteria at a commercial scale and (2) the need to ensure homogeneous soil strengthening at a large-scale. In this research, conducted in collaboration with BAM Nuttall, we present the results of large-scale test for MICP treated sand. We treat a 1 m diameter cylinder of loose sand using multiple cycles of MICP. Unconfined compressive strength tests and triaxial tests of cores taken from the treated sand result in strengths of several MPa. Our results show that bacterial biomineralization could be a viable, low carbon alternative to cement and concrete for a range of earth infrastructure applications.

Introduction

Bacterial biomineralization provides a greener solution to a diverse range of civil engineering applications, reducing the carbon footprint of construction. Most successful to-date is microbially induced carbonate precipitation (MICP). MICP is being developed for a diverse range of applications including plugging fractures [1], stabilising soils [2] and repairing buildings [3]. In MICP, bacteria are injected within the soil, followed by injection of a fluid containing urea and calcium chloride. The bacteria hydrolyse the urea, which generates bicarbonate ions, increases pH and results in the precipitation of calcite [4]. Advantages of MICP include: better penetration due to the low viscosity of the fluids, the ability to maintain free drainage in treated materials and the thousand-year durability of calcite.

Despite the growing interest in MICP for geotechnical applications, MICP still remains largely confined to the laboratory with only a very small number of large-scale experiments having been completed [5][6] and one commercial project. Use is constrained by (1) the ability to grow bacteria at a commercial scale and (2) the need to ensure homogeneous soil strengthening at a large-scale. In this research, conducted in collaboration with construction and civil engineering company BAM Nuttall, the results of a large-scale test for MICP treated sand is presented. A 1 m diameter cylinder of loose sand is treated using multiple cycles of MICP. Unconfined compressive strength tests and triaxial tests of cores taken from the treated sand result in strengths of several MPa. These results show that bacterial biomineralization could be a viable, low carbon alternative to cement and concrete for a range of earth infrastructure applications.

Materials and Methods

A radial flow cell was constructed to allow MICP treatment in sand/soil with radial injection strategies similar to those that would be used in the field (Figure 1, left). The sand was added gradually and continuously compacted by hand in the cell whilst underwater. The average initial dry density was 1581 kg/m^3 , based on the total mass of sand added, with an average porosity of 40.0%. A first run has been completed in which bacteria were injected at a high flow rate so as to prevent attachment (and hence clogging due to CaCO_3 precipitation) near the central injection point where velocities are highest. The volume of bacteria injected in each treatment cycle was approximately half the liquid volume of the cell (i.e. 0.5 Pore Volumes) so that we could evaluate the radial extent of treatment. In total, 1PV of 0.5 M urea/ CaCl_2 cementing solution was injected, at a lower flow rate, in two stages (i) 0.5 PV injection two hours after the bacteria were injected, and (ii) a further 0.5 PV injection the following morning after an overnight static reaction period. In this way, the cementing solution injection was also used to monitor changes in permeability due to CaCO_3 precipitation.

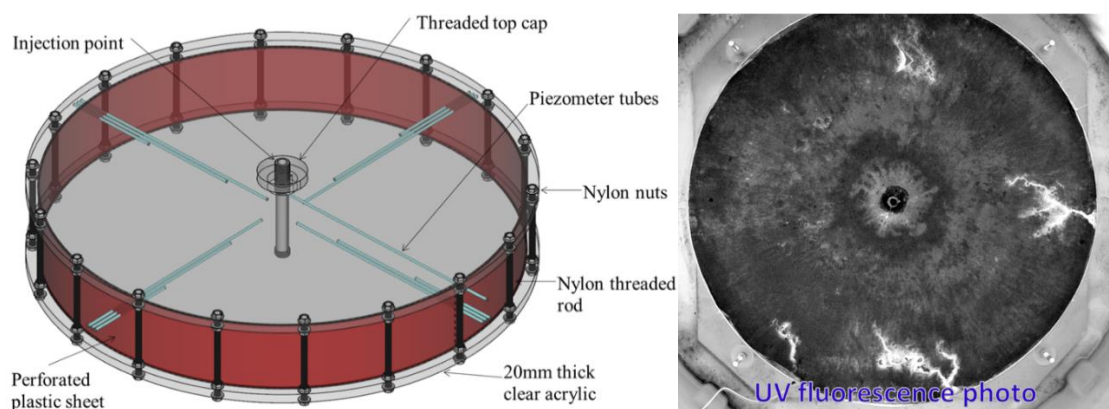


Figure 1. Left: 1m radial flow cell design. Right: overhead UV fluorescence photo taken after treatment of the sand showing high CaCO_3 concentrations in white, and low CaCO_3 concentration sand as black.

The cell was packed with loose sand. Nine treatment cycles were conducted over nine days, CaCO_3 was precipitated over a large proportion of the flow cell. This was visible on the top surface of the sand by using an ultra-violet light source and photographing the fluorescence of the CaCO_3 (Figure 2, right). There was less CaCO_3 in a ring around the injection point and also close to the outer edge of the flow cell.

Results and Discussion

The initial permeability of the sand was $1.3 \times 10^{-11} \text{ m}^2$ (typical of a medium sand, well sorted) reducing to $7.9 \times 10^{-12} \text{ m}^2$ (typical of a fine sand, well sorted) after the nine treatment cycles and the maximum pressure at any point during treatment was only 6.8 kPa, equivalent to a pressure head of 0.7 m of water. This indicates that the sand remains free-draining after treatment and confirms that low pressure equipment can be used for field-scale MICP treatment.

The MICP treatment of the (originally loose) sand resulted in sufficient cementation, in the area between the two dashed lines in Figure 2, that cores could be drilled for UCS testing. Cores were cut from the block of treated sand using a water-cooled concrete corer. The area between the two dashed circles in Figure 2 (Left) was well cemented and solid enough to stand on whilst coring.

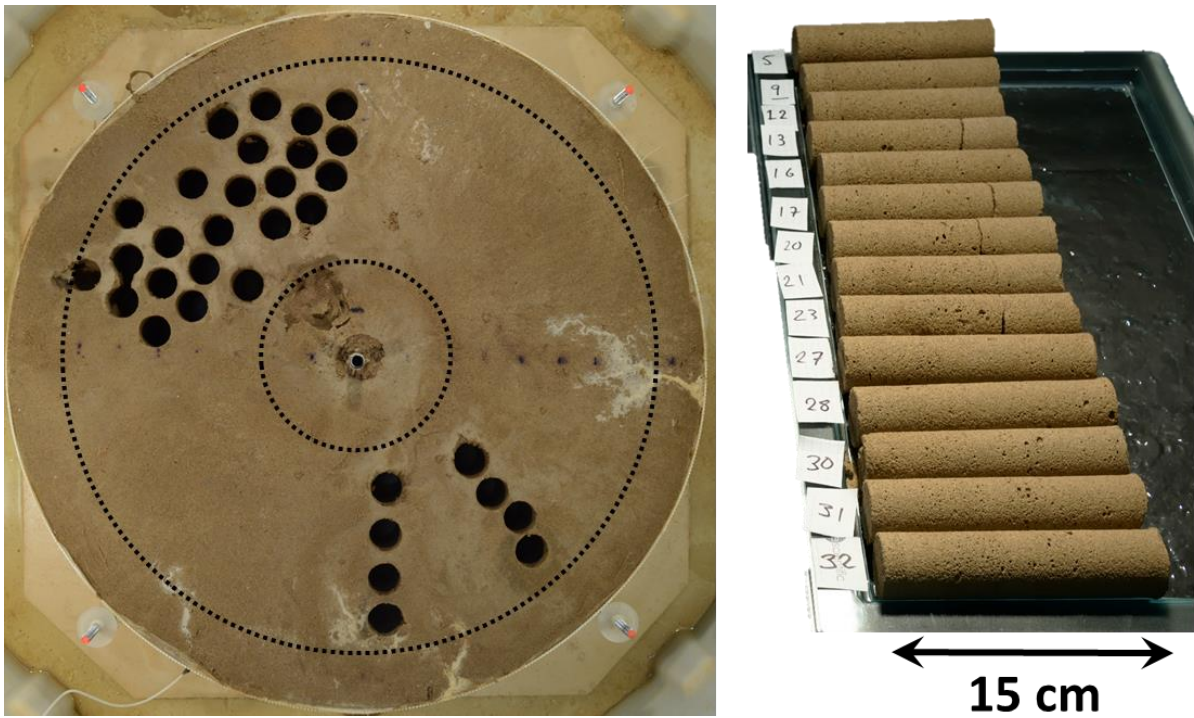


Figure 2. Left: Overhead photo of treated sand after 36mm diameter cores cut. Area between dashed circles was well cemented with CaCO_3 . Right: cores retrieved for further testing.

Cores were scanned with 2D X-ray radiography showing average density variations with depth, then cut in half (giving a 2:1 length to diameter ratio) and ends were filed smooth and planar. Approximately three quarters of the cores were capped with a high strength plaster in accordance with the standard method ASTM C617/C617M-15. The remaining cores were tested with an unbonded rubber pad, in accordance with ASTM C1231/C1231M-15. Selected cores were then scanned with 3D X-ray tomography giving a detailed map of sample density. All cores were subjected to unconfined compressive strength testing and the maximum load at failure recorded.

Figure 3 shows results for Core 9 in which there was a clear contrast in density between the lower third of the core and the upper two thirds. This contrast in density is thought to be due to the method of compacting the sand under partially saturated conditions and the vertical migration of fine particles during initial placement and compaction, rather than during MICP treatment. In future experiments the sand will be emplaced under fully saturated conditions. Core 9 (Figure 3) had a compressive strength of 4.86 MPa and failure occurred in the high porosity top region (Figure 3 C to E). To put this in context, the 36 mm diameter sample could support up to a 504 kg weight before failing.

Figure 4 shows the relationship between strength and post-treatment dry density for each 2:1 core sample along with the results from [5] which is the only comparable large-scale experiment. The unbonded capping method appears to result in lower strength and this was observed to be due to lateral expansion of the rubber pad hence, for MICP samples, use of bonded caps is preferable. In general, we achieve higher strengths for a lower dry density (which correlates with lower amounts of CaCO_3) and in less time than van Paassen indicating more efficient MICP treatment, although we also use a greater amount of bacteria. The greater spread in the data is thought to be due to heterogeneities in the initial sample dry density which are visible in the X-CT data (Figure 3); future tests in which the sand is placed under fully saturated conditions are expected to show a stronger correlation between dry density and strength.

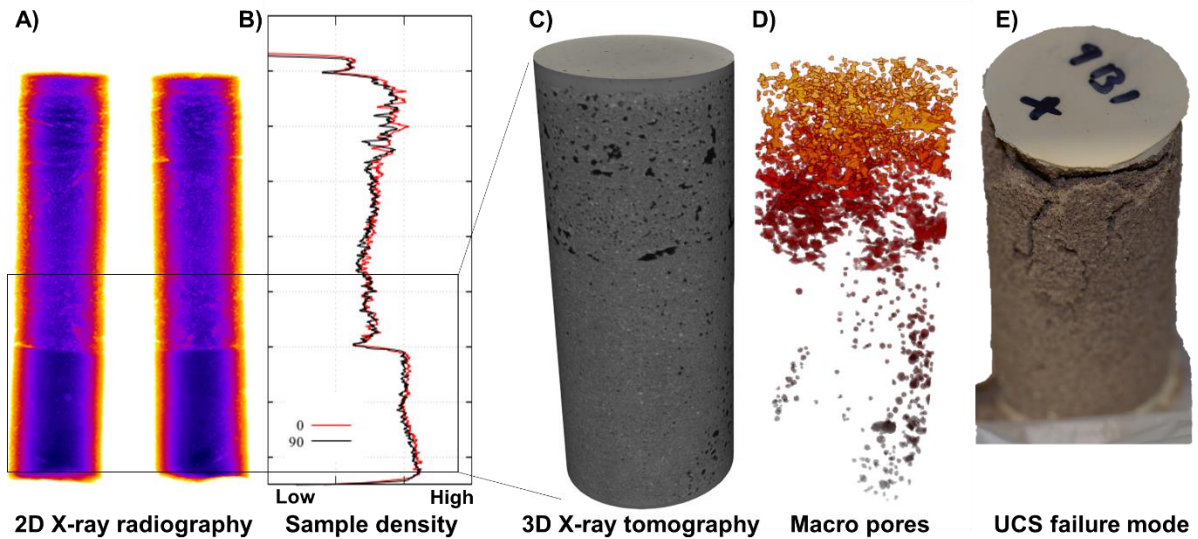


Figure 3. Radial flow cell core analysis. A) 2D X-ray scans at two orthogonal planes and B) corresponding average density profile with depth. C) 3D X-ray scan of the 2:1 core capped and prepared for UCS testing. D) Macro-pore distribution within the sample. E) Failure mode after UCS testing.

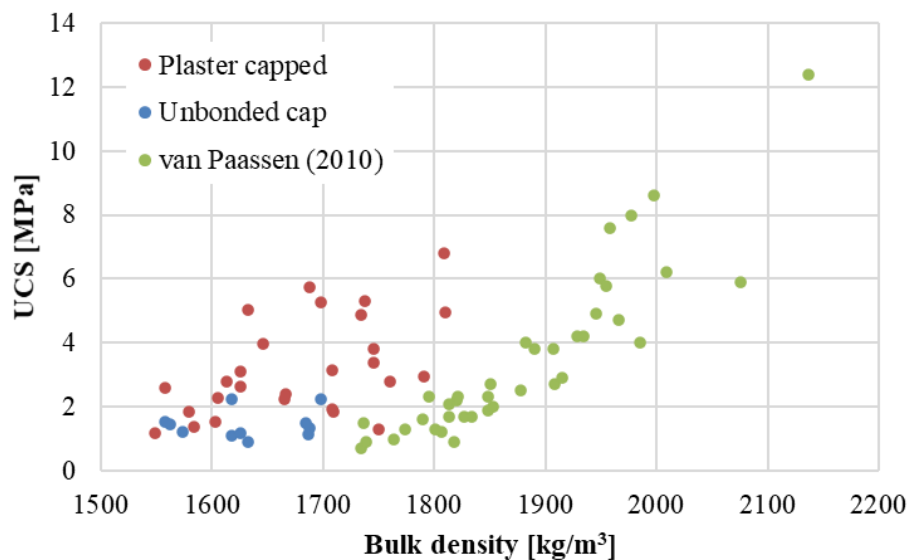


Figure 4. Unconfined compressive strength results for our cores with bonded plaster and unbonded capping methods. Results are shown in comparison to the large scale test carried out by van Paassen [5].

Conclusions

In this research the results of a large-scale test for MICP treated sand are presented. A 1 m diameter cylinder of loose sand is treated using multiple cycles of MICP. Unconfined compressive strength tests and triaxial tests of cores taken from the treated sand result in strengths of several MPa. These strengths exceed those obtained by previous researchers, when plotted against final bulk density of the treated material. Our results show that bacterial biomineralization could be a viable, low carbon alternative to cement and concrete for a range of earth infrastructure applications.

References

- [1] El Mountassir, G., Lunn, R. J., Moir, H. and MacLachlan, E.. Hydrodynamic coupling in microbially mediated fracture mineralization: Formation of self-organized groundwater flow channels, *Water Resour. Res.*, (2014). 50, doi:10.1002/2013WR013578.
- [2] Al Qabany, A. and Soga, K.. Effect of chemical treatment used in MICP on engineering properties of cemented soils. *Geotechnique*, (2013). 63(4), 331–339. <https://doi.org/10.1680/geot.SIP13.P.022>.
- [3] Minto, J. M., Tan, Q., Lunn, R. J., El Mountassir, G., Guo, H. & Cheng, X. 'Microbial mortar'- restoration of degraded marble structures with microbially induced carbonate precipitation. *Construction and Building Materials* (2018). 180, p. 44-54.
- [4] Ferris, F. G., Stehmeier, L. G., Kantzas, A., & Mourits, F. M. Bacteriogenic mineral plugging. *Journal of Canadian Petroleum Technology*, (1996). 35(8), 56–61. <https://doi.org/10.2118/96-08-06>.
- [5] L.A. van Paassen, R. Ghose, T.J.M. Van Der Linden, W.R.L. Van Der Star, M.C.M. Loosdrecht, Quantifying Biomediated Ground Improvement by Ureolysis: Large-Scale Biogrout Experiment, *J. Geotech. Geoenvironmental Eng.* 136 (2010) 1721–1728. doi:10.1061/(ASCE)GT.1943-5606.0000382.
- [6] Cuthbert, M. O., McMillan, L. A., Handley-Sidhu, S., Riley, M. S., Tobler, D. J., & Phoenix, V. R. A field and modeling study of fractured rock permeability reduction using microbially induced calcite precipitation. *Environmental Science & Technology*, (2013). 47(23), 13637–13643. <https://doi.org/10.1021/es402601g>.

Screening a suitable coating for expanded clay aggregate as bacteria carrier for manufacturing self-healing concrete

Puput Risdanareni^{1,2}, Jianyun Wang³, Nico Boon⁴, Nele De Belie¹

1: Magnel-Vandepitte Laboratory for Structural Engineering and Building Materials, Ghent University, Tech Lane Ghent Science Park, Campus A, Technologiepark Zwijnaarde 60, B-9052 Ghent, Belgium

2: Department of Civil Engineering, Faculty of Engineering, State University of Malang, Semarang Street 5, 65145 Malang, Indonesia

3: Department of Civil Engineering, Xi'an Jiaotong University, Xianning West Road 28, 710049 Xi'an, China

4 : Centre for Microbial Ecology and Technology (CMET), Ghent University, Coupure Links 653, Building A-9000, Ghent, Belgium

Abstract

Porous aggregate is a promising bacterial carrier in manufacturing bacteria-based self-healing concrete as it can retain a high amount of bacteria in its pores. However, as the pores of LWA are more open pores, the leakage of bacteria is a big problem that needs to be solved after the encapsulation process. Thus in this research, expanded clay LWA was treated in order to improve the encapsulation efficiency of *Bacillus sphaericus* (BS) for manufacturing self-healing concrete. Several coatings such as Polyvinyl Alcohol (PVA), Sodium Silicate, and Sodium Alginate were applied as surface protection on LWA by means of dipping. The ureolytic activity, pH evolution, and the leakage of bacteria from coated LWA were examined and compared to the non-coated LWA samples. The result showed that sodium alginate is suitable for LWA coating. It did not kill the bacteria, indicated by the detection of ureolytic activity in the crushed LWA sample coated with sodium alginate. In addition, sodium alginate coating on the LWA was also proven to decrease the leakage of bacterial cells from the pores of LWA.

Introduction

Bacteria-based self-healing becomes a promising autonomous self-healing method due to its compatibility with the concrete matrix. The Microbially Induced Carbonate Precipitation (MICP) method was proven to increase the durability of construction materials such as concrete and stone [1,2]. The urease active bacterium from *Bacillus* genus named *Bacillus sphaericus* was selected as the bacteria healing agent in this study due to its higher carbonate production compared to others [3].

Furthermore, the bacteria need protection in order to survive in the harsh environment of fresh concrete [4]. Several attempts on encapsulating bacteria into various carriers such as hydrogel [5], microcapsules [6], and porous aggregate [7,8] have been performed. However, cheaper and easier to apply bacterial carriers are still required in order to make self-healing concrete become accepted in the construction industry sector. Thus artificial lightweight aggregate (LWA) generated from industrial by-products such as fly ash and a commercial ready to used expanded clay aggregate can be used as bacteria carriers. Those carriers could retain a high amount of bacterial solution into their pores and are compatible with mortar or concrete mixtures. Although the LWA seems to be the ideal bacteria carrier, the leakage issue of the bacteria after encapsulation is still the main problem that needs to be solved. In previous research, vacuum treatment of LWA before encapsulation and pressure treatment afterwards had a positive impact on the encapsulation efficiency [7]. However, due to the fact that the surface of the LWA is not covered after the pressure treatment, the possibility of the bacteria to leak during mixing is still high. Thus, coating the LWA surface after the bacteria encapsulation process could be a possible solution for leakage mitigation.

In this study, Polyvinyl Alcohol (PVA), Sodium Silicate, and Sodium Alginate were selected as a coating material. Research has shown that PVA and sodium silicate effectively sealed the pores of recycled aggregate and improved the properties of its resulting concrete [9]. PVA has previously also been applied to seal sodium silicate into LWA for self-healing concrete production [10]. While sodium alginate crosslinked with calcium chloride was used as the core structure in manufacturing LWA aggregate [11,12]. However, only limited reports could be found on applying those coatings as protection for LWA impregnated with bacteria.

Summarizing, this study aims to find a suitable coating material protection for LWA impregnated with bacteria. The pH evolution and ureolytic activity were tested to monitor the viability of bacteria after the encapsulation process. In the end, the leakage of bacteria after encapsulation was also examined to see the effect of coating application on preventing the bacteria leakage.

Materials and methods

Materials

Commercial expanded clay (EC) lightweight aggregates from Argex NV with the size of 2-4 mm were used as porous bacterial carrier.

The bacterial healing agent used was *Bacillus sphaericus* (BS) LMG 22257 (Belgian Co-ordinated Collections of Micro-organisms, Ghent). The bacteria were cultured in a sterile liquid medium containing yeast extract (20 g/l) and urea (20 g/l) for 24 hours on the shaking table (120 rpm) in a room with a temperature of 28 °C. The vegetative cells were harvested by centrifuging the culture solution with the speed of 7000 rpm for 7 minutes to get the bacteria pellets. The pellets were then re-suspended in yeast extract solution (5g/l). The final concentration of the bacteria was 2×10^9 cells/ml. A flake form of 98% hydrolyzed Polyvinyl Alcohol (PVA) with the molecular weight of 146.0-186.0 from VWR was applied as the coating protection of impregnated LWA. The final concentration of PVA that was dissolved into warm distilled water (80 °C) was 8 %. While a gel form of 99% Sodium Silicate (SIL) from Sigma Aldrich was directly applied as a coating material. In addition, a powder form of sodium alginate (SAL) from Sigma Aldrich was dissolved into distilled water with the final solution concentration of 5 g/l. While a flake form of calcium nitrate tetrahydrate of 98% (VWR) dissolved into demineralized water with the desired final concentration of 54 g/l was used as medium to crosslink the sodium alginate into a stable coating gel.

Methods

Firstly, LWA was added into a penicillin bottle which was sealed with a rubber stop and metal cap and then autoclaved for 30 minutes at the temperature of 120°C. The -0.85 bar pressure was then applied to the sealed penicillin bottle followed by adding bacteria solution. After that, 1 bar pressure was applied to the penicillin bottle for 15 minutes to push the bacteria solution deep into the pores of the LWA. The next step is to transfer the impregnated LWA from the penicillin bottle to a sterilized Petri dish. Afterward, the coatings were applied by means of dipping for 30 seconds. Firstly, for sodium alginate coating, the impregnated LWA was immersed into sodium alginate solution for 10 minutes followed by immersion into calcium nitrate solution for 20 minutes to get stable gel formation. The coated LWA was then dried in a 28°C incubator for 24 hours before being examined. One-half of the coated impregnated LWAs were crushed and transferred to a sterilized urea (20 g/l) solution. The ureolytic activity of the bacteria was indicated by urea decomposition by using the Nessler method [13]. The pH evolution in the urea solution containing impregnated LWA was also monitored. The other half of the coated impregnated LWAs were then washed with distilled water to remove the bacteria that stuck on the surface of the LWA. The washed LWA were then immersed in distilled water and were left on a shaking table with a speed of 120 rpm for 1 hour. Finally, the immersion

water was taken to check the number of bacteria in it by use of the flow cytometer. However, a flow cytometry test was only performed in a sample that proved to have ureolytic activity.

Results and discussion

pH evolution

The result shows that coating application affects the pH evolution of impregnated LWA significantly (Figure 1). Samples without coating application (EC L-B) and free bacteria samples (EC-B) have pH in the range of 9-9.5. This result has a good correlation with previous research, which stated that BS cells could buffer the pH of the solution to the range of 9-9.5. [14] The control sample without bacteria (EC L-SAL/SIL/PVA) has different pH depending on its coating type. The control sample coated with sodium silicate (EC-L-SIL) has quite high initial pH of around 13. In the same group, the addition of bacteria did not improve the pH (EC-L-B-SIL). This result indicated that the bacteria cells inside the LWA might not survive with the high pH of sodium silicate. In the PVA coating group, the control sample (EC-L-PVA) has neutral pH of around 7, and the addition of bacteria (EC-L-B PVA) did not increase the pH to 9. This stagnancy of pH is not a good sign as well. In this case, the alcohol content in the PVA might also damage the bacteria inside LWA. A better condition occurs in the sodium alginate coating group. Given the initial pH of the control sample (EC L-SAL) of 8.5, bacteria inside the LWA still manage to survive, indicated by the slowly increasing pH of sample EC-L-B-SAL from 8 to 9.5 after 24 hours immersion in urea solution.

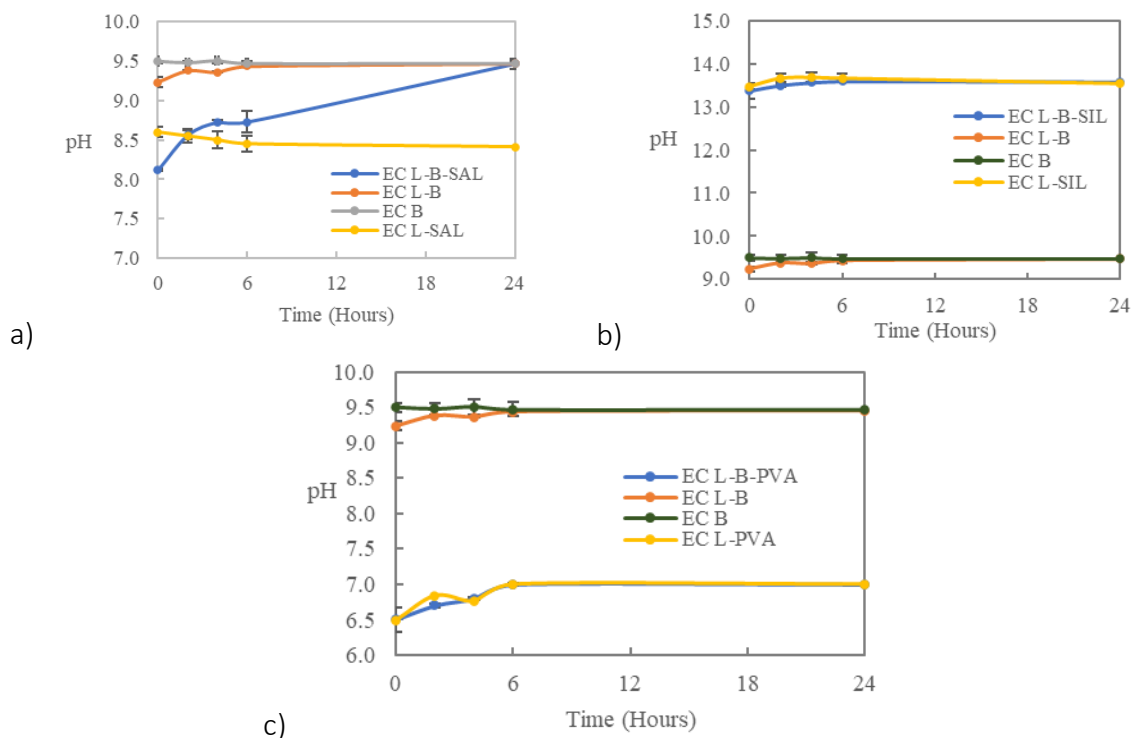


Figure 1 The effect of different coatings on the pH evolution in EC LWA: (a) sodium alginate coating (b) sodium silicate coating (c) polyvinyl alcohol coating

Ureolytic Activity

The ureolytic activity was measured by the amount of urea decomposed in the solution containing crushed LWA. Based on the result displayed in Figure 2, applying coating significantly affects the ureolytic activity of bacteria. Ureolytic activity of coated samples can only be detected on samples coated with sodium alginate (EC L-B-SAL). Even though the decomposition rate of this sample is relatively slow compared to the uncoated sample, the bacteria are still viable. On the other hand, no ureolytic activity was detected for samples

coated with sodium silicate and PVA. This result also has a good agreement with pH evolution results. Buffering in pH has only occurred in samples coated with sodium alginate.

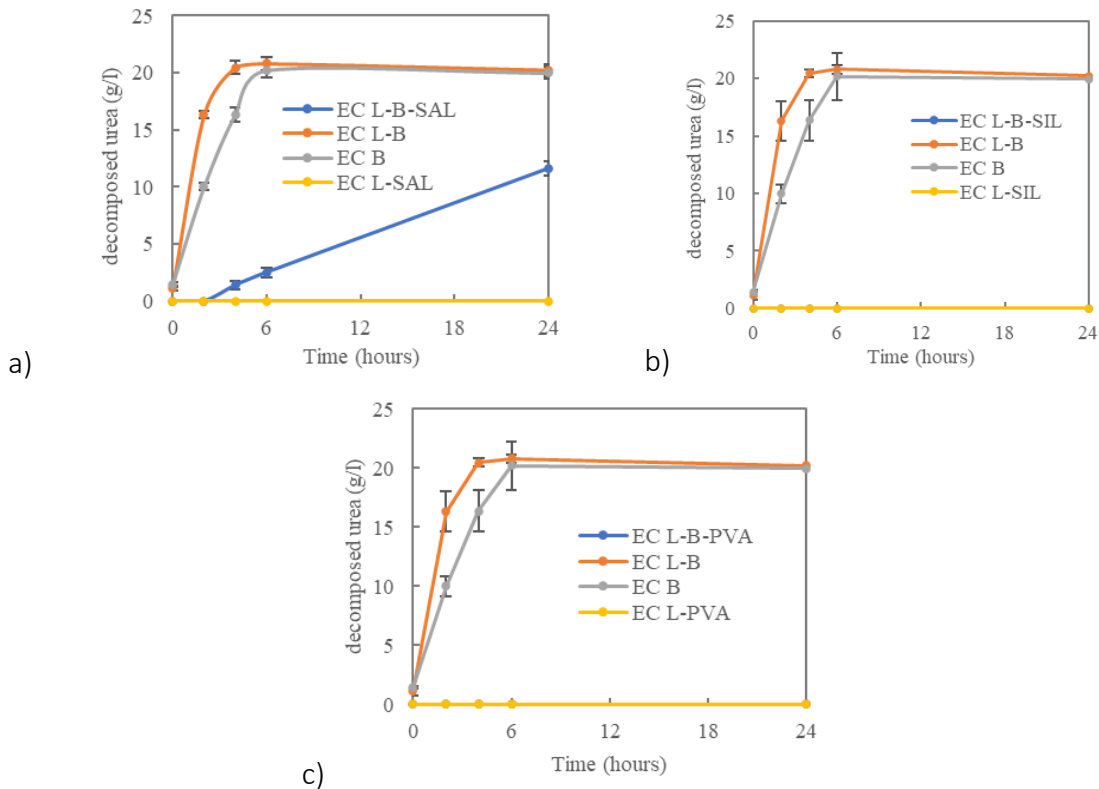


Figure 2 The effect of (a) sodium alginate coating, (b) sodium silicate coating, and (c) PVA coating on the ureolytic activity of bacteria impregnated EC LWA.

Bacteria Leakage

Based on the bacteria leakage result displayed in Figure 3, it can be seen that applying sodium alginate coating proved to reduce the leakage of bacteria after encapsulation. Without coating protection, 27.39% of bacteria were coming out from LWA's pores. By applying the sodium alginate coating, the leakage percentage was reduced gradually to 3.34 %. Previous research by Wang et al. indicated a serious leakage problem when encapsulating bacteria into diatomaceous earth, which decreased the healing efficiency of resulting self-healing concrete [15]. Thus the application of sodium alginate coating on LWA is also expected to improve the healing capacity of the resulting concrete as the leakage problem has been solved.

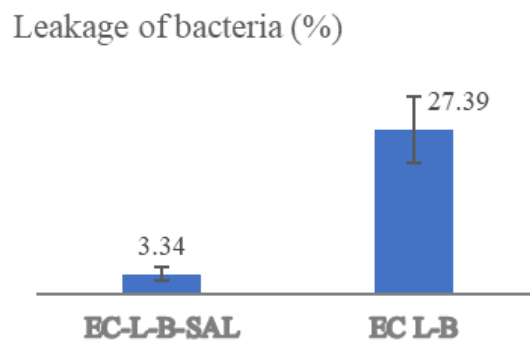


Figure 3 The effect of sodium alginate coating in the leakage of bacteria after encapsulation in EC LWA

Conclusion

Sodium alginate proved to be a potential coating material for expanded clay aggregate impregnated with *Bacillus Sphaericus* vegetative cells. This coating did not poison the bacteria, indicated by the detection of ureolytic activity after the encapsulation process. Moreover, sodium alginate coating was also proven to reduce bacteria leakage significantly.

Acknowledgment

A word of thanks goes to the Islamic Development Bank (IsDB) and The Ministry of Education and Culture of Indonesia for their financial support in preparing this paper. The authors would also like to thank the Centre for Microbial Ecology and Technology (CMET) of UGent for providing all the equipment to conduct the experiments.

References

- [1] W. De Muynck, D. Debrouwer, N. De Belie, W. Verstraete, Cement and Concrete Research Bacterial carbonate precipitation improves the durability of cementitious materials, 38 (2008) 1005–1014. <https://doi.org/10.1016/j.cemconres.2008.03.005>.
- [2] W. De Muynck, S. Leuridan, D. Van Loo, K. Verbeken, V. Cnudde, N. De Belie, W. Verstraete, Influence of Pore Structure on the Effectiveness of a Biogenic Carbonate Surface Treatment for Limestone Conservation, 77 (2011) 6808–6820. <https://doi.org/10.1128/AEM.00219-11>.
- [3] V.B. Constructies, No Title, n.d.
- [4] A. Thijssen, G. Muyzer, O. Copuroglu, E. Schlangen, Application of bacteria as self-healing agent for the development of sustainable concrete, Ecol. Eng. 36 (2010) 230–235. <https://doi.org/10.1016/j.ECOLENG.2008.12.036>.
- [5] J. Wang, A. Mignon, G. Trenson, S. Van Vlierberghe, N. Boon, N. De Belie, A chitosan based pH-responsive hydrogel for encapsulation of bacteria for self-sealing concrete, Cem. Concr. Compos. 93 (2018) 309–322. <https://doi.org/10.1016/j.cemconcomp.2018.08.007>.
- [6] J.Y. Wang, H. Soens, W. Verstraete, N. De Belie, Cement and Concrete Research Self-healing concrete by use of microencapsulated bacterial spores, Cem. Concr. Res. 56 (2014) 139–152. <https://doi.org/10.1016/j.cemconres.2013.11.009>.
- [7] F. Bravo, D. Silva, N. Boon, W. Verstraete, N. De Belie, Screening of bacteria and concrete compatible protection materials, 88 (2015) 196–203. <https://doi.org/10.1016/j.conbuildmat.2015.04.027>.
- [8] M. Alazhari, T. Sharma, A. Heath, R. Cooper, K. Paine, Application of expanded perlite encapsulated bacteria and growth media for self-healing concrete, Constr. Build. Mater. 160 (2018) 610–619. <https://doi.org/10.1016/j.conbuildmat.2017.11.086>.
- [9] S. Kou, C. Poon, Cement & Concrete Composites Properties of concrete prepared with PVA-impregnated recycled concrete aggregates, Cem. Concr. Compos. 32 (2010) 649–654. <https://doi.org/10.1016/j.cemconcomp.2010.05.003>.
- [10] R. Alghamri, A. Kanellopoulos, Impregnation and encapsulation of lightweight aggregates for self-healing concrete, 124 (2016) 910–921. <https://doi.org/10.1016/j.conbuildmat.2016.07.143>.
- [11] X. Yu Shang, J. Shan Li, Manufacturing and performance of environment-friendly lightweight aggregates with core-shell structure, J. Clean. Prod. 276 (2020) 123157. <https://doi.org/10.1016/j.jclepro.2020.123157>.
- [12] X. Shang, J. Li, B. Zhan, Properties of sustainable cellular concrete prepared with environment-friendly capsule aggregates, J. Clean. Prod. 267 (2020) 122018. <https://doi.org/10.1016/j.jclepro.2020.122018>.
- [13] F.G.F. Erris, V.P. Hoenix, Y.F. Ujita, R.W.S. Mith, Kinetics of calcite precipitation induced by ureolytic bacteria at 10 to 20 ° C in artificial groundwater, 67 (2003). [https://doi.org/10.1016/S0016-7037\(00\)00503-9](https://doi.org/10.1016/S0016-7037(00)00503-9).
- [14] J. Wang, H.M. Jonkers, N. Boon, N. De Belie, *Bacillus sphaericus* LMG 22257 is physiologically suitable for self-healing concrete, (2017) 5101–5114. <https://doi.org/10.1007/s00253-017-8260-2>.
- [15] J.Y. Wang, N. De Belie, W. Verstraete, Diatomaceous earth as a protective vehicle for bacteria applied for self-healing concrete, J. Ind. Microbiol. Biotechnol. 39 (2012) 567–577. <https://doi.org/10.1007/s10295-011-1037-1>.

Contaminant-triggered self-healing cut-off wall materials incorporating oil sorbents

Benyi Cao^{1, 2}, Abir Al-Tabbaa²

1: State Environmental Protection Key Laboratory of Soil Environmental Management and Pollution Control, Nanjing Institute of Environmental Sciences, Ministry of Ecology and Environment of China, Nanjing, China

2: Department of Engineering, University of Cambridge, Cambridge CB2 1PZ, UK

Abstract

Containment technologies are cost-effective control measures for contaminated land and hazardous waste sites. Cement-bentonite slurry trench cut-off walls are popular containment systems that act as in situ vertical barriers to confine organic and inorganic contaminants in an enclosed area. These cut-off walls are exposed to deteriorating environments during their service life, leading to an increase in permeability and even complete failure of the wall materials. Therefore, there is a need to improve the resilience of cut-off wall materials against mechanical and environmental stresses. Oil sorbents offer a self-healing solution. When cracks occur, the swelling of oil sorbents can be triggered by the ingress of organic contaminants. As a result, the swollen oil sorbents fill and seal the crack so that the low permeability of the wall materials may be recovered. The objective of this study is to investigate the self-healing performance of cement-bentonite cut-off wall materials incorporating oil sorbents. In this study, Styrene-Ethylene-Butylene-Styrene polymers were added as oil sorbents in cement-bentonite mixes at different dosages. Properties investigated were the distribution of oil sorbents, the unconfined compressive strength, permeability, and microstructure of the cement-bentonite samples. CT scan analysis revealed the uniform distribution and the swelling triggered by organic contaminants of the oil sorbents in the cementitious matrix. The effective self-healing of cracks was verified by the recovered permeability of oil sorbents-containing cement-bentonite samples.

Introduction

Cement-bentonite slurry trench cut-off walls are widely used in polluted sites for containment of the contaminants in soils because of their quick installation, low cost and low permeability. Cut-off walls are normally taken down to an impermeable stratum and are typically 600mm thick [1]. The typical cement-bentonite slurry consists of 5% bentonite, 20% cement and 75% water by weight; more recently, it is found that replacing 80% cement with ground granular blast slag (GGBS) could decrease the permeability and enhance the durability, and as a result, cement-GGBS-bentonite slurry has been more commonly used in the field [2].

The cracking of cut-off walls in contaminated sites can occur due to mechanical and environmental factors [3]. However, the formation of damage is not problematic as long as counteracted by self-healing processes. For cementitious materials, the mechanisms for achieving self-healing are classified into two categories: autogenous and autonomic self-healing. The self-healing process is termed autogenous when the recovery process uses components that could otherwise be present when not specifically designed for self-healing. The engineered addition of materials or components capable of promoting self-healing in cementitious material characterises autonomic self-healing, since the recovery process uses components that wouldn't otherwise be found in the material [4]. The self-healing processes take effect upon mechanical and chemical triggers. For example, microcapsule-based self-healing is triggered by mechanical breakage of the shell materials and superabsorbent

polymer-based self-healing is triggered by the ingress of water [5]. Following these ideas, this paper develops a novel concept to achieve self-healing of cement-bentonite slurry cut-off walls triggered by the ingress of organic contaminants through cracks. Oil sorbents (styrene-ethylene-butylene-styrene, also known as SEBS) were incorporated into cut-off wall materials by mixing the polymer particles into the cementitious slurry.

Materials and methods

The cement-bentonite samples were made from Portland cement (CEM-I, 52.5 N), OCMA-grade bentonite, GGBS, and SEBS oil sorbent polymers manufactured by M² Polymer Technologies. Cement-bentonite samples were prepared in a high-power mixer. Bentonite was first mixed with water for ten minutes to ensure the formation of a homogeneous slurry. The slurry was left to hydrate for 24 hours and then cement, GGBS and oil sorbents were added. The control cement-bentonite slurry consists of 5% bentonite, 4% cement, 16% GGBS and 75% water by weight, and the oil sorbents were added in two dosages (2% and 4%) by total weight of the cement-bentonite slurry. The samples were cast into cylindrical moulds (50mm diameter and 100mm high) and cured under a relative humidity of 100% and temperature of 20±2°C for 28 days.

The unconfined compressive strength (UCS) was obtained using a servo-hydraulic compression frame, and triplicate samples were tested. The vertical load was applied axially at a constant strain rate of 1.14 mm/min until failure, from which the strength was calculated. The permeability was determined by a constant flow rate test using triaxial cell permeameters. The cell water pressure was set at 50 kPa and maintained throughout the test, and a steady flow rate was applied at the bottom of the sample using a peristaltic pump. The recovery of permeability was investigated to assess the self-healing efficacy. After cracking using the UCS frame, the samples were immersed in liquid paraffin, which was used to represent organic contaminants in the worst-case scenario, for four hours before the recovered permeability was measured.

The scanning electron microscope (SEM) instrument was a Phenom ProX. Small chipped pieces were extracted from the crack faces of the specimens and examined under a 10kV accelerating voltage. A cracked sample with a size of 10×10×10 mm was tested by X-ray micro-CT (Nikon XT H 225 ST). X-ray energy is set as 70 kV and 85 mA; the reconstructed image matrix had a volume of 2000×2000×1000 voxels; the effective voxel size is 5.05 μm.

Results and discussion

Effects of oil sorbents addition on mechanical properties

The mean unconfined compressive strength of control and oil sorbents-containing samples is given in Figure 1, along with error bars indicating one standard deviation. The addition of oil sorbents at a dosage of up to 4% has negligible effects on the UCS values after 28 days of curing; however, the increased standard deviation in UCS suggested the oil sorbent-containing samples were less homogeneously mixed than the control samples. This is likely due to the hydrophobic properties of the oil sorbents, which resulted in relatively poor mixing quality with cementitious materials. After cracking using the UCS frame, samples were immersed in liquid paraffin for four hours for self-sealing. The second UCS tests were then conducted to study the effects of swollen oil sorbents on the UCS recovery, and the results showed no obvious recovery in UCS for samples incorporated oil sorbents. This means the incorporation of oil sorbents provides cement-bentonite mixtures with neither increased UCS strength nor increased UCS recovery.

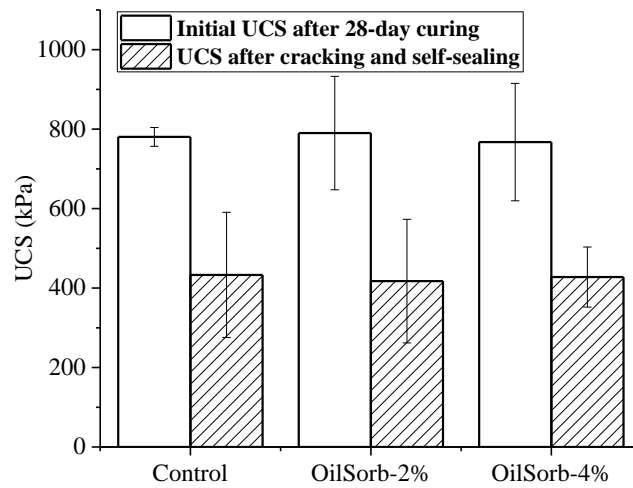


Figure 1. The effects of oil sorbents on UCS and recovery of UCS

Effects of oil sorbents addition on permeability

The effects of oil sorbents on the permeability after 28-day curing and permeability recovery after self-healing were shown in Figure 2. A marginal reduction in permeability was observed in samples incorporating 2% and 4% oil sorbents. After the cracking and sequent immersion in liquid paraffin for four hours, the recovered permeability was measured. The recovered permeabilities of oil sorbent-containing samples were significantly decreased compared to control samples from $5.0 \times 10^{-8} \text{m/s}$ to $5.8 \times 10^{-9} \text{m/s}$. The significant recovery in permeability is because the oil sorbents on crack surfaces swelled after absorbing paraffin and sealed the cracks.

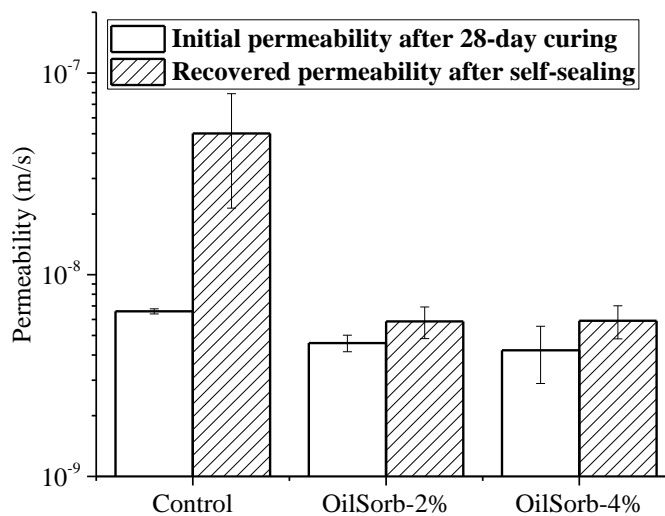


Figure 2. The effects of oil sorbents on permeability and recovery of UCS

SEM analysis

SEM images were taken of the oil sorbent-containing samples that were cured for 28 days. Representative SEM images showing the oil sorbent particles in the matrix are presented in Figure 3. The oil sorbents can be easily identified in the SEM images. They appeared dry and shrunk in the cementitious matrix. Cementitious hydration products were seen to precipitate on oil sorbents, indicating relatively good adhesion despite the hydrophobic properties of oil sorbents. The structure formed by oil sorbents also wrapped and connected cement-bentonite particles, creating a network structure in the matrix. The connection breaks when a crack propagates in the matrix, exposing oil sorbents to potential organic pollutant ingress.

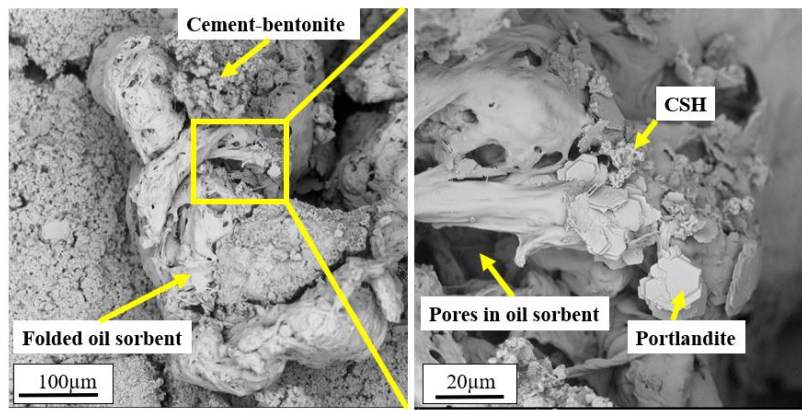


Figure 3. Typical SEM images of oil sorbents in the cement-bentonite matrix

Micro-CT scan analysis

An oil sorbent-containing cement-bentonite specimen was micro-CT scanned after cracking and immersion in liquid paraffin. After the scanning, reconstructed images were obtained with the distribution of the local linear attenuation coefficient in the form of greyscale values (Figure 4a). Three components in the specimen have different densities: cement-bentonite matrix, oil sorbents, and cracks, and they are in light grey, dark grey and black in the reconstructed image, respectively. The oil sorbents, cement hydration products and cracks were further coloured yellow, brown and black respectively to distinguish from one another clearly (Figure 4b). The homogenous distribution of oil sorbents was confirmed by checking different cross-sections of the specimen. It was shown that swollen oil sorbents blocked cracks after absorbing paraffin.

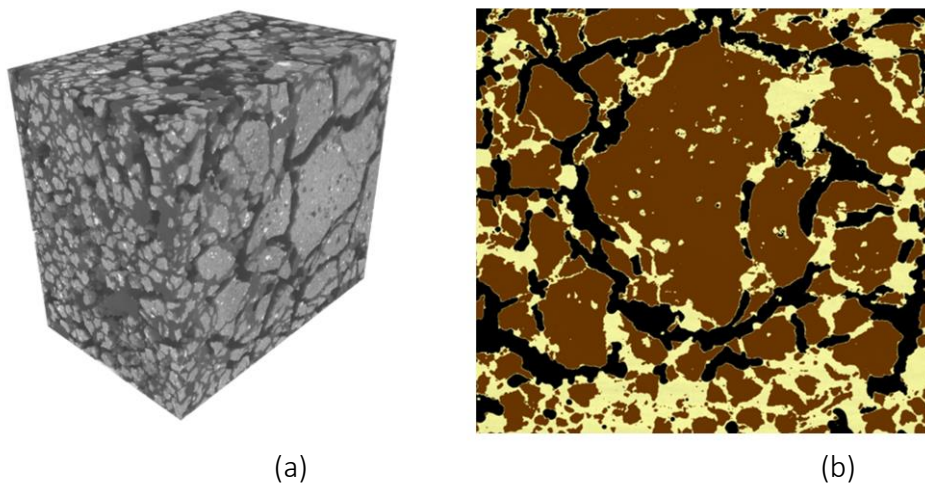


Figure 4. (a) Reconstructed 3D CT scan image of cement-bentonite samples incorporating oil sorbents; (b) 2D CT scan image (cement-bentonite: brown; oil sorbents: yellow; cracks: black)

Conclusion

The work presented here is the first attempt to introduce the concept of oil sorbent-based self-healing to cement-bentonite materials. The oil sorbent-containing cement-bentonite samples demonstrated enhanced self-healing performance in terms of the recovery of permeability. The uniform dispersion and self-healing triggered by liquid paraffin of oil sorbents were observed using micro-CT scanning. The results demonstrated the significant potential for oil sorbents as a self-healing approach for the development of more resilient cement-bentonite cut-off wall materials exposed to organic contaminants.

Acknowledgment

The support from the EPSRC-funded programme grant Resilient Materials for Life (EP/P02081X/1) is gratefully appreciated. The first author would also like to acknowledge the support from the China Scholarship Council and Cambridge Trusts for his PhD study.

References

- [1] Opdyke SM, Evans JC. Slag-cement-bentonite slurry walls. *Journal of Geotechnical and Geoenvironmental Engineering*. 2005 Jun;131(6):673-81.
- [2] Jefferis, S. "Cement-bentonite slurry systems." In *Grouting and Deep Mixing 2012*, pp. 1-24. 2012.
- [3] Joshi K, Kechavarzi C, Sutherland K, Ng MY, Soga K, Tedd P. Laboratory and in situ tests for long-term hydraulic conductivity of a cement-bentonite cutoff wall. *Journal of Geotechnical and Geoenvironmental Engineering*. 2010 Apr;136(4):562-72.
- [4] De Rooij M, Van Tittelboom K, De Belie N, Schlangen E (editors). *Self-healing phenomena in cement-Based materials: state-of-the-art report of RILEM technical committee 221-SHC: Self-Healing Phenomena in Cement-Based Materials*. Springer Science & Business Media; 2013 Apr 17.
- [5] De Belie N, Gruyaert E, Al-Tabbaa A, Antonaci P, Baera C, Bajare D, Darquennes A, Davies R, Ferrara L, Jefferson T, Litina C. A review of self-healing concrete for damage management of structures. *Advanced Materials Interfaces*. 2018 Sep;5(17):1800074.

Direct-writing and embedding of functional materials into construction materials to enable smart cities

Regana Vasanthanayagam^{1,2}, Ian Fausto Zanchetta Chittka³, Chrysoula Litina⁴, Maria Cristina Rodriguez-Rivero², Javier Orozco-Messana³, Abir Al-Tabbaa⁴, Ronan Daly²

1: Cambridge Graphene Centre, University of Cambridge, 9 JJ Thomson Avenue, Cambridge CB2 0FA, UK

2: Institute for Manufacturing, Department of Engineering, University of Cambridge, 17 Charles Babbage Road, Cambridge, CB3 0FS, UK

3: Department of Materials and Mechanical Engineering, Universitat Politècnica de València, Valencia, Spain

4: Civil Engineering Building, Department of Engineering, University of Cambridge, 7a JJ Thomson Avenue, Cambridge, CB2 0FA, UK

Abstract

Control of 2D patterns of nanomaterials by spray or inkjet printing has already shown the potential to create devices and functional surfaces for emerging product technologies such as transparent flexible electronics, printed sensors or energy storage. Here we describe the coating and embedding of functional 2D materials into the near-surface regions of composite porous construction materials, namely cement and standard ceramic tiles. Both fall within the category of mineral composites and in both cases their architectural uses mean that embedded electronics, sensors or other functions can be immediately used to support initiatives in Smart Cities. These are challenging surfaces for controlled 2D material integration and have to-date been neglected from detailed functional printing research.

These challenges will be discussed with a focus on two exciting and emerging examples. Firstly, we will report the integration of functional nanomaterials into the ceramic tile fabrication process, including compression, printing onto porous media and firing. Secondly, we will examine the integration of materials into cements at different stages of the formation process. For both spray and inkjet printing, the flow of the carrier fluid and functional materials through the composite surfaces is detailed and linked to the observed changes in functionality. Through these two examples, we show that it is critical to identify and understand the interdependencies between the advanced functionality of emerging materials and their associated manufacturing technologies.

Introduction

Cement and ceramics are essential to the infrastructure of the modern world and are common construction materials in both urban architecture and large-scale civil engineering projects such as marine and offshore construction [1,2]. There are major challenges with building maintenance, for example, £40 billion/year was spent on concrete inspection and repair in the UK alone. There is significant ongoing research into self-healing of materials in both cases [3,4], but there needs to be concurrent development of sensing techniques to enable tracking and management of materials issues. In this work, we are studying how to integrate the required electrical connections and sensing materials into the cement or ceramic materials, embedding them within the bulk to ensure stability and repeatable readings. We explore direct-writing techniques such as inkjet printing, to enable the integration of printed electronics with minimal disruption to the current manufacturing protocols and without modifying the required mechanical and barrier properties. In particular, we are focusing on how to embed these electronics within the bulk of the material, to ensure stability and long product lifetimes without degradation due to environmental conditions. The design concept is shown in Figure 1.

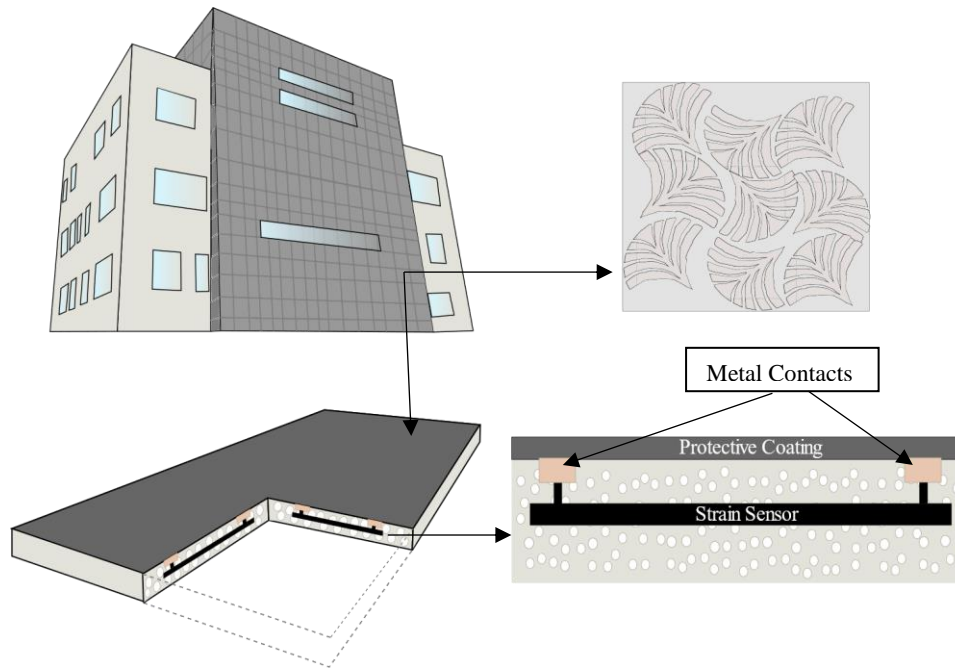


Figure 1. An inkjet printed decorative ceramic tile that includes strain sensors within the building envelope to communicate when essential maintenance will be required.

We specifically examine porcelain ceramics, which are mostly used for exterior construction and areas with high moisture. Porcelain ceramic powder is packed using high force to make a 'green' ceramic and fired at 1200°C during the fabrication process to give the hard, durable product [5]. Inkjet printing is currently used by manufacturers to decorate ceramic tiles, because it enables firms to implement late-stage customisation and avoid the traditionally large stock [6]. In 1999, no companies were offering in-line ink-jet printers for ceramic tiles, this increased to eight companies by 2009, as shown in Figure 2 [6]. This innovation led to an increased market share; therefore, it is important to consider digital modification of tiles as an industry standard. However, this has not yet been explored by firms to implement printed electronics or printed sensors. There are significant research questions that need to be tackled, which include:

- Can printing control the flow of functional materials into the bulk of the ceramic?
- How can the behaviour of the functional materials be controlled during firing?
- How will the functional tiles connect and communicate externally?
- Behaviour of the ceramic with the addition of water.

The second material that we examine, Portland cement CEM I, contains 100% cement ingredients. Specific cement formulations using this grade of cement will be explored to produce the correct composition to achieve the surface properties required to coat and embed ink on its surface. CEM 1 cement is used as it gives great strength, durability, longevity and resilience [7]. Cement is able to resist many harsh environmental conditions but may be affected by the presence of pollutants such as CO₂, and the change of temperature etc. These effects are observed as time progresses, along with shrinkage, loss of strength, the pore structure and durability [8].

Embedding ink into the cements is intrusive and therefore the mechanical properties of the cement may be diminished [9]. As cement is a very porous material, adding more liquid could weaken the structure [10].

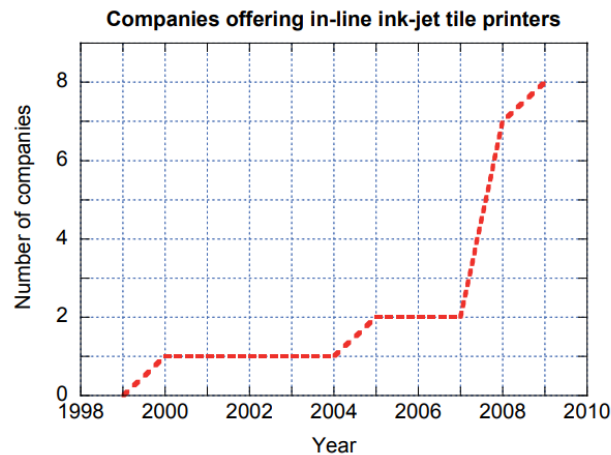


Figure 2. Numbers of companies offering commercial in-line ceramic tile printers based on ink-jet technology [6]

However, direct writing of coatings to protect regions of cement structures and embedding of sensors through printing during construction, has not yet been examined in detail. There are significant research questions that need to be tackled when digitally patterning electronics and sensors direct to the surface, such as:

- Can printing control flow of functional materials into the bulk of the material?
- How can the behaviour of the functional materials be controlled during formation?
- How will the functional tiles connect and communicate externally?
- How can carbonation be prevented in cements?
- How can the hydration of the cement be controlled?

In this presentation, we report on the initial research into specific challenges of printing electronics into both materials. This is the first step towards building sensors and interconnects into the bulk materials. There is a shared challenge about understanding the deposition and embedding of functional nanomaterials, in this case graphene, into the bulk of the material. The functional material is delivered in a carrier fluid which will travel through capillary flow and/or diffusion into the surface. We have ceramics of controlled levels of porosity, pre- and post-firing, and also cements pre- and post-curing. In each of these four states, there are different mass transfer behaviours occurring. This needs to be understood firstly in terms of the flow of liquid through each medium and secondly the flow and final connection of nanomaterials that will ensure connectivity to the outside world. Therefore, the material (porosity; density; hydration) and inks (surface tension; viscosity; deposition volumes) are carefully explored to show the potential and limitations of this direct-write approach.

While the goal is to initially integrate electronics into ceramics and cements which in the long run links to improved maintenance, we also describe planned applications of this research, such as improved barrier coatings, integration of self-healing components that are targeted to specific locations rather than throughout the bulk, integration of more complex functionality such as photovoltaics and energy storage. The presented research is a first step towards a low-cost, scalable approach taking the developments in printed electronics to answer the needs to ensure more sustainable infrastructure.

Materials and methods

Cement and ceramics were used as the model construction materials in this study. The functional materials were made into an ink to inkjet print, coat and embed conductive tracks on top of these surfaces.

The cement used was Portland Cement CEM I – strength class 42.5/52.5 N provided by Hanson – HEIDELBERG CEMENT Group (Maidenhead, UK) and complies with [11]. The superplasticiser used was MasterGlenium 51 produced by BASF (Cheshire, UK) and complies with [12]. For the ceramics, the powder used was Technical Porcelain Ceramic Powder provided by EuroAtomizado Grupo (Castellón, Spain). A control ink (50 wt. % water/glycerol) was used to study the flow of liquid through the porous materials, with the addition of fluorescence. Conductive inks include Silver Sicrys ink I50TM-119 which consists of Silver and Diethylene Glycol Monomethyl Ether from P.V. Nano Cell Ltd (Migdal Ha’Emek, Israel) and Graphink 1 (Cheltenham, UK).

The processing of the cement samples required a water to cement ratio of 0.45. For the cement paste, cement was added to a bowl with 70% of the water followed by mixing for 3 minutes. For the cement mortar, sand was added to the cement mix. 25% of the water and superplasticiser was then added and mixed for 2 minutes. The remaining 5% of water was added and mixed for 2 more minutes to ensure optimum dispersion. The mixture was then poured into the moulds and vibrated for 25 seconds to reduce the entrapped air. The moulds were left to harden for 24 hours and then cured under water for further hydration until needed for testing. The ceramic tiles were made using porcelain ceramic powder which were put into a mould. Compressive force was used to press the powder together using a benchtop material testing machine (5 ST; Tinius Olsen, Surrey, UK), the final product before firing is shown in Figure 3.

For the printing of the functional materials, an automated extrusion printer using the fisnar robot (F5200N; Fisnar, Glasgow, UK) and an inkjet printer, Dimatix printer (DMP-2800; Dimatix, Bedford, UK), was used to deposit the ink onto the surfaces of the ceramics and cements. The fisnar robot was used for the powdered ceramic where conductive ink was deposited within the bulk, compressed, and then fired. The inkjet printer was used for the compressed green ceramics and compressed fired ceramics where the conductive ink was deposited onto the surface.

For the characterisation of the inks behaviour with the ceramics and cement, an optical microscope was used to analyse the capillary flow of the ink in the porous material, using the cross-sectioning method of grind and polish. For the analysis of the porous samples, Micro CT-scanner was used to analyse the pore size distribution of the ceramic samples and to examine internal porosity.



Figure 3. Ceramic tiles before firing, made from using compressive force ranging from 500 N to 4750 N.

Results and discussion

Initial results show that, using small samples of porcelain ceramics, a range of porosities and mechanical properties can be achieved through controlling the maximum compression and compression time. This is characterised for the pre- and post-fired ceramic material and also correlated with the change in flow behaviour of printed inks in both cases. This is linked to the simple Lucas-Washburn model for capillary flow. The difference in flow behaviour of the carrier fluid and contained functional nanoparticles and graphene flakes is highlighted to show the challenge in predicting the positioning of deposited materials. Early results are included where we embed functional materials within the bulk of a fired ceramic sample and maintain, in this case, conductivity.

For cements, we examine the change in ink penetration and functional material behaviour with deposition on wet and cured cements. Again, small samples are prepared using a range of approaches and conditions. In each case, printing is carried out with model fluids and functional fluids. There is significant dependence on diffusion, rather than capillary flow in this instance and so the Lucas-Washburn model is no longer appropriate, and we explore alternative guides for choosing the deposition technique.

Conclusion

In both ceramic tile and cement industries, coating by spray or inkjet fabrication is often seen as the future paradigm in flexible manufacturing to deliver layers of protection or new functions. In this project, we are taking the first steps towards the integration of graphene-based inks into ceramic tiles to not only create barrier layers, but also conductive tracks, through-tile interconnects, electrochemical electrodes and possibly supercapacitors.

Simple 3D printed electronics built directly into mechanically robust materials could deliver enormous benefits for environment monitoring and sustainable buildings. This approach is still at a stage where a replacement is needed for layer-by-layer techniques, which are not suitable for high large-volume applications. We find here that there is a likely route forward that allows fabrication prior to the finalised material format using scalable and affordable manufacturing processes.

Acknowledgment

We acknowledge funding from EPSRC grant EP/L016087/1. The support from the EPSRC funded Resilient Materials for Life (RM4L) Programme Grant (EP/P02081X/1) is gratefully acknowledged.

Reference

- [1] W. Baomin, and D. Shuang, Effect and mechanism of graphene nanoplatelets on hydration reaction, mechanical properties and microstructure of cement composites. *Construction and Building Materials*. 2019 Vol. 228, pp. 116720.
- [2] S. Wang, W. Xu, and L. Yang, Experimental and elastoplastic model investigation on brittle-ductile transition and hydro-mechanical behaviors of cement mortar. *Construction and Building Materials*. 2019 Vol. 224, pp. 19-28.
- [3] P. Greil, Generic principles of crack-healing ceramics. *Journal of Advanced Ceramics*. 2012 vol. 1, no. 4, pp. 249-267.
- [4] P. H. Cavanagh *et al.*, Self-healing cement-novel technology to achieve leak-free wells. 2017 in *SPE/IADC Drilling Conference: Society of Petroleum Engineers*.
- [5] British-Ceramic-Tile. Ceramic vs. porcelain tiles. <https://www.britishceramictile.com/how-to-tile/ceramic-vs-porcelain-tiles> (accessed 30, January 30 2020).
- [6] I. Hutchings. "Ink-jet printing for the decoration of ceramic tiles: technology and opportunities." Qualicer. <http://www.qualicer.org/recopilatorio/ponencias/pdfs/2010234.pdf> (accessed 30, January 30 2020).
- [7] Ronimix. "Grades of cement." <https://www.ronimix.co.uk/grades-of-cement/> . (accessed 30, January 30 2020).
- [8] R. V. Venkata and A. B. Mahindrakar, Impact of aggressive environment on concrete - A review. *International Journal of Civil Engineering and Technology*. 2017 vol. 8, pp. 777-788.

- [9] S. Wen and D. D. L. Chung, "Carbon fiber-reinforced cement as a strain-sensing coating, Cement and Concrete Research. 2010 vol. 31, no. 4, pp. 665-667.
- [10] M. Pérez-Nicolás, J. Plank, D. Ruiz-Izuriaga, I. Navarro-Blasco, J. M. Fernández, and J. I. Alvarez, Photocatalytically active coatings for cement and air lime mortars: Enhancement of the activity by incorporation of superplasticizers. Construction and Building Materials 2018 vol. 162, pp. 628-648.
- [11] BS EN 197-1-2011- British Standards Method for Composition, specifications and conformity criteria for common cements.
- [12] TS EN 934-2+A1-2013 Turkish Standards Method for Admixtures for concrete, mortar and grout – Part 2: Concrete admixtures – Definitions, requirements, conformity, marking and labelling.

Session 4B Encapsulation for infrastructure materials' healing

Chair: Prof Andrew Heath

1241 *Zhang et al.* Powder-based and capsule-based crack healing agents for concrete

1182 *Litina et al.* Time-related performance of commercially applied microcapsule-based self-healing concrete

1156 *Van Mullen et al.* Evaluation of test methods for self-healing concrete with macrocapsules by inter laboratory testing

1157 *Romero Rodriguez et al.* Investigation of the micromechanical properties of the interface between PLA self-healing capsules and cementitious matrix

1109 *Norambuena-Contreras et al.* Biopolymeric microcapsules for asphalt self-healing

1149 *Guo et al.* Fracture of cementitious material containing spherical microcapsules

1127 *Alghamri and Al-Tabbaa.* Field investigation on the performance of smart aggregates for self-healing of concrete in different curing regimes

Powder-based and capsule-based crack healing agents for concrete

Xuan Zhang^{1, 2,3}, Chunxiang Qian^{1, 2,3}, Zekang Jin^{1,2,3}

1 School of Materials Science and Engineering, Southeast University, Nanjing, 211189, China;

2 Research Centre of Green Building and Construction Materials, Southeast University, Nanjing, 211189, China

3. Jiangsu Key Laboratory for Construction Materials, Southeast University, Nanjing 211189, China

Introduction

Crack is the most common disease of concrete [1]. Self-healing technology is a potential long-term solution for crack repair [2]. Compared with conventional repair methods (such as surface repair, grouting filling, and replacement methods, etc.), self-healing can achieve timely and effective repair of cracks [3, 4]. Among various approaches, bacteria-based healing has shown very promising results towards full-scale application and commercialization phase of self-healing concrete [5]. However, the bacteria-based self-healing technology still grapples with many challenges, the biggest one of which is how to ensure the long-term survival of bacteria in concrete [6]. Therefore, many kinds of healing agents that can protect bacteria have been developed, including lightweight aggregate-based [7], powder-based [8], microcapsule-based [9] and capsule-based agent. Lightweight aggregate-based bacteria concrete has yielded to improve crack sealing efficiency, but the decrease in compressive strength might limit its application [5]. Micro-capsule based agents will lead to an increase in long-term shrinkage of concrete [9]. These negative side-effects may limit the popularization and application of self-healing concrete. Therefore, the protection methods of bacteria and the added forms of self-healing agents are of great significance for engineered self-healing concrete. The powder-based and capsule-based healing agents were prepared in this study. Their self-healing capacity, effects on compressive strength and workability, bacteria recovery ability were investigated in laboratory or in real structure.

Materials and experimental methods

Healing agents

Powder-based healing agent

The appearance of healing agent containing bacteria is shown in Figure 1.



Figure 1. Powder-based healing agent

Capsule-based healing agent

To provide further protection of bacteria, a spherical capsule with a core-shell structure was designed (Figure 2). It contains two layers. The component that provides the crack repair function was stored in the inner layer. The outer layer is a low alkaline cementitious material that creates a safe chemical and physical environment for the internal bacteria. The capsule structure is shown in Figure 3. The diameter of a single capsule is 3-4mm, and the particle strength is 70-80N.



Figure 2. Capsule-based healing agent

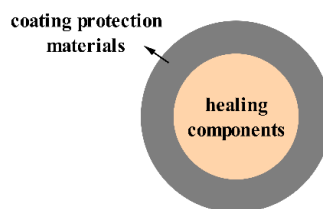


Figure 3. The structure of capsule

Preparation of self-healing concrete

Two sets of concrete were designed to test the effects of healing agents on the performance of concrete. For the powder-based healing agent, the mixture ratio is shown in Table 1. For the capsule-based healing agent, the mixing ratio is shown in Table 2.

Table 1 Mix proportion of concrete mixed with powder-based healing agent

Samples	Cement (kg/m ³)	Fly ash (kg/m ³)	Mineral powder (kg/m ³)	Water (kg/m ³)	Water reducer (kg/m ³)	Sand (kg/m ³)	Stone (kg/m ³)	Healing agent (kg/m ³)
P0	261	56	56	164	5.22	776	1072	0
P3.3	261	56	56	164	5.22	776	1072	12.892

P representing powder-based healing agent. The number behind the letter represents the percentage of cementitious materials.

Table 2 Mix proportion of concrete mixed with capsule-based healing agent

Samples	Cement (kg/m ³)	Water (kg/m ³)	Sand (kg/m ³)	Stone (kg/m ³)	Water reducer (kg/m ³)	Healing agent (kg/m ³)
C0	412	165	590	1254	2.06	0
C5	412	165	560.5	1254	2.06	29.5

C representing capsule-based healing agent. The number behind the letter represents the percentage of sand.

Test methods

The slump of the fresh concrete was tested in accordance with China Standard GB50080-2016 'Standard for test method of performance on ordinary fresh concrete'. The compressive strength of hardened concrete was tested in accordance with China Standard GB/T 50081-2019 'Standard for the test methods of concrete physical and mechanical properties'. The area rate of repaired crack is taken to characterize the repair ability of the healing agents. In order to investigate the protection function of shell on bacteria, the healing agents were soaked in the simulated pore solution of concrete. The maximum OD₆₀₀ value within 36h was used as the index to measure the ability of spore recovery, and the growth curve of spores loaded by healing agent was measured every 7 days.

Results and discussions

Influence of healing agent on slump of fresh concrete

The results of slumps of concretes mixed with healing agents are shown in Figure 4 and Figure 5. It can be seen that the powder-based healing agent increased the slump slightly and the capsule-based healing agent (Figure 5) didn't affect the slump obviously.

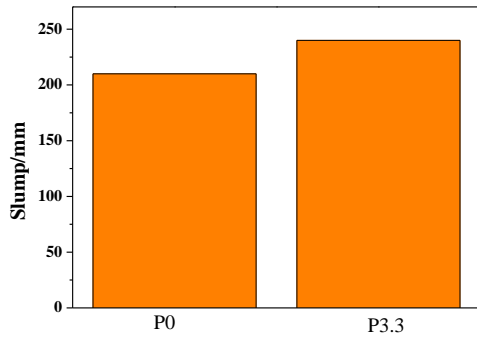


Figure 4. Slump of concrete mixture mixed with powder-based healing agent

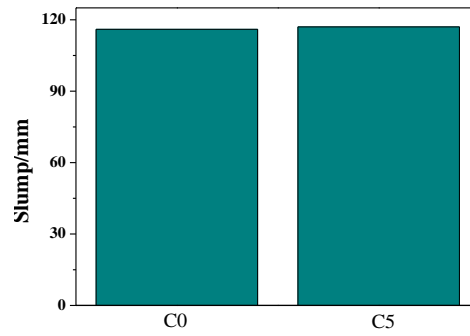


Figure 5. Slump of concrete mixture mixed with capsule-based healing agent

Influence of healing agent on compressive strength of concrete

The compressive strength of concrete with powder-based healing agents increased to a certain extent as shown in Figure 6 because of the effect of calcium resources in the healing agent. The capsule-based healing agent didn't affect the compressive strength significantly as shown in Figure 7.

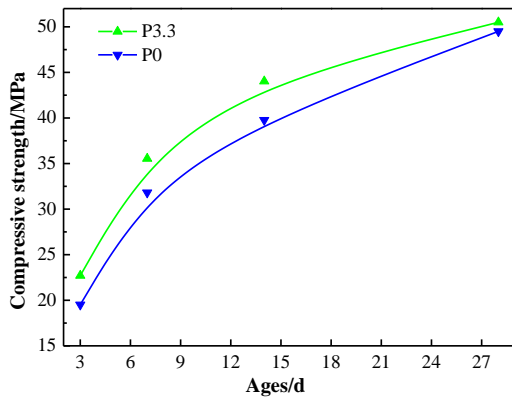


Figure 6. Compressive strength of concrete mixed with powder based healing agent

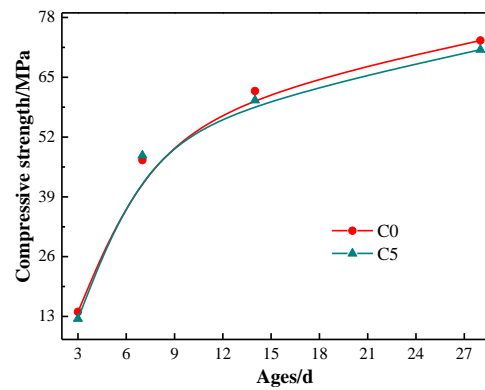


Figure 7. Compressive strength of concrete mixed with capsule based healing agent

Self-healing effectiveness

Crack with a width around 0.5 mm was prepared by spilt method. The healing area of cracks were measured after the cracked specimens were cured for 28 days. The results are listed in Table 3. Both capsule-based and powder-based healing agents can greatly improve the self-healing capacity of concrete. The healing rate of crack surface area of concrete mixed with powder-based healing agents reached 96% as shown in Table 3 and Figure 8. And the concrete with the capsule-based healing agents reached 93% as shown in Table 3 and Figure 9.

Table 3 Self-healing rate of concrete

Samples	Repair rate of crack surface area /%
P0	19
P3.3	96
C0	24
C5	93



Figure 8. Self-healing effect of concrete before and after addition of powder based healing agent

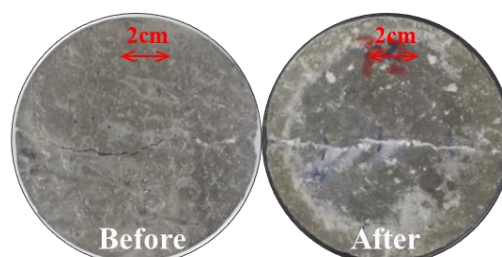


Figure 9. Self-healing effect of concrete before and after addition of capsule based healing agent

Protection of capsule

It can be seen from Figure 10 that when the spores were directly exposed to the simulated pore solution of concrete, the activity of spores were unable to maintain for more than 28 days. But under the capsule protection, the spore activity did not decrease significantly in 203 days.

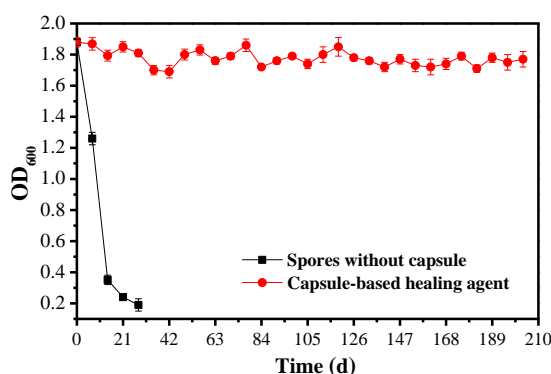


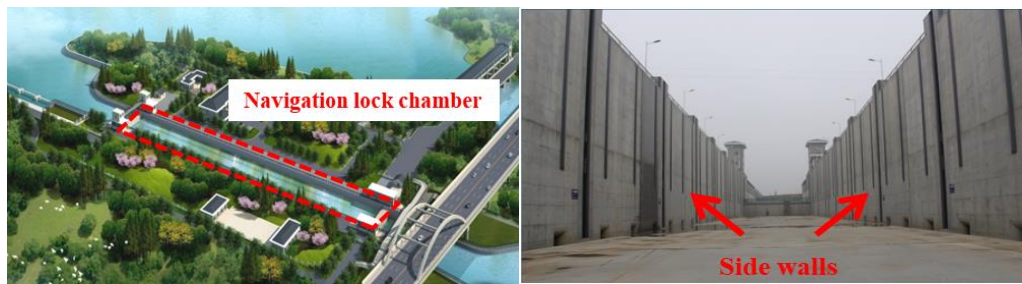
Figure 10. Protective effect of shell of capsule on bacteria

Field application

The powder-based healing agent has been applied in parts of concrete walls of navigation lock in Mangdao River in Jiangsu Province of China, Figure 11(a) and (b). The compressive strength of the wall concrete was 25 MPa. Surface cracks were observed in both normal concrete and self-healing concrete after construction. But the crack on the wall with self-healing concrete was healed at 65 days after construction and the white product can be found in the crack as shown in Figure 11 (d). Cracks on the normal concrete wall show no healing and the water seepage trace was shown in Figure 11(c).

Conclusions

The powder-based and capsule-based healing agents have been developed for healing cracks of concrete. Both of them show a good self-healing capacity and no negative effects on flow of the fresh concrete and compressive strength of hardened concrete in laboratory. Even more, the powder-based bacteria agent obtained a positive result in a real structure application. The capsule-based healing agent can provide long-term protection for activity of the loaded spores.



(a) Top view of Mangdao navigation lock

(b) Interior view of navigation lock chamber



(c) Wall with normal concrete

(d) Wall with self-healing concrete

Figure 11. Comparison of self-healing performance

Acknowledgment

This work was financially supported by the National Natural Science Foundation of China (51738003).

References

- [1] Jang, Seung Yup, Bo Sung Kim, and Byung Hwan Oh. "Effect of crack width on chloride diffusion coefficients of concrete by steady-state migration tests." *Cement and Concrete Research* 41.1 (2011): 9-19.
- [2] Pungrasmi, Wiboonluk, et al. "Evaluation of Microencapsulation Techniques for MICP Bacterial Spores Applied in Self-Healing Concrete." *Scientific reports* 9.1 (2019): 1-10.
- [3] Luo, M., Qian, C. X., & Li, R. Y. (2015). Factors affecting crack repairing capacity of bacteria-based self-healing concrete. *Construction and building materials*, 87, 1-7.
- [4] Tziviloglou, E., et al. "Bacteria-based self-healing concrete to increase liquid tightness of cracks." *Construction and Building Materials* 122 (2016): 118-125.
- [5] Wiktor, V., & Jonkers, H. M. (2016). Bacteria-based concrete: from concept to market. *Smart Materials and Structures*, 25(8), 084006.
- [6] Lee, Y. S., & Park, W. (2018). Current challenges and future directions for bacterial self-healing concrete. *Applied microbiology and biotechnology*, 102(7), 3059-3070.
- [7] Tziviloglou, E., Wiktor, V. A. C., Jonkers, H. M., & Schlangen, E. (2015). Preparation and optimization of bio-based and light weight aggregate-based healing agent for application in concrete. In *Proceedings of the 5th International Conference on Self-Healing Materials, ICSHM, Durham, USA, June 22-24, 2015*. Extended abstract.
- [8] Jonkers, H. M., Wiktor, V., Sierra Beltran, M. G., Mors, R. M., Tziviloglou, E., & Palin, D. (2015). Limestone-producing bacteria make concrete self healing. *Self-Healing Materials*, 137-148.
- [9] Wang, Xianfeng, et al. "Laboratory and field study on the performance of microcapsule-based self-healing concrete in tunnel engineering." *Construction and Building Materials* 220 (2019): 90-101.

Time-related performance of commercially applied microcapsule-based self-healing concrete

C. Litina, B. Cao, J.T. Chen, Z. Li, I. Papanikolaou, A. Al-Tabbaa

Department of Civil Engineering, University of Cambridge, Cambridge CB2 1PZ, UK

Abstract

Bringing to fruition the research on the development of tailored microcapsules for self-healing in cement based materials, this work presents details of the in situ performance of a recently developed microcapsule-based healing technology as a ready-mix self-healing admixture for real concrete applications. This involved the on-site construction of two concrete slabs in the new Civil Engineering Building at the University of Cambridge. Polymeric gelatin/gum Arabic shell and sodium silicate cargo microcapsules developed using complex coacervation, were previously up-scaled for field trial applications. The self-healing additives were added in the ready mix concrete at two different contents, 12% and 16% by vol. of cement respectively. The self-healing concrete was then deployed as a deep topping layer of 60mm on precast slabs (4.25m x 2.8m) forming part of the permanent installation of a new construction development. The performance of the site installations was monitored over 24 months through a combination of NDT methods to provide further information about internal densification, compressive strength development, durability and corrosion potential. Ultrasonic pulse velocity and rebound hammer were combined through regression analysis to propose a prediction formula to assess the compressive strength in situ. Air permeability measurements together with surface resistivity measurements were undertaken to further assess the durability of the self-healing concrete sections compared to the control. Results are presented with durability indicators confirming the in situ enhanced performance of the proposed self-healing system.

Introduction

Concrete structures remain the main driver of construction activities as concrete remains the most versatile, cost effective and widely produced building material. However, concrete structures are becoming more and more strained by increasingly more unpredictable environments and performance requirements. With increasing population and living standards demands in both developing and developed countries imposed on infrastructure, the scope of adopting or adapting new technologies to provide a higher level of confidence in the reliability of our infrastructure materials is considerable [1].

Within this remit, the benefit of self-healing infrastructure materials is recognised [2,3] and during the last decade, several concepts for self-healing concrete have been explored and some first demonstrators with self-healing concrete for commercial deployment have been constructed through national and international projects. In the UK, as part of the EPSRC funded project Materials for Life (M4L), a systematic approach for the delivery of the first generation of self-healing cementitious systems to address cracks across many length scales was realised [4–8]. The extensive system development and material testing in the laboratory was culminated by scaling up and use in the first UK full-scale field trials of self-healing concrete [4–6]. However technology update is not straightforward. The adoption in practical application requires the self-healing technologies to be tailor-designed and implemented based on the expected service conditions and expected damage [9] as well as validated long term.

Bringing to fruition the research on the development of tailored microcapsules for self-healing in cement based materials [4,6,8,10–14], this work presents details of the in situ performance of a commercial deployment of microcapsule-based self-healing concrete on a new

construction project. The performance of the site installations is being monitored over 24 months through a combination of NDT methods to provide further information about internal densification, compressive strength development, durability and corrosion potential. Results are presented with durability indicators confirming the in situ enhanced performance of the proposed self-healing system.

Materials and methods

The detailed installation forms part of the permanent structure of the new Civil Engineering Building of the proposed Department of Engineering Campus to be located in West Cambridge. Within the project’s site compound two pavement concrete slabs are specified. These are 200 mm thick grade PAV2 concrete slabs with brushed finish, 4.25 m long and 2.822 m wide. These are reinforced with an A393 mesh ($\varnothing 10$ mm bars at 200 mm centres) with a nominal top cover of 50 mm. A concept model of the structure is shown in Figure 1. For all elements of this structure, the detailed structural design was completed according to BS EN 1992. A concrete air entrained mix design was specified, for predefined expected exposure conditions, referred to as the control mix, and is detailed in Table 1. The slabs were constructed over a 4-week period where the control base slabs were initially cast and allowed to cure for 28 days before pouring in the self-healing cover concrete.

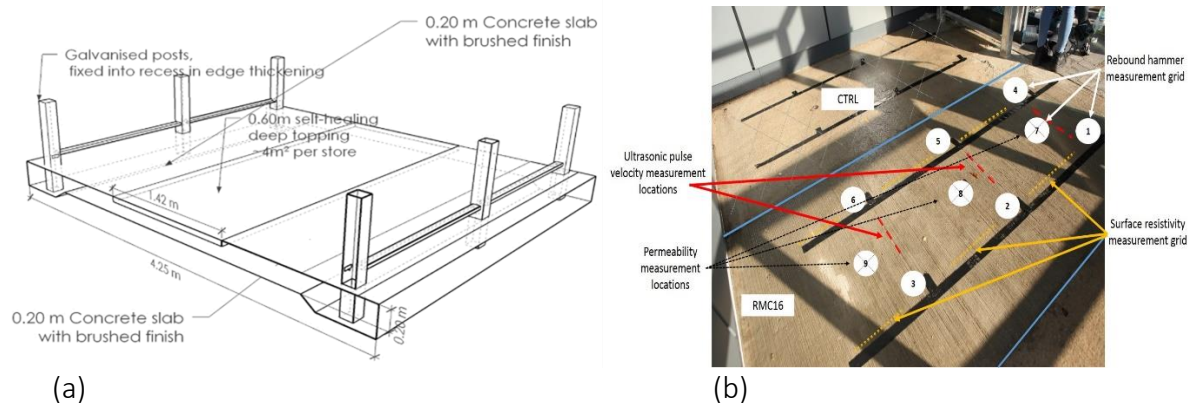


Figure. 1. (a) Concept model of the slabs and (b) Location of permeability, rebound hammer, ultrasonic pulse velocity and surface resistivity measurements.

Table 1 Composition by % weight of the ready mix C32/40 concrete (supplied by Tarmac UK)

Material	Quantity for ready mix slab (kg/m ³ unless noted otherwise)
Cement (CEM I_52.5R)	376
10/20mm Granite aggregates	733
4/10mm Granite	387
0/4mm Sand	617
Water	169 (w/c 0.45)
Admix: ChrysoAIR D /air entraining agent	0.56
Admix: Chrysoplast /RMD plasticizer	2.22

The self-healing additives used on site were polymeric gelatin/gum Arabic shell and sodium silicate cargo microcapsules developed in collaboration with Lambson using complex coacervation [8]. The microcapsules had a mean diameter of 290 μm (SD ~ 120 μm). These were previously up-scaled for field trial applications. For consideration of the suitability of the self-healing additives as part of the permanent installation a preliminary round of testing was agreed with the contractor and strength and workability requirements had to be met. The ready mix concrete was delivered on site and the two control concrete slabs poured in the

base leaving a rebate out with dimensions of 1.42 m wide, 2.822 m long and 60mm deep in each for the self-healing topping concrete to be applied. Then the self-healing additives were added in the ready mix concrete at two different contents, 12% and 16% by vol. of cement respectively. The self-healing concrete was then deployed to infill the 60mm deep layer (0.34 m³) in each precast slab.

The performance of the site installations will be monitored over 24 months through a combination of NDT methods to provide further information about internal densification, compressive strength development, durability and corrosion potential. Herein, a rebound hammer, Controls 58-C0181/C complying to EN 13791 for the non-destructive assessment of strength was employed at multiple locations on both the control and self-healing concrete slabs. A Proceq ultrasonic pulse velocity test (UPV) instrument complying with European standard EN12504-4 and BS1881:Part 203 was used to assess the compressive strength of the applied self-healing concrete sections. UPV and rebound hammer were combined through regression analysis to propose a prediction formula to assess the compressive strength in situ. Air permeability measurements using a Torrent Proceq Permeability Tester, as per SN 505 252/1, together with surface resistivity measurements are also being undertaken to further assess the durability of the self-healing concrete sections compared to the control.

Results and discussion

Indicative compatibility compressive strength results at 7 and 28 days are presented in Figure 2. Overall measured strength values from site samples were lower and were ascribed to the addition of water in the mix delivered on site to improve the workability. To assess the long-term strength development rebound hammer tests, combined with ultrasonic pulse velocity measurements will be undertaken at multiple monitoring events. Average measurements from 9 different locations are being used to profile the surface hardness of the concrete slabs. A consistent increase in recorded rebound values has been found for all slabs with time, indicating the progress of hydration and strength development. Indicatively at 12 months the overall surface hardness for all slabs is similar, within the range of 31-32.

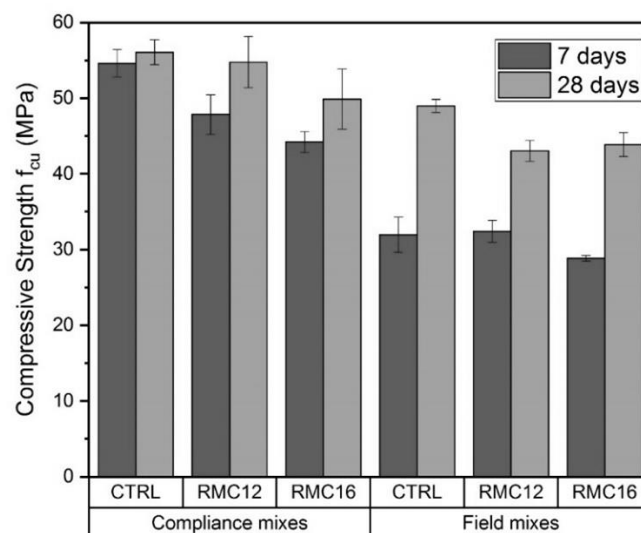


Figure 2. Lab and field result for compressive strength with increasing volume fraction (V_f) of microcapsules at 7 and 28 days respectively.

This confirms preliminary lab assessment of concrete cubes and cylinders at 28 days suggesting that any strength effects on the concrete are short-termed and do not affect the long-term performance. Ultrasonic pulse velocity testing values lie in the range of 3.2-3.95 km/s. The

general trend shows similarly an increase of measured UPV values with time, confirming the strength development of the concrete in situ. Overall the recorded values are lower than other data from literature [15]. This was attributed to the increased air content of the air entrained mixes, which could affect the time for traveling of the ultrasonic pulse wave in concrete, and thus the measured velocity. On the other hand the effect of both the addition and fraction of microcapsules on the UPV measurements seems to be beneficial.

The coefficient of air permeability is also being measured on site as it can correlate quite well with other standardized durability indicator tests [16]. The measurements from the site show similar values in the range of $\sim 10^{-16}$ kT, typical of concrete of good quality [17]. The permeability of the two microcapsule slabs at 12 months indicatively, was $7.3 \cdot 10^{-17}$ kT ($\pm 1.51 \cdot 10^{-17}$) and $3.3 \cdot 10^{-18}$ kT ($\pm 3.2 \cdot 10^{-18}$) for the RMC12 and RMC16 slabs respectively compared to $2.2 \cdot 10^{-16}$ kT ($\pm 2.2 \cdot 10^{-16}$) for the CTRL. These suggest that the microcapsule content did not negatively affect the porosity of the concrete. Moreover a further reduction of the permeability with increasing microcapsule content can be seen. Similar results were observed in the laboratory employing sorptivity measurements to evaluate the permeability of concrete and mortar samples [18]. As a further indicator of the durability of the slab the surface resistivity of the concrete was assessed. Results from site assessment confirm a very low chloride ion permeability compared with measured empirical data for real (semi-infinite) slab applications [19], showing similarly lower overall measured values.

Conclusion

Self-healing concrete using microencapsulated sodium silicate was deployed on-site as part of the permanent pavement work of the new Civil Engineering Building of the University of Cambridge. The self-healing concrete was poured as topping infills (0.34m^3) in two pre-cast slab sections. Two microcapsule contents, 12% and 16% by volume of cement were proposed for the application based on previous results on performance of these microcapsules. The practical implementation was shown to be a relatively straightforward process with the self-healing additives directly incorporated and mixed in the ready-mix concrete upon delivery on site. Non-destructive testing methods were then applied on site to monitor the performance of the self-healing slabs sections and provide further information about internal densification, compressive strength development, durability and corrosion potential. Initial results are sufficiently positive. But testing is ongoing to assess the long-term durability of the self-healing concrete in situ. This application is not only a significant step towards the acceptance of self-healing technologies by market practices but also provides invaluable feedback in the development of next generation of resilient structures.

Acknowledgment

The financial support from EPSRC for the Resilient Materials for Life (RM4L) Programme Grant (EP/P02081X/1) is gratefully acknowledged. The authors are also particularly grateful to Paul Astle of Ramboll, Cambridge, Tom Fenner of SDC, Andy Dunlop from AECOM, Simon Smith from Smith and Wallwork and Rachel Williams from Cambridge University Building Projects for their part in supporting and facilitating this commercial deployment.

References

- [1] European Commission, Business Innovation Observatory - Smart Living: Advanced Building Materials, 2014.
- [2] Lychgate, Self-healing concrete – potential applications and benefits, 2016.
- [3] D. Gardner, R. Lark, T. Jefferson, R. Davies, A survey on problems encountered in current concrete construction and the potential benefits of self-healing cementitious materials, *Case Stud. Constr. Mater.* 8 (2018) 238–247. doi:10.1016/J.CSCM.2018.02.002.
- [4] O. Teall, R. Davies, M. Pilegis, A. Kanellopoulos, T. Sharma, K. Paine, A. Jefferson, R. Lark, D. Gardner, A. Al-

- Tabbaa, Self-healing concrete full-scale site trials, in: K. Maekawa, A. Kasuga, J. Yamazaki (Eds.), Proc. 11th Fib Int. PhD Symp. Civ. Eng., Tokyo, Japan, 2016: pp. 639–646.
- [5] R. Davies, O. Teall, M. Pilegis, A. Kanellopoulos, T. Sharma, A. Jefferson, D. Gardner, A. Al-Tabbaa, K. Paine, R.J. Lark, Large Scale Application of Self-Healing Concrete: Design, Construction and Testing, *Front. Mater.* 5 (2018) 51. doi:10.3389/FMATS.2018.00051.
- [6] A. Al-Tabbaa, C. Litina, P. Giannaros, A. Kanellopoulos, L. Souza, First UK field application and performance of microcapsule-based self-healing concrete, *Constr. Build. Mater.* 208 (2019) 669–685. doi:10.1016/J.CONBUILDMAT.2019.02.178.
- [7] O. Teall, M. Pilegis, R. Davies, J. Sweeney, T. Jefferson, R. Lark, D. Gardner, A shape memory polymer concrete crack closure system activated by electrical current, *Smart Mater. Struct.* 27 (2018) 075016. doi:10.1088/1361-665X/aac28a.
- [8] A. Kanellopoulos, P. Giannaros, D. Palmer, A. Kerr, A. Al-Tabbaa, Polymeric microcapsules with switchable mechanical properties for self-healing concrete: synthesis, characterisation and proof of concept, *Smart Mater. Struct.* 26 (2017) 045025. doi:10.1088/1361-665X/aa516c.
- [9] L. Ferrara, Self-healing cement-based materials: an asset for sustainable construction industry, *IOP Conf. Ser. Mater. Sci. Eng.* 442 (2018) 012007. doi:10.1088/1757-899X/442/1/012007.
- [10] A. Kanellopoulos, T. Qureshi, A. Al-Tabbaa, Encapsulated mineral precursors for self-healing cement based composites, in: 5th Int. Conf. Self-Healing Mater., Durham, USA, 2015.
- [11] R. Alghamri, A. Kanellopoulos, A. Al-Tabbaa, Impregnation and encapsulation of lightweight aggregates for self-healing concrete, *Constr. Build. Mater.* 124 (2016) 910–921. doi:10.1016/j.conbuildmat.2016.07.143.
- [12] R. Davies, O. Teall, M. Pilegis, A. Kanellopoulos, T. Sharma, A. Jefferson, D. Gardner, A. Al-Tabbaa, K. Paine, B. Lark, Large scale application of self-healing concrete: Design, construction and testing, *Front. Mater.* (accepted) (2018).
- [13] A. Al-Tabbaa, B. Lark, K. Paine, T. Jefferson, C. Litina, D. Gardner, T. Embley, Biomimetic Cementitious Construction Materials for Next Generation Infrastructure, *Proc. Inst. Civ. Eng. - Smart Infrastruct. Constr.* (2018) 1–35. doi:10.1680/jsmic.18.00005.
- [14] L.R. Souza, Design and synthesis of microcapsules using microfluidics for autonomic self-healing in cementitious materials, Cambridge University Engineering Department, 2017.
- [15] D. Breyse, Nondestructive evaluation of concrete strength: An historical review and a new perspective by combining NDT methods, *Constr. Build. Mater.* 33 (2012) 139–163. doi:10.1016/J.CONBUILDMAT.2011.12.103.
- [16] R. Torrent, E. Denarie, F. Jacobs, A. Leemann, T. Teruzzi, Specification and site control of the permeability of the cover concrete: The Swiss approach, *Mater. Corros.* 63 (2012). doi=10.1.1.920.5175
- [17] D. Bjegović, M. Serdar, I.S. Oslaković, F. Jacobs, H. Beushausen, C. Andrade, A. V. Monteiro, P. Paulini, S. Nanukuttan, Test Methods for Concrete Durability Indicators, in: 2016: pp. 51–105. doi:10.1007/978-94-017-7309-6_4.
- [18] A. Kanellopoulos, P. Giannaros, A. Al-Tabbaa, The effect of varying volume fraction of microcapsules on fresh, mechanical and self-healing properties of mortars, *Constr. Build. Mater.* 122 (2016) 577–593. doi:10.1016/j.conbuildmat.2016.06.119.
- [19] P. Azarsa, R. Gupta, Electrical Resistivity of Concrete for Durability Evaluation: A Review, *Adv. Mater. Sci. Eng.* 2017 (2017) 1–30. doi:10.1155/2017/8453095.

Evaluation of test methods for self-healing concrete with macrocapsules by inter-laboratory testing

Tim Van Mullem¹, Giovanni Anglani², Hanne Vanoutrive³, Girts Bumanis⁴, Chrysoula Litina⁵, Marta Dudek⁶, Arkadiusz Kwiecien⁶, Abir Al-Tabbaa⁵, Diana Bajare⁴, Teresa Stryszewska⁶, Robby Caspee¹, Kim Van Tittelboom¹, Jean Marc Tulliani², Elke Gruyaert³, Paola Antonaci², Nele De Belie¹

1: Magnel-Vandepitte Laboratory, Department of Structural Engineering and Building Materials, Ghent University, Belgium

2: Politecnico di Torino, Italy

3: KU Leuven - Ghent Technology Campus, Belgium

4: Riga Technical University, Latvia

5: University of Cambridge, United Kingdom

6: Cracow University of Technology, Poland

Abstract

Self-healing of concrete is a promising way to increase the service life of structures. Innovative research is being performed, yet it is difficult to compare results due to a lack of standardised test methods. In the framework of the COST action SARCOS (CA15202) [1] six different inter-laboratory tests are being executed, in which different test methods are being evaluated for six self-healing approaches. Here, the results of the inter-laboratory test concerning mortar and concrete with macrocapsules filled with a polyurethane healing agent will be discussed. The specimens were manufactured in one laboratory and then shipped to the other five participating laboratories. All six laboratories evaluated two test methods: a water permeability test and a capillary water absorption test. For the water permeability test, mortar specimens were cracked and afterwards their crack width was controlled using an active control technique. Due to the active crack control, the crack width of 90% of the samples deviated by less than 10 μm from the target of 300 μm . This made it more straightforward to compare the permeability test results, which indicated a similar sealing efficiency for several of the laboratories. For the capillary water absorption test, concrete specimens were cracked in a crack-width-controlled three-point bending test setup without active control after unloading. Compared to the water permeability specimens, there was a lot more variation on the crack width of the capillary water absorption specimens. The variability on the crack width and differences in quality of waterproofing resulted in diverging findings in the capillary water absorption test.

Introduction

Self-healing concrete is a promising material which can repair its own defects, thereby overcoming the need for expensive manual repair interventions. Although a lot of tests have already been carried out on different types of self-healing concrete, it is often difficult to compare results from different studies as no standard methods are yet available to test the efficiency and the consequent enhancement of the self-healing concrete properties. Additionally, there are a lot of factors (age of cracking, type of crack, conditions of exposure and healing duration, through-crack stress state, etc.) which can influence the healing behaviour [2]. In the framework of the EU COST Action CA 15202 SARCOS six different inter-laboratory tests have been running to evaluate test methods to assess the efficiency of self-healing concrete. Each test focusses on a different healing mechanism. The inter-laboratory test which is described here focusses on self-healing mortar and concrete with macrocapsules. Six labs participated in this inter-laboratory test: Ghent University, Politecnico di Torino, Riga

Technical University, Cracow University of Technology, Cambridge University and KU Leuven - Ghent Technology Campus.

For the inter-laboratory test programme two different tests were evaluated: a water permeability test and a capillary water absorption test. To execute the water permeability test, mortar specimens were cast. Concrete specimens were cast to perform the water absorption test. Since the crack width has a large influence on the water permeability test results, an 'active' crack width control technique was used after cracking of the mortar specimens to limit the variation on the crack width [3]. A 'passive' crack width control technique [4], by means of crack width control during loading, was used for the concrete specimens. All specimens were cast by Ghent University and were then shipped to the participating labs. The test protocol and any deviations by a specific lab have been recorded [5].

Materials and methods

Healing agent

As healing agent a single-component polyurethane (PU) was used. The used agent has a low viscosity and polymerises when it comes in contact with moisture in the air or in the concrete. In order to prevent the polymerisation up until the moment of crack creation, the PU was encapsulated in well-sealed tubular glass capsules with an internal diameter of 3 mm. The length of the capsules was 55 mm for the mortar specimens and 60 mm for the concrete specimens. Samples containing glass capsules are referred to as CAPS, reference samples are referred to as REF.

Water permeability test on mortar specimens

To execute the water permeability test, unreinforced mortar specimens (40x40x160 mm) were made with a cast-in hole (\varnothing 5 mm) positioned with its centre 15 mm from the bottom side [3]. The mortar consisted of: 519 kg/m³ CEM I 42.5 N, 258 kg/m³ water, 1313 kg/m³ sand (0-2 mm), 89 kg/m³ limestone filler, and 0.79 l/m³ superplasticizer. For the CAPS specimens two capsules were placed at a height of 5 mm above the bottom side of the specimen so that the distance between the cast-in hole and the capsules, and the distance between the capsules and the bottom side of the specimen would be approximately equal. A Carbon Fibre Reinforced Polymer (CFRP) laminate was glued on the top side of the specimens using epoxy resin. One side of the cast-in hole of the specimens was connected to the water flow test setup. The other side was sealed. At an age of 14 or 15 days the specimens were cracked until failure in a three-point bending test setup with a span of 10 cm. Both halves of the mortar specimen stayed together due to the CFRP. Immediately after cracking the specimens were placed with their crack face upwards and the crack width was restrained under the microscope using screw jacks until the target crack width of 300 μ m was obtained. The crack width of a specimen was determined from five measurements at three different locations (15 measurements in total) along the crack mouth. The cracks at the side faces were sealed. Prior to executing the water permeability test, specimens were submerged in water for 24 h. The tube of the specimens was connected to a water reservoir at a height of 50 \pm 2 cm with respect to the cast-in hole. Water could only leak out of the bottom of the crack. The amount of leaked water was recorded over time for a minimum of 6 minutes to determine the water flow in g/min.

Capillary water absorption test on concrete specimens

To execute the capillary water absorption test, concrete specimens (60x60x220 mm) were made with 2 reinforcement bars (\varnothing 3 mm) positioned at a height of 12 mm from the bottom. The concrete consisted of: 378 kg/m³ CEM I 42.5 N, 185.2 kg/m³ water, 743 kg/m³ sand (0-5 mm), 1013 kg/m³ gravel (2-8 mm), 58 kg/m³ limestone filler, and 1.33 l/m³ superplasticizer. For the CAPS specimens, 4 capsules with a length of 60 mm were placed just above the

reinforcement, except for Lab 6 for which the CAPS specimens contained 5 capsules with a length of 49 mm, instead of 60 mm. A day before cracking, the specimens were provided with a notch (depth of 3-5 mm). At an age of 14-16 days the specimens were cracked in a crack-width-controlled three-point bending test setup, to obtain a target crack width of 300 μm . The crack width of a specimen was determined from five measurements at four different locations (20 measurements in total) along the crack mouth. After measuring the crack width, the specimens were submerged in water for 24 h, to allow for a complete polymerisation of the PU. Subsequently, the specimens were oven dried (40°C) for 2 weeks. The bottom and the sides of the specimens were waterproofed by using aluminium tape, except for a zone with a width of 14 mm centred on the crack. The dry weight of the specimens was recorded and they were then placed in a container with water so that the water level was maintained 2-3 mm above the notch. The water uptake was recorded over a period of 24 h. By plotting the water uptake (in g) versus the square root of time (in $\text{h}^{0.5}$), the sorption coefficient (SC) was determined as the slope of the trend line of the data.

Results and discussion

Water permeability test on mortar specimens

The mean crack width of the mortar specimens for the different labs is given in Figure 1 (a). Within each lab, the crack width of the REF specimens was comparable to the crack width of the CAPS specimens. Therefore, the crack width of the REF and CAPS specimens were considered together when comparing the results of the different labs in a Brow-Forsythe test (equal variances could not be assumed ($p < 0.1\%$)). This test indicated a significant result (level of significance = 5%, $p = 4.1\%$). A subsequent Tamhane's T2 post hoc test showed only a difference between Lab 1 and 2 (level of significance = 5 %, $p = 2.8\%$). It is noted that these statistical tests only gave a significant result due to the small variation on the crack width (for all labs the standard deviation of the REF, respectively CAPS series was lower than 8 μm , except for Lab 6 for which it was equal to 14 μm). Considering that for 90% of all samples the crack width of an individual specimen was within 10 μm from the target crack width of 300 μm (for 95% it was within 15 μm), it can be considered that the crack width of all labs is comparable. The low variability on the crack width is the result of the active crack width control technique which allowed to regulate the crack width precisely to the target crack width.

After measuring the crack width of the specimens and submerging them, a water permeability test was executed. The results of this test are given in Figure 1 (b). These results show more variation, as could be expected from previous research [3]. The mean water flow measured from the REF specimens is comparable for Labs 1, 3, 5, and 6. The variability on the CAPS specimens is higher than the variability on the REF specimens. This can be explained by the fact that the outflow of PU is not the same in all specimens. Table 1 shows the sealing efficiency calculated by dividing the difference between the mean water flow of the REF and CAPS specimens by the mean water flow of the REF specimens. Labs 1, 2 and 6 obtain a similar sealing efficiency of approximately 40-50%, and also Labs 3, 4 and 5 obtain a similar sealing efficiency of approximately 64-73%. Overall all labs were able to come to the same conclusion: the addition of the macrocapsules was beneficial, yet did not result in a perfect healing.

Capillary water absorption test on concrete specimens

The mean crack width of the concrete specimens for the different labs is given in Figure 2. The REF series of Lab 2 and 4, as well as the REF and CAPS series of Lab 3 and 5, did not obtain a target crack width of 300 μm (as analysed with a t-test, level of significance = 5 %).

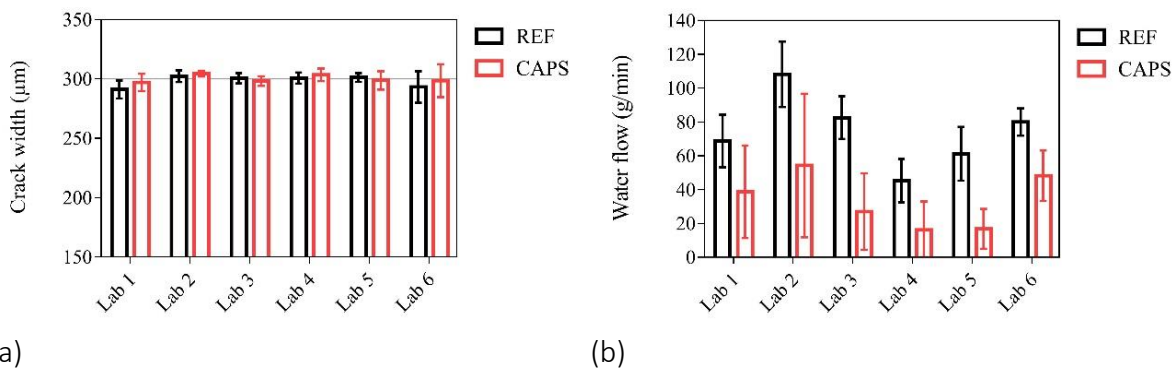


Figure 1. (a) Mean crack width of the mortar samples (error bars represent standard deviation, scale of the vertical axis is identical as for the concrete specimens); (b) Mean water flow of the mortar samples (error bars represent standard deviation)

Table 1. Sealing efficiency calculated from mean water flow

	Lab 1	Lab 2	Lab 3	Lab 4	Lab 5	Lab 6
Sealing efficiency	44%	50%	67%	64%	73%	40%

The statistical difference of the REF series of Lab 2 is related to a low standard deviation 10 µm, as the mean was equal to 290 µm, which can be considered equal to the target for practical purposes. Comparing these results with the results of the mortar specimens clearly shows that there is a much larger variation on the crack width of the concrete specimens (the standard deviation of the REF and CAPS concrete series varied from 10 µm (CAPS series Lab 2) to 76 µm (CAPS series Lab 3), while the maximum standard deviation for the mortar specimens was 14 µm (CAPS series Lab 6)). This can partly be explained by the fact that the mortar specimens have a more uniform matrix compared to the concrete specimens and thus also a different texture and crack geometry. Additionally, the larger variation is also partly a consequence of the 'passive' crack control. During loading in the three-point bending setup the crack width is precisely controlled by measurements of an LVDT or a CMOD. Yet, at the moment that the specimen is unloaded, after reaching a maximum crack width, the crack partially closes as a result of an elastic regain in the reinforcement bars. This elastic closure is not the same for all specimens, explaining the high degree of variation. A previous round robin study also used a comparable 'passive' crack control to crack reinforced mortar prisms (40x40x160 mm) [6]. The variability reported there was also much larger than the one reported in the current paper for the mortar specimens controlled in an 'active' way.

It is noted that while the target crack width after unloading was defined (300 µm), the maximum crack width under loading was left at the discrepancy of the participating labs as different displacement-controlled loading systems were used. Labs 1, 2, and 6 opened their specimens the furthest (485 µm) and they obtained results equal to the target.

The results of the water absorption tests are summarised in Table 2, where the sorption coefficients are given for the cracked REF and CAPS specimens, as well as uncracked control specimens (UNCR). There is quite a lot of variation on the results, e.g. Lab 4 obtained a sorption coefficient for the REF specimens which is more than double from what is obtained by Lab 1, 2 and 6. The variation on the crack width between the different labs does not seem to be the sole cause of these variations; the sorption coefficient of the uncracked specimens also shows a lot of variation. The quality of the waterproofing has been investigated in a follow-up study [5] and it was found that this had a significant influence.

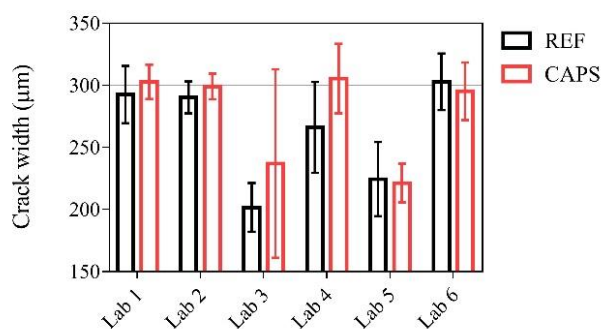


Figure 2. Mean crack width of the concrete samples (error bars represent standard deviation)

Table 2. Sorption coefficient for both uncracked specimens, reference specimens, and specimens with capsules

	Lab 1	Lab 2	Lab 3	Lab 4	Lab 5	Lab 6
SC_{REF} (g/Vh)	4.13	4.49	8.80	10.82	7.79	3.92
SC_{CAPS} (g/Vh)	4.11	4.33	6.37	9.11	7.13	3.97
SC_{UNCR} (g/Vh)	1.78	2.44	6.73	7.76	6.27	2.09

Conclusion

Results on the executed inter-laboratory test on concrete with macrocapsules showed that the target crack width of 300 µm could be obtained with great accuracy in mortar specimens as a result of the applied ‘active’ crack width control technique. The crack width has a major influence on the water permeability. Due to the equal crack widths, all labs could come to the same conclusion with regards to the sealing efficiency: the macrocapsules were beneficial, yet did not result in a perfect crack sealing.

Only three out of the six participating labs were able to obtain the target crack width in the concrete specimens used for capillary water absorption testing (after inducing cracks via a ‘passive’ crack control). Upon unloading there is an elastic regain in the reinforcement which is not controlled and which contributes to the variability of the crack width. This could have influenced the results of the capillary water absorption tests, although the quality of the waterproofing is also an important factor.

Acknowledgment

This work is the result of a joint collaboration of scientists working on the development of self-healing concrete within the framework of the European Cooperation in Science and Technology (COST) Action “Self-healing as preventive repair of concrete structures” SARCOS CA15202. T. Van Mullem and N. De Belie acknowledge the support of the grant (21SCIP-C158977-02) from the Construction Technology Research Program funded by the Ministry of Land, Infrastructure and Transport of the Korean government. Funding from the European Union’s Horizon 2020 research and innovation programme under the Marie Skłodowska-Curie grant agreement SMARTINCS No 860006 made the continuation of the collaborative work possible.

References

- [1] COST Action SARCOS homepage. <https://www.sarcos.eng.cam.ac.uk/>. Accessed June 24 2021
- [2] Ferrara L, Van Mullem T, Alonso MC, Antonaci P, Borg RP, Cuenca E, ..., De Belie N. Experimental characterization of the self-healing capacity of cement based materials and its effects on the material performance: A state of the art report by COST Action SARCOS WG2. *Construction and Building Materials*. 208 Vol 167 pp. 115-142.

- [3] Van Mullem T, Gruyaert E, Debbaut B, Caspeepele R, De Belie N. Novel active crack width control technique to reduce the variation on water permeability results for self-healing concrete. *Construction and Building Materials*. 2019 Vol 203 pp. 541-551.
- [4] Van Tittelboom K, De Belie N, Van Loo D, Jacobs P Self-healing efficiency of cementitious materials containing tubular capsules filled with healing agent. *Cement and Concrete Composites*. 2011. Vol 33 (4) pp. 497-505.
- [5] Van Mullem T, Anglani G, Dudek M, Vanoutrive H, Bumanis G, Litina C, ..., De Belie N. Addressing the need for standardization of test methods for self-healing concrete: an inter-laboratory study on concrete with macrocapsules. *Science and Technology of Advanced Materials*. 2021. Vol 21 (1) pp. 661-682.
- [6] Tziviloglou E, Wiktor V, Wang J, Paine K, Alazhari M, Richardson A, ..., Jonkers H. Evaluation of experimental methodology to assess the sealing efficiency of bacteria-based self-healing mortar: round robin test. *RILEM Conference on Microorganisms-Cementitious Materials Interactions (Delft, the Netherlands)*. 2016. pp 156-170.

Investigation of the micromechanical properties of the interface between PLA self-healing capsules and cementitious matrix

Claudia Romero Rodriguez¹, Yidong Gan¹, Hongzhi Zhang^{1,2}, Erik Schlangen¹, Branko Šavija¹

1: Department of 3MDs, Delft University of Technology, Delft 2628 BJ, the Netherlands

2: School of Qilu Transportation, Shandong University, 250002 Jinan, PR China

Abstract

Encapsulation of healing agents has been shown to be a functional methodology to obtain self-healing concrete. These capsules protect the agents during mixing but at the same time they are easily broken off or exposed during cracking, enabling the healing mechanisms. Either effect depends on the properties of the matrix, the capsules and/or their interface. In this investigation we study the interface between polylactic acid capsules and matrix through nanoindentation to obtain microhardness and modulus of elasticity at the microscale. Since these properties are representative only of the indented areas and vary depending on which cement phase(s) influence them, numerical modelling of the “2D” mapped properties through lattice fracture model was done to obtain the mechanical properties of the interface. The authors expect to understand the mechanical behaviour of the studied interface and to provide the respective mechanical properties such as tensile strength and fracture energy, that later on can be used to model the overall behaviour of the heterogeneous self-healing system.

Introduction

Autonomous self-healing (SH) of cracks in concrete is a smart solution to boost the durability of cement-based materials. A key feature of an autogenous system is the way that SH is triggered, which is closely linked to how the healing agents are incorporated into the composite. To this purpose, the healing agents are either specifically placed in prone to crack zones of the structural element (i.e. vascular systems) [1] or randomly distributed in the cement matrix, i.e. capsules [2, 3], (coated) fibres [4], where the inclusions themselves steer the crack patterns. In the latter case, mechanical triggering should be such that the overall mechanical performance of the SH composite approaches that one of the non-SH material. Although many engineered SH systems for concrete have been proposed in the past decades, there seems to be a tendency to favour encapsulation as triggering mechanism. One such example is the introduction of bacteria spores and nutrients embedded in ‘capsule-like’ particles. Regarding the latter, researches have proposed different ‘capsules’, for example ([5-7]). Encapsulation of bacterial spores is needed not only as a mechanical triggering mechanism but also to protect the alkaliphilic bacteria spores during mixing of concrete and to contain carbon sources and activation nutrients so necessary for their metabolic activity. Previous research on the use of bacteria embedded poly-lactic-acid (PLA) capsules as healing agent has proven its potential to satisfy both mechanical and functional requirements of the resulting SH system [8]. Nevertheless, the biodegradable PLA hydrolyses in alkaline environments ultimately affecting hydration kinetics of the cement paste [9]. In previous unpublished results by the authors, a rather extensive “interface zone” (IZ) was identified around the PLA particles presenting different hydration degree in comparison to the bulk paste. Thus, its effect on the mechanical properties of the interface zone (IZ) and therefore that of the SH composite needs to be investigated.

In this study we aim to quantify the tensile strength and elastic modulus of the IZ for their eventual use as input for mesoscale simulations of the SH composite. In order to do so,

mapping of the elastic modulus and the microhardness of the IZ around a PLA type H particle, embedded in cement paste, and of the bulk unaffected reference cement paste was done through nanoindentation. A similar methodology has been successfully employed in [10, 11]. The outcome was then used to simulate uniaxial tensile tests on several data sets through lattice fracture model. The resulting tensile strength and elastic modulus of the IZ were compared to the values simulated for the reference cement paste and their ratios were obtained.

Materials and methods

Ordinary Portland Cement CEM I 52.5R provided by ENCI (the Netherlands) and bacteria embedded poly-lactic-acid particles, herein called PLA type H, supplied by Basilisk (the Netherlands), were used to prepare cement paste 'H' with water-to-cement (w/c) ratio of 0.45 and extremely low particles volume content (0.6 %). The latter was selected in order to isolate the influence of each single particle on the surrounding cement paste from each other. The particles had diameter in the range 0.5-1.0 mm and a density of 1200 kg/m³. A reference cement paste with same w/c ratio was prepared to simulate the bulk cement paste regions, herein referred to as 'CP'. The pastes were cast into plastic containers with a diameter of 35 mm and a height of 70 mm and their tops sealed with plastic film and a lid for 24 hours. Demoulding followed and then curing occurred for 28 days in a moist chamber at 20 (±) 2 °C and 95 % RH.

At the end of the curing period, the samples were sawn into 3-5 mm thick slices and further cut into rectangular sections with dimensions 10x50 mm². Selected slices, containing 1 or 2 (far apart) particles, were immersed in isopropanol for approximately 7 days and further dried in an oven at 40 °C for 10 minutes. This procedure was performed for stopping hydration and drying the samples prior to preparation for the nanoindentation procedure. The resulting sections were first ground with silicon carbide paper with a mesh grade of 1200 and later polished with diamond paste (Struers) with grain sizes 9, 6, 3, 1 and ¼ µm for 15, 15, 30 and 30 minutes, respectively. After each respective step, the sections were put in an ethanol bath in an ultra-sonicator for 5 minutes in order to remove diamond and cement paste particles.

Nano Indenter (G200, KLA, USA) with a diamond Berkovich tip was used to indent the prepared sections in 6 different locations. In the case of mixture H, for each location a grid of 5 x 15 with a spacing of 10 µm was performed to measure hardness (µH) and elastic modulus (E). The orientation of the grid was such that its short side was parallel to the boundary of the PLA type H particle and its origin was right at the boundary. In the case of mixture CP, the grid consisted of 5 x 10 indents with same spacing as H. No preferred location or orientation was pursued. Using the continuous stiffness method (CSM) developed by Oliver and Pharr [12], E and µH are obtained as a continuous function of the depth of penetration of the indenter. To ensure the accuracy of measurements, a quartz standard was indented before each test. The surface approach velocity was 10 nm/s while the strain rate in the material was kept as 1/s. The maximum indentation depth was fixed at 1000 nm. A Poisson ratio of 0.2 was assumed for the calculation of the E. The average elastic modulus and hardness were calculated in the displacement range between 500 and 650 nm to avoid the scatter of lower indentation depths where surface roughness may lead to erroneous results.

Since such maps cannot lead to a conclusion on the performance of the interested material in terms of strength or elastic modulus, lattice fracture model [10, 11, 13] was used to simulate a uniaxial tensile test on the 2D meshes in which an overlay procedure mesh-maps is implemented. Mesh cell size was 1 µm and randomness of the node position within the cell was 0.2. For each lattice element with nodes i and j, the elastic modulus (E_{ij}) was calculated as a function of the interpolated nodal values E_i , E_j as suggested in [13]:

$$\frac{2}{E_{ij}} = \frac{1}{E_i} + \frac{1}{E_j} \tag{1}$$

Consequently, the shear modulus (G_{ij}) was obtained as:

$$G_{ij} = \frac{E_{ij}}{2(1+\nu)} \tag{1}$$

The ratio between measured hardness and tensile strength (f_t) used was taken as 12, as suggested in [14] and further confirmed in [15]. Whereas, the compressive strength (f_c) to tensile strength ratio was taken as 10 which has been experimentally confirmed for such length scales in [16]. The elemental tensile strength was calculated as suggested in [13]:

$$f_{t,ij} = \min(f_{t,i}; f_{t,j}) \tag{3}$$

Although it has been shown in [17] that tensile strength and elastic moduli obtained from 2D or from 3D simulations, with input parameters obtained as described above, differ somewhat in value, the orders of magnitude remain accurate and their ratio should not suffer from their differences.

Results and discussion

In Figure 1 (a, b) the 2D mappings of the tensile strength are shown for a sample of the interface zone of the PLA type H particle and for a sample of the reference cement paste. The black arrow in Figure 1 (a) indicates the boundary of the PLA particle, which has not been mapped. From the mapping examples, one can already observe the differences between degree of hydration of IZ and bulk CP. Higher local tensile strengths are obtained from the non-porous unreacted cement clinker whereas increasingly porous high- and low-density C-S-H present lower values, as has been observed elsewhere [18]. In H interface zone the number of high tensile strength and E moduli hubs is higher than in CP. This trend was observed in all indented locations. Figures 1 (a, b) also show the cracks (in red) under uniaxial tensile loading (indicated by the brown arrows), applied along the long side axis of the rectangular meshes. The observed trend for H mixture was the nucleation of cracks happening in proximity of the PLA particle boundary, suggesting weaker mechanical properties at the interface. In contrast, CP mixtures presented random locations of the cracks along the loading direction.

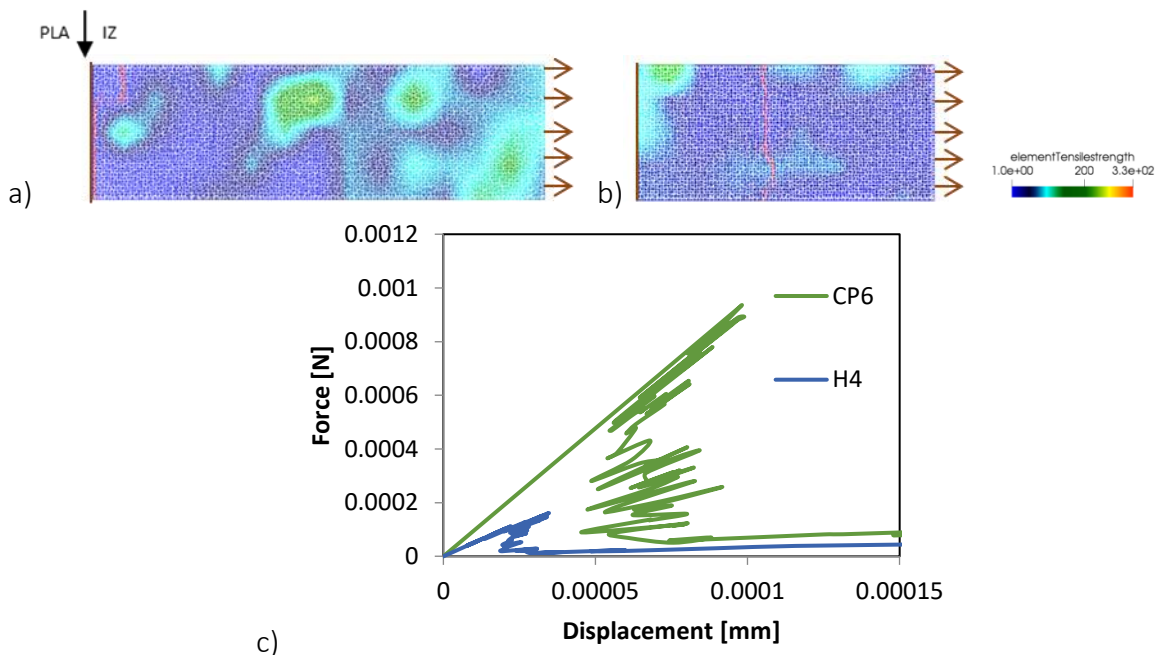


Figure 1. Tensile strength (in MPa) mapping and respective simulated Force vs. displacement curve of a data set of PLA-H IZ (a, c) and of a data set of reference cement paste (b, c). Crack patterns are shown in red.

Figure 1 (c) shows the simulated Force vs displacement response of the examples displayed in Figure 1 (a, b). The simulated E modulus and tensile strengths of H's IZ and CP are summarized in Figure 2 a) and 2 b), respectively. First of all, both E and f_t present higher scatter for the IZ in comparison to the bulk CP. Average values of both elastic modulus and tensile strength of bulk CP are higher than those simulated for the interface zone of PLA type H particles. The reference values of E and f_t for CP are close to those measured in literature for similar age, size and water-to-cement ratio [19]. Finally, the ratios between the average of simulated properties between the IZ and the bulk CP were 0.91 and 0.38 for the elastic modulus and tensile strength, respectively.

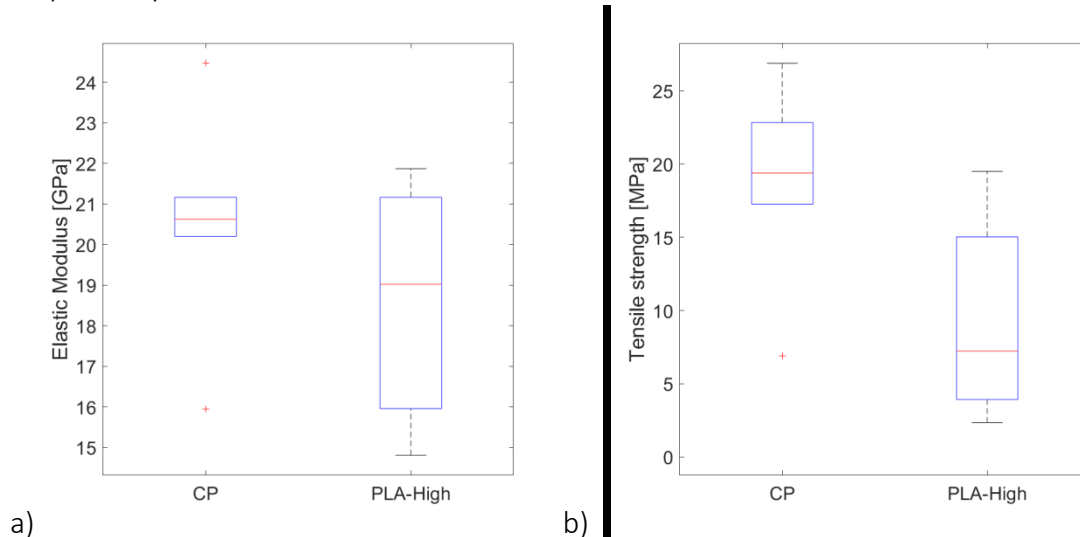


Figure 2. Simulated elastic moduli (a) and tensile strength (b) of the interface zone of the PLA-High particle and bulk cement paste.

Conclusions

The following conclusions can be drawn from the preliminary investigation of the mechanical properties of the interface zone between PLA type H and cement paste:

- E modulus and tensile strength mappings obtained from nanoindentation suggest an alteration on the local mechanical properties of the cement paste around the PLA type H particle.
- The nucleation of cracks in the IZ of mixture H near the PLA particle boundary, as well as the high scatter obtained in the simulated tensile strength values for the same, may suggest the presence of highly variable and lower local mechanical properties at the interface zone.
- The alteration of local mechanical properties for the IZ of H seems to correlate well with the dramatic decrease on tensile strength of over 60 % with respect to that of bulk cement paste.

Acknowledgment

The first author acknowledges the financial support from the Construction Technology Research Program funded by the Ministry of Land, Infrastructure and Transport of the Korean Government under the grant 17SCIP-B103706-03.

References

- [1] Li, Z., Souza, L. R. D., Litina, C., Markaki, A. E., & Al-Tabbaa, A. (2019). Feasibility of Using 3D Printed Polyvinyl Alcohol (PVA) for Creating Self-Healing Vascular Tunnels in Cement System. *Materials*, 12(23), 3872.
- [2] Mercuri, L., C. Romero Rodriguez, Y. Xu, S. Chaves Figueiredo, R. Mors, E. Rossi, G. Anglani, P. Antonaci, B. Šavija, and E. Schlangen. (2019). On The Role Of Soft Inclusions On The Fracture Behaviour Of Cement Paste.

- In Proceedings of the 10th International Conference on Fracture Mechanics of Concrete and Concrete Structures.
- [3] Li, W., Jiang, Z., Yang, Z., & Yu, H. (2016). Effective mechanical properties of self-healing cement matrices with microcapsules. *Materials & Design*, 95, 422-430.
 - [4] Romero Rodriguez, C., Chaves Figueiredo, S., Chiaia, B., & Schlangen, H. E. J. G. (2016). Induction healing of concrete reinforced by bitumen-coated steel fibres. In 9th International Conference on Fracture Mechanics of Concrete and Concrete Structures.
 - [5] Palin, D., Wiktor, V., & Jonkers, H. M. (2016). A bacteria-based bead for possible self-healing marine concrete applications. *Smart Materials and Structures*, 25(8), 084008.
 - [6] Wang, J., Van Tittelboom, K., De Belie, N., & Verstraete, W. (2012). Use of silica gel or polyurethane immobilized bacteria for self-healing concrete. *Construction and building materials*, 26(1), 532-540.
 - [7] Wang, J. Y., De Belie, N., & Verstraete, W. (2012). Diatomaceous earth as a protective vehicle for bacteria applied for self-healing concrete. *Journal of industrial microbiology & biotechnology*, 39(4), 567-577.
 - [8] Mors, R. M., & Jonkers, H. M. (2017). Feasibility of lactate derivative based agent as additive for concrete for regain of crack water tightness by bacterial metabolism. *Industrial crops and products*, 106, 97-104.
 - [9] Mors, R., & Jonkers, H. (2017). Effect on concrete surface water absorption upon addition of lactate derived agent. *Coatings*, 7(4), 51.
 - [10] Luković, M., Šavija, B., Dong, H., Schlangen, E., & Ye, G. (2014). Micromechanical study of the interface properties in concrete repair systems. *Journal of Advanced Concrete Technology*, 12(9), 320-339.
 - [11] Lv, L. Y., Zhang, H., Schlangen, E., Yang, Z., & Xing, F. (2017). Experimental and numerical study of crack behaviour for capsule-based self-healing cementitious materials. *Construction and Building Materials*, 156, 219-229.
 - [12] Oliver, W. C., & Pharr, G. M. (2004). Measurement of hardness and elastic modulus by instrumented indentation: Advances in understanding and refinements to methodology. *Journal of materials research*, 19(1), 3-20.
 - [13] Qian, Z. (2012). Multiscale modeling of fracture processes in cementitious materials. PhD Thesis, Delft University of Tehcnology, the Netherlands.
 - [14] Hlobil, M., Šmilauer, V., & Chanvillard, G. (2016). Micromechanical multiscale fracture model for compressive strength of blended cement pastes. *Cement and Concrete Research*, 83, 188-202.
 - [15] Zhang, H., Šavija, B., Chaves Figueiredo, S., Lukovic, M., & Schlangen, E. (2016). Microscale testing and modelling of cement paste as basis for multi-scale modelling. *Materials*, 9(11), 907.
 - [16] Zhang, H., Xu, Y., Gan, Y., Chang, Z., Schlangen, E., & Šavija, B. (2019). Combined experimental and numerical study of uniaxial compression failure of hardened cement paste at micrometre length scale. *Cement and Concrete Research*, 126, 105925.
 - [17] Lukovic, M. (2016). Influence of interface and strain hardening cementitious composite (SHCC) properties on the performance of concrete repairs.
 - [18] Constantinides, G., & Ulm, F. J. (2004). The effect of two types of CSH on the elasticity of cement-based materials: Results from nanoindentation and micromechanical modeling. *Cement and concrete research*, 34(1), 67-80
 - [19] Zhang, H., Šavija, B., & Schlangen, E. (2018). Towards understanding stochastic fracture performance of cement paste at micro length scale based on numerical simulation. *Construction and Building Materials*, 183, 189-201.

Biopolymeric capsules for asphalt self-healing

Jose Norambuena-Contreras¹, Jose L. Concha¹, Luis Arteaga², Irene Gonzalez-Torre¹

1: LabMAT, Department of Civil and Environmental Engineering, University of Bío-Bío, Concepción, Chile.

2: LPTC, Department of Wood Engineering, University of Bío-Bío, Concepción, Chile.

Abstract

This paper presents the synthesis and characterization of polynuclear biopolymeric capsules for asphalt self-healing. Sodium alginate biopolymer extracted from the cell wall of brown algae was used as the encapsulation material to contain Waste Cooking Oil (WCO) as a potential rejuvenating agent. Multicavity capsules were synthesized by ionic gelation. The size, surface aspect and internal structure of the WCO capsules were evaluated using Optical and Scanning Electron Microscopy. The physical-chemical properties and thermal stability of WCO capsules and their components were also evaluated. Moreover, the diffusion process and self-healing capability of the released WCO on cracked bitumen test samples were determined by image analysis through fluorescence microscopy. The main results of this study showed that the polynuclear biopolymeric capsules presented a suitable morphology to be mixed in asphalt mixture composite. WCO capsules and their components presented a good thermal stability and physical-chemical properties. It was proven that the encapsulated WCO can be diffused in the bitumen samples reducing their viscosity and resulting in healing of micro-cracks in the asphalt.

Introduction

Self-healing by the action of encapsulated rejuvenating agents has been considered as a revolutionary technology for autonomous crack-healing of asphalt materials [1]. Asphalt materials are complex viscoelastic composites mainly used for asphalt pavement construction. Cracking of asphalt materials mainly occurs due to the oxidation of the hydrocarbon compounds of bitumen [2]. When damage occurs in an asphalt material containing embedded capsules cracks appear, and eventually propagate until they reach and break a microcapsule releasing the contained rejuvenating agents. Rejuvenating agents consist of lubricating and extender oils with high proportions of maltene constituents, which restore the asphaltenes/maltenes ratio in the aged bitumen [3]. When the rejuvenating agent is released from the capsule, the molecules of the rejuvenator are diffused into the asphalt matrix and soften the aged bitumen allowing the rejuvenated bitumen to flow through the open microcracks, thus facilitating the autonomic self-healing process [4]. Figure 1 shows the concept of self-healing in asphalt using capsules.

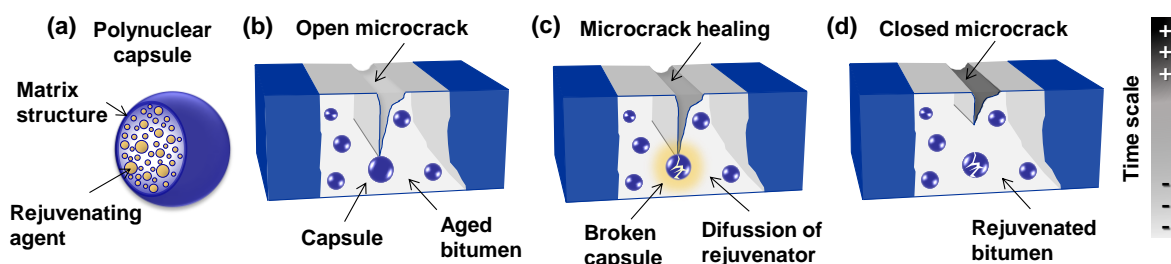


Figure 1. Concept of autonomic healing in asphalt materials by the action of encapsulated rejuvenators. Depending on their structure, capsules can be classified as either polynuclear capsules or core-shell capsules. Polynuclear capsules are spherical particles with the

encapsulated material distributed throughout a polymeric matrix structure, while core-shell capsules are spherical particles consisting of a defined core (rejuvenating agent) surrounded by a polymeric shell (membrane) structure.

Recent studies have successfully proven the use of numerous rejuvenators such as dense aromatic oil [5]; waste cooking oil [6]; sunflower oil [7]; and, recently, bio-oil from liquefied agricultural biomass waste [8] to design core-shell and polynuclear polymeric capsules for asphalt self-healing. Nevertheless, the polymers currently used for the encapsulation process, for example melamine-formaldehyde [6], can produce a potentially high environmental risk from the leaching of hazardous chemical compounds, making this technology unsuitable for extensive use in asphalt pavements [9]. This study presents the synthesis and characterization of polynuclear biopolymeric capsules for asphalt self-healing, where sodium alginate biopolymer from the cell wall of brown algae was used as the encapsulation materials to contain Waste Cooking Oil (produced after cooking and frying) as a potential rejuvenating agent for more sustainable asphalt pavements due to its lighter oil components similar to those of asphalt.

Materials and methods

Materials: Biopolymeric WCO capsules were prepared in this study. The polymeric structure of the capsules was prepared of low-viscosity grade sodium alginate (viscosity at 20 °C 200-300 cP for 2% w/v solution) provided by Buchi, and calcium-chloride dihydrate ($\text{CaCl}_2 \cdot 2\text{H}_2\text{O}$) with 70% purity provided by Winkler. Waste Cooking Oil (produced after cooking) with density 0.85 g/cm³, viscosity at 20 °C 89 cP and pH at 25 °C 4.4-4.6 was used as a sustainable rejuvenating agent. Additionally, virgin CA24 bitumen with a penetration grade 80/100 mm at 25 °C was used to quantify the WCO healing efficiency.

Preparation of WCO capsules: WCO capsules were manufactured in the laboratory by cross-linking of sodium alginate in the presence of calcium ions (Ca^{2+}) by ionic gelation, based on the procedure described by Norambuena-Contreras et al. [8]. Sodium-alginate concentrations of 2% of weight by volume of water were used to produce capsules by means of a microfluidic device that pumps the oil-in-alginate emulsion through a metal hollow needle of 1.2 mm diameter at a flow rate of 2 mL/min.

Experimental characterization: Size, surface aspect and internal microstructure of the produced WCO capsules were characterized by Optical (Leica EZ4) and Scanning Electron Microscopy (Hitachi SU 3500), respectively. Additionally, the presence of elements in the surface of polynuclear WCO capsules was evaluated by SEM through energy dispersive X-ray spectroscopy (EDX Bruker Quantax 100) for semi-quantitative determinations. Encapsulation efficiency of the WCO capsules was also quantified by a chemical procedure based on Guadarrama-Lezama et al. [10]. Bulk density and uniaxial compressive strength (at 20 °C and loading rate 0.2 mm/min) of the capsules were measured by the test method B of ASTM D792-13 [11] and ASTM D695-02a [12], respectively. FTIR-ATR of the Waste Cooking Oil (WCO) and Virgin Cooking Oil (VCO) was recorded in a Perkin Elmer Spectrum Two spectrometer between 400 and 4000 cm⁻¹ (20 Scans at 2 cm⁻¹). TGA-DTG of WCO was carried out between ambient and 600 °C at 10 °C/min in N₂ (10 mL/min) in a TA Tech Q50 thermobalance.

Results and discussion

Figure 2 presents the main results of experimental characterization of the WCO capsules. Statistical size analysis of 100 WCO capsules registered an average size of 1.649 mm (SD=0.145 mm), with a spherical and uniform geometry (Figure 2a). These capsules presented an encapsulation efficiency of WCO close to 90%. SEM-EDS observations (Figure 2d) proved that WCO capsules reveal a polynuclear structure on their surface (Figure 2b and c) with an element

composition of Ca (73%) and Na (27%), as result of the materials used for the synthesis of porous Ca-alginate matrix structure in the presence of divalent calcium cations (Ca^{2+}) allowing that the oil-in-alginate can be cross-linked.

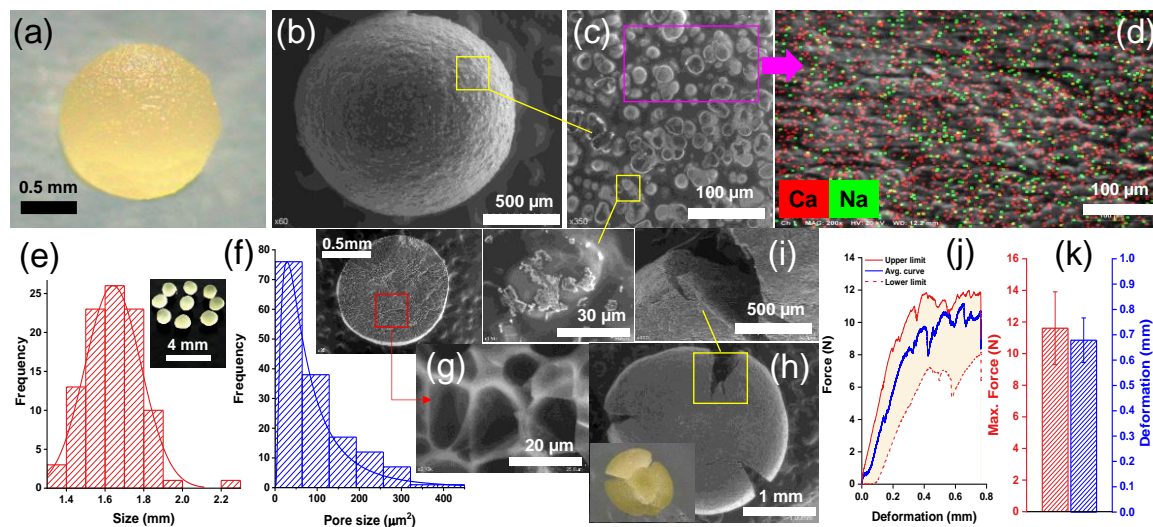


Figure 2. Experimental characterization of WCO capsules: (a) Optical image of capsule; (b) SEM image of capsule; (c) SEM detail image of polynuclear surface structure of capsule; (d) SEM-EDS observation on the capsule surface; (e) Frequency histogram of the size of capsules with Normal fitting; (f) Frequency histogram of the pore size of internal structure of capsules with Log-normal fitting; (g) SEM image of the multi-cavity (egg-box) structure into capsules; (h) SEM image of an individual broken capsule by uniaxial compression; (i) Detail by SEM image of the fracture type in the broken capsule; (j) Force and deformation average curves of the compression tests; and (k) Average values of the max. compression force and deformation.

The distribution of WCO capsule size is shown by the frequency histogram in Figure 2e, that proves the capsule size can be fitted to the Normal probability distribution (P-value 0.405 given by A-D test). Conversely, Figure 2f shows the pore size distribution of the internal multicavities of the WCO capsules. The frequency histogram proves that the capsule pore size can be fitted to the Log-normal probability distribution function (P-value 0.159 given by A-D test), with an individual average pore size of $94.58 \mu\text{m}^2$ ($\text{SD}=82,20 \mu\text{m}^2$). Additionally, Figures 2h and i show SEM images of an individual capsule and the fracture type on a capsule broken by effect of compression, respectively. This result proves that WCO capsules can break and partially release the encapsulated WCO by effect of an external trigger. Besides, biopolymeric matrix presented an elastic-plastic mechanical behaviour with breakage in plastic deformation around the propagating cracks, see Figures 2i and j. WCO capsules registered an average maximum compressive force of 11.6 N ($\text{SD}=2.3 \text{ N}$) at an average maximum deformation of 0.7 mm ($\text{SD}=0.1 \text{ mm}$), Figure 2k. This result proves that polynuclear WCO capsules can resist the asphalt manufacturing process (i.e., mixing and compaction) based on the results published by Garcia et al. [1] and Norambuena-Contreras et al. [7] (minimum compressive strength of capsules 10 N); hence, WCO capsules can be used as a resistant encapsulated rejuvenator for asphalt mixture self-healing.

Furthermore, cooking and frying activities involve the oxidation of oils with the consequent loss of unsaturation through bond breaking, additions, substitution and other well-documented reactions [13]; thus, a significant degradation of the oil is expected after the heating process. Nevertheless, the FTIR spectra recorded for both VCO and WCO are very similar (see Figure 3a). The disappearance of the $-\text{OH}$ stretching characteristic band, at 3350

cm^{-1} , in the WCO could be related to the absence of mono and diglycerides. Meanwhile, the band found at 725 cm^{-1} is typical of $-\text{CH}_2$ rocking, while those at 1100 cm^{-1} and 1250 cm^{-1} corresponds to the C-O stretching vibrations, commonly found in ethers [14]. The vibration of C-H bond in methyl groups are confirmed by the absorption bands at 1370 cm^{-1} and 1450 cm^{-1} , respectively. The strong signal at 1740 cm^{-1} is typical of carbonyl groups (C=O) in saturated aliphatic ethers, while the bands between 2850 and 3015 cm^{-1} , corresponds to symmetrical and non-symmetrical C-H stretching in methyl ($-\text{CH}_3$) and methylene ($-\text{CH}_2$) groups. The similarities in intensity, position and nature of functional groups identified by their characteristic absorption bands in both spectra (VCO and WCO), suggest that waste cooking oil is thermally stable, which supports its use as encapsulated rejuvenating agent in asphalt materials usually manufactured at temperature $160 \text{ }^\circ\text{C}$.

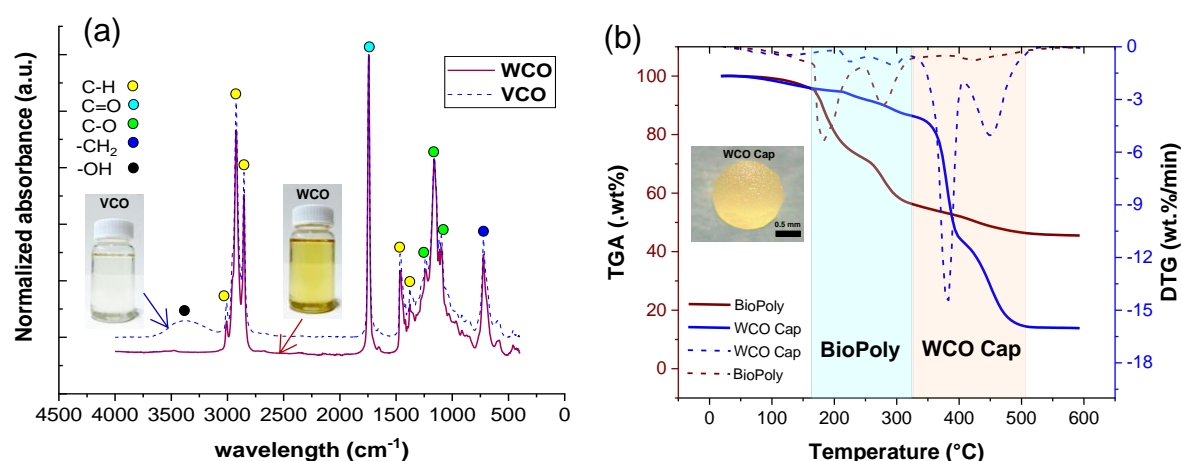


Figure 3. Results of chemical and thermal characterization of rejuvenating agents, capsule and biopolymer: (a) Normalized infrared spectra of waste and virgin cooking oil; and (b) TGA results of biopolymer (BioPoly) and WCO capsules (WCO Cap).

Additionally, the thermal stability of the biopolymer (BioPoly) used for the preparation of the WCO capsules was confirmed by the TGA curve in Figure 3b. Indeed, decomposition at 160°C -temperature of asphalt mixture preparation-, was nearly 5% for the polymer and this did not change when the WCO was encapsulated within the capsules. Two major DTG peaks corresponding to 12% and 32% wt. loss were identified for the BioPoly and, remained (with lower intensity) in the WCO Cap. The first peak at 183°C is associated to dehydration reactions in the alginate; while the second one, at 278°C , corresponds to the degradation of CaCO_3 . The weight loss below $300 \text{ }^\circ\text{C}$ is caused by the loss of hydroxyl groups in the alginate and above this temperature decarboxylation reactions take place forming CO_2 as main product [15]. The relative position of the TGA curve for the WCO capsule indicates a higher thermal stability caused by the presence of the oil encapsulated in the capsule. In fact, the first decomposition phase ends at $320 \text{ }^\circ\text{C}$ and is associated to the capsule. Above this temperature the oil decomposes according a two-stage mechanism, the first ($383 \text{ }^\circ\text{C}$) corresponding to scissoring and breakage of C-H and C-O bonds and, the second (ending at $500 \text{ }^\circ\text{C}$) corresponds to cross-linking and carbonization. Results of TGA are in line with that found in the FTIR and allows suggesting that encapsulation leads to a thermally stable material with potential to be used for asphalt self-healing applications. To prove this, healing efficiency of WCO was quantified in cracked ($200 \text{ }\mu\text{m}$ crack-width) bitumen test samples with dimensions $20 \times 20 \times 0.5 \text{ mm}$ by an inverted fluorescence microscopy (ICOE IV 5100 FL). The crack closure by WCO diffusion (oil amount 2 mg) over time was recorded taking microscopy images during a time of 85 min . Healing efficiency measured in %, was quantified as the relationship between the avg. partial

crack-width at a specific time and the avg. initial crack-width, both measured in μm . Main results show that WCO can be diffused in the bitumen samples reducing their viscosity and hence healing the open micro-cracks with a maximum healing efficiency of 70% at 85 min.

Conclusions

Based on the results, the following conclusions have been obtained: 1) Encapsulation process by simple extrusion-dripping allowed to obtain alginate-based WCO capsules with an adequate encapsulation efficiency and multicavity morphology for asphalt self-healing application. 2) WCO polynuclear capsules and their components presented a good thermal stability and physical-chemical properties. TGA and FTIR tests allows suggesting that encapsulation process leads to a thermally stable material with potential to be mixed within hot asphalt mixture with asphalt healing purposes. 3) Mechanical characterization proved that alginate-based WCO capsules can break and partially release the encapsulated WCO oil by effect of an external force trigger. 4) It was proven through transient oil-bitumen diffusion tests that the encapsulated rejuvenating agent WCO can be diffused in the bitumen test samples reducing their viscosity and hence healing micro-cracks present in the asphalt matrix.

Acknowledgment

The authors express their gratitude for the funding given by the National Research and Development Agency (ANID) through the Research Projects FONDECYT 1190027, FONDEQUIP EQMI170077 and CONICYT PIA/Apoyo CCTE 170007. Second author wishes to thank the financial support given by the University of Bío-Bío for his internal PhD scholarship granted. The authors extend their gratitude to Felipe Muñoz from LabMAT at UBB and Dr. Rodrigo Briones from CIPA-CONICYT Regional (GORE BIO-BIOR17A10003), for their technical support with some laboratory tests.

References

- [1] Gonzalez-Torre I, Norambuena-Contreras J. Recent advances on self-healing of bituminous materials by the action of encapsulated rejuvenators. *Construction and Building Materials* 2020 Vol 258 pp. 119568.
- [2] Airey GD. State of the art report on ageing test methods for bituminous pavement materials. *International Journal Pavement Engineering*. 2003 Vol 4(3) pp. 165-176.
- [3] Karlsson R, Isacson U. Investigations on bitumen rejuvenator diffusion and structural stability (with discussion). *Journal Association of Asphalt Paving Technology*. 2003 Vol 72 pp. 463–501.
- [4] Garcia A, Jelfs J, Austin CJ. Internal asphalt mixture rejuvenation using capsules *Construction and Building Materials*. 2015 Vol 101 pp. 309-316.
- [5] Su JF, Schlangen E. Synthesis and physicochemical properties of high compact microcapsules containing rejuvenator applied in asphalt. *Chemical Engineering Journal*. 2012 Vol 198-199 pp. 289-300.
- [6] Su JF, Qiu J, Schlangen E, Wang YY. Investigation the possibility of a new approach of using microcapsules containing waste cooking oil: In situ rejuvenation for aged bitumen. *Construction and Building Materials*. 2015 Vol. 74 pp. 83-92.
- [7] Norambuena-Contreras J, Yalcin E, Garcia A, Al-Mansoori T, Yilmaz M, Hudson-Griffiths R. Effect of mixing and ageing on the mechanical and self-healing properties of asphalt mixtures containing polymeric capsules. *Construction and Building Materials*. 2018 Vol. 175 pp. 254-266.
- [8] Norambuena-Contreras J, Arteaga-Perez LE, Guadarrama-Lezama AY, Briones R, Vivanco JF, Gonzalez-Torre I. Microencapsulated bio-based rejuvenators for the self-healing of bituminous materials. *Materials* 2020 Vol 13 pp.1446.
- [9] Xu S, Tabaković A, Liu X, Schlangen E. Calcium alginate capsules encapsulating rejuvenator as healing system for asphalt mastic, *Construction and Building Materials*. 2018 Vol. 169 pp. 379-387.
- [10] Guadarrama-Lezama AY, Dorantes-Alvarez L, Jaramillo-Flores ME, Pérez-Alonso C, Niranjana K, Gutiérrez-López GF, Alamilla-Beltrán L. Preparation and characterization of non-aqueous extracts from chilli (*Capsicum annum* L.) and their microencapsulates obtained by spray-drying. *Journal of Food Engineering*. 2012 Vol. 112(1-2) pp. 29-37.
- [11] ASTM D792-13, Standard Test Methods for Density and Specific Gravity (Relative Density) of Plastics by Displacement.
- [12] ASTM D695-02a, Standard Test Method for Compressive Properties of Rigid Plastics.

- [13] Rayhan B. Ahmed, Kamal Hossain, Waste cooking oil as an asphalt rejuvenator: A state-of-the-art review, *Construction and Building Materials*. 2020 Vol 230 116985.
- [14] A.E. Atabani, Sutha Shobana, M.N. Mohammed, Gediz Uğuz, Gopalakrishnan Kumar, Sundaram Arvindnarayan, Muhammad Aslam, Ala'a H. Al-Muhtaseb, Integrated valorization of waste cooking oil and spent coffee grounds for biodiesel production: Blending with higher alcohols, FT-IR, TGA, DSC and NMR characterizations. *Fuel*. 2019 Vol 244 pp. 419-430.
- [15] Zhao, W.; Qi, Y.; Wang, Y.; Xue, Y.; Xu, P.; Li, Z.; Li, Q. Morphology and Thermal Properties of Calcium Alginate/Reduced Graphene Oxide Composites. *Polymers* 2018, 10, 990.

Fracture of cementitious material containing spherical microcapsules

Shannon Guo, Mouna A. Reda, Samir E. Chidiac

Department of Civil Engineering, McMaster University, Hamilton, Ontario, L8S 4L8, Canada

Abstract

Cracks in cementitious material are unavoidable and are the root cause of most if not all concrete deterioration mechanisms. This is particularly detrimental in reinforced concrete, as cracks allow the ingress of deleterious ions, liquids and gases that cause corrosion and accelerate carbonation. In the pursuit for sustainable infrastructure, development of smart self-repairing material such as microcapsule-based self-healing concrete has become a topical research direction. However, the micro/meso-behaviour of concrete cracking in the vicinity of microcapsules has yet to be properly studied. As such, microcapsule material, geometry and quantity are not selected in a systematic manner to satisfy performance requirements.

This paper investigates the fracture mechanics of concrete containing spherical microcapsules, with a focus on the cracking mechanisms that occur in early age concrete and non-accidental cracking at a later age due to freeze/thaw, corrosion, etc. The healing effectiveness of embedded microcapsules during cracking is controlled by three mechanical properties: shell/matrix interfacial bond strength, shell strength, and shell to matrix stiffness ratio. Depending on these mechanical properties, a crack growing near a microcapsule may miss or hit the capsule, with a hit causing either successful rupturing of the shell, or crack deflection along the interface without shell rupture. An understanding of strength and stiffness compatibility between shell and matrix, and quantification of stresses developed in the concrete during cracking are necessary for microcapsule design. The developed methodology is applicable to other cracking mechanisms and can facilitate systematic material selection and microcapsule design for optimised healing output.

Introduction

Concrete at early age is particularly susceptible to cracking due to shrinkage being from drying, autogenous, etc. Cracks provide a pathway for gases, liquids and deleterious chemicals to infiltrate the concrete and undermine its structural integrity. Therefore, instantaneous self-healing of the crack openings in young concrete is pivotal for concrete durability.

Autogenous self-healing of cracks in concrete is plausible by embedding spherical capsules that contain healing agent. As cracks in concrete approach a capsule, it has been postulated that the capsule shell ruptures and releases the healing agent inside the crack. The self-healing potential and efficiency of concrete therefore depends on the success of the mechanical trigger. Accordingly, the healing effectiveness is significantly affected by the geometrical properties of the capsule and the mechanical properties and strength of the capsules and concrete [1]. Several authors proposed analytical models to study the fracture behaviour of a brittle matrix containing hollow capsules. The FEM models proposed in [2] and [3] revealed that shell rupture depends on the shell strength and brittleness and that debonding of the capsule is governed by the bond strength, geometry of the shell, and the strength and stiffness of the capsule relative to matrix. However, the sensitivity of the shell rupturing or debonding to variations in the geometry, strength and stiffness of the capsule and concrete was not studied which is fundamental for specifying the capsules range of properties that would be compatible with the design concrete. This study presents a robust analytical method to investigate the interaction between the capsules and young/matured concrete by means of

homogenization and multi-level stress analyses for determining the conditions that lead to the rupture and debonding of the capsules.

Methodology, basic assumptions, and theoretical analysis

The interaction between the microcapsules and concrete involves the determination of the state of stress and distribution in the vicinity of the capsules and the fracture energy of the cement at the interface between the concrete and capsule. The proposed micro/meso-model postulates that a) the crack path will intersect a capsule with two possible outcomes; the capsule either ruptures and releases the healing agent or the capsule debonds and stays intact, b) the capsules are dispersed and well-spaced, and c) the concrete possesses dilute distribution of cracks. Accordingly, homogenization approach is adopted to first represent the cracked concrete with an equivalent homogeneous matrix, then the interaction between the capsule and the equivalent homogeneous matrix is analyzed within the framework of continuum and fracture mechanics.

The methodology consists of three steps, as illustrated in Figure 12. By considering the RVE as a composite material consisting of cracked cement (intact cement with internal cracks) and dispersed capsules, the cracked cement is homogenized as an equivalent homogeneous matrix (Step 1). The original composite materials are treated as the homogeneous matrix containing dispersed capsules (Step 2). The interaction between capsules, cracks and cement is then simplified as an investigation for a single capsule in a homogeneous matrix subjected to far-field tensile stress σ^0 . For simplicity, only mono-sized spherical capsules are considered.

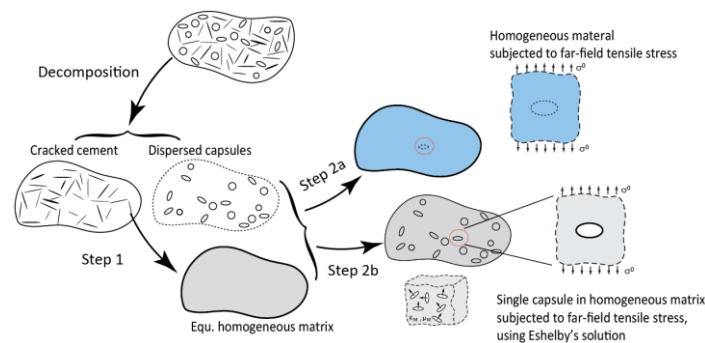


Figure 12. Decomposition of a concrete RVE containing cracks and capsules.

Step 1: Homogenization of cracked cement

Various methods have been developed to determine the effective properties of material containing random distribution of cracks with different geometries e.g., 2D circular holes, 2D straight cracks and 3D penny-shaped cracks. As an analogy for the volume fraction of defects, the crack density parameter $f_c = Na^3/V$ is introduced for 3D analysis of cracked cement, where N is the total number of cracks in a representative volume V , and a is a characteristic length of crack, which is generally selected as the half-length of a straight crack or the radius of a penny-shaped crack.

The crack density must be a low value with $f_c \ll 1$ to satisfy the assumption of dilute distribution of cracks. If the concrete is isotropic with dilute equal-sized penny-shaped cracks distributed in random orientations, then the equivalent matrix can be considered isotropic with the following elastic constants [4],

$$E_M = E_0 \left[1 + f_c \frac{16(1-\nu_0^2)(10-3\nu_0)}{45(2-\nu_0)} \right]^{-1}, \quad \mu_M = \mu_0 \left[1 + f_c \frac{32(1-\nu_0)(5-\nu_0)}{45(2-\nu_0)} \right]^{-1} \quad (9)$$

in which E , μ and ν are Young's modulus, shear modulus and Poisson's ratio of the constituents, with subscripts M and O referring to the equivalent matrix and uncracked cement, respectively.

Step 2: Analysis of dispersed capsules in an equivalent elastic matrix

The analysis is limited to dispersed uniform spherical capsules in the equivalent matrix developed in Step 1. The interaction between a single capsule with the surrounding matrix, shown in Figure 13a, is examined to determine the state of stress and deformation of the capsule. Figure 13b shows a spherical capsule of radius r in a homogeneous isotropic matrix with far-field uniaxial tensile stress σ_0 , as well as the local and global coordinate systems (Figure 2c).

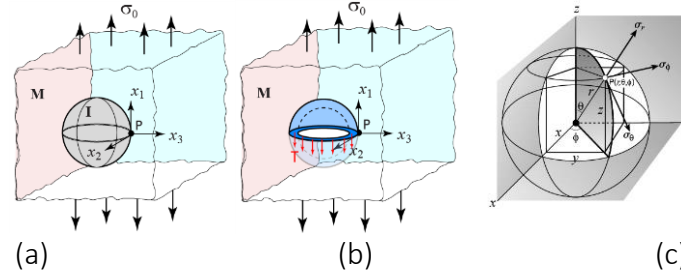


Figure 13. (a) A spherical inclusion (I) in a homogeneous isotropic matrix (M); (b) a capsule in homogeneous isotropic matrix; and (c) local and global coordinate systems [6].

The approach illustrated in Step 2a (Figure 12) will be followed to simplify the analysis, with proper consideration for relevant mechanisms of capsule rupture and debonding from concrete as follows:

- Perform homogenization operation for an equivalent matrix with embedded capsules to create an equivalent material that represents the effect of both cracks and capsules. The stiffness of the capsules is considered in the homogenization.
- Assuming the deformation of all capsules are compatible with the matrix with no interfacial debonding, calculate the tensile strain at the boundary of the capsule shell.
- Shell rupture occurs if the tensile strain exceeds the critical rupturing tensile strain of shell, or tensile stress exceeds the tensile strength of the shell. Thin-shell approximations are assumed such that stresses are uniformly distributed across the capsule shell thickness.
- Identify the condition for interfacial debonding via deformation analysis of the capsule.

For a homogeneous matrix with spherical capsules [4], the Mori-Tanaka model is adopted to calculate the effective elastic constants, where

$$K^* = K_M + c_I \frac{(K_I - K_M)K_M}{K_M + \alpha(1 - c_I)(K_I - K_M)}, \quad \mu^* = \mu_M + c_I \frac{(\mu_I - \mu_M)\mu_M}{\mu_M + \beta(1 - c_I)(\mu_I - \mu_M)}, \quad \nu^* = \frac{3K^* - 2\mu^*}{6K^* + 2\mu^*} \quad (10)$$

in which c_I is volume fraction of the capsules, K and μ are bulk modulus and shear modulus of the constituents, with subscripts M and I referring to equivalent matrix and inclusion, respectively. The two parameters α and β depend on Poisson's ratio ν_M of the matrix, where $\alpha = (1 + \nu_M)/[3(1 - \nu_M)]$ and $\beta = 2(4 - 5\nu_M)/[15(1 - \nu_M)]$. For uncracked concrete, $K_M = K_0$

and $\mu_M = \mu_0$. When the far-field stress is given, the tensile strain in x_1 direction can be estimated as $\varepsilon^* = \sigma_0 / E^*$ with $E^* = 9K^* \mu^* / (3K^* + \mu^*)$. The equivalent strain ε^* can be considered as maximum tensile strain on x_2 - x_3 plane.

As an approximation of shrinkage cracks, a crack opening analogy is used to evaluate crack-induced strain in the capsule shell. According to linear elastic fracture mechanics, for type-I cracking of circular or penny-shaped cracks, the maximum relative displacement between the crack surfaces is $\delta_{\max} = 2\xi\sigma_0 a / E$ with $\xi = 4(1 - \nu^2) / \pi$ [5]. A shrinkage crack with length $2a$ and

width δ_{max} can be considered equivalent to a penny-shaped crack of diameter $2a$ subjected to far-field tensile stress σ_0 . As a result, the tensile strain of the capsule shell can be estimated as

$$\varepsilon^* = \frac{\sigma_0}{E^*} = \frac{\delta_{max}}{2\xi a}, \quad \xi = \frac{4}{\pi}(1-\nu^{*2}) = \frac{4}{\pi} \left[1 - \left(\frac{3K^* - 2\mu^*}{6K^* + 2\mu^*} \right)^2 \right] \quad (11)$$

If the critical tensile strain of the shell at rupture is ε_{cr}^* , then $\varepsilon^* \geq \varepsilon_{cr}^*$ can be used as a criterion for capsule rupture due to elongation.

Likewise, a stress-based rupture criterion can be established by examining the stresses in the capsule shell. Referring to Figure 13(b), based on the assumption of strain compatibility used in the process of homogenization, the local stress of the capsule in the x_3 -direction on the x_1 - x_2 plane is $E_I \varepsilon^*$. The rupture of the shell wall occurs when $\sigma_{shell} \geq f_{shell}^T$, where

$$E_I \frac{\delta_{max}}{2\xi a} (\pi r^2) \geq f_{shell} (2\pi r t), \quad E_I \frac{\delta_{max}}{a} \frac{r}{t} \geq 4\xi f_{shell} \quad (12)$$

where r is the radius of the capsule, f_{shell}^T and t are the tensile strength and the thickness of the shell, respectively. It should be noted that E_I is the elastic modulus of the hollow capsule, which is lower than the elastic modulus of the capsule shell material. The tensile stress in the matrix near the interface between the matrix and the shell is $\sigma_{max} = K\sigma_0$, in which the intensity factor K depends on the geometry surrounding the crack tip and on a combination of E_0 , ν_0 , E_I and ν_I [6]. If σ_{max} is found less than the tensile strength of concrete, it is assumed that no cracking will occur in the matrix near the interface.

Next, the condition of interfacial debonding on the shell-cement interface is examined. For composite materials, additional stresses develop on the interface of different constituents due to incompatible material properties. At the local level for the capsule and the matrix (Figure 13(b)), the following relations hold for perfectly bonded interface at Point P: $\sigma_{i3}^I = \sigma_{i3}^*$ ($i=1,2,3$), $\varepsilon_{11}^I = \varepsilon_{11}^*$, $\varepsilon_{12}^I = \varepsilon_{12}^*$ and $\varepsilon_{22}^I = \varepsilon_{22}^M$. An analysis based on the theory of elasticity yields the following strains in the inclusion [4]

$$\varepsilon_{i3}^I = \frac{\mu^*}{\mu^I} \varepsilon_{i3}^* \quad (i=1,2), \quad \varepsilon_{33}^I = \frac{1}{\lambda^I + 2\mu^I} \left[(\lambda^* + 2\mu^*) \varepsilon_{33}^* + (\lambda^* - \lambda^I) (\varepsilon_{11}^* + \varepsilon_{22}^*) \right] \quad (13)$$

where $\lambda = \mu(E - 2\mu)/(2\mu - E)$ is Lamé's constants, with the superscripts $*$ and I referring to the cracked matrix and capsule, respectively. Under uniaxial tension, one expects $\varepsilon_{i3}^I = \varepsilon_{i3}^* = 0$. Moreover, it is reasonable to assume $\varepsilon_{11}^* = \sigma_0 / E^*$ and $\varepsilon_{22}^* = \varepsilon_{33}^* = -\nu^* \varepsilon_{11}^* = -\nu^* \sigma_0 / E^*$. It follows that

$$\varepsilon_{33}^I = \frac{1}{\lambda^I + 2\mu^I} \left[-\nu^* (\lambda^* + 2\mu^*) + (\lambda^* - \lambda^I) (1 - \nu^*) \right] \frac{\sigma_0}{E^*} \quad (14)$$

The interfacial normal stress is then determined as $\sigma_{33}^I = \lambda^I \varepsilon_v^I + 2\mu^I \varepsilon_{33}^I$, in which ε_v^I is the volumetric strain. Interfacial debonding occurs when σ_{33}^I exceeds the bonding strength of the capsule. Other investigations that provide more rigorous calculation of local stresses, such as Eshelby's solution [4] illustrated in Step 2b (Figure 12), are being considered.

Preliminary results and discussion

Preliminary results have been calculated for early age concrete properties from 6 hours to 28 days [7]. It should be noted no sensitivity analysis is included in this preliminary work. It is assumed that the matrix contains a dilute distribution of cracks with opening-to-depth ratio of $\delta_{max}/a = 0.1$ and 0.3 . Inclusions are modeled using typical polymer capsule properties: shell material $E_{shell} = 3.0 \text{ GPa}$, $\nu_{shell} = 0.3$; hollow capsule $E_{cap} = E_{shell}/2.5$, $\nu_{capsule} = 0.35$, $r_{capsule} = 50 \mu\text{m}$, $t_{capsule} = 5 \mu\text{m}$. Inclusions are assumed to have material strengths of typical polymer

microcapsules, with tensile strength in the range of 10-30 MPa and rupture strength up to 1.5 MPa [8]. Experimental studies show that bond strength increases with hydration as the interfacial zone densifies [9], thus the interfacial bond strength $f_{interface}$ is assumed to be approximately tensile strength of concrete. It is expected that the capsule will rupture when tensile stresses in the shell exceeds tensile strength of the shell, while debonding occurs when interfacial stress exceeds interfacial bond strength.

Table 1 presents the effect of concrete properties at early age and crack opening-to-depth ratio on the tensile stress in the capsule shell and interfacial stress at the shell-matrix boundary assuming a perfectly bonded interface. Shell stresses are significantly larger than typical shell strengths, indicating that capsules may easily be ruptured. However, as the concrete rate of elastic modulus development is faster than the rate of strength gain, there is insufficient interfacial bond strength to prevent debonding. This presents two problems that have not been addressed in existing studies:

1. The stiffness of the capsule relative to the matrix strongly affects stresses in the vicinity of the crack and capsule [10]. In the case of a compliant inclusion in a stiff matrix, high stress concentrations can develop in the inclusion due to elastic incompatibility. Stresses are further magnified due to the thin shell wall thickness. Consequently, it may be possible for high stresses to develop in the shell due to shrinkage even when stresses in the concrete do not exceed its tensile strength. This would cause premature rupture of the shell, which depletes the healing agent before crack formation.
2. Cracking due to shrinkage is predominant in early age concrete, and these cracks are detrimental to the durability of concrete structures. As such, successful shell rupture and release of the healing agent is critical at early age. However, with the slow rate of strength gain in early age concrete, cracks may propagate along the weaker interface instead of travelling through the capsule shell, leaving the capsule intact and rendering it unable to release the healing agent.

Table 1. Tensile stresses developed in shell and at shell-matrix interface [7].

Age (h)	E_0 (GPa)	ν_0	σ_{shell} (MPa)		$\sigma_{interface}$ (MPa)		$f_{interface}$ (MPa)	Failure Mode		
			$\delta/a =$	$\delta/a =$	$\delta/a =$	$\delta/a =$		$\delta/a =$	$\delta/a =$	
			0.1	0.3	0.1	0.3		0.1	0.3	
6	15.38	0.1440	159.55	478.64	1.07	3.22	0.83	Debond	Debond	
24	31.19	0.1886	161.35	484.06	1.22	3.66	3.32	Rupture	Debond	
72	35.42	0.1834	161.12	483.35	1.20	3.61	4.19	Rupture	Rupture	
168	36.21	0.1832	161.11	483.32	1.20	3.60	4.34	Rupture	Rupture	
672	40.29	0.1902	161.43	484.30	1.23	3.68	5.30	Rupture	Rupture	

Conclusions

A multiple level homogenization developed to analyze state of stress embedded spherical hollow inclusions in cracked concrete matrix revealed the importance of concrete maturity on the failure mode. These preliminary results show that material incompatibility between concrete and capsule increases stress concentrations in shell and interfaces. In early age concrete, the slower strength gain in comparison to the stiffness gain results in the debonding of capsules. Moreover, the opening-to-depth ratio of cracks is shown to influence the failure mode. Therefore, the efficiency of self healing depends on the properties of the capsules and the evolving properties of maturing concrete.

References

- [1] Guo S, Chidiac SE. Self-healing concrete: A critical review. CSCE Annual Conf., Laval, ON, Canada, June 12-15, 2019.

- [2] Li W, Jiang Z, Yang Z. Crack extension and possibility of debonding in encapsulation-based self-healing materials. *Materials*. 2017 Vol 10 pp. 589.
- [3] Gilabert FA, Garoz D, Van Paepegem W. Stress concentrations and bonding strength in encapsulation-based self-healing materials. *Materials and Design*. 2015 Vol 67 pp. 28-41.
- [4] Gross D, Seelig T. *Fracture mechanics, with an introduction to micromechanics*. (Springer-Verlag Berlin Heidelberg 2011).
- [5] Kundu T. *Fundamentals of fracture mechanics*. (Taylor & Francis Group 2008).
- [6] Murakami Y. *Theory of elasticity and stress concentration*. (Johns Wiley & Sons, Inc. 2007)
- [7] Oluokun F, Burdette E, Deatherage J. Rates of development of physical properties of concrete at early ages. *Transportation Research Record*. 1990 Vol 1284 pp. 16-22.
- [8] Reda MA, Guo S, Chidiac SE. Challenges of Self-Healing Concrete Application. *Resilient Materials 4 Life 2020 Int. Conf. (RM4L2020)*, Cambridge, UK, Sept. 14-17, 2020.
- [9] Chan Y, Li V. Age effect on the characteristics of fibre/cement interfacial properties. *Journal of Materials Science*. 1997 Vol 32 pp. 5287-5292.
- [10] White S, Sottos N, Geubelle P, Moore JS, Kessler MR, Sriram SR, Brown EN, Viswanathan S. Autonomic healing of polymer composites. *Nature*. 2001 Vol 409 pp. 794-797.

Field investigation on the performance of smart aggregates for self-healing of concrete in different curing regimes

Rami Alghamri, Abir Al-Tabbaa

Department of Civil Engineering, University of Cambridge, Cambridge, CB2 1PZ, UK

Abstract

Concrete does intrinsically possess some self-healing capacity and is able to heal microcracks autogenously. This self-healing capability is very limited and therefore researchers have attempted to improve upon it by engineering different autonomous self-healing materials and techniques. The aggregates as the major constituent of any concrete mix have the potential to significantly exploit in developing the self-healing systems. However, this has not been extensively researched. In a previous work carried out by the University of Cambridge for Materials for Life project (M4L), using the aggregates as carriers for the self-healing agents in concrete has been proposed. Lightweight aggregates (LWA) with a diameter range of 4–8 mm were impregnated with a sodium silicate solution as a potential self-healing agent. Concrete specimens containing the impregnated LWA showed ~ 80% recovery of the pre-cracking strength and 50% reduction of the water sorptivity after the healing period. However, this work has been carried out on a laboratory scale. Therefore, this work investigates the use of the developed smart aggregates for a large-scale concrete field application in different curing regimes: ambient, freshwater, saline water and wastewater. Two different types of LWA have been examined, Lytag particles with 4-8mm size and crushed pumice with 2.36-4.75mm. These aggregates have been impregnated with two different potential self-healing agent: sodium silicate and calcium nitrate. The self-healing performance of the impregnated LWA in the different curing regimes has been evaluated. Further investigations on the microstructure of the developed self-healing materials in the cracked section in the different curing regimes will be carried out.

Introduction

Concrete does intrinsically possess some self-healing capacity and is able to heal microcracks autogenously [1–3]. This self-healing capability is very limited and therefore researchers have attempted to improve upon it by engineering different autonomous self-healing materials and techniques [3,4]. Besides, aggregates as the major constituent of any concrete mix have the potential to significantly exploit in developing the self-healing systems. However, this has not been extensively researched.

In a previous work carried out by the University of Cambridge for Materials for Life project (M4L), aggregates have been proposed as carriers for the self-healing agents in concrete [5]. Lightweight aggregates (LWA) with a diameter range of 4–8 mm were impregnated with a sodium silicate solution as a potential self-healing agent. Concrete specimens containing the impregnated LWA showed ~ 80% recovery of the pre-cracking strength and 50% reduction of the water sorptivity after the healing period. However, this work has been carried out on a laboratory scale. Therefore, this work investigates the use of LWA impregnated with different liquid self-healing agents for a large-scale concrete field application in three different curing regimes: ambient, freshwater and saline water. Crushed pumice with 2-9.5 mm size have been examined. They have been impregnated with two different potential self-healing agent: sodium silicate and calcium nitrate.

Materials and Methods

Impregnated LWA system: Crushed pumice LWA imported from Yali Island, Greece were investigated as carriers for liquid self-healing agents using the vacuum impregnation technique. The properties of Pumice LWA are summarised in Table 1. The LWA were impregnated by two different solutions: (1) sodium silicate (40% wt in H₂O) with Mw= 122.06 (gmol⁻¹), Density at 20 °C = 1.39 g/ml, and pH= 12.5, and (2) calcium nitrate tetrahydrate with Mw= 236.15 g/mol, water-solubility 1.293 g/l at 20 °C and pH=5.5-7.

The impregnated LWA were then protected in a coating shell. Polyvinyl alcohol (PVA), obtained from Fisher Scientific as a 98-98.8% hydrolysed powder with an average molecular weight of 146,000-186,000g/mol, were used as the main coating material. Preparation and coating of the impregnated LWA were carried out according to the procedure thoroughly explained in [5].

Table 1: Properties of Crushed pumice LWA used in this study as provided by the manufacturer.

LWA type	Grain size mm	Specific gravity Kg/m ³	Water absorption capacity	
			% by weight	% by volume
Pumice	2.36-4.75	1210	26.7	32.3

Concrete mixtures: The fine aggregates used in the concrete mixes are natural quartz sea sand with a grain size ≤ 2 mm. The effective water absorption, tested according to ASTM C128-01, is 0.4% by weight, with a specific gravity of 2630 kg/m³. The coarse aggregates are crushed dolomite of 2.36 mm < d < 9.5 mm. The effective water absorption, tested according to ASTM C127-01, is 1.5% by weight, with a specific gravity of 2700 kg/m³. Ordinary Portland cement (PII 42.5) were used. The specific surface area of the Portland cement, tested according to ASTM C204-00, is 0.323 m²/g.

Experimental procedure: In order to investigate the in-situ self-healing performance of the impregnated self-healing system, the aggregates were tested in real scale beams. Three concrete mixes with a designed compressive strength of 30 N/mm² were prepared for this purpose. The first mix is the control (CN) which containing LWA without any healing agents; in the other two mixes, the impregnated LWA replaced a third volume of the coarse aggregates. I-Pu(S) is a mix containing sodium silicate-impregnated pumice particles and I-Pu© is containing calcium nitrate-impregnated pumice particles.

For each mix, six reinforced concrete beams of 150 mm × 200 mm × 1000 mm were prepared. The reinforcement of the beams consists of two $\Phi 12$ reinforcement bars which are equally distributed into the tensile zone (Figure 1). After the concrete casting, all concrete beams will be subjected to membrane curing in order to prevent moisture loss. Seven days after concrete casting, they were demoulded. The concrete beams were subjected to three different curing regimes: ambient, freshwater, and seawater; two beams from each mix will be cured in each curing environment.

In order to create multiple cracks in the concrete beams, they will be loaded in four-point bending after 28 days of casting (Figure 2). The supports were positioned at the ends of the beam. To make sure that the exerted load is exactly the same for each loading roller and that the load increased at the same speed for both supporters, one jack was used and the force exerted by this jack was transmitted to both rollers by means of a metal beam. The total vertical and lateral displacements were measured by three LVDTs (Figure 2). To evaluate the sealing efficiency of cracks, the initial widths of all cracks developed in each beam were measured at five marked positions by using a handheld digital microscope.



Figure 1: Mixing and casting of the concrete beams

Images were taken once the beams were unloaded to measure the residual crack width and then the images will be taken every two weeks. The average value for the five readings will be taken to analyse the crack surfaces sealing with time. Similarly, the monitoring of the crack depth was carried out every two weeks by using the ultrasonic pulse velocity method. Further details about the experiment can be found in [5].



Figure 2: (Top) the setup of the four-point bending test, (Bottom) multiple cracks in a typical beam just after loading.

Results and discussion

The self-healing efficiency in the cracked concrete beams was evaluated by monitoring the evolution of crack closure. The widths of the produced cracks were varied between 0.2- 3 mm just after load removal. Preliminary results confirmed that crystal depositions can be observed in all beams. However, the beams of I-Pu(S) and I-Pu(C) cured in water and saline water had more fillings at the crack faces; insomuch some cracks were sealed completely within 28 days (Figure 3).

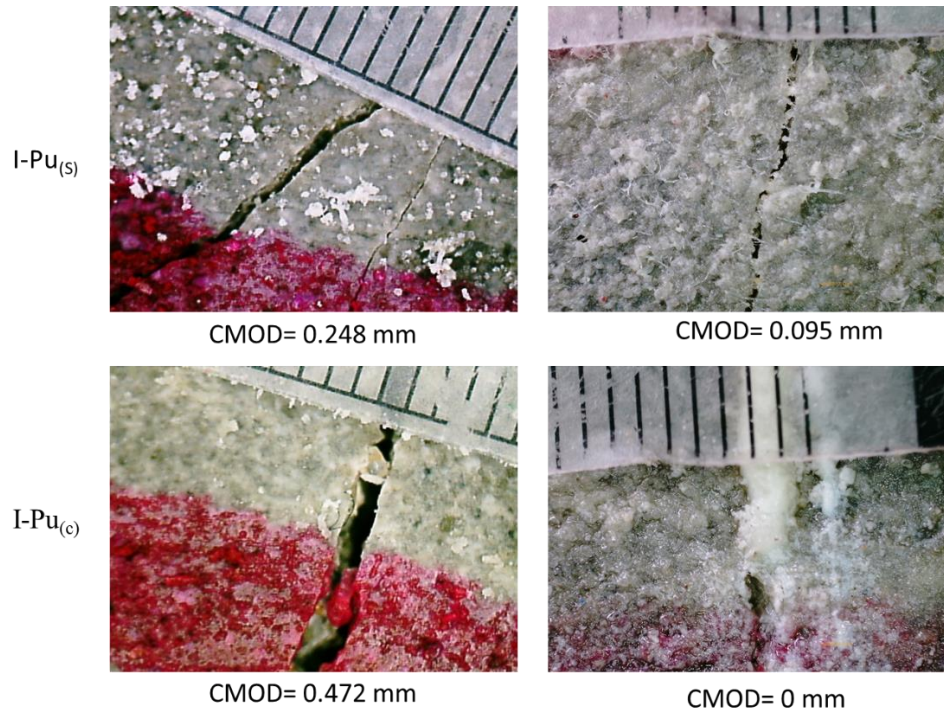


Figure 3: Representative microscopic images of the crack surfaces immediately after inducing the cracks and after cured in seawater for 28 days

As the microscopic images can provide evidence of only the sealing process at the crack surfaces, ultrasonic monitoring was used to evaluate the sealing inside the cracks. The crack depth was measured according to the wave velocity and the propagation path. As the crack plugs with the depositions and fillings, the time of the ultrasonic waves reduces [4]. The beams containing the impregnated LWA exhibited a significant decrease in the crack depth with time particularly the beams cured in freshwater and saline water as can be seen in Figure 4. As stated in [6], the self-healing processes are influenced significantly by the environments. Therefore, the healing mechanisms of the sodium silicate and calcium nitrate in the different curing regimes will be investigated in future work.

Conclusion

It could be concluded here that this work presented a successful attempt to scale up self-healing concrete containing impregnated LWA. The preliminary results showed a promising evolution of crack depth and surface width closure within 28 days. Further investigations will be carried out to evaluate the healing process in different environments.

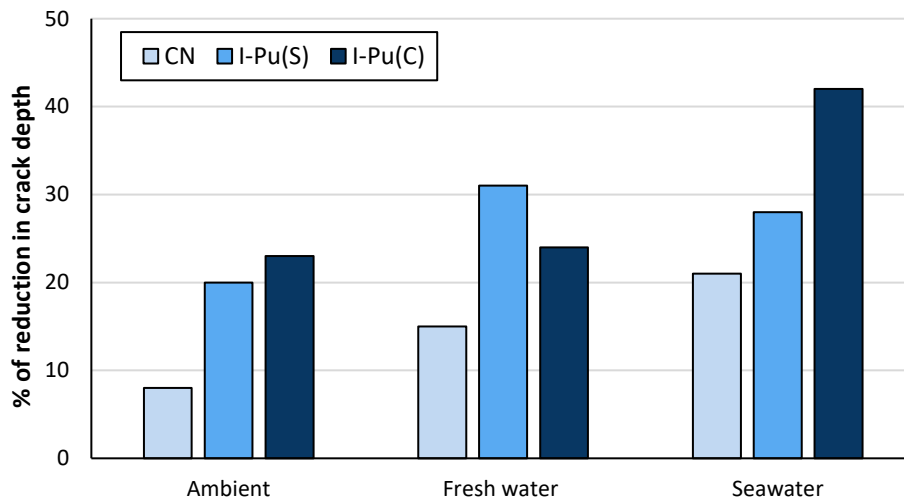


Figure 4: Reduction in the crack depth of typical beams of each mix after 28 days healing period.

Acknowledgement

The support of the fellowship for the first author from the Yousef Jameel Foundation is gratefully acknowledged. Support from the UK Engineering and Physical Sciences Research Council (EPSRC) for the Resilient Materials for Life (RM4L) programme grant (EP/P02081X/1) is also gratefully acknowledged.

References

- [1] K. Lauer and F. Slate, "Autogenous Healing of Cement Paste," *ACI J. Proc.*, vol. 52, no. 6, pp. 1083–1098, 1956.
- [2] C. Edvardsen, "Water permeability and autogenous healing of cracks in concrete," *ACI Mater. J.*, vol. 96, no. 4, pp. 448–454, 1999.
- [3] E. Schlangen and C. Joseph, *Self-Healing Processes in Concrete*. 2009.
- [4] D. Rooij, M. R., and E. Schlangen, "Self-healing phenomena in cement-based materials-State-of-the-Art report of RILEM Technical Committee," 2011.
- [5] R. Alghamri, A. Kanellopoulos, and A. Al-Tabbaa, "Impregnation and encapsulation of lightweight aggregates for self-healing concrete," *Constr. Build. Mater.*, vol. 124, pp. 910–921, 2016.
- [6] H. Huang and G. Ye, "Self-healing of cracks in cement paste affected by additional Ca²⁺ ions in the healing agent," *J. Intell. Mater. Syst. Struct.*, vol. 26, no. 3, pp. 309–320, 2015.

Session 5 Bacteria and microorganisms for civil engineering

Chair: Dr Michael Harbottle

1104 *Makita et al.* Microorganisms inhabiting concrete in the marine environment

1145 *Souid et al.* Microbial characterization for bio self-healing concrete applications

1191 *Minto et al.* Micro-Scale Processes in Microbially Induced Carbonate Precipitation

1171 *Reeksting et al.* Calcite precipitation by environmental bacteria as a method to improve durability of cementitious materials

1124 *Heriberto et al.* Calcium carbonate precipitation as function of alkaliphilic bacteria development

Microorganisms inhabiting concrete in the marine environment

Hiroko Makita¹, Keisuke Takahashi², Mari Kobayashi², Makoto Sugimura³

1: Tokyo University of Marine Science and Technology, Tokyo, Japan

2: UBE Industries, Ltd., Yamaguchi, Japan

3: Enoshima Aquarium, Kanagawa, Japan

Abstract

Recently establishment of marine infrastructure has attracted a lot of attention, such as facilities of offshore oil drilling, wind and tidal power generation. Cement could be utilized as a base material to construct the facilities. Authors have reported that hardened cement deteriorated drastically due to water infiltration and calcium leaching after one and half years exposure at deep sea conditions, and have focused on in-situ healing methods by the ability of microbes living at the deep sea areas. However, there is less study on the habitation of microbes in cementitious substance under the deep sea conditions. In order to simulate microbial activity under the deep sea conditions at a laboratory scale, a natural water tank where sea water flowing directly from natural shallow sea water near Enoshima aquarium was set up. Some groups of microbes inhabit both in deep sea and shallow sea. Sea water in the water tank was maintained at 4 °C constant and out light into the water tank was blocked. Microbial community which preferred to inhabit in hardened Portland cement pastes was investigated by exposing the specimens in the natural sea water tank. Microbial community were identified by molecular phylogenetic analyses based on the V3-V4 regions of 16S rRNA gene sequenced by the MiSeq. Our result clearly demonstrated that specific microbes in the natural sea water preferred to grow in hardened Portland cement pastes, such as Actinobacteria and Firmicutes. Actions of the microbes inhabited in the hardened Portland cement on technological properties of cement specimens have been under investigation.

Introduction

Recently, the establishment of marine infrastructure such as offshore oil rigs, and wind/tidal power plants has been attracting considerable attention. Cement is often utilized as a base material for constructing such facilities. Previously, we reported that hardened cement deteriorated drastically due to water infiltration and calcium leaching after exposure of 1.5 years under natural deep-sea conditions [1]. That previous study focused on the changes in physicochemical properties of hardened cement specimens, but the influences of microbes on the cementitious substance under deep-sea conditions have not been investigated.

Microorganisms are found everywhere in the global environment. Extreme environments, which are not habitable for humans, can be ideal for some microorganisms. Even in low temperature, high pressure and dark environments as the deep sea, and/or in the extremely high pH environment inside the concrete, some microorganisms can live and thrive [2, 3]. These microorganisms might have positive or negative effects on cement-based concrete structure exposed on the sea floor. In this study, we hypothesized microbes living in marine environment would have *in-situ* healing effects on the concrete damaged from marine exposure. Microbial healing of concrete has been studied using organic mineral precursor compounds plus spore-forming alkaliphilic bacteria [4]. When moving microorganisms from one environment to another, however, they often do not function as expected. Thus, it would be more efficient to use microorganisms derived from the same environment where the concrete structures were exposed to. In order to investigate *in-situ* healing effects by microorganisms, preferential growth of microorganisms in hardened cement structure and

changes in chemical characteristics of the cement with organic substances under the natural seawater flowing condition were measured at low temperature.

Materials and methods

In order to simulate microbial activity under deep-sea conditions at a laboratory scale, a natural seawater tank where seawater flows directly from natural shallow ocean near Enoshima Aquarium was set up. Enoshima Aquarium is located facing Sagami Bay in Japan. The water tank shown in Figure 1 is equipped with a cooling device, a submersible pump, and a pH meter with thermometer. To mimic the deep-sea environment, the amount of seawater supplied to the tank was adjusted to maintain the temperature of seawater at 4 °C. Seawater in the tank (216 L) was replaced every 8 hours and light into the water tank was blocked out. There was little difference in ion concentration between the seawater used and standard seawater. Portland cement (PC) paste specimens with the size of $\phi 50 \times 100$ mm were prepared, and cured for 28 days under sealed conditions at 20 °C before immersion into the seawater tank. Yeast extract (YE) as an organic substance were added to cement in order to increase the microbial activity as microbial activity is generally poor at low temperature. The water to cement ratio of the specimens was 0.6. The amount of YE added was 0.25 wt.% or 1.0 wt.% to cement.

The immersion test using the water tank began on September 18th, 2018. The specimens were collected after 1, 2 and 3 months elapsed. Changes of precipitated hydrates and chemical compositions were determined by X-ray diffraction (XRD) and X-ray fluorescence (XRF) analyses. Section of 10 mm from the surface of the specimens were cut and dried by immersion in acetone, then grounded. XRD data were collected using a D2 PHASER 2nd Gen (Bruker AXS) in a $\theta-2\theta$ configuration, applying Cu-K α radiation ($\lambda=1.54 \text{ \AA}$) at 30 kV of voltage and 10 mA of intensity with steps of 0.02° and 2.4° per min. The specimens were scanned between 5° and 70° 2 θ . The software used for phase identification was TOPAS (Bruker AXS). XRF was measured according to JIS R 5202.

Microbial communities were identified by cutting, grinding and extracting DNA from the specimens surface, and by performing molecular phylogenetic analysis based on the V3-V4 region of the 16S rRNA gene sequenced by MiSeq (Illumina). Microorganisms in the seawater were also analyzed in the same manner for comparative purposes.

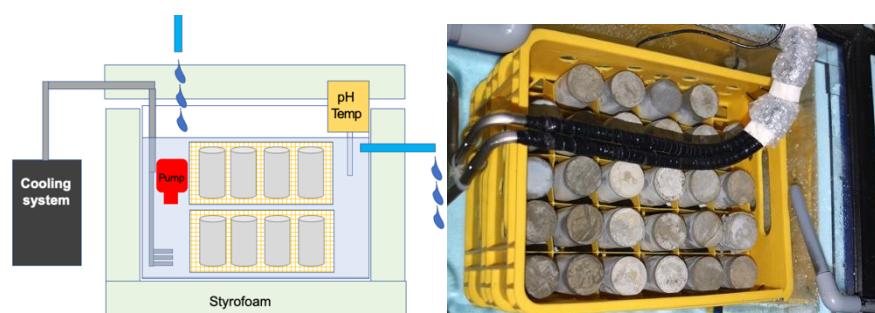


Figure 1. Schematic illustration and photo of overflowing seawater tank

Results and discussion

Figure 2 shows the visible changes in the specimens immersed in the seawater tank for 1, 2, and 3 months. No damage and cracks were observed in the specimen immersed for 1 month (A, B and C). However, after 2 months elapsed (D, E and F), both specimens with/without YE became mushy and the surface collapsed when touched by hand. Such deterioration progressed severely after 3 months (G, H and I). Little difference in the visible changes of the specimens existed between with and without YE.



Figure 2. Specimens exposed to the seawater for 1, 2 and 3 months;
 A, B and C: without YE, with 0.25 % of YE, and 1.0 % of YE after 1 month, respectively.
 D, E and F: without YE, with 0.25 % of YE, and 1.0 % of YE after 2 months, respectively.
 G, H and I: without YE, with 0.25 % of YE, and 1.0 % of YE after 3 months, respectively.

Results of the 16S rRNA gene analysis of the microbial community are summarized in Figure 3. The microbial community structure detected between specimens and the seawater were critically different. In particular, *Actinobacteria* and *Firmicutes* were virtually absent from the seawater. *Chloroflexi* was detected in the specimen immersed for 3 months but was hardly detected in seawater. These microorganisms are considered to live favorably in the environment of the cement surface. *Staphylococcus aureus* in the class *Firmicutes* which was detected in Figure 3 is known as a carbonate-forming bacterium [5]. The metabolic activity of these carbonate-forming bacterium can densify the microstructure of hardened cement and improve the durability of cement-based materials. Although *Firmicutes* member was detected in the specimen without YE after 3 months of immersion, the member was detected in the specimen with YE from 1 month of immersion. This result might indicate that YE accelerate the growth of *Firmicutes*. Sulfur-reducing bacteria in *Deltaproteobacteria* and *Nitrospira*, which are supposed to be associated with concrete degradation by their sulfur oxidation or sulfate reduction metabolism [6], were detected in seawater but not in the paste specimens.

Figure 4 shows XRD spectra in different 2θ ranges of the specimens without YE and with 0.25 % of YE immersed for 1, 2 and 3 months. These results indicate that the peaks of ettringite increase with an increase in immersion period. This increase in ettringite peaks occurred both in the specimens with and without YE. Table 1 lists chemical compositions of the specimens without YE and with 0.25% of YE immersed for 1, 2 and 3 months.

With a lengthened immersion period, the amount of calcium decreased and the amount of sulphate increased. The amount of magnesium decreased after an increase at 1 month. Changes in chemical compositions were not affected by the addition of YE.

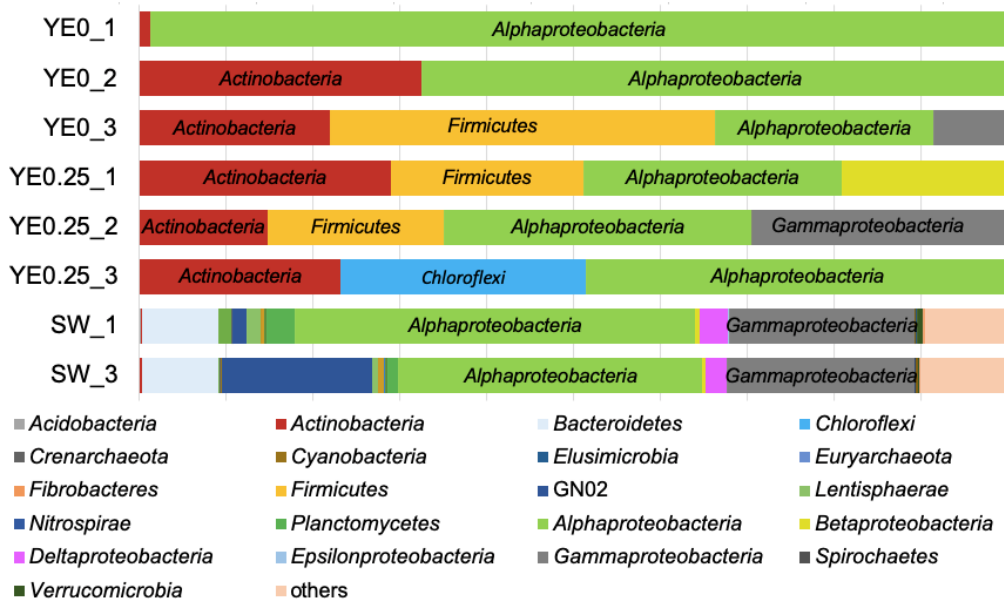


Figure 3. Relative abundances of microbial community in 16S rRNA data set from immersed specimens and seawater in the aquarium
 YE0: Specimens without YE, YE0.25: with 0.25% of YE, SW: seawater in the tank,
 _1: after 1 month, _2: after 2 months, _3: after 3months

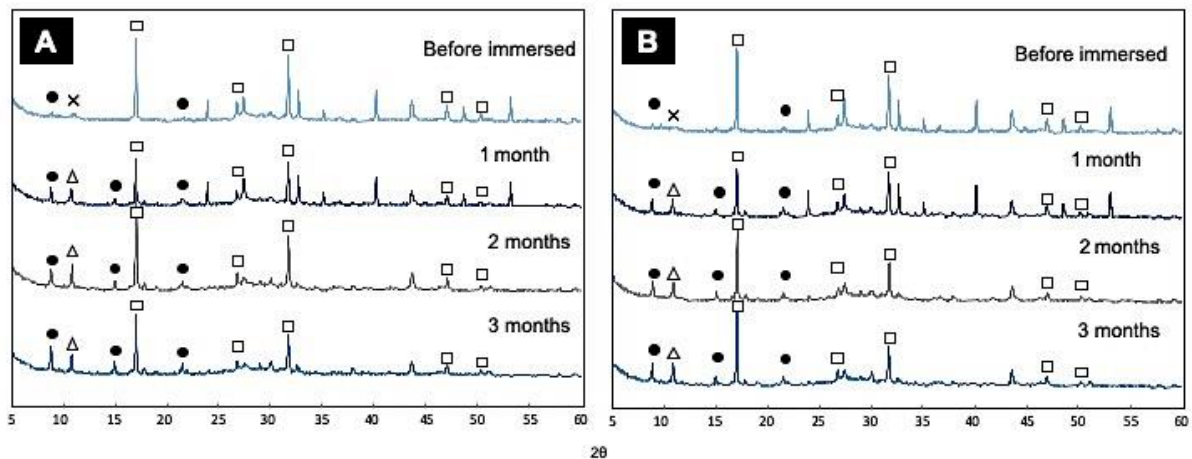


Figure 4. XRD of pastes without YE (A) and with 0.25 % of YE (B) immersed in the seawater tank at 4 °C,
 ● : Ettringite, □ : Calcium hydroxide (Portlandite), △ : Friedel's salt, × : Gypsum,
 Specimens before immersion and immersed for 1 month contain corundum as an internal standard.

Results shown in Table 1 imply that leaching of calcium hydroxide and calcium silicate hydrate could weaken the surface of the specimens. Ettringite, which induces crystallization stress and break down the weakened structure, is precipitated by infiltration of sulphate ions from seawater, decalcification and subsequent reaction with monosulphate [7]. The increase of ettringite precipitation shown in Figure 4 could enhance the surface damage shown in Figure 2. Magnesium also infiltrate to the specimens and forms magnesium hydroxide and magnesium silicate hydrates at the vicinity of the specimen surface [8]. Both magnesium-based hydrates are weak and easily scraped off, therefore the amount of magnesium decreased after an increase at 1 month as shown in Table 1.

Table 1. Chemical compositions of pastes without YE and with 0.25 % of YE immersed in seawater tank at 4 °C

	Immersion period (months)	Chemical compositions (mass%)				
		SiO ₂	CaO	MgO	Al ₂ O ₃	SO ₃
Without YE	0	13.68	45.64	0.74	3.42	1.77
	1	13.29	43.61	1.71	3.39	2.26
	2	14.29	44.99	0.81	3.85	2.65
	3	14.14	41.62	0.86	3.78	3.28
YE_0.25%	0	13.80	45.78	0.76	3.43	1.79
	1	13.19	42.86	2.13	3.37	2.35
	2	14.32	42.69	1.21	3.89	3.13
	3	14.52	44.02	0.86	3.92	3.14

However, the abovementioned severe deterioration was not observed in our previous study under the laboratory testing condition without replacement of seawater at low temperature [1]. In this study, the water flowing from natural sea is likely a dominant deteriorating factor as ion concentration at the interface between the specimen and seawater remains undersaturated to hydrates. Therefore, decalcification of calcium hydroxide and calcium silicate hydrate, precipitation of ettringite, magnesium hydroxide and magnesium silicate hydrate became more pronounced. Seawater current in the water tank could also accelerate the deterioration of the specimen surface. Figure 2 depicts that the upper part of the specimens at which seawater current was prevented by a fixture was not deteriorated compared to the middle and bottom parts of the specimens.

The difference in microbial inhabitation between without YE and with YE was clear, although less changes in precipitated hydrates and chemical compositions of immersed cement pastes with and without YE were observed. In this study, bulk samples collected from 10 mm from the specimen surface were utilized to XRD and XRF measurements. As microbial activity occurs in a micro scale and near microorganisms, micro scale measurement with wet specimens, which prevent to destroy microbial communities, is necessary.

Conclusion

The present study focused on the possibility of *in-situ* healing of cement paste specimens using microorganisms in natural seawater. Preferential inhabitation of specific microorganisms including a carbonate-forming bacterium in hardened cement pastes was observed. The difference in microbial inhabitation between without YE and with YE was clear although less changes in visual appearance, precipitated hydrates and chemical compositions of immersed cement pastes with and without YE were observed. The kinetics of chemical reaction such as decalcification and precipitation could be accelerated under low temperature and constant seawater replacement. Further research is necessary to isolate each microorganism observed in this study and investigate the effects of the microorganisms on hardened cement structure. Furthermore, the establishment of methods to evaluate the interaction between microorganisms and physicochemical properties of cement pastes warrants future efforts.

Acknowledgment

We would like to thank Dr. Yuichiro Kawabata at Port and Airport Research Institute for useful discussion. We are grateful to Prof. Takeji Takamura, Mr. Takahiro Sakamoto, Ms. Ryoko Mouri and Ms. Yuna Furukawa at Kanagawa Institute of Technology and deep-sea team at Enoshima

aquarium for their strong and heartfelt supports during this research. This work was partially supported by JSPS KAKENHI Grant Number JP18K04595.

References

- [1] Kobayashi M, Takahashi K, Yamanaka T, Makita H. Physicochemical properties and durability of cement-based materials on the deep sea floor. Proceedings of 15th International Congress on the Chemistry of Cement, Prague, 16–20 Sep. 2019
- [2] Birrien JL, Zeng X, Jebbar M, Cambon-Bonavita MA, Quérellou J, Oger P, Bienvenu N, Xiao X, Prieur D. *Pyrococcus yayanosii* sp. nov., an obligate piezophilic hyperthermophilic archaeon isolated from a deep-sea hydrothermal vent. *Int. J. Syst. Evol. Microbiol.* 2011 Vol 61, pp.2827-2831.
- [3] Takai, K., Moser, D. P., Onstott, T. C., Spoelstra, N., Pfiffner, S. M., Dohnalkova, A., Fredrickson, J. K. “*Alkaliphilus transvaalensis* gen. nov., sp. nov., an extremely alkaliphilic bacterium isolated from a deep South African gold mine”. *Int J Syst Evol Microbiol.* 2001 Vol 51 (Pt 4) pp.1245-56.
- [4] Jonkers HM and SchlangenE. Developemt of a bacteria-based self healing concrete. *Taylor Made Concrete Structures* (Taylor and Francis Press 2008).
- [5] Stabnikov V, Jian C, Ivanov V, Li Y. Halotolerant, alkaliphilic urease-producing bacteria from different climate zones and their application for biocementation of sand. *World J Microbiol Biotechnol.* 2013 Vol 29 pp.1453–1460. doi: 10.1007/s11274-013-1309-1.
- [6] Wang HL, Zhang J, Sun QL, Lian C, Sun L. A comparative study revealed first insights into the diversity and metabolisms of the microbial communities in the sediments of Pacmanus and Desmos hydrothermal fields. 2017 PLOS ONE Vol 12(7) e0181048. doi: 10.1371/journal.pone.0181048. eCollection 2017.
- [7] Jakobsen UH, De Weerd K, Geiker R. Elemental zonation in marine concrete. *Cement and Concrete Research.* 2016 Vol 85 pp.12-27.
- [8] De Weerd K and Justnes H. The effect of seawater on the phase assemblage of hydrated cement paste. *Cement and Concrete Composites.* 2015 Vol 55 pp.215–222.

Microbial characterization for bio self-healing concrete applications

Adam Souid¹, David Elliott², Omar Hamza¹

1: College of Engineering and Technology, University of Derby, Derby DE22 3AW, UK

2: Environmental Sustainability Research Centre, University of Derby, Derby DE22 1GB, UK

Abstract

Many of today's environmental problems, as well as their potential solutions, are intimately interwoven with the microbial component of the global ecosystem. The recent developments of microbial bio self-healing concrete technology were undoubtedly promoted by societal interests in environmental quality. Three principal groups of parameters can influence the mechanisms and the efficiencies of microbial self-healing concrete systems: self-healing agents, encapsulation techniques and micro-environmental conditions in and/or around the crack openings. The role of microorganisms embedded in cementitious matrix systems is to efficiently produce biogenic calcite to heal/seal the crack openings caused by mechanical, chemical and/or thermal actions.

This paper presents the characterization of the behaviour of three types of bacteria to precipitate calcium carbonate. The procedure of their application for bacterial self-healing cementitious mortar specimens at laboratory scale is validated by SEM measurements and EDX based elemental analyses. The outcomes of this research paper can contribute to increase the usefulness and the efficiency of the microbial approach applied to bio self-healing concrete technology.

Introduction

Numerous new practical applications of microbial self-healing concrete are emerging (e.g. [1] and [2]), which increase the need for innovative testing procedures and experimental approaches. These approaches are essential to assess the efficiency of this new biotechnology, for example through characterising the bacterial precipitation qualitatively and quantitatively during the autonomous healing under micro and macro-environmental conditions of the damaged structural elements. This paper aims at providing a novel approach of self-healing pilot tests of representative pre-damaged mortar elements under soil incubation conditions, representing the natural environments of significant (or parts of) infrastructures built underground e.g. tunnels, foundations of bridges, buildings, and dams. We investigated the effect of soil incubation to confirm if the self-healing process can be activated and then understand the corresponding mechanism. Mortar elements were impregnated with three bacterial strains, found naturally in the soil. A further novelty of this study lies in the approach used to pre-crack the specimens and produce small elements by using a low-cost method. The elements (produced in large quantities) allowed visual observation of the fractured bio mortar to validate the activation of bacterial self-healing after incubation stage within the fully saturation soil considered for the experiments. Characterization of bacterial precipitates on the crack-edges and cracks' cross-sections was inspected by the scanning electron microscope (SEM) and energy dispersive X-ray (EDX) analysis. The laboratory procedures (adopted in this study) will help elucidate the healing state developed in real scale damaged bio concrete substructures embedded within the ground.

Materials and Methods

The bio cementitious mortar was prepared by using Portland cement (CEM I 52.5 N) with a mixture of sand/cement = 3; calcium lactate (compressed capsules \approx 500-750 μ m)/cement =

2,5%; calcium acetate (powder)/cement = 2,5%; and bacterial spores' suspension water/cement = 0.45.

Three aerobic bacterial strains were used in this study: *Bacillus subtilis* (H50620/9), *Lysinibacillus sphaericus* (NCIMB 8218) and *Lysinibacillus sphaericus* (NCIMB 9370). After culturing according to [3], washing with sterile water a few times, spores' suspensions (1×10^9 CFU/ml) were prepared by using sterile distilled water then stored at 4 °C one week before the tests. Bacterial spores' suspension was directly added to the cementitious mixture to prepare three series of bacterial mortars.

Calcium salts cursors can affect qualitatively and quantitatively the bacterial self-healing. [4] and [5] have studied calcium salts effects on self-healing separately. A further novelty of this study lies in the investigation of the micro-impact by using multi-calcium cursors simultaneously in a mortar environment. Thus, calcium lactate was initially mixed with sand. Separately, calcium acetate was mixed with cement then added to sand and mixed well until homogenous product is obtained before adding bacterial suspension.

The specimens with geometries of 40x40x7 mm (30 bio mortar samples of each bacteria) were prepared (casted and vibrated) by using purpose-built moulds. After 20 hours of mortar casting, the specimens were demoulded and conserved under humid chambers for 24 hours then cured in water at 22 °C. After 28 days, the samples were cracked (Figures 1) and incubated under saturated sterilized soil. As soils are presenting numerous variables of conditions (microbial, chemical, mechanical and hydrological), saturated sterilized sand was chosen for this study. However, sand (granular soil) is considered as the simplest model of soil media embedding concrete infrastructures that can be studied by engineers.

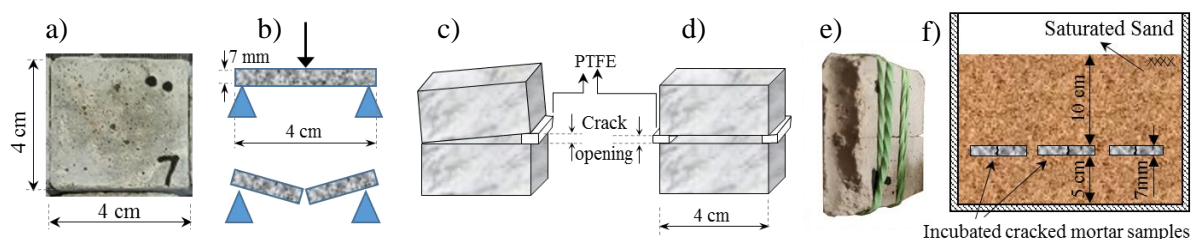


Figure 1. Process of cracks' creation and incubation of bacterial self-healing concrete samples a) Square bacterial concrete sample; b) Creation of fracture within the square concrete samples by applying a shock on the middle of span; c) and d) Crack creation models by PTFE-Teflon sheets simulating bending and direct tension cracks respectively ; e) Fractured samples tightly fastened by elastic bands before incubation; f) Bacterial cracked samples incubated in water saturated sand.

The cracks' openings are originally controlled utilizing amorphous PTFE-Teflon sheets of 100 μm and 250 μm as shown by Figures 1.c and 1.d simulating bending and direct tension effect respectively. The advantage of this method is the low-cost of standard cracks' creations without using mechanical engineering facilities that are not necessarily existing in biotechnology or in small research laboratories. The final cracks' widths are measured optically using image visualizer software "i.e. Paint" allowing to check the openings of cracks in pixels of photographed samples after step (e) of the Figure 1. After incubation, samples were dried then prepared to receive gold coating, deep observations of fractures' edges were further carried out by SEM after 6, 11, 25, 38 and 270 days. EDX spectroscopy was used to determine the chemical nature of the observed precipitation.

Results and Discussion

Table 1 and Figure 2 provide a summary of selected SEM micrographs' results of samples after 6, 11, 25, 38 and 270 days of soil incubation. The micrographs describe the micro cementitious environment of the bacterial precipitators and their precipitates. We can discuss the following points:

Bacterial precipitates and Micro-environment descriptions:

At 6 days: Mature bio vaterite crystals ($\approx 10\text{-}50\ \mu\text{m}$) were found in mortar pores. CH crystals ($\approx 10\text{-}30\ \mu\text{m}$) were observed thoroughly on CSH in addition to interesting small-like seeds crystals ($\approx 2\text{-}5\ \mu\text{m}$).

At 11 days: Clusters of biofilms and bio crystals ($\approx 10\text{-}30\ \mu\text{m}$) were observed in addition to multiple varieties of CaCO_3 based crystals like vaterite and aragonite within a micro-environment composed of CSH, a small amount of ettringite and portlandite (CH).

At 25 days: Bacterial imprints were shown on CSH with precipitated crystals around. Hollow structures of bacterial crystals were in progress. The amount of CH crystals were considerably reduced.

At 270 days: Bio self-healing formation inducing the bonding of separated fractures' lips of bio mortar specimens. Layers of mature bio crystals' depositions were observed.

Self-Healing development: Four major steps resume the bacterial self-healing development: 1) Basic crystals like-seeds production; 2) Bio minerals and clusters of crystals formation; 3) Bio micro crystalline sub-structures under construction; 4) Structured layers of bacterial self-healing construction.

Calcium cursors' effects: The mechanism of bacterial self-healing depends on the calcium cursor. The calcium acetate powder has higher solubility ($\approx 350\ \text{gr/L}$) than the compressed capsules of calcium lactate ($\approx 60\ \text{gr/L}$) at $20\ ^\circ\text{C}$.

So, while the calcium acetate was distributed homogeneously in the bio mortar, the compressed capsules (diameter $\approx 500\text{-}750\ \mu\text{m}$) of calcium lactate were distributed randomly in the bio mortar specimens. Moreover, the dissolved calcium lactate during mixing is localised essentially around their compressed granules within the bio mortar. Therefore, the effects of calcium acetate should be diffused on the cracks' cross-sections. Whereas the effects of calcium lactate were localized on and around the compressed granules of the calcium lactate initiating localized effective bacterial self-healing (similar to [6]) macro-sites (Figure 2.b, d and e) leading to the bonding of the fractured specimens. The efficiency of bacterial self-healing by using multi calcium cursors should be evaluated in future works. However, this study must be completed by another work to test the effect of each calcium salt separately in bio mortars by using the same methodology.

Bacterial effects: The SEM micrographs (Table 1) illustrate that the microstructure of the bacterial precipitates depends on bacterial strain and observation time. The bacterial crystalline structures are hollowed and can be different for the same bacteria within different phases of the microenvironment.

Soil effects: The soil compositions are expected to affect the efficiency results of bacterial self-healing (e.g. [7]). The essential point validated in this study is the affirmation that bacterial self-healing can be activated under sterile saturated granular soil (sand) regime. These points have an important impact on geotechnical and structural applications of underground infrastructures.

Conclusion

Images of calcium carbonate crystals examined under SEM were presented in Table 1 and Figure 2. The results reveal that the bacterial agents were activated and precipitated biominerals in the mortar cracks incubated within saturated sand. The SEM results conclude

that the microstructure of the bacterial precipitates depends on the bacterial strain, mortar formulation and observation time. The originality of this work lies in the proposed bio self-healing concrete pilot tests method using advantageous representative elements: 1) practical size of elements (which can be reproduced in large quantities and tested under controlled, repeatable conditions), 2) simple and controllable cracks creation by low-cost way using amorphous PTFE-Teflon sheets, 3) simultaneous usage of multi calcium salts to study the effects on the microstructures of bacterial precipitation in cementitious material incubated within soil environment. The development of bacterial precipitates and nucleation of effective healing site is validated by SEM and EDX investigations. The organic crystalline calcium carbonate-based structures, leading to effective self-healing macro sites, depend on the cementations micro-environment of the cracks' edge. Finally, the use of the methodology in academic and industrial studies is easy, simple and economic to reproduce and to investigate (possible extension to cylindrical models).

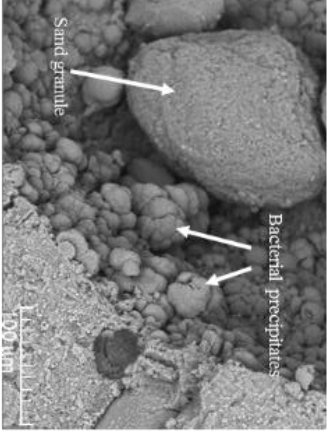
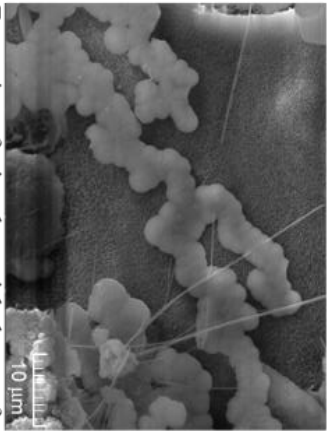
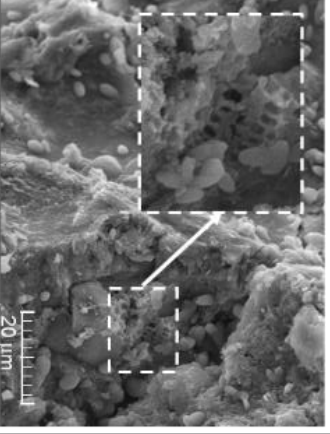
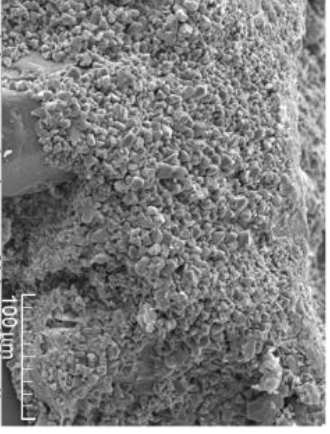
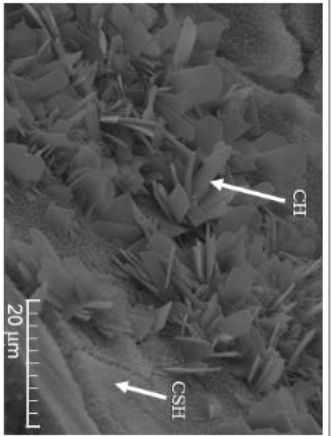
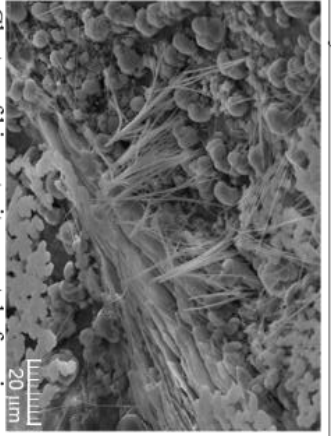
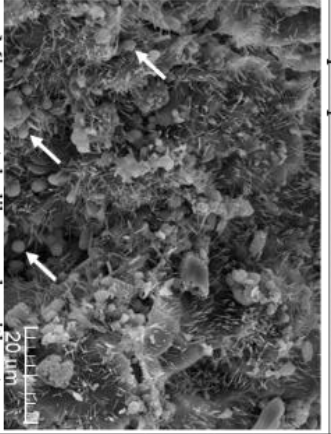
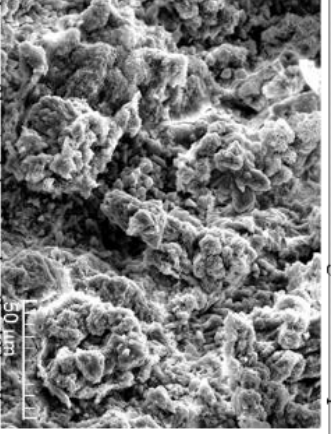
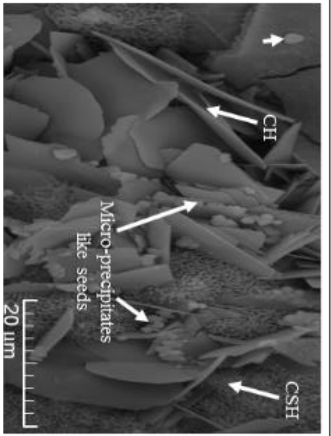
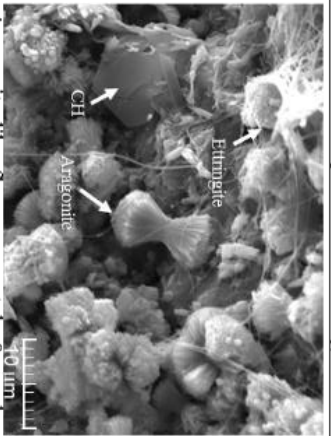
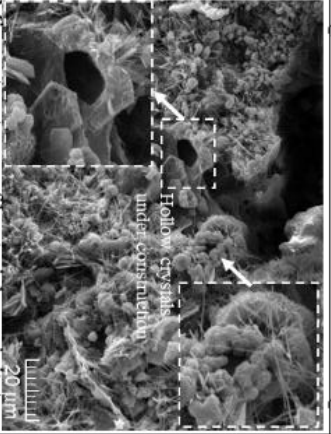
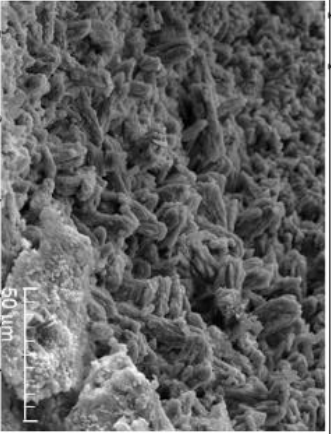
Acknowledgement

This project has received funding from the European Union's Horizon 2020 research and innovation programme under the Marie Skłodowska-Curie grant agreement No 798021 (GEOBACTICON).

References

- [1] Souid A, Esaker M, Elliott D, Hamza O, Experimental data of bio self-healing concrete incubated in saturated natural soil. *Data in brief* 2019, 26:104394. DOI:10.1016/j.dib.2019.104394.
- [2] Hamza O, Esaker M, Elliott D, Souid A, The effect of soil incubation on bio-self-healing of cementitious mortar. *Materials Today* 2020, 09, 24; doi: 10.1016/j.mtcomm.2020.100988.
- [3] Sonenshein AL; Cami B; Brevet J; Cote R. Isolation and Characterization of rifampin-resistant and streptolydigin-resistant mutants of *Bacillus subtilis* with altered sporulation properties. *Jornal of bacteriology*. 1974; 120(1):253-265.
- [4] Choco M.G.; Sang H.H.; Seong G.K.; Joo Y.P.; Chang H.K.; Jin H.J.; Jae S.S.; Effects of different calcium salts on calcium carbonate crystal. *Biotechnology and Bioprocess Eng* 2013. 18: 903-908; Doi 10.1007/s12257-013-0030-0
- [5] Achal V; Pan X; Influence of Calcium Sources on Microbially Induced Calcium Carbonate Precipitation by *Bacillus* sp. CR2. *Appl Biochem Biotechnol*. 2014; 173:307-317. DOI 10.1007/s12010-014-0842-1.
- [6] Ramin A; Muid ZAM; Moh WH; Mohanadoss P; Ali K; Jahangir M; Han SL; Optimum concentration of *Bacillus megaterium* for strengthening structural concrete. *Construction and Building Materials* 118 (2016) 180-193.
- [7] Esaker M, Hamza O, Souid A, Elliott D; Self-healing of bio-cementitious mortar incubated within neutral and acidic soil. *Mater Struct* 54, 96 (2021). DOI: 10.1617/s11527-021-01690-1.

Table 1. SEM micrographs of bacterial precipitates in micro-environments of cracks' lips of bio mortar specimens at different incubation time within saturated sand.

Time	6 days of incubation	11 days of incubation	25 days of incubation	270 days of incubation
Lysinibacillus sphaericus (NCIMB 9370)	 <p>Sand granules Bacterial precipitates</p> <p>Vaterite spherulites precipitates in pores</p>	 <p>Formation of micro bacterial cluster of crystals on CSH micro-environment</p>	 <p>Bacterial imprints & seeds like crystals precipitated on CSH surface</p>	 <p>Calcite crystals' layer of bio self-healing on the cross-section' edge of crack lip</p>
Lysinibacillus sphaericus (NCIMB 8218)	 <p>CH CSH</p> <p>CH crystals on CSH without bio minerals</p>	 <p>Cluster of bio vaterite crystals forming a basic layer of self-healing</p>	 <p>Micro-crystals like seeds without significant structure of bio self-healing</p>	 <p>Layer of bacterial crystals of self-healing precipitated on the crack cross-section</p>
Bacillus subtilis (H50620/9)	 <p>CH CSH Micro-precipitates like seeds</p> <p>Micro seeds precipitated on CH & CSH</p>	 <p>CH Ettringite Aragonite</p> <p>Aragonite like flowers crystals & seeds micro-crystals beside ettringite and CH</p>	 <p>Hollow crystals under construction</p> <p>Micro structures of bacterial precipitates formation by calcite & vaterite crystals</p>	 <p>Layer of aragonite crystals forming layer of bacterial self-healing</p>

Micro-Scale Processes in Microbially Induced Carbonate Precipitation

James M. Minto, Rebecca J. Lunn, Grainne El Mountassir, Mary M. Anderson

Civil and Environmental Engineering, University of Strathclyde, Glasgow G1 1XJ, UK

Abstract

The concept of using bacteria to control the precipitation of calcium carbonate for engineering purposes, such as increasing soil strength and decreasing permeability, is well established in lab-scale experiments. What is not so clear is how to transition from these experiments to a practical field-scale ground improvement tool.

One difficulty is that soil properties are highly site specific and also vary spatially within a site (e.g. porosity, permeability, particle shape and size distribution, mineralogical composition). Meanwhile, microbially induced carbonate precipitation relies on complex interactions between pore structure, fluid flow pathways, and injection strategies which all influence where the injected bacteria will attach, where CaCO₃ will precipitate, and which evolve over time as CaCO₃ is progressively precipitated and the pore structure is altered.

To unpick these processes and optimise MICP treatment, we use light microscopy in microfluidic devices offering high time-resolution observations of bacterial attachment and CaCO₃ crystal nucleation and growth in 2D systems. This is followed by X-ray μ CT of sand packed columns offering more complex and realistic flow conditions in which we observe the evolving pore structure and relate this to changes in the flow fields through reactive-transport modelling with the software OpenFOAM.

Results show that the processes of bacterial attachment and crystal growth are complex and highly dependent on micro-scale conditions, however feedback mechanisms, repeated treatment cycles, and operator controlled parameters such as flow velocity can act to minimise these local variations across a range of soil types.

Introduction

The concept of using bacteria to control the precipitation of calcium carbonate for engineering purposes, such as increasing soil strength [1–4] and decreasing permeability [5–7], is well established in lab-scale experiments. What is not so clear is how to transition from these experiments to a practical field-scale ground improvement technology.

One difficulty is that soil properties are highly site specific and also vary spatially within a site (e.g. porosity, permeability, particle shape and size distribution, mineralogical composition). Meanwhile, microbially induced carbonate precipitation (MICP) relies on complex interactions between pore structure, fluid flow pathways, and injection strategies which all influence where the injected bacteria will attach and where CaCO₃ will precipitate. Moreover, these interactions evolve over time as CaCO₃ is progressively precipitated and the pore structure is altered.

Currently, the most promising MICP pathway is that of urea hydrolysis using the bacterium *Sporosarcina pasteurii*. The aim of this research is to investigate the factors influencing the transport, attachment, and subsequent mobilisation of *S. pasteurii* within porous media.

Materials and methods

A type culture of bacterium *S. pasteurii* (DSM-33) was grown in yeast extract broth, incubated at 30 °C for 24 hours, centrifuged to separate cells from the broth, and re-suspended in a sterile 9 g/L NaCl solution to an optical density of 1.0 OD₆₀₀. The cells in broth were stored at 4 °C for up to a week and fresh cell suspensions in NaCl were prepared for each experiment.

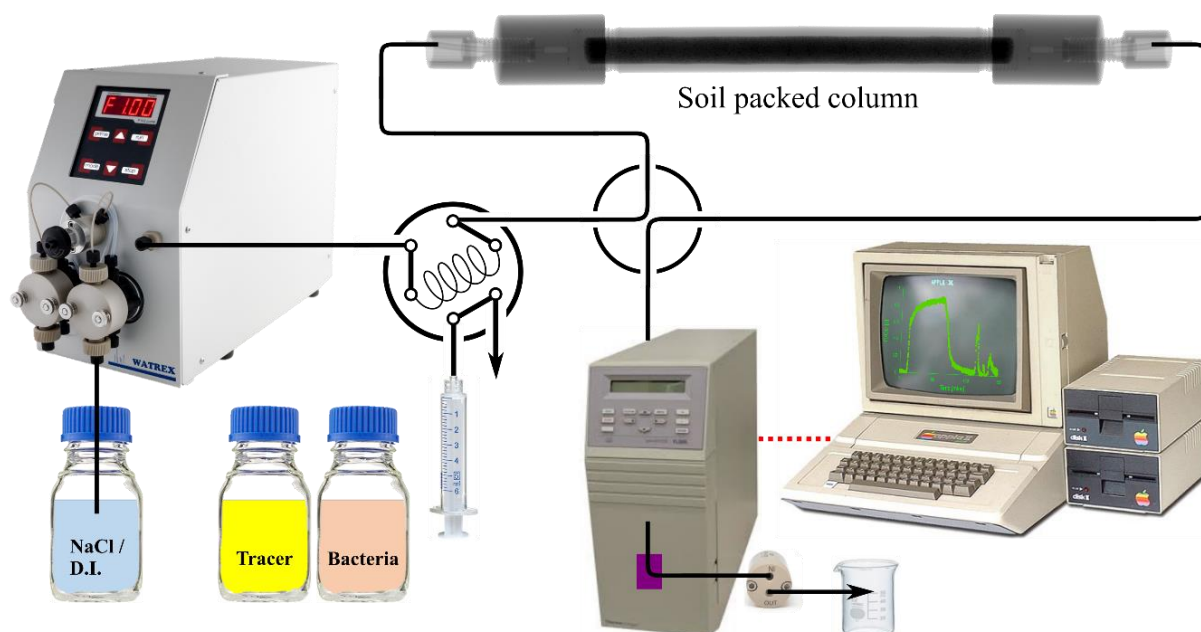


Figure 1. Experimental setup allowing continuous injection of salt solutions and controlled pulses of conservative tracer and bacteria through soil packed columns. Effluent breakthrough curves are recorded based on fluorescence. A six-way valve allows switching between injection and flushing, a four-way diagonal valve allows measurement of bacteria and tracer stock concentration, and a back pressure regulator set to 100 kPa prevents bubble formation within the system.

The experimental setup is shown in Figure 1. X-ray transparent columns 150 mm long and 4 mm diameter were packed with two different soils and fully saturated with a 9 g/L NaCl solution. The two soils were Sand 1: a lab grade quartz sand and Sand 2: a washed ‘building sand’ from a builder’s merchant. Details of the two sands are shown in Figure 2 with the main difference being that the washed building sand had a greater range in particle size distribution and particle shape, contained finer particles and thus had a lower porosity and a greater number of grain contact points.

A conservative fluorescein tracer was injected to characterise fluid flow in each soil using a six-way valve with sample injection loop to control tracer volume. Effluent breakthrough curves were recorded using a scanning fluorescence detector. A four-way valve was used to direct tracer either through the column, or directly to the detector for an influent reading. Bacteria were injected and detected in the same manner.

Results and discussion

Results are presented in the form of breakthrough curves which plot the concentration of tracer at the outlet of the column (as a ratio of the inlet concentration) against time (shown as the number of pore volumes injected). Transport of the conservative tracer was distinctly different in the two soil types (Figure 3A). In Sand 1 the effluent breakthrough curve could be fitted by a simple convection-dispersion model, whereas for Sand 2, the break-through curve could only be fitted using a two-region non-equilibrium model. This is thought to be due to the more irregular particle shape creating stagnant regions of the pore network into which the tracer could diffuse.

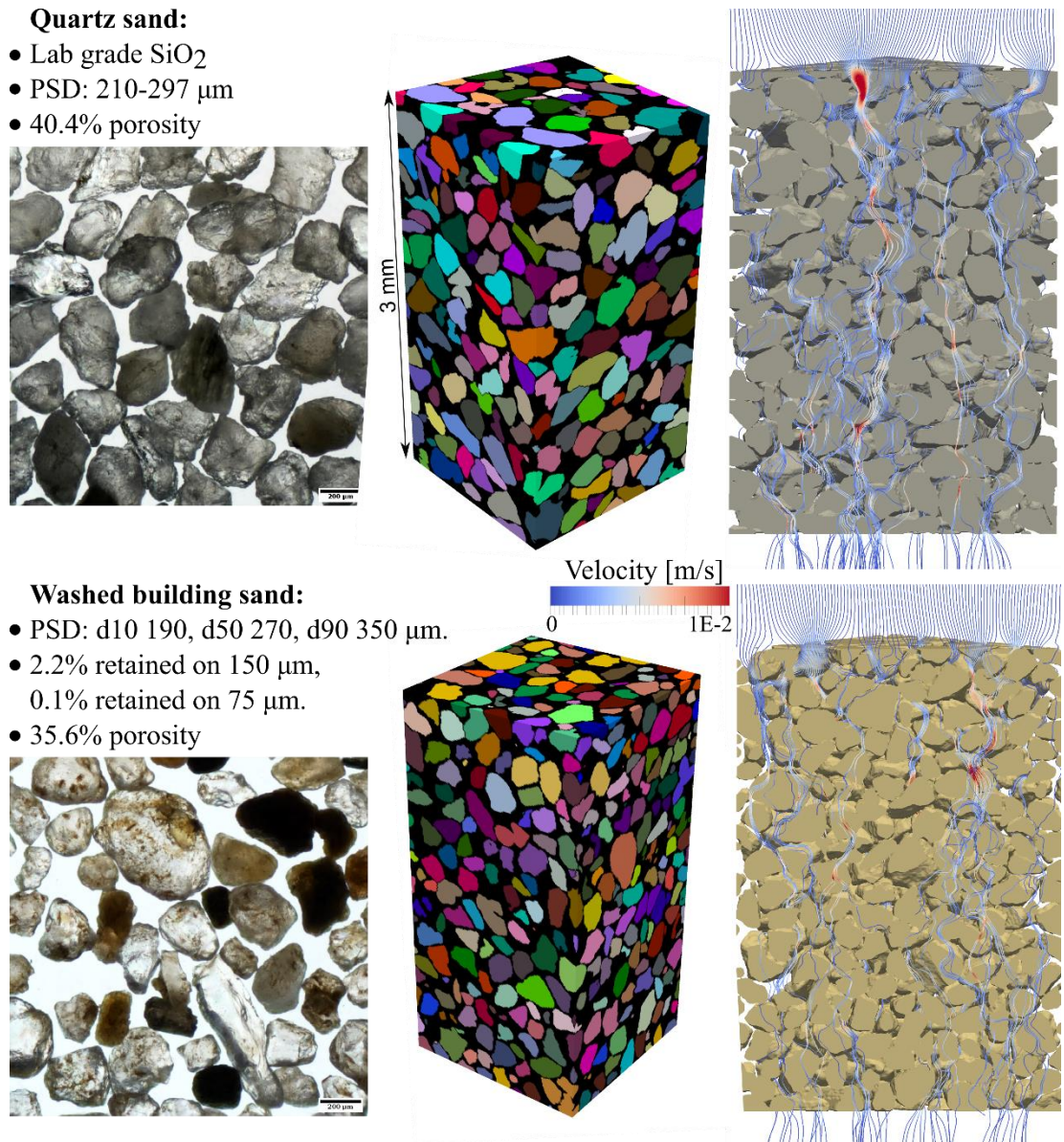


Figure 2. Top to bottom: lab grade quartz sand with near uniform particle size distribution; washed 'building sand' with greater range in particle size and shape and containing finer particles. Left to right: Optical microscope images of sand shape; X-ray μCT images of packed sand columns with individual grains separated and labelled by colour in post-processing; results of numerical flow simulation showing flow paths through the sand packs using code developed by Minto et al. [8].

Transport of the bacteria was affected by fluid velocity with higher velocities resulting in less attachment (Figure 3B), which has also been observed in sandstone cores by Tobler et al. [9]. Significantly more attachment occurs in Sand 2 (the building sand) than in Sand 1, moreover the threshold at which flow velocity affects attachment appears to be soil dependent. Finally, the absolute magnitude of attachment also depends on soil type with significantly more attachment occurring in Sand 2 than Sand 1. This is thought to be due to the irregular particles creating more contact points for physical removal of cells (filtration) and stagnant regions which promote physico-chemical removal (adsorption).

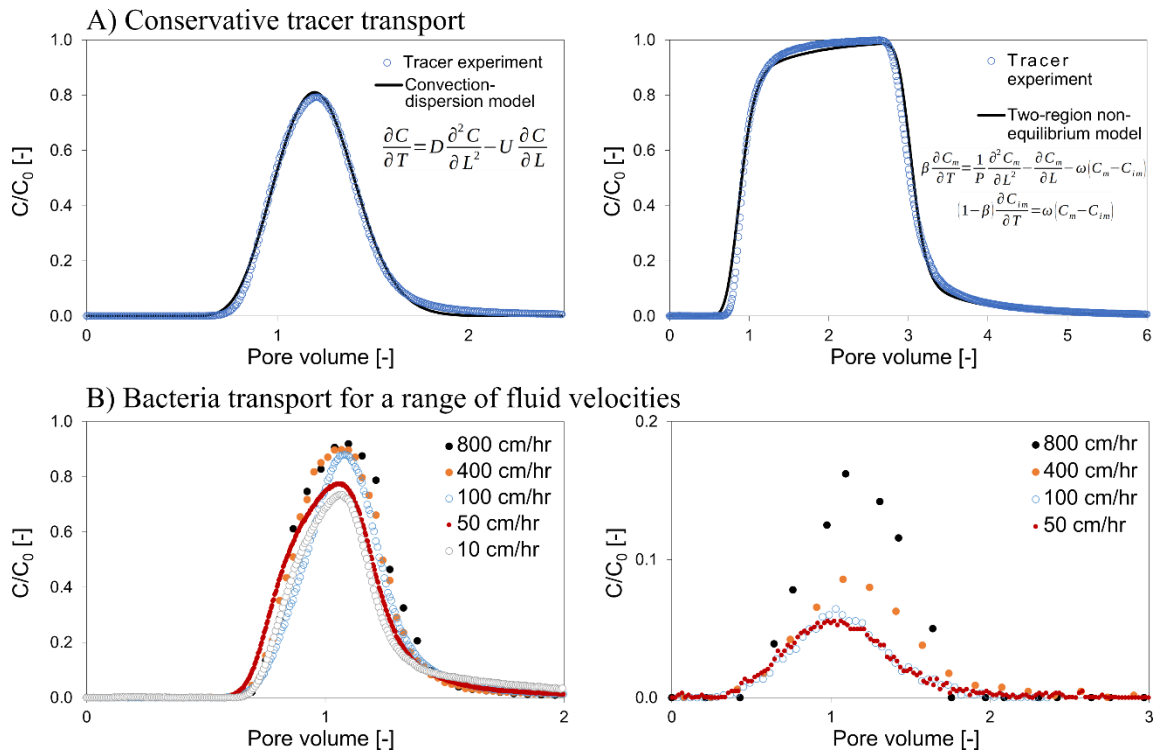


Figure 3. Effluent breakthrough curves for the quartz sand (left) and building sand (right) for A) a conservative tracer, and B) 1.0 OD₆₀₀ *S. pasteurii* in 9 g/L NaCl cell suspensions injected at different flow rates, all at 0.75 pore volumes.

Given that the columns were 150 mm long, the high retention of bacteria in Sand 2 (the building sand) could suggest that the extent of treatment around any one injection point is limited, with the result that many injection points would be required to provide uniform MICP treatment over a large area. However, this 150 mm length represents the region immediately adjacent to an injection point and, in order to access the wider volume around the injection point, it would be necessary for multiple pore volumes of bacteria to pass through this same region. By increasing the volume of bacteria injected (Figure 4), we see that retention diminishes significantly and that the soil does not continue to inhibit transport of the bacteria.

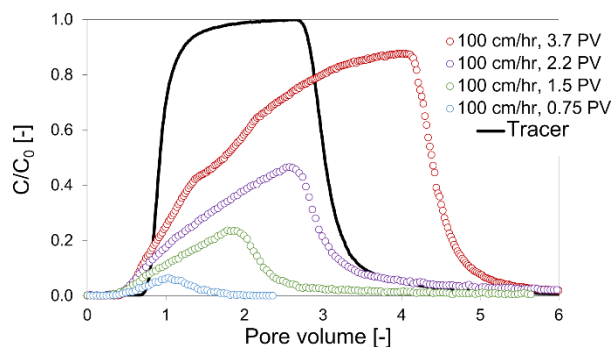


Figure 4. Effluent breakthrough curves for the building sand. 1.0 OD₆₀₀ *S. pasteurii* in 9 g/L NaCl cell suspensions injected at a constant flow rates and different durations resulting in different total pore volumes injected.

This observation is consistent with a retention mechanism of filter-blocking in which attachment sites within the porous media become occupied by bacteria and hence removal efficiency decreases over time, enabling the bacteria to be transported away from the injection point and access a greater soil volume. We hypothesise that this mechanism allows for more even distribution of bacteria within a given injection period, however the precipitation of

CaCO₃ that follows the bacterial injection would provide fresh attachment points for each subsequent treatment cycle.

Conclusion

For microbially induced carbonate precipitation to be a successful ground improvement technology, it is necessary for treatment to be uniform and predictable over large areas. This research has shown that soil properties and flow velocity must be taken into account when designing a treatment strategy. We have shown that attachment of bacteria is greatly influenced by soil properties, with more bacteria being retained within a well-graded sand compared to a uniform sand. We have demonstrated that an increase in flow velocity reduces the amount of bacteria retained and that blocking of attachment sites can help to minimise blocking of injection points.

Acknowledgment

This research was funded by the BAM Nuttall/Royal Academy of Engineering Research Chair *Biomaterial Technologies for Ground Engineering* and supported by an EPSRC Capital Award for Early Career Researchers.

References

- [1] J.T. DeJong, B.M. Mortensen, B.C. Martinez, D.C. Nelson, Bio-mediated soil improvement, *Ecol. Eng.* 36 (2010) 197–210. doi:10.1016/j.ecoleng.2008.12.029.
- [2] M.G. Gomez, B.C. Martinez, J.T. DeJong, C.E. Hunt, L.A. DeVlaming, D.W. Major, S.M. Dworatzek, Field-scale bio-cementation tests to improve sands, *Proc. Inst. Civ. Eng. - Gr. Improv.* 168 (2015) 1–11. doi:10.1680/grim.13.00052.
- [3] V.S. Whiffin, L.A. van Paassen, M.P. Harkes, Microbial Carbonate Precipitation as a Soil Improvement Technique, *Geomicrobiol. J.* 24 (2007) 417–423. doi:10.1080/01490450701436505.
- [4] L.A. van Paassen, R. Ghose, T.J.M. Van Der Linden, W.R.L. Van Der Star, M.C.M. Loosdrecht, Quantifying Biomediated Ground Improvement by Ureolysis: Large-Scale BiogROUT Experiment, *J. Geotech. Geoenvironmental Eng.* 136 (2010) 1721–1728. doi:10.1061/(ASCE)GT.1943-5606.0000382.
- [5] M.O. Cuthbert, L.A. McMillan, S. Handley-Sidhu, M.S. Riley, D.J. Tobler, V.R. Phoenix, A field and modeling study of fractured rock permeability reduction using microbially induced calcite precipitation., *Environ. Sci. Technol.* 47 (2013) 13637–43. doi:10.1021/es402601g.
- [6] J.M. Minto, E. MacLachlan, G. El Mountassir, R.J. Lunn, Rock fracture grouting with microbially induced carbonate precipitation, *Water Resour. Res.* 52 (2016) 8827–8844. doi:10.1002/2016WR018884.
- [7] A.J. Phillips, E.G. Lauchnor, J.J. Eldring, R. Esposito, A.C. Mitchell, R. Gerlach, A.B. Cunningham, L.H. Spangler, Potential CO₂ leakage reduction through biofilm-induced calcium carbonate precipitation, *Environ. Sci. Technol.* 47 (2013) 142–149. doi:10.1021/es301294q.
- [8] J.M. Minto, R.J. Lunn, G. El Mountassir, Development of a Reactive Transport Model for Field-Scale Simulation of Microbially Induced Carbonate Precipitation, *Water Resour. Res.* 55 (2019) 7229–7245. doi:10.1029/2019WR025153.
- [9] D.J. Tobler, M.O. Cuthbert, V.R. Phoenix, Transport of *Sporosarcina pasteurii* in sandstone and its significance for subsurface engineering technologies, *Appl. Geochemistry.* 42 (2014) 38–44. doi:10.1016/j.apgeochem.2014.01.004.

Calcite precipitation by environmental bacteria as a method to improve durability of cementitious materials

Bianca Reeksting¹, Kevin Paine² and Susanne Gebhard¹

1: Department of Biology and Biochemistry, Milner Centre for Evolution, University of Bath, United Kingdom

2: Department of Architecture and Civil Engineering, University of Bath, United Kingdom

Abstract

The need for greener and more sustainable technologies within the construction industry has become a concern amid growing unrest over environmental issues. Concrete is one of the most widely used construction materials worldwide but also carries significant environmental and economic costs associated with both production and maintenance. Many of these costs are exacerbated by problems with durability of concrete, often caused by the formation of cracks that influence the permeability of these structures and allow ingress of aggressive substances that cause corrosion and eventual structure failure. Microbially-induced calcite precipitation (MICP) is a process whereby the deposition of calcium carbonate can occur as a by-product of microbial metabolism. This has already been used in a diverse range of applications, including soil engineering to improve soil characteristics, bioremediation of contaminated sites, and for crack sealing in self-healing cementitious materials. We here report on our profiling of environmental bacteria and their relevance as a source of strains for use in self-healing applications. Our work has shown that different microbial metabolisms can result in different mechanisms of precipitation, possibly impacting on performance in application. This had led to further investigations of how these differences can be used to our advantage when optimising self-healing applications, with particular emphasis on crack sealing in cementitious mortars.

Introduction

The growing awareness within society regarding climate change and the recognition of the need for remedial action has prompted the development of new technologies to address problem areas. One of these problem areas is the use of concrete within the construction industry, which bears heavy environmental and economic costs. High CO₂ emissions (5-8% of global anthropogenic emissions) are associated with cement production (2)(3). These costs are amplified by durability issues in concrete structures, for example caused by cracking, which leads to ingress of water and ions, such as chlorides, that corrode internal steel reinforcements and cause eventual structural failure. Such cracks offer a target for improvement of durability in our infrastructure. If we could seal cracks and reduce the ingress of damaging substances, the lifespan of concrete structures could be extended, and the environmental price would be lower per year of use.

Calcium carbonate is an attractive candidate to use to seal cracks in concrete as it is a material that is both aesthetically pleasing as well as being compatible with concrete chemistry. It can be deposited as a by-product of microbial metabolism in a process known as microbially induced calcite precipitation (MICP), which has been occurring on a geological scale for billions of years (4). MICP has found application in several areas of environmental engineering, including bioremediation (5)(6), wastewater treatment, and soil consolidation in geotechnical applications. Many bacteria can precipitate calcium carbonate under the right environmental conditions (7), with available calcium ions, pH, and dissolved inorganic carbon (DIC) all contributing to the MICP process (8). Bacterial metabolic activity causes increases in pH and

DIC, leading to changes in the solution chemistry that lead to oversaturation of Ca^{2+} and CO_3^{2-} ions and subsequent formation of calcium carbonate precipitates (9). We have previously shown that different microbial metabolic pathways lead to variations in the mechanisms and kinetics of precipitation, with implications for application (1).

The use of MICP in self-healing of concrete offers several challenges, including an extremely alkaline environment, low nutrient availability, and large fluctuation in temperatures. Currently, most studies utilizing MICP in cementitious materials focus on utilizing a single bacterium, choice of which is often limited to a small number of species commonly used in similar studies. However, bacteria have optimum growth within a defined, often relatively narrow temperature range. As MICP requires metabolic activity, sealing of cracks in this way is restricted by the temperature range of the bacterial species utilized. The diverse environments in which concrete is used means that sealing of cracks will need to be possible in a broad temperature range, which excludes the use of a single species of bacteria. In this study we report our work on profiling environmental bacteria, isolated at different temperatures, and utilizing these bacteria in mixed culture to enable self-healing to occur over a broad temperature range.

Materials and methods

The mesophilic bacteria *Bacillus cohnii* DSM 6307B and *Bacillus pseudofirmus* DSM8715, were obtained from the German Collection of Microorganisms and Cell Cultures (DSMZ). Other mesophiles used were isolated as described in previous work (1). These bacteria had a growth optimum close to 30 °C. Psychrophiles were isolated from limestone caves, immature calcareous soils, and rock scrapings from regions in the UK. Enrichment for spore-forming bacteria was carried out by pasteurization at 80 °C for 20 minutes. Isolates were selected for growth at low temperature (7.5°C) and in alkaline conditions (pH 9). Strains capable of forming spores as well as forming visible crystals on the colony surface when grown on 0.25 B4 plates (0.1% yeast extract (W/V), 0.125% glucose (W/V), 1.5% agar, 0.25% calcium acetate, adjusted to pH 8 with NaOH) were selected for further characterisation. Pure cultures of these isolates were produced by picking individual colonies from plates, inoculating lysogeny broth (LB; 10 g l⁻¹ tryptone, 5 g l⁻¹ yeast extract, 10 g l⁻¹ NaCl) and growing overnight before storage at -80 °C in a 25% (w/v) glycerol solution.

Individual isolates were identified by amplification and sequencing of the 16S rDNA gene fragment using the 27F (5'-AGAGTTTGATCMTGGCTCAG-3') and 1492R (5'-TACCTTGTTACGACTT- 3') primers (10). Sequences were subsequently compared against the non-redundant GenBank nucleotide collection using BLASTN (<http://www.ncbi.nlm.nih.gov>). Isolates were routinely grown and maintained on LB agar adjusted to pH 8.2 with 1M Tris/HCl (pH 9). Psychrophiles had a growth optimum below 20 °C. Mesophiles were grown at 30°C and psychrophiles were grown at 7.5 °C and 15 °C, unless stated otherwise, and liquid cultures were agitated at 150 rpm. To determine optimum growth temperature and growth range of each isolate, growth curves were produced for each isolate at 7.5 °C, 15 °C, 22 °C, and 30 °C. Growth was monitored spectrophotometrically by optical density at 600 nm wavelength (OD₆₀₀) in a Tecan Spark microplate reader controlled by SparkControl™ V2.1 software.

Precipitation ability was assessed quantitatively by inoculating (1:1000) 75 ml YAC precipitation medium (10mM Tris/HCl (pH 7.8), 0.51mM III'-Salts, 5% Yeast extract, 100mM Sodium acetate) from overnight cultures and monitoring pH over time and determining the amount of insoluble calcium carbonate precipitated after 6-8 days. pH was determined using a pH electrode (Jenway 924 030, Cole-Parmer, Staffordshire UK) coupled to a pH meter (Jenway 3510 pH Meter). Insoluble calcium carbonate precipitate was recovered by centrifugation (975 × g, 2 minutes at room temperature (RT) and washed thrice in distilled water before oven drying at 50°C for 48 hours and determining dry weight. Ability of mixed cultures to precipitate calcium

carbonate at different temperatures was assessed by mixing several mesophiles and psychrophiles, in equal proportions, and using these mixed cultures to inoculate (1:1000) YAC precipitation broths. To distinguish mesophiles from psychrophiles, morphologically distinct isolates were chosen, with mesophiles forming yellow colonies and psychrophiles forming white colonies (Figure 2). Duplicate broths were incubated at 7.5 °C and 30 °C and precipitation, pH, and cell viability was monitored.

Results and discussion

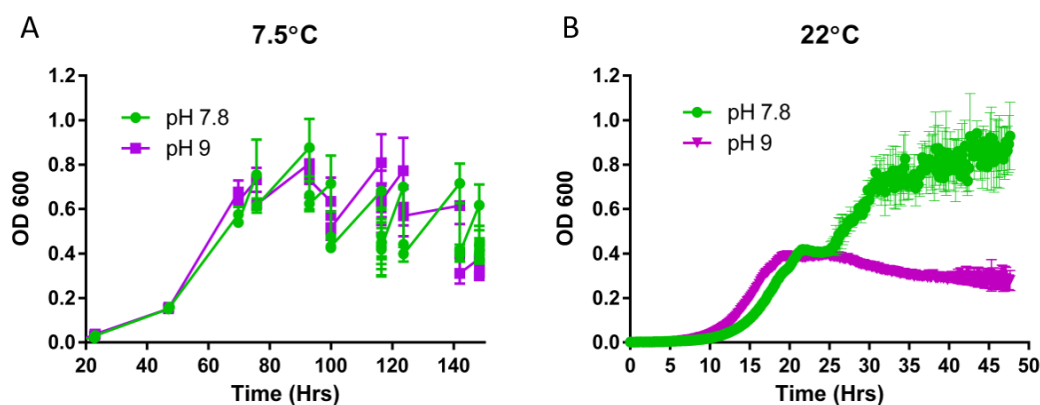


Figure 1. Representative growth curves for an individual isolate (Psy 32) at 7.5°C (A) and 22°C (B). Growth curves were carried out at both pH 7.8 (green lines) and pH 9 (purple lines). Growth measurements at 7.5°C were conducted for 6 days whilst those at 22°C were conducted over 48 hours.

Isolates were grown in neutral (pH 7.8) and alkaline (pH 9) conditions at different temperatures to determine optimal growth conditions for individual strains (Figure 1). Temperature had a profound impact on the ability of isolates to grow, with most mesophiles unable to grow at 7.5 °C and with only very limited growth for some at 15 °C. In contrast, psychrophiles grew at 7.5 °C and 15 °C. Only one of the tested psychrophiles was able to grow at 30 °C. Both mesophiles and psychrophiles displayed some growth at 22 °C. Some strains showed a pH preference, achieving better growth at one pH, but many could grow well at either pH.

Precipitation assays demonstrated that psychrophiles were able to precipitate insoluble calcium at 7.5 °C and mesophiles were able to precipitate at 30 °C. When mixed community precipitation was assessed (Figure 2), it was found that precipitation by these mixed cultures was achieved at both temperatures. It was noted that higher amounts of precipitate were recovered from mixed community broths incubated at 30 °C than at 7.5 °C (Figure 2). This could be due to the differences in solution chemistry at these different temperatures, with calcium being more soluble at lower temperature and thus larger pH changes may be required to shift the saturation point. It was found that when a mixed community was incubated at one temperature over the course of the experiment, the member for which the growth conditions were not optimal was lost. This could be mitigated by using a cycle of temperatures where one temperature was maintained for 8 hours and one for 16 hours, in which case both members of the community were maintained over 5 days (data not shown).

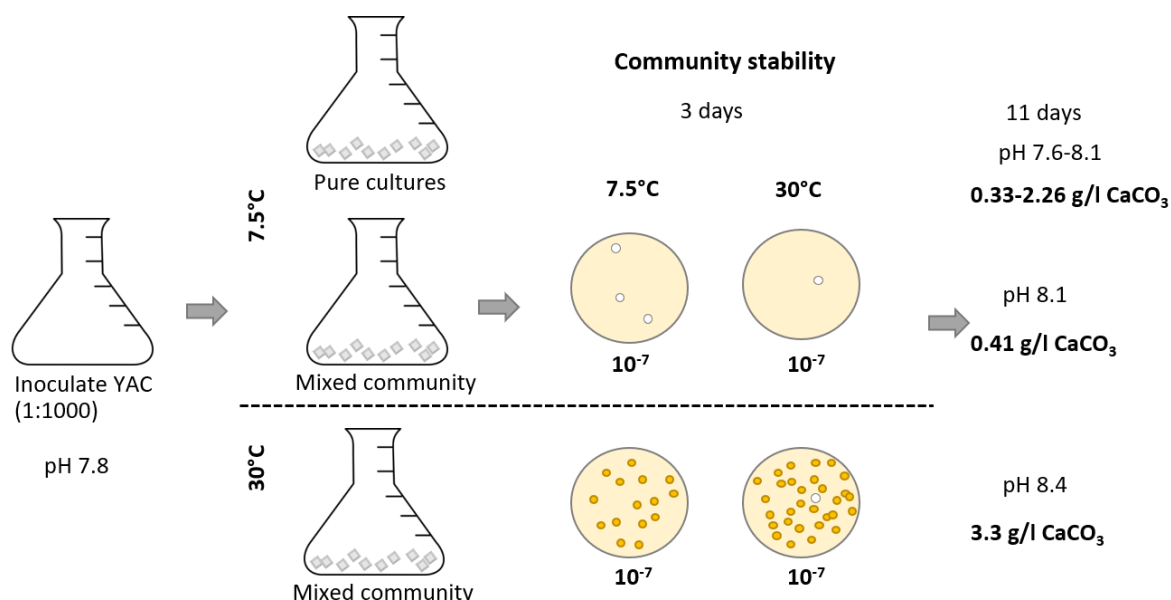


Figure 2. Mixed community precipitation assays. Precipitation broths were set-up for pure cultures at 7.5 °C and for mixed communities at both 7.5 °C and 30 °C. Mesophiles (*B. pseudofirmus*, CGN12, UBN3) grew as yellow colonies on the plates, psychrophiles grew as white colonies.

Conclusion

In this study, detailed growth information across several temperatures as well as precipitation profiles at these temperatures has allowed us to determine the individual growth and precipitation potential of mesophilic and psychrophilic bacterial isolates. This information will allow us to identify compatible partners in two-partner mixes to maximise growth and precipitation over a broad temperature range by determining whether the presence of individual members is beneficial or detrimental to growth and precipitation. The maintenance of individual members within these mixes is important, and it was seen that members can be lost when unfavourable temperatures persist. The ability to stabilise this community structure by using temperature fluctuations is an important area to investigate in future work and may in fact provide a more realistic representation of the conditions self-healing concrete would be naturally exposed to. Precipitation assays utilizing mixed cultures have demonstrated the potential for mixed communities to allow self-healing over a broad temperature range. This will be highly relevant to application, where MICP will need to occur under a range of temperatures to achieve autonomous, self-healing materials.

Acknowledgment

We acknowledge the Engineering and Physical Sciences Research Council (EPSRC; EP/PO2081X/1) and industrial collaborators/partners for funding the Resilient Materials for Life (RM4L) project.

References

1. Reeksting BJ, Hoffmann TD, Tan L, Paine K, Gebhard S. In-Depth Profiling of Calcite Precipitation by Environmental Bacteria Reveals Fundamental Mechanistic Differences with Relevance to Application. Kelly RM, editor. *Appl Environ Microbiol* [Internet]. 2020 Mar 18;86(7):e02739-19. Available from: <http://aem.asm.org/content/86/7/e02739-19.abstract>
2. Ceci A, Pinzari F, Riccardi C, Maggi O, Pierro L, Papini MP, et al. Metabolic synergies in the biotransformation of organic and metallic toxic compounds by a saprotrophic soil fungus. *Environ Biotechnol*. 2018;102:1019–33.
3. Souto-Martinez A, Arehart JH, Srubar III W V. Energy & Buildings Cradle-to-gate CO₂ e emissions vs . in situ

- CO₂ sequestration of structural concrete elements. *Energy Build* [Internet]. 2018;167:301–11. Available from: <https://doi.org/10.1016/j.enbuild.2018.02.042>
4. Mitchell AC, Dideriksen K, Spangler LH, Cunningham AB, Gerlach R. Microbially Enhanced Carbon Capture and Storage by Mineral-Trapping and Solubility-Trapping. *Environ Sci Technol*. 2010;44(13):5270–6.
 5. Achal V, Pan X, Zhang D. Remediation of copper-contaminated soil by *Kocuria flava* CR1, based on microbially induced calcite precipitation. *Ecol Eng*. 2011;37:1601–5.
 6. Wilmeth DT, Johnson HA, Stamps BW, Berelson WM, Stevenson BS, Nunn HS, et al. Environmental and Biological Influences on Carbonate Precipitation Within Hot Spring Microbial Mats in Little Hot Creek, CA. *Front Microbiol* [Internet]. 2018;9:1–13. Available from: <https://www.frontiersin.org/article/10.3389/fmicb.2018.01464>
 7. Huntzinger DN, Eatmon TD. A life-cycle assessment of Portland cement manufacturing: comparing the traditional process with alternative technologies. *J Clean Prod*. 2009;17:668–75.
 8. Boquet E, Boronat A, Ramos-Cormenzana A. Production of Calcite (Calcium Carbonate) Crystals by Soil Bacteria is a General Phenomenon. *Nature* [Internet]. 1973;246(5434):527–9. Available from: <https://doi.org/10.1038/246527a0>
 9. Hammes F, Verstraete W. Key roles of pH and calcium metabolism in microbial carbonate precipitation. *Rev Environ Sci Biotechnol*. 2002;1(1):3–7.
 10. Lane D. 16S/23S rRNA sequencing. In: Stackebrandt E, Goodfellow M, editors. *Nucleic acid techniques in bacterial systematics*. John Wiley and Sons; 1991. p. 115–75.

Calcium carbonate precipitation as a function of alkaliphilic bacteria development

Heriberto Martinez¹, Marielle Guéguen Minerbe¹, Yoan Pechaud², Thierry Sedran³

1: MAST-CPDM, Univ Gustave Eiffel, IFSTTAR, F-77447 Marne-la-Vallée, France

2: LGE, Université Paris-Est Marne la Vallée, 5 Bd Descartes 77454 Marne-la-Vallée cedex 02, France

3: MAST-MIT, Université Gustave Eiffel, F-44344 Bouguenais, France

Abstract

Some alkaliphilic bacteria have the capacity to precipitate calcium carbonate (CaCO₃) in a process called bio carbonation. This phenomenon has attracted the interest of the construction and demolition industry because such process can be applied to improve mechanical and physical properties of recycled concrete aggregates (RCA). A residual layer of cement makes the RCA very porous, increasing water permeability and compromising their performance into new concrete. If bio carbonation is used to treat RCA a layer of CaCO₃ could be formed at their surface, reducing porosity. Different alkaliphilic bacteria species specialised in CaCO₃ precipitation have been already tested on cementitious materials highlighting difficulties such as nutrient depletion and poor development due to the harsh conditions present at the surface of the materials. Two alkaliphilic bacteria species were isolated from RCA. These bacteria were able to precipitate CaCO₃ on ordinary portland cement (OPC) in form of calcite, vaterite and aragonite. This study seeks to determine the formation CaCO₃ as function of the development of these new bacteria candidates, by establishing their phase growth and inoculating them through serial dilutions into Petri plates with nutrient agar media supplied with calcium acetate [50 g/L], taking photographic evidence each 24 h on a Period of 5 days. A correlation between the bacteria growth phase and the precipitation of CaCO₃ was established. XRD (X-ray diffraction) analysis and SEM (Scanning Electron Microscopy) complemented the study by providing information about the nature and structure of the precipitates.

Introduction

Bioprecipitation of calcium carbonate (CaCO₃) offers an innovative and ecological way to treat cementitious materials [1], lengthening their lifespan by selling fissures [2], protecting them from chloride ions penetration, and enhancing their appearance in the case of concrete based monuments [3]. Bacteria are one of the most studied microorganisms on the topic capable of performing bioprecipitation through many mechanisms [4]. It is known that the efficiency of such process relies on the type of bacteria that is used to perform it [5]. The pH at the surface of cementitious materials is around 11 and 13, thus alkaliphilic bacteria is used to study the effects of bioprecipitation on these materials because they usually grow at a pH above 8 [6]. However, even alkaliphilic bacteria are not necessarily capable of developing homogeneously at the surface of such materials where the roughness and porosity are very pronounced. A heterogeneous bacteria development results in a heterogeneous bioprecipitation which does not enhance the appearance or quality of a treated material. For instance, in a previous experiment, a mortar made of ordinary portlandite cement (M-OPC) was treated by bio precipitation with *Bacillus halodurans* C-125 (alkaliphilic bacteria) to reduce its porosity and diminish water absorption. The results showed that the sporadic development of the bacteria caused a heterogeneous biodeposition of CaCO₃ [7], without favourable results. We have suggested that: (i) the roughness and porosity of the M-OPC did not allow the homogeneous distribution of nutrients on its surface, as a result, *Bacillus halodurans* C-125 just developed in

the regions where the nutrients were concentrated resulting in a heterogenous bioprecipitation (ii) a biofilm can protect bacteria from harsh conditions, so *Bacillus halodurans* C-125 unable to produce a biofilm [8][9], was vulnerable on the M-OPC when the conditions were no longer favourable, limiting its development.

To test these hypotheses we have isolated the microbiota present on recycled concrete aggregates, as has been done with other materials such as calcareous rocks [10] and degraded limestones [11]. The objective of such action was to find microorganisms with the capacity to grow at an alkaline pH forming a biofilm, and precipitate CaCO_3 . As result, 3 bacteria demonstrated to : (i) develop on nutrient media at pH 11 (ii) produce a robust biofilm, and (iii) precipitate CaCO_3 , at the surface of an M-OPC [8][12].

In this report, the growth and bioprecipitation of an isolated bacterium, named B.H, is analysed. By combining qualitative and quantitative techniques, the results provided preliminary information about, the growth phases of B.H, the time that is required to bioprecipitate CaCO_3 on a solid surface, the quantity of CaCO_3 that is precipitated, and the morphology of the crystals.

Materials and methods

Biological material and preculture

B.H was isolated from old recycled concrete aggregates stocked outdoors in Nantes, France. A 16s ribosomal RNA analysis was performed by Genotoul-GET to determine its species; the analysis associated it with *Bacillus haynesii* strain NRRL B-41327 with a percentage identity of 96.29 %. Its morphology corresponds to the *bacilli* group with the ability to form spores. This bacterium grows in nutrient (NM) and MSgg media at pH 11, and at a temperature between 25 – 30 ° C. The precultures were prepared as follow, two Erlenmeyer were filled with 35 ml of sterile nutrient broth at pH 11 (adjusted with NaCl [5M]), the flasks were inoculated with 5 ml of B.H aged of 4 days. The two flasks were incubated at 30 ± 1 ° C and 60 rpm for 3 days. One Erlenmeyer was used to perform the bacterial growth curve and the other to make the analysis of bioprecipitation on nutrient media.

Bacterium growth curve

The growth curve data of B.H was obtained by measuring the optical density (OD) of a culture for 5 days. Two Erlenmeyer of 250 ml were filled with 131 ml of sterile nutrient broth at pH 11 (adjusted with NaCl [5M]). The flasks were inoculated with 18.70 ml (equivalent to 167×10^7 UFC/mL) of the preculture aged of 3 days, making a dilution of the inoculum 1 to 8. All flasks were incubated at 30 ° C and 60 rpm. To cover the night-time in which the laboratory closes, one Erlenmeyer was inoculated at 8 h and the other at 20 h. The Erlenmeyer inoculated at 20 h represented the development of bacteria during the night, closing a cycle of 24 h. Samples of 1 ml were taken every 2 hours to measure the OD in a UV spectrophotometer at 600 nm, determining the quantity of biomass present in the culture. The obtained data were plotted in a graph of optical density against time. A CFU counting was done immediately after the inoculation.

Media preparation and bacteria inoculation

Seventeen Petri plates (\varnothing 13.5 cm x 1.7 cm) with nutrient media 1.5 % agar were prepared in sterile conditions. Fifteen media were inoculated with 275 μl (equivalent to 167×10^7 UFC/mL or 3.2×10^7 UFC/cm²) of the preculture aged of 3 days, the inoculum was dispersed homogeneously with the help of an L-shaped spreader. A CFU counting of the preculture was done instantly after the inoculation. Three ml of calcium acetate (CA) [50 g/L] were added and well distributed in the fifteen media. The two-remaining media served as a control group without being inoculated with B.H, one of them was supplied with 3 ml of CA [50 g/L]. All Petri

plates were incubated at 30 ± 1 °C for 15 days. B.H development and CaCO_3 formation was recorded by taking a picture of all the plates every day, from Monday to Friday during the incubation period.

Extraction of CaCO_3

Every three or four days, three media were selected to do microscopic observations at 50X and 100X. After their observation, the media were cut into slices and put separately into Pyrex bottles with 400 ml of distilled water. An autoclave process was then performed (121 °C, 1 atm, 15 min) to dissolve the agar, and remove the biomass by draining the supernatant. Immediately 400 ml of distilled water were added to each bottle, and the autoclave process was repeated. The sediment of all bottles was recovered by centrifugation (3000 g, 25 °C for 12 minutes in a Sigma 3-16Pk / rotor-11180), using Falcon tubes of 50 ml. After centrifugation, the pellet of each bottle was left to dry for 2 days at 40°C. Once dried, the pellets were mixed, weighed, analysed by X-ray diffraction (XRD - Anode Material: Cobalt), and by thermogravimetric analysis (TGA). The production yield (Py) was calculated from the CaCO_3 formable as a function of the amount of Ca^{2+} added to the media.

Results and discussion

Bacterial flocs were formed in all suspensions (Figure 1). Flocs are agglomerates composed of extra polymeric substances (EPS) [13], principal components of biofilm. High levels of pH can induce biofilm production [14], then it could be possible that B.H produced the flocs as a consequence of the alkalinity of the media. The presence of the flocs could have severely altered the OD readings. However, it was estimated that at pH 11 in nutrient broth: (i) the latency time was around 22 h (ii) the exponential time was estimated to be 14 h, and (iii) the doubling time of around 5 h. B.H seemed to duplicate faster when compared to the facultative alkaliphilic *Bacillus firmus* OF4 with a doubling time of 11 h at pH 11 [15].



Figure 1. Presence of flocs in the culture of B.H from its first day of incubation

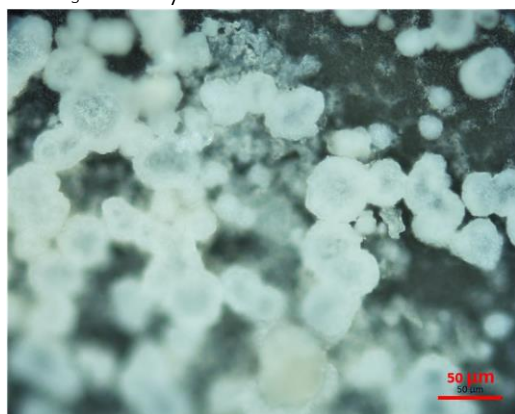
B.H colonies in form of white-cream spots appeared all over the Petri plates since the first day of incubation (Figure 2 A). Cellular agglomerates were observed on the media from the third to the fifteenth day of incubation (Figure 2 B). The microscopic observations made on the third-day post-inoculation showed the presence of CaCO_3 crystals of a size between 40 and 50 μm that covered the surface of the media quasi homogeneously (Figure 2 E, F). B.H should have formed the CaCO_3 as a consequence of the nucleation sites of its membrane or by metabolic mechanisms such as the excretion of secondary metabolites [16]–[18]. The XRD analysis characterized the precipitates as calcite and vaterite. The control media did not present bacterial development or the presence of precipitates (Figure 2 C, D). The extracted CaCO_3 was quantified by TGA. The majority of the CaCO_3 was formed during the first three days of incubation, and the quantity did not increase significantly over the next days (Figure 3). The Py was estimated at 40 %, which means that more than 50 % of the Ca^{2+} that was provided to the media is not used to form CaCO_3 . Nevertheless, if this Py is compared to that of *Bacillus halodurans* C-125 (which is of 40 % with the same Ca^{2+} intake in nutrient broth a pH 12, after

three weeks of incubation), B.H makes a faster bioprecipitation process. It is important to point out that a significant quantity of CaCO_3 could have been possibly lost during the extraction process.

A – NM + B.H + CA after 1 day of incubation B – NM + B.H + CA after 3 days of incubation C – NM + CA after 15 days of incubation D – NM after 15 days of incubation



E – microscopic observation of the precipitated CaCO_3 at 3 days 50X



F - microscopic observation of the precipitated CaCO_3 at 3 days 100X

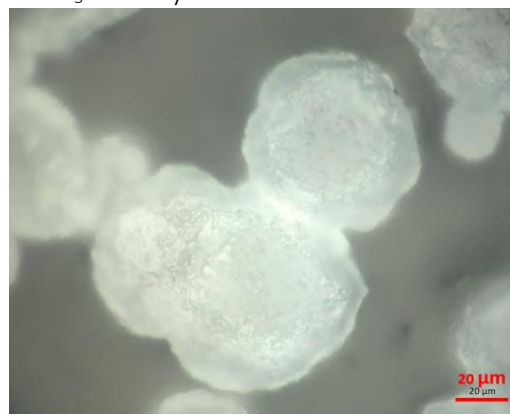


Figure 2. A - B.H colonies after 1 day of incubation, B - Presence of a homogeneous biomass mat in the media after 3 days of incubation, C - Control media with CA and without inoculum after 15 days of incubation, D - Control media without inoculum and CA after 15 days of incubation, E and F - CaCO_3 crystals precipitate on the media after three days of incubation (50 and 100X). NM – nutrient media, CA – calcium acetate.

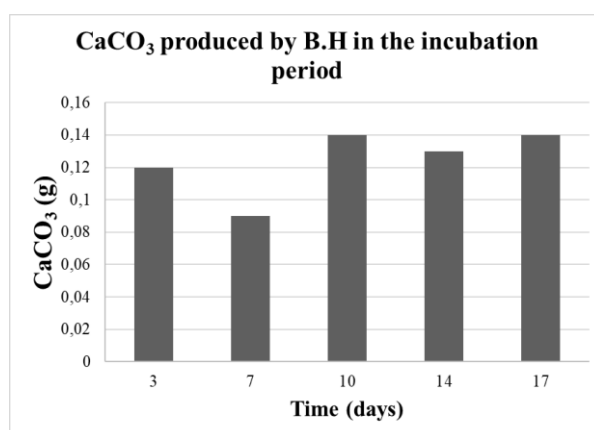


Figure 3. Quantity of CaCO_3 bioprecipitated by B.H on nutrient media at pH 11

Conclusion

Despite having estimated the doubling time, exponential, and latency phases of B.H, the presence of flocs in the suspension could have caused an important interference in the interpretation of the results. It is recommended to repeat the manipulation or employ another methodology to determine the growth curve of B.H. Moreover, it is acknowledged that

bacterial growth is different in suspension than in a solid medium, so it is not known whether it will be possible to correlate the growth phases of B.H in suspension with its growth and bioprecipitation in nutrient media. Regarding the process of bioprecipitation, it was determined that most of the CaCO₃ are precipitated during the first three days of incubation with a Py of 40%, although before drawing any conclusions, it must be confirmed that there is no significant loss of CaCO₃ during the extraction process. The conclusions are subject to change in the presentation.

Acknowledgment

The research and results reported here are supported by the French Ministry in charge of construction under the FastCarb national research program.

References

- [1] Ali, M., Abdullah, M. S., and Saad, S. A., "Effect of Calcium Carbonate Replacement on Workability and Mechanical Strength of Portland Cement Concrete," *Adv. Mater. Res.*, vol. 1115, pp. 137–141, 2015, doi: 10.4028/www.scientific.net/amr.1115.137.
- [2] Hartsock, J., "Bacteria-Infused Self-Healing Concrete," *Heron*, vol. 56, no. 1, pp. 1–12, 2011.
- [3] Rodriguez Navarro, C., Rodriguez Gallego, M., Chekroun, K. Ben, and Gonzalez Muñoz, M. T., "Conservation of ornamental stone by Myxococcus xanthus-induced carbonate biomineralization," *Appl. Environ. Microbiol.*, vol. 69, no. 4, pp. 2182–2193, 2003, doi: 10.1128/AEM.69.4.2182-2193.2003.
- [4] Wang, J., Ersan, Y. C., Boon, N., and De Belie, N., "Application of microorganisms in concrete: a promising sustainable strategy to improve concrete durability," *Appl. Microbiol. Biotechnol.*, vol. 100, no. 7, pp. 2993–3007, 2016, doi: 10.1007/s00253-016-7370-6.
- [5] Banks, E. D. *et al.*, "Bacterial calcium carbonate precipitation in cave environments: A function of calcium homeostasis," *Geomicrobiol. J.*, vol. 27, no. 5, pp. 444–454, 2010, doi: 10.1080/01490450903485136.
- [6] Anbu, P., Kang, C. H., Shin, Y. J., and So, J. S., "Formations of calcium carbonate minerals by bacteria and its multiple applications," *Springerplus*, vol. 5, no. 1, pp. 1–26, 2016, doi: 10.1186/s40064-016-1869-2.
- [7] Medevielle, M., "Utilisation de la bioprécipitation de carbonates de calcium pour améliorer la qualité de granulats de béton recyclé" (Doctoral dissertation), Université Bretagne Loire, 2017.
- [8] Martinez, H., Gueguen, M., Pechaud, Y., and Sedran, T., "Calcium carbonate precipitation of alkaliphilic bacteria on ordinary portlandite cement with a vision on recycled concrete aggregates application.," in *Proceedings of the International Workshop CO2 Storage in Concrete CO2STO2019*, 2019, p. 251.
- [9] Takami, H. *et al.*, "Complete genome sequence of the alkaliphilic bacterium *Bacillus halodurans* and genomic sequence comparison with *Bacillus subtilis*," *Nucleic Acids Res.*, vol. 28, no. 21, pp. 4317–4331, 2000, doi: 10.1093/nar/28.21.4317.
- [10] Kaur, N., Reddy, M. S., and Mukherjee, A., "Biomineralization of calcium carbonate polymorphs by the bacterial strains isolated from calcareous sites," *J. Microbiol. Biotechnol.*, vol. 23, no. 5, pp. 707–714, 2013, doi: 10.4014/jmb.1212.11087.
- [11] Dick, J. *et al.*, "Bio-deposition of a calcium carbonate layer on degraded limestone by *Bacillus* species," *Biodegradation*, vol. 17, no. 4, pp. 357–367, 2006, doi: 10.1007/s10532-005-9006-x.
- [12] Martinez, H., Gueguen, M., Pechaud, Y., and Sedran, T., "Influencing alkaliphilic bacteria development through biofilm formation on pure ordinary portlandite cement.," *Matériaux Tech.*, 2020.
- [13] Nielsen, P. H., Thomsen, T. R., and Nielsen, J. L., "Bacterial composition of activated sludge - Importance for floc and sludge properties," *Water Sci. Technol.*, vol. 49, no. 10, pp. 51–58, 2004, doi: 10.2166/wst.2004.0606.
- [14] Hošťacká, A., Čížnár, I., and Štefkovičová, M., "Temperature and pH affect the production of bacterial biofilm," *Folia Microbiol. (Praha)*, vol. 55, no. 1, pp. 75–78, 2010, doi: 10.1007/s12223-010-0012-y.
- [15] Sturr, M. G., Guffanti, A. A., and Krulwich, T. A., "Growth and bioenergetics of alkaliphilic *Bacillus firmus* OF4 in continuous culture at high pH," *J. Bacteriol.*, vol. 176, no. 11, pp. 3111–3116, 1994, doi: 10.1128/jb.176.11.3111-3116.1994.
- [16] Konhauser, K. O., "Diversity of bacterial iron mineralization," *Earth Science Reviews*, pp. 91–121, 1998, doi: 10.1016/S0012-8252(97)00036-6.
- [17] Müller, W. E. G. *et al.*, "Enzyme-accelerated and structure-guided crystallization of calcium carbonate: Role of the carbonic anhydrase in the homologous system," *Acta Biomater.*, vol. 10, no. 1, pp. 450–462, Jan. 2014, doi: 10.1016/j.actbio.2013.08.025.
- [18] Decho, A. W., "Overview of biopolymer-induced mineralization: What goes on in biofilms?," *Ecol. Eng.*, vol. 36, no. 2, pp. 137–144, 2010, doi: 10.1016/j.ecoleng.2009.01.003.

Session 6 Bacteria-based self-healing of building materials

Chair: Dr Magdalini Theodoridou

1244 *Chen and Qian*. Effect of microbial mineralization on microstructure of hardened C3S paste

1255 *Cappellesso et al.* Self-healing bacterial concrete exposed to freezing and thawing associated with chlorides

1270 *van der Bergh et al.* Development of bacteria-based repair agents for external healing of cementitious materials [POSTER]

1222 *Skevi et al.* Bacteria-based self-healing concrete in low temperature

1247 *Esaker et al.* Evaluation of the self-healing of cracked mortars incubated within sterilized and non-sterilized natural soil

1144 *Souid et al.* Microbial induced calcite precipitations of bio self-healing concrete underground exposure conditions

Effect of microbial mineralization on microstructure of hardened C₃S paste

Yanqiang Chen^{1,2,3,4} Chunxiang Qian^{1,2,3,4}

1: School of Materials Science and Engineering, Southeast University, Nanjing, 211189, China

2: Research Centre of Green Building and Construction Materials, Southeast University, Nanjing, 211189, China

3: Key Laboratory of Microbial Bio-mineralization, China Building Industry, Nanjing 211189, China

4: Jiangsu Key Laboratory for Construction Materials, Southeast University, Nanjing 211189, China

Introduction

Cement-based materials are widely used due to their good durability and compatibility. The properties of concrete, especially aesthetics and durability [1], are closely related to the properties of the surface. In 1984, Kreijger [2] pointed out that all buildings and civil facilities were directly in contact with the outside world, and concrete durability was not the same as strength for it is more dependent on the surface of the material. The composition and microstructure within the concrete's surface layer have a great influence on the performance. The mineralization of microorganism is a new surface treatment technology in cement-based materials. The carbonation of concrete and the permeability of external gases were reduced by the surface deposited calcite produced by microbial-mineralization [3]. Xue [4] demonstrated that the incorporation of bacteria into cement-based materials reduced surface efflorescence by 42.43%.

The microorganism selected in this paper was *Paenibacillus* [5], a type of carbon-fixing bacteria, and the bacteria were mixed into concrete to study the effect of microbial mineralization on the microstructure of hardened C₃S paste, such as the reaction degree of C₃S, the content of CaCO₃ and the porosity of early age hardened pastes. The study results will help better understanding the effects of bacteria on cement-based materials and guide the engineering practice.

Materials and methods

Raw materials

Tricalcium silicate

The C₃S purity was about 98.95% by QXRD [6], and the average particle diameter was 38.45 μm according to XRD analysis. The chemical composition based on XRF was shown in Table 1.

Table 1. Chemical composition of C₃S (%)

CaO	SiO ₂	MgO	Al ₂ O ₃	Na ₂ O	Sum
72.51	23.89	2.21	0.22	0.12	99.95

Microbial culture

Bacillus were domesticated for half a year in an alkaline environment before used. After being inoculated into a sterile medium and cultured at 30 °C for 24 h, the number cell was measured by flow cytometry (ACEA D2040R, China), which was 2*10⁹ cells/mL.

Mineralization experiment design

Mineralization experiment in hardened C₃S paste

A set of comparative experiments was designed. Samples in one group were C₃S paste mixed with bacteria solution under the water-solid ratio of 0.45. Samples in the other group

were pure C_3S paste. All samples were cured for 7 days in $20\pm 1\text{ }^\circ\text{C}$, $65\pm 10\%\text{RH}$ and 0.012mol/L CO_2 .

Mineralization experiment in $\text{Ca}(\text{OH})_2$ solution

The mineralization experiment in the simulated solution was further to explain the effect of microbial mineralization on the conversion of $\text{Ca}(\text{OH})_2$ to CaCO_3 . Comparative experiments were designed divided by the concentrations of $\text{Ca}(\text{OH})_2$, which were 0.0825 g/100mL , 0.165 g/100mL and 0.495 g/100mL . The simulated solution of each group was the same amount of bacteria solution or water respectively. The experiments were carried out in $20\pm 1\text{ }^\circ\text{C}$, $65\pm 10\%\text{RH}$ and 0.012mol/L CO_2 for 3 days. The mineralization products were then dried for future use.

Methods of characterization

Quantitative analysis of extent of C_3S reaction at different depths

The phases of hardened C_3S paste were quantitatively analyzed by QXRD with D8-Discover diffractometer. The sample was taken from the surface layer of hardened C_3S paste at a depth of $1\pm 0.1\text{mm}$ as shown in Figure 1. The powder was then immersed in absolute ethanol for 3 days and was dried in a vacuum oven at $60\text{ }^\circ\text{C}$ for 3 days finally.

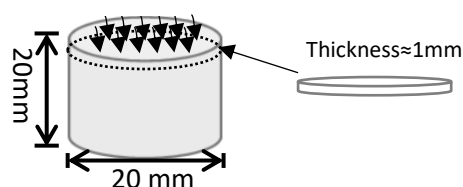


Figure 1. Schematic diagram of sample processing

Quantitative analysis of the content of CaCO_3 at different depths

TG was used to measure the content of CaCO_3 in the samples. The equipment used was Netzsch STA 449 F3. The TG curve was analysed by DTG.

Porosity measurement

X-ray tomography was used to non-destructively detect the porosity of the samples using Y.CT PRECISION S (YXLON, Germany). The images obtained by scanning the hardened paste were reconstructed by software VG Studio MAX 3.0. The smallest pore diameter resolved in this paper was $30.3\mu\text{m}$.

Results and discussion

Quantitative analysis of C_3S content at different depths

For the mineralization and control samples, the XRD patterns at different depths for different ages were shown in Figure 2. M represented the mineralization group and C represented the control group (the same applies hereinafter). The peak of $\text{Ca}(\text{OH})_2$ in the surface of the mineralization group sample was significantly lower than that of the control sample.

The results of the remaining amount of C_3S were shown in Figure 3. The C_3S content was significantly lower, indicating that the addition of microorganisms accelerated the reaction of C_3S . The decrease of C_3S content of mineralization samples might be related to the hydration promotion by bacteria as a nucleation site [7].

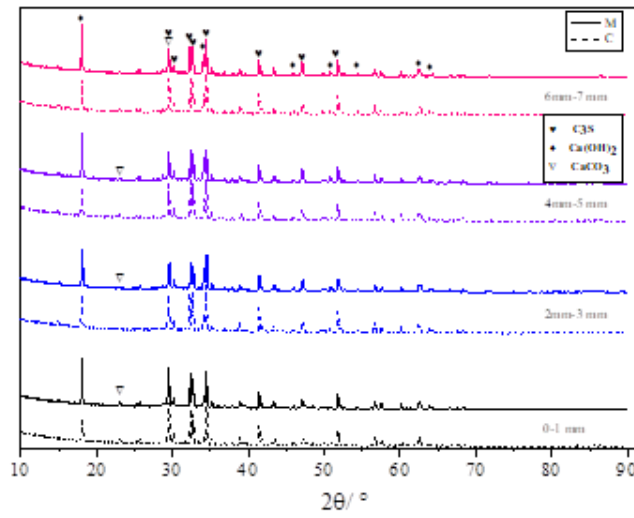


Figure 2. Peak intensity and phase at different depths from the surface layer

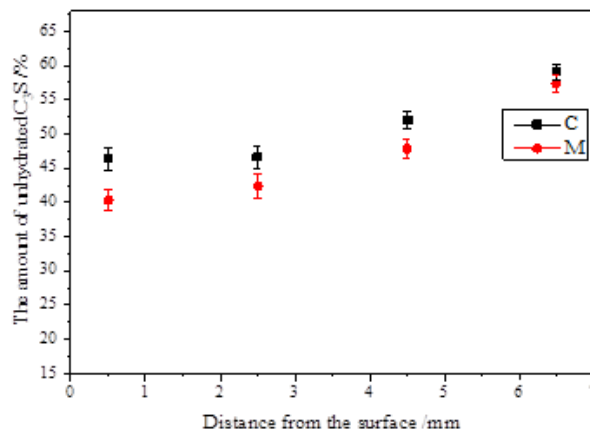


Figure 3. The amount of unhydrated C₃S at different depths from the surface layer

Quantitative analysis of CaCO₃ at different depths

Figure 4 reflected the content of CaCO₃ at different depths at different ages. Results showed that the CaCO₃ content of the mineralization group was higher than that of the control group by over 2.8% within 1mm depth.

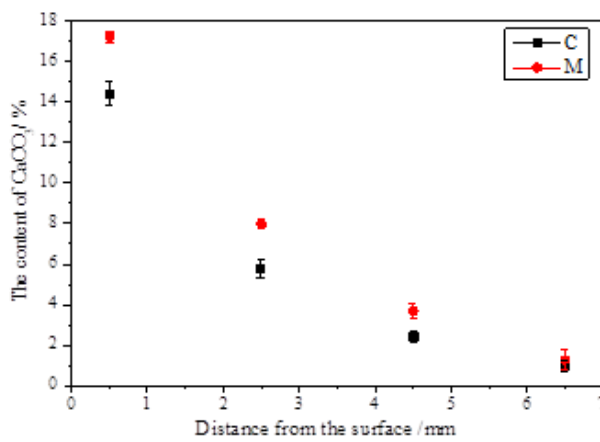


Figure 4. CaCO₃ content at different depths of mineralization/control samples

Porosity measurement

Figure 5 showed the changes in porosity under different depths of mineralization and control groups. Comparing the porosity within 1mm of the surface layer of two groups, the mineralization group decreased by 0.08%, indicating that the porosity of cement-based materials could be reduced by mineralization. Ghosh P [8] pointed out that the bio-mineralization product, calcium carbonate, was able to reduce the porosity of the sample, which was consistent with the experimental results.

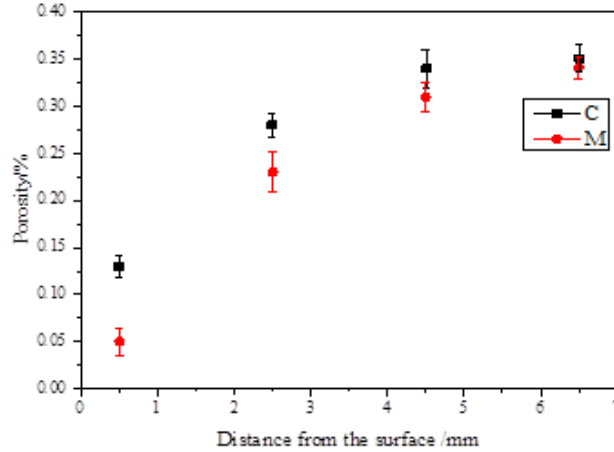


Figure 5. Porosity at different depths of mineralization/control samples

Conversion of calcium hydroxide to calcium carbonate in solution

In this section, the contents of Ca(OH)₂ and CaCO₃ were measured by TG, and the conversion rate α was used to characterize whether the addition of microorganisms has an effect on the conversion of Ca(OH)₂ to CaCO₃, as shown in Equation (1).

$$\alpha = \frac{n(\text{CaCO}_3)}{n(\text{Ca(OH)}_2) + n(\text{CaCO}_3)} \tag{1}$$

where n(Ca(OH)₂) and n(CaCO₃) were calculated from the TG diagram.

Table 2. Results of conversion rate in mineralization and control groups

Groups	Ca(OH) ₂ addition g	Solution	Solvent volume ml	Conversion rate %
J-1	0.0825	bacterial fluid	100	100
NJ-1	0.0825	deionized water	100	100
J-2	0.165	bacterial fluid	100	94.91
NJ-2	0.165	deionized water	100	90.16
J-3	0.495	bacterial fluid	100	82.86
NJ-3	0.495	deionized water	100	57.55

As shown in table 2, when adding 0.0825g/100mL and 0.165 g/100mL Ca(OH)₂, the difference of conversion rate between the mineralization and control group was small. However, when adding 0.495g/100mL Ca(OH)₂, the conversion rate in the mineralization group was 82.86%, while it was 57.55% in the control group. The difference indicated that the addition of microorganisms had a significant effect on the conversion of Ca(OH)₂ to CaCO₃ when the Ca(OH)₂ solution was saturated.

Figure 6 showed SEM images of CaCO₃ in the mineralization and control groups. The CaCO₃ formed in the mineralization group were mainly polyhedrons, and there were a small number of spherical particles. The CaCO₃ formed in the control group were mainly the oblique

hexagonal lattice structure, and the crystal particle size was larger and the distribution was more uniform, with the presence of flake or rhombohedral single crystal, twin crystal and aggregates.

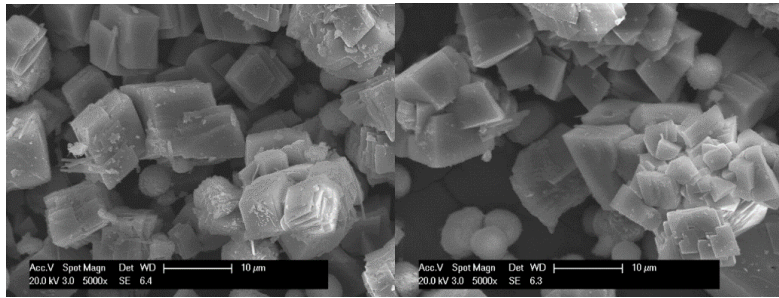


Figure 6. SEM image of CaCO_3 in the mineralization (left) and control (right) groups.

This experiment showed that microbes could promote the formation of CaCO_3 when they were in the pore solution of cement-based materials with external CO_2 assessed. Since the volume of CaCO_3 is larger than that of Ca(OH)_2 , the addition of microorganisms could effectively reduce the porosity of cement-based materials.

Conclusion

- The addition of microorganisms was able to promote the hydration of C_3S .
- The content of CaCO_3 in mineralization group was significantly higher than that in the control group.
- The addition of microorganisms had a significant effect on the conversion of Ca(OH)_2 to CaCO_3 .

Acknowledgment

The authors appreciate the financial support from the National Natural Science Foundation of China (Grant No.51738003).

References

- [1] Uchikawa H, Hanehara S, Shirasaka T, et al. Effect of admixture on hydration of cement, adsorptive behavior of admixture and fluidity and setting of fresh cement paste[J]. *Cement & Concrete Research*, 1992, 22(6):1115-1129.
- [2] Kreijger P C. The skin of concrete composition and properties[J]. *Matériaux Et Construction*, 1984, 17(4):275-283.
- [3] De Muynck W, Cox K, De Belie N, et al. Bacterial carbonate precipitation as an alternative surface treatment for concrete[J]. *Construction and Building Materials*, 2008, 22(5): 875-885.
- [4] Xue B, Qian C. Mitigation of efflorescence of wallboard by means of bio-mineralization[J]. *Frontiers in Microbiology*, 2015, 6:1155.
- [5] Chen Y, Qian C, Zhou H. Characterization Methods for the Effect of Microbial Mineralization on the Microstructure of Hardened C_3S Paste[J]. *Advances in Materials Science and Engineering*, 2020, 2020.
- [6] Nish F, Takeuchi Y, Maki I (1985). Tricalcium silicate $\text{Ca}_3\text{O}[\text{SiO}_4]$: the monoclinic superstructure [J]. *Zeitschrift für Kristallographie*. 172: 297-314.
- [7] Lee J C , Lee C J , Chun W Y , et al. Effect of Microorganism *Sporosarcina pasteurii* on the Hydration of Cement Paste[J]. *Journal of Microbiology and Biotechnology*, 2015, 25(8).
- [8] Ghosh P , Mandal S , Chattopadhyay B D , et al. Use of microorganism to improve the strength of cement mortar[J]. *Cement & Concrete Research*, 2005, 35(10):1980-1983.

Self-healing bacterial concrete exposed to freezing and thawing associated with chlorides

Vanessa Giaretton Cappelleso^{1,2}, Tim Van Mullen¹, Elke Gruyaert², Kim Van Tittelboom¹, Nele De Belie¹

1: Ghent University, Department of Structural Engineering and Building Materials, Technologiepark Zwijnaarde 60, 9052 Gent, BE

2: KU Leuven, Department of Civil Engineering, Materials and Constructions, Ghent Technology Campus, Gebroeders De Smetstraat 1, 9000 Ghent, BE

Abstract

Recently, researchers have focussed on the development of self-healing strategies in order to guarantee high performance regarding the durability of concrete structures. Exposing self-healing concrete to extreme conditions and evaluating its behaviour is the first step in understanding how the self-healing mechanism performs under these conditions. Nevertheless, there are limited studies subjecting self-healing concretes to harsh conditions combining extreme low temperatures and salt attack. Therefore, we concentrate in this study on freezing and thawing conditions with de-icing salts, specifically with sodium chloride. It is an innovative assessment of self-healing concrete including commercially manufactured bacteria as healing agent. The objective is to ensure that autonomous crack healing occurs, restricting chloride ingress, extending the service life, and reducing the effect of degradation. The study presents the influence of the exposure conditions through permeability tests, microscopic investigations, scaling analyses, and chloride penetration. The permeability tests showed complete sealing after freezing and thawing cycles. Nevertheless, the healing products were removed together with material that was scaled off the surface due to cyclic freezing and thawing. The bacteria enhanced the properties of the concrete, resulting in less scaling and chloride penetration. However, chloride penetration through the crack cannot be prevented.

Introduction

The efficiency of self-healing concrete has been reported multiple times in literature showing the great potential of this technique to heal cracks. However, many of these studies were performed under ideal exposure conditions. Therefore, knowing how the self-healing concrete resists extreme conditions is extremely important to transfer this technology to practice. There are different self-healing mechanisms and several extreme conditions that need to be studied in depth. Hence, it will be possible to design structures with the most suitable self-healing mechanism for each extreme condition. A combination of cold temperatures and salt attack represents a realistic condition prevailing in cold countries which results to damage noticed in infrastructure such as highways, bridges, bike paths, ports, etc. There are two different types of deterioration due to freezing and thawing: internal cracking due to freezing and thawing cycles [1][2], and surface scaling, generally due to freezing in the presence of de-icing salts [3][4]. The cyclic freezing and thawing can produce a high pore pressure related to the water phase change inside the pores leading to the initiation of cracks within the concrete matrix [1][2]. In this study, we investigated a self-healing concrete produced with commercially manufactured bacteria as healing agent exposed to freezing and thawing conditions with de-icing salts. The study presents the influence of the exposed conditions through permeability tests, microscopic investigation, scaling analyses, and chloride penetration.

Materials and methods

Self-healing mechanism.

The healing agent is available in powder form and is a commercial product composed of bacterial spores (*Bacillus cohnii*) and calcium lactate as carbon source. Both are encapsulated through the extrusion of the carbon sources and the bacterial spores followed by grinding of the extrudate. The pellets have dimensions less than 2 mm. The bacteria-based concrete, depending on the dosage of the healing agent, has the ability to heal cracks up to 0.8 mm under laboratory conditions [5]. The recommended healing agent dosage is 5-15 kg/m³ concrete. This study investigates a dosage of 10 kg/m³.

Concrete specimens.

Self-compacting concrete with a water-to-cement (W/C) ratio of 0.45 was used. It respects the maximum W/C required by EN-206 1 [6] for freeze-thaw attack with de-icing salt in high water saturation, considering XF4 being the exposure class. A concrete with high strength and flow was chosen to achieve better resistance and to allow to distinguish the improvement provided by the use of the healing agent. The concretes contained per m³ 853 kg sand 0/4, 263 kg gravel 2/8, 434 kg gravel 8/16, 360 kg CEM I 52.5 N, 240 kg limestone filler, 162 kg water and 3.22 kg superplasticizer. The content of the healing agent was 10 kg/m³. The concrete had a slump class SF2 and the average 28-day compressive strength was 80 MPa with 2.97 MPa of standard deviation for the reference concrete, and 71 MPa with 3.02 MPa of standard deviation for bacterial concrete. The geometry of the cast cylindrical specimens is 100 mm in diameter and 50 mm in height. After casting, the specimens were stored in an air-conditioned room with a temperature of 20±2 °C and a relative humidity of at least 95% for 24 hours. Subsequently, samples were demoulded and placed in this room until 28 days. At this age cracks were created in part of the specimens. Realistic cracks were made by the Brazilian splitting test producing average crack widths of 170±50 µm. After crack creation, the specimens were submerged in water with the cracks that would be exposed facing downwards for 28 days to allow healing. The uncracked specimens were placed in the same conditions as the cracked concrete samples.

Crack width measurements.

The crack width of realistic cracks was measured at eleven places along the crack length at the top side with three measurements performed on each image. The measurements were executed with a stereomicroscope, Leica S8 APO with DFC 295 camera. The locations were fixed to allow analysis of the same place after exposure. In order to do so, a 3D printed template was used with some tag points. This method was used instead of a method where marks are applied on the samples surface to indicate crack measurement locations as the surface could be destroyed during the freeze-thaw cycles.

Freeze-thaw with de-icing salts.

The experiment was based on the standard CEN/TS 12390-9 [7]. For the uncracked concrete the standard was followed. However, for the cracked concrete samples some adaptations to the standard were required. The protection of the crack is the most important factor, as one of the steps in the experiment is to glue the specimen into a PVC tube of 70 mm in height and 110 mm in internal diameter. The procedure is to fill the gap between the specimen and the wall of the PVC tube with epoxy resin with a low viscosity (Figure 1a). If the crack is not well protected, the epoxy resin may enter the crack filling part of it. The way to avoid this is to protect the crack by a tape with a high adherence. Aluminium tape was used at the locations where the tape did not have to be removed after the test (Figure 1b). The bottom of the specimens used for the water permeability test was sealed with white masking tape (Figure 1c), and then aluminium butyl tape on top to avoid leakage during the freeze-thaw test (Figure

1dd). Finally, the specimens were placed into an insulating material (Figure 1Figuree), covered with the chloride solution, protected with a resistant plastic, and inserted into a freeze-thaw chamber.

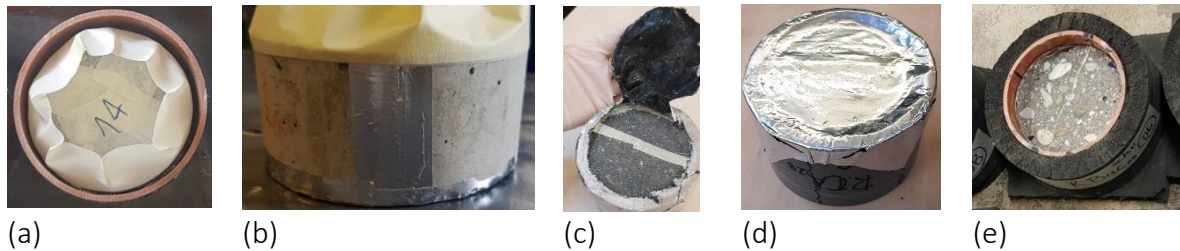


Figure 1. Concrete specimens glued into a PVC tube (a), the aluminium tape protecting the crack before gluing into a PVC tube (b), the white masking tape protecting the crack allowing removal after exposure at the bottom of the specimen (c), aluminium butyl tape placed on the bottom to avoid leakage during the test where the specimen is shown upside down (d), and insulation system applied while testing in the freeze-thaw chamber

Self-healing efficiency.

The water flow test with a constant water head (25 cm) was used to assess the permeability, hence, the self-healing efficiency. A method similar to the one of Shin et al. [8] was used. The permeability was measured at the time of crack creation, after healing, and after freeze-thaw exposure. Three specimens were used for each combination for water flow test. Microscopic images were collected at each time step using the same microscope as the one used to measure the crack widths. The collection of scaled material was performed at time steps as specified in the standard CEN/TS 12390-9 [7]. To collect the scaled material from the test surface, the surface was rinsed with demineralized water using a spray bottle. The brush as recommended by the standard was avoided because the formed healing products could be destroyed, affecting the results. The chloride penetration was measured perpendicular to the crack, after splitting the specimens, at the end of the freeze-thaw cycles. Once the surface was dry, a 0.1 mol/L silver nitrate solution was sprayed on the fractured cylinder halves to visualize the chloride ingress. The location of the colour change boundary was measured from the top every 5 mm for cracked concrete, and every 10 mm for uncracked concrete by discarding 10 mm from the edges. The entrance through the crack horizontally was quantified in the middle of the specimen height.

Results and discussion

Crack healing efficiency after exposure.

The self-healing efficiency was quantified by performing a water flow test (Figure 2Figure a) before (28 d) and after the healing period (56 d), as well as after the freeze-thaw exposure (112 d). Both the reference (REF) and bacterial (BAC) concretes showed a reduction in the permeability after the healing period demonstrating sealing capacity. Likewise, both concretes showed significant healing during freeze-thaw exposure. The REF concrete was sealed for 78% after the healing period in case of specimens with an average crack width of $175 \mu\text{m} \pm 31 \mu\text{m}$, and nearly 100% after freeze-thaw exposure. In contrast, the BAC concrete sealed for 70% in case of specimens with an average crack width of $163 \mu\text{m} \pm 37 \mu\text{m}$, and 93% after exposure. Although the BAC concrete had a lower average crack width, it showed somewhat lower healing efficiency in the water flow test, probably because of the parallel-walled crack that permitted leaching forming weak stalactites. The method used for crack creation generates through-going cracks, and differences in the crack width on both surfaces are unavoidable. Despite the fact that the crack width is on average similar on both surfaces, generally, the width

at the top surface is slightly different from the width at the bottom surface. These variations cause variability in the water flow test, although the mean value of different specimens is the same.

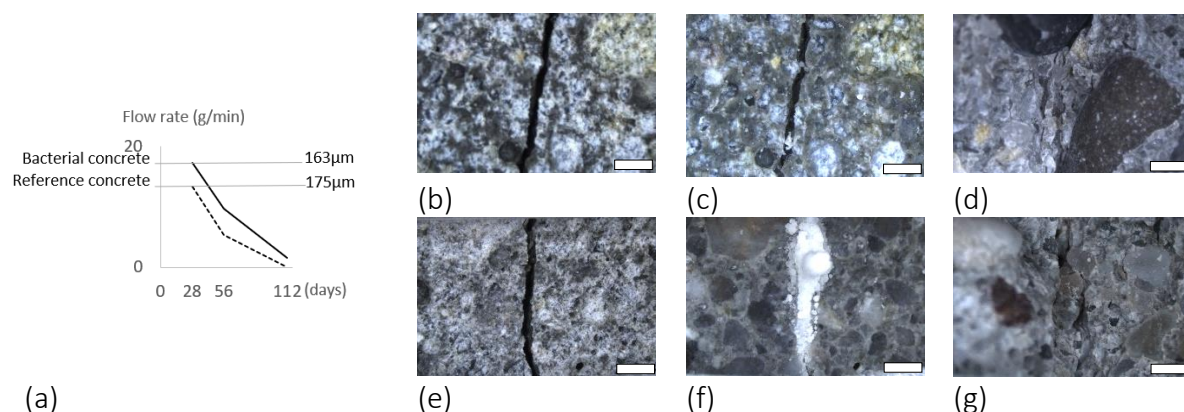


Figure 2. Water flow rate (a). Crack images for reference concrete with 220 μm of width (b) at the crack creation day, (c) after healing period, (d) after exposure to freeze-thaw cycles, and for bacterial concrete with 215 μm of width (e) at the crack creation day, (f) after healing period, (g) after exposure to freeze-thaw cycles. The scale bar represents 1 mm.

Cracks that cross the specimen increase the leaching of calcium hydroxide on the bottom surface combined with the intense production of calcium carbonate from the bacteria. In addition, the gravity in a submerged condition contributed to the production of a huge amount of healing product in the crack surface facing downwards. These factors caused formation of stalactites along the crack (Figure 2f). The stalactites did not have resistance enough to survive the water flow test and some small holes were created at the location of the stalactites needles. The holes allowed the water to cross the crack, increasing the permeability. On the other hand, REF concrete did not demonstrate crack closure as shown by microscopic analysis (Figure 2c). Further research should focus on samples located in a wet environment with flexural cracks, as it is expected that the tendency for stalactite formation of the BAC concrete will be lower. Note that the healing product was damaged due to freezing as observed in the microscopic analyses (Figure 2g).

Resistance of autonomously healed concrete to scaling and chloride penetration.

The scaling results after 56 days are given in Figure 3a. The BAC concrete decreased the scaling by $89\% \pm 3.2\%$ for uncracked concrete, and $91\% \pm 2.3\%$ for cracked concrete compared to the REF concrete. For the REF uncracked concrete, scaling was reduced by $25\% \pm 2.9\%$ compared to the REF cracked concrete, while for the BAC uncracked concrete it was reduced by $12\% \pm 1.7\%$ compared to the BAC cracked concrete. Therefore, the BAC concrete increases the resistance to scaling, reducing significantly damage caused by loss of material due to freezing. The small difference in the scaling between uncracked concrete and cracked concrete, for REF and BAC concretes, shows that there was not only an increase in the surface strength of the material but a widespread improvement in resistance throughout the sample. Chloride penetration has also been reduced for BAC concrete, both uncracked and cracked (Figure 3c and Figure 3e), compared to REF concrete (Figure 3b and Figure 3d). The BAC uncracked concrete decreased the chloride penetration by 46% compared to the REF uncracked concrete. The BAC cracked concrete decreased the chloride penetration from the surface by 35% compared to the REF cracked concrete. The horizontal penetration by the crack did not show a significant difference between both concretes, but depends largely on the crack widths as well as the internal crack geometries. The improvements in the resistance to scaling and

chloride penetration generated by the use of self-healing concrete produced with bacteria are possibly due to a densification of the concrete or due to changes in the porosity increasing the air-entrainment in the bacterial concrete. This is currently further investigated.

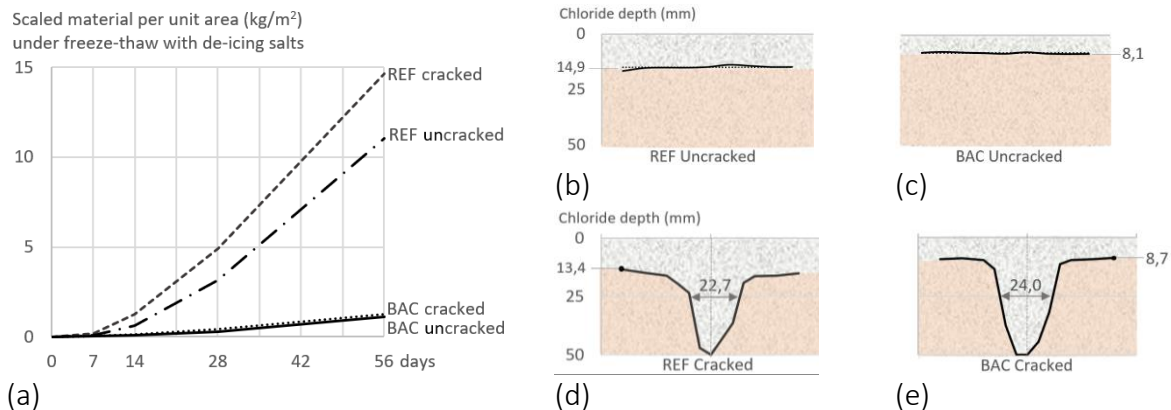


Figure 3. Scaling under freeze-thaw with de-icing salts (a). Depths of chloride penetration with gray colour representing the area with chlorides for uncracked reference concrete (b), uncracked bacterial concrete (c), cracked reference concrete (d), and cracked bacterial concrete (e)

Conclusion

The bacterial concrete showed better performance under freezing and thawing conditions. There are two possible hypotheses (1) the densification due to the healing products increased the resistance of the concrete, or (2) the healing agent induced a microstructure with greater distribution and amount of porous, that is, bringing the benefits of the air-entrainment. Further studies need to be done to understand the actual factors. The freeze-thaw condition contributes to the internal healing measured by water permeability; however, chloride penetration through the crack cannot be prevented. The generated healing products in the crack were damaged by scaling due to freezing during the exposure period. Although the bacteria have less or no proven efficiency at low temperatures, cycles between low and high temperatures may have contributed to the reactivation of spores in periods of positive temperature. While in freezing conditions, they may regress to spores to survive for the next activation period. Although, the healing period may have contributed to the good performance of the bacterial concrete.

Acknowledgment

This project has received funding from the European Union's Horizon 2020 under the Marie Skłodowska-Curie grant agreement No 860006. The healing agent was provided by Basilisk and TU Delft, the latter being a beneficiary of SMARTINCS. acknowledge the support of the grant (21SCIP-C158977-02) from the Construction Technology Research Program funded by the Ministry of Land, Infrastructure and Transport of the Korean government.

References

- [1] Z. Liu and W. Hansen, "Effect of hydrophobic surface treatment on freeze-thaw durability of concrete," *Cem. Concr. Compos.*, vol. 69, pp. 49–60, May 2016, doi: 10.1016/j.cemconcomp.2016.03.001.
- [2] M. J. Al-Kheetan, M. M. Rahman, S. H. Ghaffar, M. Al-Tarawneh, and Y. S. Jweihan, "Comprehensive investigation of the long-term performance of internally integrated concrete pavement with sodium acetate," *Results Eng.*, vol. 6, no. March, p. 100110, Jun. 2020, doi: 10.1016/j.rineng.2020.100110.
- [3] M. Pigeon, J. Marchand, and R. Pleau, "Frost resistant concrete," *Constr. Build. Mater.*, vol. 10, no. 5, pp. 339–348, Jul. 1996, doi: 10.1016/0950-0618(95)00067-4.
- [4] L. Basheer and D. J. Cleland, "Freeze–thaw resistance of concretes treated with pore liners," *Constr. Build. Mater.*, vol. 20, no. 10, pp. 990–998, Dec. 2006, doi: 10.1016/j.conbuildmat.2005.06.010.
- [5] R. Mors and H. M. Jonkers, "Bacteria-based self-healing concrete: evaluation of full scale demonstrator

- projects," *RILEM Tech. Lett.*, vol. 4, pp. 138–144, Apr. 2020, doi: 10.21809/rilemtechlett.2019.93.
- [6] EUROPEAN COMMITTEE FOR STANDARDIZATION, *NBN EN 206-1: Concrete - Part 1: Specification, performance, production and conformity*. Belgium- Brussels, 2001, p. 72.
- [7] EUROPEAN COMMITTEE FOR STANDARDIZATION, *PD CEN / TS 12390-9: 2016 BSI Standards Publication. Testing hardened concrete Part 9: Freeze-thaw resistance with de-icing salts - Scaling*. 2016.
- [8] K. J. Shin, W. Bae, S.-W. Choi, M. W. Son, and K. M. Lee, "Parameters influencing water permeability coefficient of cracked concrete specimens," *Constr. Build. Mater.*, vol. 151, pp. 907–915, Oct. 2017, doi: 10.1016/j.conbuildmat.2017.06.093.

Development of bacteria-based repair agents for external healing of cementitious materials

[POSTER]

John Milan van der Bergh¹, Snežana Vučetić², Olja Šovljanski², Bojan Miljević², Siniša Markov², Jonjaua Ranogajec², Michael Riley¹, Ana Bras¹

¹School of the Built Environment, Liverpool John Moores University, Byrom Street, Liverpool, L3 3AF, UK

²Faculty of Technology, University of Novi Sad, Bul. cara Lazara 1, 21000 Novi Sad, Serbia

Introduction and Aim

- Self-healing techniques using bacteria based systems have been extensively studied, but the agent is usually added during the manufacture stage
- Our aim was to develop a **bacteria-based system for external healing/sealing**
- After our preliminary study, research was continued to include an additional bacterial culture, *Bacillus cohnii*
- Possible application for buildings already in service

Materials

- Pre-cracked cement mortar beams CEM I 42.5 (EN196-1) treated with bio liquid repair system applied by dropping technique
- Bio liquid systems: suspension of *Sporosarcina pasteurii* or *Bacillus cohnii* (+ respective nutrient solutions)

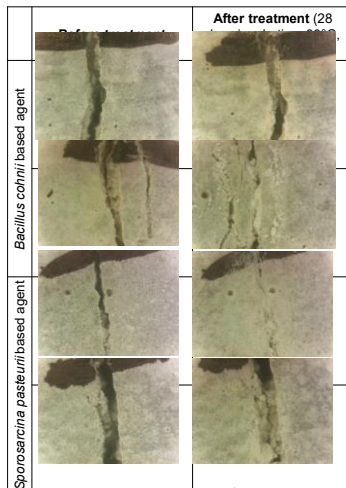
Methods

- Crack observation (optical microscopy)
- Capillary absorption test
- Compressive strength test



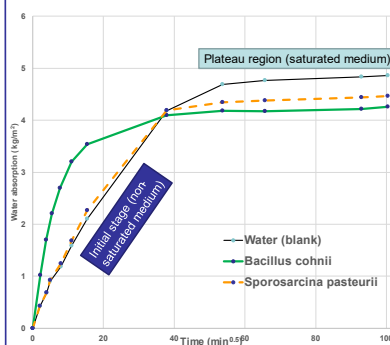
Results and Discussion

Crack Observation



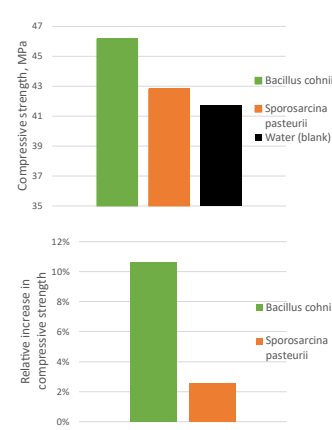
Visual inspection confirmed that treatment with bio-agents resulted in visible formation of sealing material – products of metabolism

Capillary Absorption Test



- *B. cohnii* sample had higher water absorption in the initial stage, but lower absorption in the plateau region than both *S. pasteurii* and blank samples
- The *S. pasteurii* sample had very similar behaviour to the blank sample in the non-saturated part, but lower absorption in the saturated part, which is a desirable result. It can be concluded that *S. pasteurii* had very good overall performance in terms of reduction of capillary absorption in both the non-saturated and saturated medium part of the graph.

Compressive Strength Test



- Evidently, *B. cohnii* bio-agent demonstrated better improvement of mechanical characteristics than *S. pasteurii*, even though *S. pasteurii* exhibited better sealing properties

Conclusions

- *S. pasteurii* based bio-agent had better **sealing characteristics** as determined by capillary absorption
- *B. cohnii* based bio-agent had better **mechanical characteristics** – compressive strength recovery
- Further research efforts should include testing potential synergetic effect of combining the two bacterial cultures

Acknowledgments

The authors of this paper would like to thank the Royal Society research grant RGS11191304—Research Grants 2019 Round 1, ICE R&D Enabling Fund, Royal Academy of Engineering, COST action CA15202 “Self-Healing as Preventive Repair of Concrete Structures (SARCOS)”, and the Serbian Ministry of Education, Science and Technological development (Project No. 451-03-9/2021-14/200134) for enabling the development of this work.

Further info: Van Der Bergh, J.M.; Miljević, B.; Šovljanski, O.; Vučetić, S.; Markov, S.; Ranogajec, J.; Bras, A. Preliminary Approach to Bio-based Surface Healing of Structural Repair Cement Mortars. *Constr. Build. Mater.* 2020, 248, 118557; Van Der Bergh, J.M.; Miljević, B.; Vučetić, S.; Šovljanski, O.; Markov, S.; Riley, M.; Ranogajec, J.; Bras, A. Comparison of Microbially Induced Healing Solutions for Crack Repairs of Cement Based Infrastructure Sustainability 2021, 13, 4267.

Bacteria-based self-healing concrete at low temperature

Lorena Skevi¹, Bianca Reeksting², Susanne Gebhard², Kevin Paine¹

1: BRE Centre for Innovative Construction Materials, University of Bath, Claverton Down, BA2 7AY Bath, UK

2: Department of Biology and Biochemistry, University of Bath, Claverton Down, BA2 7AY Bath, UK

Abstract

Cracking in concrete is an inevitable problem that can severely impair the durability of the structures and shorten their service life. A solution to the problem is self-healing concrete, an innovative material that has can detect and heal its own cracks, minimizing the need for external repair. Bacteria have been investigated for self-healing concrete due to their ability to induce the precipitation of calcium carbonate through their metabolic activities, thus sealing the cracks. In this investigation, bacteria-based self-healing of concrete in low temperatures is attempted. The self-healing efficiency of cement mortars with two different bacteria, a psychrophilic strain and the non-psychrophilic *B. cohnii*, was assessed in two different temperatures, at 10 °C and 20 °C. Bacteria spores were encapsulated in aerated concrete granules (ACG) which replaced part of the sand in the mortar mix. Nutrients and precursors were added directly in the mix. The effect of the cracking age on self-healing capacity was also investigated with cracks generated at 28 and 180 days. Self-healing performance was evaluated by visual observation with an optical microscope and by the water permeability of the samples before and after the healing. The results showed a clear lead of the psychrophilic strain in low-temperature self-healing against *B. cohnii*, which could only contribute to healing at 20 °C. Crack healing at both temperatures was more efficient for early age cracks. Possibility of combining the two strains for achieving self-healing in different temperatures will be investigated in the near future.

Introduction

Various types of cracks occur inevitably in concrete, affecting the durability of the material and consequently the structure's service life. Monitoring of the cracks and external repair throughout a structures' life is vital for expanding their lifespan but is also expensive and technically challenging [1]. In the UK approximately 35% of the country's total construction budget is spent on the maintenance and repair of existing structures, which in 2020 accounted for approximately £57.9 billion [2]. Self-healing concrete has been investigated over the past decade as a potential solution to this problem. A biological approach towards self-healing concrete is bacteria-based self-healing (BBSH) in which bacterial spores are employed in concrete as healing agents. In the presence of nutrients and when water flows through the cracked area the spores germinate and induce the precipitation of calcite through their metabolic activities, thus sealing the crack. Addition of the spores in protective carriers has been shown to increase the viability of the bacteria in the highly alkaline and stressful environment of concrete [3].

Numerous self-healing systems using different bacteria, nutrients and carriers have been studied reporting significant healing of cracks up to 1 mm wide [4, 5]. In the majority of the research so far mesophilic bacteria that grow optimally at 30 °C have been employed and therefore healing has been demonstrated at environmental temperatures ranging from 20 °C to 30 °C. However, temperature lower than that can negatively affect both the growth of bacteria [6] and the rate of Microbially Induced Calcite Precipitation (MICP) [7]. It is thus essential to examine the efficiency of BBSH concrete at lower temperatures to ensure its

application in realistic environmental conditions. Only few studies have addressed this issue to date [8, 9]. Palin et al. [8] used *Bacillus halmapalus* and Su et al. [9] *Lysinibacillus sp.* in cement mortars and demonstrated significant healing of cracks 0.4 mm wide at 8 °C and 7 °C respectively.

In this study, bacteria-based self-healing of concrete at low temperature was investigated using two bacterial strains, a mesophile and a psychrotroph. The self-healing efficiency of the cement mortars was examined both at low (7.5 ± 2 °C) and room temperature (20 ± 2 °C) and compared for both strains over a period of one month.

Materials and methods

Mesophilic bacteria of the strain *Bacillus cohnii* DSM 6307B (German Collection of Microorganisms and Cell Cultures (DSMZ)) were used in this study, along with a psychrotrophic species, named Psy39, that was isolated from natural limestone regions in the UK, based on its ability to grow both at low-temperatures and in alkaline environments. Portland limestone cement, CEM II/A-L 32.5R, was used for making the cement mortar samples. Yeast extract was used as the organic food source for the bacteria and calcium nitrate was used as the precursor calcium source for promoting calcium carbonate precipitation. The sand used conformed to BS EN 196-1.

Spores of the bacteria were encapsulated in commercially available aerated concrete granules (ACG) before being added to the mortar mix. The encapsulation process has been described in detail by Tan et. al [10]. More specifically, spores were added in distilled water and ACG of 1-4 mm size were impregnated in the spore-bearing water solution under vacuum. To avoid an early germination of the spores when contacting the nutrients during mixing, the granules were dried in the oven at 50 °C for 24 hours and were then coated with a layer of PVA. Spore-loaded granules replaced 6% of the sand by volume in the mortar mix, while 1% of yeast extract and 5% of calcium nitrate by mass of cement were diluted in the mixing water and added directly in the mortar mix. Two types of bacterial samples were prepared in this way, BIO-M containing the mesophile *B. cohnii* and BIO-P containing the psychrophile Psy39.

In addition to the bacterial samples, plain cement mortar samples without bacteria and nutrients (reference – REF) and samples containing only nutrients (control – CTRL) were prepared as benchmarks. Two sets of samples were made for testing the healing at two temperatures, at 7.5 ± 2 °C and 20 ± 2 °C. In order to save materials, especially high-cost spores, 40x40x65 mm samples were prepared in two layers, one containing the healing agents, i.e. the bacteria and nutrients, and one layer of plain mortar, as shown in Figure 1a. To be consistent all samples were prepared in this manner. A triplet of samples was prepared for each type and for the two sets resulting in a total of 24 samples, 6 per mix design. Table 1 gives the mix design for each type of samples used in this study. Mixing of mortars was done according to BS EN 196-1. Specimens were demoulded 48 hours after casting and were cured in water at 20 °C for 28 days, until the day of cracking.

Table 1. Composition of the 3 mortar types used in this study.

	Cement (g)	Water (g)	Sand (g)	Spore- loaded ACG (g)	Yeast extract (g)	Calcium nitrate (g)
REF	184	92	552	-	-	-
CTRL	184	92	552	-	9.1	2
BIO - M	184	92	519	13	9.1	2
BIO - P	184	92	519	13	9.1	2

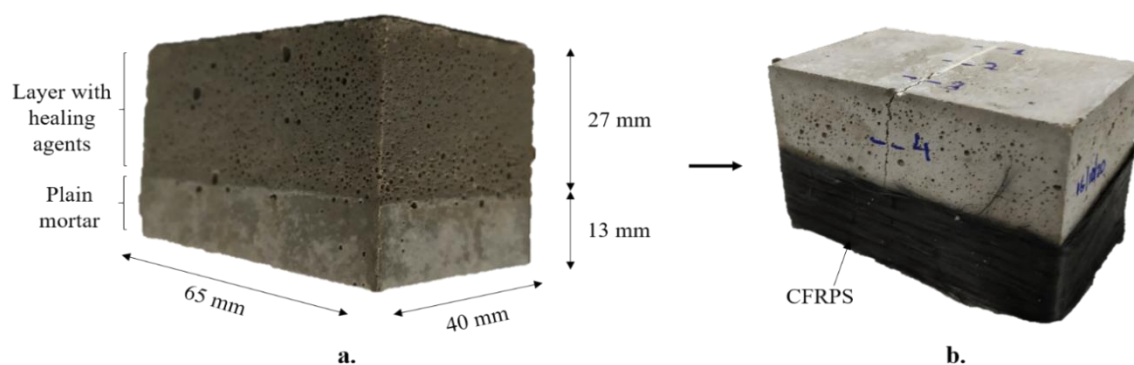


Figure 1: a. Specimen casted in two layers b. Cracked specimen wrapped with CFRP.

Cracks were created by applying three-point bending on the samples. Before cracking, the plain mortar layer of the samples was wrapped with carbon fibre reinforced polymer strips (CFRPS) to avoid complete splitting of samples (Figure 1b). To facilitate cracking a notch of approximately 1.5 cm depth was introduced in the middle of the samples. Crack opening was controlled with a crack mouth opening displacement gauge so that a crack width of about 0.4-0.5 mm was obtained. Cracked samples were semi-submerged in tap water in separate containers at room temperature ($20 \pm 2 \text{ }^\circ\text{C}$) or in a fridge at $7.5 \pm 2 \text{ }^\circ\text{C}$ as appropriate. Self-healing efficiency of the mortars was assessed with a LEICA M205C light optical microscope. Crack width of all samples was measured immediately after cracking and then weekly up to 28 days of healing. Healing ratio was calculated by Equation (1).

$$H_w = ((W_0 - W_t) / W_0) \times 100 \% \quad (2)$$

Where:

W_0 : crack width before healing, immediately after cracking.

W_t : crack width after t time of healing

Results and discussion

Healing ratios of all samples after 7, 14, 21 and 28 days of healing at $20 \text{ }^\circ\text{C}$ and $7.5 \text{ }^\circ\text{C}$ are shown in Figure 2. First, the graphs reveal that the critical percentage of healing for all sample types is achieved during the first 7 days of healing at both temperatures. As expected, reference samples (REF) of plain mortar presented the lowest healing ratio of all samples, and the limited healing witnessed can be attributed to autogenous healing. This occurs mainly by the reaction of calcium hydroxide that is present in cementitious composites with atmospheric carbon dioxide that permeates the cracked area. Control samples (CTRL) containing yeast extract and calcium nitrate healed to a greater extent than reference samples. Being a calcium source, calcium nitrate has contributed to additional available calcium in the material, leading to greater calcium hydroxide availability and therefore likely led to increased formation of calcium carbonate following carbonation. Healing of both REF and CTRL samples did not seem to be affected by the temperature. In contrast, BIO-M samples, containing the mesophilic spores of *B. cohnii* in addition to yeast extract and calcium nitrate, showed better healing at $20 \text{ }^\circ\text{C}$ than at $7.5 \text{ }^\circ\text{C}$. In the first case, a slightly higher healing than the CTRL samples was obtained by BIO-M samples indicating the strong contribution of the calcium nitrate addition to the healing. At lower temperature, though, the healing ratio of BIO-M samples was lower than that of the CTRL which suggests the poor performance of *B. cohnii* at $7.5 \text{ }^\circ\text{C}$. On the other hand, the healing ratio of BIO-P samples, in which the psychrotrophic Psy39 was used, was significantly higher than that of all other samples at both temperatures, reaching 78.6% and 85.2% at $20 \text{ }^\circ\text{C}$ and $7.5 \text{ }^\circ\text{C}$, respectively.

Healing of the bacterial samples at 20 °C and 7.5 °C can be visually compared in Figure 3 and 4 respectively where images of the cracked samples obtained with an optical microscope before (0 days) and after 28 days of healing are presented. It is obvious that the healing product formed in BIO-M samples was denser at 20 °C than at 7.5 °C where a thin and brittle layer was formed. Cracks of BIO-P samples on the other hand were covered by a crystalline and homogenous layer at both temperatures. EDX measurements (not shown here) confirmed that the product formed on the surface of the cracks was calcium carbonate.

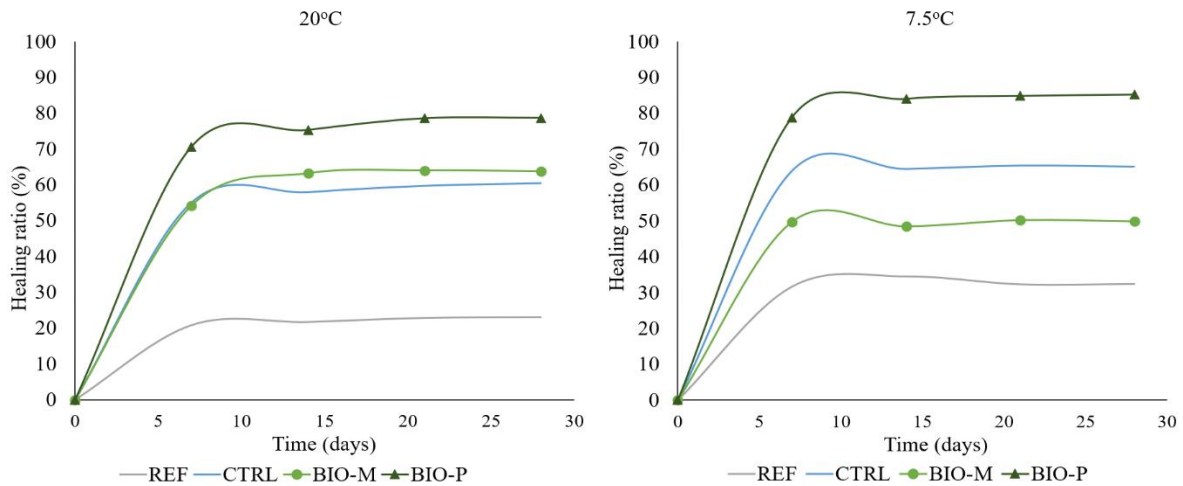


Figure 2: Healing ratio of the specimens at 20 °C and 7.5 °C.

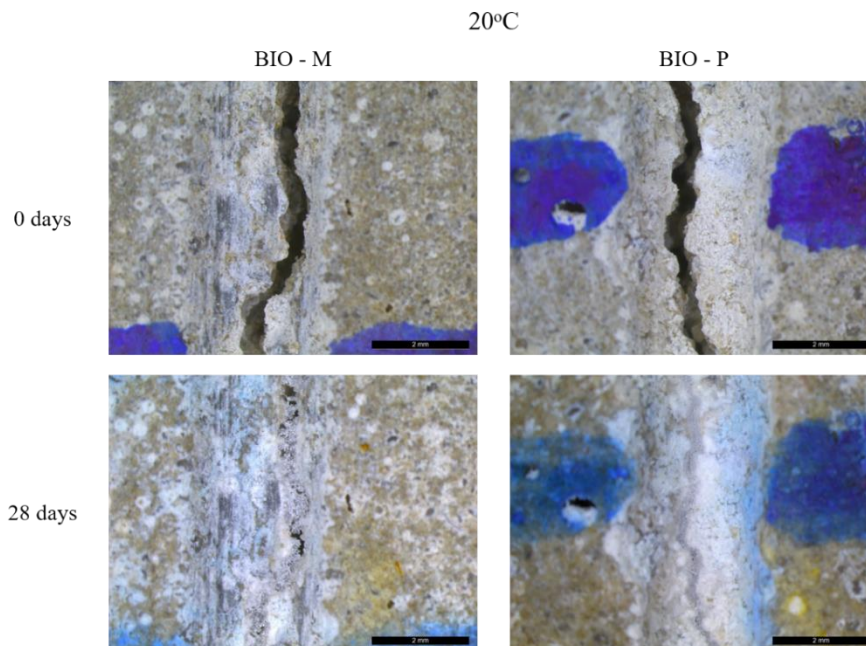


Figure 3. Optical microscope images of bacterial samples before (0 days) and after 28 days of healing at 20 °C. BIO-M: samples with the mesophile *B. cohnii* and BIO-P with the psychrotrophic Psy39.

Conclusion

In this study the self-healing efficiency of cement mortars with two different bacteria, a mesophilic and a psychrotrophic strain, was assessed at both 7.5°C and 20°C. The results showed that samples with mesophilic bacteria underperformed at low temperature in contrast to samples with the psychrotrophic strain, which presented significant healing both at low and

room temperature. It is therefore demonstrated that temperature is a significant factor to be taken into consideration in the research of bacteria-based self-healing concrete.

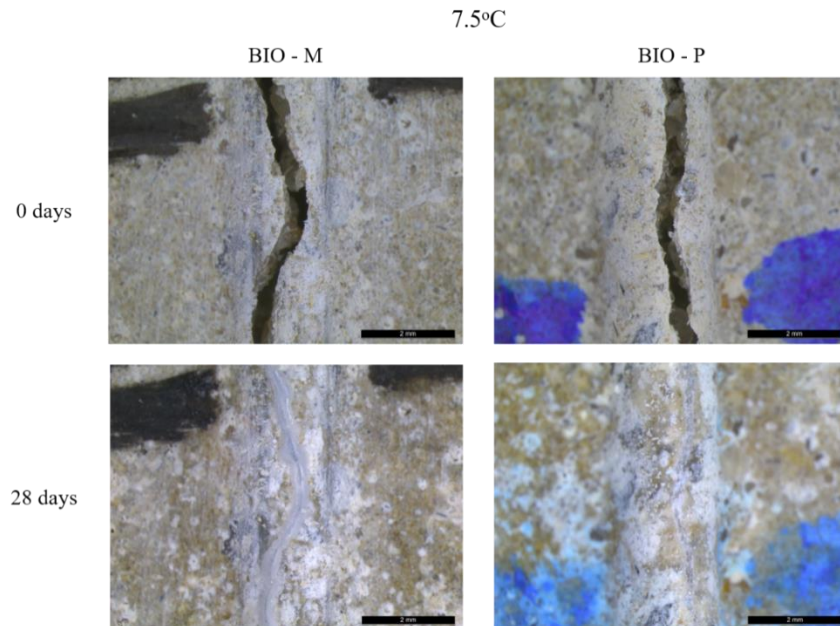


Figure 4. Optical microscope images of bacterial samples before (0 days) and after 28 days of healing at 7.5 °C. BIO-M: samples with the mesophile *B. cohnii* and BIO-P with the psychrotrophic Psy39.

The psychrotrophic Psy39 used here shows high potential in achieving efficient self-healing at a wide range of temperatures, hence offering great prospects for real applications of this technology.

Acknowledgment

This investigation is part of a PhD project supported by the BRE Trust and research supported by UKRI-EPSC (Grant No. EP/P02081X/1, Resilient Materials 4 Life, RM4L).

References

- [1] Gardner D, Lark R, Jefferson T, Davies R. A survey on problems encountered in current concrete construction and the potential benefits of self-healing cementitious materials. *Case Studies in Construction Materials*. 2018 Vol 8 pp. 238-47.
- [2] Office for National Statistics. Output in the construction industry. February 2021.
- [3] Van Tittelboom K, De Belie N, De Muynck W, Verstraete W. Use of bacteria to repair cracks in concrete. *Cement and Concrete Research*. 2010 Vol 40 pp. 157-66.
- [4] Ersan YC. Biotechnology offers more durable and sustainable cementitious composites. *Microorganisms-Cementitious Materials Interactions*. 2018. Toulouse, France.
- [5] Jiang L, Chen H, Ren L, Luo M. Sugar-coated expanded perlite as a bacterial carrier for crack-healing concrete applications. *Construction and Building Materials*. 2020 Vol 232.
- [6] Deng W, Wang Y. Investigating the Factors Affecting the Properties of Coral Sand Treated with Microbially Induced Calcite Precipitation. *Advances in Civil Engineering*. 2018 Vol 2018.
- [7] Peng J, Liu Z. Influence of temperature on microbially induced calcium carbonate precipitation for soil treatment. *PLOS ONE*. 2019 Vol. 14.
- [8] Palin. A Bacteria-Based Self-Healing Cementitious Composite for Application in Low-Temperature Marine Environments. *Biomimetics*. 2017 Vol 2.
- [9] Su Y, Feng J, Zhan Q, Zhang Y, Qian C. Non-ureolytic microbial self-repairing concrete for low temperature environment. *Smart Materials and Structures*. 2019 Vol 28.
- [10] Tan L, Reeksting B, Ferrandiz-Mas V, Heath A, Gebhard S, Paine K. Effect of carbonation on bacteria-based self-healing of cementitious composites. *Construction and Building Materials*. 2020 Vol. 257.

Evaluation of the self-healing of cracked mortars incubated within sterilized and non-sterilized natural soil

Mohamed Esaker¹, Omar Hamza¹, David Elliott², Adam Souid¹

1: College of Engineering and Technology, University of Derby, Derby DE22 3AW, UK

2: College of Natural and Life Science, University of Derby, Derby DE22 1GB, UK

Abstract

The incubation conditions for concrete specimens is a significant factor in the mechanism of self-healing. This study aims to investigate the effect of the presence of microbial and organic materials within soil on the autogenous and bio self-healing. This was achieved by incubating cracked cement mortar specimens into fully saturated sterilized and non-sterilized soil. The crack sealing developed in the specimens during the incubation period in both soil conditions were evaluated and compared. Visual inspection, water absorption test, scanning electron microscopy (SEM), and Energy Dispersive X-ray (EDX) were conducted to evaluate the healing process. The experimental results showed that the crack healing ratio and water absorption of specimens incubated within the natural saturated soil (non-sterilized) were different from those incubated within sterilized saturated soil. In addition, the results of (SEM) and (EDX) evidenced the presence of calcite precipitated on the crack surface in all specimens.

Introduction

Recent studies (1, 2) have shown that bacterial based self-healing is a promising solution to seal concrete micro-cracks and limiting the deterioration of concrete structures. The observed crack healing is affected by many factors such as crack age, incubation period, and exposure conditions. For example, cracks can be completely healed when specimens incubated in water either fully submerged for the entire incubation period (1) or subjected to wet-dry cycles (3) and they are partially healed when specimens exposed to humid air (4). However, research to date has not investigated the effect of soil environment where parts of concrete structures such as foundations, retaining walls, bridge piers, and tunnels which are exposed to.

Natural soil and engineered aggregates contain chemicals, organic materials and microbes which contribute to the concrete exposure conditions and may significantly affect the performance of autogenous and autonomous healing of concrete cracks. This research aims to investigate the effect of the presence of microbials and organic materials within the soil on the performance of self-healing by incubating cracked cement mortar specimens (Control Mortar, CM) mixed with nutrients into sterilized (SS) and non-sterilized (NSS) natural saturated soil. The bio self-healing performance within ground was also investigated by incubating cracked bio cement mortar specimens (Bio-Mortar, BM) within saturated natural soil.

Materials and test methods

Preparation of bacterial agent

Bacillus subtilis H50620/9 (supplied by Philip Harris, UK) were cultivated in growth media was prepared as described by Sonenshein et al. (5). The culture was incubated in a shaker at 125 rpm and a temperature of 36 °C for three days (6) until spores were formed. The spores were first checked under a microscope (LABOPHOT-2, Nikon) using spore stain test and then harvested using a centrifuge machine at a high speed (3390 RCF) for 10 min and then washed twice using distilled water (7). The centrifuged spores were re-suspended in distilled water and kept at a temperature of 2 °C for the concrete mixtures. The concentration of spores in the suspension was about 1.4×10^7 CFU/ml.

Preparation of mortar specimens and crack creation

Control (CM) and Bio-Mortar prisms specimens (BM) with dimensions of 4 x 4 x 16 cm were prepared according to BS EN 196-1. The Blue Circle Cement (CEM II/B-V 32.5R) was first mixed with standard sand, nutrient (calcium lactate) and then followed by adding water. For BM specimens, around 10% of the mix water was replaced by the bacterial spores. The mix proportions for the two different types of specimens are summarized in Table 1. In order to avoid failure during the generation of cracks, the specimens were reinforced by placing a fibre mesh at the centre of the specimens. After 28 days of standard curing, the specimens were cracked using three-point load test. The induced cracks were controlled via a Linear Variable Differential Transducers (LVDT) and generated with different widths range between 100 µm to 350 µm measured at regular intervals.

Table 1: Mixture proportion of the mortar specimens.

Ingredient (Kg/m ³)	Control Mortar (CM)	Bio-Mortar (BM)
Cement	450	450
Sand	1350	1350
Water	225	200
Nutrients	9	9
Bacterial spores	-	25

Soil preparation/incubation process

After the creation of cracks, the specimens were divided into three groups as indicated in Table 2. The BM and CM cracked specimens were immediately incubated within saturated natural soil classified as described in (8). In order to investigate the effect of microbes that are naturally present within the soil, the CM specimens were incubated into saturated sterilized and non-sterilized soil. The soil was sterilized in the oven at a temperature of 120 °C for two days. The BM and CM specimens were incubated in separate plastic boxes to avoid cross contamination.

Table 2: Incubation medium of cracked mortar specimens.

Specimens type	No of specimens	Exposure condition
Bio-Mortar (BM)	6	Natural saturated soil (NSS)
Control Mortar (CM)	6	Natural saturated soil (NSS)
Control Mortar (CM)	6	Serialized saturated soil (SS)

Evaluation of crack healing efficiency

Crack healing quantification

The healing ratio for all specimens was calculated using image J software. For each mix group listed in Table 2, a total of 18 microscopic images were taken homogeneously along the crack length before and after incubation. In preparation for the inspection after incubation, it was essential to perform ultrasonic cleaning using water to remove any remaining soil particles. The healing percentage was taken as the decrease in area fraction of crack identified by the black pixels of the images corresponding to the cracks present in a microscopic image after incubation. The healing percentage of cracks was calculated using equation 1.

$$\text{Healing ratio } \% = \frac{A_i - A_f}{A_i} \times 100 \tag{1}$$

Where A_i is the area of crack before incubation, and A_f is the final area of crack after incubation
Capillary water absorption test

The water absorption test was conducted according to BS EN 13057:2002. The initial weight of all specimens was recorded and then the testing face of each specimen was placed on two

plastic strips in a tray fitted with a loose lid to prevent air movement around the specimens during the test. The tray was filled with distilled water to a depth of about 2 ± 1 mm over the level of the plastic strips. The absorption and the sorptivity coefficient (S) were calculated using the following equations.

$$I = \frac{m_t}{a \cdot d} \quad (2)$$

$$S = \frac{I}{\sqrt{t}} \quad (3)$$

Where m_t is the change in specimen mass in grams at time t , a is the exposed area of the specimen in mm^2 , d is the density of the water in g. mm^{-3} , and S is the sorption coefficient $\text{mm}/\sqrt{\text{s}}$

Results and discussion

Crack healing quantification results

After 100 days of incubation, the specimens were taken out from their incubation environments to quantify the self-healing efficiency. Figure 1 shows images of CM and BM specimens incubated in different environmental conditions. It can be clearly seen that BM specimens were sealed by white precipitation. Specimens incorporated with nutrient (CM) incubated in non-sterilized soil (NSS) were partially healed by white precipitated material.

The healing ratio for all mixes and incubation conditions are illustrated in Figure 2, where specimens containing bacterial agent (BM) exhibit a greater healing ratio (about 76%) compared to the other specimens not containing bacterial agent (CM) (around 46% in NSS and 29% in SS). In comparison with CM specimens incubated in SS, CM incubated in NSS showed a relative increase in healing ratio and this could be explicated by the metabolic conversion of nutrients by bacteria.

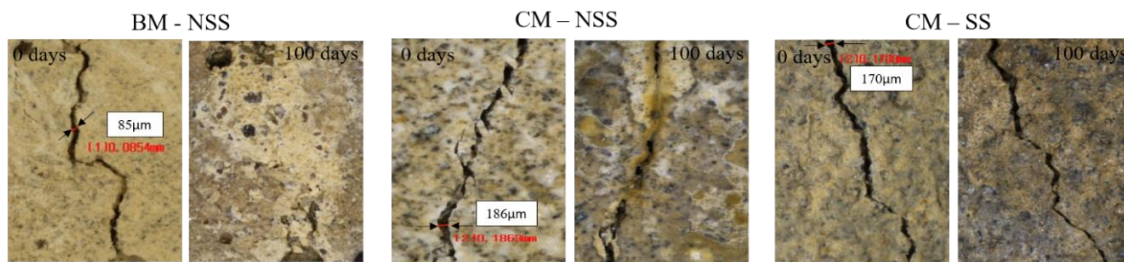


Figure 1: Microscopic images of cracks before and after incubation for mixtures BM and CM

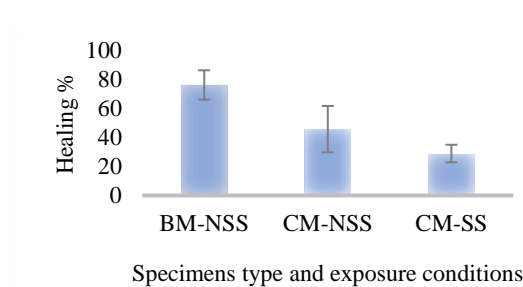


Figure 2: The average crack healing ratio after 100 days of incubation

Capillary water absorption test results

The relationship between the mass of absorbed water per unit inflow area and the square root of time was plotted in Figure 3. As illustrated in the figure, the change in sorptivity index value of the CM specimens incubated in NSS ($1.170 \times 10^{-4} \text{ mm.s}^{-1}$) is overall higher than those of the CM specimens incubated in SS ($8.308 \times 10^{-5} \text{ mm.s}^{-1}$). This implies that the presence of bacteria within soil led to around 34% reduction in the sorptivity index values in comparison with the values observed in the CM incubated in SS. The lowest post-incubation absorption rate was attained for specimens incorporated with bacterial agent (BM) incubated in NSS, as a result of

the deposition of healing products which fills pores and continuous channels that passing the water and therefore reduce the amount of water taken up in the crack by capillary suction. The absorption results were consistent with the visual inspection and indicated that the absorption behaviour was related to the crack healing ratio.

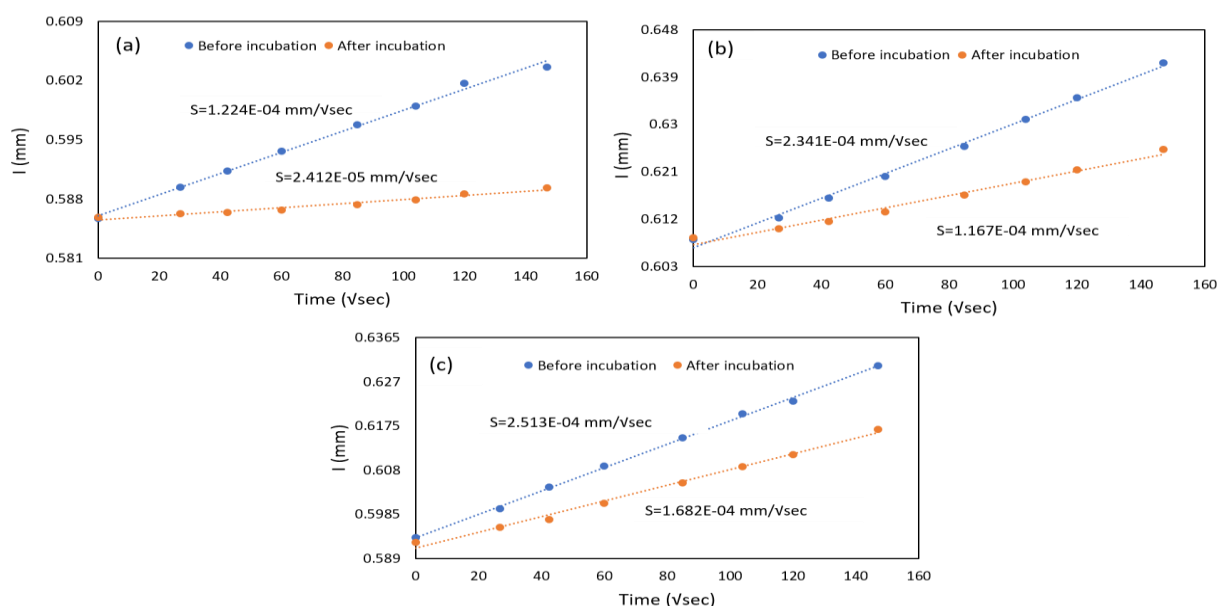


Figure 3: Change in water absorption of the cracked specimens before and after incubation. (a) BM specimens incubated in NSS, (b) CM incubated in NSS, (c) CM incubated in SS.

Microstructure analysis of healing products

The SEM and EDX analysis (Figure 4) indicated that the microstructure of precipitated material at crack surfaces of BM and CM specimens incubated in NSS were crystals of calcium carbonate and the major elements of the mineral precipitate were calcium, carbon, and oxygen. Therefore, it can be concluded that cracks were sealed by precipitated calcium carbonate crystals. The microstructure analysis of CM specimens incubated in SS showed that the main structure was formed by crystals of calcium hydroxide and ettringite, which was formed as a result of the reaction of sulphate compounds with calcium aluminate in the cement. Calcium carbonate crystals were also observed and the probable reason for that is due to the reaction of carbon dioxide presented in water with the calcium hydroxide produced by hydration of calcium oxide (3). The major elements were characterized by EDX were silicate and oxygen which can be attributed to forming calcium silicate hydrate (C-S-H) due to the ongoing hydration of cement particles. Therefore, we conclude that cracks were sealed by precipitated calcium carbonate crystals, and that the process was enhanced in the presence of naturally occurring soil bacteria.

Conclusion

The present study investigated the effect of ground exposure conditions on the efficiency of bio self-healing concrete. In addition to that, the influence of naturally occurring microbes presented within soil on self-healing was investigated by incubating cracked cement mortar specimens mixed with nutrient (calcium lactate) into saturated sterilized (SS) and non-sterilized soil (NSS). From the results, the main conclusions can be drawn as follow:

- The self-healing ratio for bio-mortar specimens (BM) was greater than the control mortar specimens (CM) which did not contain bacterial spores.
- The healing percentage of BM specimens incubated in NSS is significantly higher (37%) compared to CM specimens incubated in the same soil condition.

- Indigenous bacteria naturally present within soil can enhance the mortar self-healing process.

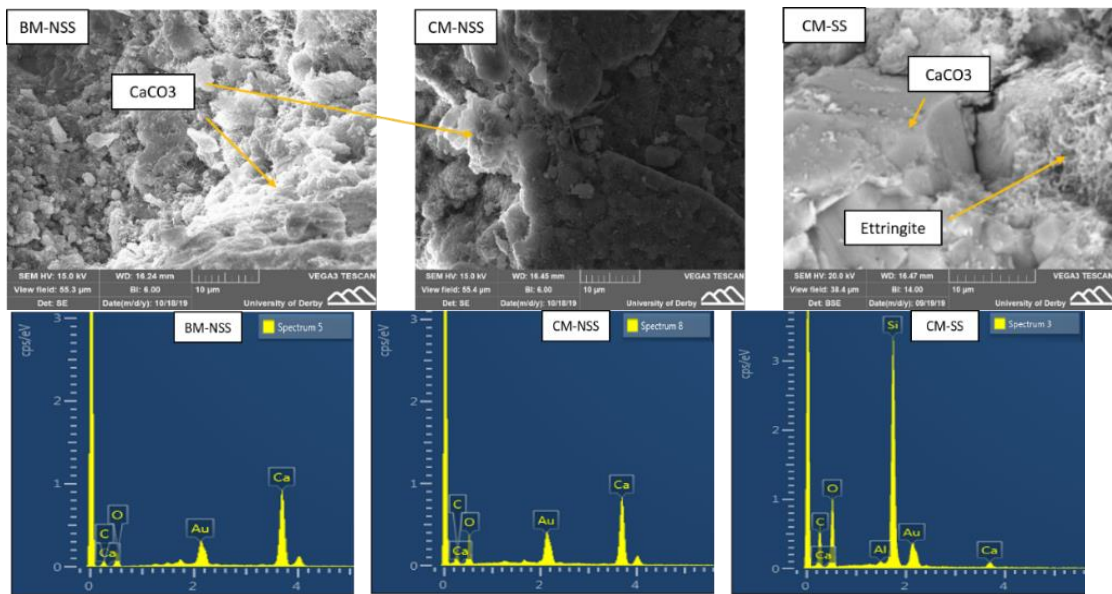


Figure 4: SEM images and EDX analysis of precipitations at cracks surface

Acknowledgment

The authors appreciate the financial support of the University of Derby for this research.

References

- [1]. Zhang J, Liu Y, Feng T, Zhou M, Zhao L, Zhou A, et al. Immobilizing bacteria in expanded perlite for the crack self-healing in concrete. *Construction and Building Materials*. 2017;148:610-7.
- [2]. Luo M, Qian C-x, Li R-y. Factors affecting crack repairing capacity of bacteria-based self-healing concrete. *Construction and building materials*. 2015;87:1-7.
- [3]. Wang J, Soens H, Verstraete W, De Belie N. Self-healing concrete by use of microencapsulated bacterial spores. *Cement and Concrete Research*. 2014;56:139-52.
- [4]. Wang J, Van Tittelboom K, De Belie N, Verstraete W. Use of silica gel or polyurethane immobilized bacteria for self-healing concrete. *Construction and building materials*. 2012;26(1):532-40.
- [5]. Sonenshein AL, Cami B, Brevet J, Cote R. Isolation and characterization of rifampin-resistant and streptolydigin-resistant mutants of *Bacillus subtilis* with altered sporulation properties. *Journal of bacteriology*. 1974;120(1):253-65.
- [6]. Hamza O, Esaker M, Elliott D, Souid A. The effect of soil incubation on bio self-healing of cementitious mortar. *Materials Today Communications*. 2020 Sep 1;24:100988.
- [7]. Esaker M, Hamza O, Souid A, Elliott D. Self-healing of bio-cementitious mortar incubated within neutral and acidic soil. *Materials and Structures*. 2021 Apr;54(2):1-6.
- [8]. Souid A, Esaker M, Elliott D, Hamza O. Experimental data of bio self-healing concrete incubated in saturated natural soil. *Data in brief*. 2019 Oct 1; 26:104394.

Microbial induced calcite precipitations of bio self-healing concrete underground exposure conditions

Adam Soud¹, Omar Hamza¹, David Elliott², Mohamed Esaker¹

1: College of Engineering and Technology, University of Derby, Derby DE22 3AW, UK

2: College of Natural and Life Science, University of Derby, Derby DE22 1GB, UK

Abstract

Technologies involving encapsulated microbial agents within concrete might be more preferable to engineered self-healing concrete because they are eco-friendly reflecting a world of biomimicry, and may uphold a commercial and societal values if considered from the perspective of new concept of bio economy. Research developments on bacterial cementitious material have been showing a promising solution for the super structural concrete that can seal or heal cracks. This previous research has been developed in laboratory under water and air wet/dry cycles incubation conditions.

However, concrete structures are built on and/or in soil, where cracks are difficult to be detected and then to be repaired on the right time. Therefore, the bio self-healing concrete technologies might be an attractive solution for the geotechnical engineering communities for improving underground buildings and infrastructures. The aim of this work is to investigate bacterial cementitious specimens, at laboratory scale, to be incubated in soil exposure conditions after cracking creation. Specimens of microbial self-healed concrete are observed and analysed under SEM and EDX based elemental analyses. The outcomes of this research work are highly relevant to the construction industry and the knowledge produced by the present and the near future perspectives will have an economic, financial and societal impact.

Introduction

For several billions of years, functional and biological systems have been evolved enabling the kingdoms of life to develop self-repairing mechanisms of diverse types of damage [1]. Inspired by the self-healing of bones fractures, we explored in this paper the viability of the idea to use bacterial self-healing concrete for underground structural elements. The self-repairing of bones fractures occurs through the process of osteology [2], which can be aided by bone immobilisation and restricted movement. If the fracture is displaced or if it is complex, surgery may be necessary. By the analogy of the mechanism of repairing transverse bones fractures (Figure 1. d), we want to demonstrate, in a simple manner, the capacity of bacteria embedded in concrete to precipitate calcite and to repair fractured concrete specimens incubated in different types of soil under water saturation regime. Self-healing strategies (particularly bacteria-based self-healing) are regarded as a promising solution to reduce the high maintenance and repair cost of concrete infrastructures. The research to date has tended to focus on the self-healing process in air or water environment [3]. Our aim is to extend the application of bacterial self-healing concrete to geotechnical engineering. As a key of fact, infrastructures are built on and in the ground, where part of their concrete structures are inevitably embedded in soil environments with all sorts of ground variables: chemical, microbial, hydrological and mechanical. The global framework (hypothesis) of our research work is that different ground conditions could impact the efficiency of bacterial self-healing concrete. So, the first step in our research was to investigate the activation of bacterial self-healing of concrete incubated within simple soils' models (free chemicals and free bacteria) under a full saturation regime. From the soil mechanics' point of view, the ground medias are primarily subdivided into three types: granular, cohesive and rocky. The micro-structure (e.g.

Grain-size and soil porosity) of each soil model surrounding concrete micro/macro cracks could affect the bacterial self-healing efficiency that we are not evaluating in this article.

This paper presents the methodology followed to investigate and to prove the capacity of bacterial agents, embedded within cementitious mixtures by two different methods (direct add and light weight aggregates), to precipitate calcite and repair fractures under soil environment by analogy to the self-repairing model of bones' fractures. Visual and deep observations and analyses confirmed fractures repairing in addition to the nature and the morphologies of calcite based crystals precipitated by bacterial actions under three different types of soil environments.

Materials and methods

The bacterial self-healing agent used in this study was non-ureolytic *Bacillus subtilis* H50620/9 (supplied by Philip Harris, UK). After cultured according to [4] and harvested, a spores' suspension was prepared by using sterile distilled water then stored at 4 °C prior to the tests. Two methods of embedding spores of bacterial healing agents in the cementitious mixture were used:

- Direct add: Bacterial spores and nutrients were directly added to the cementitious mixture. Small balls of bacterial mortar were then made by hand (Figure 1. a) to conduct our investigations about the viability of our proposal to use bacterial self-healing concrete within soil environments. Cementitious mortar was prepared by using a mixture of Sand/cement = 3 with calcium lactate/cement = 2% and bacterial spores suspension (water/cement=0.5). By using CFU tests of the initial bacterial spores' suspension, the spores concentration is estimated as $3.5E+5$ spores/cm³ of mortar.
- Encapsulation in light-weight aggregates: to immobilize bacteria, expanded perlite (1-3mm particles size) were impregnated with bacteria spores and nutrients (Yeast extract 0.03 g/g perlite and calcium acetate 0.3g/g perlite) according to [5]. The capsules were dried at 40 °C for 2 days until a constant weight was achieved. Bacterial light-weight aggregates concrete is mixed by using bacterial expanded perlite (22.5 Kg/m³), sand (761 Kg/m³), cement (450 Kg/m³), calcium lactate (1% of cement) and water (225 L/m³). Small specimen (like cylindrical finger) has taken from the mixture to conduct our experiments underground conditions (Figure 1. a). The concentration of spores is estimated as $14E+5$ spores/cm³ concrete (after CFU tests of bacterial perlite).

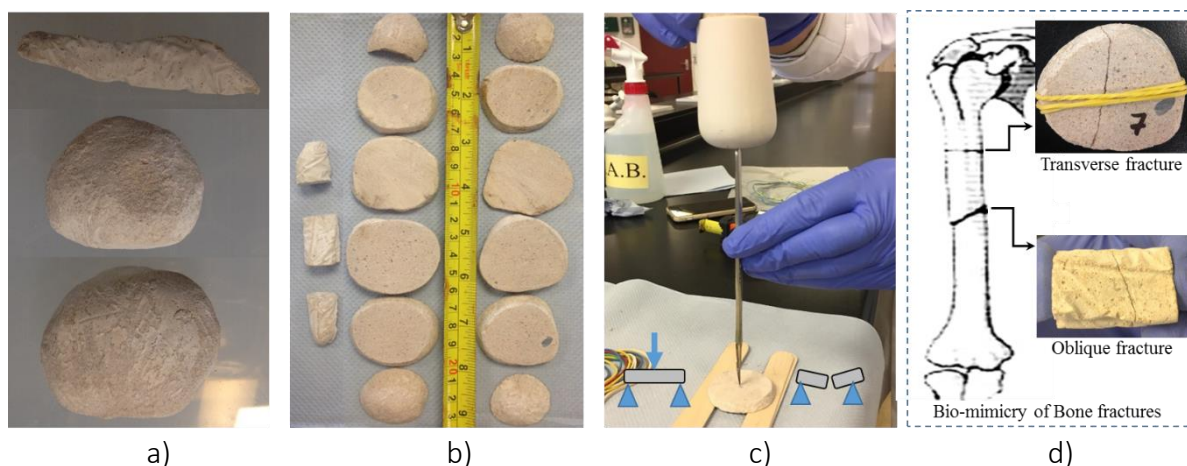


Figure 1. a) Two types of cementitious mixture samples including cylindrical finger containing bacterial (self-healing) agents encapsulated within expanded perlite, and balls containing bacterial agents added directly to mortar mixture; b) Discs obtained from the balls' samples (sliced into six discs each), and cylindrical finger (cut into three small samples); c) Creation of

fracture within the discs' samples by applying a shock on the middle of span; d) Bio-mimicry model of bones fractures compared to fractured bacterial self-repairing samples.

After 30 days of curing in water at 20 °C, specimens were cut totally into 12 small discs (6 discs from each bacteria direct add ball sample) and 3 small like cylinders (encapsulated perlite concrete finger sample) as shown in Figure 1.b. Fracture introduction was created by applying a shock on the middle span of each sample (Figure 1. c). The fractured parts were assembled and fastened by elastic bands (as fractured bones model shown in Figure 1. d) to be investigated after incubation in water saturated soil. For this purpose, three types of soils (Table 1) were used to incubate fractured samples as illustrated in Figure 2 and indicated in Table 2. The sterile soils were filled gently by hand under flame (i.e. under sterile environment) in sterilized bags in two layers of 10 cm each. Samples were placed on the middle height of the incubating soil bags then saturated by using sterile demineralized water until complete water immersing of the top soils' surfaces. Then the total height of each soil bag was 20 cm.

Table 1. Soil types description and preparation to incubate fractured samples of bacterial concrete

Soil ID	Soil Description / EN standard	Preparation before use
Soil-1	Ballast railway aggregates 31 – 50 mm washed 7 times / EN13450	Oven-dried at 121°C for 24 hours.
Soil-2	Sand for concrete 0.063 – 2.0 mm / EN 13139	
Soil-3	Mixture of clay (<9%) with sand (<47%) and ballast aggregates up to 50 mm / BS EN 13285	



Figure 2. a) Fractured samples tightly fastened by elastic bands before incubation; b), c), d), e), f), and g) Samples incubations in Soil-1, Soil-2 and Soil-3 before saturation; h) Storage of sterile bags containing saturated soils during the incubation of fractured samples.

At the end of the incubation period of 50 days, the specimens were removed, gently, from their incubation environments (soil and water) to visually inspect the fractures' healing. The specimens were cleaned in distilled water by using an ultrasound device (Figure 3. a). At the end of the cleaning process, the elastic bands were removed (Figure 3. b, c and d) and the specimens were visually inspected. The results of the observed self-repaired samples are presented in Table 2.

Deep observations (Figures 4 and 5) of the precipitated materials in fractures' lips were further carried out by Scanning Electron Microscope (SEM). The chemical compositions of the precipitates were examined by Energy Dispersive X-Ray Spectrometry (EDX) (Figure 5. g). In preparation for the scanning works of the observed specimens (after incubation in soil and ultrasound cleaning), it was necessary to dry the specimens and break some of them to be coated by gold to scan the cross-section of the fractures' lips (Figure 5).

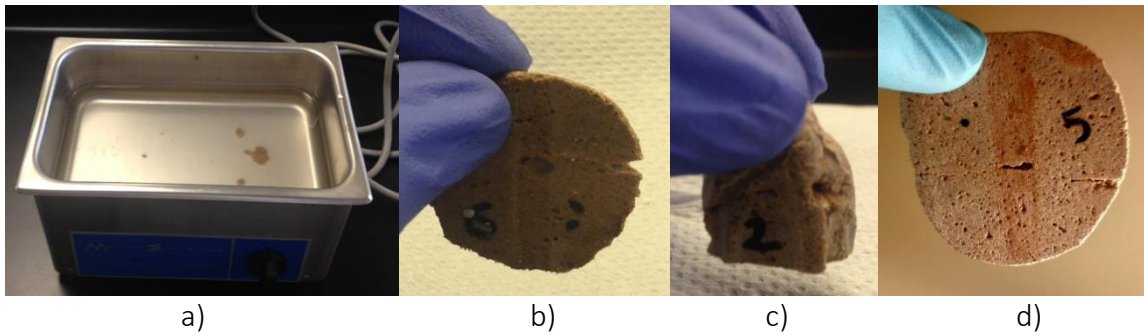


Figure 3. a) Ultra sonic water cleaning tools used to gently remove any soil particles adhered to the surface of samples after incubation; b), c) and d) Self-repaired samples: visual inspection of initially fractured samples after incubation, cleaning and elastic bands being removed.

Results and discussion

Table 2, Figures 4 and 5 summarize the results of the methodology followed to inspect the activation of bacterial agents precipitating calcite under different soil environments in fully saturation regime. Bacterial calcite precipitation was activated to repair/bond fractures of mortar (Figure 4) and lightweight aggregates concrete (Figure 5) in the three saturated soil media. The orientation of fracture in the incubation environments was inspected and seems not affecting the activation of the self-repairing of fractured samples. Table 2 shows that samples 1, 2, 3, 4, 9, 10 and 12 are not bonded. This is possibly due to the following reasons: 1) the fastening of the fractured parts might have affected the efficiency of the self-repairing, particularly if fractures' lips are not opposite (same results observed in osteology during the healing period of transverse fractures' bones) or not in touch; 2) the soil movement during the transfer of bags and soil dig up to take samples out of the soil after incubation. This could induce damage of the fresh bacterial healing; and 3) the motility of bacteria (non immobilized in direct add) can affect the efficiency of bio self-repairing when bacteria immigrate out of samples into water saturated soil macro environment.

Table 2. Visual inspection results of self-repaired fractured concrete samples incubated in saturated soils

Self-healing Method	Direct add of bacterial self-healing agents												Bacterial agents in Perlite capsules		
	1	2	3	4	5	6	7	8	9	10	11	12	1	2	3
Sample N°	1	2	3	4	5	6	7	8	9	10	11	12	1	2	3
Incubation Media	Soil3	Soil2	Soil1	Soil2	Soil3	Soil1	Soil1	Soil2	Water	Soil2	Soil3	Water	Water	Soil2	Soil2
Fracture orientation during incubation															
Visual inspection of Fractured pieces after incubation	Not bonded	Not bonded	Not bonded	Not bonded	Bonded	Bonded	Bonded	Bonded	Not bonded	Not bonded	Bonded	Not bonded	Bonded	Bonded	Bonded

The presence of white precipitates was observed in the environments surrounding the non-bonded fractured' samples. These precipitates are collected and confirmed as bacterial limestone precipitates by SEM micrographs and EDX analysis of their chemical composition. The difference of bacterial crystals shown in figure 4 and figure 5 is due to mortar/concrete

formulation and nutrients added to the cementitious mixtures. Moreover, the EDX analyses (Figure 5) of pointed zones of the surface of precipitates that have been observed on the samples' borders of the cross-section show that the CaCO_3 based crystalline structure are not pure calcite. There is a significant difference in (C) and CO_2 values suggesting spectrums 1/2 are possibly the result of partial erosion of CaCO_3 into CaO and spectrums 3/4 is possibly purer CaCO_3 perhaps with some organic (C) content. However, we can't be exactly sure as both (C) and (O) values can be raised artificially sometimes due to sample orientation (e.g. because the surface is not flat and overlap with neighbouring particles/elements).

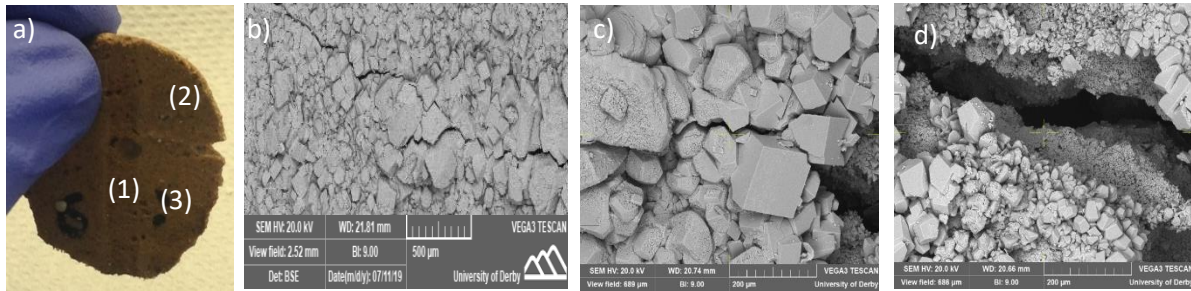


Figure 4. a) Zones (1), (2), and (3) of self-repaired fracture surface of the sample 6 inspected under Scanning Electron Microscope (SEM) after gold coating. b), c), and d) SEM micrographs of fracture closure and bacterial limestone crystals on zones (1), (2), and (3) respectively.

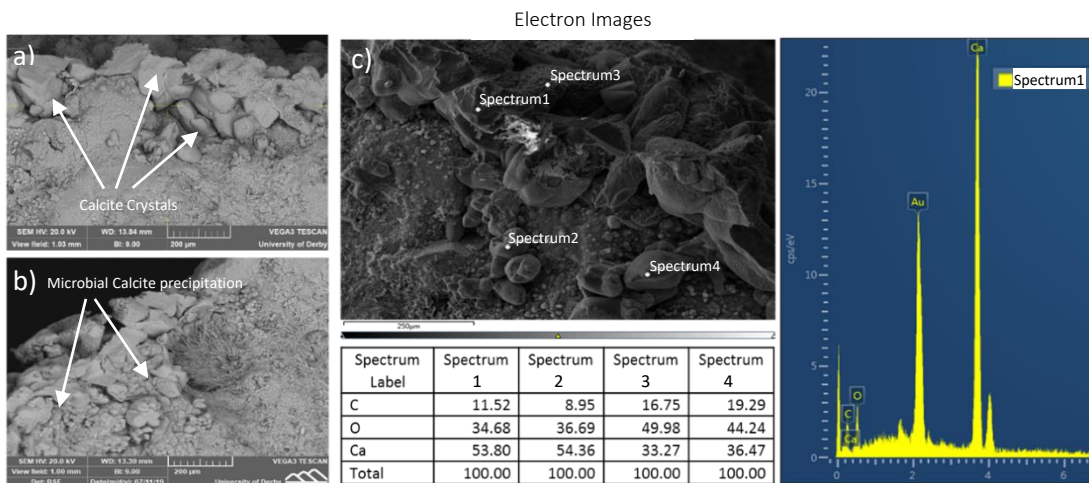


Figure 5. Encapsulated microbial aggregates concrete – sample2: a) and b) Limestone precipitates SEM micrographs on surrounding zones of the repaired cross-section after incubation. c) Electron Image and Energy Dispersive X-Ray Spectroscopy of the microbial calcium carbonate based precipitation on surrounding edge of the cross-section.

Conclusion

The self-repairing of fractured bones systems is a biologically inspired design and a biomimetic approach to investigate new ideas and concept of solutions to self-seal or (partially) heal damage or fractures in cementitious materials. Interestingly, the concept was applied to investigate the viability of the solution of using bacterial self-healing cementitious materials for underground infrastructures

Embedded bacteria in cementitious materials were found to be capable to precipitate calcite crystals to seal damage and to repair fractured samples at a laboratory scale. SEM observations and EDX analyses confirmed that mineral precipitations on the fractures' surfaces and lips were calcite crystals. The developed procedure in this work are easily reproducible in academic and

industrial laboratories and can be generalized for small size square and cylindrical bio concrete/mortar samples.

Acknowledgement

This project has received funding from the European Union's Horizon 2020 research and innovation programme under the Marie Skłodowska-Curie grant agreement No 798021 (GEOBACTICON). This research work has also received funding from a PGTA scholarship awarded by the University of Derby (E&T-15- PGTA-0717). The authors would thank Dr. Graham Souch for his appreciated help.

References

- [1] Speck O, Speck T. An Overview of Bioinspired and Biomimetic Self-Repairing Materials. *Biomimetics* 2019, 4, 26; doi:10.3390/biomimetics4010026.
- [2] McRae R. *Pocket Book of Orthopaedics and Fractures*. (2nd edition. Edinburgh: Churchill Livingstone 2006).
- [3] Kunamineni V; Meena M; Shirish V. D. Bacterial based self healing concrete – A review. *Construction and Building Materials*. 152(2017) 1008-1014
- [4] Sonenshein AL; Cami B; Brevet J; Cote R. Isolation and characterization of rifampin-resistant and streptolydigin-resistant mutants of *Bacillus subtilis* with altered sporulation properties. *Journal of bacteriology*. 1974; 120(1):253-265.
- [5] Alazhari M; Sharma T; Heath A; Cooper R; Paine K; Application of Expanded perlite encapsulated bacteria and growth media for self-healing concrete. *Construction and Building Materials* 160(2018) 610-619.

Session 7 Self-healing composites and advance monitoring

Chair: Dr Marcus Perry

1152 *Shimizu et al.* Self-healing capability of fibre reinforced cementitious composites using different types of by-products

1102 *Tang and Al-Tabbaa.* Preliminary study of developing a self-healing strain-hardening cementitious composite (SHCC) for cyclic loading conditions

1155 *Tulliani et al.* Polypropylene/CNT strain gauges for structures monitoring

1250 *Pellegrino and Stathaki.* Automatic smart concrete quality control using supercomputing

Self-healing capability of fibre reinforced cementitious composites using different types of by-products

Riccardo Maddalena¹, Koshi Shimizu², Tomoya Nishiwaki²

1: School of Engineering, Cardiff University, Cardiff CF24 3AA, UK

2: Graduate School of Engineering, Tohoku University, Sendai 980-8579, Japan

Abstract

Self-healing concrete represents nowadays an environmentally friendly alternative solution to conventional building materials. For crack widths in the range of few microns to 0.1 mm concrete has the ability to heal itself with a mechanism known as autogenous healing. In this case, the water that penetrates cracks will further hydrate unhydrated particles to form either calcite or calcium (aluminium) silicate hydrate phases. Waste by-product materials such as silica fume, fly ash and ground granulated blast-furnace slag (GGBS) exhibit a high “pozzolanic” reactivity, due to their small particle size and the presence of unhydrated products. However, little is known about their healing potential, especially when they are combined together as a replacement of Portland cement.

In this study, the mechanical properties and healing potential of concrete specimens using different mixes of waste materials and plastic fibres were investigated. Fibre reinforced cementitious composites (FRCC) with different percentage of by-product materials (i.e., silica fume, fly ash, and granulated ground blast-furnace slag) were subjected to mechanical, physical, and indirect tests. Results showed that all the mixes exhibited a healing efficiency higher than conventional Portland cement composites, along with improved mechanical strength and overall reduction in porosity.

Introduction

In terms of durability of reinforced concrete (RC) structures, concrete crack generation leads to more serious deterioration due to ingress of harmful ingredients such as carbon dioxide and chloride. On the other hand, crack generation is unavoidable during the long lifetime of RC structures. In addition, labour-saving technologies are strongly required in especially advanced countries, including Japan where faces to the drastically declining population and the aging of the construction engineers/workers. Based on this background, research on various kinds of self-healing concrete has been carried out last 2 decades. Even in ordinary concrete, cracks with small enough width (e.g., less than 0.1 mm) can be filled in an atmosphere where moisture is supplied [1]. In case of fibre-reinforced cementitious composite material (FRCC), it has been confirmed that self-healing capability can be enhanced because of crack controlling characteristics and existence of bridging reinforcing fibres. In particular, larger crack width of approximately 0.3 mm can be healed on FRCC with polyvinyl alcohol (PVA) fibre which provides polarity due to hydroxyl group [2].

In addition, from the environmental point of view, supplementary cementitious materials (SCMs) derived from industrial by-products are attractive to reduce CO₂ emissions by replacement for cement. Although previous studies of self-healing concrete using SCMs, which give slower hydration process than conventional cement improved the self-healing effect [3-5]. However, few studies have conducted the self-healing effect of various SCM applications in FRCC. In this paper, the effect of SCM on the self-healing performance of FRCC is examined by water absorption test and the pore size distribution measurement.

Materials and methods

Employed materials in this study are followings. Ordinary Portland cement (C, density 3.16 g/cm³, specific surface area 3230 cm²/g) was used as cement. Silica sand No. 6 (S, density 2.6 g/cm³, average particle size 212 μm) was employed as fine aggregate. As SCMs, silica fume (SF, density 2.2 g/cm³, mean particle size 0.15 μm), fly ash (FA, Type II for JIS A 6201:2015 [6], density 2.23 g/cm³, specific surface area 4170 cm²/g), and ground granulated blast-furnace slag (GB, density 2.91 g/cm³, specific surface area 4230 cm²/g) were used. Super plasticizer of polycarboxylic acid copolymer (SP, specific gravity 1.05 g/cm³) and PVA fibre (diameter 40 μm, length 12 mm, density 1.3 g/cm³, tensile strength 1560 MPa.) were also employed. Experiments were carried out on 5 series with different mix proportions as shown in Table 1. CO is the control. SF, FA, and GB with single SCM, and TE with total 50% substitution by 3 types of SCM were used.

Table 1. Sample series and mix proportions (wt. %)

	B (Binder)				S/B	W/B	SP/B	PVA (vol.%)
	C	SF	FA	GB				
CO	100	—	—	—				
SF	90	10	—	—				
FA	80	—	20	—	40	40	0.9	2
GB	80	—	—	20				
TE	50	10	20	20				

Compressive strength, splitting tensile strength, bulk density ρ_b , true density ρ_m and porosity Φ were measured. In these tests, cylindrical specimens with a radius of 50 mm and a height of 100 mm were used. The test was carried out at 28 days of age, and the mean value of the three specimens was used as a representative value.

Water Absorption Test

The water absorption test described in ASTM C 1585 [7] was carried out to evaluate the self-healing properties. Three conditions were employed; before introducing the crack (before crack), immediately after introducing the crack (after crack), and after 28 days of water curing from the crack introduction (after self-healing). The specimens were dried at 60 °C for 5 days before the test. Cracks were introduced at 28 days by the split tensile test. To control the residual crack width of 0.3 mm, the crack mouth opening displacement (CMOD) was measured by the clip gauge. As the schematic diagram of the water absorption test as shown in Figure 1, the bottom surface of the test specimen was placed in the water tank so that it was immersed in water for about 2 mm. The mass change due to water absorption was measured with time of 1, 4, 9, 16, 25, 36, 49, 64, 81, and 100 minutes from the test start. The results were converted as the relationship between water absorption per bottom area W [mm³/mm²] and square root of time \sqrt{t} [s^{0.5}].

Figure 2 shows the expected self-healing effect regarding water absorption. Before the crack generation, the water penetrates through the FRCC matrix micro-voids. On the other hand, the water absorption increases because the water can be pulled up by capillary suction in case of the specimen with crack. After self-healing process (cured in water bath), the amount of water absorption decreases because the self-healed crack can block by water penetration. Therefore, it is considered that the amount of water absorption will be before crack < after self-healing < after crack.

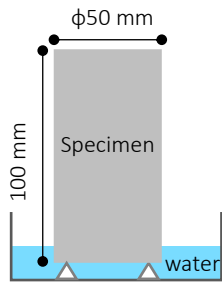


Figure 1. Schematic diagram of water absorption test

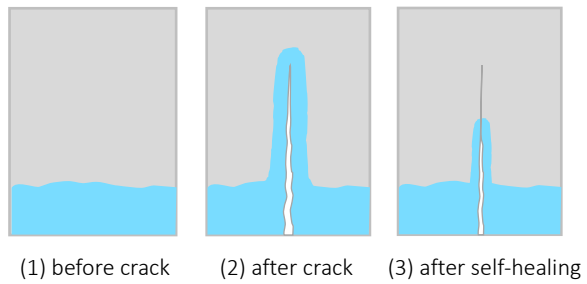


Figure 2. Changes in water absorption due to self-healing

The pore size distribution measurement

The pore size distribution was measured in accordance with the mercury intrusion porosimetry method. Two conditions were employed; cracked specimens stored in a climate room (cracked) and the specimens cured in water for 28 days after crack introducing (healed). The samples were cut into 5 mm cubes using a concrete saw. Five cubes for each condition were collected, thus, 10 samples were measured in total. The contact angle between the mercury and the sample was set to 130°, and the surface tension of the mercury was set to 0.485 N/m. The pressure was applied from 0.0138 MPa to 227.476 MPa.

Results and discussion

Table 2 shows the results of the collected physical properties. The compressive strength F_c of FA and GB is approximately 10 ~ 15% lower than CO at 28 days due to late pozzolanic reaction following the hydration process. On the other hand, the splitting tensile strength F_t of CO is smaller than all series with SCMs. The porosity of SF and TE mixed with silica fume is small. This is considered to be due to the formation of a dense micro-structure by the microfiller effect of silica fume.

Table 2. Physical properties (standard deviation in brackets.)

	F_c [MPa]	E [GPa]	F_t [MPa]	Φ [%]	ρ_b [g/cm ³]	ρ_m [g/cm ³]
CO	60.6 (1.00)	34.4 (3.36)	4.52 (0.01)	27.6 (0.26)	1.80 (0.00)	2.49 (0.01)
SF	68.0 (0.46)	30.3 (4.26)	5.91 (0.49)	25.4 (0.18)	1.77 (0.00)	2.37 (0.01)
FA	53.2 (1.48)	28.4 (0.78)	5.94 (0.46)	27.7 (0.25)	1.76 (0.01)	2.43 (0.01)
GB	50.8 (1.46)	28.3 (0.86)	5.67 (0.32)	28.7 (0.18)	1.74 (0.00)	2.45 (0.00)
TE	63.2 (6.32)	28.9 (0.65)	6.86 (0.28)	23.2 (0.18)	1.75 (0.00)	2.29 (0.00)

Water Absorption Test

Figure 3 shows the results of the water absorption test. Here, only the control CO and TE, which showed the largest recovery rate, are shown due to the paper limitation. The water absorption of “after crack” is the largest among all conditions. Regarding “after self-healing”, the water absorption reaches less than “before crack” in case of TE, however, CO is not. These graphs have almost line relationship with the correlation coefficient of more than 0.97 in all results. These slopes are defined as the sorptivity (the water absorption coefficient) [mm/min^{0.5}] in ASTM C 1585 [7]. Figure 4 shows the relative sorptivity which was normalized by the “before crack” as the reference. After self-healing, the relative sorptivity of SF, FA and TE are the same or less than “before crack” due to the closure of the fine crack after the self-healing. Here, the recovery rate R is defined to evaluate self-healing performance. R is calculated by Equation (1). This equation was made based on equation [8], which determines the strength recovery rate.

$$R = \frac{S_c - S_h}{S_c - S_u} [\%] \tag{1}$$

Here, R is a recovery rate [%], S_u is the sorptivity of “before crack”, S_c is the sorptivity of “after crack”, and S_h is the sorptivity of “after self-healing”. Figure 5 shows the R values of each series. From this graph, the recovery rates of SF, FA, and TE exceeded 100%. This is because the progress of the pozzolanic reaction of SCMs during 28 days water curing could enhanced the more dense micro-structure as the self-healing phenomena.

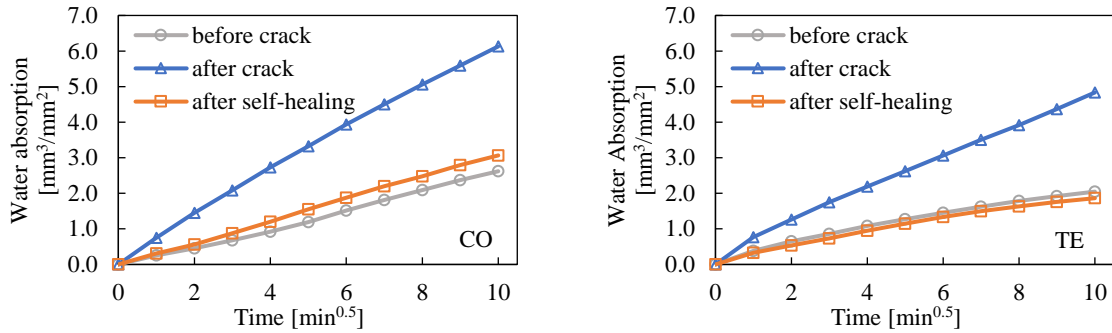


Figure 3. The results of water absorption test

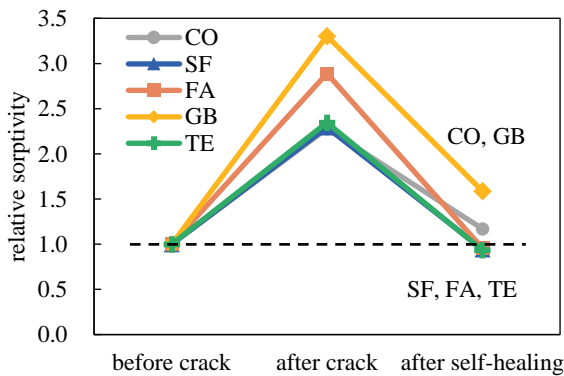


Figure 4. Relative sorptivity

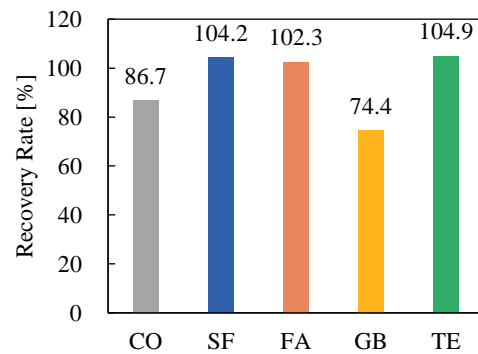


Figure 5. Recovery Rate

The pore size distribution measurement

Figure 6 shows the results of pore size distribution measurement. Here, as with the water absorption test, only the CO and TE results are shown. In case of CO, the peak diameter at the “cracked” stage shifted smaller at the “healed” stage. FA and GB also show the similar trends. These SCMs results may indicate that the pores were filled by precipitations due to the progress of pozzolanic reaction during the recuring process. In the case of TE and SF with silica fume, the peak diameter did not change from cracked to healed, but the relatively large pores with the range of 0.1 ~ 1 μm decreased, and the smaller pores with less than 0.1μm increased. This can be regarded as the SF and TE, which had a finer structure than the other series at the time of after cracking, were further densified during recuring process. It is considered that this difference in the change in pore size distribution led to the difference in self-healing performance in the water absorption test of CO and TE.

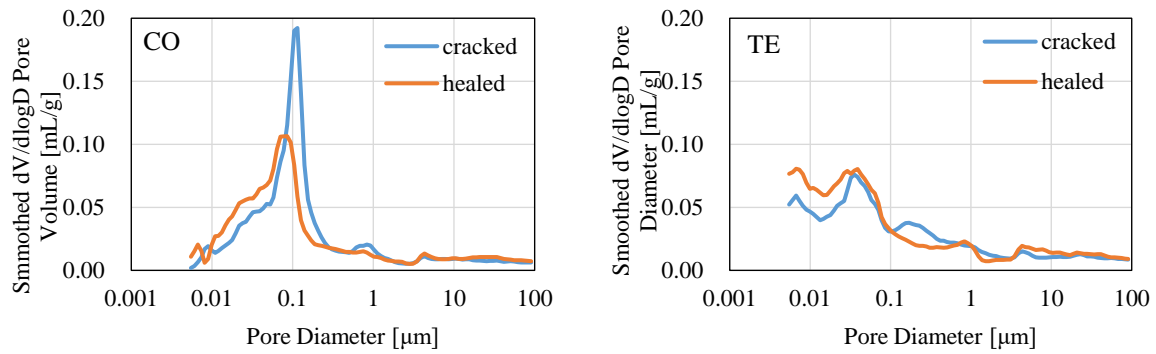


Figure 6. results of pore size distribution measurement

Conclusion

The self-healing performance of FRCC using different SCMs and PVA fibres was evaluated by water absorption test and the pore size distribution measurement. The findings obtained are described below;

- 1) The results of the water absorption test in three conditions of “before crack”, “after crack”, and “after self-healing” shows that the self-healing capability can be confirmed by the relative sorptivity.
- 2) The recovery rate, which was defined as the strength recovery rate, was proposed as a quantitative evaluating indicator of the self-healing capability of water permeability.
- 3) The pore size distribution shifted smaller during recuring by self-healing process of the pozzolanic reactions of SCMs.

Acknowledgment

The authors are deeply grateful to JSPS Postdoctoral Fellowships for Research in Japan (Fellowship ID: PE19722).

References

- [1] C. Edvardsen, Water permeability and autogenous healing of cracks in concrete, *ACI Mat. J.*, 96 (1999) 448–454.
- [2] T. Nishiwaki, M. Koda, M. Yamada, H. Mihashi, and T. Kikuta, Experimental Study on Self-Healing Capability of FRCC Using Different Types of Synthetic Fibers, *J. Adv. Concr. Technol.*, 10 (2012) 195–206.
- [3] R. Maddalena, H. Taha, D. Gardner, Self-healing potential of supplementary cementitious materials in cement mortars: Sorptivity and pore structure, *Dev. Built Environ.*, 6 (2021) 100044.
- [4] S.H. Na, Y. Hama, M. Taniguchi, O. Katsura, T. Sagawa, M. Zakaria, Experimental investigation on reaction rate and self-healing ability in fly ash blended cement mixtures, *J. Adv. Concr. Technol.* 10 (2012) 240–253.
- [5] H. Huang, G. Ye, D. Damidot, Effect of blast furnace slag on self-healing of microcracks in cementitious materials, *Cem. Concr. Res.* 60 (2014) 68–82.
- [6] JIS A 6201, Fly ash for use in concrete, (2015).
- [7] ASTM C 1585-04, Standard Test Method for Measurement of Rate of Absorption of Water by Hydraulic-Cement Concretes (2004).
- [8] X.F. Wang, Z.H. Yang, C. Fang, N.X. Han, G.M. Zhu, J.N. Tang, F. Xing, Evaluation of the mechanical performance recovery of self-healing cementitious materials – its methods and future development: A review, *Const. Build. Mater.*, 212 (2019) 400–421.

Preliminary study of developing a self-healing strain-hardening cementitious composite (SHCC) for cyclic loading conditions

Zixuan Tang, Abir Al-Tabbaa

Department of Engineering, University of Cambridge, Cambridge CB2 1PZ, UK

Abstract

Seismic attacks cause huge amount of property damage and loss of life every year. The repair work after earthquakes is often costly and inefficient. The damage is often more destructive in developing countries due to their weak infrastructure. Civil engineers have dedicated to reducing the seismic damage and the maintenance work on infrastructure in different ways. Ductile materials can be developed to bear the seismic loading, and self-healing techniques can be applied to reduce the repair work. Strain-hardening cementitious composites (SHCC) is a unique type of high performance fibre reinforced cementitious composites (HPFRCC) which exhibits extremely high strain capacity under tension. Based on micromechanics design and the synergetic interactions between fibres and cement matrix, effective fibre bridging and load transfer can be realized to achieve the strain-hardening effect. Under tensile or flexural loading, multiple fine cracks generate on the material to realize the deformation. Compared with traditional steel-reinforced concretes or fibre-reinforced concretes, SHCC has larger shear resistance, energy absorption capacity and damage tolerance, making it a promising seismic-resistant material. Moreover, the multiple fine cracking behaviour of SHCC has been proven to greatly improve the material durability and self-healing ability due to various factors. This study aims to investigate the self-healing behaviour of SHCC under different simulated seismic (cyclic) loadings. The recovery of mechanical and transport properties was studied by conducting uniaxial tensile tests, resonant frequency tests and water permeability tests. The reduction in surface crack widths was measured under optical microscope. The healing products were studied by SEM/EDX tests.

Introduction

Cracking is regarded as inevitable in cement-based materials. Water or air can easily penetrate through cracks, induce corrosion and negatively affect the mechanical properties and durability of structures. Cementitious materials inherently have an autogenous self-healing mechanism to close small cracks and recover mechanical properties relying on continuing hydration and calcium carbonate precipitation [1]. However, only very small cracks (below 100 μm) could be healed slowly [2,3]. Therefore, it would be beneficial to limit the crack widths so as to promote self-healing.

Earthquake waves often apply dynamic and cyclic loadings to infrastructure in a short time and impair the integrity of structures. The damage after seismic attacks is often destructive and the repair work is costly and difficult to conduct. Ductile materials could be developed to bear cyclic loadings and reduce the damage, and self-healing techniques could be applied to eliminate the repair and maintenance work.

Fibre reinforced strain-hardening cementitious composites (SHCC) have been put forward as a promising seismic-resistant material which exhibits extremely high strain capacity under tension ($> 3\%$), high shear resistance and energy absorption capacity [4,5]. Different from traditional fibre-reinforced concrete with low ductility, SHCC is based on micromechanics design and can generate multiple fine cracks to realize a strain-hardening behaviour. Compared with traditional steel-reinforced concrete with large cracks, SHCC has limited crack widths (typically $< 100 \mu\text{m}$) due to effective fibre bridging. Thanks to this, the durability and self-healing ability of SHCC is greatly improved [6,7]. This research aims to develop a self-

healing SHCC for seismic loading conditions, and this preliminary study focuses on investigating the mechanical behaviour of SHCC under monotonic and cyclic flexural loadings and evaluating its potential self-healing ability. The crack widths and healing were observed under a stereoscope. The fibre-matrix interface was studied by SEM-EDX analysis.

Materials and methods

Materials and specimen production

CEM-I 52.5N High strength Portland cement (C) supplied by Hanson UK and fine silica sand (S) (maximum grain size: 250 μm) were adopted. Fly ash (FA) with a fineness category of N according to BS EN 450-1 was supplied by CEMEX UK. No coarse aggregates were involved. A polycarboxylate-based superplasticiser (SP) and a viscosity modifying admixture (VMA) were adopted to control the fresh properties and to achieve uniform and homogeneous fibre distribution in SHCC, both supplied by Sika UK. Polyvinyl alcohol (PVA) fibres with 1.2% surface oil coating were manufactured by Kuraray, Japan. The tensile strength is 1.56 GPa, the elastic modulus is 41 GPa, the elongation is 6.5%, the diameter is 40 μm and the length is 12 mm. The mix proportions are given in Table 1.

Table 1. The mix proportions of SHCC investigated

Ingredients	Cementitious material/binder		Aggregates		Chemical admixtures		
	C	FA	S	W	SP	VMA	Fibre
Mass ratio	1	1.2	0.8	0.58	1.69%	0.49%	4.80%
Unit weight (kg/m^3)	542	650	434	314	9.18	2.67	26

Cement, sand and fly ash were first dry mixed, and then a pre-mixed water solution containing SP and VMA was added and thoroughly mixed. Then a flow table test according to BS EN 12350-5 was performed and the spread was 290 ± 10 mm. Lastly, fibres were added and uniformly mixed. The fresh SHCC mixture was then cast into moulds. For high moisture curing, the specimens were stored in a high moisture container at $97 \pm 2\%$ relative humidity (RH) and 20 ± 2 °C until the required age was reached. For ambient curing, the specimens were placed in laboratory air with $50 \pm 5\%$ RH and a temperature of 20 ± 2 °C.

Methods

Compressive strength tests were conducted on cubic specimens ($40 \times 40 \times 40$ mm³). Triplicate specimens were tested according to BS EN 196-1. The density of SHCC was calculated based on 24 cubic specimens. Secant modulus of elasticity in compression was tested based on BS EN 12390-13 using cylindrical specimens with a dimension of $\varnothing 75 \times 150$ mm³.

Four-point flexural tests were conducted on prisms ($300 \times 50 \times 26$ mm³) under displacement control. The loading span was 80 mm and the supporting span was 240 mm. Three kinds of tests were performed, i.e. monotonic loading tests, one-side loading-unloading cyclic tests and reversed cyclic tests. The midspan deflection of each specimen was recorded by a laser extensometer. The specimens were then placed in high moisture condition for 28 days for self-healing study.

Leica DM 2700 M stereoscope was used for counting the crack number and measuring the crack widths after the flexural tests. The width of each crack was measured from the bottom surface of the specimens based on at least three points. The changes in cracks after the 28-day healing were also observed.

Scanning electron microscopy with an energy-dispersive X-ray spectroscopy detector (SEM-EDX) was used to study the fibre-matrix interfaces and the substance on the fibre surface.

Results and discussion

Mechanical characteristics

The average density of SHCC was 2050 kg/m³. The compressive strength under high moisture condition was 75.42 (± 2.00) MPa at 28 days. The 7-day initial modulus of elasticity was 13.3 GPa and the stabilised modulus of elasticity was 14.0 GPa.

7-day SHCC prisms all exhibited deflection-hardening behaviour under monotonic flexural loading. The flexural stress-deflection curves are presented in Figure 1(a). Representative characteristics are summarised in Table 2. Multiple fine cracks were generated before a localised crack appeared, as shown in Figure 1(b). Measured under stereoscope, the crack width was 51(±19) µm.

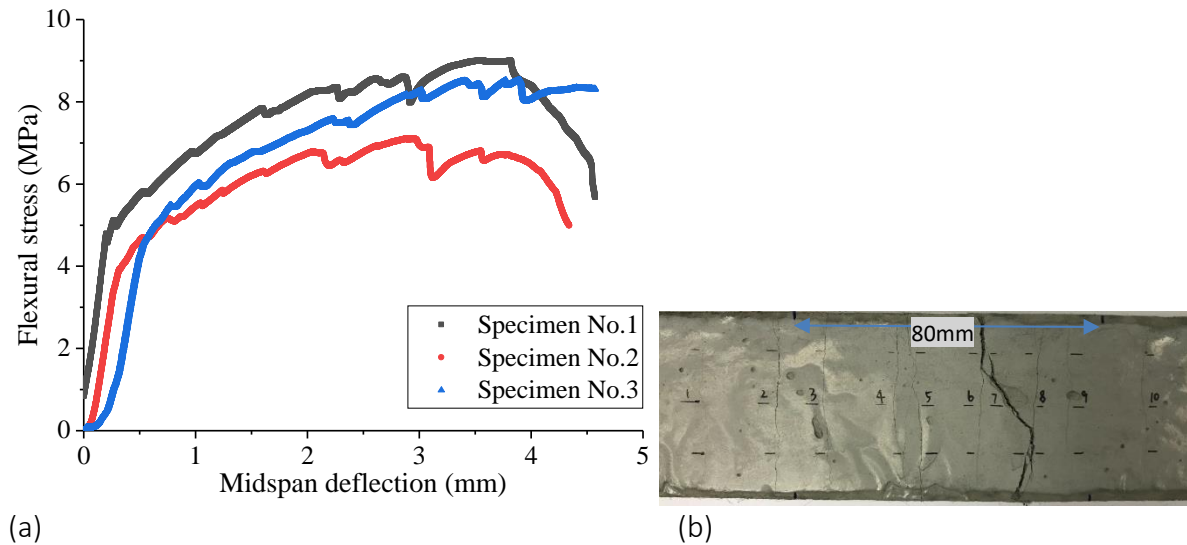


Figure 1. (a) Flexural stress-deflection curves of 7-day SHCC; (b) crack pattern of multiple fine cracks with one localised wide crack

Table 2. Characteristics of 7-day SHCC under monotonic flexural loading

First cracking strength (MPa)	First cracking deflection (mm)	Modulus of rupture (MPa)	Deflection capacity (mm)	Flexural stiffness (MPa/mm)
4.46 (±0.40)	0.26 (± 0.04)	7.90 (±0.91)	3.79 (±0.44)	19.13 (±1.41)

7-day SHCC prisms were tested under one-side loading-unloading cycles (Test A) and fully reversed loading cycles (Test B). The resulting stress-deflection curves are given in Figure 2. The envelop curves of the cyclic testing results were close to the monotonic stress-deflection profile, showing that the specimen still experienced a hardening phase and a softening phase under cyclic loading. The flexural stiffness in the loading branch of each cycle reduced rapidly as the cycle number increased.

The cracking pattern of multiple parallel fine cracks was similar to that of monotonic tests. In Test A, the cracks only generated on the bottom face of the specimens. In Test B, the reversed force could help close or reduce previous cracks in one half part of the specimen while re-opening old cracks or generating new cracks in the other half part. These were in accordance with stereoscope observation. The crack width in Test A (59±16 µm) was larger than that in Test B (39±12 µm), indicating that the cracks in Test B had a higher potential of being self-healed according to previous studies [8].

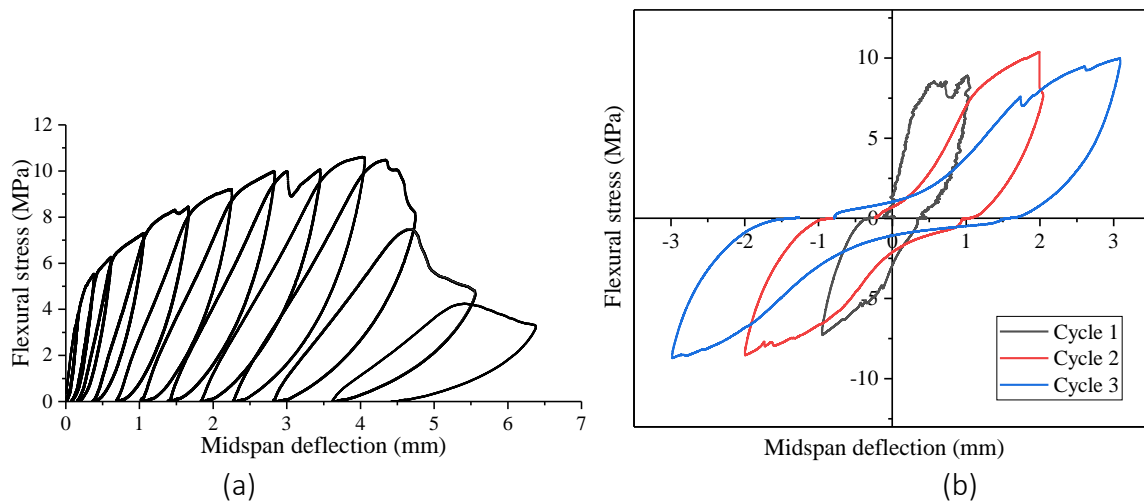


Figure 2. Flexural stress-deflection curves of (a) cyclic loading-unloading tests; (b) reversed cyclic tests

Microstructure analysis

It is shown in SEM images that PVA fibres in cracks were either bridging the crack or ruptured or pulled out due to crack opening (Figure 3(a)(b)). Moreover, the fibres were covered with cementitious materials according to both SEM images and EDX analysis (Figure 3(c)), which were probably calcium silicate hydrate (C-S-H), unhydrated cement particles or fly ash (in circular shapes). The latter two are essential for continuing hydration and pozzolanic reaction, which promote autogenous self-healing. This is in agreement with [9], i.e. the PVA fibres with a high polarity could act as a core for autogenous healing products to precipitate on, so the cracks could be filled more efficiently.

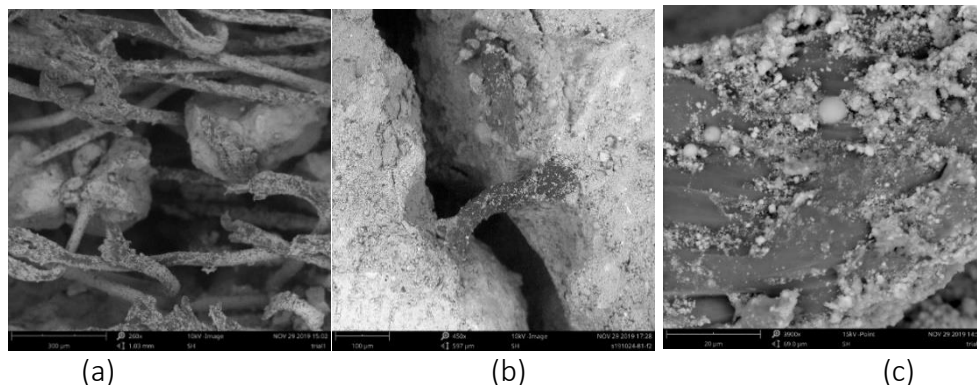


Figure 3. SEM images of (a) pulled-out or ruptured fibres; (b) bridging fibres being partially pulled out; (c) hydration products and unhydrated particles on fibre surface.

Self-healing evaluation

After the cracked SHCC went through 28-day autogenous self-healing, only crack locations in direct contact with water exhibited reduction in crack widths, as observed under stereoscope, which should be attributed to a higher availability of water or moisture in these regions. For example, the crack width for the reversed cyclic test (Test B) decreased to $33(\pm 11) \mu\text{m}$, which was probably due to the precipitation of C-S-H and/or calcite in cracks (Figure 4). Further confirmation of the chemical compositions would be conducted by EDX analysis.

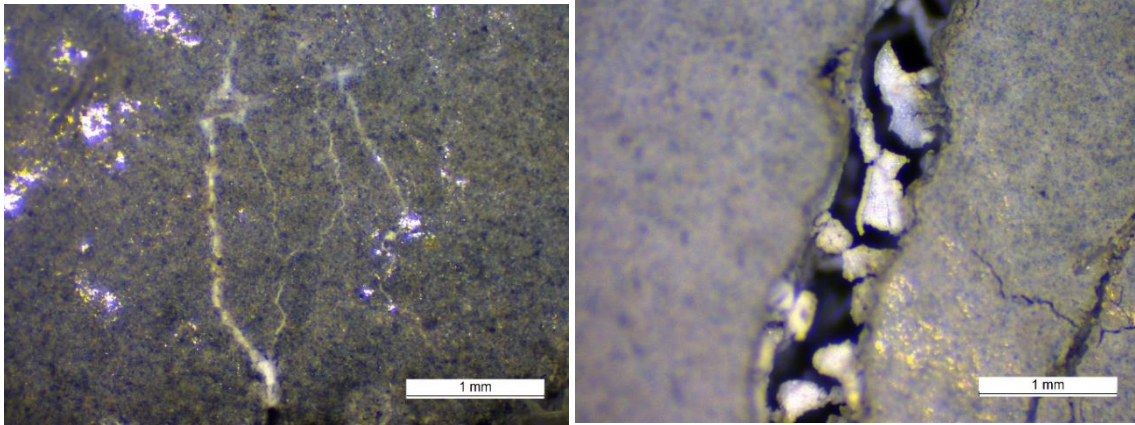


Figure 4. Stereoscope images of white healing products in cracks: (a) fine cracks $< 50 \mu\text{m}$; (b) crack $\approx 500 \mu\text{m}$.

After the 28-day healing, the specimens were re-loaded. The stiffness in the first reloading cycle was similar to that in the last preloading cycle, rather than decreasing a lot, showing that the self-healing process had a potential of recovering mechanical properties of SHCC. With appropriate healing conditions in the future (e.g. with sufficient water and/or CO_2 supply), the SHCC investigated could have a higher potential of self-healing, including more efficient and robust crack closure and recovery of mechanical properties.

Conclusion

- All the 7-d SHCC specimens exhibited deflection-hardening and multiple cracking behaviour under either monotonic or cyclic flexural loading. The general characteristics under cyclic loading could be described by the envelopes of the stress-deflection curves, which were close to the monotonic results. The flexural stiffness reduced after every loading-unloading cycle.
- In the reversed cyclic tests, the reversed force could close or reduce previous cracks at one half part of the specimens, resulting in smaller cracks than those in the one-side loading-unloading tests.
- The fibres were covered with cementitious materials and hydration products according to SEM-EDX analysis, confirming that PVA fibres with a high polarity could become a habitat for autogenous healing products to form, facilitating large cracks to be healed.
- After 28-day self-healing, the reduction in crack widths could be attributed to the formation of new C-S-H or calcite with sufficient water supply. The recovery or maintenance of stiffness could be a good indication of recovery of mechanical properties.

Acknowledgment

The financial support from the EPSRC for the Resilient Materials for Life (RM4L) Programme Grant (EP/P02081X/1) is acknowledged. The financial support from the Cambridge Commonwealth, European and International Trust (CCEIT) for the first author's PhD research, is appreciated.

References

- [1] de Rooij M, Van Tittelboom K, De Belie N and Schlangen E. Self-healing phenomena in cement-based materials. (Springer 2013).
- [2] Huang H, Ye G, Qian C and Schlangen E. Self-healing in cementitious materials: materials, methods and service conditions. *Materials and Design*. 2016 Vol 92 pp. 499–511.
- [3] De Belie N, Gruyaert E, Al-Tabbaa A, Antonaci P, Baera C, Bajare D, Darquennes A, Davies R, Ferrara L, Jefferson T, Litina C, Miljevic B, Otlewska A, Ranogajec J, Roig-Flores M, Paine K, Lukowski P, Serna P, Tulliani JM, Vucetic

- S, Wang J and Jonkers HM. A review of self-Healing concrete for damage management of structures. *Advanced Materials Interfaces*. 2018.
- [4] Li VC. From micromechanics to structural engineering - the design of cementitious composites for civil engineering applications. *Journal of Structural Mechanics and Earthquake Engineering*. 1993 Vol 10 No 2 pp. 37–48.
- [5] Li VC. On Engineered Cementitious Composites (ECC) - a review of the material and its applications. *Journal of Advanced Concrete Technology*. 2003 Vol 1 No 3 pp. 215–230.
- [6] Yildirim G, Keskin ÖK, Keskin SBl, Şahmaran M and Lachemi M. A review of intrinsic self-healing capability of engineered cementitious composites: recovery of transport and mechanical properties. *Construction and Building Materials*. 2015 Vol 101 pp. 10–21.
- [7] Van Zijl GPAG and Wittmann FH. *Durability of strain-hardening fibre-reinforced cement-based composites (SHCC)*. (Springer 2011).
- [8] Wu M, Johannesson B and Geiker M. A review: self-healing in cementitious materials and engineered cementitious composite as a self-healing material. *Construction and Building Materials*. 2012 Vol 28 pp. 571–583.
- [9] Nishiwaki T, Koda M, Yamada M, Mihashi H and Kikuta T. Experimental study on self-healing capability of FRCC using different types of synthetic fibers. *Journal of Advanced Concrete Technology*. 2012 Vol 10 pp. 195–206.

Polypropylene/CNT strain gauges for structures monitoring

Bartolomeo Coppola¹, Luciano Di Maio², Paola Antonaci³, Loredana Incarnato², Jean-Marc Tulliani¹

1: Department of Applied Science and Technology (DISAT), Politecnico di Torino, Torino, Italy

2: Department of Industrial Engineering (DIIN), University of Salerno, Salerno, Italy

3: Department of Structural, Geotechnical and Building Engineering (DISEG), Politecnico di Torino, Torino, Italy

Abstract

Carbon nanotubes (CNT) have been widespread used thanks to their extraordinary mechanical, thermal and electrical properties. Specifically, polymer/CNTs composites are used as high-performance composites, thermal insulators and sensors. Polymer/CNTs are excellent sensing materials if the electrical percolation threshold (EPT) is exceeded. The aim of this work was to produce polypropylene (PP)/CNT sensors to be used in the field of structures monitoring. For this reason, three PP/CNTs blends (1, 2 and 5 wt%, respectively) were prepared via a melt-blending process in a twin-screw extruder. Then, ribbon-shaped sensors were produced. Finally, such sensors were immersed in prismatic samples of a cementitious mortar and cured for 28 days in water. As expected, higher the CNTs content, higher the elastic modulus of PP/CNTs sensors (3841 MPa, 4471 MPa and 5191 MPa for 1%CNTs, 2%CNTs and 5%CNTs, respectively). Moreover, also a slight increase of tensile strength was observed. Mortar samples containing PP/CNTs sensors were tested in three-point bending mode to determine electrical impedance variation (ΔZ) under load. No meaningful variations were observed for samples containing 1%CNTs and 2%CNTs sensors, denoting that they were below the EPT value. On the contrary, a ΔZ of approx. 100 MOhm was measured in the case of 5%CNTs up to a load of 1250 N. In particular, impedance starts to increase for load values between 350-450 N and a Gauge Factor (GF), i.e. the ratio between ΔZ due to the applied strains and the initial impedance value, of 90% was determined.

Introduction

Cement-based mortars and concrete are the most used materials on Earth (4.1 Gt of cement were produced in 2017, according to Cembureau estimations [1]). While their structural properties have been deeply studied, relatively less attention has been dedicated to their functional properties [2]. The addition to cement-based materials of electrically conducting particles, such as carbon fibers [3], steel fibers [4], carbon black [5] or nickel [6] powder or carbon nanotubes [7] may significantly increase their electrical conductivity while maintaining or even improving their mechanical properties [2]. Strain-sensitive sensors are among the latest developed smart cementitious materials. This self-monitoring ability is achieved by correlating the change in the applied loads with electrical resistance or impedance values variations of the material. Then, the deformation or tension state can be estimated through the resistance changes allowing the emergence and spread of damage and microfractures to be continuously monitored. The most suitable self-monitoring materials are non-conductive fiber-reinforced cementitious and composite materials due to the higher sensitivity to changes in electrical resistance of non-conducting or poorly conducting matrices [2].

The remarkable mechanical and electrical properties of carbon nanotubes (CNTs) suggest that they are ideal candidates for creating smart cementitious composites. However, the problem of providing good fiber dispersion has become an essential issue requiring serious consideration and resolution [2]. To this aim, acid functionalization is often used to disperse CNTs in the cementitious matrix but, CNTs toxicity can be increased [8, 9]. In this work, to avoid

the problem of CNTs dispersion in the cement paste, polypropylene (PP)/CNT sensors were produced. Polymer/CNTs are excellent sensing materials for structural health monitoring (SHM) if the electrical percolation threshold (EPT) is exceeded. For this reason, three PP/CNTs blends (1, 2 and 5 wt%, respectively) were prepared via a melt-blending process in a twin-screw extruder and evaluated as stress-strain sensors in mortars.

Materials and methods

A conductive polypropylene (PP)-based masterbatch (PLASTICYL PP2001) containing multiwalled CNTs (MWCNT, 20 wt%, Nanocyl NC7000) was used for composites preparation (Nanocyl, Sambreville, Belgium). According to Nanocyl datasheets, the average diameter, the average length and the carbon purity of NC7000 MWCNT are 9.5 nm, 1.5 μm and 90%, respectively. PP and PP2001 pellets were opportunely mixed to dilute the initial CNTs concentration (20 wt%) to three fixed concentrations: 1, 2 and 5 wt%. PP/CNT composites nomenclature indicates MWCNT concentration (e.g. PP/CNT-5 is the mixture containing 5 wt% of MWCNT). PP/CNT pellets were produced using a laboratory pelletizer from the extruded strand which was quenched using a cold-water bath. Ribbon-shaped sensors were then produced using a single screw extruder equipped with a rectangular die. The effective dispersion of CNTs in the PP matrix was assessed by Field Emission-Scanning Electron Microscopy (FE-SEM) observations. Finally, such strips were immersed in prismatic samples of a cementitious mortar (water / cement (CEM II/B-LL 32.5 R) / normalised sand ratio of 1/2/6; $4 \times 4 \times 16 \text{ cm}^3$) (Figure 1a). The samples were kept in a sealed bag with a container full of water for one day to prevent water evaporation and were cured for 28 days in water. PP/CNT strips were located in the inferior part (1/3 from the bottom, where tensile stresses are higher) of a PMMA mold before mortar casting.

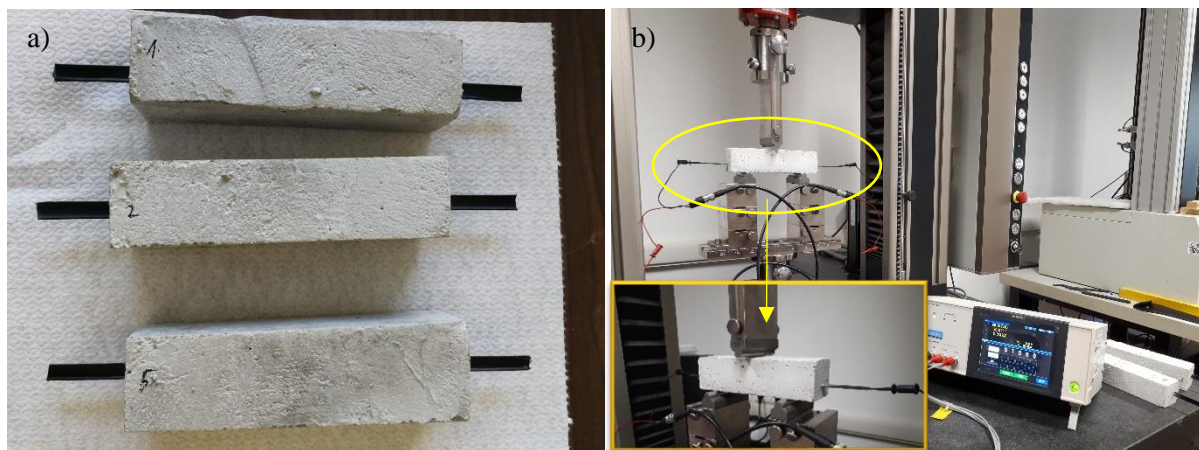


Figure 1. a) Mortar samples containing PP/CNTs and b) experimental setup

Tensile tests were conducted on rectangular strips (12 cm long having a gauge length of 5 cm) according to ASTM D638 and ISO 527-1 with a universal testing machine (Sans CMT6000 series, Shenzhen City, China) equipped with a load cell of 1 kN. Tensile tests were performed at a crosshead speed of 5 mm/min to determine the elastic modulus (E) of the specimens. Mechanical properties are the average of five measurements conducted for each sample. Self-sensing ability of PP/CNT composites was determined by means of 3-point bending tests carried out using a universal testing machine (Zwick Roell 2014, Ulm, Germany) equipped with a load cell of 50 kN at a strain rate of 0.25 mm/min (Figure 1b). Tests were stopped at a maximum load of 1500 N to avoid sample failure and allow cyclic tests. Indeed, each sample was loaded and unloaded three times to verify measurements reproducibility and possible decay of the self-sensing ability over the time. PP/CNT resistivity was assessed considering

impedance variation (ΔZ) under load. Impedance, Z , was measured using an impedance analyzer (LCR meter IM3533, HIOKI EE. Corp., Japan) imposing a ΔV of 1 V and a frequency of 5 kHz. The gauge factor, $GF(\%)$, was calculated as the ratio between impedance variation (ΔZ), at the maximum achieved strain (approx. 0.55%), and initial impedance value (Z_0), according to equation 1:

$$GF(\%) = \Delta Z/Z_0 \times 100 \quad (1)$$

Results and discussion

As expected, higher the CNTs content, higher the elastic modulus of PP/CNTs sensors (819 MPa, 890 MPa and 926 MPa for 1% CNTs (PP/CNT-1), 2% CNTs (PP/CNT-2) and 5% CNTs (PP/CNT-5), respectively) (Figure 2). Moreover, also a slight increase of tensile strength was observed and a contextual decrease of elongation at break. Mortar samples containing PP/CNTs sensors were tested in three-point bending mode to determine electrical impedance variation (ΔZ) under load. No meaningful variations were observed for samples containing 1% CNTs and 2% CNTs sensors (curves not shown), denoting that the sensors were below the EPT. Thus, a fourth sample was prepared with 3% CNTs (PP/CNT-3). The results of the impedance measurements on PP/CNT-3 and PP/CNT-5 samples under load are displayed in Figure 3. PP/CNT-3 nanocomposites reported an impedance decrease starting from about 250 N and then showed a constant value after approx. 1000 N (Figure 3a). This behavior can be explained considering that the electrical percolation threshold is not yet reached and once the load is applied, CNTs reorganization occurs due to the applied strain and Poisson's ratio. This change in the CNTs spatial distribution leads to a slight decrease of Z value for PP/CNT-3 nanocomposites ($\Delta Z = 13 \text{ M}\Omega$, considered as absolute value and a Gauge Factor (GF) of 1660%). On the contrary, a ΔZ of approx. 100 $\text{M}\Omega$ was measured in the case of 5% CNTs up to a load of 1500 N (Figure 3b). Specifically, impedance starts to increase for load values between 350-450 N and a GF of 141,600% was measured.

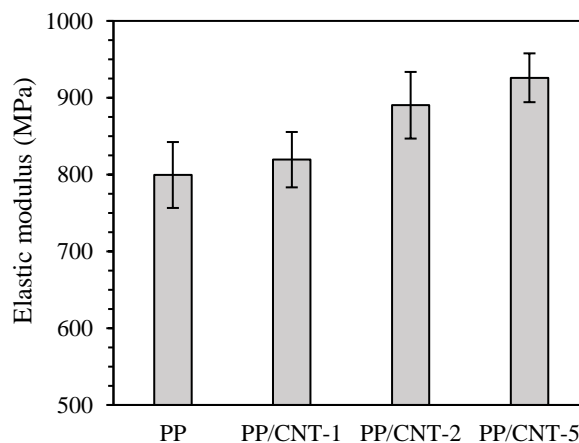


Figure 2. Elastic modulus of the PP and PP/CNTs composites and b) impedance (Z) vs. load for PP/CNT-5

The distribution and dispersion of CNTs in PP/CNT composites was investigated using a FESEM and a micrograph took on cryogenically fractured surface of 5% PP/CNT is reported in Figure 4a. CNTs partially agglomerate (white arrows of Figure 4a) but these agglomerates are rather homogeneously dispersed in the PP matrix. CNTs morphology and degree of dispersion can be deduced from Figure 4b in which it is evident that CNTs are entangled and curved but spaced in the polymer matrix.

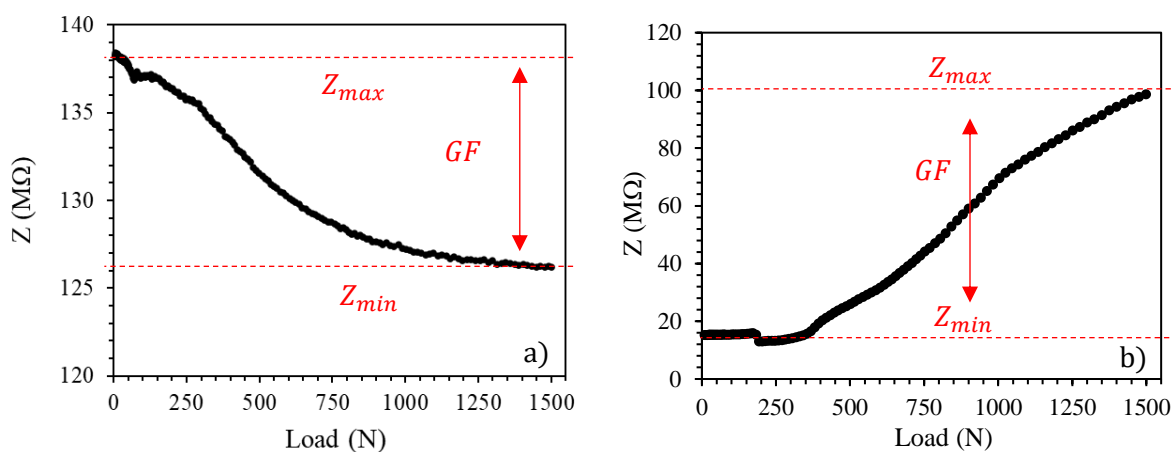


Figure 3. Impedance (Z) vs. load for a) PP/CNT-3 and b) PP/CNT-5

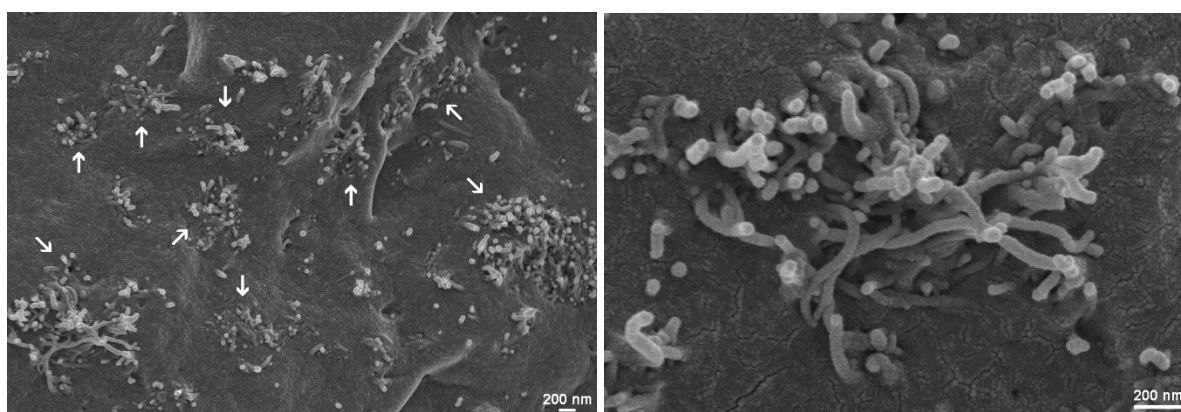


Figure 4. FESEM micrograph of: a) 5% PP/CNT composite ($\times 50,000$) and b) detail of the lower left corner of the same image ($\times 150,000$)

Conclusion

PP/CNT composites with different CNTs concentrations (i.e. 1, 2, 3 and 5 wt%) were prepared and tested as strain-gauge for structures monitoring. In particular, PP/CNT composites were embedded in a cementitious mortar and tested in 3-point bending mode recording impedance variation at increasing load. PP/CNT composites with 1 and 2 wt% didn't show significant results while PP/CNT composites while those with 5 wt% of CNTs showed very promising results. Indeed, impedance started to increase even at very low loads (between 350-450 N) and returned at the initial value once that the load was removed. Moreover, at increasing CNTs content, an increase of elastic modulus was obtained in the PP/CNTs composites. In conclusion, PP/CNT composites with 5 wt% of CNTs can be successfully used as strain-gauge sensors.

References

- [1] <https://cembureau.eu/media/1716/activity-report-2017.pdf> (accessed 16 December 2019)
- [2] Materazzi AL, Ubertini F, D'Alessandro A. Carbon nanotube cement-based transducers for dynamic sensing of strain. *Cement and Concrete Composites*. 2013 Vol 37 pp. 2–11.
- [3] Chen PW, Chung DDL. Carbon fiber reinforced Concrete for smart structures capable of non-destructive flaw detection. 1993 *Smart Materials and Structures*. Vol 2 pp. 22–30.
- [4] Chung DDL. Review functional properties of cement-matrix composites. 2001 *Journal of Materials Science* Vol 36(6) pp. 1315-1324.
- [5] Han B, Ou J. Embedded piezoresistive cement-based stress/strain sensor. 2007 *Sensors and Actuators, A: Physical*. Vol 138(2) pp. 294-298.
- [6] Han BG, Yu Y, Han BZ, Ou JP. Development of a wireless stress/strain measurement system integrated with pressure-sensitive nickel powder-filled cement-based sensors. 2008 *Sensors and Actuators, A: Physical*. Vol 147(2) pp. 536-543.

- [7] Li GY, Wang PM, Zhao X. Pressure-sensitive properties and microstructure of carbon nanotube reinforced cement composites. 2007 *Cement and Concrete Composites* Vol 29 pp. 377–82.
- [8] Figarol A, Pourchez J, Boudard D, Forest V, Akono C, Tulliani JM, Lecompte JP, Cottier M, Bernache-Assollant D, Grosseau P. In vitro toxicity of carbon nanotubes, nano-graphite and carbon black, similar impacts of acid functionalization. 2015 *Toxicology in Vitro* Vol 30(1) pp. 476-485.
- [9] Figarol A, Pourchez J, Boudard D, Forest V, Tulliani JM, Lecompte JP, Cottier M, Bernache-Assollant D, Grosseau P. Biological response to purification and acid functionalization of carbon nanotubes. 2014 *Journal of Nanoparticle Research* Vol 16(7) Article number 2507.

Automatic smart concrete quality control using supercomputing

Erika Pellegrino, Tania Stathaki

Electrical and Electronic Engineering, Imperial College London

Abstract

Over the last decade the civil infrastructure has been experiencing a diffused deterioration that raises several concerns related to the economic and the environmental impacts. For this reason, extending the service life of structures has become a key objective in the field of building engineering. In particular, self-repairing materials can play an important role because they prevent several deterioration factors and reduce the human intervention.

Methods based on Computer Vision and Artificial Intelligence can help researchers during the quality assessment of these new materials, but they require a huge amount of data to be processed in order to extract relevant features and measurements. Moreover, being the process carried out manually, the repetitive performances, the limitations and the subjectivity in human vision cause decreased work ability and errors in reading measurement instruments. In order to cope with these problems, this paper proposes a variational method to detect cracks in images along with a parallel implementation on heterogeneous High Performance Architectures aiming both at automatizing the whole process and at reducing its execution time.

Introduction

The concrete infrastructure requires a constant monitoring due to the deterioration caused by several factors. In current practice the detection of defects is absolved manually by inspectors, but this modality is time consuming and error prone [1,3]. This task is critical also for assessing the concrete quality [2]. Due to availability of cheaper devices, image-based techniques have been gaining in popularity, but they require large volumes of data to be processed as quickly as possible. The detection of fractures is still challenging in image processing. The main reasons are that they have a complex topology, a thickness similar to the image resolution and are easily corrupted by noise.

One of the scopes of this paper is to propose a variational model to detect cracks in images. It is well known that classical edge detection techniques based on gradient information are not successful with these structures. The intuitive idea is that, assuming that a fracture can be modelled by an indicator function supported by a smooth curve, it can be approximated by a sequence of functions whose Hessian blow up in its perpendicular direction, while their gradient is null. Motivated by these observations, showing that a suitable model should involve higher order derivatives, we propose a crack recovery method that falls within second order variational models. It is based on the Blake-Zisserman [4] functional or, to be more precise, on its approximation by elliptic functionals defined on Sobolev spaces [5]. In this paper we propose an implementation on High Performance Computing (HPC) architectures that are designed to execute massive parallel tasks.

The paper is organized as follow: in Section 'Mathematical Model and Parallel Implementation' we describe the mathematical model and the parallel implementation, in Section 'Numerical Results' we discuss performance results and in Section 'Conclusion' we draw some conclusions.

Mathematical Model And Parallel Implementation

Variational methods have addressed successfully problems such as image segmentation and edge detection. They propose as solution a minimizer of a global energy. A first example is

described by Mumford and Shah (MS) in their famous paper [8] where they proposed a first order functional, whose minimization determines an approximation of the image by means of a piecewise smooth function and detects edges as singularities in the image intensity. However, this model is not suitable for cracks because they do not represent singularities in the intensity function, but in its gradient instead. For this reason, we propose a second order variational model based on the Blake-Zissermann (BZ) functional [4]. This was introduced with the aim of overcoming some limitations of the MS approach, such as the over segmentation and the lack in detecting gradient discontinuities. Being the original formulation not suitable for numerical treatment, we had to work on a different approach that is based on the approximation proposed by Ambrosio and Tortorelli (AT) for the MS functional [6,7]. In their model, they replaced the unknown discontinuity set by an auxiliary function which smoothly approximates its indicator function. In our case two auxiliary functions are introduced as indicators of both intensity discontinuity and gradient discontinuity sets. As numerical minimization algorithm we chose an “inexact” block-coordinate descent scheme (BCD) in order to address the heterogeneous environment. Although the model is global, several numerical experiments have highlighted that the solutions weakly depend on boundary conditions and are energetically close to the initial data. This motivate the adoption of a tiling scheme to address very large images: the minimizer is assembled by merging together local solutions restricted to portion of images.

Numerical Results

We tried our methods on images of cracks taken in tunnels in Greece and back-scattered electron images of concrete samples. In the former case the challenge was to reconstruct the whole structure avoiding the effect of the noise and the environmental conditions (i.e. lights). In both cases the structures have been detected correctly (Figure 1,2). As future work, It would be interesting to compare the quality of the reconstruction with labelled dataset provided by the engineers involved in the assessment process.

In order to reduce the execution time and to provide a automatic procedure we tested a sequential implementation with a parallel one based on the OpenMP framework that implements two strategies for collaboratively executing a program on an environment composed by devices of different types (aka heterogeneous architectures). The experiments were performed both on a commodity PC and on a High Performance Computing cluster at Imperial College. A sequential version was executed on a workstation equipped with a processor Intel (R) Xeon CPU E6-79 at 3.40 GHz with 32GB of RAM and total number of cores 12, running an Ubuntu 18.04 operating system. The parallel version based was executed on a heterogeneous cluster equipped with x86-64 processors, running a CentOS 7.6 operating system. Overall, the results show a significant reduction in the execution time with respect to the sequential algorithm. In the latter the aim was to “insulate” the structure from the complex texture in the background.

Table 1. Run time comparison for a single image

	run time (s)
sequential	13.184868
parallel 24 cores	1.056701
parallel 48 cores	0.5915374

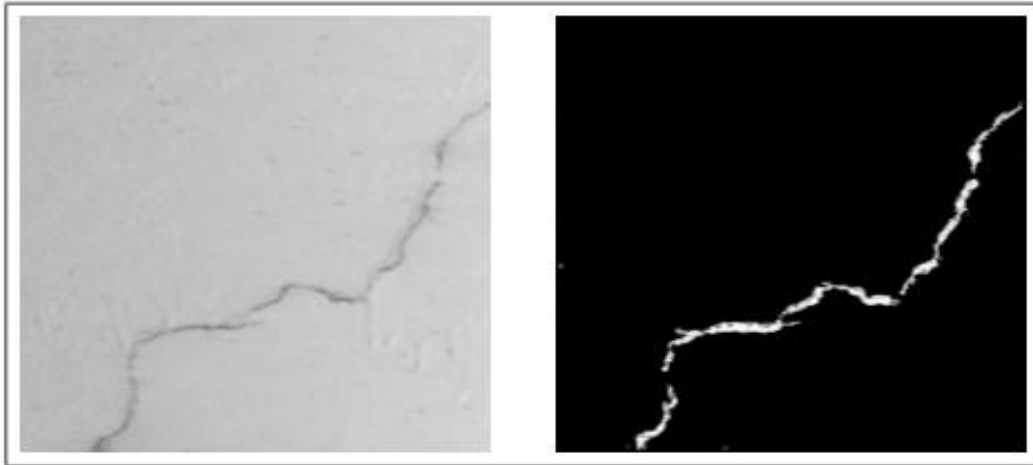


Fig. 1. Crack on a concrete wall

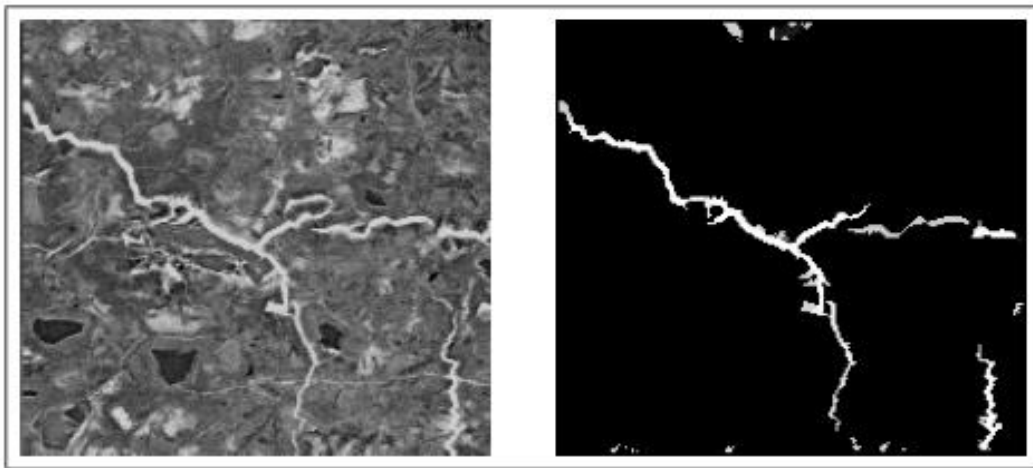


Fig. 2. Microcracks on a BSE microscopy of concrete materials

Conclusions

In this paper we proposed a variational method to detect cracks in images and a parallel implementation targeting modern High Performance Computing architectures with the aim of automatizing the detection process and of reducing its execution time. We got promising results for both the quality of the reconstruction and the reduction of its duration.

As future plan, we would like to test our procedure on real world scenarios in order to understand if it could be used as useful tool for assessing the building infrastructure and the concrete quality. We plan also to reduce further the execution time by designing a domain specific hardware accelerator tailored specifically to detect cracks in real time. Moreover, it would be interesting to understand how the algorithm work with isotropic structures such as bubbles.

Acknowledgement

We would like to thank the National Technical University of Athens for having provided images of cracks in the tunnels of Egnatia Motorway in Metsovo and the Concrete Durability Laboratory at Imperial College London for the back-scattered electron images.

References

1. Protopapadakis, E., Voulodimos, A., Doulamis, A., Doulamis, N. and Stathaki, T., 2019. Automatic crack detection for tunnel inspection using deep learning and heuristic image post-processing. *Applied Intelligence*, pp.1-14.
2. Lee, H.X.D., Wong, H.S. and Buenfeld, N.R., 2016. Self-sealing of cracks in concrete using superabsorbent polymers. *Cement and Concrete Research*, 79, pp.194-208.
3. Dams, B., Sareh, S., Zhang, K., Shepherd, P., Kovac, M. and Ball, R., 2017. Aerial additive building manufacturing: three-dimensional printing of polymer structures using drones. *Proceeding of the Institution of Civil Engineers: Construction Materials.*, pp.1-12.
4. Blake, A. and Zisserman, A., 1987. *Visual reconstruction*. MIT press.
5. Ambrosio, L., Faina, L. and March, R., 2001. Variational approximation of a second order free discontinuity problem in computer vision. *SIAM Journal on Mathematical Analysis*, 32(6), pp.1171-1197.
6. Ambrosio, L. and Tortorelli, V.M., 1990. Approximation of functional depending on jumps by elliptic functional via t-convergence. *Communications on Pure and Applied Mathematics*, 43(8), pp.999-1036.
7. Ambrosio, L. and Tortorelli, V.I.N.C.E.N.Z.O., 1992. On the approximation of free discontinuity problems.
8. Mumford, D. and Shah, J., 1989. Optimal approximations by piecewise smooth functions and associated variational problems. *Communications on pure and applied mathematics*, 42(5), pp.577-685.

Session 8A Advance Manufacturing for Civil Engineering and self-healing

Chair: Prof Jean-Marc Tulliani

1115 *Souza and Al-Tabbaa*. A high throughput microfluidic platform for production of microcapsules for self-healing in cementitious materials

1185 *De Nardi et al*. Advanced 3D printed mini-vascular network for self-healing concrete

1108 *Litina and Al-Tabbaa*. Advanced manufacturing platform for microcapsule-based self-healing cementitious materials

1166 *Sweeney et al*. Injection moulding of 'Spheritet' component for concrete reinforcement

1164 *Sweeney et al*. Concrete crack closure and reinforcement using high performance shape memory polymers (SMP)

1142 *Balzano et al*. Modified hybrid shape memory polymer tendons for enhanced concrete crack closure

A high throughput microfluidic platform for production of microcapsules for self-healing in cementitious materials

Lívia Ribeiro de Souza, Abir Al-Tabbaa

Department of Engineering, University of Cambridge, Trumpington Road, Cambridge CB2 1PZ, UK

Abstract

Microfluidics offer the possibility of microencapsulation while fine tuning capsule properties, such as size, shell thickness, mechanical properties, and interfacial bonding. However, the production rate of microcapsules has hindered the application of the technology to self-healing in cementitious materials. Typically, the laminar flow used for the formation of the double emulsion relies on flow rates ranging from 0.5-1 mL/g; as a result, the amount of material produced is not sufficient to assess the self-healing performance of the microcapsules in the matrix. To overcome this problem, we investigate a microfluidic platform for the high throughput of production of double emulsion. This parallelised platform offers the option for multiple microchannels, thus resulting in up to a 40-fold increase on the production rates of microcapsules. We demonstrate the successful implementation of our device for the production of microcapsules for self-healing, encapsulating hydrophobic core material and inorganic cores such as sodium silicate and colloidal silica. We investigated the mechanical characteristics of the microcapsules to achieve reliable and repeatable results in a broad range of mechano-responsive scenarios. Focusing of physical triggering, the size and shell thickness were investigated, as well as the mechanical characterisation using Dynamic Mechanical Analysis and microindentation. In addition, we performed the functionalisation of the produced capsules aiming to attract water molecules during the mixing process and facilitate the interfacial bonding between the capsule and the cementitious matrix. We envision that this platform will have a fundamental impact on laboratory tests to understand the mechanisms capsule-based performance of different healing agents.

Introduction

Encapsulation of a wide range of cargo materials and control over shell properties is of considerable importance to investigate the performance of capsule based self-healing in cementitious materials. Microfluidics offer the possibility of microencapsulating while fine tuning capsule properties, such as size, shell thickness, mechanical properties, and interfacial bonding [1]. However, the low production rate of microcapsules has hindered the application of the technology to self-healing in cementitious materials. Typically, single chips produce double emulsion at flow rates ranging between 0.5 to 1 mL h⁻¹; as a result, the amount of material produced is not sufficient to assess the self-healing performance of the microcapsules in the matrix. To perform lab scale tests to assess recovery in transport and mechanical properties after the self-healing in mortar, ~150 g of capsules are necessary [2]. This yield could only be achieved by 150 h producing microcapsules, at an encapsulation efficiency of 100%, which makes the test very time-consuming. A promising route to achieve a higher throughput of microcapsules is the use of parallelised microchannels in a platform. Microchips with several microchannels in parallel can be used simultaneously, markedly increasing the throughput of double emulsions. This system can offer up to a 40-fold increase in the current rates of microcapsules produced, decreasing the time necessary to achieve this material. In this paper, we investigate a microfluidic platform for the high throughput of production of double emulsion. We demonstrate the successful implementation of our device for the production of microcapsules, encapsulating hydrophobic mineral oil as model core material. We demonstrate the formation of monodisperse double emulsion, as well as the control over the

shell thickness. By using UV-polymerisation, we solidify the outer layer of the double emulsion to achieve a core-shell structure. We confirm core retention using thermogravimetric analysis. We envision that this platform will have a fundamental impact on laboratory tests to understand the mechanisms capsule-based performance of different healing agents due to its versatility to produce capsules with a wide range of core and shell materials.

Materials and methods

To produce the double emulsion, a microfluidic device with four flow-focusing channels in parallel, placed in a Telos device (Dolomite Microfluidics, UK), as shown in Figure 1. To obtain the suitable wettability for the production of double emulsion, the first part of the chip is hydrophobic while the second part is hydrophilic with a gasket connecting the two parts. The diameter of the channel is 300 μm for the first junction and 500 μm for the second junction. Double emulsions are formed using mineral oil (light, Sigma Aldrich, density of 0.838 g mL^{-1} , viscosity 29.3 $\text{mPa}\cdot\text{s}$) for the inner phase, trimethylolpropane ethoxylate triacrylate (ETMPTA, Sigma Aldrich, density 1.11 g mL^{-1} , viscosity 73.3 $\text{mPa}\cdot\text{s}$) with 1 vol% of photoinitiator hydroxy-2-methylpropiophenone for the middle phase, and 5 % (w/w) poly(vinyl alcohol) (PVA, M_w 13000-23000, 87-89% hydrolysed, viscosity 4.99 $\text{mPa}\cdot\text{s}$) for the continuous phase. The fluids were injected using pressure pumps (Dolomite Microfluidics, UK) at typical flow rates of 9-40 $\mu\text{L}/\text{min}$, 25-30 $\mu\text{L}/\text{min}$ and 250-370 $\mu\text{L}/\text{min}$ for the inner, middle and outer fluids, respectively. The polymerisation of the shell took place using a UV-lamp (Omniculture, 50% opening) exposed over the collection tube shortly (Figure 1) after the formation of the double emulsion droplets to minimise the effect of the density mismatch between the core and shell [3]. The resultant microcapsules were collected in an aqueous solution of 10 wt% PVA solution to prevent the agglomeration of the microcapsules during the polymerisation.

The produced double emulsions and microcapsules were observed with an optical microscope (OM) (DM 2700 M, Leica, Germany). To assess the thermal stability and oil content, the microcapsules were dried for 2 days before the thermogravimetric analysis (TGA) using PerkinElmer STA6000 between 50 and 700 $^{\circ}\text{C}$ at a rate of 5 $^{\circ}\text{C}/\text{min}$, under air atmosphere.



Figure 1 - Microfluidic platform showing the three pumps, the Telos device, the high-speed microscope and the box where the double emulsion is collected while being UV-polymerised.

Results and discussion

To demonstrate the use of microfluidic chip with 4-parallel channels to form monodisperse double emulsion, we produce oil-in-oil-in-water (o/o/w) double emulsions using mineral oil as inner phase. For middle phase, we use ETMPTA and PVA 5% as outer phase. Oil is selected as model core for the inner phase, as the double emulsion can be produced without the addition of surfactants. The chip produces highly monodisperse double emulsion, as shown by the optical microscopic image in Figure 2. Here, o/o/w double emulsions are produced at pressure of 2000, 6000 and 4000 mbar for inner, middle and outer phase, respectively, resulting in flow rates of 2360, 1800 and 21840 $\mu\text{L h}^{-1}$ for inner, middle and outer phase, respectively. The double emulsions present an average diameter of $602 \pm 8.6 \mu\text{m}$ and shell thickness of $53 \mu\text{m}$. We analyse ~ 7 double emulsions produced to assess the size distribution of the droplets (Figure 2a), as shown by the histogram of the outer diameters in Figure 2b. The double emulsions produced have a narrow size distribution, with a coefficient of variance (CV) is inferior to 1% for the outer diameter within the same junction and $\sim 1.4 \%$ for the all for junctions combined.

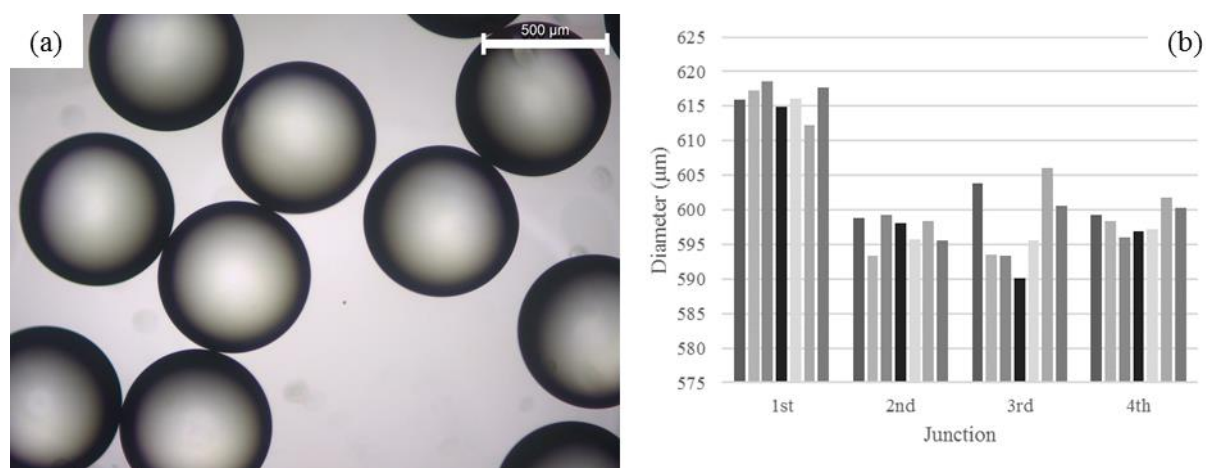


Figure 2 - (a) Microscope image of monodisperse double emulsion produced in the third junction of the microfluidic device. (b) size distribution of outer diameter double emulsion, where the inner, middle and outer flow rate were 2360, 1800 and 21840 $\mu\text{L h}^{-1}$ for inner, middle and outer phase, respectively.

We investigate the effect of varying the flow rate to of the inner phase to tune the shell thickness of the double emulsion. The relative shell thickness (h) is defined as a function of the flow rate ratio of the middle acrylate phase over the inner phase ($q_{\text{middle}}/q_{\text{inner}}$). By invoking mass conservation [4], h is calculated in Equation 1:

$$h = \frac{D_{\text{outer}} - D_{\text{inner}}}{D_{\text{outer}}} = 1 - \left(1 + \frac{q_{\text{middle}}}{q_{\text{inner}}}\right)^{-1/3} \quad 1$$

where D_{outer} and D_{inner} are the outer and inner diameter of the double emulsion, respectively. To control the size of the core droplets, we vary the inner phase flow rate from 570 to 1720 $\mu\text{L h}^{-1}$ while keeping the acrylate phase constant at 1300 $\mu\text{L h}^{-1}$ and the continuous PVA phase constant at 15000 $\mu\text{L h}^{-1}$. As show in in Figure 3, as the inner flow rate increases, we form double emulsions with larger core sizes. The shell thickness is calculated using Equation 1, ranging between 50 to 87 μm . By decreasing the shell thickness, we have larger core-shell ratios, increasing the payload with core material and the likelihood of the capsule to be physically triggered.

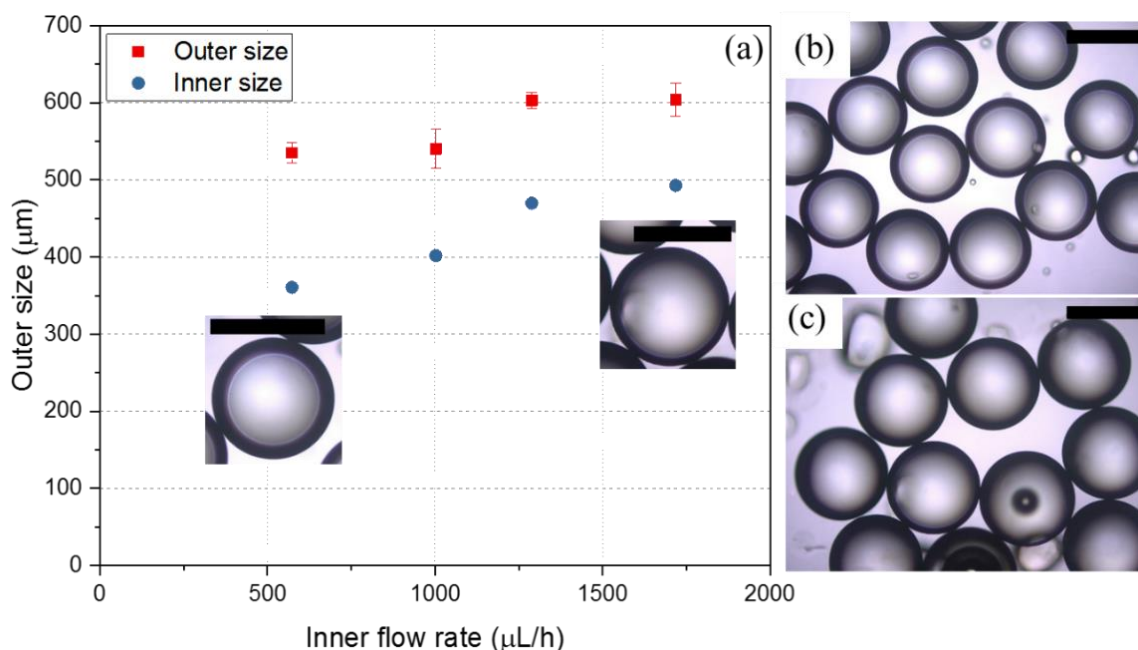


Figure 4 – Variation of outer and inner size of the double emulsion versus inner flow rate using a single microchip with 4-junctions in parallel. (a) Variation in Q_{inner} to produce double emulsions with various sizes of core drops, while keeping the acrylate and continuous phase constant at 1300 and 15000 $\mu\text{L h}^{-1}$, respectively. Microscope image of double emulsion produced at flow rates of (b) 570, 1300 and 15000 $\mu\text{L h}^{-1}$, and (c) 1720, 1300 and 15000 $\mu\text{L h}^{-1}$, for inner, middle and outer phase, respectively. Scale-bar represents 500 μm .

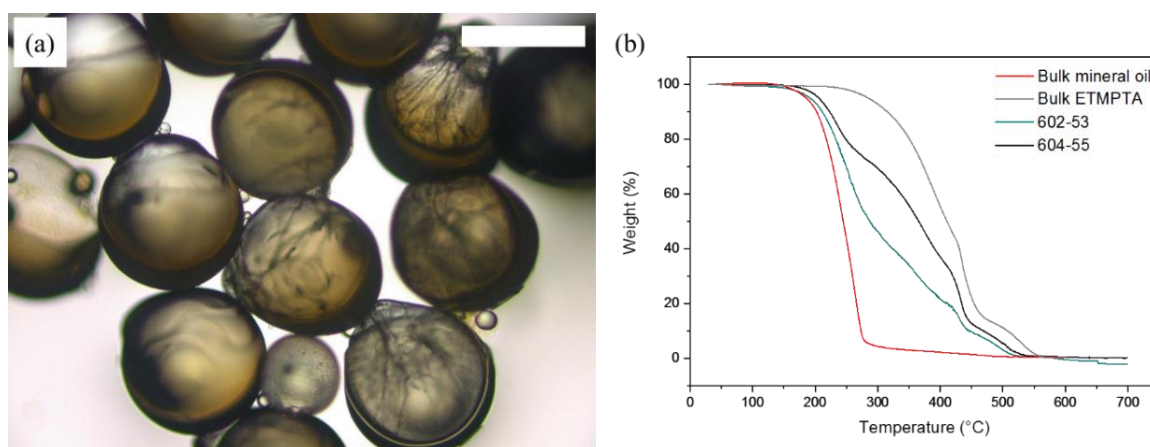


Figure 4 – (a) Image of microcapsules formed from O/O/W double emulsion templates using photocrosslinkable acrylate liquid as the shell phase and mineral oil as core. Scale-bar represents 500 μm . (b) TGA curves of the bulk shell material (grey line) and the mineral oil (red line) and the microcapsules with OD of 602 μm and shell thickness of 53 μm (teal line) produced with at flow rates of 2360, 1800 and 21840 $\mu\text{L h}^{-1}$ for inner, middle and outer phase. And the microcapsules with OD of 604 μm and shell thickness of 55 μm produced at flow rates of 1720, 1300 and 15000 $\mu\text{L h}^{-1}$, for inner, middle and outer phase, respectively.

To form the microcapsules, we solidify the shell phase by crosslinking the monomers constituting the droplet shell using UV-light. The double emulsion produced using the microchip is collected in a PVA 10% solution to prevent agglomeration [1], while being exposed to the UV-light. Core-shell structure is formed, as shown in the optical microscope image in Figure 4a. Due to the density mismatch between mineral oil and ETMPTA leads to the formation of spatially inhomogeneous microcapsules [3]. The retention of mineral oil inside of

the microcapsules is demonstrated by the thermogravimetric analysis (TGA) of the microcapsules with size 604 and 602 μm , and shell thickness of 55 and 53 μm , respectively. The thermal degradation of neat mineral oil under air atmosphere takes place between 150 and 300 $^{\circ}\text{C}$, as observed in the red line of Figure 4. However, the decomposition curve of the bulk sample of the acrylate shell (grey line) is not complete before 550 $^{\circ}\text{C}$. For the microcapsules at 400 $^{\circ}\text{C}$, all the oil is likely to be decomposed while the shell is still present. Thus, by contrasting the decomposition curve of the microcapsules (black and teal line) with the shell (grey line) at 400 $^{\circ}\text{C}$, the shell material was calculated to be 39% for the 602-53. Thus, the mass balance of 61% was attributed to mineral oil as a core. For the sample produced at the pressure of 1250, 4500 and 2700 mbar, resulting flow rates of 1720, 1300 and 15000 $\mu\text{L h}^{-1}$, for inner, middle and outer phase, respectively, the produced double emulsion was 604 ± 21 μm and shell thickness of 55 μm , the calculated shell thickness from the TGA is 67% and the mineral oil encapsulated is 33%. The difference in mineral oil encapsulated was mainly attributed to the density mismatch, and the escape of the core during polymerisation. To minimise the density mismatch and produce capsules with homogenous shells, the core density needs to be enhanced, by encapsulation other materials, such as emulsified sodium silicate [2].

The amount of microcapsules produced per hour varied between 2.9 g for the flow rates of to 1720 and 1300 $\mu\text{L h}^{-1}$, for inner and middle, respectively. The maximum amount of capsules produced using a single chip was 4.0 g per hour using a flow rate of 2360 and 1800 mg h^{-1} for inner and middle, respectively. The modular approach allows another 9 devices to be put in parallel. This could result in a 10-fold increase, of microcapsules, resulting in ~ 700 g per day. This amount is suitable for lab-scale size of tests, where approximately 100g of material are necessary to test mechanical properties, sorptivity and crack closure to assess self-healing performance. It is important to mention that this values were obtained at the maximum pressure allowed by the pump. According to the manufacturer, the flow rates could be up to 6 g/h for one chip. The values are close to the maximum capacity reported in the literature for the production of microcapsules using microfluidics [3].

Conclusion

We describe a microfluidic device with 4-junction in parallel used to produce double emulsion at a flow rate between 2.7 to 4 mg h^{-1} . The chip produces monodisperse double emulsion with diameter ranging between 520 to 600 μm , and shell thickness between 50 to 90 μm . We produce microcapsules using the double emulsion as template. We confirm the encapsulation of mineral oil using thermogravimetric analysis with a core content of 30-60% . The system with 4-channels in parallel produces microcapsules in a range of 2.9-4g, which is enough to produce capsules for lab scale tests in 40h. By using other 3 chips in parallel, this time will be reduced to 10 h. The system works robustly and no clogging is observed, indicating the material could be produced in a couple of days. This approach markedly enhances the potential of the technique to produce capsules with a wide array of materials for lab scale tests of self-healing performance.

Acknowledgment

This work is supported by UKRI-EPSC (Grant No. EP/P02081X/1, Resilient Materials 4 Life, RM4L).

References

- [1] Souza LR, Al-Tabbaa A. Microfluidic fabrication of microcapsules tailored for self-healing in cementitious materials. *Construction and Building Materials*. 2018 Vol 184 pp 713-722.
- [2] Kanellopoulos A, Giannaros P, Al-Tabbaa A. The effect of varying volume fraction of microcapsules on fresh, mechanical and self-healing properties of mortars. *Construction and Building Materials* 2016 Vol 122 pp 577-593.
- [3] Datta SS, et al. Delayed buckling and guided folding of inhomogeneous capsules. *Phys. Rev. Lett.* 2012 Vol 109 pp 134302
- [4] Hennequin Y, et al. Synthesizing Microcapsules with Controlled Geometrical and Mechanical Properties with Microfluidic Double Emulsion Technology. *Langmuir* 2009 Vol 25 pp 7857-7861
- [3] Nawar S, et al. Parallelizable microfluidic dropmakers with multilayer geometry for the generation of double emulsions. *Lab Chip*. 2020 Vol 20 pp 147-154.

Advanced 3D printed mini-vascular network for self-healing concrete

Cristina De Nardi, Diane Gardner, Tony Jefferson
School of Engineering, Cardiff University, Cardiff CF24 3AA, UK

Abstract

Following biomimetic design principles, several vascular network techniques have been studied over the last few decades. Promising vascular networks, using a variety of materials, have been proposed as a mechanism to achieve self-healing in concrete, however the advent of readily constructible structural elements that form part of the permanent works on a construction project has yet to be realised. Recent studies have focused on mini-vascular networks (MVNs); hollow channelled units formed using 3D printable polymers. These 3D tetrahedral units (so called TETs) have demonstrated the ability to respond efficiently to damage by releasing single-component, air-cured healing agents, stored inside the TETs. In order to make the MVN healing system more adaptable to different damage events and to overcome the potentially short shelf life of single-component healing agents, the design of the TETs has been improved. Ligaments are now formed from dual co-axial hollow channels (d-TETs) which allow the storage of bi-component healing agents. The system has given proof of good stability; the healing agents are activated only when the crack occurs, the action of which fractures the dual-channel ligaments and allows the polymerization process to occur. A range of healing agents, including epoxy resin, sodium silicate and nanolime have been explored, with encouraging initial results. The results showed the potential of d-TETs to adequately deliver the bi-component healing agents to zones of damage and allow sufficient reaction of the components in situ to achieve partial recovery of the undamaged flexural strength of the concrete.

Introduction

Mimicking blood and nutrient circulation networks in biological systems, recently vascular networks have been proposed by several researchers as innovative technology for self-healing concrete structures. To overcome the inherent weakness of hollow capsules concerned with their "one use only" design, researchers at Cardiff University developed a new method to form two-dimensional vascular network for cementitious materials [1], and proven the efficacy of this healing system in a set of full-scale site trials [2]. Moreover, 3D vascular networks, based on a biomimetic design that follows Murray's law were 3D printed and cast in small prismatic beams by Li et al [3], and showed the efficiency of delivering the pumped sodium silicate (SS) resulting in strength recovery up to 34% after 28 days. However, despite the success of vascular networks, there is a concern regarding their impact on the concrete manufacturing and casting process, so the advent of a full-scale system is yet to be realized. An alternative approach was proposed by De Nardi et al [4], encompassing the insertion of mini-vascular networks (MVNs), so called TETs into the cementitious matrix. It was noted that the TETs are able to store sufficient healing agent to cure serviceability-sized cracks in concrete, healing a multiple occurrence of damage with a ceiling value of 20% recovery of flexural strength after the first loading cycle [5]. In order to improve the healing efficacy whilst overcoming the challenges concerned with the potentially short shelf life of single-component healing agents, attention has been directed towards co-axial hollow channels TETs (d-TETs) which allow the storage of bi-component healing agents. In this context, a range of healing agents, including epoxy resin, sodium silicate solution and nanolime dispersion have been explored.

Materials and methods

The initial stages of the development d-TETs t involved modifications to a standard 3D tetrahedral unit in order to host a bi-component healing agent. The aim of this first stage was to optimize the design as well as the printing process to satisfy the bi-component healing agent requirements, namely i) the ability to store the two components without premature mixing; ii) the ability to be fully watertight when inserted into a cementitious matrix; iii) the ability to prevent any chemical interactions with the healing agent components. The ligament design was improved by adding an inner co-axial channel, as represented in Figure 1.

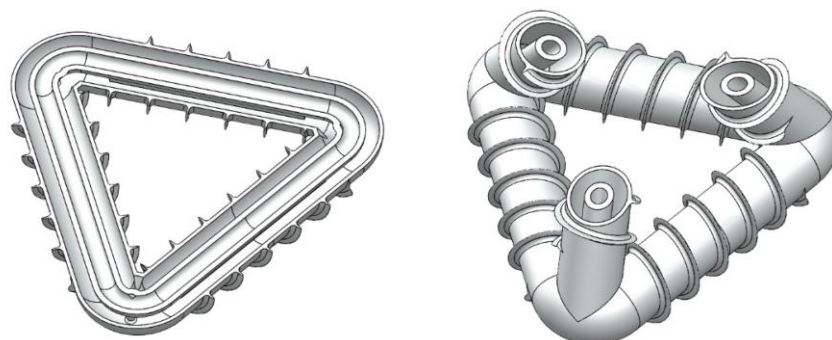


Figure 1 Co-axial hollow channels (d-TETs) design.

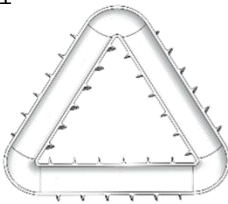
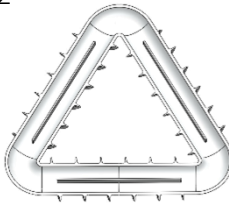
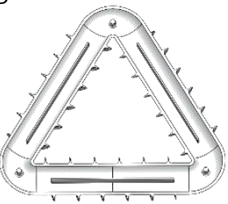
Three variants of d-TET were printed from clear PLA, purchased from Innofil3D BASF, using an Ultimaker2® printer (Utrecht, The Netherlands) with a 0.25 mm nozzle. The main printing parameters are summarized in Table 1. The properties of the d-TETs' variants are summarised in Table 1. Primarily, a 6mm external diameter ligament was taken as a starting point, since it proved to rupture at the designed crack opening of 0.3mm [5] whilst the dimension of the internal channel was chosen to store a commercial bicomponent adhesive in the ratio 1:5.

Table 1 Printing parameters

Printing parameters	
Nozzle	0.25 mm
Support type	buildplate
bottom_layers	12
cool_fan_speed	80
infill_sparse_density	100
support_infill_rate	10
support_z_distance	0.15
top_bottom_pattern	zigzag
top_bottom_thickness	0.25
top_layers	14
wall_line_count	2
wall_thickness	0.25
xy_offset	0.01

The d-TETs were filled with healing agents; either ink, a commercially available bi-component epoxy resin, sodium silicate ($\text{Na}_2\text{O}_3\text{Si}$) solution and nanolime (CaOH_2) solution, marked as Nanorestore® by the Company CTS Europe and produced by CSGI – University of Florence. For the sake of comparison, a sample containing two single channel TETs, filled with SS as described in [5] were also cast.

Table 1 d-TETS variants properties

Variant	1	2	3
			
Edge's length (mm)	42	45	45
Ribs	Spiral, pitch 5mm	Spiral, pitch 5mm	Spiral
External channel diameter (mm)	6	8	8
Inner channel diameter (mm)	2	3	3
External wall thickness (mm)	0.5 mm (0.25 x2)	0.5 mm (0.25 x2)	0.5 mm (0.25 x2)
Inner wall thickness (mm)	0.25 mm	0.5 mm (0.25 x2)	0.75 mm (0.25 x3)
Supports	NO	Along the base ligaments	Along the base ligaments + punctual elements at the corner

One d-TET of each variant were then manually placed in the centre third of a concrete prism mould (75 x 75 x 255mm), and concrete was then cast around them. The mix constituents and proportions of the concrete comprised CEM II/A-L1 32,5R cement (562 kg/m³), 0-2mm fine aggregate sand (562 kg/m³), 0-10mm coarse aggregate crushed limestone (1124 kg/m³), and water (253 kg/m³).

Following 7 days of curing, a 5mm notch was created and the prisms were loaded until a crack mouth opening displacement (CMOD) of 0.35 mm was recorded using a 3-point bending test under CMOD control. Control specimens without TETs were cast at the same time.

The effectiveness of healing can be evaluated by calculating the strength gained after the healing period ($\bar{\sigma}_{\text{healed}}^k$) with respect to the residual strength measured at the maximum pre-cracked opening ($\bar{\sigma}_{\text{damaged}}^k$) and comparing it to the maximum stress exhibited by the same specimens in undamaged conditions ($\bar{\sigma}_{\text{undamaged}}^k$)[5]. The index of strength recovery η_{σ}^k (%) is defined as in equation (1) [6].

$$\eta_{\sigma}^k = \frac{\bar{\sigma}_{\text{healed}}^k - \bar{\sigma}_{\text{damaged}}^k}{\bar{\sigma}_{\text{undamaged}}^k - \bar{\sigma}_{\text{damaged}}^k} \quad (1)$$

Results and discussion

Variant 1 performed poorly in a watertightness test, visible leakage of ink was observed from the inner channels, mainly concentrated at the corners. Moreover, the small diameter of the inner channel was incompatible with the injection process so that the Variant 2 design was improved increasing the healing agent volume and the overall functionality. A few supports to the inner channels were also placed in the middle of the base ligaments with the aim to enhance the stability during the printing, however some internal leakages were still evident at the ligament's junction. Finally, in Variant 3 discrete supports were added at the corners, and the wall thickness of the internal channels was increased (up to 0.75 mm), thereby reaching the full watertightness. At a crack width of 0.35 mm visual observations of the prisms containing ink filled d-TETs clearly show indication of d-TETs breakage and release of ink, as evidenced in Figure 2



Figure 2 Evidence of d-TETs breakage

The results of the pre-cracked and post healed specimens are presented in terms of load vs CMOD responses in Figure 3. The presence of d-TETs marginally reduces the flexural strength of the specimens tested after 7 days (-10%), as already previously experienced in samples containing single channel tested at early stages [5]. Specimens containing either 2 single channel TETs or 1 d-TETs filled with SS pre-cracked and exposed to laboratory conditions for 14 days, confirmed positive healing results, with a load recovery index of 17% and 18% respectively. As a matter of fact, the volume of healing agent stored in a d-TET (7440 mm³) has been slightly increased with respect to 2 single channel TETs (6630 mm³). Samples containing d-TETs filled with the bi-component epoxy resin did not show any evidence of strength recovery. Even if both components of the epoxy resin have low viscosity, and thus assuming that they were both released in the damage zone at the same time, the polymerisation reaction may not have taken place because the right mix ratio of the two compounds was not achieved properly.

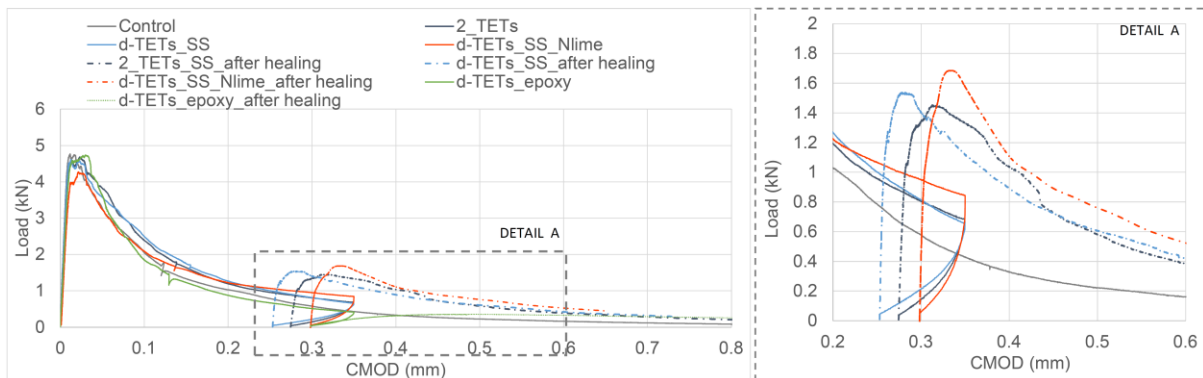


Figure 3 Load-CMOD results for Variant 3 d-TETs

Samples containing d-TETs filled with SS and nanolime showed a recovery strength of 27%. It may be reasonably assumed that the addition of nanolime, at the time of the damage, has promoted the reaction healing between SS and calcium hydroxide already present in the matrix to form C-S-H gel [7]. It also appears that the extra amount of calcium hydroxide, available in liquid form into the crack has also enhanced the transport of the healing agent due to the capillary rise so that the crack plane coverage in the cross-section approached 100%.

Conclusion

The experimental results indicate that the d-TETs variant 3 yielded the best results with respect to the requirements of hosting a bi-component healing agent. Samples containing d-TETs filled

with a bi-component epoxy, showed no evidence of the release of both reacting components in the right stoichiometry, upon the d-TETs' breakage. The result of this mis-mixing ratio led to the polymerisation reaction failure. Interestingly, d-TETs filled with SS and nanolime dispersion highlighted a strength recovery up to 27 % in prismatic concrete beams. The tests performed to date have opened the path to a new approach for TETs, which encompasses the simultaneous storage of a healing agent and an enhancer of healing, that will both be available at the time of damage in the vicinity of any crack formation.

Acknowledgment

Financial support from the Engineering and Physical Sciences Research Council (EPSRC) for this study (Project No. EP/P02081X/1) is gratefully acknowledged. The authors thank Dr Borgioli and CTS Europe for providing the product Nanorestore®.

References

- [1] G. D. Davies Robert, Jefferson Anthony, Lark Robert, "A novel 2d vascular network in cementitious materials," in *FIB Proceedings*, 2015.
- [2] R. Davies *et al.*, "Large Scale Application of Self-Healing Concrete: Design, Construction, and Testing," *Front. Mater.*, vol. 5, p. 51, 2018.
- [3] Z. Li, L. R. De Souza, C. Litina, A. E. Markaki, and A. Al-tabbaa, "A novel biomimetic design of a 3D vascular structure for self-healing in cementitious materials using Murray 's law," *Mater. Des.*, vol. 190, p. 108572, 2020.
- [4] C. De Nardi, D. Gardner, A. Jefferson, T. Selverajoo, and G. Evans, "Durable Concrete for Infrastructure under Severe Conditions. Smart Admixtures, Self-responsiveness and nano additions," in *Durable Concrete for Infrastructure under Severe Conditions Durable Concrete for Infrastructure under Severe Conditions*, 2019, no. September, pp. 19–23.
- [5] C. De Nardi, D. Gardner, and A. D. Jefferson, "Development of 3D Printed Networks in Self-Healing Concrete," *Materials (Basel, Switzerland)*, vol. 13, no. 6. Resilient Materials for Life (RM4L) Research Group, School of Engineering, Cardiff University, Wales CF243AA, UK., 2020.
- [6] L. Ferrara, V. Krelani, F. Moretti, M. Roig Flores, and P. Serna Ros, "Effects of autogenous healing on the recovery of mechanical performance of High Performance Fibre Reinforced Cementitious Composites (HPFRCCs): Part 1," *Cem. Concr. Compos.*, vol. 83, pp. 76–100, 2017.
- [7] H. Huang and G. Ye, "Application of sodium silicate solution as self-healing agent in cementitious materials," no. 1993, 2011.

Advanced manufacturing platform for microcapsule-based self-healing cementitious materials

C. Litina, A. Al-Tabbaa

Department of Civil Engineering, University of Cambridge, Cambridge CB2 1PZ, UK

Abstract

Emerging research over the last two decades has focused particularly on imparting self-healing biomimetic attributes to composite materials for infrastructure and construction through the development of tailored microstructures, such as microcapsules and microparticles. These advanced composites require microcapsules with controlled size characteristics and micro-properties to deliver the desired functionalities. However, the fabrication of microcapsules and microparticles in the scale required with well-defined structures and compositions is challenging and highly variable with the traditional methods of emulsion polymerisation commonly used industrially. Membrane emulsification is a promising new technique that can be deployed as a scalable modular conduit for the consistent and continuous production of single and complex emulsions. This work reports on the development of a manufacturing platform based on membrane emulsification for microcapsule-based self-healing cementitious materials. The feasibility of single and double emulsion production with wall formation as a secondary step through UV radical polymerisation was explored using a discrete membrane emulsification dispersion cell. The operational parameters (pressure, dispersed phase flux, temperature, shear rate) are established and optimised for the specific phase characteristics (viscosity, density, interfacial tension) to achieve precise control of emulsion droplets and maintain a high encapsulation of core content (high payload). The emulsifier type and concentration are investigated to ensure stability of the formed emulsion. Finally the formed microcapsules were characterised and their release performance in the cementitious matrix established.

Introduction

One of the most exciting and fledgling trends in material innovation that is set to revolutionise many industries are biomimetic and in particular self-healing materials. Self-healing materials are designed to repair their own damage, thus providing enhanced performance, safety and sustainability through reduced inspection, repair and disruption costs. Recent advances have emerged with scientific breakthroughs in self-healing technologies for cementitious materials [1,2]. Amongst these, engineered microparticles or microcapsules filled with repair agents, that can be added to the material and rupture as cracks begin to form, releasing their content and repairing the material show particular promise.

To date, several microencapsulation techniques have been explored to deliver a range of repair materials and functionalities for self-healing applications relying on bulk emulsification methodologies. However, these are hard to control and lead to polydisperse systems [3]. Significant effort has been dedicated into optimisation of the droplet breakdown procedures in particular in terms of emulsification process scale-up. Within this remit production of emulsions using drop-by-drop approaches is of growing interest as it allows greater control over droplet size distribution and properties. Such approaches include the use of flow focusing (microfluidic) devices or controlled pore-size membranes (membrane emulsification - ME). The distinguishing features of the latter deviating from traditional technologies is that rather than continuously breaking down droplets to smaller sizes till the final required size is achieved, each droplet is produced individually with the final desired dimensions. One step formation of droplets offers not only greater control over emulsion microstructural attributes allowing

reliable consistent and repeatable creation of desired emulsion structures [4] but also the lower energy input results in fewer thermal and shear effects on those emulsion constituents [5]. Moreover these advantages over traditional breakdown methods allow modular and easy scale-up bespoke droplet formation with low energy and material consumption [6]. Here droplets are produced individually in a single step when the dispersed phase is pressed through a microporous membrane. Then droplets are formed on the other side of the membrane that is in contact with the continuous phase at the opening of each pore [5–7]. Once the droplets reach critical dimensions they detach into the continuous phase either due to spontaneous deformation driven by free-energy minimization or through shearing generated by a continuous phase flow over the membrane surface [6].

Researchers at the University of Cambridge have already begun investigating flow-focusing approaches to encapsulate self-healing agents in microcapsules with polymeric acrylate shells leading to advanced shell functionalities and performance [8,9]. This work builds on these promising formulations and reports on the development of a manufacturing platform based on membrane emulsification focusing on the potential of this controlled emulsification process as a technique to generate microcapsules for the systematic investigation of capsule-based self-healing cement-based materials.

Materials and methods

Trimethylolpropane ethoxylate triacrylate (ETMPTA) and the photoinitiator hydroxy-2-methylpropiophenone used to initiate the polymerisation of the acrylate were purchased from Sigma Aldrich, UK and formed the photocurable oil phase. Poly(vinyl alcohol) (PVA, MW 31000-50000, 98-98.8% hydrolysed, ACROS Organics, Belgium) was used as a surfactant to tune the interfacial tension and the viscosity of the aqueous phases. To produce emulsions (single or double), PVA concentrations ranging between 2-10% by weight were considered. All chemicals were used without further purification.

During the formulation stage which included optimisation of phase ratio and concentrations of components, emulsions were produced using a Dispersion Cell (Micropore Technologies, UK) fitted with a flat disc hydrophilic nickel membrane placed under a paddle stirrer. The dispersed phase was injected through the membrane into the continuous phase at a constant flow rate of 1ml/min with a syringe pump. The volume of the continuous phase in the cell was 90cm³. Once the best formulation was determined, continuous membrane emulsification (crossflow) with a tubular nickel hydrophilic membrane was investigated. The dispersed and continuous phases were injected using peristaltic pumps (Ismatec MCP-Z, Cole-Palmer, UK). A constant flow rate of 180ml/min was adopted for the continuous phase while the dispersed phase flow rate was varied (30,60,90 ml/min) to investigate its effect. In both systems 20 µm membranes with 200 µm pore spacing were used. The produced emulsions were transferred into a beaker with controlled stirring. A complete set up of the discrete cell and crossflow systems is shown in Figure 1.

Particles were then obtained through a second step free radical polymerisation of the photocurable oil phase initiated by UV irradiation. A UV-lamp Omnicure Series 1500 was used. During the shell formation stage the emulsions were stirred to prevent droplets from agglomerating. Formed particles were collected and washed. Droplet/particle size and diameter were observed and analysed through optical microscope (DM 2700 M, Leica, Germany) and the microstructure formation was confirmed with a scanning electronic microscope (SEM, Pro G2, Phenom, Netherlands).

Results and discussion

The ability to form simple oil-in-water (o/w) emulsions was investigated as a droplet template for the formation of solid core microparticles. The versatility of the membrane to produce solid particles with was demonstrated by using a mixture of ETMPTA as the dispersed phase.

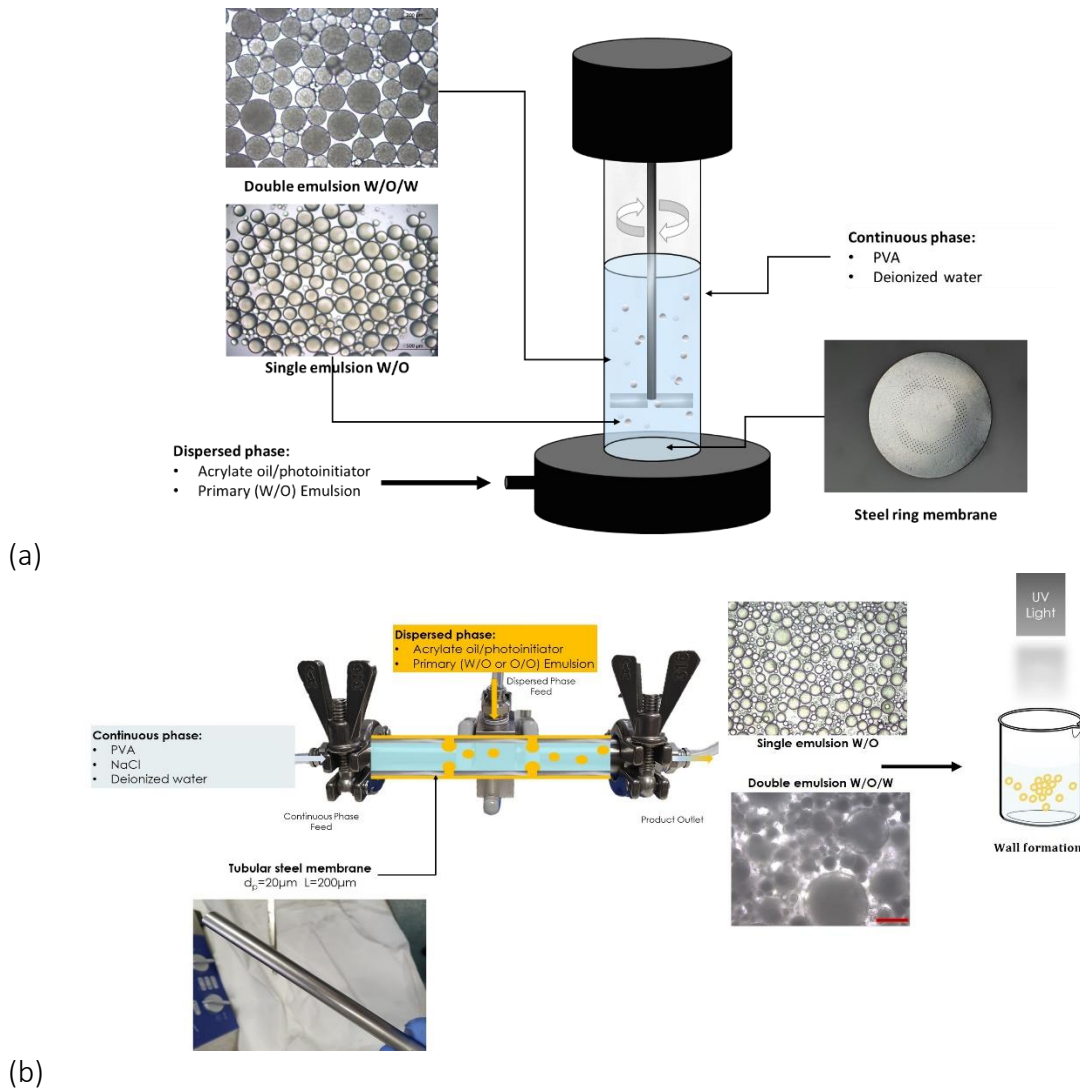


Figure 1. (a) Dispersion Cell setup used for the production of single and double emulsions and (b) Crossflow continuous setup for continuous emulsion production.

Microparticles were then obtained by crosslinking the photocurable oil phase in the single emulsion droplets in the collection vessel. Formed microparticles are presented in Figure 2a and c. The effect of viscosity of the continuous phase was considered by modifying the content of PVA stabiliser. Four different contents were assessed (10%/5%/2%/1%) by weight of solution. It was found that decreasing the content lead to a reduction of the viscosity of the outer phase, increasing the droplet size and improving size distribution. However it affected the stability of the final emulsion leading to agglomeration during polymerization.

The proposed platform was also investigated for the production of core-shell structures. Water-in-oil-in-water droplets (w/o/w) were generated using a two part emulsification process. The first emulsion, w/o, comprised of a model aqueous phase in an oil acrylate wall forming solution. PVA was used in the water phase to stabilize this inner emulsion. Water plays a key role in self-healing of cement-based materials, enabling autogenic healing reactions or acting as a carrier for mineral healing compounds. The emulsion was formed by mixing the water core (5% PVA by weight) in the ETMPTA and photoinitiator solution to create a 20% by

weight final emulsion in a homogenizer at 10000rpm for 2min. The emulsion was still stable after 2 hours. This then formed the dispersed phase to be injected through the membrane to form the final w/o/w emulsion. This final double emulsion formed the template to investigate the production of liquid core microcapsules, where the shell can then be created by crosslinking the middle phase of the final emulsion in the collection medium (Figure 2b and c). The feasibility of translating the two-step microencapsulation system from the discrete dispersion cell to higher throughputs was assessed through the use of a crossflow membrane emulsification device. Results of initial investigations (Figure 3) illustrate similar mean particle sizes and geometries for membranes of the same pore opening and pitch confirming the robustness of the platform for the production of both particulate systems. The operational parameters (pressure, dispersed phase flux) are being assessed and further work is underway to optimise for the specific formulation characteristics.

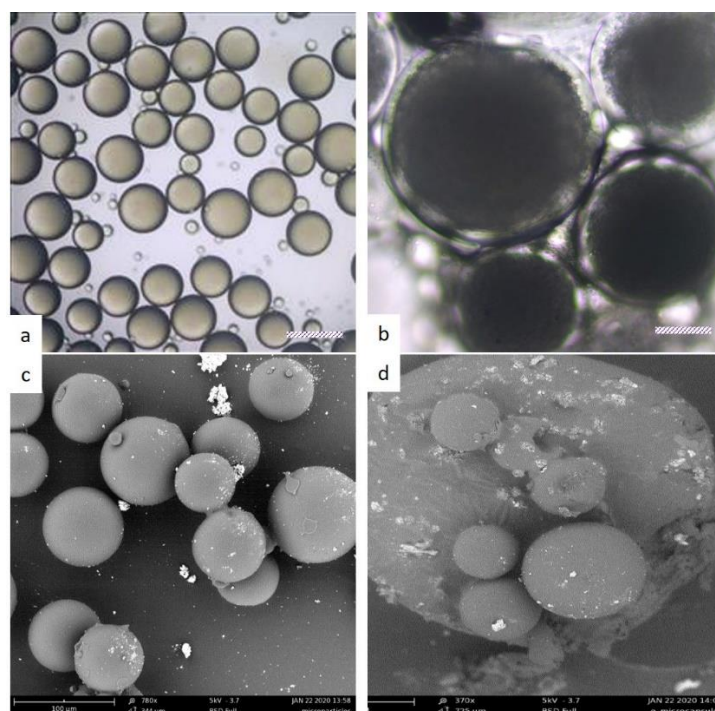


Figure 2. Optical microscope images of (a) the single emulsion droplets before polymerisation and the (b) double emulsion core-shell structures; and SEM images of the formed and dried (c) microparticles and (d) microcapsules.

Conclusion

For the first time, membrane emulsification was used to produce microcapsules and microparticles as delivery systems for self-healing in cementitious materials. Simple and double emulsions were formed and UV-polymerised to form particulate and core-shell structures respectively, using water as model core. Initial steps towards establishing a high throughput manufacturing platform have been successful but further work towards optimising the operational parameters is needed. The manufacturing platform and formulation outlined in this work can be further extended to encapsulate a range of typical healing agents used for self-healing in cementitious materials. This opens up new opportunities for a wider adoption and use of functional microsized additions to promote self-healing and other biomimetic attributes in construction.

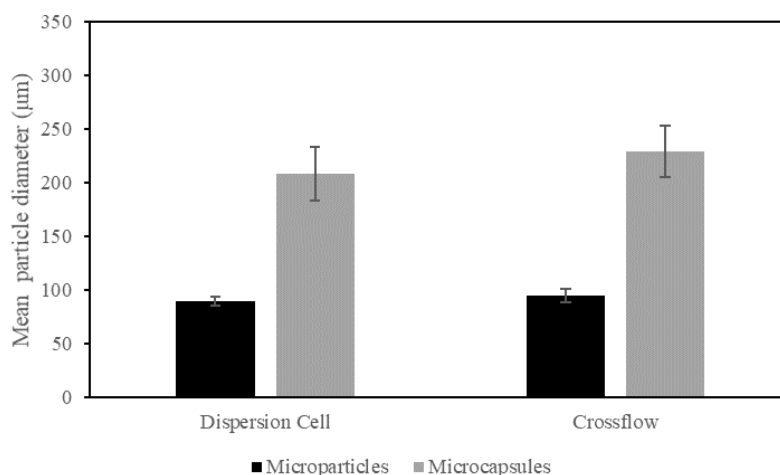


Figure 3. Mean particle diameters of polymerised particles produced using the discrete and continuous membrane emulsification platform.

Acknowledgment

The financial support from EPSRC for the Resilient Materials for Life (RM4L) Programme Grant (EP/P02081X/1) is gratefully acknowledged.

References

- [1] de Rooij M, Van Tittelboom K, De Belie N, Schlangen E. 2013 Self-Healing Phenomena in Cement-Based Materials State-of-the-Art Report of RILEM Technical Committee 221-SHC: Self-Healing Phenomena in Cement-Based Materials, Springer Netherlands.
- [2] De Belie N, Gruyaert E, Al-Tabbaa A, Antonaci A, Baera C, Bajare D, Darquennes A, Davies R, Ferrara L, Jefferson T, Litina C, Miljevic B, Otlewska A, Ranogajec J, Roig-Flores M, Paine K, Lukowski P, Serna P, Tulliani JM, Vucetic S, Wang J, Jonkers HM. 2018 A Review of Self-Healing Concrete for Damage Management of Structures, *Advanced Material Interfaces*. 1800074 pp 1–28. doi:10.1002/admi.201800074.
- [3] Schröder V, Schubert H. 1999 Production of emulsions using microporous, ceramic membranes, *Colloids Surfaces A Physicochemical and Engineering Aspects* Vol 152 pp 103–109. doi:10.1016/S0927-7757(98)00688-8.
- [4] Vladislavljević GT, Kobayashi I, Nakajima M. 2012 Production of uniform droplets using membrane, microchannel and microfluidic emulsification devices, *Microfluidics and Nanofluidics*. Vol 13 pp 151–178. doi:10.1007/s10404-012-0948-0.
- [5] Charcosset C, Limayem I, Fessi H. 2004 The membrane emulsification process—a review, *Journal of Chemical Technology and Biotechnology* Vol 79 pp 209–218. doi:10.1002/jctb.969.
- [6] Giorno L, De Luca G, Figoli A, Piacentini E, Drioli E. 2009 Membrane Emulsification: Principles and Applications, in: *Membrane Operations*, Wiley-VCH Verlag GmbH & Co. KGaA, Weinheim, Germany, 2009: pp. 463–497. doi:10.1002/9783527626779.ch21.
- [7] Vladislavljević GT, Williams RA. 2006 Manufacture of large uniform droplets using rotating membrane emulsification, *Journal of Colloid Interface Science*. Vol 299 pp 396–402. doi:10.1016/J.JCIS.2006.01.061.
- [8] Souza L, Al-Tabbaa A. 2018 Microfluidic fabrication of microcapsules tailored for self-healing in cementitious materials, *Construction and Building Materials* Vol 184 pp 713–722. doi:10.1016/j.conbuildmat.2018.07.005.
- [9] Souza LR, Al-Tabbaa A, Rossi D, 2019 Taking a microfluidic approach to the production of self-healing construction materials, *Metal Powder Report* Vol 74 pp 121–125. doi:10.1016/J.MPRP.2019.01.001.

Injection moulding of 'Spheritet' component for concrete reinforcement

John Sweeney¹, Glen Thompson¹, Ben R Whiteside¹, Tony Jefferson², Diane Gardner², Robert Davies², Brunella Balzano², Riccardo Maddalena², Cristina-Luminita Tuinea-Bobe¹

1: Polymer IRC, Faculty of Engineering and Informatics, University of Bradford, Bradford, BD7 1DP, UK

2: School of Engineering, Cardiff University, Cardiff CF24 3AA, UK

Abstract

A tetrahedral component was designed to act as concrete reinforcement. The component named 'Spheritet' aims to prevent crack formation due to its geometry. The component was initially manufactured by 3D printing, a manufacturing method not suitable for mass production and limited due to the material choices. In order to mass-produce the device via injection moulding a mould tool was required. The difficulty of mould design rests with the component's open structure and lack of symmetry planes. The paper will detail the design procedure and the manufacturing procedure of the 'Spheritet'. Furthermore, the material selection is closely related with the application: the 'Spheritet' needs to be of sufficient strength to resist cracks and to withstand the concrete mixing step, while being inert chemically during this process. Two glass filled materials were tested for this purpose and met the specifications.

Introduction

An open-structure polymer component has been designed to act as concrete reinforcement. The component, which we refer to as a 'Spheritet', has a designed geometry such as to prevent crack propagation. The geometry is such that the devices do not naturally form regular stacks and so do not provide opportunities for crack planes to form; when there is a sufficient loading, potential crack paths all go through a spheritet. The prototype was made using 3D printing, a manufacturing method not suitable for mass production and offering limited material choices. In order to mass-produce the device via injection moulding a mould tool was required. The difficulty of mould design rests with the component's open structure and lack of symmetry planes. This paper will detail the design and the manufacturing procedure of the spheritet. Furthermore, the material selection is closely related with the application: the spheritet needs to be of sufficient strength to resist cracks and to withstand the concrete mixing step, while being inert chemically during this process. Two glass filled materials were tested for this purpose and met calculated criteria for their mechanical properties.

Materials and methods

Material selection

For the fabrication of the spheritet we require materials that present mechanical properties capable of withstanding the forces developed in concrete during crack development. In addition to the application requirements, the injection moulding process runs at very high pressures, with fast cooling that can induce different morphologies in the skin/bulk layers of the components. Two materials were shortlisted based on previous experiments, one a polyoxymethylene (POM) and the other a polyethylene terephthalate (PET), both glass-reinforced. The first was DuPont Delrin 525GR NC000 with a 25% glass reinforcement, which is specified as very high strength, stiffness and deflection temperature and excellent resistance to creep. The PET material was DuPont Rynite 530 N010 which has 30% glass reinforcement and is specified as possessing an outstanding balance of strength, stiffness, toughness and chemical resistance. Tensile Test specimens (1BA, ISO 527- 2) with a 25mm gauge length and 1mm thickness were injection moulded on a Fanuc Roboshot S-2000i-5A and mechanically

tested on an Instron 5568 with a 3-point bend fixture at a crosshead speed of 21.6 mm/min (strain rate 0.005 s^{-1}) and tensile test fixture at a crosshead speed of 10mm/min (strain rate 0.005 s^{-1}).

Mould design

The spheritet is a complex structure aiming to prevent crack propagation in concrete. The complexity of the structure follows from the concept that the assembly of spheritets include polymer sections that will intercept any crack plane. Injection moulding is well established as one of the main processes for producing plastics components at a mass scale. It was adopted for spheritet manufacture as it is a fast process capable of producing large numbers of identical parts with high precision and low cost. Typically, polymeric material is introduced into the injection moulding heated barrel via the hopper where a reciprocating screw plasticises the material. It is then metered and fed into a temperature-controlled mould that defines the shape of the component, via a channel system (the gate and runner). During the process multiple parts can be manufactured simultaneously (multi-cavity tool) or as a single component shot. Due to the complexity of the proposed part a single shot approach was proposed, and the refinement of the component geometry in Solidworks was required (Figure 1): The design comprises crack intercepting sections with ribs and four anchorages for better fixation in concrete. The principal mould design problem related to finding an appropriate split line for the mould and finding a way to eject the part successfully.

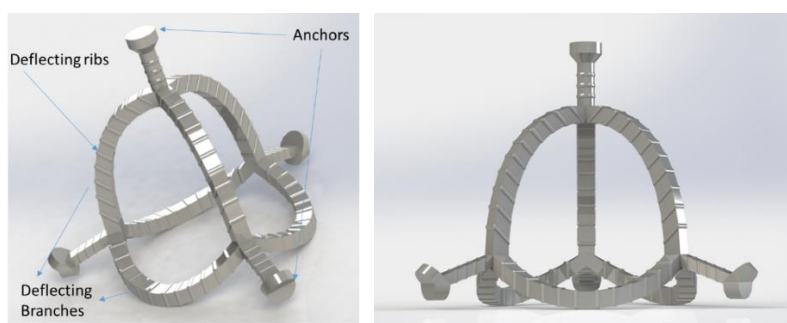


Figure 1. Solid model of the spheritet component

The mould was designed to eject the part by the movement of three sliding plates. The details of the branches, ribs and anchorages were produced using Electrical Discharge Machining (EDM) and Computer Numerical Control (CNC) machining (Figure 2).

The fixed part of the mould containing the mould core was manufactured using the same techniques (Figure 3). Seven alignment pins were required for the alignment of the plates of the tool, with three of them fixed on the sliding cores. The successful function of the tool is based on the simultaneous movement of the three sliding cores in synchrony with the injection moulding toggle movement. As the machine starts to open the mould the sliding cores start to move sideways to release the plastic component that subsequently is ejected. A robot was programmed to extract the samples from the mould tool and transfer them into containers. The moulding was performed on a Fanuc Roboshot S-2000i100A using the parameters in Table 1.

Table 1. Polymers parameters and properties

Polymer	Drying Temperature	Injection Temperature	Mould Temperature
POM (Delrin 525GR NC000)	80 °C	210 °C	80 °C
PET (Rynite 530 N010)	120 °C	280 °C	90 °C

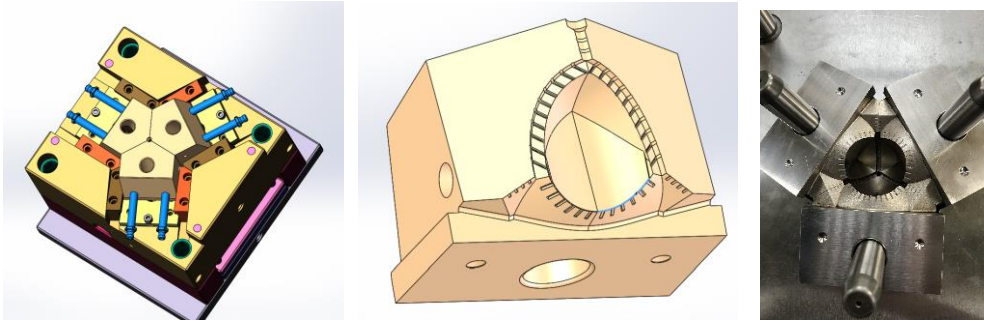


Figure 2. Plates and side mover on the mobile side: left – model of the mobile mould side closed, middle – model of the detail of the sliding core, right – picture of the mould cavity after machining



Figure 3. Mould core: left – model of the mould, right – picture of the core with the alignment pins housing

Results and discussion

Material testing

The Delrin material showed consistent behavior in tensile and three-point bend tests. The tensile strength was very consistent at around 145 MPa with specimens fracturing mid gauge-length. The average flexural modulus was 7800 ± 40 MPa.

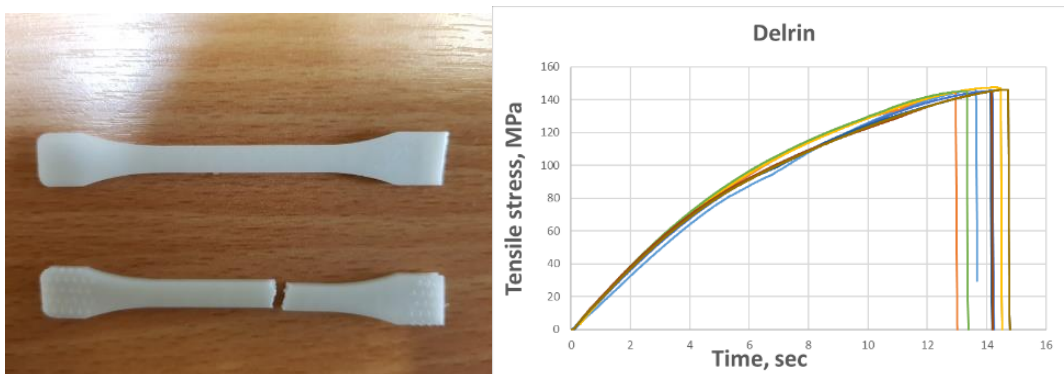


Figure 4. Delrin material samples before and after testing left, results of the tensile test on the right

Rynite 530 NC010 tensile strengths were very consistent at around 144 MPa, with the specimens fracturing mid gauge-length. The average flexural modulus was 8032 ± 108 MPa. Both materials are suitable for the application.

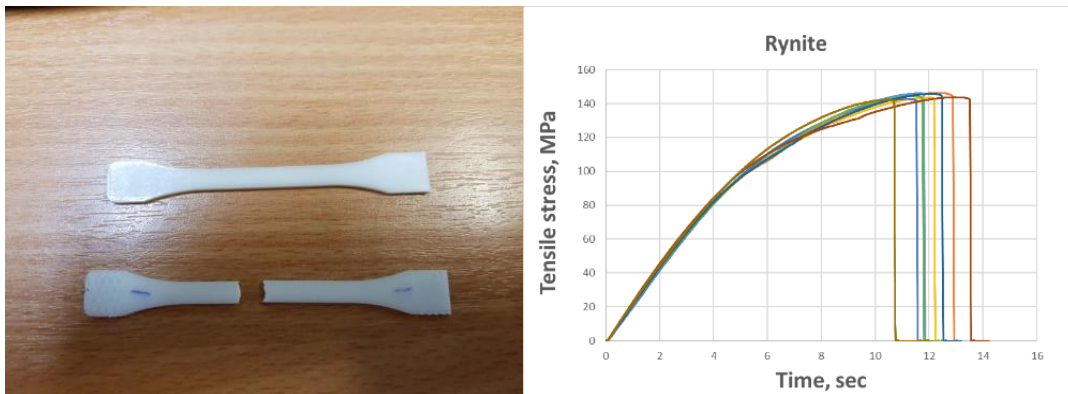


Figure 5. Rynite 530 NC010 material samples before and after testing left, results of the tensile test on the right

Spheritet reinforced material testing

The spheritets were embedded in concrete to obtain beams which were mechanically tested in 3-point bend. The concrete beam size was 100x100x500 mm. 50 spheritets were mixed into each beam.

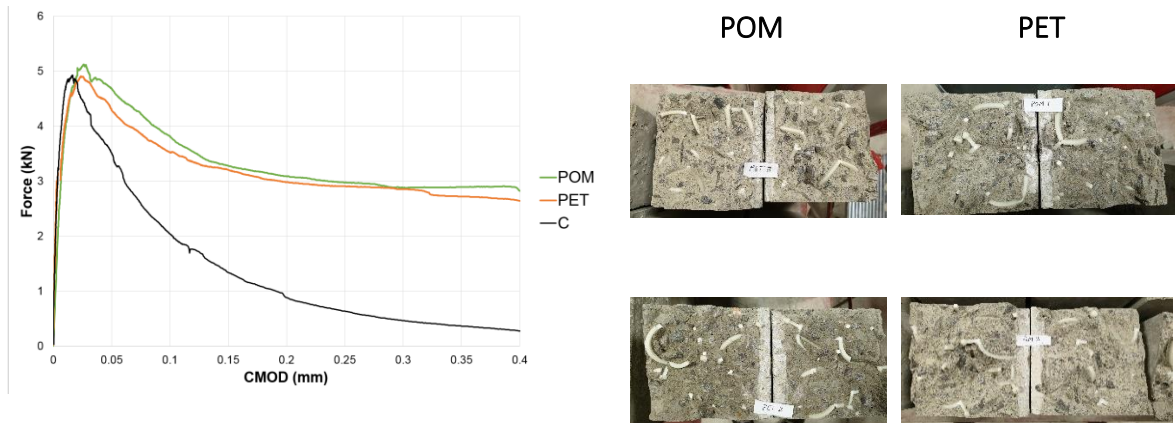


Figure 6. Mechanical testing of beams. On left are shown applied force against crack opening for POM and PET based spheritets (averages of three tests). C is for unreinforced concrete. Typical fracture surfaces are shown on the right.

Figure 6 shows that the presence of spheritets does not influence significantly the initial load peak, which is associated with crack initiation. However, their presence does greatly influence subsequent crack propagation, with much higher loads than for the control beams at CMOD of 0.4 mm. The two spheritet materials do not appear to perform significantly differently at this stage.

Conclusion

Spheritets can be successfully produced by injection moulding. They have been shown to inhibit crack propagation. However, there is a significant loss of load after the peak. Identification of the vulnerable regions of the spheritets will guide design improvements to improve performance. There is no significant difference in performance of the two materials used.

Acknowledgment

EPSRC Resilient Materials for Life (RM4L) EP/P02081X/1

Concrete crack closure and reinforcement using high performance shape memory polymers (SMP)

John Sweeney¹, Glen Thompson¹, Ben R Whiteside¹, Tony Jefferson², Diane Gardner², Robert Davies², Brunella Balzano², Riccardo Maddalena², Cristina-Luminita Tuinea-Bobe¹

1: Polymer IRC, Faculty of Engineering and Informatics, University of Bradford, Bradford, BD7 1DP, UK

2: School of Engineering, Cardiff University, Cardiff CF24 3AA, UK

Abstract

This paper concentrates on a fabrication method of SMP tendons and other devices to be used in a strengthening and reinforcement systems for concrete. The goals of this work encompass systems both to confine the cementitious matrix during the setting process to close or inhibit cracks, and also to provide reinforcement during service.

Two materials were investigate to be used for the SMP devices: Polyethylene Terephthalate (PET) and Poly(methyl methacrylate) (PMMA). Manufacturing has been carried out using extrusion to produce solid section fibres or tube, followed by die and mandrel drawing to induce molecular orientation. Converging dies were used to produce SMP tendons from solid section fibre. For other devices, oriented tube is required and is produced using a combination of a conical mandrel to induce circumferential orientation, and a converging die to add axial orientation. For tube SMP, process conditions were developed to produce an optimised combination of shape memory and compressive strength. SMP fibres have been developed with shrinkage force levels of around twice those of commercial products.

Introduction

Molecular orientation in polymers has been known as a phenomenon for many decades. It can be used to produce polymers with increased stiffness and strength, with technology developed for highly extended and very stiff fibres in the 1970s [1]. Techniques for producing larger section material by deformation in the solid phase to induce orientation continued in the 1970s and 1980s. Processes such as hydrostatic extrusion [2], roll drawing [3] and die-drawing [4] were developed and were successful in producing high modulus material. For polyethylene with a modulus of ~ 1 GPa in the isotropic state, hydrostatic extrusion could produce material with extension ratio of around 25 and modulus 60 GPa [2]. Similar examples are available for other processes and materials; for instance, for a polypropylene with a modulus of ~ 1 GPa in the isotropic state, die-drawing to an extension ratio of 16 has produced material with a modulus of 23 GPa [5]. Strength and fracture toughness can also be enhanced [6]. All methods of obtaining molecular orientation have the potential to produce shape memory polymer (SMP) as well as stiff material.

Die-drawing is one of the more tractable technologies that does not have the requirement of high pressure and is also capable of producing material with a range of cross-sectional shapes, both hollow and solid. For these reasons we have adopted it for the manufacture of the SMP reported in this paper.

We report here two case studies of the use of an SMP to assist in the strengthening of concrete. In the first, SMP fibres installed in bundles (tendons) within concrete at the setting stage, and triggered so as to induce compressive forces in the concrete to suppress the microcrack development. In the second, a compound device consists of a prestressed tensile element within an SMP tube. The stress in the prestressed element is transferred to the concrete on triggering of the SMP tube, to apply reinforcement forces.

Materials and methods

For both applications, a commercial grade of polyethylene terephthalate (PET) material (Dow Lighter C93) was used. This is an amorphous polymer, and so its shape memory behaviour is controlled by its glass transition temperature T_g ; orientation must be imposed at around this temperature, and shape recovery is also achieved near T_g . For this material, $T_g \approx 78 \text{ }^\circ\text{C}$ according to manufacturer's figures. This makes the triggering temperature compatible with the setting concrete environment.

Tendons for crack suppression

Firstly the material was made into fibres by melt extrusion, using a twin-screw extruder operating at $270 \text{ }^\circ\text{C}$, extruding through a 4mm die into a cooling bath to achieve a final fibre diameter of 1.8 mm. The second stage of the process was to introduce molecular orientation into the fibres. The technique of die-drawing was used [4]. Fibre at room temperature was pulled through a 1.5 m length fan-assisted oven with a controlled air temperature. On exit from the oven, it entered a converging conical die with cone angle 30° and final diameter 1 mm, held at a constant temperature. After the die the fibre was gripped by a caterpillar-type haul-off device operating at a constant linear speed. Maximum orientation was achieved by using a high haul-off speed of 1 m/min and lowering the oven temperature to just above the temperature where stress-whitening, indicating void damage, was observed. The final diameter of the oriented product was 0.9 mm, corresponding to a draw ratio of 4.0. Shrinkage restraint forces on the fibres were measured using a load cell while the fibres were heated in an oven in air in air at $90 \text{ }^\circ\text{C}$. Results are shown in Figure 1 [7], showing stresses up to 35 MPa.

Oriented SMP tubes

The die-drawing process can be used on hollow sections to make hollow products. Circular cylinders can be die-drawn, as shown in Figure 2, to produce material that is oriented in both the axial and hoop directions. In the device illustrated in Figure 3, the SMP has two roles: to resist the compressive forces imposed by the prestressed tensile element and maintain the devices integrity before deployment; and to be triggered after installation in concrete, so that the SMP tube itself applies a compressive force, together with the force from the tensile element that is then released. For the first role, the tube's compressive strength is important. While axial orientation increases tensile strength

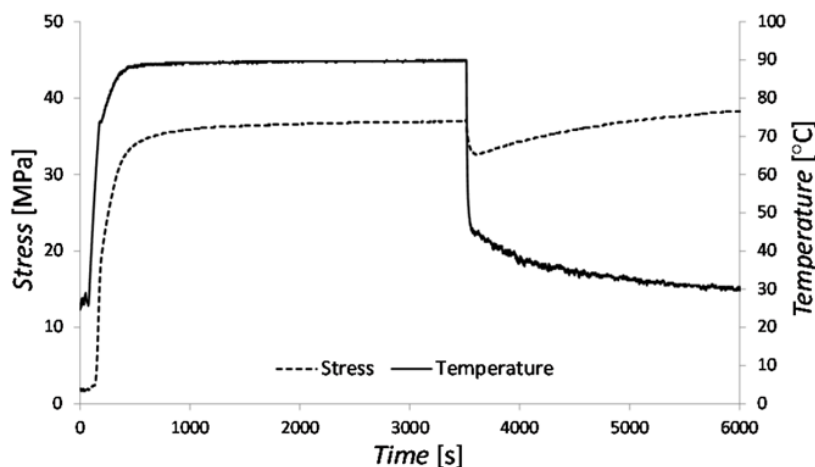


Figure 1. Shrinkage restraint forces developed in SMP fibres on heating to $90 \text{ }^\circ\text{C}$ [7]

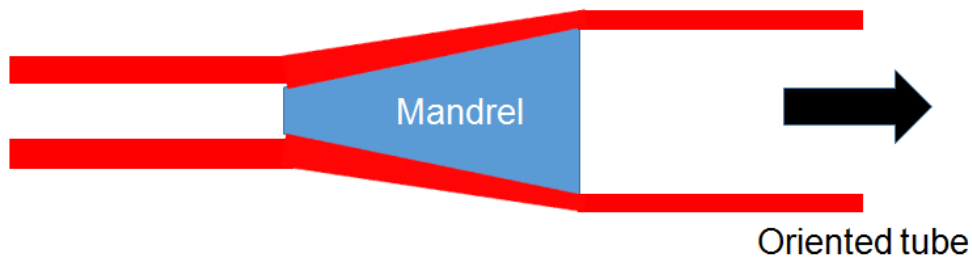


Figure 2. Production of biaxially oriented tube by drawing over a diverging mandrel.

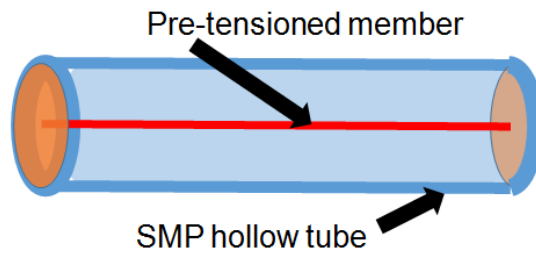


Figure 3. Prestressed reinforcement device.

Efficiently, its effectiveness is less so for compressive strength. However, the relative levels of molecular orientation in the hoop and axial directions has a complex effect on the axial compressive strength, as compressive failure will cause tensile extension in the hoop direction. The drawing parameters were adjusted to produce various levels of hoop and orientation in an attempt to optimise the compressive strength.

Results and discussion

Tendons for crack suppression

To measure the capability to heal cracks, tendons were installed in concrete beams which were tested in three-point bend [8]. Tendons were installed along the beam axis in the tensile region – see Figure 4.

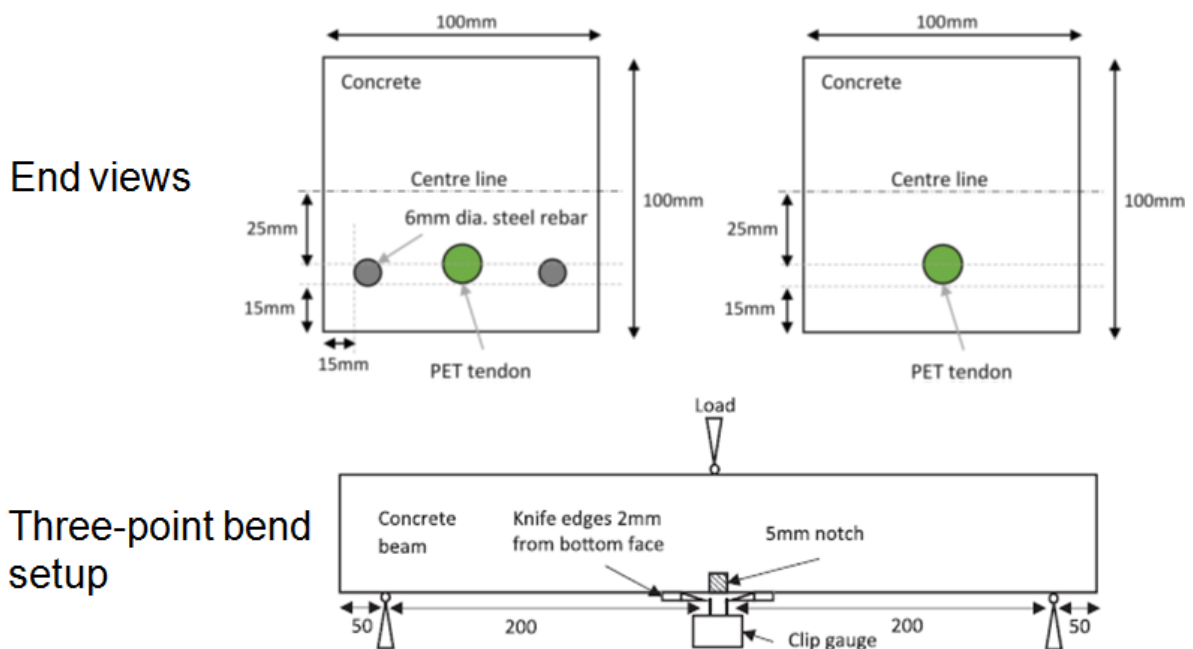


Figure 4. Three-point bend setup and location of tendons, all dimensions in mm

Two test configurations were used, one with PET tendons only and the other with accompanying steel reinforcement. During testing, images of cracks were measured using optical microscopy and a DIC system used to measure strain via a speckle pattern sprayed onto the sides of the beams. Beams with tendons were compared with controls. Results of such a comparison are shown in Figure 5, in terms of load-crack opening behaviour. Activation of the tendon produces substantial crack closure, and on reloading the force obtained is close to that of the initial loading.

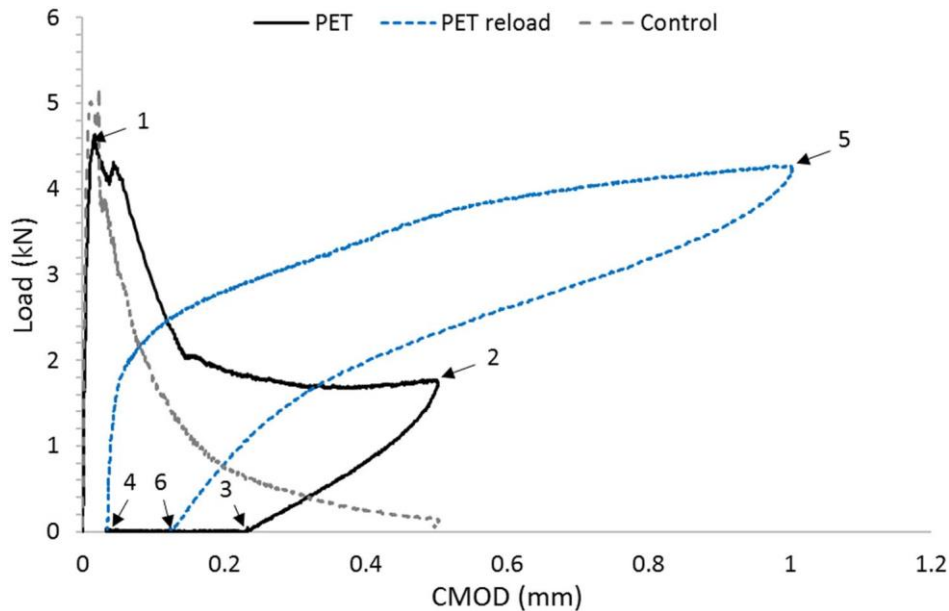


Figure 5. Three-point bend results comparing beams with tendons (PET) and Control [8]. Tendon is activated at point 3 and closes crack to point 4.

Oriented SMP tube device

Improvements in tensile strength of the SMP tubes were achieved by suitably balancing the levels of hoop and axial orientation. The strengths obtained are such as to produce viable devices with useful levels of preload in the tensile element. The devices are being developed further, increasing the tensile loads in the central members and developing the SMP tubes appropriately. Processes are being developed to produce the devices of Figure 3 continuously.

Conclusion

SMPs are being used to improve concrete structural integrity in a number of ways. High performance PET fibres have been produced by die-drawing and developed to provide high levels of shrinkage restraint force.

SMP tubes, with complex molecular orientation fields, have been developed by mandrel drawing to withstand high compressive loads before activation and enable effective prestressed reinforcement devices.

Acknowledgments

EPSRC Materials for Life (M4L) project (EP/K026631/1), EPSRC Resilient Materials for Life (RM4L) EP/P02081X/1, Costain Group PLC.

References

- [1] Cappacio G, Gibson AG, Ward IM. Ultra-high modulus polymers, Ciferiri, A, Ward, IM (Eds.) (Elsevier Applied Science 1979).
- [2] Gibson AG, Ward IM, Cole BN, Parsons B, Hydrostatic extrusion of linear polyethylene. *Journal of Materials Science* 1974 Vol 9 pp1193-1196.
- [3] Zachariades AE, Porter RS (Eds.) *The strength and stiffness of polymers.* (Marcel Dekker Publications 1983).
- [4] Coates PD, Ward IM. Die drawing: Solid phase drawing of polymers through a converging die. *Polymer Engineering and Science* 1981 Vol 21, 612-618.
- [5] Vgenopoulos D, Sweeney J, Grant CA, Thompson GP, Spencer PE, Caton-Rose P, Coates PD. Nanoindentation analysis of oriented polypropylene: Influence of elastic properties in tension and compression. *Polymer* 2018 Vol 151 pp 197-207.
- [6] Sweeney J, Duckett RA, Ward IM. The fracture behaviour of oriented polyethylene at high pressures. *Proceedings of the Royal Society London A* 1988 Vol 420 pp 53-80.
- [7] Teal O, Pilegis M, Sweeney J, Jefferson A, Lark R, Gardner D. Development of high shrinkage polyethylene terephthalate (PET) shape memory polymer tendons for concrete crack closure. *Smart Materials and Structures* 2017 Vol 26 045006.
- [8] Teal O, Pilegis M, Davies R, Sweeney J, Jefferson A, Lark R, Gardner D. A shape memory polymer concrete crack closure system activated by electrical current. *Smart Materials and Structures* 2018 Vol 27 075016.

Modified hybrid shape memory polymer tendons for enhanced concrete crack closure

Brunella Balzano¹, John Sweeney², Cristina Tuinea-Bobe², Glen Thompson², Anthony Jefferson¹

1: School of Engineering, Cardiff University, Cardiff CF24 3AA, UK

2: Department of Mechanical and Energy Systems Engineering, University of Bradford, Bradford BD7 1DP, UK

Abstract

This paper presents the results of a second experimental campaign carried out to test the modifications made to the original design of the crack-closure system introduced by Balzano et al. 2020. Following the successful results of the initial tests, this work aims to address and solve the problems highlighted in the previous work on the hybrid tendons. The anchorage assembly was modified in order to reduce the slippage and improve the overall performance of the reinforcement.

Introduction

The presence of cracks on the concrete surface has long been known as a major threat for the service life of a structure and repairs and maintenance still constitute a big burden on the whole-life cost of concrete structures [1]. The introduction of engineering self-healing technologies offers a novel tool to enhance the durability of concrete structures, by enabling the material of self-maintenance, hence extending the longevity of the concrete itself [2]. Several technologies have been developed and tested providing the concrete with the capacity of healing its cracks [3] [4] [5] [6].

An alternative to crack “healing” is offered by shape memory tendons, embedded in the structural element, that, when activated, release a shrinkage potential which provides crack-closure mechanism [7]. Balzano et al. 2020 [8] proposed the study of innovative high-performance hybrid tendons, result of a combination of shape memory polymers (i.e. PET) and aramid fibres (i.e. Kevlar®). The latter were tested against their capability of offering both crack-closure and a reliable flexural reinforcement by embedding them in small mortar beams. The experimental campaign showed that the novel hybrid tendons successfully developed stress for crack-closing. Furthermore, the presence of aramid fibres enhanced the flexural performance of the cracked mortar beams. A numerical model, based on the hinge model for cracked beams, was also implemented to model the experimental results. The numerical code highlighted some problems related to the technology which reduced the overall performance of the hybrid tendons. This work presents the results of a second experimental campaign carried out to test a modified version of the hybrid tendons with the aim of reducing the slippage at the anchorage.

Materials and methods

Balzano et al. 2020 [8] presented the design of the hybrid tendons which is reported in Figure 1. The tendons are made by two elements: the first is an outer cylinder (or sleeve) made of pre-drawn PET; the second consists of a prestressed core formed from Kevlar® rope. The PET tubes were manufactured using a commercial grade of PET through a die-drawing process adapted for the production of tubes [7][8]. The raw material is heated above its glass transition temperature, stretched to orientate the molecules and cooled down to then freeze the new length. The shape memory polymer can be activated via heating at a temperature of circa 120-130 °C.

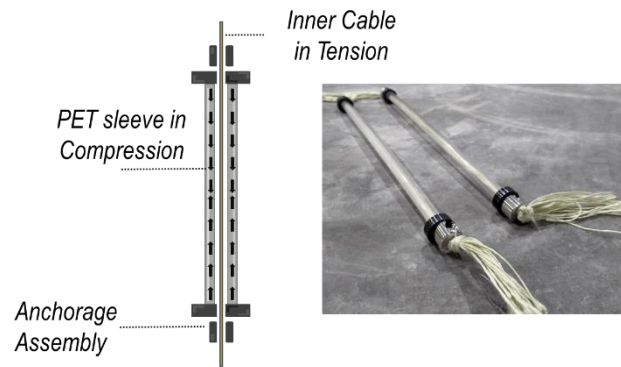


Figure 1. Hybrid Tendons

One could argue that the exposure to high temperatures could affect the mechanical response of the cementitious material. However, evidences in literature [9][10] show that up to 150/200 °C the strength loss is negligible. Moreover, for the specific application the mortar/concrete will be exposed to heat only for a limited amount of time (1 hour at most). It is then safe to assume that no serious damage is to be expected because of heat exposure, as a prolonged exposure to heat is more likely to induce instead serious consequences. The PET tubes are characterized by an external diameter of 8.6 mm and 1.5 mm thickness. The mechanical properties of the PET are reported in Table 1.

Kevlar® is an organic fibre belonging to the family of the aramid fibres and is characterised by a relatively high tensile strength. The mechanical properties of the Kevlar® are also given in Table 1.

Table 1. Mechanical Properties of the PET and the Kevlar®

		PET		Kevlar®	
		Average	CV %	Average	CV %
Tensile Strength	MPa	117.7	1.75	740	11.4
Compression Strength	MPa	84.07	9.78	-	-
Young Modulus	MPa	1380	1.52	7023	0.96

Initially the inner cable is stressed elastically until the desired pre-stress is reached. The whole system is then locked and now in a self-equilibrated state (Figure 1). This pre-stressed core is indeed restrained by the outer PET cylinder until the latter is activated, at which point the tensile pre-load in the core and the shrinkage potential of the cylinder are released. The hybrid tendon is then embedded and anchored in a concrete or mortar structural element. Once cracking has occurred, the hybrid tendon is activated via heating. This triggers the sleeve's shrinkage potential, thereby releasing the tensile force stored in the inner cable, which then applies a compressive force to the cementitious beam via the tendon's anchorages. In addition to post-tensioning the beam, the Kevlar® inner (core) cable also provides unbonded reinforcement. A modification was made to the original anchorage assembly with the aim of addressing the problem of to the slippage already highlighted in the numerical modelling of the previous experimental campaign [8].

In order to explore the behaviour of the revised hybrid tendon, a 75x75x255 mm beam with four embedded tendons was tested. As shown in Figure 2 the specimen contained a central notch to accommodate the CMOD gauge and was loaded in three-point bending. The cement

mortar for the beam specimens was prepared using Portland cement CEM II A/L 32.5 R (CAS number 65997-15-1), standard quartz sand (CAS number 14808-100 60-7) as fine aggregate and tap water. Cement (c) and sand (s) were mixed in a c/s ratio of 1:3 by mass, and water (w) was added at a w/c ratio of 0.55 by mass. The mix proportions of cement, water and sand were 439.6 kg/m³: 1318.7 kg/m³: 241.8 kg/m³ respectively. The sand was passed through a 2mm sieve and then oven dried.

Three 100x100x100mm cubes and three 100x200 mm cylinders were produced in order to perform compression and splitting tests in accordance with BS EN 12350-1:2000 and BS EN 12390-6:2009 respectively. Table 2 reports the compressive cube strength (f_{cu}) and tensile splitting strength (f_{cyl}) of the mortar paste after 7 days of curing.

Table 2. Cube strength (f_{cu}) and Cylinder strengths (f_{cyl}) at 7 days

	f_{cu} (7 days)	f_{cyl} (7 days)
	MPa	MPa
Mean (MPa)	14.4	1.3
CV (%)	4.8	3.7

Figure 2 also shows the tendons configurations and the geometry of the inner core. The inner core of the hybrid tendons was made by combining two 2.3 mm and two 4 mm ropes and prestressing the cable with an initial prestressing force of 900 N each for a total of 3.6 kN per beam.

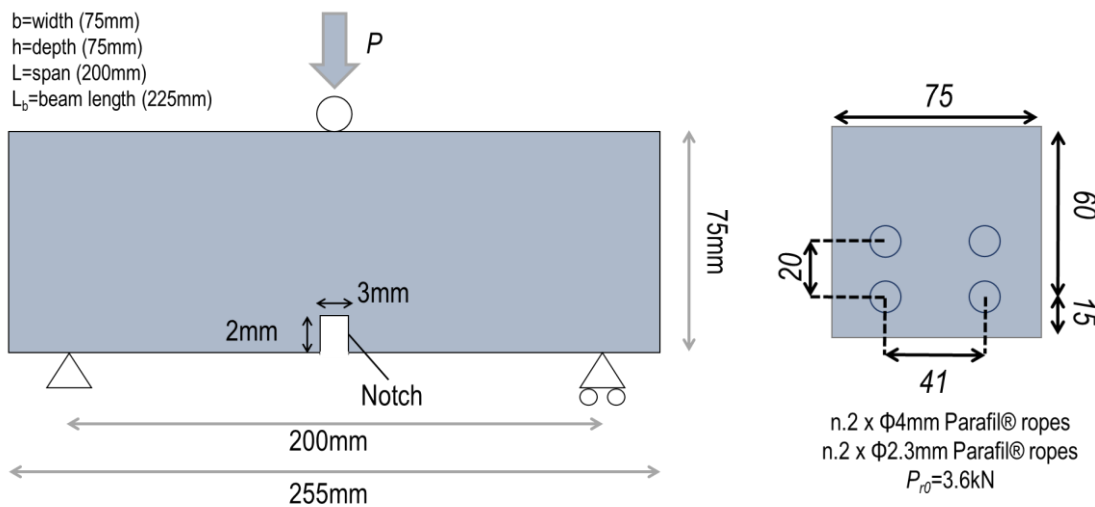


Figure2. Mortar Beam Test Configuration and Hybrid Tendons Scheme

The specimen was subjected to three-point loading in order to induce a central crack. Once the crack opening reached the value of 0.3 mm, the specimen was then unloaded and removed from the loading machine. The crack width was measured immediately after unloading and then the hybrid tendons were heat activated by placing the mortar beam in the oven at 120 °C for 45 mins. The crack width was re-measured after activation, once the specimens had cooled to the ambient temperature. The mortar beam was then re-loaded in three point bending to the maximum value the CMOD gauge could record prior failure.

Results and discussion

Figure 3 and 4 show the Force-CMOD response of the specimen before and after the activation of the hybrid tendon.

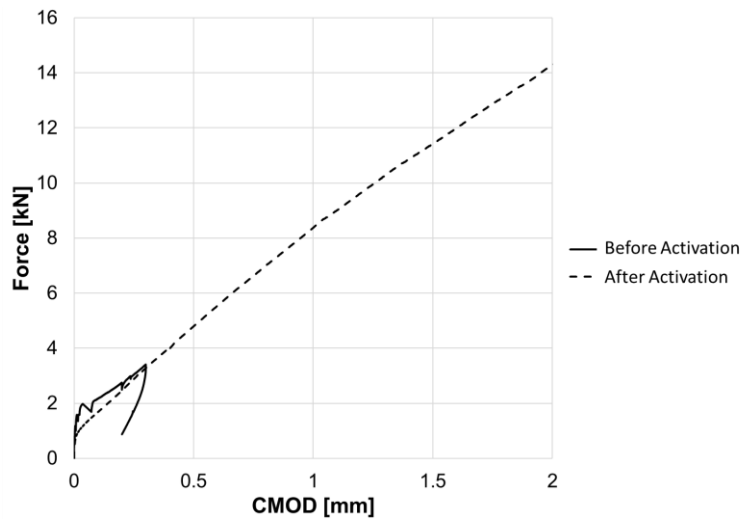


Figure 3. Force-CMOD graph before and after the activation of the Hybrid Tendons

Figure 4 shows the crack width measurement before and after the tendons' activation and it's evident how the stress released upon activation successfully closed the cracks previously impressed to the mortar beam.

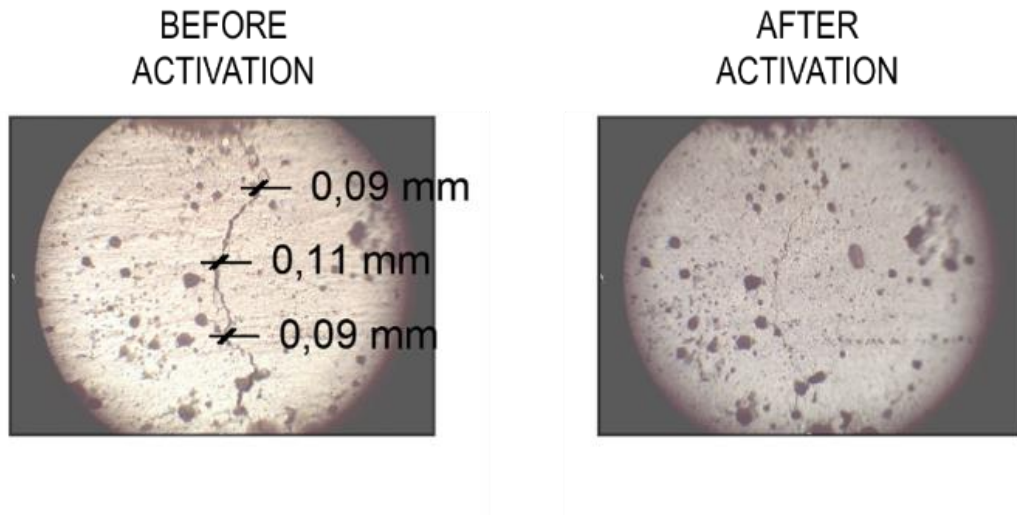


Figure 5. Crack aperture measurements before and after the hybrid tendons' activation

Figure 5 shows the comparison between the Force-CMOD graph of the beam with the former hybrid tendon and the one tested in this work. It can be observed how the slippage was reduced thanks to the introduction of new anchorage assembly. According to Balzano et al. 2020, in the previous version of the hybrid tendon a slippage of 0.43 mm was estimated. Its value is now reduced to 0.23mm, resulting also in an improvement of the load-carrying capacity at the ultimate state. The hybrid tendons showed enough pre-stress to close the serviceability level cracks in mortar specimen.

Conclusion

This work confirmed the efficiency of the hybrid tendons as crack-closure mechanism and as a reinforcement in the post-cracked phase. The new anchorages improved the overall response as flexural reinforcement by significantly reducing the slippage.

The study is however at its early stages and the design is in continuous changing in order to address and solve other issues associated to this technology (i.e. manufacturing, cost, activation system).

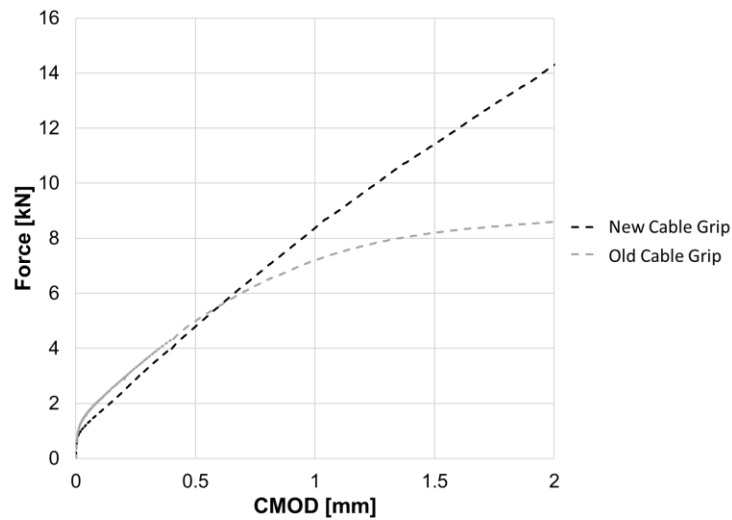


Figure 6. Comparison between the cracked beams Force-CMOD graph with the old and the new Cable Grip design

Acknowledgment

This work is supported by UKRI-EPSC (Grant No. EP/P02081X/1, Resilient Materials 4 Life, RM4L).

References

- [1] Gardner, D. et al. (2018). A survey on problems encountered in current concrete construction and the potential benefits of self-healing cementitious materials. *Case Studies in Construction Materials* 8, pp. 238-247.
- [2] Li, V. C. and Herbert, E. (2012) 'Robust Self-Healing Concrete for Sustainable Infrastructure', *Journal of Advanced Concrete Technology*, 10(6), pp. 207–218.
- [3] Jonkers, H. M. et al. (2010) 'Application of bacteria as self-healing agent for the development of sustainable concrete', *Ecological Engineering*, 36(2), pp. 230–235. doi: 10.1016/j.ecoleng.2008.12.036.
- [4] Souza, L. and Al-Tabbaa, A. (2018) 'Microfluidic fabrication of microcapsules tailored for self-healing in cementitious materials', *Construction and Building Materials*. The Authors, 184, pp. 713–722.
- [5] De Belie, N., Gruyaert, E., Al-Tabbaa, A., Antonaci, P., Baera, C., Bajare, D., Darquennes, A., Davies, R., Ferrara, L., Jefferson, T., Litina, C., Miljevic, B., Otlewska, A., Ranogajec, J., Roig-Flores, M., Paine, K., Lukowski, P., Serna, P., Tulliani, J.-M., Vucetic, S., Wang, J., Jonkers, H. M., *Adv. Mater. Interfaces* 2018, 5, 1800074.
- [6] Ferrara, L. et al. (2018) 'Experimental characterization of the self-healing capacity of cement-based materials and its effects on the material performance: A state of the art report by COST Action SARCOS WG2', *Construction and Building Materials*. Elsevier Ltd, 167, pp. 115–142.
- [7] Teall, O. et al. (2017) 'Development of high shrinkage polyethylene terephthalate (PET) shape memory polymer tendons for concrete crack closure', *Smart Materials and Structures*. IOP Publishing, 26(4).
- [8] Balzano, B., Sweeney, J., Thompson, G., Jefferson, A. Enhanced Concrete crack closure with Hybrid Shape Memory Polymer Tendons. Currently submitted at *Engineering Structures*, Elsevier.
- [9] Djaknoun, S., Ouedraogo, A., Benyahia, A. (2012). Characterisation of the behaviour of high-performance mortar subjected to high temperatures. *Construction and Building Materials* 28, pp.176-186.
- [10] Yazici, S., Sezer, G., Sengul, H. (2012). The effect of high temperature on the compressive strength of mortars. *Construction and Building Materials* 35, pp. 97-100.

Session 8B Advances and measurements in self-healing and self-immunising materials

Chair: Dr Iulia Mihai

1170 *Bras et al.* Self-healing bio-concrete – a sustainable solution for structures and infrastructures

1248 *Xie and Al-Tabbaa.* Self-immunity in cementitious materials for protection against corrosion

1245 *Zomorodian et al.* Efficiency of Inhibitors in corrosion protection of reinforcing steel in synthetic pore water

1137 *Frandsen et al.* Experimental investigation of water vapor diffusivity in bio-based building materials by a novel measurement method

Self-healing bio-concrete – a sustainable solution for structures and infrastructures

Ana Bras¹, Hazha Mohammed², Ismini Nakouti³

1: Built Environment and Sustainable Technologies (BEST) Research Institute, Liverpool John Moores University, Liverpool L3 2ET, UK

2: Built Environment and Sustainable Technologies (BEST) Research Institute, Liverpool John Moores University, Liverpool L3 2ET, UK

3: Centre for Natural Products Discovery (CNPD), School of Pharmacy and Biomolecular Sciences, Liverpool John Moores University, Liverpool L3 3AF, UK

Abstract

In the UK, hundreds of million pounds are spent per year on the maintenance and repair of concrete infrastructure. A significant number of Reinforced Concrete structures that were built for a working life of 50 years have exceeded serviceability limits or are close to limits due to steel reinforcement corrosion. There is a limited understanding of the self-healing concretes exposed to chlorides from seawater regarding their durability. This motivates a deep study on optimisation of the behaviour of reinforced concrete (RC) specially exposed to wet/tidal-splash environments. Current encapsulation of the healing agent affects the mechanical properties of RC and studies are lacking on the long-term durability. This enormous economic impact could be reduced, by better evaluation of the lifecycle of concrete structures and by using durable bio-concrete materials in design and retrofit phases. The paper shows short and long-term results of laboratory tests of self-healing concretes exposed to difference environments. An increased concrete service life will be achieved due to optimisation of bio-concrete self-healing behaviour tailored for specific durability contexts.

Introduction

RC corrosion costs the UK £23b per year and is one of the major durability challenges leading to rust formation, cracking, spalling, delamination and degradation of structures. Continuous inspection and maintenance is crucial to avoid reduction of the serviceability limits due to steel reinforcement corrosion. Considerable labour costs are incurred relating to repairs, on contrast, in nature, damage can usually be self-healed and structures durability enhanced. Such impacts occur globally, for instance India, where RC corrosion costs between 3-4%/year of the national gross domestic product (level growing and tends to increased construction levels and lack of regulation).

Existing concrete repairing techniques are highly expensive and time-consuming [1], whilst bio-consolidation provides a cutting-edge biotechnology applicable to consolidation, repair, protection and improvement of construction materials. Precipitation of calcite in cementitious materials (Microbially Induced Calcium-carbonate Precipitation (MICP)) is the most common method and acts as a biosealant. The hypothesis is that bacteria with calcium nutrient source can form a) calcium carbonate precipitations and b) biologically induce chemical precipitations in which an organism creates an optimal extracellular micro-environment of mineral phases [2]. The strength of the bacterial concrete in principle will be more than the normal concrete, but production of i) ammonium ions through the ureolytic pathway results in nitrogen oxide emission to the atmosphere ii) ammonium could lead to ammonium salts leading to possible reinforcement corrosion or conversion of ammonium to nitric acid, which could damage the concrete structure [3]. There is a limited understanding of the self-healing concretes exposed to chlorides from seawater regarding their durability. This motivates a deep study on

optimisation of the behaviour of reinforced concrete (RC) specially exposed to environmental exposures [4]. This knowledge can contribute to decrease the enormous economic impact, by better evaluation of the lifecycle of concrete structures and by using durable bio-concrete materials in design and retrofit phases. The paper shows short and long-term results of laboratory tests of self-healing concretes exposed to difference environments. An increased concrete service life will be achieved due to optimisation of bio-concrete self-healing behaviour tailored for specific durability contexts.

Materials and methods

Binders

This study used Ordinary Portland cement (CEM I) according to the specification set in BS EN 197-1, with a class of strength of 52.5N. Ground granulated blast furnish slag (GGBS) was also used to produce a CEMIII/A (CEMIII). It was sourced in UK from Hanson Cement Limited, according to the requirements of the British Standard BS EN 15167-1 for utilisation within mortar and concrete.

Aggregates

The sand used in this research is from the Tarmac factory, UK, and is according to the British Standard BS EN ISO 9001. The aggregate used in this research sourced in UK, 10mm and 20mm coarse aggregates were also used in the concrete, provided by Travis Perkins.

Concrete mix design

Four concrete compositions were prepared and casted – CEMI and CEMIII/A with and without bioproduct. For each concrete composition three cubes of size 150 x 150 x 150 mm and six cylinders with diameter of 100mm and a height of 200mm were prepared and casted. The amount of bacteria added in to each concrete batch was controlled in order to maintain the same concentration of cells using the techniques presented in [5-7] (Figure 1). Table 1 presents the mix design.

Table 1 - CEMI and CEMIII concrete mix design.

Concrete Composition	kg/m3	Concrete Composition	kg/m3
CEMI 52.5N	450	CEMIII/A	450
Agg. 20mm	712	Agg. 20mm	712
Agg. 10mm	610	Agg. 10mm	610
Sand	335	Sand	335
Water	202.5	Water	202.5
w/b	0.45	w/b	0.45
Bio-agent	0% and 2.1%	Bio-agent	0% and 2.1%

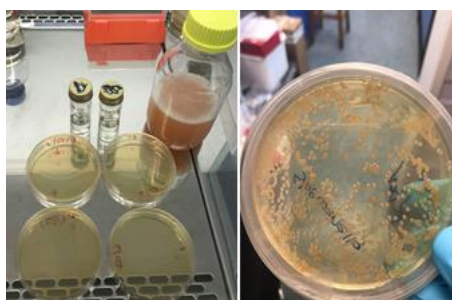


Figure 1 – Serial dilution of the bio-agent [5]

Results and discussion

Concrete Compressive strength

Three samples per composition with 150 mm size concrete cubes were loaded to failure according to EN 12390-4. The following figure (Figure 2) show the results obtained for concretes with cement type CEM I, CEMIII with and without bioproduct (BIO).

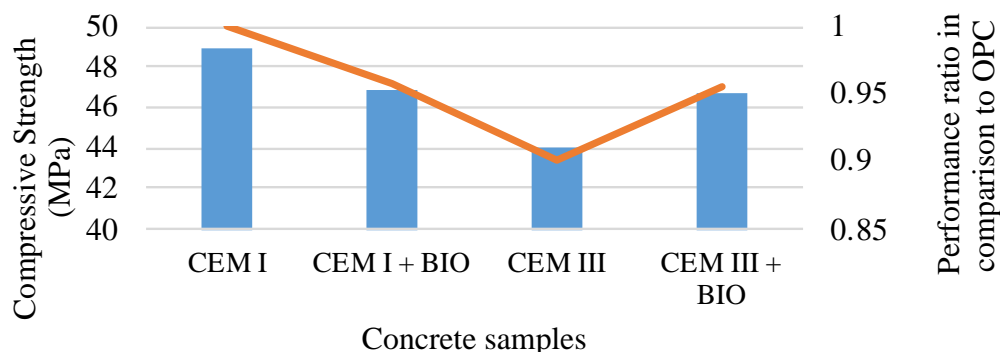


Figure 2 – Compressive strength of concretes tested at 28 days. The coefficient of variation varied between 2-6% for the tested samples

The previous figure shows that the self-healing behaviour in concrete type CEMIII+BIO enhances the compressive strength in comparison without the use of bioproduct. Bioproduct decreases by 5% the compressive strength of concrete made with CEMI. However, for CEMIII the increase is of 10%.

Capillary water absorption

Capillary tests were carried out according to EN 1015-18. Samples were placed in oven at 30°C for a period of 8 days until the mass change was less than 0.1%. This test was continued until the water absorption for each sample had stabilised. Weight of the samples were registered at 0', 5', 15', 30', 1h, 2h, 3h, 21h up to 28 days, until the water absorption reached to asymptotic value. The following figure presents the results of water absorption via capillary tests for concretes CEMI CEMIII with and without bioproduct (Figure 3a). Water absorption via capillary tends to reduce at least 25% if self-healing behaviour is introduced in a Concrete type CEMIII (CEMIII+BIO). The self-healing behaviour does not change the maximum water absorbed by the concrete CEMI. However, the there is a decrease in the water absorption velocity if self-healing is used in CEM I and CEMIII concretes.

Non-steady state chloride migration test

The performance of concrete was quantified in terms of durability, as regards corrosion of steel reinforcement, with and without the presence of self-healing behaviour. The chloride migration coefficient for each concrete composition was determined by the NT BUILD 492 method and is a measure of the resistance of the tested material to chloride penetration. Figure 3b presents the ratio evolution with time of the migration coefficient in comparison to the references (CEMI and CEMIII at 28 days). A decrease in the migration rate is associated with an increase of the RC service life. The previous results demonstrate that there is a reduction of the chloride migration coefficient if self-healing behaviour is introduced in the concrete. It is shown that the chloride migration coefficient can reduce 30% for CEMI with BIO and 50% for CEMIII with BIO, which substantially increase the RC service life. It is also clear that the bioproduct has a better short and long term performance if mixed in a concrete CEMII

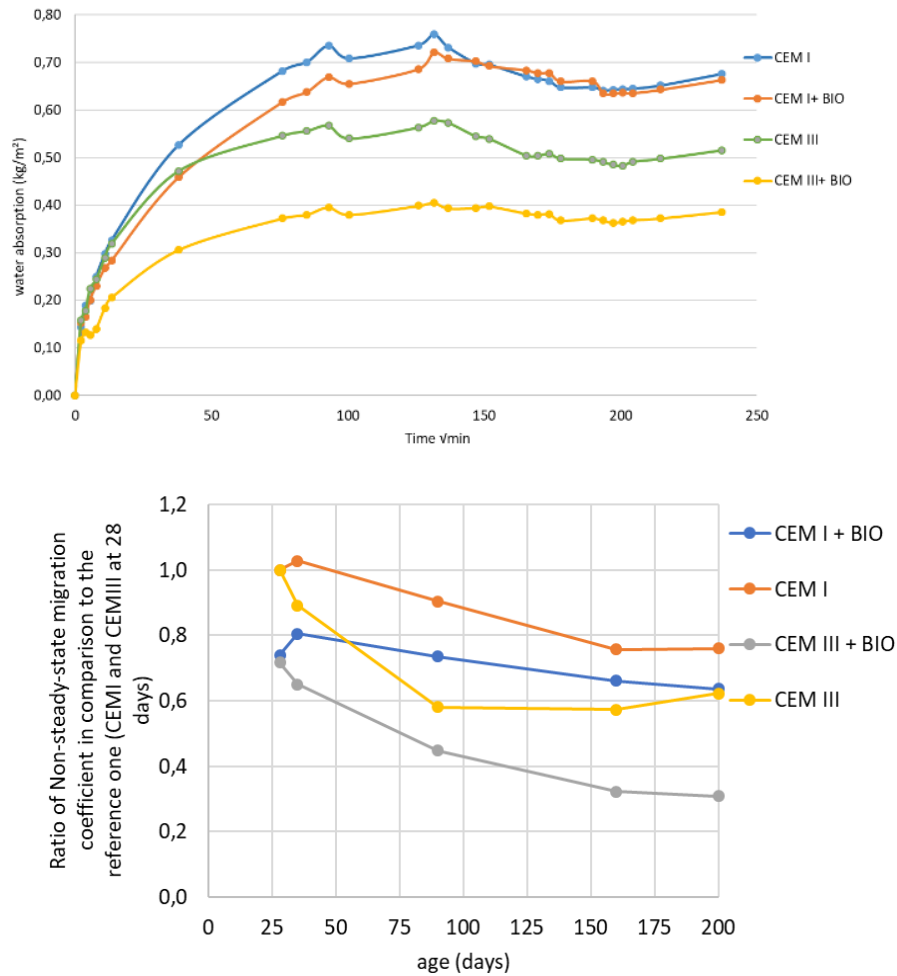


Figure 3 – (a) Water absorption via capillary for concretes tested at 28 days and for 2 weeks. (b) Ratio of non-steady-state migration coefficient in comparison to the references (CEM I and CEM III with and without bioproduct (CEM I+BIO and CEM III+BIO) at 28 days)

Conclusion

This paper presents some results on self-healing concrete with a focus on providing reinforcement against corrosion. The previous results demonstrate that water absorption via capillary tends to reduce at least 25% if self-healing behaviour is introduced in a Concrete type CEM III (CEM III+BIO). There is also a reduction of the chloride migration coefficient in concretes with self-healing behaviour. It is shown that the chloride migration coefficient can reduce 30% for CEM I with BIO and 50% for CEM III with BIO, which substantially increase the RC service life. It is also clear that the bioproduct has a better short and long term performance if mixed in a concrete CEM III.

Acknowledgment

The author of this paper would like to thank the research grant from Royal Society RGS\R1\191304 - Research Grants 2019 Round 1, the grant from the ICE R&D Enabling Fund and the grant 272002/ S0001/ 911BUE that enabled the development of this work.

References

[1] Vijay et al, Bacteria based self-healing concrete – A review, Constr and Building Materials, Vol 152, 2017, pp1008-1014

- [2] Khaliq et al, Crack healing in concrete using various bio influenced self-healing techniques, Constr and Building Materials
Vol 102, 2016, pp 349-357
- [3] De Muynck et al, Microbial carbonate precipitation in construction materials: A review, Ecological Engineering, Vol36, Issue 2, 2010, pp 118-136
- [4] Brás A, Faustino P. (2018) Impact of Repairs on Embodied Carbon Dioxide Expenditure for a Reinforced Concrete Quay, Proceedings of ICE - Engineering Sustainability, Volume 172 Issue 2, 2019, pp. 87-97
- [5] Bras, A.; van der Bergh, J.M.; Mohammed, H.; Nakouti, I. Design Service Life of RC Structures with Self-Healing Behaviour to Increase Infrastructure Carbon Savings. Materials 2021, 14, 3154. <https://doi.org/10.3390/ma14123154>
- [6] Mohammed H, Ortoneda-Pedrola M, Nakouti I, Bras A, Experimental characterisation of non-encapsulated bio-based concrete with self-healing capacity, Construction and Building Materials, Volume 256, 2020, <https://doi.org/10.1016/j.conbuildmat.2020.119411>
- [7] van der Bergh, J.M.; Miljević, B.; Vučetić, S.; Šovljanski, O.; Markov, S.; Riley, M.; Ranogajec, J.; Bras, A. Comparison of Microbially Induced Healing Solutions for Crack Repairs of Cement-Based Infrastructure. Sustainability 2021, 13, 4287. <https://doi.org/10.3390/su13084287>

Self-Immunity in cementitious materials for protection against corrosion

Zijun Xie, Abir Al-Tabbaa

Department of Civil Engineering, University of Cambridge, Cambridge CB2 1PZ, UK

Abstract

Deterioration of steel reinforcement in cement-based structures induced by corrosion has been reported as a major durability problem worldwide, which can directly affect infrastructures in terms of safety, economy, and sustainability. The addition of corrosion inhibitors is a promising technique to solve this problem because it is relatively effective, economical and easy to handle. However, most of the corrosion inhibitors can be harmful to the environment and with limited functionality. Our work proposes an alternative approach for corrosion inhibition, using layered double hydroxides (LDHs) to capture chloride ions and protect the surrounding concrete. As part of this research work a novel modified hydrotalcite was synthesized by intentionally intercalating a particular inhibitor anion to replace the carbonate. This modified hydrotalcite has the ability to prevent both the chloride-induced corrosion and shows great potential for carbonation-induced corrosion, by releasing inhibitor anions and capturing chloride or carbonate ions. A Multi Reference Electrode (MuRE) sensing system based on a series of linear-Ni-made-electrodes to measure the local potential of steel reinforcement was used to monitor the corrosion process and define the efficiency of the proposed inhibitor. The corrosion potential profile was obtained, and localisation of the corrosion initiation was made possible. The initial results indicated that the calcined hydrotalcite had five times the chloride capture capacity (0.1g/g) than uncalcined hydrotalcite (0.02g/g). The results of this research confirmed the feasibility of using LDHs as a concrete corrosion inhibitor in cementitious mixes.

Introduction

Concrete is the most widely used construction material all around the world. Corrosion of the reinforcing steel is a major threat in durability and serviceability of concrete infrastructures. Expansive corrosion products propagate in the concrete cover and subsequently leads to cracking and spalling of concrete in the cross-sectional area, which in turn causes the insufficient tensile capacity and leads to the damage and even collapses of structures [1]. Over the last two decades, more research projects focused on the development of new or modified materials in order to prevent corrosion initiation or hinder corrosion propagation, as well as to understand their underlying working mechanism.

It is believed that hydrotalcite has the potential to prevent corrosion by binding chloride into concrete. It occurs both naturally and synthetically with the general chemical formula of $[\text{Mg}_6\text{Al}_2(\text{OH})_{16}]\text{CO}_3 \cdot 4\text{H}_2\text{O}$, and the molar ratio of $\text{Al}^{3+}/(\text{Mg}^{2+}+\text{Al}^{3+})$ can be modified based on application and demand [3]. Hydrotalcite exhibits a layered crystal structure, which comprises positively charged hydroxide layers and carbonate anions located in the interlayer region together with water molecules. The anions can be exchanged with a wide range of inorganic and organic anions such as chloride ions in the surrounding solution [10]. Thus, hydrotalcite can prevent corrosion by absorbing and binding chloride ions in its interlayer space. However, the naturally occurring hydrotalcite has relatively low anion exchange capacity because the affinity of carbonate anion is higher than chloride ions. Therefore, hydrotalcite is normally calcined within a certain temperature range to remove the carbonate anions in the crystal

structure and increase its anion exchange capacity [5]. Calcination above 500°C generally causes the decomposition of the hydrotalcite and the formation of a mixed layer of magnesium-aluminium oxide. This mixed metal oxide can absorb anions from aqueous solution and gradually reconstruct the original structure of hydrotalcite. This phenomenon is called the structural memory effect and indicates the reutilization of the regenerated hydrotalcite as an anion sorbent [7].

The goal of this study is to evaluate the role of calcined hydrotalcite in capturing chloride ions as promising green corrosion inhibitor and to find the maximum capturing capacity of chloride ion over time. The results of the project will significantly reduce the costs of infrastructure maintenance and improve the safety and sustainability of future construction.

Materials and methods

The synthetic hydrotalcite used in this work with molecular formula $[\text{Mg}_6\text{Al}_2(\text{OH})_{16}]\text{CO}_3 \cdot 4\text{H}_2\text{O}$ was obtained from Sigma-Aldrich (UK). The molecular weight is equal to 603.98g/mol. Its relative density is 2.0g/ml at 25 °C and the product is insoluble in water. According to Ke et al. (2016), calcined hydrotalcite was produced by thermally treating hydrotalcite at 500 °C for 3 hours, and then cooling down to room temperature. After that, it was stored in a sealed container until testing to prevent any contamination especially from water and CO_2 . This procedure was followed here in the preparation of calcined hydrotalcite. The solid samples of hydrotalcite and calcined hydrotalcite were characterized by X-ray diffraction using a Siemens D500 diffractometer with $\text{Cu-K}\alpha$ radiation (40kV and 40mA). The scanning regions were between 5° and 70° of 2θ values, at a rate of 0.5s/step.

The absorption capacities of hydrotalcite and calcined hydrotalcite were obtained in two steps. The first step was to determine the optimum duration of hydrotalcite ion exchange capacity. For this purpose, 2g powder of hydrotalcite and 2g powder of calcined hydrotalcite were mixed with a 50mL NaCl solution respectively. To simulate the average salinity in seawater, 1.75g NaCl powder was dissolved in 50mL deionised water to achieve a 3.5% NaCl solution by mass. The suspension was then sealed and put on a shaker at 20°C. The shaking durations were 2, 4, 6, 8, 14, 16, 18, 20, 22, 24, and 48 hours in order to obtain an optimum duration of exchange capacity. For each time slot, three specimens were prepared.

For the second step, to evaluate the maximum chloride binding capacity of calcined hydrotalcite, a constant mass of calcined hydrotalcite (2g) was added to 50mL NaCl solution with a range of different concentrations of chloride solutions, and the same reaction duration was maintained. The optimum reaction duration to allow the uptake of chloride to reach equilibrium was defined from step 1. For each concentration of chloride solution, three samples were prepared. In both steps, the mixtures were then all decanted using filter paper and the concentration of free chloride ions in the filtrate solution was measured by a chloride selective electrode. Thus, the chloride captured by calcined hydrotalcite was determined by the following Equation1 [5].

$$q_e = \frac{(C_0 - C_e)V}{m} \quad [1]$$

where q_e is the absorption loading of calcined hydrotalcite at equilibrium (mg/g), V is the volume of solution (L), C_0 and C_e are the initial and equilibrium concentrations of chloride ions (mg/L) respectively, and m is the mass of adsorbent (g).

Results and discussion

Figure 1 shows the X-ray diffraction patterns of hydrotalcite and the corresponding calcined hydrotalcite samples heated at 500 °C for 3 hours. The hydrotalcite sample showed a typical

hydrotalcite-type pattern: sharp and intense lines at low 2θ values of $11.5^\circ(003)$, $21.5^\circ(006)$ and $34.5^\circ(009)$ and less intense lines at higher angular values [8]. The calcined hydrotalcite sample presented diffraction peaks, which were characteristic to a mix of magnesium and aluminium oxide.

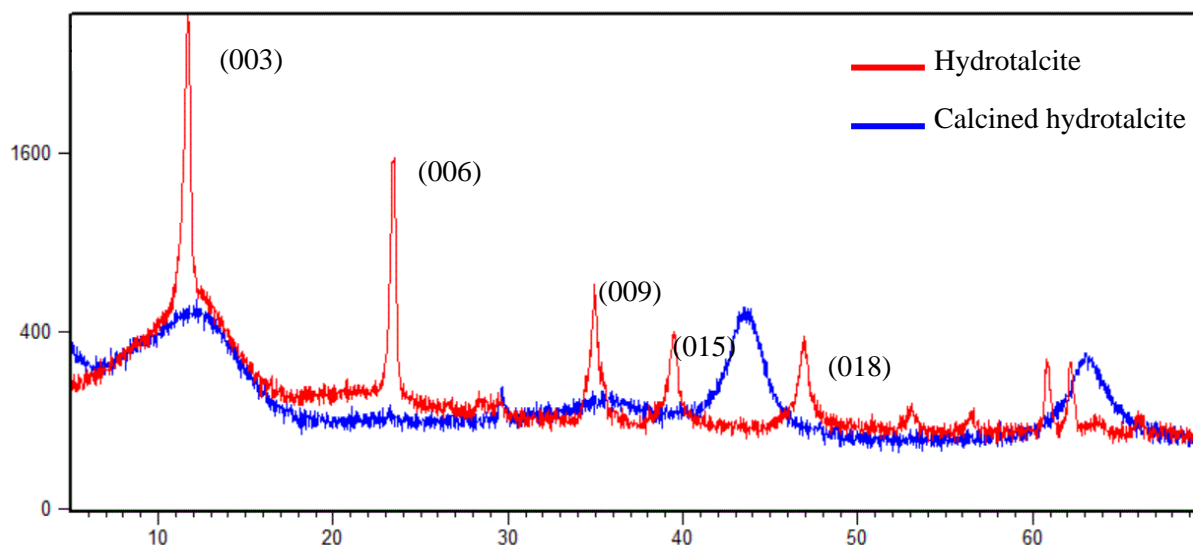


Figure 1: XRD pattern of hydrotalcite and calcined hydrotalcite

The chloride binding capacity of hydrotalcite and calcined hydrotalcite over time are shown in Figure 2. It can be seen that there was a rapid absorption of chloride ions during the first 8 hours for both materials, and then it slowed down and reached a plateau from 24 hours onwards. It was likely because the ion exchange of hydrotalcite tends to start on the edges or in the external part of the lamellar structure, where the ions are readily available to be exchanged [9]. The subsequent reduction in growth was probably due to the restricted internal ion exchange which strongly depends on the diffusion of the anions. Consequently, the 24-hour reaction duration was selected as the appropriate duration needed for assessing the maximum chloride binding capacity of calcined hydrotalcite.

The main difference between hydrotalcite and calcined hydrotalcite was in the extent of chloride binding. After 8 hours, the chloride binding capacities of hydrotalcite and calcined hydrotalcite were 14mg/g and 67mg/g respectively and after 24 hours they were 20 mg/g and 105 mg/g respectively. Calcined hydrotalcite showed much higher chloride binding efficiency, which was nearly 5 times more than that of hydrotalcite. This large difference had been expected because of the different mechanisms of chloride absorption between hydrotalcite and calcined hydrotalcite. The reason was that during calcination, the interlayer water of hydrotalcite was released, which was followed by the decomposition of the interlayer carbonate to magnesium-aluminium oxide solid. When a chloride-containing solution was added to hydrotalcite, chloride ions would diffuse into the interlayer regions to replace the carbonates. However, according to hydrotalcite relative preference of anions, hydrotalcite shows greater affinity for carbonates compared to chloride ions [6]. In contrast, in the calcined hydrotalcite, chloride ions can be directly absorbed because no layered structure would occur. To determine the optimum conditions for the maximum chloride binding capacity of calcined hydrotalcite, the Langmuir adsorption model as shown in Equation 2 was used to fit the experimental data [11]. As shown in Figure 3, the Langmuir isotherm fits well with the chloride absorption data of calcined hydrotalcite, and the correlation coefficient (R^2) is equal to 0.97.

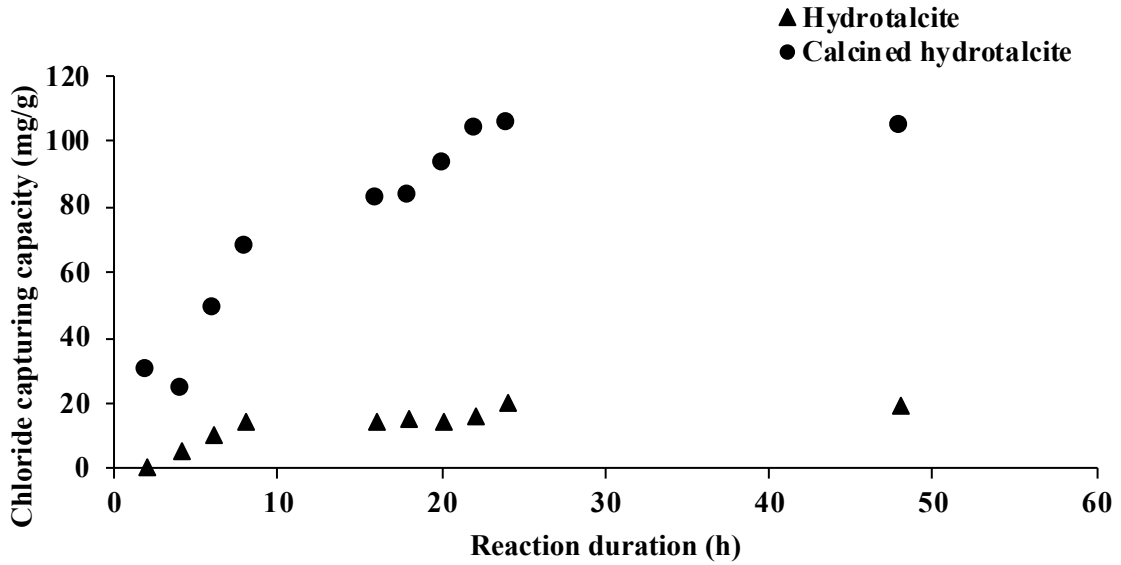


Figure 2: Average chloride binding capacity of hydrotalcite (triangle) and calcined hydrotalcite (dot) as a function of contact time

The maximum chloride binding capacity was equal to 155 mg/g, while the initial and equilibrium chloride concentrations were equal to 800 mg/L and 180 mg/L in the NaCl solution respectively. The evaluated maximum chloride binding capacity of calcined hydrotalcite in the NaCl solution is close to the stoichiometric value (168 mg/g) [5].

$$q_e = \frac{QbC_e}{1+bC_e} \tag{2}$$

where, Q and b are the Langmuir constants, C_e is the equilibrium chloride concentration in the solution (mg/L), q_e is the absorption loading of calcined hydrotalcite at equilibrium (mg/g).

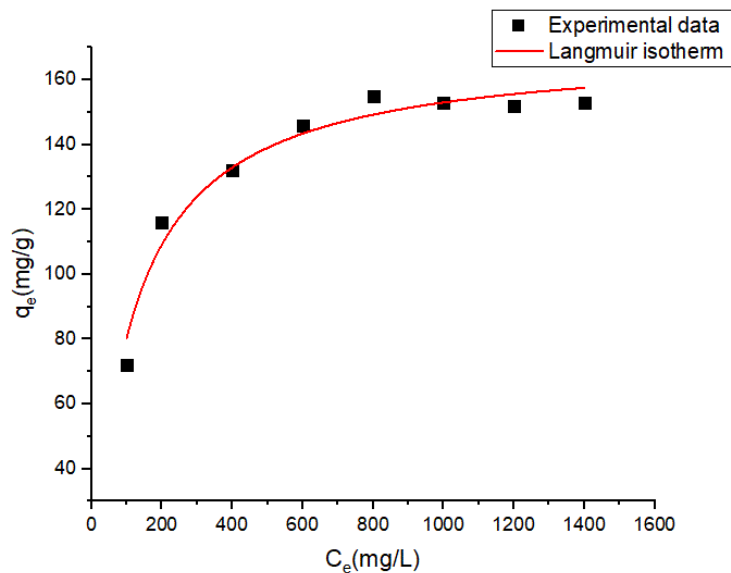


Figure 3: Equilibrium isotherms of the chloride removal by calcined hydrotalcite at room temperature: experimental data (dots) are fitted to the Langmuir model (curve)

Conclusion

The following conclusions from this research can be drawn

- Calcined hydrotalcite can capture considerable quantities of chloride ions while the hydrotalcite could only capture limited chloride ions.
- The optimum reaction duration to obtain the maximum amount of chloride ions captured in calcined hydrotalcite is 24 hours. In addition, the maximum chloride binding capacity of calcined hydrotalcite is determined to be 155 mg/g, close to the stoichiometric value (168 mg/g).

Therefore, the results demonstrate the high chloride ion removal efficiency of calcined hydrotalcite, and consequently confirm the potential applicability of calcined hydrotalcite for reinforced concrete corrosion inhibitors.

References

- [1] Bertolini L., Elsener B., Pedersen, P., Redaelli, E. and B. Polder, R. Corrosion of steel in concrete: Prevention, Diagnosis, Repair. 2nd ed. Weinheim, Germany: Wiley-VCH. 2013 p.71.
- [2] Granados Correa, F. and Serrano Gómez, J. Kinetic and thermodynamic parameters of 99Mo sorption on thermally treated hydrotalcite. *Journal of Radioanalytical and Nuclear Chemistry*, 268(1). 2006. pp.95-101.
- [3] Kayali, O., Khan, M. and Sharfuddin Ahmed, M. The role of hydrotalcite in chloride binding and corrosion protection in concretes with ground granulated blast furnace slag. *Cement and Concrete Composites*, 34(8). 2012. pp.936-945.
- [4] Ke, X., Bernal, S.A., Provis, J.L. Controlling the reaction kinetics of sodium carbonate-activated slag cements using calcined layered double hydroxides. *Cem. Concr. Res.* 81. 2016. pp. 24–37.
- [5] Lv, L., He, J., Wei, M., Evans, D.G., Duan, X. Uptake of chloride ion from aqueous solution by calcined layered double hydroxides: Equilibrium and kinetic studies. *Water Res.* 40. 2006. pp.735–743.
- [6] Parker, L.M., Milestone, N.B., Newman, R.H. The Use of Hydrotalcite as an Anion Absorbent. *Ind. Eng. Chem. Res.* 34. 1995. PP. 1196–1202.
- [7] Stanimirova, T.S., Kirov, G., Dinolova, E. Mechanism of hydrotalcite regeneration. *J. Mater. Sci. Lett.* 20. 2001. pp. 453–455.
- [8] Wang, Z., Lu, P., Zhang, X., Wang, L., Li, Q. and Zhang, Z. NO_x storage and soot combustion over well-dispersed mesoporous mixed oxides via hydrotalcite-like precursors. *RSC Advances*, 5(65). 2015. pp.52743-52753.
- [9] Yang, Z., Fischer, H., Polder, R. Laboratory investigation of the influence of two types of modified hydrotalcites on chloride ingress into cement mortar. *Cem. Concr. Compos.* 58. 2015. pp. 105–113.
- [10] Yang, Z., Polder, R.B., Mol, J.M.C. Modified hydrotalcites as chloride scavengers and inhibitor release agents for improved corrosion protection of reinforced concrete. *Heron* 62. 2017.
- [11] Yoon, S., Moon, J., Bae, S., Duan, X., Giannelis, E.P., Monteiro, P.M. Chloride adsorption by calcined layered double hydroxides in hardened Portland cement paste. *Mater. Chem. Phys.* 145. 2014. pp. 376–386.

Efficiency of Inhibitors in corrosion protection of reinforcing steel in synthetic pore water

Amir Zomoridan, Regeane Bagonyi, Abir Al-Tabbaa

Department of Engineering, University of Cambridge, Cambridge CB2 1PZ, UK

Abstract

Steel is highly susceptible to corrosion when exposed to the chloride ions. Corrosion increases potential of failure in reinforced concrete structures especially in marine environments. Various inhibitors have been used to prolong the lifetime of the reinforcing steel. However, there is insufficient information about the effect of these inhibitors in synthetic pore water and carbonated solution in the presence of chloride ions.

The aim of this work is to evaluate the efficiency of the inhibitors such as calcium nitride, potassium nitride, casein, and amino acid (11-aminoundecanoic acid, and p-aminobenzoic acid) in corrosion protection of reinforcing steel. Reinforcing steel was exposed to synthetic pore water with combined different concentration of chloride ions and carbonated solution. The performance of each inhibitor in different solutions and the chloride threshold for initiation of corrosion process were investigated using electrochemical techniques. The corrosion current density was obtained with the use of linear polarization test. Electrochemical Impedance Spectroscopy (EIS) and open circuit potential were recorded for each test to evaluate the passivation mechanism of inhibitors. Results indicate that corrosion protection of reinforcing steel depends on the inhibitor and concentration of chloride ions in the solution.

Introduction

The corrosion of reinforcing steel is one of the major causes of failures of reinforced concrete and has a detrimental effect on the national economy. Improvement in corrosion protection enhances the durability and service life of the concrete structure [1]. Concrete provides physical and chemical protection to the embedded steel. This physical barrier retards the ingress of aggressive ions such as chloride, carbon dioxide, sulphate, oxygen and moisture and its high alkalinity provides chemical protection by forming stable iron oxide on the surface of the reinforcement [2]. This protective oxide layer, the passive layer, however, may undergo destruction from carbonation or from the penetration of high amounts of chloride ions to the reinforcing steel [3]. The subsequent formation of expansive corrosion products on the surface of the reinforcement causes cracking and spalling of the concrete, which in turn introduces easier paths for the aggressive ions to reach the reinforcement. The breakdown of the passive layer in reinforced concrete is associated with the concentration of the chloride ions in the vicinity of the rebar surface. The minimum amount of chloride concentration which initiates breakdown of the passive layer is known as the chloride threshold value. This value is influenced by various factors such as the chemical composition of the pore solution, alkalinity, used admixtures and the type of inhibitor [4].

Application of inhibitors is a cost-effective method in comparison to other techniques such as cathodic protection or chloride extraction and increases the chloride threshold value [5,6]. Various types of inhibitors have been proposed; their mechanism of corrosion protection varies depending on the nature of the inhibitors. Organic inhibitors, due to the high vapour pressure, can penetrate through the concrete and stop any corrosion activity on the surface of reinforcement [7]. On the other hand, inorganic inhibitors, such as nitrate, act as oxidizing

anions and passivate the steel in the absence of oxygen [8]. There is, however, no agreement on the protective efficiency of inhibitor types in a concentrated chloride solution.

The aim of this research, therefore, is to evaluate the efficiency of different types of organic and inorganic corrosion inhibitors at different $[Cl^-]/[OH^-]$ molar ratios in pore media.

Materials and methods

Commercial reinforcing steel was obtained from a local supplier and sectioned into plates with a diameter and thickness of 10 mm and 3 mm respectively. The chemical composition of the rebar is depicted in table 1. All electrochemical tests were performed in pore solution with the following chemical composition: 0.1 M NaOH + 0.3 M KOH + saturated $Ca(OH)_2$. This solution is similar to the pore solution extracted from cement paste samples with $w/c=0.42$ which were wet cured for 7 days [9]. All electrochemical tests were performed in a 200ml corrosion cell using a potentiostat PGSTAT 204 AUTOLAB. A three-electrode electrochemical cell consisting of a platinum plate as a counter electrode, an Ag/AgCl reference electrode and a rebar with a surface of 1 cm^2 as the working electrode. Four inhibitors including sodium nitrate (0.05 M), 11-aminoundecanoic acid (0.05 M), p-aminobenzoic acid (0.05 M) and casein (2 g/l) were used in pore solution with various chloride concentrations. Electrochemical tests were performed to investigate the efficiency of inhibitors and corrosion protection of the rebar in pore solution with open circuit potential (OCP) and potentiodynamic polarisation test.

Table 1: Chemical composition of the reinforcing steel

Chemical composition	C	Mn	Si	S	Cr	Ni	Cu	Fe
Reinforcing steel	0.19	0.82	0.13	0.02	0.1	0.14	0.57	Balance

Results and discussion

The OCP of the reinforcing steel was measured for 24 hours while immersed in the synthetic pore solution. The initial value of the OCP in the non-chloride solution was about -0.55 mV and it gradually shifted to a more positive potential (Figure 1). The increase in potential is related to the formation of the passive oxide film on the reinforcing steel. The protective hydroxide $Fe(OH)_2$ or stable iron oxide, according to the thermodynamic diagram of Pourbaix, is formed in the alkaline synthetic pore solution [10]. The increase of OCP over time is a result of the formation/growth of the protective oxide layer on the reinforcing steel. However, the growth rate of the protective layer is limited and the OCP reaches a plateau after 20 hours of immersion. The final OCP value after the formation of the protective layer is about -0.25 mV. The addition of chloride to the synthetic pore solution has a detrimental effect on the OCP and shifts it to the cathodic potential as the chloride concentration increases. It can clearly be seen that there is no breakdown in OCP until the Cl/OH ratio reaches 2.

At the critical concentration, when the ratio of Cl /OH reached 2, a significant breakdown in potential is observed which clearly indicates that corrosion has been initiated in the reinforcing steel. The corrosion potential in this solution reaches the value of -0.48 mV and shows small fluctuations within a range of 0.03 mV of this potential.

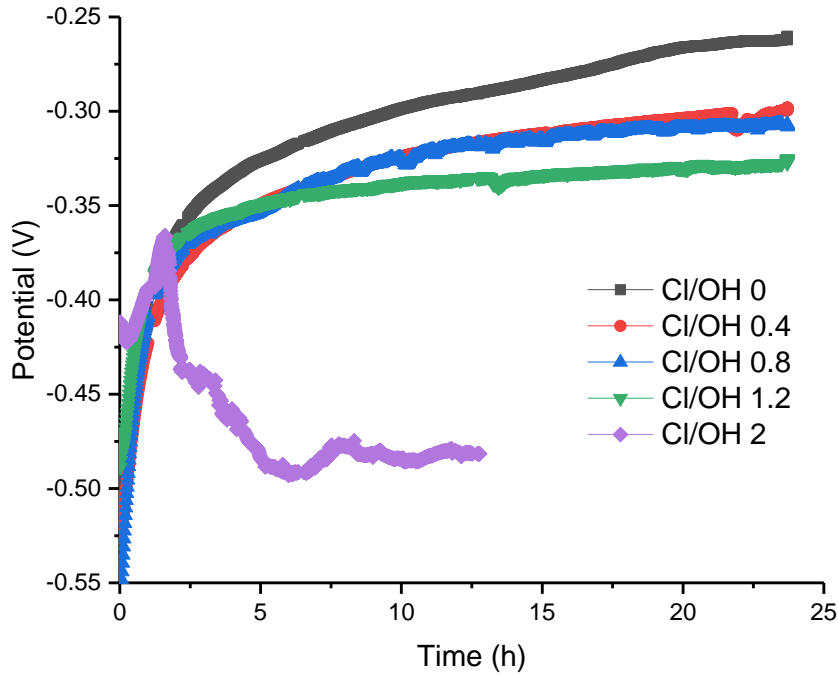


Figure 1: OCP measurement of rebar in synthetic pore solution at different ratio of Cl/OH
 The addition of inhibitors to the pore solution containing the critical concentration of chloride ions strongly influences the OCP values. The variation of OCP in the presence of inhibitors is depicted in Figure 2

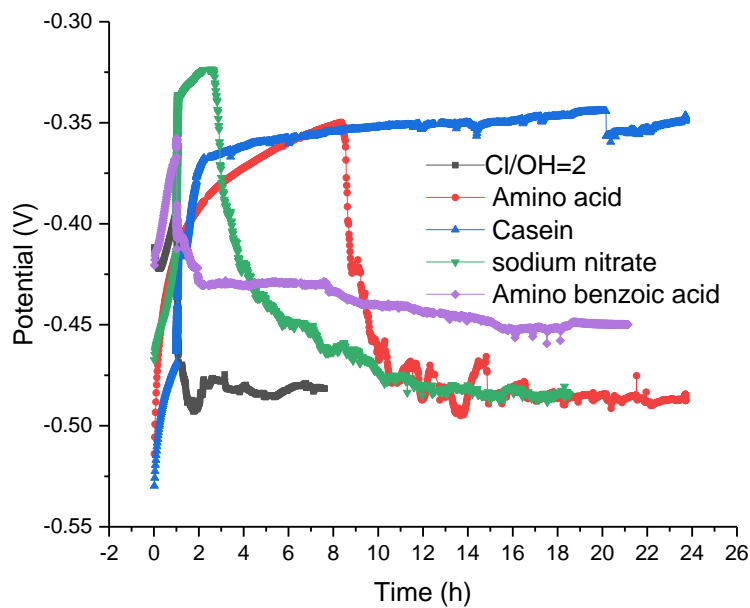


Figure 2: OCP measurement of rebar in synthetic pore solution with different inhibitors at critical concertation of Cl/OH ratios

Research indicated that active corrosion of rebar embedded in cement is identified with an OCP value lower than -0.273 mV. However, it is known that several parameters influence the OCP such as availability of oxygen, concrete porosity and presence of inhibitors. Here, sodium nitrate as an inhibitor in the critical concentration of chloride in the pore solution is found to shift (-0.48mV) the potential of the reinforcing steel to a more positive value. However, the

increase of OCP was limited to the first few hours and a subsequent breakdown in OCP was observed with a potential shifting to the cathodic values close to the corroding rebar (-0.48mV). The application of amino acid as the second inhibitor promoted a limited shift to a positive potential for only 8 h; it then exhibited a breakdown towards the corroding potential. Similarly, when aminobenzoic acid is used as an inhibitor, the OCP breaks down, but nonetheless after this collapse the recorded OCP potential was -0.42 mV which is still higher than the corroding potential of the rebar (-0.48 mV). Although this potential is more anodic (more positive) than the corroding potential, there is a high risk of corrosion initiation over a longer immersion time. Casein, the green inhibitor, shifted the OCP of the corroding rebar to the noble values and no significant decrease or breakdown in OCP was observed during immersion in pore solution. In addition, the formation of the passive layer in the presence of casein is promoted as casein is absorbed into the surface and a stable complex of iron oxide/casein is formed. The OCP value of the passivated rebar in presence of casein is about -0.32 mV which is 0.280 mV higher than the corroding OCP potential.

To corroborate the OCP results with another electrochemical technique, potentiodynamic studies were performed in pore solutions with and without inhibitor at a Cl/OH ratio of 2. All the tests were performed after 24h of immersion in the pore solution and results are shown in Figure 3.

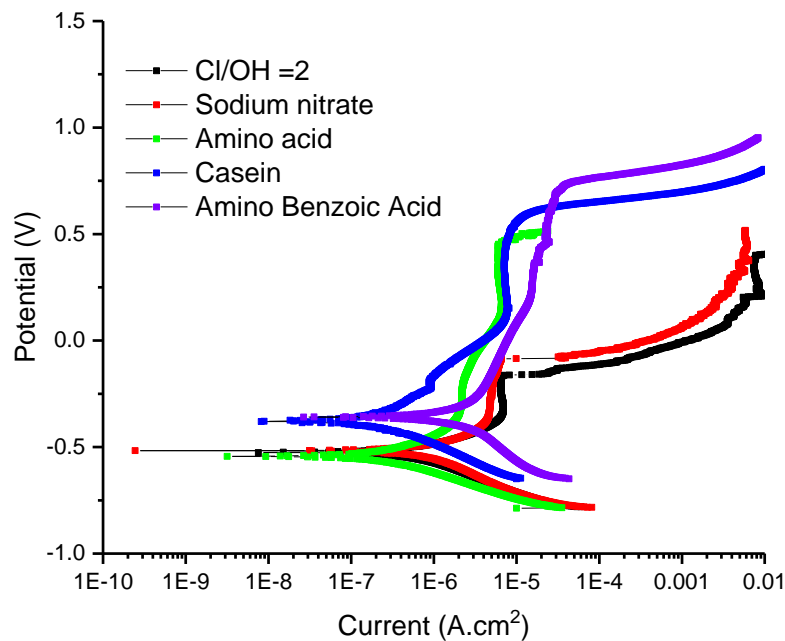


Figure 3: Potentiodynamic polarisation of rebar in pore solution contains different inhibitors

The potentiodynamic results represent the corrosion potential, passivity of reinforcing steel and breakdown potential of the passive film with and without inhibitors. The potentiodynamic polarisation of the rebar without inhibitors shows the formation of a passive layer within the potential range of -0.350 mV to -0.240 mV (Figure 3). The formation of this passive layer even in the high chloride concentrated solution is the consequence of exposing the rebar in the high alkaline pore solution. However, the attack of chloride ions destroys the passive layer at $E_{pit} = -0.240\text{mV}$ which this potential is known as the pitting potential. The current density of this passive layer during the anodic scan is higher than the rebar with inhibitors indicating the higher corrosion rate of rebar. The difference of the current density in the solution with and without sodium nitrate is not significant but this shift is still detectable. Amino acid significantly decreases the anodic current density, but the cathodic current and corrosion potential remain

unchanged. The mechanism of amino acid inhibition is based on blocking the anodic reactions and subsequently lower the current density during anodic scan. Amino acid provides the stable passive layer with the constant current density. This passive layer, however, breaks down at $E_{\text{pit}} = 0.460$ mV which is significantly higher than the pitting potential of sodium nitrate ($E_{\text{pit}} = -0.240$ mV) meaning a much higher resistance to the chloride attack compared to the sodium nitrate inhibitor. Aminobenzoic acid changes the corroding potential (-0.51 mV) to the more noble value (-0.41 mV) but the corrosion current density was higher than the samples without inhibitors and even in an anodic scan higher current density can be seen in comparison to the other inhibitors. The main advantage of the aminobenzoic acid is that this inhibitor shows a breaking potential at $E_{\text{pit}} = 0.640$ mV. Although the pitting potential is high, the passive layer with constant current density was not formed during the anodic scan which may link to the weak absorption of inhibitor in the surface. The casein provided a passive film in the broad potential range during the anodic scan. In addition, corrosion potential shifted to the positive potential and a passive film with the constant current density was observed.

Conclusion

The corrosion behaviour of rebar in various concentrations of chloride solution with and without inhibitors was studied and the following conclusions are drawn.

- The open circuit potential (OCP) of reinforcing steel in the solution without inhibitors shows a clear relation between chloride concentration, OCP value and the corrosion potential of the reinforcement. Increasing chloride concentration shifts OCP potential to the more cathodic value. The first radical change in OCP due to the increase of chloride concentration demonstrates the chloride threshold value and subsequent corrosion initiation. However, the OCP value for pore solution containing inhibitors may not link to the corrosion potential or the corrosive state of concrete. Inhibitors in the synthetic pore solution may polarise the potential of the rebar and subsequently the identification of corrosion based on only OCP value may not be a safe evaluation.
- Different types of inhibitors were evaluated in this research and it was found that casein as a green inhibitor can sufficiently protect the reinforcing steel in the solution with chloride threshold concentration. The aminobenzoic acid, casein, amino acid, and sodium nitrate provide higher breaking potential than the reference sample. The passive layer, however, in case of aminobenzoic acid was not characterised with constant current density which may be caused by insufficient surface adhesion of this inhibitor.

Acknowledgment

Authors acknowledge Engineering and Physical Science Research Council (EPSRC) for funding Resilient Materials 4 Life (RM4L) under EP/P02081X/1 project.

References

1. Sohail, M. G. *et al.* Electrochemical behavior of mild and corrosion resistant concrete reinforcing steels. *Constr. Build. Mater.* (2020). doi:10.1016/j.conbuildmat.2019.117205
2. Das, J. K. & Pradhan, B. Effect of cation type of chloride salts on corrosion behaviour of steel in concrete powder electrolyte solution in the presence of corrosion inhibitors. *Construction and Building Materials* 208, 175–191 (2019).
3. James, A. *et al.* Rebar corrosion detection, protection, and rehabilitation of reinforced concrete structures in coastal environments: A review. *Constr. Build. Mater.* 224, 1026–1039 (2019).
4. Cao, Y. *et al.* Critical chloride content in reinforced concrete — An updated review considering Chinese experience. *Cement and Concrete Research* (2019). doi:10.1016/j.cemconres.2018.11.020
5. Wilson, K., Jawed, M. & Ngala, V. The selection and use of cathodic protection systems for the repair of

- reinforced concrete structures. *Constr. Build. Mater.* 39, 19–25 (2013).
6. Andrade, C., Alonso, C., Acha, M. & Malric, B. Preliminary testing of Na₂PO₃F as a curative corrosion inhibitor for steel reinforcements in concrete. *Cem. Concr. Res.* 22, 869–881 (1992).
 7. Gartner, N., Kosec, T. & Legat, A. The efficiency of a corrosion inhibitor on steel in a simulated concrete environment. *Mater. Chem. Phys.* (2016). doi:10.1016/j.matchemphys.2016.08.047
 8. Paridah, M. . *et al.* We are IntechOpen , the world ' s leading publisher of Open Access books Built by scientists , for scientists TOP 1 % . *Intech i*, 13 (2016).
 9. Poursaei, A. Corrosion of steel bars in saturated Ca(OH)₂ and concrete pore solution. *Concr. Res. Lett.* 1, 90–97 (2010).
 10. Beverskog, B. & Puigdomenech, I. Revised Pourbaix diagrams for iron at 25-300°C. *Corros. Sci.* (1996). doi:10.1016/S0010-938X(96)00067-4

Experimental investigation of water vapor diffusivity in bio-based building materials by a novel measurement method

Kirstine Meyer Frandsen, Yovko Ivanov Antonov, Hicham Johra, Per Møldrup, Rasmus Lund Jensen

Department of the Built Environment, Aalborg University, Aalborg, DK

Abstract

At present, the building industry accounts for 30 – 50% of raw material consumption in Europe. The exhaustion of natural resources and increased demand for housing with the rising world population underlines a growing need for sustainable building materials. Bio-based materials show significant potential in being renewable materials with low or negative embodied energy. Furthermore, they show high interaction with surrounding water vapor when compared to conventional building materials, demonstrating their potential for application in passive design strategies. However, the implementation of these bio-based materials requires an understanding of the hygrothermal processes that occur in the porous media. Water vapor diffusivity is needed when analyzing moisture transport as one of the primary mechanisms in the presence of water vapor gradients.

This study involves the experimental determination of the vapor diffusivity using a novel measurement method, commonly applied in soil physics research. It works by applying oxygen as a non-reactive tracer gas to determine the gas diffusion coefficient, to which the water vapor diffusivity is related. The new method solves the potential problem of simultaneous water vapor diffusion and sorption and is more time-efficient than the standard Dry Cup/Wet Cup methods. Relative diffusivities are determined and compared for bio-based and mineral materials. The active porosity is measured on the same samples using a pycnometer, which allows for the determination of pore network tortuosity and other characteristics in the material at different moisture contents. The found hygrothermal properties are subsequently used in our companion paper for improved accuracy of building simulations.

Introduction

At present, the building industry accounts for 30 – 50% of raw material consumption in Europe. The exhaustion of natural resources and increased demand for housing with the rising world population underlines a growing need for sustainable building materials. Bio-based materials, such as hempcrete, show significant potential in being renewable materials with low or negative embodied energy and good thermal properties [1–5]. They also exhibit significantly higher moisture dynamics in comparison to conventional building materials [6]. This demonstrates their potential for application in passive design strategies through their moisture buffering capabilities [7]. However, the appropriate application of hempcrete requires a thorough understanding of the hygrothermal processes that occur in such highly porous media.

Moisture transport is governed by mechanisms such as convection, diffusion, capillary suction and moisture storage and may occur in both vapor and liquid form [8]. Diffusion is of particular importance in bio-based materials, due to often-high porosity and therefore large air-filled pore spaces. Current predictions of hygroscopic behavior require the specifics of a material's moisture storage capabilities (sorption isotherms) and diffusion (water vapor permeability) [9]. At present, diffusion is obtained by measuring water vapor permeability through the time-costly Wet Cup/Dry Cup method [10], which can be translated into moisture diffusivity by Fick's

law [4,11]. However, while denoted as diffusivity, cup method also includes additional moisture mechanisms such as sorption, capillary condensation, surface diffusion and liquid transfer. In this study, a novel measurement method is used to determine water vapor diffusivity in porous hempcrete materials. The method measures the relative gas diffusivity by applying a non-reactive tracer gas, which is consequently related to water vapor diffusivity. It is commonly applied in soil physics research field [12–14] but is a new approach to evaluating moisture transport within building materials. This experimental method allows for water vapor diffusion in the air-filled pore space to be observed, neglecting evaporation and condensation at the water-air interfaces and liquid transfer in the water-filled pore spaces [11]. An in-depth comparison with Collet's molded hempcrete (MHC) [4] is provided to evaluate the impact of different experimental methods in determining water vapor diffusivity.

Materials and methods

The Oxygen Diffusion Apparatus 2020 (ODA 20), shown in Figure 1 **Error! Reference source not found.**(a), measures gas diffusivity by using oxygen as a tracer gas. Oxygen is used due to its non-reactive properties (physically, chemically and biologically) [14]. These properties ensure that specific diffusion is measured in the air-filled pore spaces of the material, and that additional moisture mechanisms are absent.

The apparatus consists of an air-tight chamber, which contains an oxygen sensor (FIGARO KE-25). The chamber is initially flushed with N_2 to remove any present oxygen. The sample is sealed onto the open-ended side of the chamber using an air-tight rubber O-ring. Oxygen then diffuses through the sample into the chamber, where oxygen levels are consistently measured at an interval of 1 second.

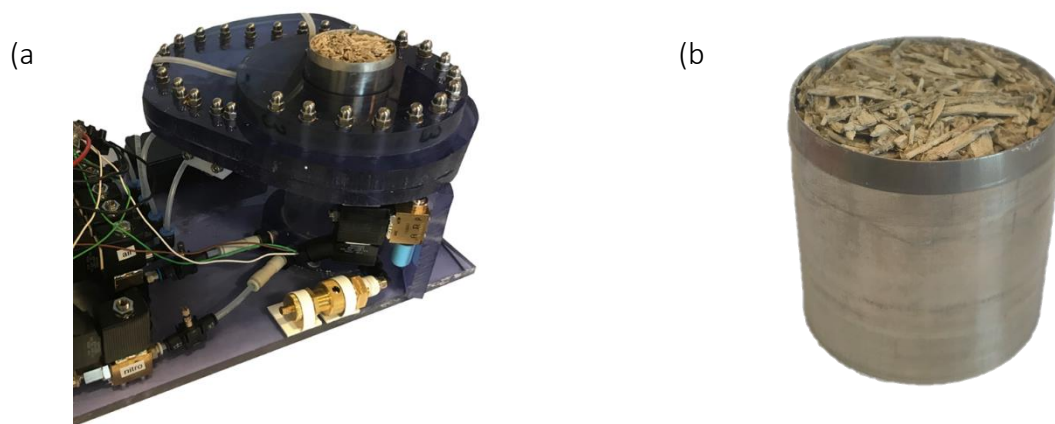


Figure 1 (a) The Oxygen Diffusion Apparatus 2020 (ODA 20) with an inserted hempcrete sample. (b) A hempcrete sample molded in a metal cylinder.

The measurement is complete once the chamber has reached oxygen levels of 20.9% (ambient air). One measurement takes approximately 1-3 hours, depending on the porosity of the material. This is a clear improvement compared to the time-costly Wet Cup/Dry Cup Method [10]. The rate of diffusion is used to calculate the oxygen diffusion coefficient D_p [$m^2 s^{-1}$]. This is then translated into the relative gas diffusivity (D_p/D_o), to enable water vapor diffusion to be calculated. D_o is the gaseous diffusion coefficient, derived from literature, of a gas system, e.g. O_2 or H_2O in air, which are shown in Table 1. By utilizing this relation, the oxygen diffusion coefficient $D_{p,O}$ may be translated into gas diffusion coefficient for water vapor $D_{p,WV}$ through the sample. Water vapor diffusivity is commonly calculated by water vapor permeability measurements using Equation (1) [4].

Table 1 Gas diffusion coefficients for oxygen and water vapor in air.

Gas system	Diffusion coefficient D_o [$\text{cm}^2 \text{s}^{-1}$]	Reference
O ₂ in air	0.205	[14]
H ₂ O in air	0.248	[15]

In this study, the inverse equation is used to calculate the water vapor permeabilities based on experimentally derived water vapor diffusivities.

$$D_{p,WV} = \frac{\delta_p \cdot P_s}{\rho_0 \cdot \xi} \quad (1)$$

Where δ_p is the water vapor permeability [$\text{kg m}^{-1} \text{s}^{-1} \text{Pa}^{-1}$], P_s is the saturated vapor pressure [Pa], ρ_0 is the dry density [kg m^{-3}] and ξ is the sorption capacity [-].

Two hempcrete materials were investigated in this study: Low-Hemp mix (LH-mix) and High-Hemp mix (HH-mix). The hempcrete materials differ in their compositions by the hemp-shive to lime binder ratios with respective dry densities of 312 kg m^{-3} and 156 kg m^{-3} . Additional material properties may be examined in [1]. The samples were molded directly into sample rings of height 51 mm and diameter 53 mm (volume 100 cm^3); a sample is shown in Figure 1(b). Each sample was measured once at four different relative humidities: oven-dry, 44% RH, 60% RH and 80% RH. Equilibrium moisture content was reached at each RH in chambers with saturated salt solutions.

Results and discussion

The derived gas diffusion coefficients D_p for hempcrete depict a negative linear relation with moisture content, as observed in Figure 2 **Error! Reference source not found.**. As moisture content increases, the presence of adsorbed water molecules (initial monolayer and subsequent multilayers) narrows the air-filled pore space and limits the passage for diffusion. Three clusters of measured data points maybe be observed for both HH-mix and LH-mix respectively, despite measurements conducted at four different RH levels. This depicts the impact of sorption in hempcrete, where there is little distinction in the moisture content between 44% and 60% RH. The linearity of the diffusion coefficients differs from de Vries' non-linear depiction of water vapor diffusivity vs moisture content, which includes effects from effusion, sorption and liquid transfer [16]. These effects are not present due to the application of the non-reactive tracer gas.

The relative gas diffusivity is higher for the more porous HH-mix than LH-mix. However, both material mixes exhibit significant diffusive properties, which correlates to the highly porous structure of hempcrete. Oxygen diffusivity in the hempcrete materials range from 3.1×10^{-6} to $5.0 \times 10^{-6} \text{ m}^2 \text{ s}^{-1}$. In comparison, the oxygen diffusivity of less porous concrete has been found to range from 5.0×10^{-8} to $3.9 \times 10^{-7} \text{ m}^2 \text{ s}^{-1}$ [17]. The total porosity of hempcrete is commonly around 72-80% [4], whereas concrete has a total porosity of 9 – 20% [17].

A significant observation is made in the magnitude of water vapor diffusivities. For clarification, results derived from the novel method are denoted as gas diffusivity (of water vapor), and the effective diffusivity derived from water vapor permeability measurements for MHC in [4] are denoted as water vapor diffusivity. Gas diffusivities range from 3.7×10^{-6} to $5.9 \times 10^{-6} \text{ m}^2 \text{ s}^{-1}$. However, water vapor diffusivities of MHC range from 1.3×10^{-9} to $7.3 \times 10^{-9} \text{ m}^2 \text{ s}^{-1}$ [4].

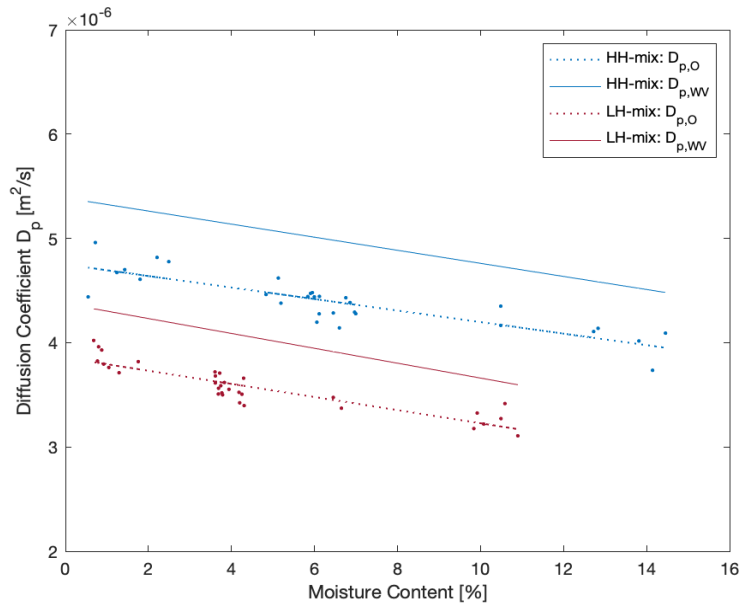


Figure 2 Respective oxygen and water vapor diffusion coefficients $D_{p,O/WV}$ of two different hempcrete material mixes as a function of moisture content

The large magnitude difference implies that the effective diffusion is significantly reduced due to effects such as sorption, surface diffusion, effusion and capillary condensation, as mentioned in [4,11]. Based on this, the gas diffusivity may be expressed as the independent diffusivity, whereas the water vapor diffusivity obtained from the cup method is the effective diffusion. This introduces the retardation factor R , which is an expression for the effect of the additional processes that are present during water vapor diffusion [18]. By calculating water vapor permeabilities from derived gas diffusivities, R has been determined as the relation between $\delta_{p, gas}$ and $\delta_{p, Collet}$, observed in Table 2 to calculate the effective permeabilities $\delta_{p, effective}$. Resultant permeabilities are visualized in companion paper (no. 1138).

Table 2 Water vapor permeabilities calculated from gas diffusivity ($\delta_{p, gas}$), Collet's MHC ($\delta_{p, Collet}$) and normalized by R ($\delta_{p, effective}$). R is the retardation factor calculated by the relation between $\delta_{p, gas}$ and $\delta_{p, Collet}$.

$\delta_{p, gas}$		$\delta_{p, Collet}$ [4]			R	$\delta_{p, effective}$		
RH	HH	LH	RH	MHC		RH	HH	LH
0%	5.2E-9	5.6E-9	23%	2.9E-11	360	0%	1.4E-11	1.6E-11
44%	1.9E-8	1.9E-8	50%	4.6E-11		44%	5.1E-11	5.4E-11
60%	2.0E-8	2.2E-8	70%	5.6E-11		60%	5.7E-11	6.0E-11
80%	3.7E-8	4.6E-8	84%	6.3E-11		80%	1.0E-10	1.3E-10

Conclusion

This paper introduces a novel measurement method for the determination of water vapor diffusivity in porous building materials. The method neglects effects such as sorption, capillary condensation and surface diffusivity, providing the independent diffusivity in comparison to the effective diffusivity derived by the conventional Wet Cup/Dry Cup method. Additional benefits include improved time-efficiency. A large retardation factor is needed to account for the additional processes that occur during water vapor diffusion. This underlines the need for further studies to thoroughly understand the moisture mechanics that occur on a microscopic

scale. Results also show that increased hemp-shive to binder ratios increases diffusivity. Diffusion decreases as moisture content increases, due to the narrowing of air-filled pore spaces. As expected, hempcrete shows highly diffusive properties in comparison to conventional concrete. The derived permeabilities are subsequently used in our companion paper (no. 1138) for improved accuracy of building simulations.

Acknowledgment

This study is funded by the grant no. 8022-00032B “Non-Equilibrium of Water Vapor Sorption in Building Materials [NOWA]” from the Independent Research Fund Denmark.

References

- [1] Y.I. Antonov, R.L. Jensen, P. Møldrup, M. Pomianowski, Comparison of salt solution and air drying methods for moisture fixation in highly porous building materials, in: *Energy Procedia*, 2017. doi:10.1016/j.egypro.2017.09.753.
- [2] T. Colinart, P. Glouannec, M. Bendouma, P. Chauvelon, Temperature dependence of sorption isotherm of hygroscopic building materials. Part 2: Influence on hygrothermal behavior of hemp concrete, *Energy and Buildings*. 152 (2017) 42–51. doi:10.1016/j.enbuild.2017.07.016.
- [3] F. Collet, S. Pretot, Experimental highlight of hygrothermal phenomena in hemp concrete wall, *Building and Environment*. 82 (2014) 459–466. doi:10.1016/j.buildenv.2014.09.018.
- [4] F. Collet, J. Chamoin, S. Pretot, C. Lanos, Comparison of the hygric behaviour of three hemp concretes, *Energy and Buildings*. (2013). doi:10.1016/j.enbuild.2013.03.010.
- [5] Y.I. Antonov, R.L. Jensen, P. Møldrup, Hemp-Lime Performance in Danish Climatic Context. Thermal Conductivity as a Function of Moisture Content, in: *CLIMA 2016 - Proceedings of the 12th REHVA World Congress*, 2016.
- [6] S. Amziane, F. Collet, S. Report, R.T. Committee, Bio-aggregates Based Building Materials, 2017. doi:10.1007/978-94-024-1031-0.
- [7] E. Latif, M. Lawrence, A. Shea, P. Walker, Moisture buffer potential of experimental wall assemblies incorporating formulated hemp-lime, *Building and Environment*. (2015). doi:10.1016/j.buildenv.2015.07.011.
- [8] C. Rode, Combined heat and moisture transfer in building constructions, Kgs. Lyngby, Denmark, 1990.
- [9] C. Rode, K. Grau, Whole building hygrothermal simulation model, in: *American Society of Heating, Refrigeration and Air-Conditioning Engineers, Recent Advances in Energy Simulation: Building Loads, Symposium CH-03-09, Chicago, United States*, 2010.
- [10] DS/EN ISO 12572, Hygrothermal performance of building materials and products – Determination of water vapour transmission properties – Cup method, *Dansk Standard*. (2016).
- [11] D.A. De Vries, Simultaneous transfer of heat and moisture in porous media, *Transactions, American Geophysical Union*. 39 (1958) 909–916. doi:10.1029/TR039i005p00909.
- [12] A.C. Resurreccion, T. Komatsu, K. Kawamoto, M. Oda, S. Yoshikawa, P. Moldrup, Linear model to predict soil-gas diffusivity from two soil-water retention points in unsaturated volcanic ash soils, *Soils and Foundations*. (2008). doi:10.3208/sandf.48.397.
- [13] S. Zhihui, W. Bing, G. Yuanshi, Determination of gas diffusion coefficients in soils with different porosities, *Transactions of the Chinese Society of Agricultural Engineering*. 31 (2015) 108–113. doi:10.11975/j.issn.1002-6819.2015.15.015.
- [14] P. Schjøning, M. Eden, P. Moldrup, L.W. De Jonge, Two-chamber, two-gas and one-chamber, one-gas methods for measuring the soil-gas diffusion coefficient: Validation and inter-calibration, *Soil Science Society of America Journal*. 77 (2013) 729–740. doi:10.2136/sssaj2012.0379.
- [15] W.E. Forsythe, *Smithsonian physical tables*, 9th ed., Smithsonian Institution, Washington, 1959.
- [16] C. Feng, H. Janssen, Y. Feng, Q. Meng, Hygric properties of porous building materials: Analysis of measurement repeatability and reproducibility, *Building and Environment*. (2015). doi:10.1016/j.buildenv.2014.11.036.
- [17] I.S. Yoon, Comprehensive Approach to Calculate Oxygen Diffusivity of Cementitious Materials Considering Carbonation, *International Journal of Concrete Structures and Materials*. (2018). doi:10.1186/s40069-018-0242-y.
- [18] J.H. Dane, G.C. Topp, *Methods of Soil Analysis. Part 4 - Physical Method*. Soil Science Society of America Book Series No. 5, Soil Science Society of America, WI, USA, 2002.



The abstracts and posters appearing in this book comprise the proceedings of the RM4L2020 International Conference, held between the 20th and 22nd of September 2021. The posters presented reflect the authors' opinions and are published as presented and without change (formatting and minor editing expected). Their inclusion in this publication does not necessarily constitute endorsement by the editors, RM4L, or Cardiff University.

ISSBN 978-1-3999-0832-0

Published by Cardiff University

For information

Cardiff University, Queen's Building, The Parade, CF24 3AA.

Email: MaddalenaR@cardiff.ac.uk

Please use the following format to cite material from these proceedings:

Author, AB, Author, XY, and Author, DE (2021), Title of paper, **Proceedings Resilient Materials 4 Life 2020 (RM4L2020)**, Maddalena R, Wright-Syed M, (RM4L Eds), pp. a–b, Cardiff, UK, 20-22 Sep 2021, ISBN 978-1-3999-0832-0

Copyright © 2021 RM4L and Cardiff University.

Copying of material in these Proceedings for internal or personal use, or for the internal or personal use of specific clients is permitted without charge by RM4L and Cardiff University. Other copying for republication, resale, advertising, or promotion, or any form of systematic or multiple reproduction of any material from these Proceedings is prohibited except with permission in writing from Cardiff University.

The RM4L2020 is organised by the UKRI-EPSRC funded Programme Grant Resilient Materials 4 Life (RM4L) and supported by



American Concrete Institute
Always advancing



The Institute of
Concrete Technology



The Institution of
StructuralEngineers



applied sciences

an Open Access Journal by MDPI